Sound propagation over mixed impedances

Thesis

SOUND PROPAGATION OVER MIXED IMPEDANCES

Thesis submitted by

N.W. Heap B.Sc.

for the degree of

Doctor of Philosophy

VOL. 1.

Faculty of Technology

The Open University

Milton Keynes

England

Date of submission: 1·10·82

Date of award: 8·11·82

September 1982

ProQuest LLC
789 East Eisenhower Parkway
P.O. Box 1346
Ann Arbor, MI 48106 - 1346

Abstract

Outdoor propagation of surface transportation noise is strongly influenced by reflections from the ground surface due to the creation of an intereference pattern. The result is an attenuation with distance over and above that expected from simple spherical divergence and atmospheric absorption.

A review of literature shows that ground effects can be characterised by a spherical wave reflection coefficient and a normal surface impedance. Theoretical solutions of point to point propagation over three different ground surface models (local reaction, extended reaction and a rigid backed layer) are described and the first two are shown to give good estimates of the excess attenuation as a function of distance.

Methods for measuring the normal surface impedance are discussed and experimental measurements reported. It is concluded that an indirect method employing the local reaction theoretical solution gives reasonable estimates over the frequency range 1-70 kHz.

For practical applications the homogeneous ground surface is modified to include the effects of impedance discontinuities. The theoretical solutions are compared with the results obtained from experiments on laboratory models built to a notional scale of 1:100. In the case of the source over a rigid surface and receiver over an acoustically soft ground surface, it is shown that (a) for a low noise source (e.g. cars) the impedance discontinuity has negligible effect and (b) that for elevated sources (e.g. lorries) the excess attenuation is increased relative to that of a homogeneous surface.

The double discontinuity introduced by a rigid strip in an acoustically soft ground surface is also examined. Experimental results indicate the effect of the strip is insignificant for strip widths less than 10% of the source receiver separation distance. For wider strips it is found that prediction can be improved by postulating an increased average surface impedance.

Declaration

I declare that no part of the material contained in this thesis has previously been submitted for a degree or other qualification to the Open University or any other institution.

Acknowledgements

The author wishes to record his sincere graditude to his supervisor Dr. K.A. Attenborough, Senior Lecturer in Engineering Mechanics, for his encouragement and patience throughout the nine long years of this work.

I am also indebted to my academic colleagues in the Electronics Design and Communications Discipline for their support and understanding, to the Technical Staff for their assistance with the construction of some of the experimental apparatus and to the Secretaries for preparing this lengthy and complicated manuscript.

The first three years of this work was supported by a grant from the Science Research Council.

CONTENTS

Figure Captions Chapter 2

Figure 2.1 Right handed Cartesian coordinate system.

Figure 2.2 Geometry of plane wave propagation over a plane surface.

Figure 2.3 Predicted excess attenuation for plane wave propagation over a rigid surface. Source and receiver heights 1 m, separation distance 20 m.

Figure 2.4 Predicted excess attenuation for plane wave propagation over a resilient surface. Source and Receiver heights 1 m, separation distance 20 m.

Figure 2.5 Geometry for plane wave propagation over an interface between two semi-infinite media.

Figure 2.6 Predicted excess attenuation for plane wave propagation over an extended reaction boundary. Source and receiver heights 1 m, separation distance 20 m.

Figure 2.7 Predicted excess attenuation for plane wave propagation over a locally reacting boundary. Source and receiver heights 1 m, separation distance 20 m.

Figure 2.8 Geometry for plane wave propagation over a layered boundary.

Figure 2.9 Predicted excess attenuation for plane wave propagation over a rigid backed layer. Source and receiver heights 1 m, separation distance 20 m, layer depth 0.05 m.

Figure 2.10 Geometry for propagation over two semi-infinite half surfaces.

Figure Caption Chapter 3

Figure 3.1 Geometry for point to point propagation over an interface between two semi-infinite media.

Figure Captions Chapter 4

Figure 4.1 Geometry for Rasmussen's iteraterative procedure for a half rigid half soft boundary.

Figure 4.2 Reciprocity calculation for half rigid half soft boundary Source height 1 m, receiver height 0.1 m, separation distance 10 m.

Figure 4.3 Reciprocity calculation for half rigid half soft boundary Source height 1 m, receiver height 0.1 m, separation distance 60 m.

Figure 4.4 Thin barrier geometry for DeJong's empirical propagation Model.

Figure 4.5 Surface integral geometry for Simpson and Hothersall's discontinuous boundary model.

Figure 4.6 Geometry for rigid strip boundary model.

Figure Captions Chapter 5

Figure 5.1 Circuit diagram of an impedance bridge.

Figure 5.2 Block diagram of two port network.

Figure 5.3 Graph for determining SWR at the surface from the SWR measured at the first two minima (after Kilmer).

Figure 5.4 Magnitude of the total sound pressure in an impedance tube as a function of distance (after Ando).

Figure 5.5 Extrapolation of the reflection coefficient at x = 0 (after Ando).

Figure 5.6 Geometry for free-field impedance measurement (after Sides and Mulholland).

Figure 5.7 Geometry for transfer function impedance measurement (after Chung and Blazer).

Figure Captions Chapter 7

Figure 7.1 Free-field corrections for microphones 4135 and 4136 with protecting grid.

Figure 7.2 Free-field corrections for type 4135 without protecting grid.

Figure 7.3 Free-field corrections for type 4138 with protecting grid.

Figure 7.4 Free-field corrections for type 4138 without protecting grid.

Figure 7.5 Air Jet Model Noise Source (after Delany et al).

Figure 7.6 1/3rd Octave free-field spectrum of Air Jet Noise Source.

Figure Captions Chapter 8

Figure 8.1 Bruel and Kjaer Standing Wave Apparatus Type 4002.

Figure 8.2 Block diagram of the instrumentation used for the Impedance Tube measurements.

Figure 8.3 Block Diagram of the instrumentation used for the Free-Field impedance measurements.

Figure 8.4 Free-field trace of Sound Pressure above the rigid backing at 12.5 kHz.

Figure 8.5 Free-Field trace of Sound Pressure above the Artificial Grass at 1.6 kHz.

Figure 8.6 Effect of normal surface impedance value upon the location of the interference minima.

Figure 8.7 Block diagram of the instrumentation used for the experimental determination of excess attenuation.

Figure 8.8 Comparison of predicted and measured excess attenuation for propagation over the artificial grass surface. Source height 5 cm, receiver height 5 cm, separation distance 100 cm.

Figure 8.9 Comparison of predicted and measured excess attenuation for propagation over the fibreboard surface. Source height 5 cm, receiver height 5 cm, separation distance 100 cm.

Figure 8.10 Comparison of predicted and measured excess attenuation for propagation over the fibreboard surface. Source height 9 cm, receiver height 10 cm, separation distance 100 cm.

Figure 8.11 Block diagram of the instrumentation used for the direct and reflected pulse measurements.

Figure 8.12 Measured direct and reflected pulses. Source height 15 cm, receiver height 60.3 cm, separation distance 52.7 cm.

Figure 8.13 Direct and Reflected pulses and their corresponding spectra.

Figure 8.14 Calculated reflection coefficient for the rigid surface. Source height 15 cm, receiver height 60.3 cm, separation distance 52.7 cm.

Figure 8.15 Calculated reflection coefficient for the rigid surface. Source height 15 cm, receiver height 15 cm, separation distance 100 cm.

Figure 8.16 Calculated reflection coefficient for the artificial grass surface. Source height 15 cm, receiver height 62 cm, separation distance 49.5 cm.

Figure 8.17 Calculated reflection coefficient for the fibreboard surface. Source height 15 cm, receiver height 70.3 cm, separation distance 49.2 cm.

Figure 8.18 Measured direct and reflected pulses and corresponding Power Cepstrum for the rigid surface. Source height 15 cm, receiver height 60.3 cm, separation distance 52.7 cm.

Figure 8.19 Impulse response for the rigid surface, extracted from the Power Cepstrum of Figure 8.18 (b).

Figure 8.20 Power Cepstrum before and after subtraction of the direct pulse contribution.

Figure 8.21 Long duration impulse response and corresponding reflection coefficient for a rigid surface.

Figure 8.22 Short duration impulse response and corresponding reflection coefficient for a rigid surface.

Figure 8.23 Extracted impulse response and corresponding minimum phase impulse response for a rigid surface.

Figure 8.24 Reflection coefficients calculated from the extracted impulse response and the minimum phase impulse response for a rigid surface.

Figure 8.25 Extracted impulse response and calculated reflection coefficient for the artificial grass surface. Source height 15 cm, receiver height 15 cm, separation distance 100 cm.

Figure Captions Chapter 9

Figure 9.1 Block diagram of the instrumentation used for the point to point propagation measurements.

Figure 9.2 Comparison of measured and predicted excess attenuation for propagation over a rigid surface. Source height 5 cm, receiver height 5 cm, separation distance 100 cm.

Figure 9.3 Effect of source height upon the location of the interference minima.

Figure 9.4 Comparison of measured and predicted excess attenuation for a rigid surface versus source height.

Figure 9.5 Comparison of excess attenuation over a rigid surface predicted by (a) coherent source theory (b) fluctuating spherical wave theory. Solid circles are measured values. Source and receiver heights 1.2 m, separation distance 15 m (after Daigle).

Figure 9.6 Predicted excess attenuation for propagation over a rigid surface when the source is modelled as a linear array of point sources.

Figure 9.7 Comparison of measured and predicted excess attenuation after correcting the predicted values for source height, source bandwidth and finite size.

Figure Captions Appendix A

Figure A.1 Floor plan of Anechoic Chamber

Figure A.2 Block Diagram of Anechoic Calibration Experiments Instrumentation.

Figure A.3 Spherical Divergence Measurements.
Pure Tones ½" Microphone and Protection Grid.

Figure A.4 Spherical Divergence Measurements.
Random Noise, ½" Microphone and Protection Grid.

Figure A.5 Spherical Divergence Measurements.
Aire Jet Source, ¼" Microphone and Protection Grid.

Figure A.6 Spherical Divergence Measurements.
Air Jet Source ¼" Microphone without Protection Grid.

Figure A.7 Spherical Divergence Measurements.
Air Jet Source ¼" Microphone and Nose cone.

Figure A.8 Spherical Divergence Measurements.
Air Jet Source 1/8" Microphone and Nose cone.

Figure Captions Appendix B

Figure B.1 Block diagram of basic spark discharge circuit.

Figure B.2 Storage Capacitor Voltage versus time.

Figure B.3 Series triggered spark discharge circuit.

Figure B.4 Parallel triggered spark discharge circuit.

Figure B.5 Spark discharge circuit with thyristor switch.

Figure B.6 Block diagram of spark source calibration instrumentation.

Figure B.7 Measured spark discharge.

Figure B.8 Measured Spectra of spark discharge.

Figure B.9 Spark discharge pulse duration versus trigger pulse duration.

Figure B.10 Spark source spectrum versus trigger pulse duration.

Figure B.11 Deviation from Inverse Square Law for Spark Source.

Figure captions for Appendix D

Figure D.1 Predicted excess attenuation above a rigid surface for octave bands of noise (after Sutherland).

Chapter 1

1.1 Introduction

Growing concern at the increase in community noise levels has led to the concept of noise pollution, and caused many national and state regulatory authorities to enact measures to reduce the rate of increase.

Particular attention has been paid to road traffic, identified as the major contributor to community noise levels [1.1], but other noise sources include: high speed trains, construction sites and consumer appliances such as lawnmowers.

Governmental legislation has been introduced to control the maximum permissible noise level of new vehicles [1.2] and to empower local authorities to establish noise abatement zones and a Noise Level Register [1.3]. Furthermore, local authorities have also been encouraged to set maximum permissible boundary noise levels for new industrial planning applications.

All these measures have been aimed at reducing the noise level at the source, but in many cases the scale of the reduction is dictated by economic and practical considerations [1.4].

Community noise levels are unlikely to fall as a consequence of controls on the maximum noise emitted by new vehicles, because of the very large number of older noisier vehicles. In Canada, certain States of the United States of America and Australia, regulations

have been introduced to limit the noise level of vehicles in use. The vehicle is subject to an annual inspection and will fail if the emitted noise level exceeds a predefined maximum [1.5, 1.6, 1.7]. The permissible noise levels are set by defining the percentage of vehicles likely to fail the test. As yet no similar annual test is enforced in the United Kingdom.

Along with control at source, the Government of the United Kingdom has introduced legislation that enables households to obtain compensation for exposure to noise from new road improvement schemes [1.8]. Furthermore, through the Noise Insulation Regulations 1973, revised 1975 [1.9], the Land Compensation Act 1972, requires Local Authorities to carry out, or make grants towards the cost of work of insulating certain houses. Insulation is mandatory in the case of new or improved roads opened after the 16th October 1972, when the properties are, or will be within 15 years, subject to an increase in road traffic noise of at least 1 dBA and to a total level of 68 dBA on the L_{10} (18 hour) index*, measured at a point 1 metre in front of the most exposed window.

In the case of the new roads, rather than improvement schemes, the noise level at the building facade may have to be predicted according to the method outlined in the regulations.

---

*L_{10} is the sound level in dBA which is exceed for 1 tenth of a period of one hour between 0600 and 2400 hours on a normal working day. L_{10} (18 hour) is the arithmetic average of all the levels of L_{10} during a period from 0600 to 2400 hours on a normal working day.

The measurement of noise emission from vehicles and the prediction of building facade noise levels require an understanding of the propagation of sound through the air, and in particular the influence of the ground surface.

Standard measurement and prediction methods have been published [1.9, 1.10, 1.11], but due to the lengthy consultation process required prior to publication, such documents rarely reflect the state of the art. A recent review of Noise Control legislation in Australia [1.7] indicates both the unfairness and the inadequacy of current vehicle noise measurement procedures. Similar comments apply equally to traffic noise prediction schemes.

1.2 Purpose of this Thesis

The prime objective of this thesis is to review and evaluated recent developments in the theoretical solutions for the prediction of sound waves propagating over flat absorbing surfaces in a calm and stable atmosphere.

Of particular interest is the problem of mixed boundary conditions, whereby part of the surface is absorbing and part is rigid. A potential solution for the case of a narrow rigid strip in an otherwise absorbing surface has been developed and forms one of the original contributions of this study.

The work has direct relevance to the community noise problem outlined above, but is equally applicable to the problems of aircraft noise prediction, auditoria design and noise reduction in ventilation duct work.

Wind and temperature gradients and near surface turbulence have a significant influence upon outdoor sound propagation, and as yet there are no methods for making quantitative corrections for their effects. In view of this it was decided to use laboratory models to aid in the evaluation process.

These models were not precisely scale versions of outdoor propagation paths, but the source receiver geometries were selected on the basis of a notional 1:100 scale of the source and receiver heights and separation distances commonly encountered in road traffic noise problems.

The influence of an absorbing surface can be characterised by its surface impedance ratio, that is the ratio of pressure to particle velocity at the surface. Measurement of the surface impedance is a difficult enough task over the frequency range associated with traffic noise spectra, but the problems are magnified at the much higher frequency range used for acoustical modelling.

A secondary objective has therefore been an examination of the methods of measuring surface impedance over the frequency range 1-100 kHz.

1.3 Broad Outline of the Work Undertaken

At the commencement of this study in 1973 there were no acoustical experimental facilities or equipment at the Open University. As a consequence much time and effort has been expended in developing, designing and obtaining the necessary facilities. Little of this work has been detailed in this thesis because it is not of direct relevance, but a brief outline is given below.

The first digital signal processing system used for the high frequency impedance measurements was designed and built by the author. The system comprised two high speed analogue to digital converters linked to a mini-computer by direct memory access channels. The maximum sampling rate of 256 kHz per channel was the fastest attainable due to the limitations of the computer memory read/write cycle time.

Captured data or calculated spectra could be displayed on an oscilliscope screen. The X and Y display coordinates were obtained from digital to analogue conversion of data store in speciific memory locations via additional high speed direct memory access channels.

This system proved invaluable in establishing the suitability of the measurement procedures, but the limited availability of computer memory (16384 words) restricted the amount of data that could be captured and processed. However, once the general technique was proven it was possible to justify the purchase of a commercial digital signal processing system. The system used for the measurements reported in this thesis incorporated a Nicolet 660 Digital Spectrum Analyser. The arrangement is detailed in Chapter 8.

A computer controlled microphone positioning system has been developed for the anechoic chamber. The first design utilised a variable speed d.c. motor and a taut-wire drive belt. However, the repositioning accuracy was found to be unacceptable for high frequency measurements. The second and present system utilises a large stepping motor and toothed belt drive and is capable of

positioning the microphone to within 0.5 mm over the full 2 m of travel.

Extensive computer software has been written and tested to support the experimental study. Special purpose programs for interfacing measurement equipment, such as the digital signal processor and stepping motor controller, have been written as well as a comprehensive graphical display package. A small local area network has also been developed to enable experimental data to be transferred between the various computer installations used during this study.

1.4 Thesis Layout

In Chapter 2 a brief review wave is given of plane wave theories for predicting propagation over various types of ground surface. Plane wave reflection coefficients are derived for these surfaces and the results used to predict the pressure field at a receiver.

Chapter 3 reviews the theoretical solutions for point to point propagation at grazing angles of incidence and long separation distances for three types of boundary condition. These are semi-infinite medium, local reaction and rigid backed layer.

Solutions for the mixed boundary conditions are reviewed in Chapter 4, and an asymptotic solution for a rigid strip in a finite impedance boundary is developed. The solution assumes a local reaction model for the impedance surface, and is valid for long separation distances.

Chapter 5 reviews methods for measuring the normal surface impedance of porous materials and describes the basic theory and limitations of the methods selected for this study.

The basic concepts and definitions of digital signal processing are introduced in Chapter 6, together with a description of the equipment used for the experimental measurements.

In Chapter 7 the basic rules of acoustic scale modelling are introduced, together with specifications for the transducers used as noise source and receiver. Factors the influence the measurement signal to noise ratio, such as electrical noise and atmospheric absorption, are also discussed.

Chapter 8 details the experimental procedures and techniques for determining the normal surface impedance of the model materials. The values obtained from the selected methods are compared and one set selected for use in the theoretical prediction evaluation.

The experimental measurement of excess attenuation is detailed in Chapter 9. The theoretical predictions are compared to the measured values, and the effects of source height, bandwidth and turbulence discussed. The final section exaimines the impact the theoretical predictions might have upon the prediction of road traffic noise.

In the final chapter the thesis is summarised and suggestions as to further developments made.

References Chapter 1

1.1 Waller, R.A.: The Measurement and Control of the Impact of Noise From New Roads.
J. Inst. Highway Engs. 10-17 October 1972

1.2 Motor Vehicles (Construction and Use) Regulations 1973,
Statutory Instruments 1973 No.24, H.M.S.O. 1973

1.3 The Control of Noise (Measurement and Registers)
Regulations 1976, Statutory Instruments 1976 No.37, H.M.S.O. 1976

1.4 Taylor, R.: Progress in the Reduction of Noise from Road Transport in the United Kingdom.
Paper 780386 SAE Congress, Detroit 1980

1.5 Welbourne, E.R.: Regulation of Motor Vehicle Noise in Canada.
Paper 780385 SAE Congress Detroit 1980

1.6 Close, W.H.: Surface Transportation Noise - The Role of the US Department of Transportation.
Paper 780383 SAE Congress Detroit, 1980

1.7 Snow, R. and Law, R.: Motor Vehicle Noise Control Legislation in Australia.
Paper 780384 SAE Congress Detroit, 1980

1.8 Land Compensation Act, 1973 (1973 Ch. 26)

H.M.S.O. 1973

1.9 The Noise Insulation Regulations 1975.

Statutory Instruments 1975 No. 1763 H.M.S.O. 1975

1.10 Planning and Noise, Department of the Environment. Circular 10/73.

H.M.S.O. 1973

1.11 Delany, M.E., Harland, D.G., Hood, R.A. and Scholes, W.E.: The Prediction of Noise Levels L_{10} due to Road Traffic.

J.S.V. (48) 305-325. 1976

Chapter 2

Plane wave radiation models

2.1 Introduction

Theoretical solutions to the problem of predicting the far field pressure above the ground surface due to a plane wave source are available in most standard acoustic texts [2.1, 2.2, 2.3]. Perhaps it is appropriate then to explain their inclusion in this study.

The main reason is that a plane wave solution provides an asymptotic approximation for the identical point-source problem. This is true for both the mathematical and physical models. In the mathematical case the plane wave solution may be used to check either the long-range limiting behaviour of an exact point source solution, or as is more often the case, the leading terms of an approximate one. Physically the plane wave solutions may be useful at large source/receiver separation distances. The main advantage of such solutions is that they require significantly less time to compute and are less expensive to use in community noise prediction schemes.

The main texts used in the preparation of this chapter were: Kinsler and Frey [2.1], Morse and Ingard [2.2] and Brehkovskikh [2.3].

2.2 Formulation of the problem

The general problem can be stated as finding a solution to the second order partial differential equation

$$(\nabla^2+k^2)\,\Phi(r,t) = f(r,t) \qquad 2.1$$

governing the steady-state sound field from a plane-wave source in a homogenous medium. This is the so called reduced wave equation or Helmholtz equation.

$\Phi(r,t)$ is a scalar velocity potential and $f(r,t)$ is a generalised forcing function that describes the generation of energy by the source.

This general equation is adapted to individual problems by the introduction of appropriate boundary conditions, which specify the behaviour of the field at the boundaries of the medium.

Unless otherwise stated, it will be assumed throughout that the propagation medium is air, with a characteristic impedance of ρc (i.e. product of density and velocity). The wavenumber k will be taken as real for air, and a harmonic time dependance will be assumed.

The total field radiated by a plane-wave source in an unbounded medium is defined by the equation

$$\Phi(r,t) = A.\exp\left[i(k.r-\omega t)\right] \qquad 2.2$$

where:

A = an arbitrary amplitude constant,

r = general position vector in three dimensional space

The velocity potential form of equation 2.2 is used throughout, since this simplifies the mathematics by reducing the solution to a scalar function rather than a vector function. This simplification is justified by postulating that for the problems of interest in this study air may be regarded as a non-viscous medium, and may therefore be treated as an irrotational fluid (i.e. no shear wave).

The field may also be expressed in terms of the pressure or particle velocity by means of the relationships:

$$p = \rho \frac{\partial \Phi}{\partial t} = -i\omega\rho\Phi \qquad 2.3$$

$$u = -\text{grad}\ \Phi = \frac{1\partial\Phi}{\partial x} + \frac{m d\Phi}{\partial y} + \frac{n\partial\Phi}{\partial z} \qquad 2.4$$

where 1, m and n are the unit vectors along the coordinate axes x, y, z.

A right handed Cartesian system of coordinates is used throughout. Along these coordinates the position vector r has components

$$x = r \sin \Theta \cos \phi$$

$$y = r \sin \Theta \sin \phi$$

$$z = r \cos \Theta$$

with the angles Θ and ϕ as defined in Figure 2.1.

2.3 Rigid boundary solution

The appropriate condition for a rigid boundary is that the normal component of the velocity is zero at the surface of reflection. The source and receiver geometry is shown in Figure 2.2.

It is assumed that the wave extends to infinity along the y axis. The boundary condition can be written as

$$-\text{grad } \Phi = 0$$

At the surface this can be further simplified to

$$\frac{-\partial \Phi}{\partial z} = 0 \qquad 2.5$$

An alternative expression can be obtained by utilising equation 2.3, which expresses the boundary condition in terms of the pressure gradient as

$$-\frac{\partial p}{\partial z} = 0 \text{ or } \frac{\partial p}{\partial n} = 0$$

where n is the outward pointing normal vector.

The total field at the receiver will be the sum of the incident wave and the scattered wave. The scattered wave may be analysed as a specularly reflected component, and a diffracted or non specular component.

The boundary condition requires that the total pressure gradient is zero at the surface z=0, that is

$$\frac{\partial (p_i + p_s)}{\partial z}_{z=0} = 0$$

Separating out the time coordinate, Φ_i and Φ_s can be substituted for p_i and p_s, and the boundary condition re-written as

$$\frac{\partial (\Phi_i + \Phi_s)}{\partial z}_{z=0} = 0 \qquad 2.6$$

therefore

$$\frac{\partial \Phi_s}{\partial z} = \frac{-\partial \Phi_i}{\partial z} \qquad 2.7$$

The incident and scattered velocity potentials are

$$\Phi_i = A \exp\left[ik(x\sin\Theta_i - z\cos\Theta_i)\right] \quad (-i\omega\rho) \qquad 2.8$$

$$\Phi_s = B \exp\left[ik(x\sin\Phi_i - z\cos\Theta_i)\right] \quad (-i\omega\rho) \qquad 2.9$$

In view of the fact that there are two unknowns and only one boundary condition, a solution is obtained by postulating that the scattered wave can be expressed in terms of the incident wave. The scattered wave can be written as

$$\Phi_s = A.Rp \exp\left[ik(x\sin\Theta_r + z\cos\Theta_r)\right] \qquad 2.10$$

Substituting equations 2.8 and 2.10 into equation 2,7 gives

$$-k\cos\Theta_i A. \exp(ikx\sin\Theta_i) = -k\cos\Theta_r A.Rp \exp(ikx\sin\Theta_r) \qquad 2.11$$

A solution independant of x can only result if

$$k \sin \Theta_i = k \sin \Theta_r \qquad 2.12$$

This is the acoustic equivalent of Snell's Law, stating that the angle of reflection equals the angle of incidence.

Collecting like terms and simplifying equation 2,11, an expression for the reflection coefficient is obtained as

$$R_P = 1$$

The total pressure at the receiver can be obtained by summing the direct and reflected (scattered) waves. A convenient method of presenting this information graphically is to normalise the received pressure field by plotting the ratio of total field to direct field. The result is termed the excess attenuation.

Figure 2.3 shows the excess attenuation as a function of frequency for the rigid boundary condition. The source and receiver heights are 1 m and the separation distance is 20 m. It can be seen that at low frequencies the total field is double that due to a plane-wave source in an unbounded space. A null in the field occurs at those frequencies for which the product of wavenumber, k, times the path length difference, δ, is equal to even multiples of π, that is $k\delta = n\pi$ $n = 2,4,6...$

2.4 Resilient boundary solution

The boundary condition for a resilient surface is that the total pressure at the surface be zero, that is

$$p_i + p_s = 0 \qquad 2.13$$

As before this may be written in terms of velocity potentials as

$$\Phi_s = -\Phi_i \qquad 2.14$$

Substituting equations 2.8 and 2.10 into this expression, and following the same line or argument, it can be shown that

$$R_p = -1$$

For a resilient boundary therefore, the reflected wave is of equal amplitude to the incident wave, but is 180 degrees out of phase.

The excess attenuation for a resilient boundary is shown in Figure 2.4. The source and receiver geometry is identical to that of the rigid boundary example.

At low frequencies the field is almost zero due to the destructive interference between the direct and reflected wave. The nulls occur at those frequencies for which $k\delta = n\pi$ $n = 0,1,3,5....$

2.5 Two media solution

A more general boundary condition exists for the interface between two semi-infinite isotropic media. For convenience the interface is located along the plane z=0 as shown in Figure 2.5.

The boundary equations can be written down using the principles of continuity of pressure and continuity of particle velocity. Expressing these in terms of the velocity potentials gives

$$i\omega\rho_1 \Phi_i + i\omega\rho_1 \Phi_r = i\omega\rho_2 \Phi_t \quad \text{continuity of pressure} \qquad 2.15$$

$$\frac{\partial\Phi_i}{\partial z} + \frac{\partial\Phi_r}{\partial z} = \frac{\partial\Phi_t}{\partial z} \quad \text{continuity of velocity} \qquad 2.16$$

Since there are three unknowns and only two equations, a solution can only be obtained by postulating that the reflected and transmitted waves can be expressed in terms of the incident wave.

These three waves are

$$\Phi_i = A \exp\left[ik_1(x\sin\Theta_i - z\cos\Theta_i)\right] \qquad 2.17$$

$$\Phi_r = A \exp\left[ik_1(x\sin\Theta_r + z\cos\Theta_r)\right] \quad .Rp \qquad 2.18$$

$$\Phi_t = A \exp\left[ik_2(x\sin\Theta_t - z\cos\Theta_t)\right] \quad .Tp \qquad 2.19$$

where Rp is the plane wave reflection coefficient and Tp is the plane wave transmission coefficient. Substituting these expressions into equation 2.15 and 2.16, for the plane z=0, gives

$$i\omega\rho_1 A \exp(ik_1 x\sin\Theta_i) + i\omega\rho_1 A.Rp \exp(ik_1 x\sin\Theta_r) = i\omega\rho_2 A.Tp \exp(ik_2 x\sin\Theta_t) \qquad 2.20$$

and

$$-ik_1\cos\Theta_i A \exp(ik_1 x\sin\Theta_i) + ik_1\cos\Theta_r A.Rp \exp(ik_1 x\sin\Theta_r) = ik_2\cos\Theta_t A.Tp \exp(ik_2 x\sin\Theta_t) \qquad 2.21$$

Since the solution must be independent of x, then

$$k_1 \sin\Theta_i = k_1 \sin\Theta_r = k_2 \sin\Theta_t \qquad 2.22$$

Utilizing equation 2.22 enables equations 2.20 and 2.21 to be rewritten in the form

$$-\rho_1 A(1+Rp) = -\rho_2 A.Tp \qquad 2.23$$

and

$$-ik_1\cos\Theta_i A.(1-Rp) = ik_2\cos\Theta_t A.Tp \qquad 2.24$$

Adding equations 2.23 and 2.24 enables one to eliminate Rp and so derive the following expressions for the transmission coefficient,

$$Tp = \frac{2\cos\Theta_i}{\rho_2 c_2 \cos\Theta_i + \rho_1 c_1 \cos\Theta_t} \qquad 2.25$$

The reflection coefficient is obtained by substituting equation 2.25 into 2.23. This gives an expression of the form

$$Rp = \frac{\rho_2 c_2 \cos\Theta_i - \rho_1 c_1 \cos\Theta_t}{\rho_2 c_2 \cos\Theta_i + \rho_1 c_1 \cos\Theta_t} \qquad 2.26$$

Normally the reflection coefficient is written in terms of the specific or relative acoustic impedance as

$$Rp = \frac{Z\cos\Theta_i - \cos\Theta_t}{Z\cos\Theta_i + \cos\Theta_t} \qquad 2.27$$

where

$$Z = \rho_2 c_2 / \rho_1 c_1$$

Equation 2.26 shows that the density and sound velocity of the lower medium must be known before the total pressure field at the receiver can be calculated. These parameters can be measured or estimated using the techniques described in Chapter 5.

$\cos \theta_t$ is termed the angle of refraction, and is related to the angle of incidence by Snell's Law. Rearranging equation 2.22 $\cos \theta_t$ is given by

$$\cos \theta_t = \sqrt{1 - (\frac{k_1}{k_2})^2 . \sin^2 \theta_i}$$

Introducing an index of refraction $n = c_1/c_2 = k_2/k_1$, a more convenient notation is

$$\cos \theta_t = \sqrt{1 - \sin^2 \theta_i / n^2}$$

Hence Rp may be written as

$$Rp = \frac{Z \cos \theta_i - \sqrt{1 - \sin^2 \theta_i / n^2}}{Z \cos \theta_i t \sqrt{1 - \sin^2 \theta_i / n^2}}$$

The ratio of total pressure/direct pressure at a receiver 1m above an interface between air and a semi-infinite porous medium is shown in Figure 2.6. The source height is 1m and the separation distance is 20m. The lower medium is modelled by a surface having a flow resistivity of 10 000 Mks units.

2.6 Local reaction solution

In many cases of practical interest it can be shown that the ratio of pressure to normal particle velocity* is constant along the boundary surface. Physically this means that the motion of any single point on the surface is independent of the motion of any other point on the surface.

Such surfaces are completely characterised by their normal surface impedance Z_s, that is the ratio of pressure and particle velocity measured at normal incidence, and the angle of incidence of the reflected wave.

Expressions for the pressure and particle velocity at a point just above the surface can be obtained from equations 2.3, 2.4, 2.17 and 2.18. The pressure is given by

$$p_1 = i\omega\rho\Phi = i\omega\rho\, A \exp\left[ik(x\sin\theta_i - z\cos\theta_i)\right] + B \exp\left[ik(x\sin\theta_r + z\cos\theta_r)\right]$$

---

*Some authors use the term volume velocity

and the particle velocity by

$$u_1 = \frac{\partial \Phi}{\partial z} = ik\cos\Theta_i \, A \exp\left[ik(x\sin\Theta_i - z\cos\Theta_i)\right] - ik\cos\Theta_r \, B \exp\left[ik(x\sin\Theta_r + \cos\Theta_r)\right]$$

Because the pressure and particle velocity must be continuous across the boundary, the ratio p_1/u_1 must equal the ratio p_2/u_2. But $p_2/u_2 = Z_2$. Therefore

$$p_1/u_1 = Z_2 \qquad 2.28$$

To solve for the coefficients A and B, one must gain postulate a reflection coefficient of the form B = Rp. A.

At the surface z = 0, equation 2.28 may be written

$$\frac{p_1}{u_1} = \frac{i\omega\rho A(1+Rp)e^{ikx\sin\Theta_i}}{ik\cos\Theta_i A(1-Rp)e^{ikx\sin\Theta_i}} = Z_1 \qquad 2.29$$

Simplifying this expression gives a reflection coefficient of the form

$$Rp = \frac{Z_1 - \rho c/\cos\Theta}{Z_1 + \rho c/\cos\Theta} \qquad 2.30$$

Defining a specific normal impedance*

$$Z_s = Z/\rho_1 c_1$$

and a specific normal admittance

$$\beta_s = 1/Z_s$$

the reflection coefficient may also be written as

$$R_p = \frac{Z_s \cos\Theta - 1}{Z_s \cos\Theta + 1} \qquad 2.31$$

$$R_p = \frac{\cos\Theta - \beta_s}{\cos\Theta + \beta_s} \qquad 2.32$$

An alternative method of obtaining this result is to recognise that the local reaction definition implies that any energy transmitted into the lower medium must propagate normal to the surface, otherwise the motion of adjacent points on the surface would not be independent. Substituting $\Theta_t = 0$ in equation 2.26 gives

$$R_p = \frac{\rho_2 c_2 \cos\Theta_i - \rho_1 c_1}{\rho_2 c_2 \cos\Theta_i + \rho_1 c_1}$$

---

*For the interface between two semi-infinite media Z_s = the specific (or relative) characteristic impedance.

Dividing throughout by $\rho_2 c_2$, the characteristic impedance of the lower layer, Rp becomes

$$R_p = \frac{\cos\theta_i - 1/Z_s}{\cos\theta_i + 1/Z_s} = \frac{\cos\theta_i - \beta_s}{\cos\theta_i + \beta_s}$$

Figure 2.7 shows the predicted ratio of total pressure/direct pressure using the local reaction for a surface having a flow resistivity of 10 000 Mks units. The dashed line curve, obtained from the two media solutions, is shown for comparison.

2.7 Layered boundary solution

The final ground surface model that will be examined is that of a layered boundary. This has been shown to have application in predicting the field above forest floors [2.4] and snow [2.5].

The geometry of the incident and reflected waves and the boundary are shown in Figure 2.8.

Consider first the pressure within the layer

$$i\omega\rho\Phi = p_2 = i\omega\rho_2 \left[Ae^{-ik_2 z\cos\theta_t + Be^{ik_2 z\cos\theta_t}}\right] e^{ik_2 x\sin\theta_t} \qquad 2.33$$

$$\frac{-\partial\Phi}{\partial z} = u_2 = \left[ik_2\cos\theta_t Ae^{-ik_2 z\cos\theta_t} - ik_2\cos\theta_t Be^{ik_2 z\cos\theta_t}\right] e^{ik_2 x\sin\theta_t} \qquad 2.34$$

At the bottom of the layer the ratio $p_2/u_2 = Z_3$, which corresponds to the simple impedance boundary, hence using the known solution for this case it can be shown that

$$B/A = \frac{Z_3 - Z_2}{Z_3 + Z_2} \qquad 2.35$$

where $Z_3 = \rho_3 c_3 / \cos\Theta_{t3}$

$Z_2 = \rho_2 c_2 / \cos\Theta_{t2}$

At the top of the layer Z = d the ratio ρ_2/u_2 = Zin the effective input impedance of the layer as viewed from medium 1. Z_{in} is therefore given by:

$$Z_{in} = \frac{i\omega\rho_2}{ik_2\cos\Theta_{t2}} \left[\frac{Ae^{ik_2 d\cos\Theta_{t2}} + Be^{ik_2 d\cos\Theta_{t2}}}{Ae^{ik_2 d\cos\Theta_{t2}} - Be^{ik_2 d\cos\Theta_{t2}}} \right] \qquad 2.36$$

$$= \frac{\rho_2 c_2}{\cos\Theta_{t2}} \left[\quad \right]$$

$$= Z_2 \left[\quad \right]$$

Dividing throughout by A,

$$Z_{in} = Z_2 \frac{e^{ik_2 d\cos\Theta_{t2}} + B/A.e^{ik_2 d\cos\Theta_{t2}}}{e^{ik_2 d\cos\Theta_{t2}} + B/A.e^{ik_2 d\cos\Theta_{t2}}} \qquad 2.37$$

Substituting equation 2.35 into 2.37 gives:

$$Z_{in} = Z_2 \left[\frac{e^{-if} + \frac{Z_3 - Z_2}{Z_3 + Z_2} e^{if}}{e^{-if} - \frac{Z_3 - Z_2}{Z_3 + Z_2}} \right] \qquad 2.38$$

where $f = k_2 d\cos\Theta_{t2}$

Using the definition of the hyperbolic tangent, Z_{in} can be written as:

$$Z_{in} = Z_2 \left[\frac{Z_3 - Z_2 \tanh(if)}{Z_2 - Z_3 \tanh(if)} \right]$$

The plane wave reflection coefficient for the rigid backed layer can be obtained by inspection from equation 2.35, that is:

$$R_L = \frac{Z_{in} - Z_1}{Z_{in} + Z_1} \qquad 2.39$$

A case of special interest is the rigid backed layer, for which $Z_3 \to \infty$ and Z_2 is given by:

$$Z_2 = \frac{\rho_2 c_2}{\cos\theta_{t2}} \cdot \frac{\rho_1 c_1}{\cos_i} \qquad 2.40$$

It then follows that:

$$R_L = \frac{\cos\theta - \frac{\cos\theta_{t2}}{Z_s}\tanh(-if)}{\cos\theta + \frac{\cos\theta_{t2}}{Z_s}\tanh(-if)} \qquad 2.41$$

This is of the same form as equation 2.32 so the admittance of the rigid backed layer β_L can be written as:

$$\beta_L = \beta_s \cos\theta_{t2} \tanh(-if) \qquad 2.42$$

where β_s is the specific admittance of the layer. Substituting for $\cos\theta_{t2}$, the angle of refraction in the layer, equation 2.42 becomes:

$$\beta_L = \frac{\rho_1}{\rho_2} \cdot (n^2 - \sin^2\theta_i)^{\frac{1}{2}} \tanh(-if)$$

Substituting for f in this expression gives:

$$\beta_L = \frac{\rho_1}{\rho_2} \cdot (n^2-\sin^2\theta_i)^{\frac{1}{2}} \tanh(-ik_2 \cdot \frac{k_1}{k_2} d(n^2-\sin^2\theta_i)^{\frac{1}{2}}) \qquad 2.43$$

hence:

$$\beta_L = \frac{\rho_1}{\rho_2} \cdot (n^2-\sin^2\theta_i)^{\frac{1}{2}} \tanh\left[-ik_1 d(n^2-\sin^2\theta_i)^{\frac{1}{2}}\right]$$

The specific impedance of the layer can be obtained from expression:

$$Z_L = 1/\beta_L$$

hence:

$$Z_L = \frac{\rho_2 \coth\left[-ik_2 d(n^2-\sin^2\theta_i)^{\frac{1}{2}}\right]}{\rho_1 (n^2-\sin^2\theta_i)^{\frac{1}{2}}}$$

Figure 2.9 shows the predicted values for the ratio total pressure/ direct pressure for a 0.05m thick rigid backed layer of material having a flow resistivity of 10 000 Mkz units. The dashed curve shows the two-media solution values for comparison

2.8 Two semi-infinite half surfaces

A boundary condition of particular practical significance is that of two semi-infinite half surfaces, where one half surface is rigid and the other half surface has a finite impedance. Such a boundary is commonly encountered in traffic noise propagation problems, whereby the source is located over a rigid tarmacadam or concrete road, and the receiver is located over grassland.

Morse and Ingard [2.2] offer an approximate solution for plane waves incident upon a discontinuous boundary, based upon the Helmholtz-Huygens integral. The solution is composed of two parts, the direct field, plus a scattered field obtained from the integral of a source distribution of the boundary. The geometry of the incident and scattered waves is shown in Figure 2.10.

The general solution for the pressure at the receiver is given by an integral equation of the form

$$p_r(r) = p_i(r_o) + \iint_S \left[G(r/r_o) \frac{\partial}{\partial n} p(r) - p(r) \frac{\partial}{\partial n} G(r/r_o) \right] dS \qquad 2.44$$

$p_i(r_o)$ is the direct wave and $p(r)$ the pressure on the surface due to the source, as determined by the boundary conditions. $G(r/r_o)$ is the Green's function for the boundary with the source located at r_o and the receiver at r.

The derivatives of equation 2.44 are taken with respect to the outward pointing normal of the surface enclosing the source. For the coordinate system used here, one may write

$$\frac{\partial}{\partial n} = -\frac{\partial}{\partial z}$$

The integral expression may be simplified by means of the techniques described in Sections 3.4 and 4.2.2 to give

$$p_r(r) = p_i(r) + ik\beta \int_0^\infty p(r).G(r/r_o)dx_o \qquad 2.45$$

since $\frac{\partial}{\partial n} p(r) = 0$ for a rigid surface, and $\frac{\partial}{\partial n} G(r/r_o) = ik\beta G(r/r_o)$ for the finite impedance surface, assuming local reaction.

The Green's function takes the form:

$$G(r/r_o) = \frac{1}{4}\left[H_o'(kr_o) + H_o'(kr)\right]$$

Morse does not give a final expression for the total field, but draws some conclusions for a numerical evaluation of equation 2.45. He states that for a given angle of incidence the field concentrated along the reflected ray exhibits a diffraction pattern described by the Fresnel functions C(u) and S(u). The reflection coefficient corresponds to an average of that of the two half surfaces.

Well away from the discontinuity of the boundary, the reflected wave behaves as though it were due to a reflection from a single continuous boundary.

Such a plane wave model is of limited use for many outdoor propagation problems, but does provide an indication of the received pressure in the far field.

References Chapter 2

2.1 Kinsler, L.E. and Frey, A.R.: Fundamentals of Acoustics.
Wiley. 1962.

2.2 Morse, P.M., Ingard, K.U.: Theoretical Acoustics.
McGraw-Hill. 1968.

2.3 Brekhovskikh, L.M.: Waves in Layered Media.
Academic Press. 1960.

2.4 Talaske, R.H.: The Acoustic Impedance of a Layered Forest Floor.
Noise Control Laboratory, Pennsylvania State University.
PA16802 USA. 1980.

2.5 Tilloston, J.G.: Attenuation of Sound Over Snow-Covered Fields.
JASA (39) 171-173. 1966.

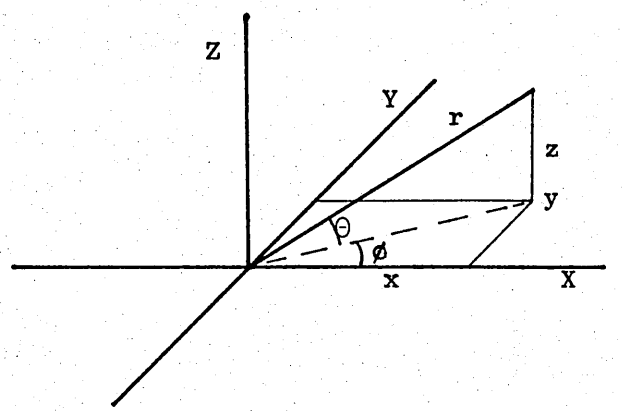

Figure 2.1
Right Handed Cartesian Co-ordinate System

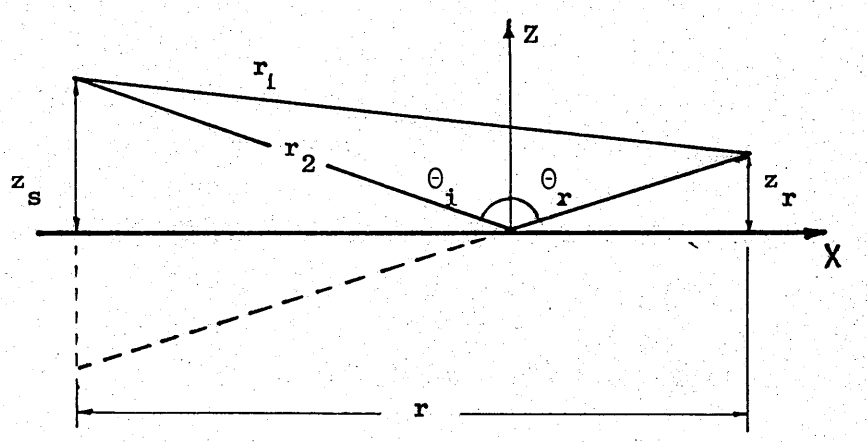

Figure 2.2
Geometry of Plane Wave Propagation over a Plane Surface

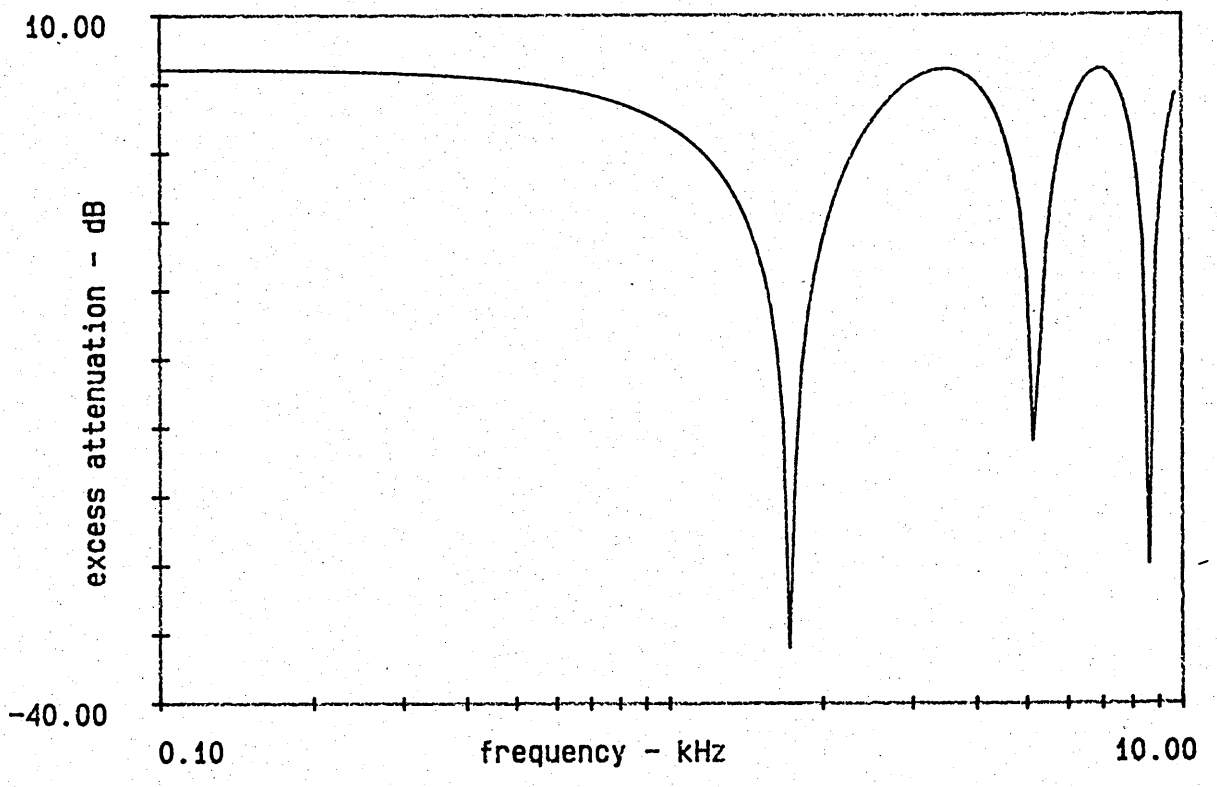

Figure 2.3
Predicted excess attenuation for plane wave propagation over a rigid surface. Source and receiver heights 1 m, separation distance 20 m.

Figure 2.4
Predicted excess attenuation for plane wave propagation over a resilient surface. Source and Receiver heights 1 m, separation distance 20 m.

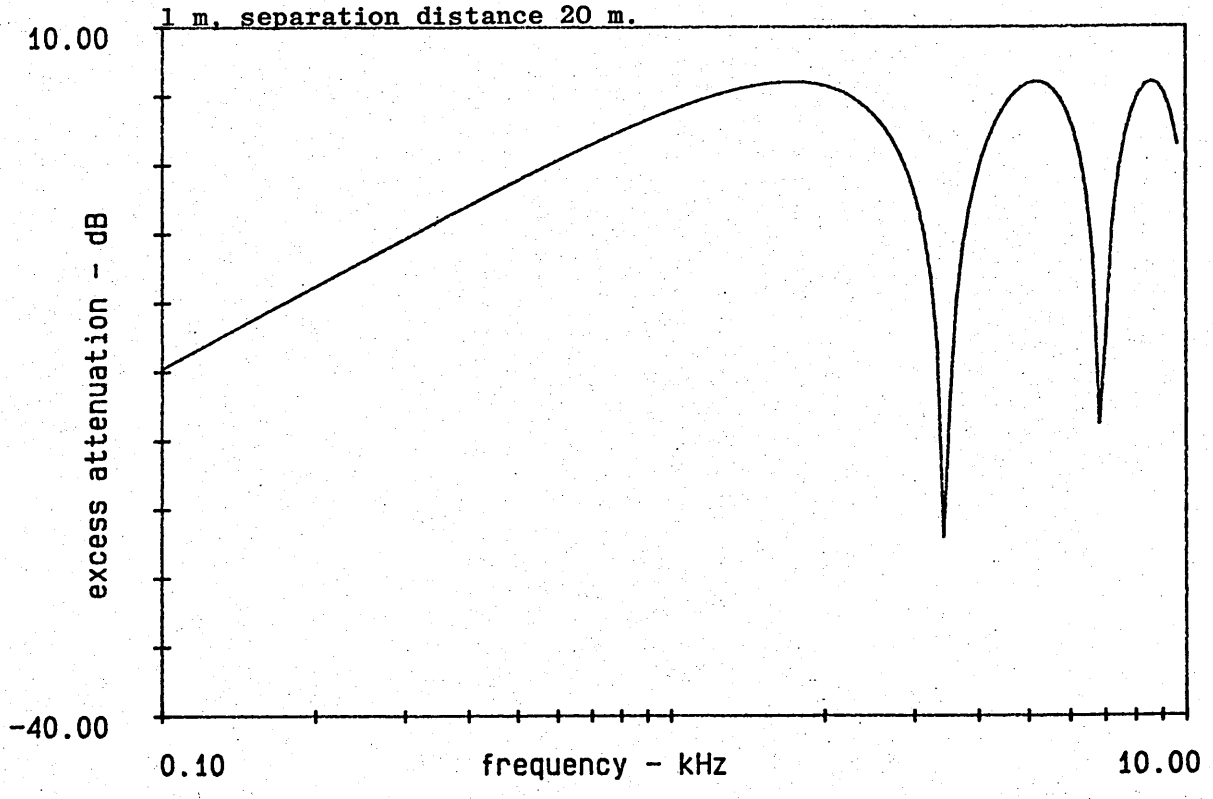

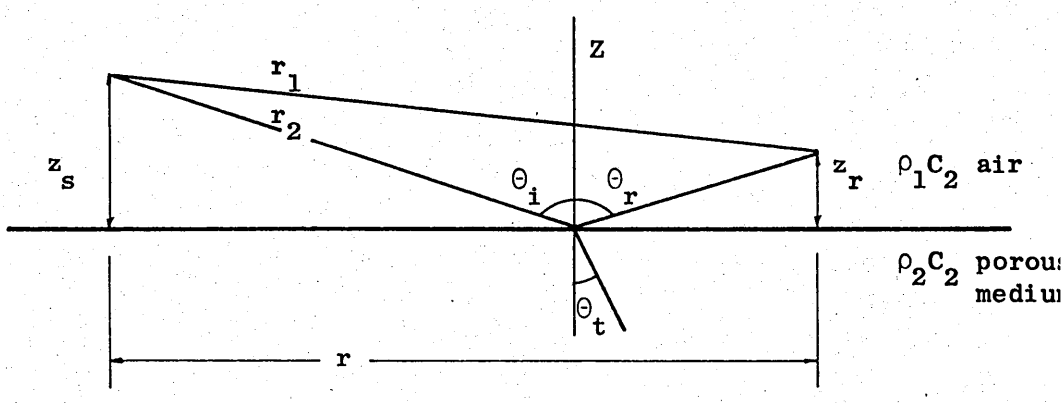

Figure 2.5
Geometry for Plane Wave Propagation over an Interface between Two Semi-Infinite Media

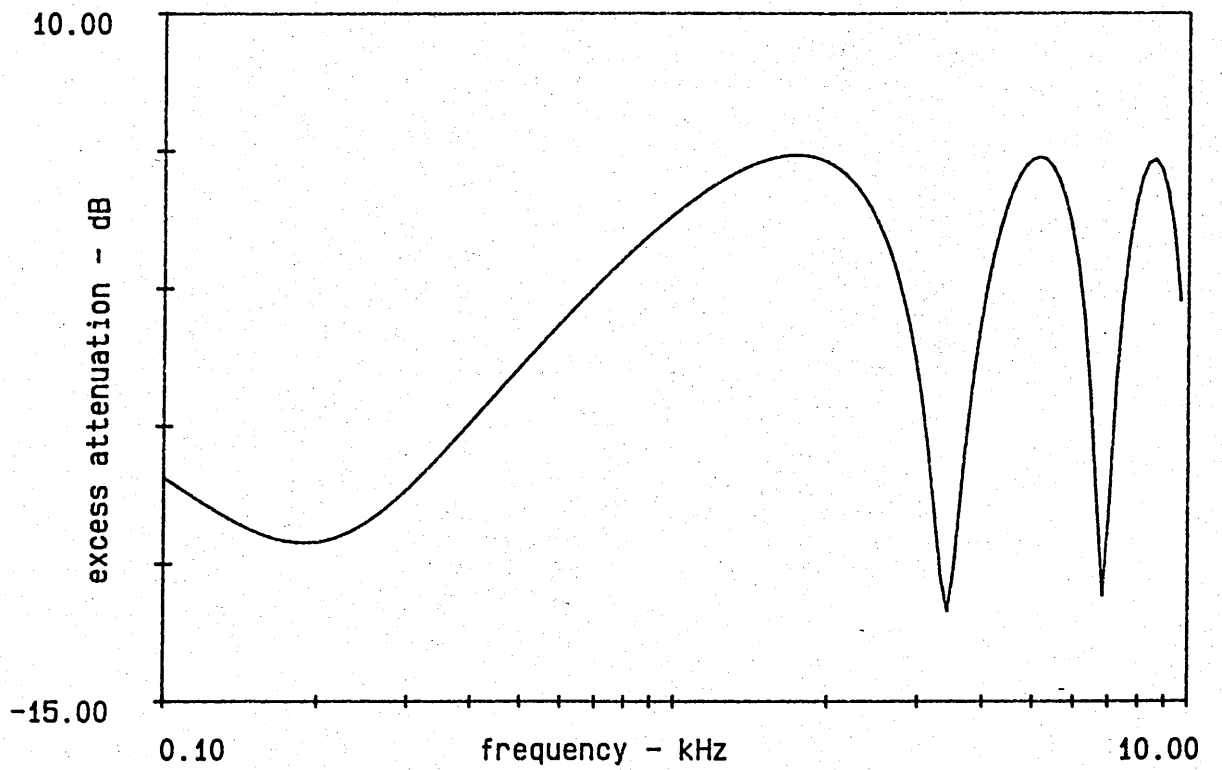

Figure 2.6
Predicted excess attenuation for plane wave propagation over an extended reaction boundary. Source and receiver heights 1 m, separation distance 20 m.

Figure 2.7
Predicted excess attenuation for plane wave propagation over a locally reacting boundary. Source and receiver heights 1 m, separation distance 20 m.

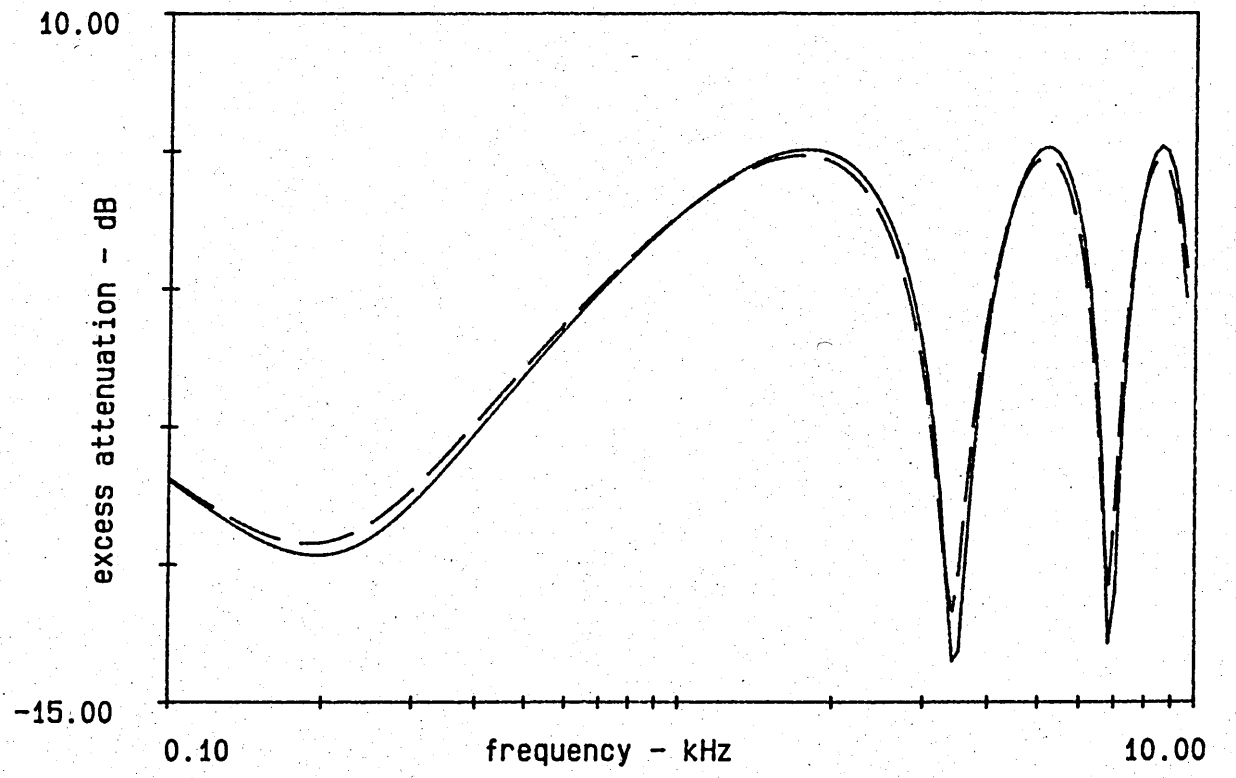

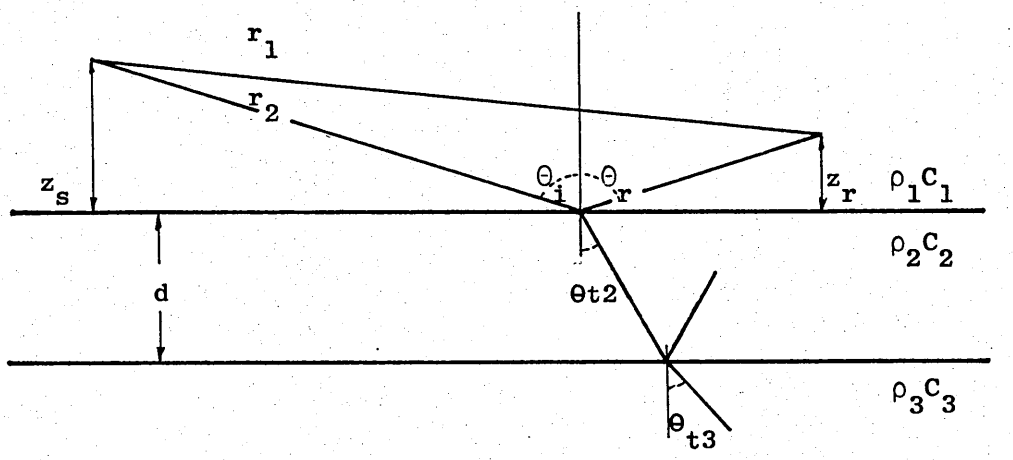

Figure 2.8
Geometry for Plane Wave Propagation over a Layered Boundary

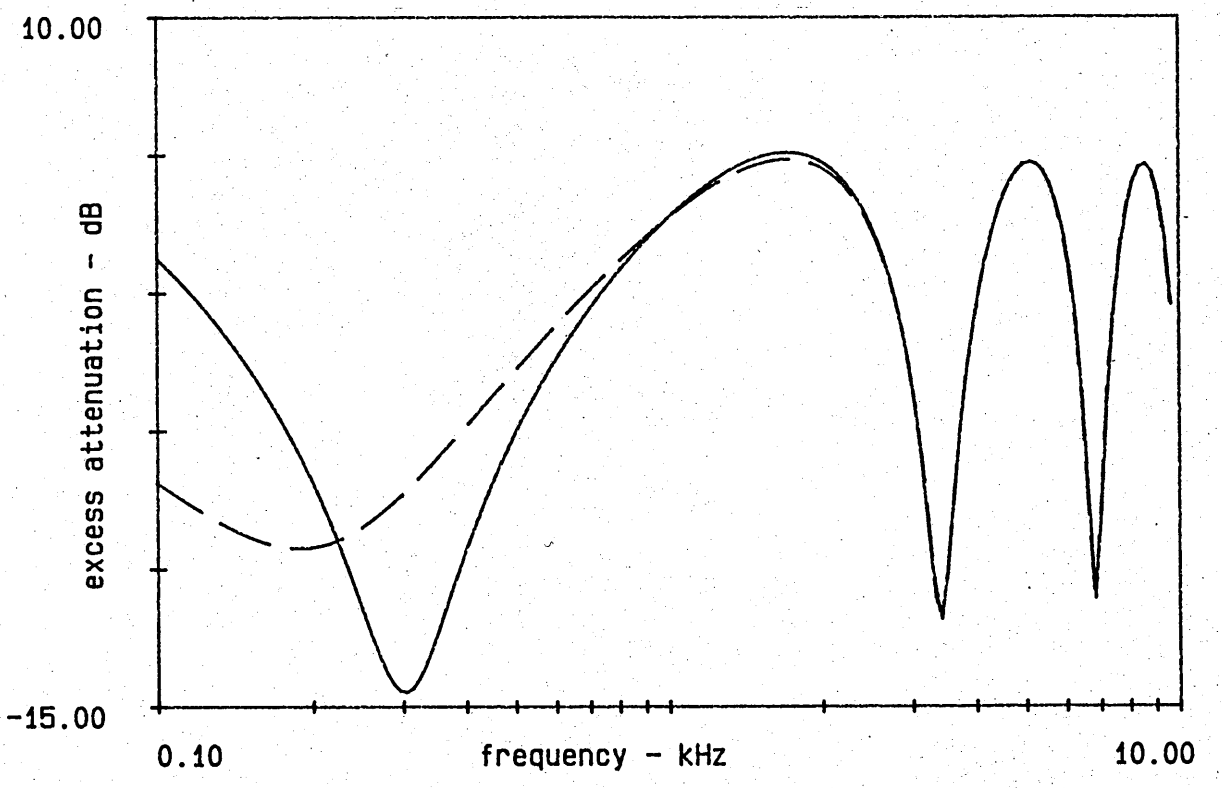

Figure 2.9
Predicted excess attenuation for plane wave propagation over a rigid backed layer. Source and receiver heights 1 m, separation distance 20 m, layer depth 0.05 m.

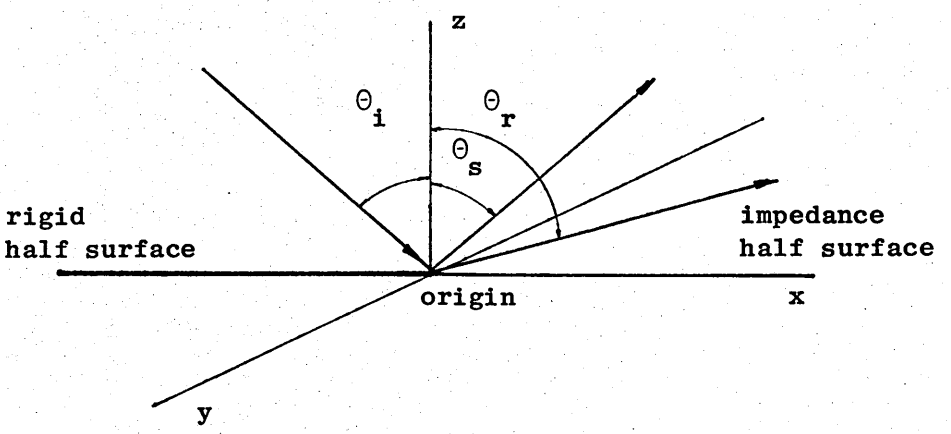

Figure 2.10
Geometry for propagation over two semi-infinite half surfaces

Chapter 3

Point source radiation models

In this chapter are reviewed the theoretical solutions to the problem of point to point propagation over a plane surface under the conditions of a stable atmosphere.

The general problem is formulated in exactly the same manner as for plane incident waves. That is one seeks a solution to the reduced wave equation (Helmholtz equation) subject to specified boundary conditions.

In the case of a point source, a solution cannot be obtained by the method of separating coordinates. Instead it is necessary to utilize either one of the transform techniques or the Greens function.

3.1 Formulation of the problem

The equation governing the steady-state sound field radiated from a point source in a homogeneous medium, is the inhomogeneous Helmoholtz equation:

$$(\nabla^2 + k^2)\,\Phi(r,t) = f(r,t) \qquad 3.1$$

where Φ (r,t) is the required velocity potential at the field point, and f(r,t) is the forcing function describing the generation of energy at the source. (Note that a harmonic time dependence of the form $\exp(-i\omega t)$ is assumed.)

The general solution to the homogeneous equation:

$$(\nabla^2 + k^2)\Phi_H = 0 \qquad 3.2$$

will be written as:

$$\Phi_H = \frac{Ae^{ikr_2}}{4\pi r_1} + \frac{Be^{ikr_2}}{4\pi r_2} \qquad 3.3$$

The factor 4π is a scaling term describing the source strength and disappears upon integrating over a volume of space. Equation 3.3 describes the field radiated into unbounded space by a point source.

The utility of the function Φ_H lies in the principle of superposition. This enables a solution of equation 3.1 to be written as the sum of homogeneous and inhomogeneous solutions, or as they are more commonly known, the complementary function and the particular integral.

Once the velocity potential has been obtained, the sound pressure or particle velocity can be found from the relations:

$$p = i\omega\rho\Phi \qquad 3.4(a)$$

$$u = -\text{grad}\ \Phi \qquad 3.4(b)$$

3.2 Integral transformations

A solution to equation 3.1 can be found by assuming that it may be written as an expansion in terms of elementary waves. Banos [3.1] postulates the particular integral solution of equation 3.1 can be obtained from a threefold summation of elementary plane waves.

Consider a point source $\Phi(r_1) = \exp(ikr_1)$, where $r_1^2 = x^2 + y^2 + z^2$. If $\Phi(r)$ is regarded as a function of x only, it has the Fourier transform

$$F(k_x,y,z) \doteq \int_{-\infty}^{\infty} \Phi(x,y,z)\ \exp(-ik_x x)dx \qquad 3.5$$

where k_x is the transform variable, equivalent to a wave number in transform space. Transforming $F(k_x,y,z)$ with respect to y gives:

$$F(k_x,k_y,z) \doteq \int_{-\infty}^{\infty} F(k_x,y,z)\ \exp(-ik_y y)dy \qquad 3.6$$

with k_y as the transform variable. A final transformation, this time of $F(k_x,k_y,z)$ with respect to z, produces:

$$F(k_x,k_y,k_z) = \int_{-\infty}^{\infty} F(k_x,k_y,z)\ \exp(-ik_z,z)dz \qquad 3.7$$

Combining equations 3.5, 3.6 and 3.7 results in the triple Fourier transform:

$$F(k_x,k_y,k_z) = \int_{-\infty}^{\infty}\int_{\infty}^{\infty}\int_{\infty}^{\infty}\Phi(x,y,z)\ \exp(-k_x x,\ -k_y y,\ -ik_z z)dxdydz \qquad 3.8$$

The function $\Phi(x,y,z)$ can be obtained by inverse transformation of equation 3.8, which gives:

$$\Phi(x,y,z) = \frac{1}{(2\pi)^3} \int \int_{-\infty}^{\infty} F(k_x,k_y,k_z)\ \exp(+ik_x x + ik_y y \ldots$$

$$\ldots + ik_z z)dk_x dk_y dk_z \qquad 3.9$$

Thus if $F(\ )$ can be found, then $\Phi(\ )$ is known through equation 3.9.

$F(\ )$ is obtained from a triple transform of 3.1. Such a transformation shows that:

$$F(k_x,k_y,k_z) = \frac{4\pi\ A\ \exp(-ik_z z)}{k_x^2 + k_y^2 + k_z^2 - k^2} \qquad 3.10$$

Substituting equation 3.10 into 3.9 results in an expression for $\Phi(\ )$ in terms of a summation of elementary plane waves:

$$\Phi(r) = \frac{1}{(2\pi)^3} \int\int_{-\infty}^{\infty}\int \frac{4\pi A e^{-i(k_x x + k_y y + k_z z)} dk_x dk_y dk_z}{(K^2 - k^2)} \qquad 3.11$$

Each plane wave has direction cosines $(k_x/k, k_y/k, k_z/k)$ and is weighted by the factor $4\pi A/(K^2 - k^2)$ where:

$$K^2 = k_x^2 + k_y^2 + k_z^2$$

The Fourier transform enables one to expand a spherical wave into a set of plane waves, by means of a triple integral over transformed wave number space.

3.3 Sommerfeld's expansion

A second integral transform, frequently used in solving differential equations, is the Fourier-Bessel transform. Consider the two dimensional Fourier transform:

$$F(k_x,k_y) = \frac{1}{(2\pi)^2} \int_{-\infty}^{\infty}\int f(x,y) \exp(-ik_x x - ik_y) dxdy \qquad 3.12$$

On making the substitutions:

$$r^2 = x^2 + y^2 + z^2,\ x = r\cos\theta,\ y = r\sin\theta,\ k_x = K\cos\phi$$
$$K^2 = k_x^2 + k_y^2$$
$$k_y = K\sin\phi$$

then

$$F(k_x,k_y) = \frac{1}{(2\pi)^2} \int_0^{\infty} f(r).r.dr \int_0^{2\pi} \exp(iKr\cos(\theta - \phi)) d\theta \qquad 3.13$$

since $dxdy = rdrd\theta$ and $k_x x + k_y y = r\,K\cos(\theta - \phi)$.

But the argument of the second integral is periodic, so that:

$$\int_o^{2\pi} \exp iKr\cos(\theta - \phi)\ d\theta = \int_o^{2\pi} \exp\left[iKr\cos\theta\right]d\theta \qquad 3.14$$

The right hand expression is just the integral form of $2\pi.J_o(Kr)$, where $J_o(Kr)$ is the Bessel function of the 1st kind and zeroth order.

The transform for $F(k_x,k_y)$ can therefore be written:

$$F(k_x,k_y) = \int_o^{\infty} r.f(r).J_o(Kr)dr \qquad 3.15$$

and the inverse transform for f(r) becomes:

$$f(r) = \frac{1}{(2\pi)^2} \int_o^{\infty} F(k_x,k_y)e^{-i\omega K} J_o(Kr)dk \qquad 3.16$$

The weighting function $F(k_x,k_y)$ can be found from the two dimensional transform of equation 3.1.

Using the Fourier-Bessel transform Sommerfeld [3.2] was able to show that a spherical source can be expanded into a set of elementary cylindrical harmonics. A final expression for the expansion is given below:

$$\frac{e^{ikr}}{r} = \int_o^{\infty} \frac{K\,J_o(Kr)}{(K^2 - k^2)^{\frac{1}{2}}} \exp\left[-i(K^2 - k^2)^{\frac{1}{2}}z\right]dK \qquad 3.17$$

Brekhovskikh [3.3] shows that an alternative, but closely related, expression can be obtained by making the substitution:

$$J_o(Kr) = \frac{H_o'(Kr) - H_o'(-Kr)}{2} \qquad 3.18$$

Here $H_o'(Kr)$ is the Hankel function of the 1st kind and zeroth order.

Equation 3.17 can now be written as:

$$\frac{e^{ikr}}{r} = \frac{1}{2}\int_{\infty}^{\infty} \frac{KH_o'(Kr)}{\left(K^2 - k^2\right)^{\frac{1}{2}}} \exp\left[i(K^2-k^2)^{\frac{1}{2}}z\right]dK \qquad 3.19$$

3.4 The Green's function

Not all differential equations lend themselves to solutions by transform methods, and so other techniques are required. One technique utilises the Green's function.

Suppose it is required to solve the equation:

$$(\nabla^2 + k^2)\, g(r/r_o) = -\delta(r - r_o) \qquad 3.20$$

which defines the propagation, in an unbounded medium, of a unity amplitude, harmonic source. $\delta(r - r_o)$ is the three dimensional Dirac delta function.

Morse and Ingard [3.4] show that the general form of $g(r/r_o)$ is:

$$g(r/r_o) = \frac{e^{ikR}}{4\pi R} \qquad 3.21$$

where $R = (r - r_o)$, and is the distance between the source point r_o, and the field point r. $g(r/r_o)$ is known as the Green's function for a source in an unbounded medium.

The utility of the Green's function is best demonstrated by two examples. Firstly consider the field $f(r)$ at a point r due to a distribution of unit sources $\rho(r_o)$. The total field is obtained from the volume integral:

$$f(r) = \int_V g(r/r_o)\ \rho(r_o)\, dV \qquad 3.22$$

Secondly, suppose we require the field $f(r)$ at a point r due to a distribution $\gamma(r)$ of unit sources on a surface. The total field is found from the surface integral:

$$f(r) = \int_S g(r/r_o)\ \gamma(r_o)\ dS \qquad 3.23$$

These equations show that the field at any point can be expressed as a summation of unit sources, either in space or over a surface.

Equations 3.22 and 3.23 may be combined to satisfy any inhomogeneous boundary conditions since the boundary conditions can be satisfied by an appropriate distribution of surface sources. The homogeneous solution can be obtained from the volume integral of a suitable distribution in space of unit sources.

Green's functions find application in solutions of the Helmholtz-Hyguens Radiation Integral. This integral follows from Green's integral, and Gauss' theorem, and is based on the fact that the field inside a given volume is determined by the power of any sources within it, plus the power entering the volume from outside or reflected by the boundary. The Helmholtz-Huygens integral is usually written in the form:

$$f(r) = \int_V \rho(r_o)\, g(r/r_o)\, dv + \int_S \left[g(r/r_o) \frac{\partial}{\partial n} \gamma(r_o) - \gamma(r_o) \cdot \frac{\partial}{\partial n} g(r/r_o)\, ds \right] \qquad 3.24$$

where

r is the field point;

r_o is the source point;

$\rho(r_o)$ is the volume distribution of unit sources;

$\gamma(r_o)$ is the surface distribution of unit sources;

$\frac{\partial}{\partial n}$ is the gradient of the outward pointing normal.

In most cases of practical interest the form of the volume integral is known, it is simply that of a point source radiating in an unbounded medium. The surface integral provides for the appropriate distribution of unit sources on the surface to satisfy the boundary conditions.

3.5 A Rigid Surface

The boundary condition for a rigid surface is that the normal component of the particle velocity is zero. If u = 0, then from 3.4(b):

$$-\text{grad}\ \Phi = 0 \qquad 3.25(a)$$

or alternatively

$$\frac{\partial p}{\partial u} = 0 \qquad 3.25(b)$$

According to Morse and Ingard [3.4] an appropriate Green's function is:

$$g(r_2/r_1) = \frac{e^{ikr_1}}{4\pi r_1} + \frac{e^{ikr_2}}{4\pi r_2} \qquad 3.26$$

where the first term on the right hand side corresponds to the field due to the direct wave, and the second term is the field due to an image source below the reflecting surface.

At the boundary $g(r_2/r_1)$. $\frac{\partial p}{\partial n} = 0$ and, since the source and image fields cancel at all points, $p \frac{\partial}{\partial n} g(r_2/r_1) = 0$, therefore the total field is:

$$f(r_2) = \int_v g(r_2/r_1)dV \qquad 3.27$$

The solution for a rigid boundary is therefore:

$$\Phi = \frac{e^{ikr_1}}{r_1} + \frac{e^{ikr_2}}{r_2} \qquad 3.28$$

3.6 A resilient surface

Following exactly the same procedure as for a rigid surface, the solution for a resilient surface can be shown to be:

$$\Phi = \frac{e^{ikr_1}}{r_1} - \frac{e^{ikr_2}}{r_2} \qquad 3.29$$

In this case the Green's function is:

$$g(r_2/r_1) = \frac{e^{ikr_1}}{4\pi r_1} - \frac{e^{ikr_1}}{4\pi r_2} \qquad 3.30$$

which can be seen to satisfy the boundary condition $p = 0$ at the surface.

3.7 Interface between two semi-infinite media

In this section are reviewed the solutions pertaining to the propagation of a spherical wave over the interface between two semi-infinite isotropic media. Such a model presumes the ground to be a homogeneous porous medium characterised by a density and sound velocity, both of which may be complex.

The source and receiver are located in the upper medium and the interface lies along the plane $z = 0$, as shown in Figure 3.1.

The total velocity potential in the upper medium is:

$$\Phi_i(r) = \Phi_{il} + \Phi_{s1} \qquad z>0 \qquad 3.31$$

the superposition of a direct and scattered field. Note that in general the scattered wave will be assumed to include any specularly reflected contribution.

The velocity potential in the lower medium is:

$$\Phi_2(r) = \Phi_{s2}(r) \qquad z<0 \qquad 3.32$$

consisting of just

the refracted wave. The three components Φ_{il}, Φ_{sl} and Φ_{s2} can all be expressed in terms of the summation of elementary waves, either plane or cylindrical, using the Fourier and Fourier-Bessel transforms.

Explicit expressions for these components have been published by several authors, and they are reveiwed in the following sub-sections.

3.7.2 Rudnick's Solution

Rudnick [3.5] developed a solution for the two-media (or extended reaction) boundary, by postulating that for a source on the interface, the scattered potential in the upper medium could be expressed as:

$$\Phi_{sl} = \int_{\infty}^{\infty} f(K)\ J_o(Kr) e^{-(K^2 - k_1^2)^{\frac{1}{2}} z_r}\ dK \qquad 3.33$$

where f(K) is a weighting function to be determined from the boundary conditions and K is the transformed wavenumber.

Using equation 3.17, the direct field can be epxressed in terms of the Bessel function J_o as:

$$\Phi_{il} = \int_{\infty}^{\infty} \frac{KJ_o(Kr)}{\sqrt{K^2-k_1^2}} e^{-(K^2-k_1^2)^{\frac{1}{2}}z} r\, dK \quad z > 0$$

Summing the expressions for the direct and scattered fields, the total field in the upper medium becomes:

$$\Phi_1 = \int_o^{\infty} \left[\frac{K}{\sqrt{K^2-k_1^2}} + f(K) \right] J_o(Kr) e^{-(K^2-k_1^2) z} r\, dK \qquad 3.34$$

After applying the boundary conditions, to determine the weighting function $f_1(K)$, Rudnick showed that the total field is given by:

$$\Phi_1 = 2\rho_2 \int_o^{\infty} \frac{J_o(Kr_1)}{\rho_2 l + \rho_2 m} e^{-lz} r dK \qquad 3.35$$

where:

$$l = (K^2-k_1^2)^{\frac{1}{2}}$$
$$m = (K^2-k_2^2)^{\frac{1}{2}}$$

ρ_1 = density of upper medium

ρ_2 = density of lower medium

Rudnick then assumed that equation 3.35 could be generalised for a source on the interface, by adding the source displacement. This results in a total field given by:

$$\Phi_1 = 2\rho_2 \int_o^{\infty} \frac{J_o(Kr)}{\rho_2 l + \rho_1 m} e^{-l(z_r + z_s)} K dK \qquad 3.36$$

However, it has been shown [3.6] that the total field cannot be represented by a single integral, and that the correct form of equation 3.36 is:

$$\Phi_1 = \frac{e^{ikr_1}}{r_1} + \frac{e^{ikr_2}}{r_2} - 2\rho_1 \cdot \int \frac{J_o(Kr)\, m e^{-\ell(z_r+z_s)} K dK}{(\rho_2 \ell + \rho_1 m)} \qquad 3.37$$

Utilising a transformation due to Van der Pol [3.7], and following an analysis of Norton's [3.8], Rudnick derived an approximate solution for the total field in the upper medium as:

$$\Phi_1 = \frac{e^{ikr_1}}{r_1} + \frac{e^{ikr_2}}{r_2} \left[Rp + (1-Rp) F(W) \right] \qquad 3.38$$

where Rp is the plane wave reflection coefficient:

$$Rp = \frac{\rho_2 c_2 \cos\theta_i - \rho_1 c_1 (1 - k_1^2 \sin^2\theta_i / k_2^2)^{\frac{1}{2}}}{\rho_2 c_2 \cos\theta_i + \rho_1 c_1 (1 - k_1^2 \sin^2\theta_i / k_2^2)^{\frac{1}{2}}} \qquad 3.39$$

and F(W) is a correction factor that acts on the strength of the image source to compensate for the effects of the interface. F(W) is given by:

$$F(W) = 1 + i2(W)^{\frac{1}{2}} e^{-W} \int_{-i\sqrt{W}}^{\infty} e^{-u^2} du \qquad 3.40(a)$$

F may also be written in terms of the complementary error function as:

$$F(W) = 1+i\sqrt{\pi}.W\ e^{-W}\ \mathrm{erfc}(-i\sqrt{W}) \qquad 3.40(b)$$

The argument of F is called the numerical distance, and is defined by Rudnick as:

$$W = \frac{2ikr_1}{(1-Rp)^2}\left(\frac{\rho_1 c_1}{\rho_2 c_2}\right)^2 . (1-k_1{}^2\sin^2\Theta_i/k_2{}^2) \qquad 3.41$$

For numerical purposes, series expansions of F(W) are available. When $|W|<<1$, that is k_1r_2 not very large, β small and $\Theta_i \simeq \pi/2$

$$F(W) = 1 + i\pi^{\frac{1}{2}}\ We^{-W}.e^{2-2W^2} + \frac{(2W^2)^2}{1.3} \quad \frac{(2W^2)^3}{1.3.5} \cdots$$

which is an absolutely convergent power-series expansion. When $|W| > 1$:

$$F(W) \simeq 2i\pi^{\frac{1}{2}}\ We^{-W}e^2\ H[-\mathrm{Im}(W)] - \frac{1}{2W^2} - \frac{1.3}{(2W^2)^2} - \frac{1.3.5}{(2W^2)^3} - \cdots.$$

which is a semi-convergent asymptotic expansion.

H [ ] is the Heaviside step function defined by

$$H[-\mathrm{Im}(W)] = \begin{cases} 1, & \mathrm{Im}(W)<0 \\ 0, & \text{otherwise} \end{cases}$$

There are two important conditions imposed by Rudnick in deriving his solution. The first is that $|\rho_1 c_1/\rho_2 c_2| \simeq 1$, that is the impedances of the two media must be similar. The second is that k_2 must have a large imaginary part so as to ensure that the field from the image is concentrated about the image point.

Measurements of the normal specific admittance of institutional grassland have shown that at high frequencies (f > 1 kHz) $\rho_1 c_1/\rho_2 c_2 \simeq 1$, but at low frequencies $\rho_1 c_1/\rho_2 c_2 \ll 1$. Thus Rudnick's first condition is only met at high frequencies. His second condition implies that at short separation distances the boundary must behave as one of local rather than extended reaction.

3.7.3 Paul's Solution

Paul [3.9] derived a solution for the two-media boundary by following through the work of Banos and Wesley [3.10]. This expression for the total field in the upper medium is:

$$\Phi_1 = \frac{e^{ikr_1}}{r_1} - \frac{e^{ikr_2}}{r_2} + V(h,r) \qquad 3.42$$

Where:

$$V(h,r) = 2\rho_2 \int_0^\infty \frac{J_o(Kr)e^{-\ell h}}{\rho_2\ell+\rho_1 m} KdK \qquad 3.43$$

$h = z_r + z_s$

r = the horizontal separation distance

$\ell = (K^2 - k_1^2)^{\frac{1}{2}}$

$m = (K^2 - k_2^2)^{\frac{1}{2}}$

Using identities relating Bessel functions to Hankel functions, equation 3.43 can be re-written as:

$$V(h,r) = \rho_2 \int_{-\infty}^{\infty} \frac{e^{-\ell h}.H_o(K.r)}{\rho_2\ell+\rho_1 m} KdK \qquad 3.44$$

and the integration is now along the entire real axis of the complex K plane.

Two branch cuts are required to make this integrand single valued. Paul chooses the vertical cuts specified by:

$$\mathrm{Re}(K) = \pm \mathrm{Re}(k_1), \text{ cut } C_1$$

and

$$\mathrm{Re}(K) = \pm \mathrm{Re}(k_2), \text{ cut } C_2$$

The integration along the real axis can be transformed into a contour integration by the addition of the integral of V(h,r) over a semi-circle of infinite radius (see Morse and Ingard page 16); since this integral will vanish a $|K| \to \infty$.

Thus the exact solution for V is given by:

$$V(h,r) = -\int_{C_1} - \int_{C_2}$$

the sum of the contributions from the branch cuts C_1 and C_2.

Under the condition $\theta < \sin^{-1}(+n)$, the integral over C_1 does not contribute to the final solution, hence V(h,r) may be written:

$$V(h,r) = V^2(h,r) + U(\Theta-\Theta_b).V^1(h,r) \qquad 3.45$$

where:

$$V^2(h,r) = \int_{C_2}$$

$$V^1(h,r) = \int_{C_1}$$

$$U(X) = 1 \text{ if } x > 0$$
$$\text{or}$$
$$= 0 \text{ if } x < 0$$

$$\Theta_b = \sin^{-1}(\pm n)$$

By applying the transformations:

$$K = k_1\cos\Theta$$

and

$$K = k_2\cos\Theta$$

Paul is able to evaluate V^2 and V^1 using the method of steepest descents.

The solution for $V^2(h,r)$ is a double integral and can be written as:

$$V(h,r) = \frac{i4k_1 e^{i\ell k r_1}}{\pi} \int_{\infty}^{\infty}\int_{o}^{\infty} F(x,y)e^{-(x^2+y^2)/2}dydx \qquad 3.46$$

where:

$$F(x,y) = \frac{\sin(\omega+\Theta_i)\cos(\omega+\Theta_i)\ d\omega/dx}{\left[M\sqrt{n^2-\sin^2(\omega+\Theta_i)}+\cos(\omega+\Theta_i)\right].\ \sqrt{(4_i k_1 r\sin(\omega+\Theta_i)-y^2)}} \qquad 3.47$$

$$\omega = \Theta - \Theta_i$$

$$\frac{x^2}{2} = -2ik_1 r_1 \sin^2(\omega/2)$$

$$d\omega/dx = \frac{1}{\sqrt{ik_1 r_1}.\cos(\omega/2)}$$

Expanding the function F(x,y) into a double Taylor series and integrating term by term, Paul derives an asymptotic solution for $V^2(h,r)$. However, this solution is not valid as the first term of the denominator of equation 3.47 tends to zero because of the existence of a pole located close to the saddle point.

The problem can be remedied by utilising the technique of subtraction of the pole [3.1]. $V^2(h,r)$ is decomposed into two parts: $V^P(h,r)$ the contribution from the pole, and $V^S(h,r)$ the contribution from the steepest descent integral.

$V^P(h,r)$ is obtained by expanding F(x,y) in the vicinity of the pole and integrating term by term.

The resultant series is subtracted, term by term, from $V^2(h,r)$ to give $V^s(h,r)$ the contribution from the branch cut integral. Paul gives the leading terms for $V^s(h,r)$ as:

$$V^s(h,r) = \frac{2(1-M^2)^{-1}Q^{-\frac{1}{2}}\exp\left[ikr-kh(1-n^2)^{\frac{1}{2}}(1-M^2)^{-\frac{1}{2}}\right]}{\rho_1 r\left[1-M^2(1+n^2)+n^2M^4\right]^{1/4}}$$

$$\times \left\{1 + \frac{G_1}{ik_1r} + \frac{G_2}{2(ik_1r)^2}\right\} \qquad 3.48$$

where:

$$Q = 2M^{-2}(1-n^2)^{-1}\left[\left(\frac{1-M^2n^2}{1-M^2}\right)^{\frac{1}{2}}-1\right]$$

$$G_1 = \frac{k_1h}{2}(1-n^2)^{-\frac{1}{2}}+M^2\left[-9\frac{(1-2n^2+n^4)}{128}\cdot(1-n^2)^{-1}\right.$$

$$\left. - \frac{k_1h}{16}(1+n^2)(1-n^2)^{-\frac{1}{2}} + \frac{k_1^2h^2}{8}\right]$$

$$G_2 = \frac{-k_1h}{4}(1-4n^2)(1-n^2)^{-\frac{1}{2}}+\frac{3k_1^2h^2}{4}(1-n^2)^{-1}$$

The second branch cut integral is also evaluated using the method of steepest descent. It is sufficient here to give the final result for V(h,r), which is:

$$V(h,r) = \frac{2\cos\Theta_i e^{ik_1 r_1}}{r_1(\cos\Theta_i + M(n - \sin\Theta_i)^{\frac{1}{2}}} \left[1 + \frac{F}{ik_1 r_1} + \ldots\right] +$$

$$+ U(\Theta_i - \Theta_o) \frac{2ik_2 r_1 M \exp\left[ik_2 r_1 (\sin\Theta_1 + n^{-1}(1-n^2)^{\frac{1}{2}}\cos\Theta_i\right]}{(ik_1 r_1)^2 \rho_2 (1-n^2)\sqrt{\sin\Theta_i}\left[\sin\Theta_i - n(1-n^2)^{\frac{1}{2}}\cos\Theta_i\right]} 3/2 \qquad 3.49$$

where:

$$F = -1 - \frac{\sin 2\Theta_i}{\cos\Theta_i(\cos\Theta_i + M\sqrt{n^2 - \sin^2\Theta_i})} + 1 - \frac{\cos\Theta_i}{\sin^2\Theta_i}$$

$$x \left[\cos\Theta_i + \frac{2M\cos^2\Theta_i - 3M\sin^2\Theta_i}{2(n^2 - \sin^2\Theta_i)^{\frac{1}{2}}} + \frac{M\cos^2\Theta_i \sin^2\Theta_i}{2(n^2 - \sin^2\Theta_i)^{3/2}}\right] x$$

$$x \left[\cos\Theta_i + M\sqrt{n^2 - \sin^2\Theta_i}\right]^{-1} + \frac{\sin^2\Theta_i}{n^2 - \sin^2\Theta_i}$$

$$x \left[\frac{\sqrt{n^2 - \sin^2\Theta_i} + M\cos\Theta_i}{M(n^2 - \sin^2\Theta_i)^{\frac{1}{2}} + \cos\Theta_i}\right]^2$$

$$\Theta_b = \sin^{-1}(\pm n) \qquad 3.50$$

Paul's first paper provides a solution valid for large separation distances, and either small or large angles of incidence. In a later paper [3.14] he develops a solution valid over the entire hemisphere above the interface. However, in this second paper he fails to take account of the possible contribution from any poles in the complex plane.

3.7.4 Modifications to Paul's solution

Paul's work has formed the basis for several recent treatments of the two media problem, notably those of Attenborough et al [3.11] and Corbin [3.12].

Attenborough specialised entirely to near grazing incidence on porous ground, whereas Corbin expands Paul's treatment to include different types of media. Starting with equation 3.44, Attenborough chose to use hyperbolic branch cuts in the K plane rather than Paul's vertical cuts. These new cuts which are defined by:

$$\mathrm{Re}(\ell) = \pm \mathrm{Re}\ (k_1)$$

and

$$\mathrm{Re}(m) = \pm \mathrm{Re}\ (k_2)$$

which together with the transformation $K=k_1\sin\Theta_1$, rather than $K=k_1\cos\Theta_1$, have the advantage that the branch cut integral C_1 disappears in the complex Θ plane.

Furthermore, using the known properties of porous materials, i.e. $|\rho_1/\rho_2| \ll 1$, $|\beta| < 1$ and $\mathrm{Re}(n) > 1$ and $\mathrm{Im}(n) > 0$, Attenborough shows that not only is there only one pole to consider in the contour integration, but also that the branch cut integral C_2 can be ignored.

Equation 3.45 can now be written as:

$$V(h,r) = \begin{cases} V^2(h,r) + V^s & \mathrm{Re}(\Theta_p - \Theta_i) > 1 \\ V^2(h,r) & \text{else} \end{cases} \qquad 3.51$$

$$\Theta_p \simeq \pi/2 - nM$$

The term V^S is the contribution from the residue of the pole at Θp and is part of the total field only when the pole lies within the steepest descent path contour: it can be written as

$$V^S = \frac{-Ak_1 \exp(-ik_1 hA)}{2(1-M^2)} H_o' \left[k_1 r(1-A^2)^{\frac{1}{2}}\right]$$

where

$$A = \frac{M(n^2-1)^{\frac{1}{2}}}{(1-M^2)}$$

The contribution from V^S can be seen to decay exponentially with increasing height above the surface similar to a surface wave. Hence this term has become known as the surface wave pole or surface wave contribution.

When this pole approaches the saddle point, it limits the radius of convergence of the Taylor series expansion of the integral $V^2(h,r)$. The effect of this pole can be removed by the technique of subtraction of the pole as outlined previously.

Using this method, Attenborough is able to show that the pole contribution in $V^2(h,r)$ exactly cancels that of V^s and so the surface wave pole disappears as an explicit part of the total field. However, this does not remove the pole's influence from the total field.

The approximate solution for the total field is given by:

$$\Phi_t = \frac{e^{ik_1 r_1}}{4\pi r_1} - \frac{e^{ik_1 r_2}}{4\pi r_2} - \frac{k_1 A}{4(1-M^2)} \cdot \operatorname{erfc} \frac{ix_o}{\sqrt{2}} \; H'_o \quad \ldots \quad 3.52$$

$$\ldots \left[kr(1-A^2)^{\frac{1}{2}}\right] \times \exp(ik_1 hA) . + V^R$$

where:

$$V^R \simeq \frac{e^{ik_1 r_1}}{2\pi r_2} \left\{ \frac{\cos\Theta_i}{\cos\Theta_i + M(n^2 - \sin^2\Theta_i)^{\frac{1}{2}}} + \frac{A}{\sqrt{2}(1-M^2)} \cdot \right.$$

$$\left[1 + \frac{1+A\cos_i}{(1-A^2)^{\frac{1}{2}}\sin\Theta_i} \right]^{\frac{1}{2}} \cdot \frac{1}{A+\cos\Theta_i} + \frac{1}{ik_1 e_2} \times$$

$$\left[\frac{F\cos\Theta_i}{\cos\Theta_i + M(n^2 - \sin^2\Theta_i)^{\frac{1}{2}}} + \frac{A}{\sqrt{2}(1-M^2)(A+\cos\Theta_i)} \right.$$

$$\left(1 + \frac{1+A\cos\Theta_i}{\sin\Theta_i (1-A^2)^{\frac{1}{2}}} \right)^{\frac{1}{2}} \left(\frac{1+A\cos\Theta_i + (1-A^2)^{\frac{1}{2}}\sin\Theta_i}{2(A+\cos\Theta_i)^2} + \right.$$

$$\left. \left. \left. + \frac{1}{8\sin\Theta_i (1-A^2)^{\frac{1}{2}}} \right) \right] \right\}$$

$$A = M \left(\frac{(n^2-1)}{(1-M^2)} \right)^{\frac{1}{2}}$$

F is as previously defined in equation 3.50.

Equation 3.52 can be expressed in terms of the plane wave reflection coefficient, a form that will prove of use in later sections.

The result is:

$$\Phi_t = \frac{e^{ik_1 r_1}}{4\pi r_1} + \frac{e^{ik_1 r_1}}{4\pi r_2} \left\{ Rp + B \left[(1-Rp).F(\omega) \right] \right\} \qquad 3.53$$

where B is given by:

$$B = \frac{\cos\theta_i + Mn(n^2 - \sin^2\theta_i)^{\frac{1}{2}}}{\cos\theta_i + \beta_s(1-n^{-2})^{\frac{1}{2}}/(1-M^2)^{\frac{1}{2}}} \quad \frac{(1-n^{-2})^{\frac{1}{2}}}{(1-\sin^2\theta_i/n^2)^{\frac{1}{2}}} \quad x$$

$$x \quad \frac{\left[(1-M^2)^{\frac{1}{2}} + \beta_s(1-n^{-2})^{\frac{1}{2}}\cos\theta_i + \sin\theta_i(1-\beta_s^2)^{\frac{1}{2}}\right]^{\frac{1}{2}}}{(1-M^2)^{3/2}(2\sin\theta_i)^{\frac{1}{2}}(1-\beta_s^2)^{1/4}}$$

$$F(\omega) = 1 + i\sqrt{\pi}\ \omega\ e^{-\omega^2}\ \mathrm{erfc}(-i\omega)$$

$$\omega^2 = X_o^2/2$$

$$= ik_1 r_2\left[1 + (\beta_s\cos\theta_i(1-n^{-2})^{\frac{1}{2}} - \sin\theta_i(1-\beta_s^2)^{\frac{1}{2}}/(1-M^2)^{\frac{1}{2}}\right]$$

$$\mathrm{Im}(\omega) > 0$$

Corbin has extended Paul's basic solutions to include the following boundary types:

(i) Fluid/Fluid

(ii) Porous Medium/Fluid

(iii) Fluid/Elastic Solid

(iv) Elastic solid/Elastic solid

The source and receiver may be located in either medium.

Corbin follows Banos' and Paul's work closely, and makes use of the technique of subtraction of the first order pole. Rather than repeat the development in detail it will suffice to give just the final results.

The total velocity potential is given by:

$$\Phi_t = \frac{e^{ik_1 r_1}}{r_1} - \frac{e^{ik_1 r_2}}{r_2} + \Phi\ (z_s, r, z_r) \qquad 3.54$$

where $\Phi\ (z_s, r, z_r) = V^S + V^P + V$

$$V_s = \frac{G_o(h,r)}{ik_1 r}\left[1 + c\sum_{=1}^{2} \frac{G_1(h)}{(ik_1 r)^c}\right]$$

$$V^P = \frac{i\pi k_2 M(1-n^2)^{\frac{1}{2}}}{(1-M^2)^{\frac{1}{2}}}\ e^{-\frac{X_o^2}{2}}\ H_o^1(k_1 r)\,\mathrm{erfc}(-i\frac{X_o}{\sqrt{2}}$$

$$V = \frac{F(h,r)}{(ik_2 r)^2}\left[F_o + \sum_{c=1}^{2} \frac{F_1(h)}{(ik_2 r)^c}\right]$$

$$G_o\ (h,r) = \frac{2ik_1}{\sqrt{2}(1-M^2)}\ \frac{\tau M}{\sqrt{\sigma.\lambda}}\ e^{ik_1 r}\ .\ e^{k_1 h\tau}$$

$$G_1(h) = \frac{ik_1 h}{2} + M\left[\frac{i(1-n^2)^{-\frac{1}{2}}}{2}\ .\ ik_1 h + \frac{i(1-n^2)^{-\frac{1}{2}}}{3}\ (ikh)^3\right]$$

$$+ M^2\left[\frac{-9}{128}(1-n^2) + \frac{1}{16}(7+n^2)(ik_1 h)^2 - \frac{(1-n^2)(ik_1 h)^4}{8}\right]$$

$$G_2(h) = -(ik_1 h)^2 + \frac{(ik_1 h)^4}{4} + M\left[i(1-n^2)^{-3/2}(1-4n^2)(ik_1 h)\right.$$

$$\left. - i\frac{(1-n^2)^{-\frac{1}{2}}}{6}\ (1-4n^2)(ik_1 h)^3 + 1(1-n^2)^{-\frac{1}{2}}(ik_1 h)^5\right]$$

$$F\ (h,r) = \frac{2in^2 k_2}{(1-n^2)^{\frac{1}{2}}}\ .\ e^{ik_2 r}\ .\ e^{ik_1 h(1-n^2)^{\frac{1}{2}}}$$

$$F_o = \frac{-M}{(1-n^2)^{\frac{1}{2}}}$$

$$F_1(h) = \frac{-M}{(1-n^2)^{3/2}} \left[-2(1+2n^2)+3n^2(1-n^2)^{\frac{1}{2}}(ik_1h)+6M^2n^2 \right]$$

$$F_2(h) = \frac{-n^2M}{(1-n^2)^{5/2}} \{24(3+2n^2)-3(12+13n^2)+15n^2(ik_1h)^2$$

$$\cdot (1-n^2) - M^2 \left[24(3+7n^2)-60n^2(1-n^2)^{\frac{1}{2}}(ik_1h) \right] +$$

$$+ 120\, M^4n^2 \}$$

$$X_o = i(2ik_ir) \left[\left(\frac{1-M^2n^2}{1-M^2} \right)^{\frac{1}{2}} -1 \right]^{\frac{1}{2}}$$

3.7.5 Fillipi and Habault Solution

Fillipi and Habault have also examined the two media problem [3.13]. They show that equation 3.1 can be transformed to:

$$\left[\frac{d^2}{dz^2} + K_1^2 \right] \hat{p}_1 = f(r_1t) \qquad 3.55$$

where:

$$K_1^2 = -4\pi^2 \varepsilon^2 + k_1^2$$

$$\hat{p}_1 = F(p_1) = 2\pi \int_o^\infty J_o(2\pi\varepsilon r) p_1(r,z) r dr$$

$\hat{p}_1$ is the Fourier transform of p_1, the sound pressure, in a new cylindrical coordinate system (r,Θ).

By transforming the boundary conditions, the solution to equation 3.55 becomes:

$$\hat{p}_1 = \frac{e^{ik_1(z-z_s)}}{2iK_1} + A(\varepsilon) \cdot \frac{e^{iK_1(z+z_s)}}{2iK_1} \qquad 3,56$$

where:

$$A(\varepsilon) = \frac{(\rho_2 K_1 - \rho_1 K_2)}{(\rho_2 K_1 + \rho_2 K_2} \qquad 3.57$$

$$K_2^2 = -4\pi^2 . \varepsilon^2 - k_2^2$$

The solution to the problem is obtained by inverse transformation of equation 3.56.

To simplify the inverse transformation, Fillipi and Habault expand equation 3.57 to give:

$$A(\varepsilon) = \left(\frac{1+M^2}{1-M^2}\right) + \frac{2M^2(k_2^2-k_1^2)}{(1-M^2)^2(b^2-K^2)}$$

$$- \frac{2M}{1-M^2} \cdot \frac{K_1}{K_2} - \frac{2M}{(1-M^2)^2(b^2-K^2)} \frac{K_1}{K_2} \qquad 3.58$$

where:

$$b^2 = \frac{k_1^2 - M^2 k_2^2}{1-M^2}$$

The first term of equation 3.58 can be identified with an image source of strength:

$$\frac{1-M^2}{1+M^2}$$

The second term corresponds to the field of a simple source distribution over the infinite plane $z=z_s$ and can be inverted by use of the convolution theorem. The third and fourth terms correspond to the fields of dipole distributions over the infinite plane $z=-z_s$, and can also be inverted by means of the convolution theorem.

The final solution for the total pressure at the receiver is:

$$p = \frac{e^{ik_1 r_1}}{4\,r_1} + \frac{1-M^2}{1+M^2}\,\frac{e^{ik_1 r_1}}{4\,r_1} - \frac{iM^2(k_2^2-k_1^2)}{2(1-M^2)^2}$$

$$\times \int\int_{-\infty}^{\infty} \frac{\exp\left[ik_1((x-u)^2+(y-v)^2+(z+z_s)^2)^{\frac{1}{2}}\right]}{4\pi((x-u)^2+(y-v)^2+(z-z_s)^2)^{\frac{1}{2}}}$$

$$H_o^1(b(u^2+v^2)^{\frac{1}{2}})\,du\,dv$$

$$+ \frac{M}{1-M^2}\,\frac{d}{dz}\int\int_{-\infty}^{\infty} \frac{\exp(ik_2\,u^2+v^2)}{u^2+v^2} \cdot \frac{\exp(ik_1)x-u)^2+(y-v)^2+(z-z_s)^2}{4\pi\sqrt{(x-u)^2+(y-v)^2+(z-z_s)^2}}$$

$$- \frac{iM}{4(1-M^2)^2}\,\frac{d}{dz}$$

$$\int\int\int\int_{-\infty}^{\infty} \frac{\exp(ik_2\sqrt{f^2+g^2})}{\pi\sqrt{(f^2+g^2)}} \cdot H_o\left[b((u-f)^2+(v-g)^2)^{\frac{1}{2}}\right] \cdot$$

$$\frac{\exp(ik_1\sqrt{(x-u)^2+(y-v)^2+(z-z_s)^2}}{4\pi\sqrt{(x-u)^2+(y-v)^2+(z-z_s)^2}}\quad df\,dg\,du\,dv \qquad 3.59$$

where u,v,f,g are the coordinates of the sources on the plane of integration and x,y,z are the coordinates of the receiver.

When the source and receiver are on the boundary, equation 3.59 can be simplified; because the double layer potentials reduce to the half layer density only.

Fillipi and Habault develop two asymptotic solutions, one for the near field and one for the far-field. The near field solution is:

$$p = \frac{2}{(1-M^2)} \frac{e^{ik_1 r}}{4\pi r} + \frac{2M}{(1-M^2)} \frac{e^{ik_1 r}}{4\pi r} + \frac{\rho_1{}^2 . M . (k_2{}^2 - k_1{}^2)}{2\pi (1-M^2) . \sqrt{(b^2 - k_1{}^2)}}$$

$$x \log \left[\frac{k_1 + i\sqrt{b^2 - k_1{}^2}}{b} \right] + \frac{\rho_2{}^2 M (k_2{}^2 - k_1{}^2)}{2 (1-M^2) \sqrt{b^2 - k_2{}^2}} \cdot \log \left[\frac{k_2 - i\sqrt{b^2 - k_2{}^2}}{b} \right] \qquad 3.60$$

The far field solution is:

$$p = \frac{2ik_1}{M^2 (k_1{}^2 - k_2{}^2)} \cdot \frac{e^{ik_1 r}}{4\pi r} \qquad 3.61$$

However, the range of validity of equation 3.60 has recently been questioned as discussed in section 3.8.1.

3.8 Local Reaction Solution

In many cases of practical interest, such as propagation over institutional grassland and ploughed fields, the ground surface may be assumed to be locally reacting.

Such a boundary model is advantageous because the reflection from the surface may be calculated knowing only the surface normal impedance, a quantity which is relatively easily measured. Furthermore, this impedance is independent of the angle of incidence.

A necessary and sufficient condition for use of the local reaction assumption can be obtained by comparing equations 2.27 and 2.31. Using Snell's Law the plane wave reflection coefficient for an extended reaction boundary may be written as:

$$R_p = \frac{Z \cos\theta_i - \sqrt{1 - \sin^2\theta_i / n^2}}{Z \cos\theta_i + \sqrt{1 - \sin^2\theta_i / n^2}} \qquad 3.62$$

If $|n^2| >> 1$ then the term under the square root is approximately equal to 1, and equation 3.62 becomes:

$$R_p = \frac{Z \cos\theta_i - 1}{Z \cos\theta_i + 1}$$

which is the plane wave reflection coefficient for a locally reacting boundary.

A local reaction solution can be obtained from equation 3.52 by employing appropriate conditions. The conditions are:

(i) $|n^2| >> 1$

(ii) $|\beta| < 1$

(iii) $|M^2| << 1$

Using conditions (i) and (iii), the term $M(n^2-\sin^2\theta_i)^{\frac{1}{2}}$, which appears in the definition of B, in equation 3.52, can be written as:

$$M(n^2-\sin^2\theta_i)^{\frac{1}{2}} \simeq Mn = \beta_n$$

where β_n is the specific normal admittance.

Applying these approximations to equation 3.52, the solution for a locally reacting surface can be written as:

$$\Phi_{LR} = \frac{e^{ik_1 r_1}}{4\pi r_1} + R_p \frac{e^{ikr_2}}{4\pi r_2} - \frac{k\beta_n}{4} \; x \qquad 3.63$$

$$\text{erfc}\left(\frac{-iX_o}{\sqrt{2}}\right) H_o'\left[kr(1-\beta_n^2)^{\frac{1}{2}}\right].e^{-ikh\beta_n} + V^{LR}$$

where:

$$V^{LR} = \frac{\beta_n}{2\pi} \cdot \frac{e^{ikr_2}}{r_2(\beta_n+\cos\theta_i)} \left\{ \frac{1}{\sqrt{2}} \left(\frac{1+\beta_n\cos\theta_i}{(1-\beta_n^2)^{\frac{1}{2}}\sin\theta_i} + 1 \right)^{\frac{1}{2}} + \right.$$

$$\frac{1}{ikr_2(\beta_n+\cos\theta_i)^2} \left[-(1+\beta_n\cos\theta_i) + \frac{\sin\theta_i(1-\beta_n^2)^{\frac{1}{2}}}{8\sqrt{2}} \right. \; x$$

$$1 + \left(\frac{1 + \beta_n \cos\Theta_i}{\sin\Theta_i (1-\beta_n^2)^{\frac{1}{2}}}\right)^{3/2} \left(\frac{1 + \beta_n \cos\Theta_i}{\sin\Theta_i (1-\beta^2)^{\frac{1}{2}}} + 3\right)\Bigg]\Bigg\}$$

$$\frac{X_o^2}{2} = ikr_2 \left[1 + \beta_n \cos\Theta_i - (1 - \beta_n^2)^{\frac{1}{2}} \sin\Theta_i\right]$$

$$R_p = \frac{\cos\Theta_i - \beta_n}{\cos\Theta_i + \beta_n}$$

Further simplifications may be made for particular surfaces, so for $|\beta_n^2| << 1$, the so called hard boundary, the solution becomes:

$$\Phi_{LR} = \frac{e^{ikr_1}}{4\pi r_1} + \frac{e^{ikr_2}}{4\pi r_2} \left[R_p + (1-R_p)\, F(w)\right] \qquad 3.64$$

where:

$$F(w) = 1 + i\sqrt{\pi}\ w\ e^{-w^2}\ \text{erfc}(-iw)$$

$$w = \left(\frac{ikr_2}{2}\right)^{\frac{1}{2}} (\beta_n + \cos\Theta_i) \quad \text{Im}(w) > 0$$

This solution has been derived by several authors, [3.13, 3.14, 3.15, 3.16] and their work is reviewed more completely by Attenborough et al [3.11].

In a recent paper [3.17] Habault and Filippi question the accuracy of equation 3.63 beyond terms of $O(r_2^{-1})$. They offer an alternative solution based upon surface wave and layer potential representations. The solution is:

$$\Phi_{LR} = \frac{e^{ikr_1}}{4\pi r_1} + \frac{e^{ikr_2}}{4\pi r_2} \left| R_p + \frac{2i(1+\beta_s \cos\theta_i)}{kr_2(\cos\theta_i+\beta_s)^3} \right| \qquad 3.65$$

The range of validity of this expression has been questioned [3.18], since the radius of convergence of the series is limited by the presence of a pole. As such equation 3.65 is only useful at high frequencies or large source receiver separation distances when the numerical distance, w, is greater than 1. For $|W|>5$ the difference between the solutions 3.73 and 3.74 is negligible.

3.9 Rigid Backed Layer Solution

Certain types of ground surface exhibit a reactive term of the characteristic impedance that changes sign [3.19]. This phenomenon can be displayed by a rigid backed layer. The change of sign occurs at frequencies for which the layer depth is approximately a quarter wave length.

Pao and Evans [3.20] used an asymptotic solution due to Brekhovskikh [3.21] to calculate the propagation of sound over natural ground cover. The trees and shrubs form a layer and the ground surface is assumed rigid. The total field at the receiver is given by the expression:

$$\Phi_o = \frac{e^{ikr_1}}{4\pi r_1} + \frac{e^{ikr_2}}{4\pi r_2} \left\{ R_L + \frac{1}{ikr_2} \left[\tfrac{1}{2} R_L'' (1-\cos\theta_i) - \cos\theta_i R_L' \right] \right\} \qquad 3.66$$

R_L' and R_L'' are the first and second derivatives of the plane wave reflection coefficient for a layer, with respect to $\cos\Theta_i$. An alternative expression for the third term is:

$$\frac{1}{ikr}\left[R_L'' + \cot\Theta_i\, R_L'\right]$$

where R_L' and R_L'' are derivatives with respect to Θ_i.

Pao and Evans chose to use a reflection coefficient that only accounted for a single reflection from within the layer. Their expression is:

$$R_L = \frac{\cos\Theta_i - \beta_1}{\cos\Theta_i + \beta_1} + \frac{4\beta\cos\Theta_i \cos d_t(\cos\Theta_i - \beta_2)\Psi}{(\cos\Theta_t + \beta_1\cos\Theta_i)^2(\cos\Theta_t + \beta_2)} \qquad 3.67$$

where β_1 is the specific admittance of the layer with respect to air, β_2 is the specific admittance of the layer with respect to the rigid backing Θ_t is the angle of refraction within the layer.

The function Ψ accounts for the phase change of a wave reflected from the rigid backing and is given by:

$$\Psi = \exp\left[2id\,(n^2 - \sin^2\Theta_i)^{\frac{1}{2}}\right]$$

where d is the depth of the layer.
It is not clear why Pao and Evans chose this somewhat unrealistic model; because it is relatively straightforward to employ the correct reflection coefficient as defined by equation 2.45.

Substituting for the angle of refraction $\cos\Theta_i$ gives:

$$R_L = \frac{\cos\Theta_i - \beta_s/n(n^2-\sin^2\Theta_i)^{\frac{1}{2}}\tanh(-if)}{\cos\Theta_i + \beta_s/n(n^2-\sin^2\Theta_i)^{\frac{1}{2}}\tanh(-if)}$$

$$= \frac{\cos\Theta_i - M(n^2-\sin^2\Theta_i)^{\frac{1}{2}}\tanh(-if)}{\cos\Theta_i + M(n^2-\sin^2\Theta_i)^{\frac{1}{2}}\tanh(-if)} \qquad 3.68$$

The first and second derivatives of R_L can be obtained after some tedious algebra. The results are:

$$R_L' = -\frac{2Mi}{p^2}\left[(n^2-1)(n^2-\sin^2\Theta_i)^{\frac{1}{2}}\cot(\alpha) - \cos^2\Theta_i kd \right.$$

$$\left. \operatorname{cosec}^2(\alpha)\right]$$

$$R_L'' = \frac{2Mi}{p^3}\left[(n^2-1)(n^2\sin^2\Theta_i)^{-3/2}(3\cos\Theta_i + 2(n^2-1)).\right.$$

$$\cot^2(\alpha) - 2M\cos\Theta_i(n^2-1)(n^2-\sin^2\Theta_i)^{\frac{1}{2}}\cot(\alpha) -$$

$$i\cos\Theta_i kd\left[(n^2-1)(n^2-\sin^2\Theta_i)^{-1} + 2Mi(n^2-\sin^2\Theta_i)^{\frac{1}{2}}\right].$$

$$\operatorname{cosec}^2(\alpha)\cot(\alpha) - M\cos\Theta_i kd(n^2-1)(n^2-\sin^2\Theta_i)^{-\frac{1}{2}}$$

$$\operatorname{cosec}^2(\alpha) + 2i\cos^4\Theta_i k^2d^2(n^2-\sin^2\Theta_i)^{-\frac{1}{2}}\operatorname{cosec}^4(\alpha) -$$

$$\left. 2i\cos^3\Theta_i kd\operatorname{cosec}^2(\alpha).\cot^2(\alpha)\right]$$

where: $\alpha = kd(n^2-\sin^2\Theta_i)^{\frac{1}{2}}$ and

$$P = i\cos\Theta_i\cot(\alpha) - M(n^2-\sin^2\Theta_i)^{\frac{1}{2}}$$

Thomasson has also addressed the problem of a layered boundary [3.22]. He shows that the field above a rigid backed layer can be expressed as the sum of the field above a locally reacting boundary and a correction.

The correction term is:

$$\Phi_e = \frac{\beta_s d}{2n^2} \frac{\partial}{\partial \beta_s} \left[(\beta_s^2 - 1)\Phi_{LR} + 2\beta_s^2 \Phi_H - \frac{\beta_s^2}{ik} \frac{\partial}{dz} \Phi_H \right] \qquad 3.69$$

where:

$$\Phi_H = \frac{e^{ikr_2}}{4\pi r_2}$$

and Φ_{LR} is as given in equation 3.73.

Under the condition that $|n^2| >> 1$, $\Phi_e \simeq 0$ so that the total field over the rigid backed layer equals that over a locally reacting boundary provided that the normal point admittance β_s is replaced by:

$$\beta' = \frac{n\rho_1}{\rho_2} \cdot \frac{\tan(nk_2 d)}{i} = \frac{\beta_s \tan(nk_2 d)}{i}$$

This expression is just that of the specific admittance for a rigid backed layer, as given by equation 2.46, after applying the condition:

$$(n^2 - 1 + \cos^2\theta_i)^{\frac{1}{2}} \simeq n$$

and the relationship:

$$\frac{\tan(x)}{i} = \tanh(-ix)$$

The approximation amounts to postulating that any wave refracted into the layer and reflected by rigid backing is dissipated by the layer medium.

An alternative derivation has been suggested by Habault and Fillippi [3.23] using a layer potential representation for the reflected wave. Their asymptotic solution is:

$$\Phi_L = \frac{e^{ikr_1}}{4\pi r_1} + \frac{e^{ikr_2}}{4\pi r_2}\left[R' - \frac{i}{2kr_2}\left(\frac{2Z'\cos\Theta_i}{(Z'\cos\Theta_i+f)^2}(2f+f'\cot\Theta_i + f'')\right) - \frac{4Z'}{(Z'\cos\Theta_i+f)^3}(f\sin\Theta_i+f'\cos\Theta_i)(Z'\sin\Theta_i-f')\right] \qquad 3.70$$

where:

$$R' = \frac{Z'\cos\Theta_i - f}{Z'\cos\Theta_i + f}$$

$$Z' = \frac{i\rho_2 k_1}{\rho_1 k_2} \qquad \tan(k_2 d) = \frac{i\tan(k_2 d)}{Mn}$$

$$f = K\tan(Kk_2 d)/\tan(k_2 d)$$

$$f' = \frac{\partial f}{\partial \Theta_i} \qquad f'' = \frac{\partial^2 f}{\partial \Theta_i^2}$$

$$K = (1-\sin^2\Theta_i/n^2)^{\frac{1}{2}} = \cos\Theta_t$$

R' is the plane wave reflection coefficient for the rigid backed layer, as can be shown by substituting the value for f into the expression for R'.

The authors state that for numerical solutions in the far field, only the first two terms of equation 3.70 are required. Using the next term "increases widely the validity range of this approximation". Under such conditions it is reasonable to expect that equations 3.66 and 3.70 should give similar results. In fact it is possible to show that the leading terms of these solutions are identical.

Unfortunately neither solution is valid for small separation distances, because of the existence of a surface wave pole. However, they could prove useful engineering solutions for community noise problems.

References Chapter 3

3.1 Banos, A.: Dipole Radiation in the Presence of a Conducting Half-Space.
Pergamon. 1966.

3.2 Sommerfeld. A.: Partial Differential Equations in Physics.
Academic Press. 1964.

3.3 Brekhovskikh, L.M.: Waves in Layered Media.
Academic Press. 1960.

3.4 Morse, P.M., Ingard, K.U.: Theoretical Acoustics.
McGraw-Hill. 1968.

3.5 Rudnick, I.: The Propagation of an Acoustic Wave Along a Boundary.
JASA (19) 348-356. 1947.

3.6 Hayek, S.I., Attenborough, K. and Lawther, J.M.: Sound Propagation over Absorptive Ground Planes.
Task A Report on Contract DoI-FH-11-9515. 1980.

3.7 Van der Pol, B.: Theory of the Reflection of the Light from a Point Source by a finitely Conducting Flat Mirror, with an Application to Radio telegraphy.
Physica (2) 843-853. 1935.

3.8 Norton, K.A.: The Propagation of Radio Waves over the Surface of the Earth and in the Upper Atmosphere.
Proc. IRE (24) 1367-1387, 1936 and (25) 1203-1236, 1937.

3.9 Paul, D.I.: Acoustical Radiation from a Point Source in the Presence of two Media.
JASA (29) 1102-1109. 1957.

3.10 Banos, A. and Wesley, J.P.: The Horizontal Electric Dipole in a Conducting Half Space.
University of California. Marine Physical Labs. S10 References 53-33 and 54-31. 1954.

3.11 Donato, R.J.: Propagation of a Spherical Wave Near a Plane Boundary with a Complex Impedance.
JASA (60) 34-39 1976

3.12 Corbin, J.C.: Theoretical and Experimental Investigation of Acoustic Point Source Radiation in the presence of a Reflecting and Refracting Plane. Final Report on contract NAS8-21414. 1969.

3.13 Filippi, P.J.T. and Habault, D.: Reflection of a Spherical Wave by a Plane Interface between a Perfect Fluid and a Porous Medium.
J.S.V. (56) 97-103. 1978.

3.14 Paul, D.I.: Wave Propagation in Acoustics Using the Saddle Point Method.
J. Math. Phys. (38) 1-15. 1959.

3.15 Chien, C.F. and Soroka, W.W.: Sound Propagation along an Impedance Plane.
J.S.V. (43) 9-20. 1975.

3.16 Thomasson, S.I.: Reflection of Waves from a Point Source by an Impedance Boundary.
JASA (59) 780-785. 1976.

3.17 Habault, D. and Philippi, P.J.T.: Ground Effect Analysis: Surface Wave and Layer Potential Representations.
J.S.V. (79) 529-550. 1981.

3.18 Attenborough, K.A., Heap, N.W., Richards, T.L. and Sastry, V.V.S.S.: Comments on 'Ground Effect Analysis: Surface Wave and Layer Potential Representations.
J.S.V. (to be published).

3.19 Talaske, R.H.: The Acoustic Impedance of a Layered Forest Floor. M.Sc. Thesis. Noise Control Laboratory, Pennsylvania State University, PA16802. 1980.

3.20 Pao, S.P. and Evans, L.B.: Sound Propagation over Simulated Ground Cover.
J.A.S.A. (49) 1069-1075. 1971.

3.21 3.3 p255.

3.22 Thomasson, S.I.: Sound Propagation Above a Layer with a Large Refractive Index.
J.A.S.A. (61) 659-674. 1977.

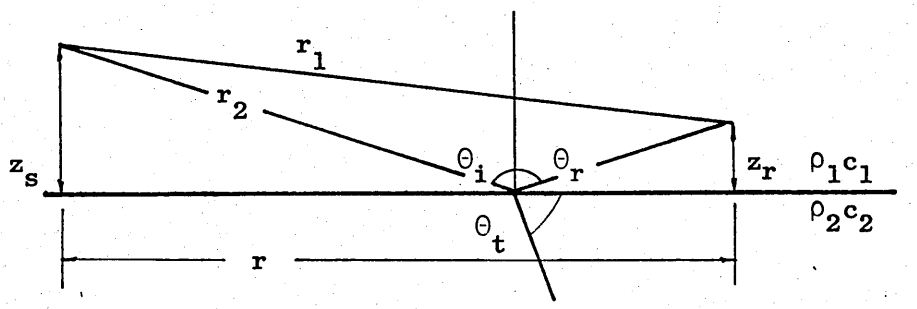

Figure 3.1
Geometry for Point to Point Propagation over an Interface between Two Semi-Infinite Media

Chapter 4

Mixed Impedance Boundaries

The solutions for propagation over a plane interface described in Chapter 3 only apply when the source and receiver are located over a continuous surface. For the most important community noise problem, road traffic, this is not the case. The receiver is usually sited over a finite impedance boundary such as the ground, but the source is located over a hard tarmacadam or concrete road.

The significance of such a surface impedance discontinuity had not been recognised until recently. The discontinuity produces a diffracted wave that interferes with the direct and reflected waves, so as to reduce the attention relative to that for a single impedance surface.

Solutions for two cases of special interest are reviewed in this chpater. The first is for a boundary composed of two semi-infinite half surfaces and the second for a rigid strip across a finite impedance boundary. A comparison of the predicted and measured values is left until Chapter 9.

4.1.2 Rasmussen's Model

The complexity of the point source model has led several authors to examine various numerical approximation techniques. Rasmussen [4.1] has proposed a method based upon Huygens principle for the decomposition of a progagating wavefront.

Consider the case shown in Figure 4.1. The source is located over the rigid half surface and the receiver over the finite impedance one. The pressure at the receiver can be calculated by summing the contributions from an array of elemental point sources. These sources are distributed across some surface located in the propagation path.

Rasmussen suggests using a vertical plane, erected normal to the ground surface, along the line of the discontinuity. Each source is located by a number pair (m,n) where m corresponds to the vertical position and n to the horizontal. The strength of each elemental source is calculated from the expression for the velocity potential over a rigid boundary, thus:

$$\Phi_{m,n} = \Phi_{i,m,n} + \Phi_{r,m,n} \qquad 4.1$$

$$\Phi_{i,m,n} = \frac{e^{ikr_{1,m,n}}}{4\pi r_{1,m,n}}$$

$$\Phi_{r,m,n} = \frac{e^{ikr_{2,m,n}}}{4\pi r_{2,m,n}}$$

The velocity potential at the receiver, Φ_t, is the sum of the contributions from the elemental sources, where each source propagates over a finite impedace boundary. The resultant velocity potential is therefore:

$$\Phi_t = \sum_{m,n} \left\{ \frac{e^{ikr_{3,m,n}}}{4\pi r_{3,m,n}} + \frac{e^{ikr_{4,m,n}}}{4\pi r_{4,m,n}} \left[Rp+(1-Rp)F\right] \right\} \qquad 4.2$$

Equation 4.2 is just a multiple application of equation 3.64, the solution for a locally reacting boundary.

Equation 3.64 assumes that each source is a point source of unit strength. A direct application of equations 4.1 and 4.2 would, therefore, give an incorrect result; because each elemental source on the vertical plane represents a fraction of the energy from a single point source. A weighting factor must be introduced to account for the pressure distribution across the vertical plane.

Rasmussen adopts a ray approach, and calculates the net outward flow through a small square surface surrounding the point source. For an area segment δa, the source strength (radiating into a half space) is given by:

$$A_{m,n} = 2(-ik + \frac{1}{r_{1,m,n}}) \frac{e^{ikr_{1,m,n}}}{4\pi r_{1,m,n}} . \quad \delta a. \quad \frac{D}{r_{1,m,n}} \qquad 4.3$$

$$+ 2(-ik + \frac{1}{r_{2,m,n}}) \frac{e^{ikr_{2,m,n}}}{4\pi r_{2,m,n}} . \quad \delta a. \quad \frac{D}{r_{2,m,n}}$$

D is the length of the normal from the source to the vertical plane.

The first term of the weighting factor is derived from the x component of the divergence of the vector field, and the ratio D/r accounts for spherical divergence.

The recommended spacing between elemental sources is 0.2λ and the vertical plane dimensions are 40λ wide and 20λ high. However, in

view of the symmetry across the vertical plane the horizontal width can be reduced by 2 and the strength of each elemental source doubled.

The excess attenuation predicted by this numerical solution compares well with results from equation 3.64 for large source receiver distances. However, the same is not true for all source receiver geometries.

Rasmussen states "it is not clear from the above considerations that the reciprocity requirement is fulfilled. However, test calculations have indicated that reciprocity is fulfilled for this calculation procedure". This statement was tested for several source-receiver geometries but the results showed that some restrictions must be imposed. In particular it was found that reciprocity does not hold for short separation distances and low frequencies. This is not surprising in view of the approximations inherent in equation 3.64, which is only valid for $kr>>1$ and $\theta_i \simeq \pi/2$.

Figure 4.2 shows the predicted excess attenuation for a source 1 m high, a receiver 0.1 m high and a separation distance of 10 m. The solid line is for the source over the rigid half boundary and the dashed line for the reciprocal case. The results are significantly different at high frequencies.

The differences arise because the angle of incidence is too large. At 100 Hz the sould wavelength is approximately 3.4 m so the heights of the elemental sources on the vertical plane range

from 0.34 m (0.1λ) to 68 m (20λ). The angle of incidence ranges from 75^{o} for the lowest elemental source to 4^{o} for the highest.

Figure 4.3 shows the predicted excess attenuation for the same two cases, but for a separation distance of 60 m. The results show very good agreement and indicate that the principle of reciprocity holds. For this increased separation distance, the range for the angle of incidence is from 87^{o} for the lowest source on the vertical plane to 23^{o} for the highest.

A recent note by Rasmussen [4.2] shows that equation 4.2 can be derived using a Green's Function solution and a surface integral. The surface corresponds to a vertical plane (or screen) extending to infinity along the line of the discontinuity.

The solution takes the form:

$$\Phi_t = \Phi_L + \iint_S \left[\Phi_L \frac{\partial \Phi_t}{\partial n} - \Phi_t \frac{\partial \Phi_L}{\partial n}\right] ds \qquad 4.4$$

where Φ_t is the velocity potential at the receiver and Φ_L is the solution for the impedance boundary.

Rasmussen chooses a Rayleigh solution for Φ_t, stating that:

$$\Phi_t \simeq 2\ \Phi_L$$

$$\frac{\partial \Phi_t}{\partial n} \simeq 2\ \frac{\partial \Phi_L}{\partial n}$$

If the screen is hard, then:

$$\Phi_t = \Phi_L - 2 \iint_S \left[\Phi_L \frac{\partial \Phi_L}{\partial n}\right] ds \qquad 4.5$$

since the screen extends to infinity, the source is obscured from the receiver and so $\Phi_t = 0$ and:

$$\Phi_L = 2 \iint_S \left[\Phi_L \frac{\partial \Phi_L}{\partial n}\right] ds \qquad 4.6$$

Substituting the appropriate values for Φ_L and $\partial\Phi_L/\partial n$, Rasmussen obtains an approximate expression for $\Phi_L(r_R/r_S)$ the velocity potential at the receiver taking into account the impedance discontinuity. The solution is:

$$\Phi_L(r_R/r_S) = 2 \int_0^\infty \int_{-\infty}^{\infty} \left[\frac{e^{ikr_1}}{4\pi r_1} + Q_1 \frac{e^{ikr_2}}{4\pi r_2}\right] \cdot$$

$$\cdot \left[(-ik + \frac{1}{r_3}) \frac{e^{ikr_3}}{4\pi r_3} x_R + (-ik + \frac{1}{r_4}) Q_2 \frac{e^{ikr_4}}{4\pi r_4} x_R\right] dydz \qquad 4.7$$

which is equivalent to the numerical solution given by equation 4.2.

This derivation assumes that Q_1 and Q_2 vary slowly with horizontal distance, therefore, it is possible to use the method of stationary phase to approximate the integral over y. For large k the solution becomes:

$$\Phi_t = x_R (8\pi k)^{\frac{1}{2}} \frac{e^{-i\pi/4}}{16\pi^2} \int_0^\infty \frac{e^{ik(r_1+r_3)}}{(r_3^3 r_1 (r_1+r_3))^{\frac{1}{2}}}$$

$$+ Q_2 \frac{e^{ik(r_1+r_4)}}{(r_4^3 r_1(r_1+r_4))^{\frac{1}{2}}} + Q_1 \frac{e^{ik(r_2+r_3)}}{(r_3^3 r_2(r_2+r_3))^{\frac{1}{2}}}$$

$$+ Q_1 Q_2 \frac{e^{ik(r_2+r_4)}}{(r_4^3 r_1(r_2+r_4))^{\frac{1}{2}}} \Big] \quad dz \qquad 4.8$$

The obvious advantage of this solution is the reduction in computational effort. Furthermore, Rassmussen states that if the solution is derived assuming the screen to be soft, it can be shown that the principle of reciprocity is satisfied. However, care must still be taken to avoid those geometries for which equation 3.64 is not a good approximate solution.

4.1.2 De Jong's Model

De Jong [4.3] has derived a semi-empirical solution based upon barrier diffraction theory. The surface is treated as an opened-out wedge-shaped barrier. The velocity potential at the receiver is given by the expression:

$$\phi_r = \frac{e^{ikr_1}}{4\pi r_1} + Q \frac{e^{ikr_2}}{4\pi r_2} + \phi_{diff} \qquad 4.9$$

where Q is the spherical wave reflection coefficient, defined by:

$$Q = R_p + (1-R_p)\, F(w)$$

with the other variables are given in equation 3.64. De Jong suggests that ϕ_{diff} can be approximated by:

$$\phi_{diff} \simeq (Q_1-Q_2)\ \{\ \frac{e^{i\pi/4}}{\sqrt{\pi}}\ \Big[\text{sign}(\pi-\chi_o-\chi)$$

$$\frac{e^{ikr_1}}{4\pi r_3}\ .\ F\Big[(k(r_3-r_1))^{\frac{1}{2}}\Big] + \text{sign}(\pi-\chi_o-\chi)$$

$$\frac{e^{ikr_2}}{4\pi r_3}\quad F\Big[(k(r_3-r_2))^{\frac{1}{2}}\Big]\}\qquad 4.10$$

where sign(α) = -1 for $\alpha < 0$

+1 for $\alpha \geq 0$

and F denotes the Fresnel integral:

$$F(\beta) = \int_{\beta}^{\infty} e^{iw^2}\,dw$$

The other variables are defined in Figure 4.4.

When the reflection point is located at the discontinuity, the solution becomes:

$$\phi = \frac{e^{ikr_1}}{4\pi r_1} + \frac{Q_1+Q_2}{2}\quad \frac{e^{ikr_2}}{4\pi r_2} - \frac{e^{-\pi/4}}{\sqrt{\pi}}\ .\ \text{sign}(\pi+\chi_o-\chi)$$

$$\frac{e^{ikr_1}}{4\pi r_2}\ F\Big[(k(r_2-r_1))^{\frac{1}{2}}\Big]\ (Q_1-Q_2)$$

For $k(r_2-r_1) \gg 1$ and source and receiver not close to the boundary the solution reduces to:

$$\phi \simeq \frac{e^{ikr_1}}{4\pi r_1} + \frac{(Q_1+Q_2)}{2}\ \frac{e^{ikr_2}}{4\pi r_2}\qquad 4.11$$

This implies that the reflected wave is described by the average of the two reflection coefficients, a finding in agreement with Morse and Ingard's plane wave solution discussed in Chapter 2.

De Jong has compared his approximate solution with both scale model and outdoor measurements and found reasonable agreement. However, Rasmussen found that the solution failed for small source and receiver heights especially at low frequencies.

4.1.3 Numerical Evaluation of the Helmholtz-Huygens Integral

Several authors have described approximate solutions based upon numerical integration of the Helmholtz-Huygen integral:

4.12

$$p(r) = p_i(r_1) + \int_s \left[G(r_2/r_1) \frac{\partial}{\partial n} p(r_2) - p(r_2) \frac{\partial}{\partial n} G(r_2/r_1) \right] ds$$

Simpson and Hothersall [4.4] propose using the following expressions:

$$p(r_1) = \frac{e^{ikr_1}}{4\pi r_1}$$

$$G(r_2/r_1) = \frac{e^{ikr_2}}{4\pi r_2}$$

Substituting these into the integral of equation 4.12, the reflected wave can be written as:

$$\phi_1 = \int_{-\infty}^{+\infty}\int_{-\infty}^{\infty} \left[\frac{e^{ikr_2}}{4\pi r_2} \frac{\partial}{\partial n} \frac{e^{ikr_1}}{4\pi r_1} - \frac{e^{ikr_1}}{4\pi r_1} \frac{\partial}{\partial n} \frac{e^{ikr_2}}{4\pi r_2} \right] ds \qquad 4.13$$

According to Skudrzyk [4.5]:

$$\frac{\partial}{\partial n}\left(\frac{e^{ikr}}{r}\right) \simeq 2\cos\Theta \ \frac{\partial}{\partial r}\left(\frac{e^{ikr}}{r}\right)$$

where Θ is the angle between the normal and r, so the solution for the reflected wave becomes:

$$\phi_r = \frac{}{2\pi} \iint_{-\infty}^{\infty} \left[\cos\Theta_i\left(1 + \frac{i}{kr_1}\right) - \cos\Theta_r\left(1 + \frac{i}{kr_2}\right)\right] \cdot \frac{e^{i(k(r_1+r_2)-\pi/2)}}{r_1\, r_2}\, ds \qquad 4.14$$

with the geometric variables as defined in Figure 4.5.

Simpson suggests that this solution can be extended to a boundary of finite impedance by introducing the plane wave reflection coefficient inside the surface integral of equation 4.14. Such an approximation is not unreasonable for $kr \gg 1$, which is a pre-condition for the validity of this solution.

Equation 4.9 can be solved numerically by dividing the surface into small elemental areas for which Θ_i, Θ_r, r_1 and r_2 can be determined. Simpson suggests that $\lambda/4$ is a reasonable side length for each elemental square and that the total surface area should be at least $2r^2$, where r is the horizontal separation distance.

Numerical evaluation of this solution for a continuous rigid boundary gives results in close agreement with the known solution. However, it tends to underestimate the negative excess attenuation at low frequencies for an impedance boundary.

The errors arise from the use of the plane wave reflection coefficient, rather than the spherical one.

Klein and Myncke [4.5] recognised such a limitation and proposed a solution based upon Thomasson's model for a locally reacting surface of finite impedance. Their solution is:

$$\phi = G(r_2/r_1) - ik \int_{s_1} G(r_2/r_1)\, \phi_T\, ds_1 \qquad 4.15$$

where ϕ_T is given by equation 3.73 and:

$$G(r_2/r_1) = \frac{e^{ikr_1}}{4\pi r_1} - \frac{e^{ikr_2}}{4\pi r_2}$$

The choice of Green's Function means that the integration is limited to the finite impedance half-surface.

Comparison between theory and outdoor experiments reported by the authors is not good, but this is claimed to be due to the effects of turbulence near the ground which creates phase instability. The interference of the direct and reflected waves is known to be particularly sensitive to this phenomenon.

4.1.4 Approximate Analytical Solutions

Asymptotic solutions for the discontinuous boundary solution have been derived by several authors. In general these solutions utilise the method of steepest descent to approximate the function under the integral to produce a result valid in the far field.

Naghieh and Høyek [4.6] use functiontheoretic methods to derive an integral equation solution to the mixed boundary problem. The integral is evaluated by replacing it with the first term of its

Taylor series and using the method of pole subtraction together with a steepest descent path contour.

The resulting solution includes a reflected wave, three diffracted waves and a surface wave due to each impedance, as well as the direct wave.

The reflected and surface waves depend upon the impedance of the surface under the receiver, whilst the diffracted waves depend on the difference of the impedance of the two planes. These findings are in agreement with the empirical model developed by De Jong.

Durnin and Bertoni [4.7] have examined the special case of both source and receiver on the ground. Starting with a Helmholtz-Huygens integral formulation, the authors use the steepest descent method to derive an approximation solution.

Rasmussen has found that the Naghieh and Hayek solution over-estimates the negative excess attenuation at low frequencies.

4.2 The Rigid Strip

4.2.1 The rigid strip set in an impedance boundary is an idealised model to the problem of aircraft noise propagation across an airfield or traffic noise propagation across a grass playing area crossed by a service road, a feature common to many multistorey blocks of flats.

A closed form solution for the wave equation for this boundary condition has not been found in the literature, but it is possible to derive an approximation solution for large source receiver separation distances.

At first sight it would appear that equation 4.9 can be modified to give three surface integral contributions for the reflected wave. The first surface extends from infinity to the near side of the strip, the second across the width of the strip and the third from the far edge of the strip to minus infinity.

Such a solution requires considerable computational effort; because the contribution from the impedance surface must be calculated by a numerical integration scheme.

4.2.2 The Greens Function Solution

An alternative solution that requires a single numberical integration across the surface of the strip. Consider the source receiver geometry in Figure 4.6, which sows a rigid strip extending from a/2 to -a/2 in the x direction and from ∞ to $-\infty$ in the y direction.

According to Green's Theorem, the velocity potential at the receiver $\Phi(r_r/r_3)$ is given by

$$\Phi(r_r/r_s) = \Phi_i + \iint_s \left[\Phi_i \frac{\partial \Phi}{\partial n} - \Phi \frac{\partial \Phi_i}{\partial n}\right] dS \qquad 4.15$$

where Φ_i is a solution of

$$(\nabla^2 + k^2)\ \Phi_i = \delta(r_r - r_s)$$

and the surface s consists of the hard and soft surfaces denoted by S_h and S_s respectively.

The contribution from the soft surface can be obtained directly as follows. On S_s, Φ_i satisfies the boundary condition

$$\frac{\partial \Phi_i}{\partial n} - ik\beta\Phi_i = 0 \text{ on the surface } z = 0$$

therefore $\frac{\partial \Phi_i}{\partial n} = ik\beta\Phi_i$, where β is the surface admittance. The soft surface is assumed to be locally reacting so that β is independent of the angle of incidence.

Substituting this expression into the soft surface integral gives

$$\iint_{S_s} = \iint_{S_s} \left[\Phi_i \frac{\partial \Phi}{\partial n} + ik\beta\Phi.\Phi_i\right] dS \qquad 4.17$$

which can be written in the form

$$\iint_{S_s} = \iint_{S_s} \Phi_i \left[\frac{\partial \Phi}{\partial n} + ik\beta\Phi\right] dS$$

The function Φ can be any single valued function whose derivatives are continuous [4.9]. Φ must satisfy the same impedance boundary condition as Φ_i on S_s hence, the integral $\iint_{S_s} = 0$.

The total velocity potential at the receiver is therefore just

$$\Phi(r_r/r_s) = \Phi_i + \iint_{S_h} \left[\Phi_i \frac{\partial \Phi}{\partial n} - \Phi \frac{\partial \Phi_i}{\partial n}\right] ds \qquad 4.18$$

A closed form solution for Φ_i does not exist, but as a first approximation one can use equation 3.64 for the local reaction boundary, denoted by Φ_{LR}.

On the rigid strip the function Φ must satisfy the condition

$$\frac{\partial \Phi}{\partial n} = 0,$$

therefore

$$\Phi(r_r/r_s) = \Phi_{LR} - \iint_{S_h} \Phi \frac{\partial \Phi_{LR}}{\partial n} \, dS \qquad 4.19$$

The surface integral is commonly referred to as the scattered velocity potential Φ_s.

The integral of equation 4.19 can only be solved approximately by making certain assumptions about the two functions Φ and Φ_{LR}. Two cases have been examined, leading to somewhat different solutions.

4.2.3 Approximate solutions for $\partial\Phi_{LR}/\partial n$ and Φ

The first approximate solution assumes that Φ_{LR} is a reasonable estimate of the Green's Function satisfying the local reaction boundary condition, hence

$$\frac{\partial \Phi_{LR}}{\partial z} = -ik\beta\Phi_{LR} \qquad \text{on } z = 0 \qquad 4.20$$

The second case requires that Φ_{LR} be differentiated explicitly. After some algebra it can be shown that

$$\frac{\partial \Phi_{LR}}{z} = \frac{-e^{ikr}}{4\pi r}\left[\frac{-ikz_s}{r} + \frac{z_s}{r^2}\right] - Q\,\frac{e^{ikr}}{4\pi r}\left[\frac{ikz_s}{r} - \frac{z_s}{r^2}\right] \qquad 4.21$$

$$- \frac{e^{ikr}}{4\pi r} \cdot \frac{\partial Q}{\partial z} \qquad \text{on } z = 0$$

where r is the horizontal separation between the source and the receiver and z_s is the source height. The term $\partial Q/\partial z$ varies slowly with height above the surface, hence it is possible to write $\partial Q/\partial z \simeq 0$.

The Rayleigh solution for Φ on the strip is just $2.\Phi_d$, that is twice the direct field [4.10]. Substituting equation 4.20 into 4.19 leads to an approximate solution of the form

$$\Phi(r_r/r_s) = \Phi_{LR} + \iint_{S_h} \left[2ik\beta\Phi_{LR}.\Phi_d\right] dS$$

Expressing the surface integral as a double integral over x and y and letting $\Phi_d = \frac{e^{ikr}}{4\pi r}$ gives

$$\Phi_s = ik\beta \int_{-\infty}^{\infty}\int_{-a/2}^{a/2} \frac{e^{ikr_d}}{2\pi r_d}\left[\frac{e^{ikr_1}}{4\pi r_1} + Q\,\frac{e^{ikr_2}}{4\pi r_2}\right] dxdy \qquad 4.22$$

where r_d is the distance from the source to the elemental surface area dxdy.

Because r_1, r_2 and Q are independant of x and y, the term in square brackets may be taken outside the integral. The scattered potential can therefore be written as

$$\Phi_s \simeq \frac{ik\beta}{2\pi} \left[\frac{e^{ikr_1}}{4\pi r_1} + Q \frac{e^{ikr_2}}{4\pi r_2}\right] \int_{\infty}^{\infty} \int_{-a/2}^{a} \frac{e^{ikr}}{r} \, dxdy \qquad 4.23$$

Substituting equation 4.21 into 4.19 reads to an expression for β_s of the form

$$\Phi_s \simeq \frac{[1-Q]}{2\pi} \left(\frac{ik}{r_d} - \frac{1}{r_d^2}\right) \frac{e^{ikr_d}}{4\pi r_d} z_s \int_{\infty}^{\infty} \int_{-a/2}^{a/2} \frac{e^{ikr}}{2} \, dxdy \qquad 4.24$$

The differences in the two solutions arise from the approximations made in deriving expressions for $\partial\Phi_{LR}/\partial n$.

The integral term of equations 4.23 and 4.24 cannot be expressed in closed form, but can be evaluated numerically on a digital computer. Care must be taken when truncating the integration along y; because the exponential term is periodic and hence r must be large to ensure that the integral tends to some limiting value.

4.2.4 Limiting Values of the Approximate Solutions

Three limiting cases can be found for the rigid strip solution:-

(i) zero width strip

(ii) infinite width strip

(iii) impedance of soft boundary $\rightarrow \infty$

Equations 4.23 and 4.24 can be shown to behave correctly in the case of $a/2 \rightarrow 0$; because the integral goes to zero. When the impedance of the boundary $\rightarrow \infty$, $\beta \rightarrow 0$ and equation 4.23 equals zero. The solution is just

$$\Phi(r_r/r_s) = \frac{e^{ikr_1}}{4\pi r_1} + Q\,\frac{e^{ikr_2}}{4\pi r_2}$$

and because Q = 1 for $\beta = 0$, this becomes the solution for a rigid boundary. Equation 4.24 also equals zero because Q = 1, and therefore the contents of the first bracket equals zero.

In the case of an infinitely wide strip, $a/2 \to \infty$, it can be shown that

$$\int_{-\infty}^{\infty}\int_{-\infty}^{\infty} \frac{e^{ikr}}{r}\,dxdy \to \frac{2\pi r}{ikz_s}$$

Substituting this value into equation 4.24 gives

$$\Phi_s \quad \frac{e^{ikr_1}}{4\pi r_1} + Q\,\frac{e^{ikr_2}}{4\pi r_2} + (1-Q)\,\frac{e^{ikr}}{4\pi r}$$

Assuming that $r_1 \simeq r_2 \simeq r$, then $\Phi_s \frac{e^{ikr}}{2\pi r}$ the solution for a source close to a rigid boundary.

Making the same substitution in equation 4.23 enables one to write

$$\Phi_s \simeq \frac{\beta^z s}{r}\left[\frac{e^{ikr_1}}{4\pi r_1} + Q\,\frac{e^{ikr_2}}{4\pi r_2}\right]$$

As $r \to \infty$ so $\Phi_s \to 0$ and the total velocity potential becomes

$$\Phi(r_r/r_s) \simeq \frac{e^{ikr_1}}{4\pi r_1} + Q\,\frac{e^{ikr_2}}{4\pi r_2}$$

the solution for a locally reacting boundary. Only by invoking the condtion $\beta \to 0$ can equation 4.23 give the correct solution in the limit $a/2 \to \infty$. If is felt that the solution should tend to the rigid boundary solution independant of β. However, numerical computation of equations 4.23 and 4.24 have shown the former to be less sensitive

of equations 4.22 and 4.23 have shown the former to be less sensitive to errors in the evaluation of the integral term.

A closed form solution to the wave equation for this boundary condition has not been found in the literature, but it is possible to derive a numerical solution for large source-receiver separation distances.

One possible solution can be obtained by modifying equation 4.9. Intead of a single surface integral, the reflected field is calculated from three. The first over the surface from the source to the first edge of the strip, the second over the strip itself and the third from the far edge of the strip to the receiver. The first and third integrals take account of the finite impedance and the second the rigid strip.

This solution requires considerable computational effort, since the contribution from the impedance surface must be calculated numerically.

can be evaluated by dividing the surface into small elemental areas and summing the contributions.

The source and receiver positions, relative to the strip are shown in Figure 4.7. The variable 'r' is the distance from the source to the elemental surface area, and is given by,

$$r = \sqrt{(D+x)^2+(y_o-y_1)^2+z_o^2}$$

The elemental surface dimensions can be specified in terms of the incident wavelength. Experience with the numerical solutions for the half soft - half rigid boundary suggest 0.2λ along the y axis and 0.01λ across the strip.

The total surface area can also be defined in terms of the wavelength, since it is reasonable to expect the diffracted wave to be concentrated about the specularly reflected ray. The symetry of the boundary means that the field need only be calculated for half the strip length in the y direction and the result doubled to obtain the total result. Once again experience suggests a maximum length of 40λ in the y direction.

References Chapter 4

4.1 Rasmussen, K.B.: Sound Propagation Over Level Terrain.
Report No. 33 Technical University of Denmark. 1982.

4.2 Private Communication

4.3 De Jong, B.A.: Rekenmodellen omde invloed te voorspellen van een asfalt-grasorergang en van de afschermung van een wal.
Technical University of Delft. 1978.

4.4 Simpson, S. and Hothersall, D.C.: Aspects of Noise Propagation in Complex Environments. Section 2.
Report on Grant No. GR/A29746 SRC. 1981.

4.5 Klein, C. and Myncke, H.: Sound Propagation over Flat Terrain with an Impedance Jump.
Inter Noise. 1981.

4.6 Naghieh, M. and Hayek, S.I.: Diffraction of a Point Source by two Impedance Covered Half-Planes.
J.A.S.A. (69) 629-637. 1981.

4.7 Durnin, J. and Bertoni, H.L.: Acoustic Propagation over Ground having Inhomogeneous Surface Impedance.
J.A.S.A. (70) 852-859. 1981.

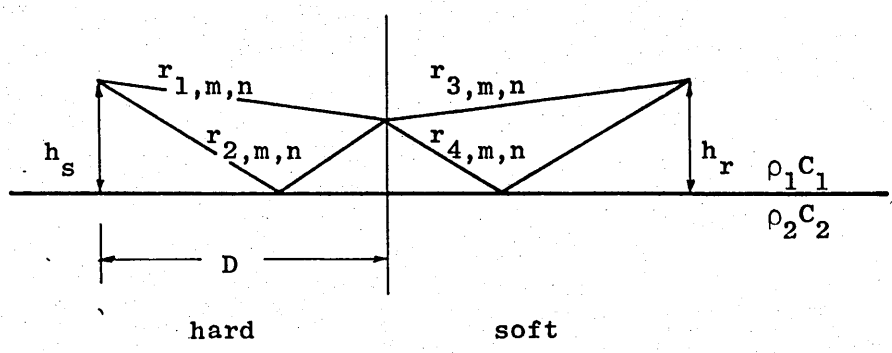

Figure 4.1
Geometry for Rasmussen's Iterative Procedure for a Half Rigid-Half Soft Boundary

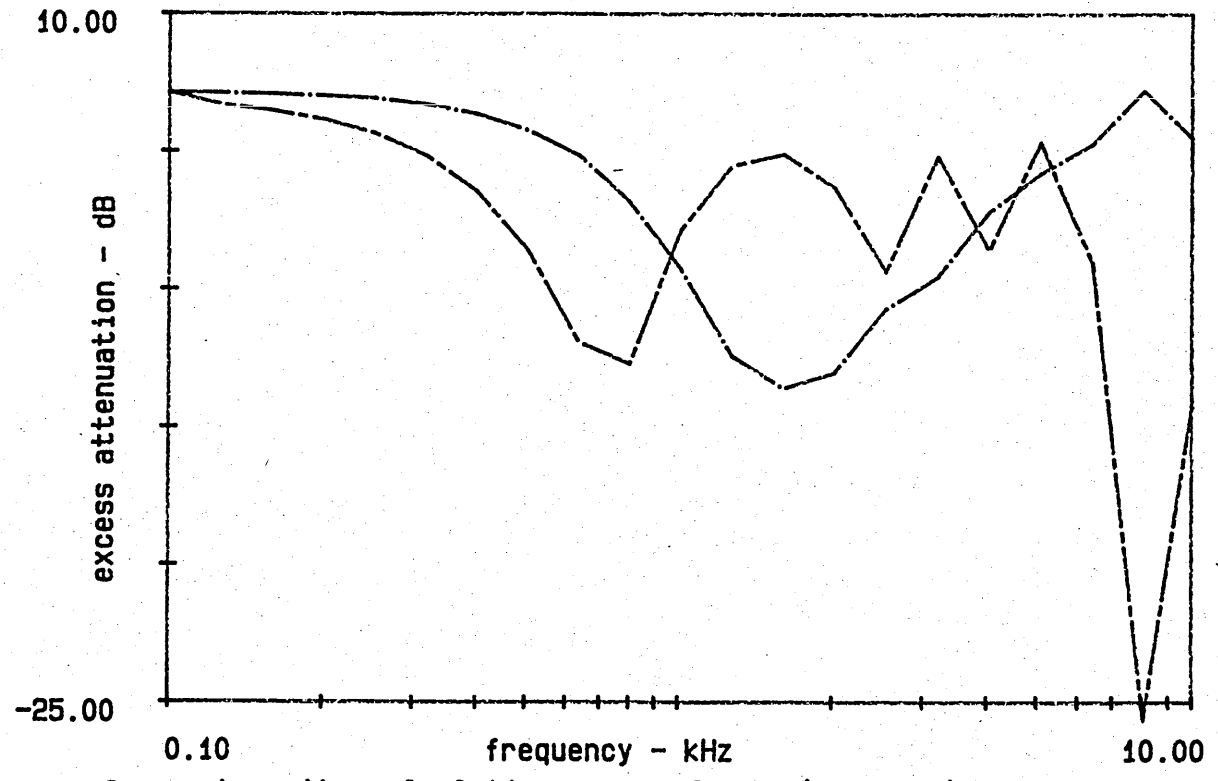

Figure 4.2 reciprocity calculation - grassland (1, 0.1, 10)

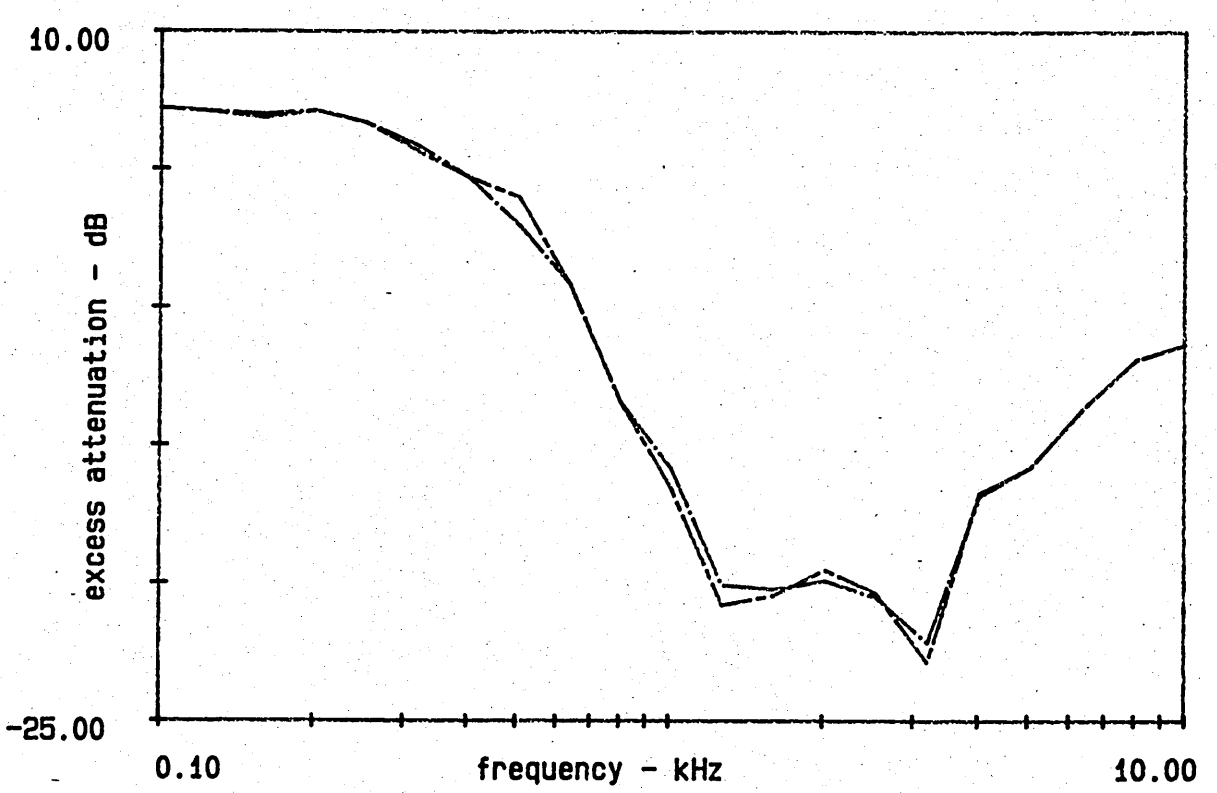

Figure 4.3 reciprocity calculation - grassland (1, 0.1, 80)

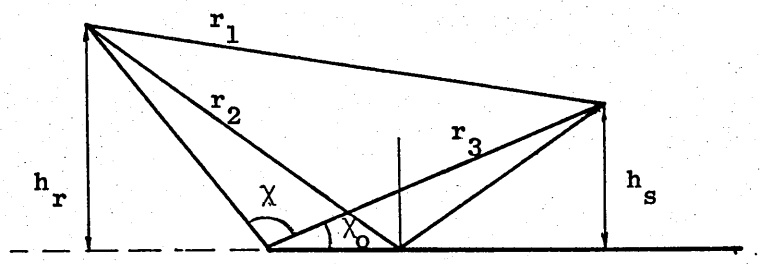

Figure 4.4
Thin Barrier Geometry for De Jong
Empirical Propagation Model

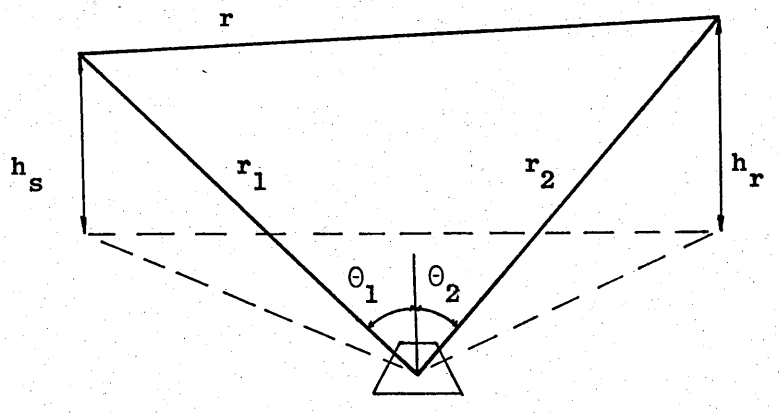

Figure 4.5
Surface Integral Geometry for Simpson and Hothersall
Discontinuous Boundary Model

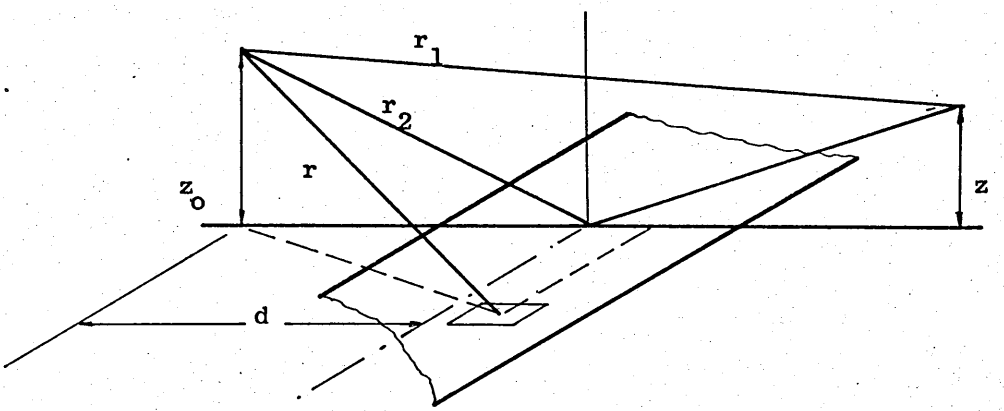

Figure 4.6
Geometry for Rigid Strip Boundary Model

Chapter 5

Methods for measuring the acoustic impedance of porous materials

The contents of the last two chapters have shown that the ground surface can be completely characterized by two complex parameters: the impedance and the propagation constant. This chapter reviews the experimental techniques for determining these parameters.

5.1 There are numerous methods for measuring the impedance of porous materials. An early review paper by Beranek [5.1] summarized many of these and a later text [5.2] described these methods in detail, discussing the advantages and disadvantages of each.

For his review, Kilmer [5.3] divided the methods into three categories:

(i) surface methods;

(ii) transmission line methods;

(iii) comparison methods.

However, advances in signal processing techniques and instrumentation have lead to the development of other methods as recently reviewed by Singh [5.4]. These can be categorized as:

(iv) indirect methods;

(v) impulse methods;

(vi) transfer function methods.

The basis for each of these methods is briefly outlined below.

5.1.1 Surface methods

This is the most fundamental of all the methods; since it tries to measure directly the surface pressure, p, and the particle velocity, u, of the material. The impedance is calculated from the ratio p/u. However, it is rarely used because of the difficulty of measuring u, which requires a pressure gradient microphone sufficiently small in size to avoid disturbing the sound field at the surface.

5.1.2 Transmission line methods

All the methods in this category rely upon measuring the interference pattern set up by the direct and reflected pressure waves in front of the material under investigation. The impedance is calculated from the expression

$$Z = \frac{1 + R_p}{1 - R_p} \qquad 5.1$$

where R_p is the plane wave reflection coefficient.

Transmission line methods have been used extensively to measure the impedance of the ground surface and will be examined in greater detail later.

5.1.3 Comparison methods

The techniques in this category make use of an acoustic bridge, analogous to the electrical impedance bridge. Consider the Impedance bridge circuit shown in Figure 5.1. If no current flows between A and B the circuit is said to be in balance, therefore

$$Z_x = Z_1 . \frac{Z_2}{Z_3}$$

To measure the unknown impedance Z_x, Z_2 and Z_3 are normally given fixed equal values, and Z_1 is varied until the bridge balances.

For an acoustic bridge, balance is achieved when there is no net pressure differential between the equivalent points A and B, and hence no volume flow.

Although the theory is very simple, practical bridges are difficult to construct and use because of the problem of producing a variable impedance Z_1. Z_2 and Z_3 are often electrical networks, rather than acoustic elements; since it is easier to produce a wide range of controlled impedance values from electrical components.

Practical versions of the bridge have been described in the literature [5.5, 5.6], but they have not gained wide acceptance.

5.1.4 Indirect methods

These methods have been developed to enable one to determine the specific impedance of a material for oblique angles of incidence [5.7, 5.8]. Measurements of the pressure above the surface are compared with theoretical predictions. By

adjusting various parameters in the theory, it is possible tc obtain some measure of agreement between the measured pressure field and the theoretical prediction and hence obtain a value for the surface impedance.

The technique is extremely questionable since there are more unknowns than can be determined by the available equations. However, by limiting the range of these variables it has been possible to obtain reasonable agreement with the results obtained from other methods.

5.1.5 Impulse methods

The specific normal impedance of a material is related to the reflection coefficient R_p by the expression

$$Z = \frac{1 + R_p}{1 - R_p}$$

hence the impedance can be calculated from a measured reflection coefficient.

The direct and reflected sound can be separated either in the time or space domains if a short duration signal is used to generate the incident pressure wave. Once separated, a simple division is all that is required to measure the reflection coefficient.

The methods can suffer from signal-to-noise ratio problems, especially over hard surfaces, due to the limited energy that can be generated with a pulse. In addition, they are difficult to use at near grazing incidence because of the small path length (and therefore time) difference between the arrivals of the direct and reflected pulses.

5.1.6 Transfer function methods

These methods are really a further development of the impulse methods, but since they use steady-state signals do not suffer to the same extent from signal-to-noise ratio problems.

Consider the two port system shown in Figure 5.2. x(t) is the input to the system, y(t) the output and h(t) is the impulse response of the system. If x(t), y(t) and h(t) have Fourier transforms X(f), Y(f) and H(f) respectively, it can be shown that

$$H(f) = Y(f)/X(f) \qquad 5.2$$

H(f) is called the complex transfer function and is equal to the reflection coefficient.

Although not new, transfer function methods have only recently become popular because of the advent of digital spectrum analysers, which enable measurements to be carried out quickly and reliably.

5.1.7 The Hibert Transform Method

A Legeay [5.9] has recently outlined another indirect method, based upon the Hilbert Transform.

Under certain conditions the magnitude and phase of the reflection coefficient of a surface are inter-dependant and related by the Hilbert Transform. In particular the phase of the reflection coefficient can be calculated from its magnitude using the expression:

$$\Theta(\omega_o) = \frac{1}{\pi}\int_{-\infty}^{\infty} \frac{\mathrm{Log}|R(\omega)|}{\omega-\omega_o}\,\partial\omega$$

where $|R(\omega)|$ is the magnitude of the measured reflection coefficient. In general the magnitude of the reflection coefficient can be measured more accurately than the phase; because it is not influenced by errors in estimating the surface height. This method would therefore appear to offer some advantage over the alternatives, especially for estimating the phase at high frequencies.

Unfortunately the Hilbert Transform relationship only holds for minimum-phase systems. Such systems are characterised by transfer functions that have no zeros in the right-hand half of the complex 'S' plane, that is: the real part of the zero must be negative.

There is no apriori reason why porous materials should be minimum phase, hence Legeay goes on to show that it is possible to express any reflection coefficient as the cascade of a minimum phase component and several all-pass components. Each all-pass component is used to cancel the effect of one of the zeros in the right half of the plane and the combined effect of the all-pass components is to reduce the system to one of minimum phase.

The location of the zeroes can be estimated from the magnitude of the reflection coefficient, and the sign of the phase shift at the zero. An appropriate set of all-pass components can be defined from this information and combined with the measured reflection coefficient $R_m(\omega)$ to produce a new estimate $R'(\omega)$, that is:

$$R'(\omega) = R_m(\omega) * A_2(\omega) \ldots A_n(\omega)$$

where $A_n(\omega)$ represents the frequency response of the nth all-pass component $|R'(\omega)|$ can be used to calculate a new phase estimate for the reflection coefficient of the material.

Legeay shows that the results calculated using this technique are comparable to those obtained by an impedance tube.

5.2 Measuring the impedance of modelling materials

One of the major tasks of this study has been the experimental evaluation of the prediction theories presented in Chapters 2 and 3. As already explained it was decided to conduct this evaluation with the aid of laboratory models rather than full scale measurements outdoors.

The measurement methods chosen were influenced by the choice of modelling frequencies and the available instrumentation used to conduct the tests. Of the methods discussed in the previous section, categories (i) and (iii) were eliminated because the necessary exerpimental rigs were not readily available. Of those remaining all have been used, albeit over a restricted frequency range in the case of some of them.

The following sections examine the chosen methods in more detail and discuss some of their limitations in the context of measuring the impedance of modelling materials.

The bandwidth of the measurements was set at 1-100 kHz. The lower limit was chosen on the basis of the performance of the anechoic chamber and the low frequency output power of the model noise sources. The upper limit was set by the bandwidth of the available instrumentation.

The methods that will be described are:

(i) standing wave tube;
(ii) free field interference;
(iii) indirect;
(iv) impulse;
(v) transfer function.

5.3 The standing wave tube

The standing wave tube (impedance tube) method is probably the most widely used technique for measuring the acoustic absorption and impedance of porous materials. The first experiments were conducted around 1902. The tube itself may be either square or circular in cross-section.

The technique requires the probing of the standing wave in front of the sample to determine the ratio of the sound pressure at the maxima and minima, the standing wave ratio, and the position of the first minimum with respect to the sample surface. The sample is normally held at one end of the tube with its surface normal to the tube axis. The acoustic source is located at the other end of the tube. A small diameter probe tube is used to measure the pressure variations along the length of the tube.

Such standing wave tubes have been used to measure the impedance at oblique angles of incidence [5.13]. However, the discussion here will be restricted to the case of normal incidence.

The basic equations for the impedance tube will be developed and solved, and in later sections the effects of tube attenuation, probe end correction, frequency stability and sample fixing will be discussed. These factors are especially important when measuring the relatively high impedances associated with ground surfaces.

5.3.1 Rigid termination

The simplest case to examine is that for a rigidly terminated loss-less tube. Since there is no energy lost at the reflecting surface, the reflected wave equals the incident wave. Consider a plane wave travelling along the axis of the tube. The pressure of the incident wave can be expressed as

$$p_i = P_o\, e^{i(kx-\omega t)}$$

If there are no tube losses the reflected wave is given by

$$p_r = P_o\, e^{i(-kx-\omega t)}$$

The total pressure at any point x along the tube is the sum of the incident and reflected waves, that is

$$p(x) = P_o\, e^{-i\omega t}\left[e^{ikx} + e^{-ikx}\right]$$

Dropping the time dependent term and using well known trigonometric identities, the presssure at the surface x = 0 can be written as

$$p(x) = 2P_o \cos(kx)$$

The volume velocity u can be calculated from the expression

$$u(x) = \frac{-1}{i\omega\rho} \frac{dp}{dx}$$

$$= \frac{-2P_o}{i\rho c} \sin(kx)$$

Since the pressure and normal velocity must be constant across the surface, the impedance of the surface must equal the ratio p/u, therefore at x = 0

$$Z_s = p/u = i\rho c\ 2 \cot(kx)$$

$$Z_s = \infty$$

The pressure along the tube will vary between 0 and $2P_o$. The maxima will occur at the points for which cos(kx) = 1 and the minima will occur at points for which cos(kx) = 0.

5.3.2 Non-rigid termination

In this case some of the incident energy will be absorbed by the sample. Furthermore, the material may introduce a phase shift between the incident and reflected waves. Assuming a reflection coefficient of the form $P_o e^{-\gamma}$, the total pressure in the tube can be written as

$$p(x) = P_o\left[e^{ikx} + e^{-ikx-\gamma}\right]$$

The volume velocity u is

$$u = \frac{P_o}{\rho c}\left[e^{ikx} - e^{-ikx-\gamma}\right]$$

The surface normal impedance of the sample at $x = 0$ can be shown to be given by the expression

$$Z_s = \rho c\left[\frac{1 + e^{-\gamma}}{1 - e^{-\gamma}}\right] \qquad 5.3$$

Rearranging this equation it is possible to separate the real and imaginary parts of the impedance. They are:

$$R_s = \frac{\rho c \tanh(\gamma'/2)\left[1 + \tan^2(\gamma''/2)\right]}{\tanh^2(\gamma'/2) + \tan^2(\gamma''/2)} \qquad 5.4(a)$$

$$X_s = \frac{\rho c \tan(\gamma''/2)\left[\tanh^2(\gamma'/2) - 1\right]}{\tanh^2(\gamma'/2) + \tan^2(\gamma''/2)} \qquad 5.4(b)$$

where

$$\gamma = \gamma' + i\gamma''$$

5.3.3 Non-rigid termination and tube attenuation

The effect of conducting measurements within a tube is to introduce additional energy dissipation. Air viscosity, non-smooth walls, non-rigid walls and air absorption all introduce attenuation over and above that due to a non-rigid sample.

The simplest way to account for these losses is to introduce an additional attenuation factor α, so that the incident pressure wave becomes

$$p_i = P_o e^{ikx_1} . e^{-\alpha x_1}$$

and the reflected pressure becomes

$$p_r = P_o e^{-ikx_2-\gamma} . e^{\alpha x_2}$$

The total pressure in the tube can then be written as

$$p(x) = P_o \left[e^{ikx_1-\alpha x_1} + e^{-ikx_2+ x_2-\gamma} \right]$$

The volume velocity is obtained by differentiating to give

$$u(x) = \frac{-i(ik-\alpha)}{\omega\rho} P_o \left[e^{ikx_1-\alpha x_1} - e^{-ikx_2-\alpha x_2-\gamma} \right]$$

and the surface normal impedance at x = 0 is given by

$$Z_s = \frac{\omega\rho}{(k-\alpha)} \quad \frac{1 + e^{-\gamma}}{1 - e^{-\gamma}}$$

Dividing through by k this becomes

$$Z_s \doteq \frac{\rho c}{1 - \frac{\alpha}{k}} \left[\frac{1 + e^{-\gamma}}{1 - e^{-\gamma}} \right]$$

The effect of tube attenuation is therefore to introduce a factor $k/(k - \alpha)$ into the impedance.

An approximate expression for α, due to Kirchhoff [5.14], is

$$\alpha = 2.77.10^{-5} \, f^{\frac{1}{2}}/r \quad \text{nepers/cm}$$

where

c = the speed of sound in air

f = frequency of excitation

r = radius of tube in cms

However, experimental measurements suggest values of α calculated from this expression should be increased by 15%. Beranek [5.1] quotes an experimental value for α of

$$\alpha = 3.18.10^{-5} \, \frac{f^{\frac{1}{2}}}{r} \quad \text{nepers/cm}$$

To this value must be added a correction for air absorption along the tube.

ASTM document C 384-58 gives the following expression for α

$$= 2.95 \; 10^{-5} \; \frac{f^{\frac{1}{2}}}{r} \quad \text{nepers/cm}$$

5.4 Corrections to measured values of the standing wave ratio

5.4.1 Tube attenuation

The surface normal impedance cannot be measured directly with an impedance tube. Instead one measures the standing wave ratio and the phase shift to obtain the reflection coefficient and hence the impedance from equation 5.1.

Consider first the case of a non-rigid termination and no tube attenuation. To calculate the surface normal impedance Z_s, it is only necessary to calculate the value of γ. Kilmer has shown that

$$e^{-\gamma'} = \frac{10^{L/20} - 1}{10^{L/20} + 1} \qquad 5.6$$

and

$$\gamma'' = \pi(1 - 2d) \qquad 5.7$$

where L = standing wave ratio (dB) = $20 \log_{10}(1/r)$ $r = \frac{|P_{min}|}{|P_{max}|}$

$$d = \frac{x_{min\ 1}}{x_{min\ 2} - x_{min\ 1}}$$

$x_{min\ 1}$ = distance from sample surface to first pressure minimum

$X_{min\ 2}$ = distance from sample surface to second pressure minimum

For the case of non-rigid termination and tube attenuation it is not possible to obtain a direct solution. Instead Kilmer uses a pragmatic approach to develop a graphic solution. Two standing wave ratios are measured.

$$L1 = SPL_{max} - SPL_{min\ 1}$$

$$L2 = SPL_{max} - SPL_{min\ 2}$$

SPL_{max} is the sound pressure level of any maximum along the length of the tube, $SPL_{min\ 1}$, is the sound pressure level at the first minium and $SPL_{min\ 2}$ is the level at the second minimum.

By plotting the graph of L-L1 versus L1-L2, shown in Figure 5.3, it is possible to obtain an estimate of L based upon the measured values of L1 and L2. Kilmer found that the relationship between L-L1 and L1-L2 was independent of frequency, but dependent upon the phase angle of the reflection coefficient.

Morse [5.15] has suggested an alternative scheme for correcting the measured standing wave ratio for tube attenuation. He recommends plotting the measured pressures of the maxima and minima on semi-logarithmic graph paper and extrapolating the values to x = 0 to give the value of L.

Ando [5.16] and Joffe [5.17] have also proposed extrapolation schemes to account for the effects of tube losses which can introduce significant errors into the impedance estimate for hard surfaces. In view of the similarity of the two methods, only Ando's will be described here.

Figure 5.4 shows the sound pressure within the tube as a function of distance from the sample surface. The magnitude of the minima decrease S with increasing distance from the surface because of the tube/air attenuation factor $e^{-\alpha x}$. Ando shows that provided $2\alpha x_n \leq 0.1$ the reflection coefficients calculated for each successive minimum will lie on a straight line as shown in Figure 5.5. The reflection coefficient at the surface x = 0 can be obtained by extrapolating this straight line to the $|R|_N$ axis.

The attenuation coefficient can be obtained from the slope of the line which is given by

$$\text{slope} = -2\alpha|R|$$

The argument of the reflection coefficient can be calculated for any minimum location using the expression

$$\gamma'' = (2n + 1)\pi - 2kx_n + \delta_n \quad (n = 0,1,2\ldots) \qquad 5.8$$

where

$$\delta_n = \sin^{-1}\{ \frac{\alpha}{2k} [\frac{e^{2\alpha x_n}}{R} - \frac{|R|}{e^{2\alpha x_n}}] \}$$

The main advantages of this method are its simplicity and the fact that α need not be estimated prior to extrapolation and correction. Ando shows that the estimated values of α tend to be greater than the measured, and suggests this may be due to the fact that the actual value of α is determined by the conditions of the tube and the gas within it.

5.4.2 Probe end correction

When a small diameter probe tube is used to sample a pressure field, the pressure measured is not that at the end of the tube, but rather the pressure some small distance beyond its end. Morse [5.15] states that this effect is due to the interaction of the column of air within the tube and the mass of air outside.

The implications for the impedance tube are that the measured distances for the positions of the maxima and minima will be incorrect, and hence the calculated phase shift γ'' will be in error. There are several equations that enable one to estimate a correction for the effect of an unflanged small diameter tube.

Morse [5.15] suggests that for a tube length less than half a wave length the end correction is approximately

$$c_e = -1.4a - 1.6a$$

independent of frequency, whilst [5.18] gives

$$c_e = -a(0.11ka - 0.64)$$

a function of frequency. a is the radius of the probe tube.

ASTM document C384-58 recommends that the end correction be measured in a tube with a rigid termination. If the measured distances to the first and second minima are d_1 and d_2 respectively, then the actual distances x_1 and x_2 are given by

$$x_1 = d_1 - c_e$$

$$x_2 = d_2 - c_e$$

For a rigid termination $x_1 = x_2/3$, from which it can be shown that

$$c_e = d_1 - 0.5(d_2 - d_1) \qquad 5.9$$

5.4.3 Frequency stability

Experimental experience has shown that it is essential to monitor the frequency of excitation and the air temperature within the tube, otherwise the calculated wavelength may be erroneous. Two temperature related factors contribute to the error.

(i) The temperature of the air mass in the tube may differ from that outside, hence the velocity of sound and therefore the wavelength calculated from the outside air temperature will be in error.

(ii) The frequency of the driving oscillator will drift with temperature, as well as other factors.

An estimate of the size of the error can be obtained by considering the percentage error in the wavelength due to a change in temperature. The speed of sound, C, is given by

$$C = 331.15.(1 + t/273.15)^{\frac{1}{2}} \qquad 5.10$$

where t is the ambient air temperature in ^{o}K above $0^{o}C$. A 5% change in temperature produces a 0.29% change in wavelength. At 1 kHz this would produce a 2 mm error in the wavelength or a 2^{o} error in the phase estimate of the impedance.

However, it would appear that temperature alone cannot account for the observed discrepancies. Other factors that might be taken into account are:

(a) Dispersion - the Rayleigh, Kirchhoff, Helmholtz model for wave motion in a cylindrical tube allows for the possibility of a complex velocity of sound which is frequency dependent.

(b) Viscosity - the interaction of a viscous fluid, in this case air, and a rough tube wall will produce a non-uniform velocity profile across the tube.

(c) Non-rigid - if the walls of the tube are not rigid they will radiate energy to the outer air. Morse and Ingard [5.19] show that for flexible walls the velocity in the tube will differ from that in free air, and the effect is frequency dependent.

However, it is not intended to examine these factors further in this study.

5.4.4 Sample fixing

The measured phase of the surface normal impedance is sensitive to errors in the location of the sample surface, especially at high frequencies. For plastic foam or rigid framed materials the acoustic surface is normally taken to be the actual surface of the sample. Tufted and high-impedance samples, such as grassland, present a much greater problem; because the active surface appears to lie somewhere between the backing material (e.g. soil) and the end of the tufts. The effect of surface mislocation is to produce a large scatter in the estimates of the surface impedance. This scatter can be reduced by varying the nominal surface location by a few millimetres [5.20].

Edge conditions may also have a significant effect; since the theory assumes an exact fit between the tube walls and the sample. Cutting and fitting rigid framed materials is straight forward, but flexible samples present several problems. the cutting may compress the sample thereby increasing its impedance at the edges. If the sample is cut oversize, the edges may become clamped during fitting and an air gap introduced behind the sample. When this air gap equals a quarter wave length the backing changes from rigid to soft, thus invalidating the equations for the pressure distribution in the tube.

When the sample is cut undersize, air may penetrate down the sides and behind the sample. The impedance seen by the pressure wave will be a combination of that of the sample and the rigid backing.

Donato [5.21] has made an attempt to analyse the effects of edge clamping, but the results are inconclusive.

5.5 Limitations of the standing wave tube

The equations derived in the last section are based upon plane wave propagation within the standing wave tube. At sufficiently high frequencies it is possible to excite transverse modes within the tube and so produce particle motion parallel to the sample surface. According to Rayleigh [5.22] the first transverse mode occurs at a frequency whose wave length equals 3.41 times the radius of the tube. Beranek [5.2] states that for axial excitation this first mode is not excited, so the frequency range may be increased by a factor of two. However, the work reported in this study assumed the lower limit as the basis for calculating the maximum usable frequency in the tube.

The lower frequency limit of a tube is dictated by the need to measure at least one minimum, preferably two, and is determined by the tube length. In order to use the correction techniques to compensate for tube attenuation, it was decided to measure the location of at least two minima thus necessitating a minimum length of half a wave length.

The minimum tube length and maximum diameter required to cover the range of frequencies of interest for modelling are:

Frequency	Minimum length m	Maximum diameter m
1 kHz	170.10^{-3}	200.10^{-3}
100 kHz	$1.7.10^{-3}$	2.10^{-3}

The values quoted above are based upon a velocity of sound of 340 m/s.

The problems associated with the construction and use of a 2 mm diameter tube ruled out the use of the standing wave method to measure the impedance of the modelling materials over the full frequency range. Instead a commercial tube, B & K 4002, was used over the range 0.2-6.5 kHz.

One further limitation of the standing wave tube is that it cannot be used to measure the impedance of very hard materials. Table 5.1 shows the absorption coefficient as a function of L, from which it can be seen that for $\alpha < 0.01$, $L > 50$ dB. To achieve a 50 dB signal-to-noise ratio within the tube can be difficult.

Table 5.1

L/dB	a
5	0.92
10	0.73
15	0.51
20	0.33
25	0.20
30	0.12
35	0.07
40	0.04
45	0.02
50	0.01

5.6 Free Field Interference Method

The free-field interference method has been used extensively to measure the angular dependance of the impedance of porous materials. A sample of the material, large enough to avoid edge diffraction effects, is mounted on a rigid backing through which a small probe tube may pass. The whole apparatus is housed in an anechoic chamber to minimise unwanted reflections.

The technique was first described by Ingard and Bolt [5.23] and subsequently revised and modified by others [5.9, 5.24]. The analysis described here is that due to Sides and Mulholland [5.11].

Consider a point source S_1 located above the surface and inclined at an angle Θ to the normal and its image S_2, as shown in Figure 5.6. The total pressure at a point x above the surface is the superposition of the direct and reflected waves such that:

$$p = \frac{P_i}{r_i} e^{ik(r_1-ct)} + \frac{P_r}{r_2} e^{ik(r_2-ct)} \qquad 5.11$$

where P_i and P_r are the amplitudes of the direct and reflected waves respectively.

If $x \ll h$ then p may be written in the form:

$$p = \frac{P_i}{h} e^{i(kh-\omega t)} \left[\frac{e^{-ikx\cos\Theta}}{1-\frac{x}{h}\cos\Theta} + \frac{P_r}{P_i} \frac{e^{ikx\cos\Theta}}{1+\frac{x}{h}\cos\Theta} \right] \qquad 5.12$$

which can be shown to reduce to:

$$p = \text{constant} \left[\cosh^2\left(x+\frac{x}{h}\cos\Theta\right) - \cos^2(\beta - kx\cos\Theta) \right]^{\frac{1}{2}} \qquad 5.13$$

The normal impedance of the layer is given by:

$$z(\Theta) = \frac{\rho_c \tanh(x+i\beta)}{\cos\Theta(1+i/kh)} \qquad 5.14$$

If the standing wave ratio and the distance to the first minimum are found, then x and β are given by:

$$\beta = \pi + kd_1\cos\Theta \qquad 5.15$$

$$x = \frac{\log_e}{2} \left[\frac{e^{-(d_1\cos\Theta)/h} + r.e^{-(d_2\cos\Theta)/h}}{e^{(d_1\cos\Theta)/h} - r.e^{(d_2\cos\Theta)/h}} \right] \qquad 5.16$$

where $d_2 = d_1 + \lambda/4\cos\Theta$, $r = |p_{min}| \; / \; |p_{max}|$ and λ is the wavelength of the source.

The real and imaginary parts of the impedance can be obtained by separating the expression for $z(\Theta)$ and substituting for β to give:

$$R = \frac{\rho c \; kh\left[kh \sinh 2\alpha + \sin(2kd_1\cos\Theta)\right]}{2\cos\Theta(1+k^2h^2)\left[\cosh^2\alpha - \sin^2(kd_1\cos\Theta)\right]} \qquad 5.17$$

$$X = \frac{\rho c\, kh\left[\sin 2\alpha + \sin(2kd_1\cos\theta)\right]}{2\cos\theta(1+k^2h^2)(\cosh^2\alpha - \sin^2(kd_1\cos\theta))} \qquad 5.18$$

Under the condition that $h\to\infty$, a plane incident wave approximation can be used to simplify the expressions for R and X, hence:

$$R_\theta = \frac{\rho c\ 2r\ \sec\theta}{1+r^2-(1-r^2)\cos(2kd_1\cos\theta)} \qquad 5.19$$

$$X_\theta = \frac{\rho c(1-r^2)\sin(2kd_1\cos\theta)\sec\theta}{1+r^2-(1-r^2)\cos(2kd_1\cos\theta)} \qquad 5.20$$

As with the standing wave tube, corrections must be applied to the measured standing wave ratio and the distance to the first minimum.

One major limitation of the free field techniqnes described is that they cannot be used for grazing angles of incidence or for measurements near the surface.

5.7 Indirect methods

The need to measure the acoustic impedance at grazing angles of incidence has led to the development of the so-called 'indirect method' of estimation. The technique is straightforward, but does require the existence of an adquate model for predicting the sound pressure at a point above the surface, such as those described in Chapter 3.

A source and receiver are positioned close to the ground surface, and the received pressure is measured as a function of frequency. This is compared to the pressure predicted by a theorectical model using surface impedance as an input variable.

Obviously this method requires an initial estimate of the surface impedance, or preferably upper and lower bounds. Thomasson [5.8] has proposed a technique for deriving this first estimate based upon a four parameter model of a homogeneous ground. This model enables one to express the admittance as a function of the four parameters a, b^1, c^1 and d such that:

$$\beta = a(b^1/c^1)\tan(b^1c^1f/d)/i \qquad 5.21$$

where:

$$a = \rho_o c_o \left|K\rho\Omega\right|^{\frac{1}{2}}/\rho$$

$$b = \arg\left[(K\rho)^{\frac{1}{2}}\right]$$

$$c = \sigma/\rho$$

$$d = \left[\left|K\rho\,\Omega\right|^{\frac{1}{2}} 2\pi z_1\right]^{-1}$$

$$b^1 = e^{ib}$$

$$c^1 = \left[1+ic(2\pi f)^{-1}\right]^{\frac{1}{2}}$$

$$0 < \arg(c^1) < \pi/4$$

a approaches the specific characteristic impedance at high frequencies, 2b is the phase angle of the complex compressibility, c is the ratio flow resistivity to effective density and d is inversely proportional to thickness.

The other input parameters for the model are:-

c_o velocity of sound in air

K compressibility of the fluid in the layer (may be complex)

Ω porosity of the layer

σ the specific flow resistivity of the layer

ρ dynamic air density

ρ_o density of air

By adopting a fixed source-receiver geometry, it is possible to calculate a set of theoretical response curves for different values of the four parameters a, b^1, c^1 and d. Comparing the measured response with this set of predicted ones, it is possible to obtain estimates for the upper and the lower bounds of the four parameters. A computer program can be used to search between these bounds for the best fit between measured and predicted pressure responses.

Thomasson also tried admittance models based on only three parameters, but claims that although simpler to use because of the reduction in the degrees of freedom, they were more difficult to apply to the experimental data.

Bass and Bolen [5.25] have used a similar scheme for estimating surface admittance, but based upon Donato's prediction model. They adjust the real and imaginary parts of the admittance so as to minimise the square of the error between measurement and prediction. However, even though this method only requires two input variables to the predictive model, it can still

be difficult to obtain consistent results for the final estimate of admittance, due to the number of degrees of freedom.

A third scheme, and the one adopted for this study, utilises an empirical model for surface impedance developed by Delany and Bazley [5.26].

They performed an analysis of fibrous porous absorbents covering various grades of glass fibres and mineral wools. The surface impedance and flow resistivity of these materials were measured and regression analysis used to obtain a power law relationship between them. These relationships are, in Mks units:

$$R/\rho c = 1+0.0571.C^{-0.754}$$
$$X/\rho c = 0.087.C^{-0.732} \qquad 5.22$$

where:

$C = f\rho/\sigma$

σ = flow resistivity

f = frequency

ρc = characteristic impedance of air

k_o = wavenumber in air

ρ = density of air

Power law relationship were also established for the real and imaginary parts of the complex propagation constant $\gamma = \gamma' + \gamma''$ of the porous material. They are:

$$'/k_o = 1+0.0978.C^{-0.7}$$
$$''/k_o = 0.189.C^{-0.595} \qquad 5.23$$

The obvious advantage of this ground surface model is that only one input variable, the flow resistivity is required to calculate the predicted pressure response.

Initial values of the flow resistivity can be established by comparing the porosity of the unknown surface to a known one, or using a table of flow resistivity such as that produced by Embleton and Piercy 5.34 given below.

Table 5.2 Ground Surface Flow Resistivity

Ground Cover	Flow Resistivity Mks Units x 10^3
snow	2 - 20
forest floor	25 - 50
ploughed and disked sandy loam	≃ 50
grassland	150 - 300
settled earch with weed cover	800 - 1000
limestone chips ½" - 1"	800 - 2000
hard compacted quarry dust	1000 - 2000
compacted sandy silt	≃ 1000
concrete and mature asphalt	> 20 000

Porosity is not always a good indicator of flow resistivity; because flow resistivity depends upon the cross-sectional area of the pores rather than the number of pores.

Delany and Bazley suggested bounds for the validity of their empirical relationship in terms of bounds on the frequency/flow resistance ratio such that:

$$0.01 \leqslant C \leqslant 1$$

Mechel [5.27] has proposed alternative expressions to extend the range of application of this model. He suggests that for:

$0.016 \leq f/\sigma < 1$

$$R/\rho c = 1+0.0489(C)^{-0.754} \qquad 5.24$$

$$X/\rho c = 0.087(C)^{-0.731}$$

$$\gamma'' = 1+0.0978(C)^{-0.695} \qquad 5.25$$

$$\gamma' = 0.189\ (C)^{-0.693}$$

and for $C < 0.016$

$$z_c/\rho c = i\left\{[2\pi\ (C)]^{-1} - i1.403\right\}\ (\gamma/k_o)^{-1} \qquad 5.26$$

$$\gamma/k_o = [1.466+i0.212(C)]^{\frac{1}{2}} \qquad 5.27$$

Bies and Hansen [5.28] have also proposed modifications to the basic power law expressions, and furthermore suggest that equations 5.22 and 5.23 may be valid for $C > 1$. However, this point has recently been questioned [5.29].

Although the indirect method has gained wide acceptance, it is open to one major criticism, and that is that its justification is circular. The theory that is used to determine the impedance estimate, is also the one used to test the validity of the estimate. However,

the objections can be minimised by using several test geometries to obtain a mean value of impedance.

5.8 Impulse methods

Impulse methods for the measurement of acoustic impedances have developed rapidly in recent years, due primarily to advances in signal processing techniques.

In the basic method a short duration pulse is emitted by the source and picked up by the receiver. For an omni-directional source two distinct pulses will be received, the direct and the reflected. The latter will be delayed and attenuated with respect to the former because of path length differences and surface characteristics. The magnitude of the reflection coefficient can be calculated from the expression:

$$|R(\omega)| = \left|\frac{S_2(\omega)}{S_1(\omega)}\right| \qquad 5.28$$

where $S_1(\omega)$ is the frequency response of the direct pulse and $S_2(\omega)$ the frequency response of the reflected pulse, obtained by Fourier Transformation of the measured pulses.

The phase of the reflection coefficient is more difficult to determine; because it is not possible to distinguish between a phase shift resulting from a pure time delay and that due to the surface. If the location of the acoustic surface were known precisely, then it would be possible to calculate the phase shift due to the path length difference and extract this linear component from the measured phase shift.

The surface location problem is not unique to impulse methods, it exists for all the impedance measurement techniques. However, since a single impulse is used to predict the impedance over a broadband of frequencies, any error in locating the surface can distort the phase estimate at high frequencies.

The main advantages of the basic impulse technique are that measurements need not be conducted in a free-field and that it can be used for all angles of incidence, because it does not rely on any propagation theory for determination of the impedance. However, there are two major limitations to successful measurements, they are:

(i) Signal to Noise Ratio

(ii) Pulse overlap

5.8.2 Improving the Signal to Noise Ratio

The bandwidth of the measured frequency response is determined by the width of the pulse, the narrower the pulse the greater the bandwidth. In the time domain the energy in the pulse is related to the product of amplitude and width, and in a real system this energy is limited by the power handling capabilities and frequency response of the source transducer.

In the frequency domain this energy is distributed across the entire measurement bandwidth, (Parseval's theorem states that the total energy in the time domain must equal the total energy in the frequency domain), and so at some frequencies the energy from the source may not be very much greater than that of the system noise level. Low signal to noise ratios may lead to poor estimates in the magnitude and phase of the impedance.

Several methods have been suggested to overcome this limitation, all involving the use of tone bursts rather than pulses. Such bursts may be either multiple cycles of a pure tone, or single cycles of a sweep across a fixed bandwidth. The pure tone bursts give the highest signal to noise ratio; since all the energy is concentrated into a small part of the frequency spectrum.

The swept tone burst has the advantage of a greater measurement bandwidth.

An alternative technique for increasing the signal to noise ratio is that of signal averaging or signal enhancement. Repetitive occurrences of the pulse are summed, together with the noise, but since the noise is uncorrelated its mean value tends to zero leaving a clean version of the pulse. The improvement in the signal to noise ratio is given by:

$$\Delta S/N = 10 \log_{10} n$$

where n is the number of pulses averaged.

Synchronous detection is essential for signal averaging to work satisfactorily. In the case of pulses the leading or trailing edge of the signal itself may be used fo synchronisation. Pure tone and swept tone bursts may present special problems; because few commercial oscillators provide facilities for controlling the initial phase of the burst. However, this particular problem can be overcome by the use of digital rather than analogue signal generation [5.30].

5.8.3 The Pulse Overlap Problem

The second major limitation of pulse techniques is that of pulse overlap. For the basic impedance measurement method to work the direct and reflected pulse must be separable. This means that the width of the direct pulse must not exceed the travel time corresponding to the path length difference, that is:

$$T_d < \frac{R_2 - R_1}{c} \simeq \frac{2Hh}{rc}$$

where R_1 and R_2 are the direct and reflected path lengths respectively, c is the speed of sound, H is the source height, h the receiver height and r the horizontal separation distance.

At grazing incidence the path length difference is very small and it may not be possible to generate a sufficiently short pulse. In such cases the two pulses overlap and cannot be separated in the time domain.

5.8.4 The Power Cepstrum

Bolton and Gold [5.31] have proposed a measurement method that can cope with a limited degree of overlap; it is based upon the methods of homomorphic deconvolution.

When the pulses overlap, the reflected pulse becomes convolved with the direct pulse, and so the measured frequency response is the product of the direct and reflected pulse transforms. The multiplication makes it impossible to separate the pulses in the frequency domain. However, if the natural logarithm function of the frequency response is found and the result Fourier Transformed, then the multiplication is converted to addition and the reflected pulse can be separated from the direct. The inverse Fourier transform of the logarithm of the frequency response is called the cepstrum.

The following analysis, taken from Bolton and Gold's paper shows how the cepstrum can be used to extract the plane wave reflection coefficient from the measurement at a single receiver.

The total pressure at the receiver $P_t(t)$ can be written as the sum of the direct and reflected pulses in the form:

$$P_t(t) = p(t) + \frac{R_1}{R_2}\ p(t) * h(t-\tau) \qquad 5.29$$

where $p(t)$ is the direct pulse, R_1 and R_2 are the direct and reflected path lengths and $h(t-\tau)$ is the

impulse response of the surface. The symbol '*' represents convolution in the time domain.

Taking the Fourier Transform of equation 5.29, the frequency response at the receiver can be written as:

$$P_t(\omega) = P(\omega) \left[1 + \frac{R_1}{R_2} H(\omega) e^{-i\omega t}\right] \qquad 5.30$$

Bolton and Gold apply the power cepstrum, which means taking the logarithm of the magnitude squared of the frequency response, the phase is discarded. The square modulus of the received pulse is given by:

$$|P_t(\omega)|^2 = |P(\omega)|^2 \{1 + \frac{R_1}{R_2} H(\omega)e^{-i\omega t}\left[1 + \frac{R_1}{R_2} H(\bar{\omega})e^{i\omega t}\right] \qquad 5.31$$

Taking the natural logarithm gives:

$$\ln |P_t(\omega)|^2 = \ln|P(\omega)|^2 + \ln \left[1 + \frac{R_1}{R_2} H(\omega)e^{-i\omega t}\right] + \ldots$$

$$\ldots \ln \left[1 + \frac{R_1}{R_2} H(\bar{\omega})e^{i\omega t}\right] \qquad 5.32$$

The terms containing the surface impulse response can be expanded using the series representation of the logarithm:

$$\ln (1+Z) = z - \frac{z^2}{2} + \frac{z^3}{3}$$

since $\left|\frac{R_1}{R_2} H(\omega) e^{i\omega t}\right| < 1.$

Performing the expansion and taking the inverse Fourier transform gives the power cepstrum of the received pulse as:

$$\hat{p}_t(t) = \hat{p}(t) + \frac{R_1}{R_2} h(t-\tau) + \left(\frac{R_1}{R_2^2}\right)^2 h(t-\tau) \frac{h(t-\tau)}{2} \qquad 5.33$$

$\hat{p}(t)$ is the power cepstrum of the direct pulse. The remaining terms represent the contribution of the reflected pulse. The term $R_1/R_2\ h(t-\tau)$ is the required surface impulse response modified by the spherical spreading term R_1/R_2. If this term is extracted from $\hat{p}_t(t)$, it can be inverse Fourier Transformed to give the reflection coefficient. It is not possible to obtain the direct and reflected pulse; because the phase information of the frequency response was discarded. However, for impedance measurements reconstruction of the pulses is not required.

.5 The Complex Cepstrum

An alternative deconvolution procedure exists, based upon the complex cepstrum which is defined as

$$\hat{P}_t(t) = \ln[P(\omega)] \qquad 5.34$$

where $P(\omega)$ is the frequency response of the combined direct and reflected pulses. The logarithm of the frequency response can be written in terms of the magnitude and phase as:-

$$\hat{P}_t(t) = \ln[P(\omega)] + i \arg[P(\omega)] \qquad 5.35$$

Care must be exercised when calculating the term $\arg[P(\omega)]$; because most arctangent functions will compute the principle value of the phase. The result is a discontinuous phase function. As discussed in Section 6.7 the phase must be continuous in order to satisfy the requirements of the homomorphic mapping used to establish the deconvolution process. The phase discontinuities can be removed by a technique referred to as phase unwrapping.

Tribolet has suggested a phase-unwrapping algorithm based upon integrating the phase derivative. This procedure has been adopted for this study and found to work successfully for partially overlapped pulses.

The main advantage of the two deconvolution procedures is that measurements of surface impedance can be made at much greater angles of incidence than is possible with the basic free-field method. The main penalty for this is the extensive computational effort required.

5.9 Transfer Function Methods

The final class of impedance measurement techniques examined in this study are the so called transfer function methods, which rely on measuring some form of cross-spectral property between two microphones positioned above the surface. Measurements may be made within a free-field or a tube, provided there are no extraneous reflections to distort the cross-spectral estimate.

The transfer function of a system is defined as

$$H(f) = Y(f)/X(f)$$

where Y(f) is the complex spectrum of the output and X(f) is the spectrum of the input. This simple expression can only be used when it is possible to make independant estimates of the direct and reflected pressures, which correspond to the

the input and outputs of the system. In the case of steady-state excitation above a reflecting surface it is not possible to separate the direct and reflected pressure fields using a single microphone. Chung and Blazer [5.10] have proposed a technique using two microphones which does enable measurements of the surface transfer function. The following description is based upon their work, but uses a frequency domain analysis rather than the time domain of the original authors.

Consider the geometry shown in Figure 5.7. Let the total pressure at microphone 1 be $P_1(f)$ and at microphone 2 $P_2(f)$. $P_1(f)$ and $P_2(f)$ may be written in terms of the direct and reflected fields as

$$P_1(f) = P_{1d}(f) + P_{1r}(f) \qquad 5.36$$

$$P_2(f) = P_{2d}(f) + P_{2r}(f) \qquad 5.37$$

Let $H_{12}(f)$ be the transfer function for the pressure field between the two microphones, such that:

$$P_2(f) = H_{12}(f).P_1(f) \qquad 5.38$$

then $P_2(f)$ can be written as

$$P_{2d}(f) + P_{2r}(f) = H_{12}(f)\left[P_{1d}(f) + P_{2r}(f)\right] \qquad 5.39$$

The direct and reflected pressures at microphone 2 can be written in terms of the pressures at microphone 1 and the direct and

reflected transfer functions, therefore

$$P_{2d}(f) = H_d(f).P_{1d}(f) \qquad 5.40$$

and

$$P_{2r}(f) = H_r(f).P_{ir}(f) \qquad 5.41$$

Equating total pressures:-

$$H_d(f).\ P_{1d}(f) + H_r(f).\ P_{1r}(f) = H_{12}.P_{1d}(f) + H_{12}.P_{1r}(f)$$

then

$$P_{1r}(f)\ \left[H_r(f) - H_{12}(f)\right] = P_{1d}(f)\ \left[H_{12}(f) - H_d(f)\right]$$

The reflection coefficient measured at microphone 1 is the ratio $P_{1r}(f)/P_{1d}(f)$ which is given by

$$R_1(f) = \frac{P_{1r}(f)}{P_{1d}(f)} = \frac{H_{12}(f) - H_d(f)}{H_r(f) - H_{12}(f)} \qquad 5.42$$

Similarly it can be shown that the reflection coefficient measured at microphone 2 is given by

$$R_2(f) = \frac{P_{2r}(f)}{P_{2d}(f)} = \frac{H_r(f)}{H_d(f)} \left[\frac{H_{12}(f) - H_d(f)}{H_r(f) - H_{12}(f)}\right] \qquad 5.43$$

The reflection coefficient at the surface, R(f), can be obtained from either of $R_1(f)$ or $R_2(f)$, by making a phase correction for the height of the microphone above the surface, therefore

$$R(f) = R_1(f).\ e^{j2k(l+s)} \qquad 5.44$$

or

$$R(f) = R_2(f)\ e^{j2kl} \qquad 5.45$$

If the propagation medium can be assumed non-dispersive, then the direct and reflected transfer functions $H_d(f)$ and $H_r(f)$ are just phase corrections and are given by

$$H_d(f) = e^{-jks}$$

$$H_r(f) = e^{+jks}$$

The measured transfer function $H_{12}(f)$ is dependant upon the frequency response characteristics of the two microphones. In particular small phase differences between the microphones can introduce significant errors into the phase estimate of the reflection coefficient. These errors can be minimised by measuring the frequency response of each microphone and correcting the subsequent transfer function estimates.

Chung and Blazer suggest an alternative scheme, which relies upon measuring a mean value of $H_{12}(f)$. A first estimate is made with the microphones in one position, this is denoted by $H^o_{12}(f)$ and the second estimate, $H^s_{12}(f)$, with microphone positions reversed. The mean value of the transfer function is given by

$$\overline{H_{12}}(f) = \left[H_{12}^{o}(f) \cdot H_{12}^{s}(f)\right]^{\frac{1}{2}} \qquad 5.46$$

The reflection coefficients $R_1(f)$ and $R_2(f)$ are calculated using $\overline{H_{12}}(f)$ rather than $H_{12}(f)$. The impedance of the surface can be obtained from the reflection coefficient at the surface using equation 5.44, this gives

$$\frac{Z(f)}{\rho c} = \frac{j\,\overline{H_{12}}(f)\,\sin(kl) - \sin\left[k(l-s)\right]}{\cos\left[k(l-s)\right] - \overline{H_{12}}(f)\,\cos(kl)} \qquad 5.47$$

The frequency range of this technique is limited by the destructive interference that occurs when the spacing between the microphones equals half a wave length. To avoid such effects, the spacing s should be chosen such that

$$s \leq \frac{c}{2fm}$$

where c is the velocity of sound, and fm is the maximum measurement frequency.

Glaretas [5.35] has recently combined the transfer function and indirect methods for measuring the oblique incidence impedance ratio of ground surface.

The technique utilises two microphones located vertically above the surface. The position of these microphones is dictated by the need to ensure that the interference dips due to the ground surface occupy different portions of the measurement bandwidth. This maximises the signal to noise ratio of the calculated transfer function.

In the case of a locally reacting surface, equation 3.64 is used to calculate the complex pressure field at each microphone for a particular geometry as a function of frequency. The transfer function can then be calculated using equation 5.58.

An iterative computation procedure is used to determine the surface admittance ratio that minimises the difference between the measured and calculated transfer function.

According to Glaretas, one of the main advantages of the method is its relative insensitivity to errors in the location of the ground surface. This is due to the fact that at grazing incidence the path length difference between the direct and reflected wave is small, and so the linear phase term error introduced is also small.

References Chapter 5

5.1 Beranek, L.L.: Precision Measurement of Acoustic Impedance
JASA (12) 3-13 1940

5.2 Beranek, L.L.: Acoustic Measurements
J. Wiley 1949

5.3 Kilmer, R.D.: Evaluation and Prediction of Sound Absorbing Characteristics of Composite Acoustic Absorbers for Normally incident Plane Waves
M.Sc Thesis, Pennsylvania State University 1974

5.4 Singh, R.: Acoustic Impedance Measurement Methods
Shock and Vibration Digest Volume 14 No.2 1982

5.5 Schuster, K.: Measurement of Acoustic Impedances by Comparison
Electr. Nachr. - Tech. (13) 164-176 1936

5.6 Robinson, N.W.: An Acoustic Impedance Bridge
Phil Mag (23) 665-680 1937

5.7 Johnason, H.G.: The Propagation of Sound Over Ground with and without Acoustic Barriers
Report 18 Lund Institute of Technology Sweden 1971

5.8 Thomasson, S.I.: Theory and Experiments on Sound Propagation above an Impedance Boundary
Report 75 Lund Institute of Technology Sweden 1977

5.9 Legeay, V.: Application of the Discrete Hilbert Transform to the Evaluation of Acoustic Reflection Coefficients
Ph.D Thesis University of Maine 1981

5.10 Chung, J.Y. and Blazer, D.A.: A New Method of Measuring In-Duct Acoustic Properties I & II
Eng Mechs Dept General Motors Research Labs
Report No. GMR-3167 1979

5.11 Sides, D.J. and Mulholland, K.A.: The Variation of Normal Layer Impedance with Angle of Incidence
JSV (14) 139-142 1971

5.12

5.13 Shaw, E.G.: The Acoustic Waveguide I & II
JASA (25) 224-231 1953

5.14 Beranek, L.L.: Noise Reduction and Control
Wiley 1968

5.15 Morse, P.M.: Sound and Vibration 2nd Edition
McGraw Hill 1948

5.16 Ando, Y.: An Extrapolation of Measuring the Reflection Coefficient by An Acoustic Tube
Applied Acoustics (2) 95-99 1969

5.17 Joffe, L.: A Criterion for the Use of Linear Regression Analysis in the Determination of Low Values of Absorption Coefficient using the Impedance Tube Method
Applied Acoustics (7) 139-146 1974

5.18 Ando, Y.: Probe Microphone Directivity and Acoustic Centre of a Probe Microphone
J Acoust Soc Japan (24) 335-342 1968

5.19 Morse, P.M. and Ingard, K.U.: Theoretical Acoustics
McGraw-Hill 1968

5.20 Talaske, R.H.: The Acoustic Impedance of a Layered Forest Floor
M.Sc Thesis Pennslyvania State University 1980

5.21 Donato, R.J.: Model Experiments on Surface Waves
JASA 63 700-703 1978

5.22 J.W. Strutt, Lord Rayleight: Theory of Sound I & II
Dover 1945

5.23 Ingard, K.V. and Bolt, R.H.: A Free-Field Method of Measuring the Absorption Coefficient of Acoustic Materials
JASA (23) 509-516 1951

5.24 Ando, Y.: The Interference Pattern Method of Measuirng the Complex Reflection coefficient of Acoustic Materials at oblique Incidence
Electronics and Comms in Japan (5) 303-310 1968

5.25 Bass, H.E. and Bolen, L.N.: Propagation of Sound Through the Atmosphere: Effects of Ground Cover
US Army Research Office DAAG-29-76-G-0258

5.26 Delany, M.E. and Bazley, E.N.: Acoustical Properties of Fibrous Absorbent Materials
Applied Acoustics (3) 105-116 1970 and NPL Aero Report Ac37 1969

5.27 Mechel, F.P.: Ausiveitung der Absorberformel van Delany and Bazley zu tiefen Frequenzen
Acustica (35) 210-213 1976

5.28 Bies, D.A. and Hansen, C.H.: Flow Resistance Information for Acoustical Design
Applied Acoustics (13) 357-391 1980

5.29 Attenborough, K.A.: Acoustical Chateristics of Porous Materials
Physics Reports (82) 181-227 1982

5.30 Wilson, P.: An Application of Direct Memory Transfers
Institute of Acoustics Meeting 9th June 1981

5.31 Bolton, J.S. and Gold, E: The Application of Cepstral Techniques to the Measurement of Reflection Coefficients Insitu.
RMIT Report 121007

5.32

5.34 Embleton T.W. and Piercy.: Excess Attenuation or Impedance of Common Ground Surfaces Characterised by Flow Resistance JASA (65) page 563 Supplement No.1 Spring 1979

5.35 Glaretas, C.: Acoustical Properties of the Ground Ph.D Thesis Pennsylvania State University 1981

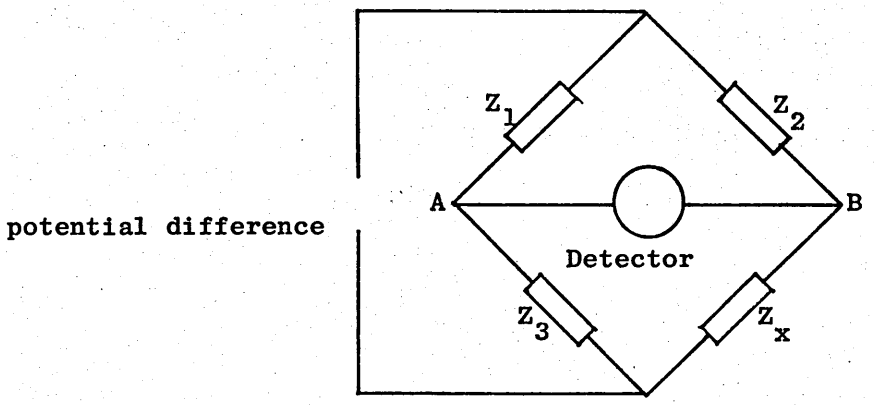

Figure 5.1
Circuit diagram of an impedance bridge

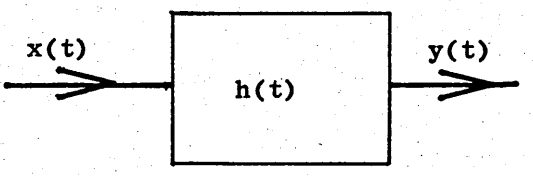

Figure 5.2
Block diagram of two port network

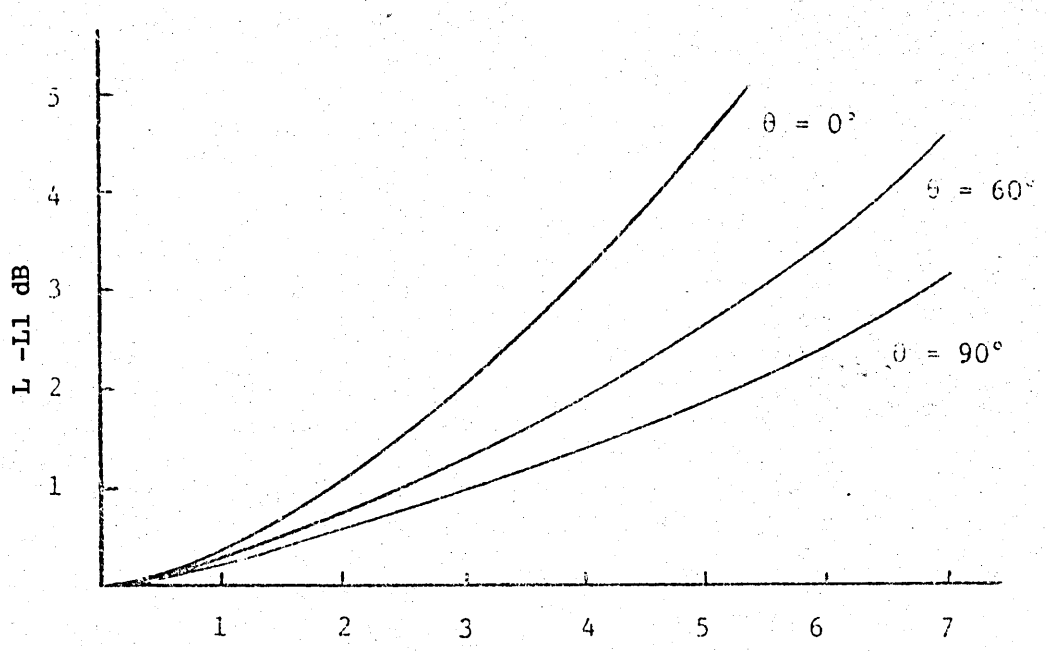

Figure 5.3
Graph for determining SWR at the surface from the SWR measured at the first two minima (after Kilmer)

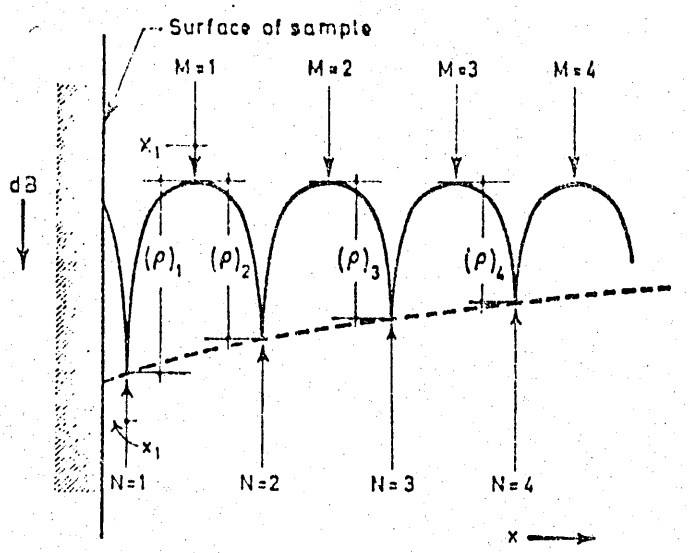

Figure 5.4
Magnitude of the total sound pressure in an impedance tube as a function of distance (after Ando)

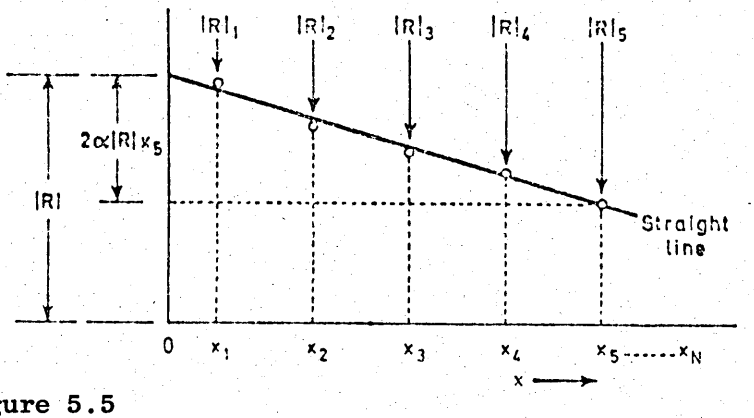

Figure 5.5
Extrapolation of the reflection coefficient at x = 0 (after Ando)

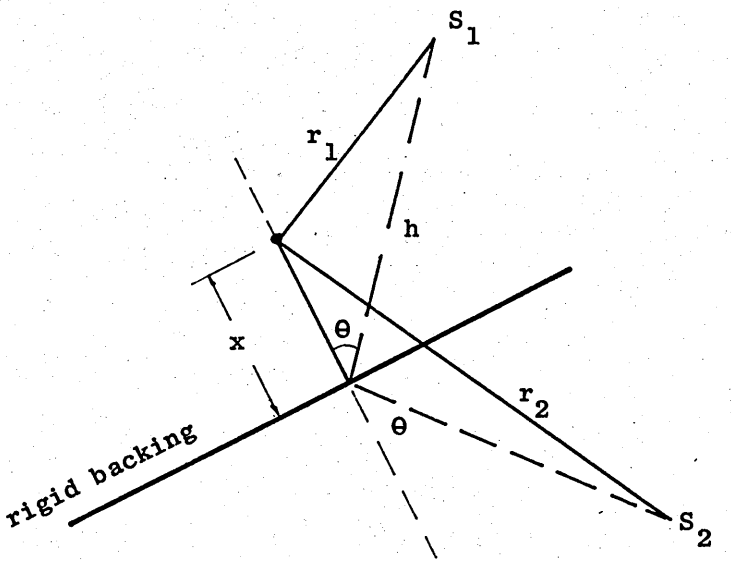

Figure 5.6
Geometry for free-field impedance measurement (after Sides and Mulholland)

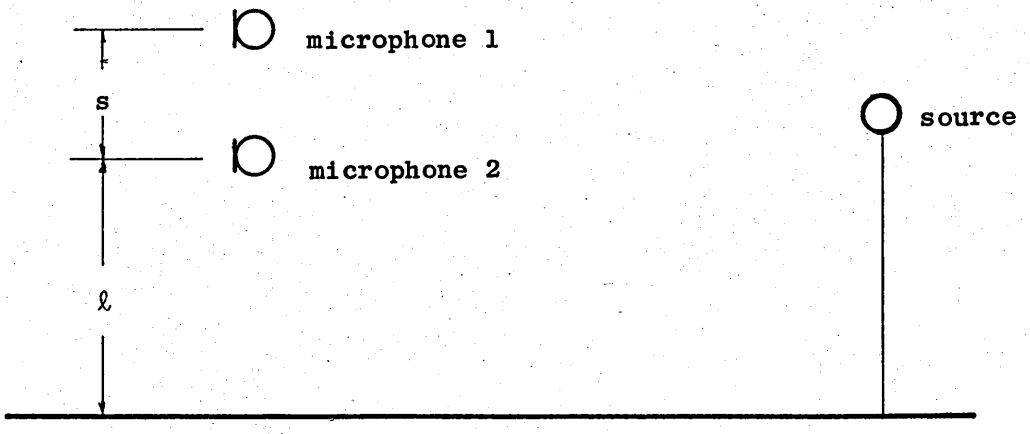

Figure 5.7
Geometry for transfer function impedance measurement (after Chyng and Blazer)

Chapter 6

Digital Signal Processing Techniques

The purpose of this chapter is to review of the basic concepts of digital signal processing, and in particular the definitions and equations used in this study. The following analysis assumes that the system under investigation is linear and therefore obeys the rules of superposition.

6.1 Sampling and Conversion

The starting point of the analysis is a signal x(t), which is sampled at a rate given by Shannon's sampling rule. This rule states that the signal must be sampled at a rate at least twice the bandwidth of the signal. Since all the signals to be analysed can be considered to be baseband signals, that is having a bandwidth extending from d.c. to fHz, the sampling rate, s, must be such that:

$$s \geqslant 2f \text{ samples per second}$$

f is called the Nyquist frequency.

The bandwidth of the sampled signal must take account of any extraneous signal sources such as electronic noise, otherwise the energy present above the Nyquist frequency will appear at lower frequencies due to aliasing, and hence corrupt the spectral analysis. This effect can be minimised by low pass filtering of the signal prior to sampling.

The sampling process converts the continuous signal x(t) into a discrete series of samples at intervals dt where:

$$dt = 1/s \text{ secs}$$

The new series is represented by:

$$x(n) \quad n = 1,2,3,....N$$

where N is the maximum number of samples. The sequence x(n) is called an ensemble.

The conversion from continuous to discrete (analogue to digital) involves the process of quantization, by which each sample x(n) is represented by a codeword or number representing the amplitude of the signal. In a binary system the range of numbers available is limited by the number of bits in a binary codeword such that:

$$n = 2^b$$

where n is the number of codewords and b is the number of bits in the codeword. Hence each codeword must represent a small but finite range of the continuous analogue signal. The difference between the analogue value and the digital representation is called the quantization error. The converted signal may be modelled as the sum of the true signal plus a noise-like signal due to the quantization error.

The error limits the accuracy of the conversion process. One way to quantify the effects is in terms of the signal to noise ratio [6.2]:

$$S/N = 20 \log_{10} 2^b$$

This expression shows that each additional bit added to the codeword increases the S/N ratio by 6 dB. The model given above is over-simplified; because it does not take account of the statistical nature of the noise. However, it does serve as a useful rule of thumb for engineering purposes.

6.2 Signal Enhancement in the Time Domain

Quantization errors are not the only source of noise present in signals. All electronic circuits give rise to noise of

various types which add to and degrade the signal. Hence amplifiers, and filters are potential sources of noise. Provided the noise is uncorrelated with the signal and has an expected mean value of zero, its effects upon the signal can be minimised by signal averaging. The improvement in the S/N ratio is given by:

$$\Delta S/N = 10 \log_{10} (m)$$

where m is the number of ensembles averaged [6.2].

Although averaging can minimise the effects of electrical noise, it cannot in general reduce quantization noise. However, the presence of a small amount of noise in the original signal x(t) can drastically reduce quantization effects. Horlick [6.1] has shown that adding white noise, with an amplitude about five times the quantization interval, and averaging over 1000 ensembles effectively removes the quantization noise. If the amplitude of the electronic noise is too small, it may be advantageous to add white noise from a generator.

6.3 The Discrete Fourier Transform

The basis of most of the signal processing conducted in this study is the Fourier Transform pair, defined by:

$$X(f) = \int_{-\infty}^{\infty} x(t)\ \exp(-i2\pi ft)dt \qquad -\infty<f<\infty$$

and

$$x(t) = \frac{1}{2\pi} \int_{-\infty}^{\infty} X(f)\ \exp(i2\pi ft)df \qquad -\infty<t<\infty$$

The equivalent expressions for digital computation require discrete time and frequency components of finite duration, so that the transform pair become:

$$X(k) = \sum_{0}^{N-1} x(n)\ \exp(-i\ \frac{2\pi nk}{N})\ k = 0,1,2...(N-1) \qquad 6.1$$

$$x(n) = \frac{1}{N} \sum_{0}^{N-1} X(k)\ \exp(i\ \frac{2\pi nk}{N})\ n = 0,1,2...(N-1) \qquad 6.2$$

The frequency components, or spectral estimates, X(k) represent the energy in the signal over a finite bandwidth b where:

$$b = \frac{1}{T} = \frac{1}{dt.N}$$

and T is the total duration of the ensemble.

Implicit in the finite duration assumption of the discrete Fourier Transform is that the sequence x(n) has been 'windowed'. Mathematically the sequence has been multiplied by the function:

$$U(n) = 1 \quad 0 \leqslant n \leqslant N-1$$

$$0 \quad \text{elsewhere}$$

The multiplication in the time domain transforms to a convolution in the frequency domain, hence the spectral estimates are modified by the frequency response of the window. The problem does not arise if the sample is totally contained with the window, as is usually the case for transient signals. For continuous signals the errors caused by windowing can be minimised by careful selection of the window function [6.2].

The spectral analysis equipment used for the experimental measurements described in Chapters 8 and 9 employs a Hanning squared window defined by the expression:

$$W(t) = 1 - \cos^4(\pi\tau/T)$$

where τ is the sample interval and T the total duration of the window [6.3].

The effect of such a window to is attenuate the beginning and end of the recorded time sequence. This wastes valuable data, so provision is made to overlap parts of the total data sequence x(n) to produce the finite duration sequences $x_m(n)$, n = 0 - N-1

If 50% overlap is used, the finite sequences are made up as follows:

$$x_1(n) = x(0) \ldots x(N-1)$$
$$x_2(n) = x(N/2) \ldots x(3N/2-1)$$
$$x_3(n) = x(N) \ldots x(2N-1)$$
$$x_4(n) = x(3N/2) \ldots x(5N/2-1)$$

6.4 Spectral estimation

A single application of equation 6.1 produces a raw spectral estimate governed by a χ^2 distribution with 2 degrees of freedom. Additional smoothing is essential to obtain practical estimates with more suitable statistical properties [6.2].

Transient signals averaged in the time domain do not require additional smoothing in the frequency domain.

The frequency smoothing can be performed either of two ways depending upon the measurement system. For long transform lengths adjacent spectral estimates can be averaged, to form a new estimate of bandwidth $b' = b.\ell$ where ℓ is the number of raw estimates.

Alternatively spectral estimates from short time sequences can be averaged. This is referred to as segment averaging and is the procedure adopted by most special purpose digital spectrum analysers. In either case the normalised standard error due to random variations is given by:

$$\varepsilon = \sqrt{1/\ell}$$

6.5 Cross-spectral functions

Measurement of the reflection coefficient, impedance or admittance of a surface are based upon estimates of the frequency response function. The pressure reflection coefficient of a surface is defined by the expression:

$$R(\omega) = \frac{p_r(\omega)}{p_d(\omega)} \qquad 6.3$$

where $p_r(\omega)$ and $p_d(\omega)$ are the complex energy spectra of the direct and reflected pressure waves respectively. $R(\omega)$ may also be determined from the corresponding time-domain functions.

By convention the input and output sequences of a linear system are denoted by $x(t)$ and $y(t)$ respectively. The system is characterised by its impulse response $h(\tau)$.

$x(t)$, $y(t)$ and $h(\tau)$ are related by the convolution integral such that:

$$y(t) = \int_{o}^{\infty} h(\tau)x(t-\tau)dt$$

Fourier transforming this result gives:

$$Y(f) = H(f).\ X(f) \qquad 6.4$$

$H(f)$ is termed the transfer function of the system.

In general $Y(f)$ and $X(f)$ are complex functions, but few spectrum analysers calculate averages of $Y(f)$ and $X(f)$; because unless the sampling process is synchronous, the phase estimate behaves as a random variable and the estimates of $Y(f)$ and $X(f)$ tend to zero.

The transfer function can be estimated from the cross-spectrum of the input and output of the system, together with the spectrum of the input. The cross spectrum is defined as:

$$G_{xy}(f) = X(f)^{*}Y(f)$$

and the transfer function as:

$$H(f) = \frac{G_{xy}(f)}{X(f)} \qquad 6.5$$

Bendat and Piersol [6.2] also point out that this equation provides an unbiased estimate of the transfer function whereas equation 6.4 does not.

6.6 Coherence function

In practical measurement systems it is impossible to exclude all sources of extraneous noise, hence spectral estimates will be contaminated. One method of quantifying the degree of contamination is to calculate the Coherence Function, which is defined as [6.2]:

$$\gamma^2_{xy}(f) = \frac{|G_{xy}(f)|^2}{|X(f)| . |Y(f)|} \qquad 6.6$$

For linear systems, $\gamma^2_{xy}(f)$ can be interpreted as the fractional proportion of the mean square value of the output y(t) which is contributed by the input x(t) at frequency f.

Confidence limits for the transfer function H(f) can be determined from the expression below:

$$|\hat{H}(f)| - \hat{r}(f) \leqslant H(f) \leqslant |\hat{H}(f)| + \hat{r}(f) \qquad 6.7$$

$$\emptyset(f) - \hat{\Delta\emptyset}(f) \leqslant \emptyset(f) \leqslant \emptyset(f) + \hat{\Delta\emptyset}(f) \qquad 6.8$$

where:

$|\hat{H}(f)|$ is the transfer function gain estimate

$\phi(f)$ is the transfer function phase estimate

$\Delta\hat{\phi}(f) = \sin^{-1}\left[\hat{r}(f)/|\hat{H}(f)|\right]$

$\hat{r}(f) = +\sqrt{\hat{r}^2(f)}$

$$f\hat{r}^2(f) = \frac{2}{(n-2)} F_{2,n-2,x}\left[1 - \gamma^2_{xy}(f)\right] \frac{Y(f)}{X(f)}$$

$n = 2bT$ = number of degrees of freedom

$F_{2,n-2,x}$ = 100 x percentage point of an F distribution with $n_1 = 2$ and $n_2 = n-2$ degrees of freedom

6.7 The Cepstrum

Two forms of the cepstrum are in common use, the power cepstrum and the complex cepstrum. The power cepstrum is defined as:

$$\hat{p}(n) = F^{-1}\{\ln(|F(x(n))|) + i\,o)\}$$

and the complex cepstrum as:

$$\hat{c}(n) = F^{-1}\{\ln(|F(x(n))|) + i \arg F(x(n))\}$$

where F and F^{-1} denote forward and inverse Fourier transforms respectively.

For a real input sequence x(n), both cepstra are real functions, and the power cepstrum is the even part of the complex cepstrum.

Computation of the power cepstrum presents no special problems, but the definition of the argument of F(x(n)) in the complex cepstrum does.

The object of using the complex cepstrum is to enable deconvolution of two signals. The multiplicative operation in the time domain, convolution, is transformed to addition in the cepstrum. If a sequence x(n) is the convolved product of two sequences $x_1(n)$ and $x_2(n)$, then:

$$\ln[x(n)] = \ln[x_1(n).x_2(n)]$$
$$= \ln[x_1(n)] + \ln[x_2(n)]$$

This implies that:

$$\ln|x(n)| = \ln|x_1(n)| + \ln|x_2(n)|$$
$$\arg[x(n)] = \arg[x_1(n)] + \arg[x_2(n)]$$

The second requirement can only be met if arg [x] is a continuous function of x.

Since most algorithms used to compute the phase term produced the principal value, arg [x] can be made continuous by adding 2π radians to the phase each time it passes through zero. This simple method will only work if the phase increment is smaller than 2π. For a transient signal with a long time delay from start of sampling to onset of pulse, the phase increment at high frequencies may exceed π. The delay must be removed prior to computation of arg[x] [6.3].

The sample points of the computed cepstrum (power or complex) are termed quefrencies and have units of time.

The positive time samples are referred to as the causal sequence and the negative time samples the acausal sequence. This follows directly from the basic definition of linear time invariant systems, because the output of a causal system is zero up until the time the input starts. An acausal system can produce an output prior to the start of the input.

The cepstral samples concentrated around zero positive time are termed the low time components, and the remainder the high time components.

6.8 Digital processing equipment

The majority of the signal processing tasks undertaken during this study were executed on a commercial spectrum analyser, the Nicolet 660. This is a dual channel analyser performing a Fourier Transform on 1024 data points, to produce a frequency response of 512 spectral components. The available functions calculated and the main operating characteristics are shown in Table 6.1.

Only two of the five operating modes were used, the signal Enhancement and Dual Channel. In the signal enhancement mode the instrument computes a time domain ensemble average of up to 9999 samples. This mode was used for all the transient data analysis. Unfortunately, the Nicolet will not perform any cross-spectral estimates

in this mode, so that the data has to be transferred to a computer for additional processing.

The dual channel mode was used for cross-spectral estimates and transfer function calculations using an air jet noise source. The instrument calculates a frequency domain ensemble average of up to 9999 samples.

All data and intermediate results from the Nicolet were stored on a small general purpose minicomputer, a Nova 4/C. Furthermore, this machine provided a convenient means of transferring experimental data to a VAX/780 computer for further processing.

A graphics terminal and plotter proved invaluable peripherals to the computers for examining and modifying the experimental data prior to numerical calculation of frequency response impedance or homomorphic deconvolution.

Table 6.1 Nicolet Spectrum Analyser Operation Characteristics

Modes of Operation

(i) Signal averaging
(ii) Single channel (2048 point transform)
(iii) Dual channel (1024 point transform)
(iv) Correlation
(v) Probability

Averaging modes

(i) Summation
(ii) Exponential (RC network averaging)
(iii) Sweep (maximum redundancy)
(iv) Peak
(v) Transient

Function calculated

(i) Instantaneous spectrum
(ii) Average spectrum
(iii) Cross spectrum
(iv) Transfer function
(v) Coherence
(vi) Coherent output power
(vii) Auto-correlation function
(viii) Cross-correlation function
(ix) Impulse response

Operating characteristics

(i) Bandwidth d.c.-100 kHz
(ii) Spectral resolution 5.10^{-3}-250 Hz
(iii) Antialiasing filter 8th order elliptic
(iv) Input signal range 0-20 V peak
(v) Analogue conversion resolution 12 bits (1 part in 4096)

References Chapter 6

6.1 Horlick, G.: Reduction of Quantization Effects by Time Averaging with Added Random Noise

6.2 Bendat, J.S. and Piersol, A.G.: Random Data: Analysis and Measurement Procedures
Wiley 1971

6.3 Oppenheim, A.V. and Schafer, R.W.: Digital Signal Processing
Prentice Hall 1975

Chapter 7

General Considerations for Acoustic Modelling

7.1 Evaluation of the excess attenuation prediction schemes, described in Chapter 3, by comparison with outdoor experimental measurements often proves inconclusive. There are several contributing factors of which the most important are: wind and temperature gradients, near surface turbulence, non-plane surfaces and non-homogeneous surface properties.

Careful selection of measurement sites and times can minimise the influence of these factors, but they are difficult to eliminate entirely.

For this reason it was decided to use acoustic models to carry out the evaluation. This chapter examines the basic requirements of such models and describes the selection of appropriate transducers.

7.2 Basic Modelling Rules

If a model system is to reproduce all the relevant properties of the original system faithfully, two conditions must be fulfilled. The first condition is that the model system must be similar to the original in all important characteristics, and the second is that the laws relating the various parameters in the original must apply unaltered to the parameters in the model.

Consider for example the condition of geometric similarity. It is well known that the interaction of sound waves with objects

depends upon the wavelength of the sound and the dimensions of the bodies or surfaces involved. Hence the relative dimensions of obstacle and wavelength must be faithfully transferred from original to model.

A second requisite of acoustic modelling is that of kinematic similarity, since the velocity of sound is involved. If air provides the propagation medium in original and model, then the velocity of sound is maintained constant. This imposes a time scale factor, as can be shown by considering the dimensionless quantity characterising reference times (the Thomson Number) as follows:

$$\frac{T_m V_m}{L_m} = \frac{T_o V_o}{L_o} \qquad 7.1$$

where T, V and L are time, velocity and length respectively, and the m and o subscripts refer to the model and original.

Since $V_m = V_o$ then:

$$\frac{T_m}{T_o} = \frac{L_m}{L_o} \qquad 7.2$$

and the time scale factor equals the length scale factor. Thus maintaining the same sound velocity in the original and the model requires that the model frequencies be increased with respect to the original, and that all model times be scaled downward.

In general the scale factor must also be applied to the materials used to model the real surface; so that the impedance at the model frequencies equals that at the full scale frequencies.

The prime objecting the model experiments conducted during this study was to evaluate the theoretical predictions for point to point propagation. Such predictions should be valid for all values of ground impedance satisfying the basic assumptions inherent in the derivation of the far-field solutions of Chapter 3. Furthermore, there are many problems associated with measuring the impedance of materials at high frequencies as discussed in Chapter 8.

In view of this, the properties of the modelling materials have not been scaled exactly, although the size of the anechoic chamber relative to the typical propagation distances of traffic noise suggested a notional scale factor of 1 : 100. This scale factor has been used to determine the model source and receiver geometry. As a consequence, it is more appropriate to refer to the experimental technique as laboratory modelling, rather than as acoustic scale modelling.

7.3 Requirements of a Model Receiver

The basic requirements of a receiver are small size, high sensitivity and wideband frequency response. Size is important for two reasons, firstly because directivity is related to the ratio of diaphragm diameter to wavelength and hence a small microphone better approximates an omni-directional receiver, and secondly because the reduction in diaphragm mass improves the high frequency response of the microphone. The only disadvantage of a small diaphragm diameter is its small surface area which results in a low microphone sensitivity.

Table 7.1 gives the sensitivity and frequency response of the Bruel and Kjaer ½", 1/4" and 1/8" microphones, and shows that each halving of the diaphragm diameter reduces the sensitivity by approximately a quarter, but doubles the upper limit of the frequency response.

Table 7.1

Microphone Type	Nominal Diameter	Sensitivity mV/Pa	Frequency Response (pressure) ±2 dB limits
B & K 4134	½"	12.5	30 kHz
B & K 4136	¼"	4	70 kHz
B & K 4138	1/8"	1.0	140 kHz

Figures 7.1-7.4 show the directivity of these microphones at various frequencies, measured both with and without a protection grid [7.1]. It is clear from these figures that the directional characteristics of the microphones are improved by using them without a protecting grid. Bruel and Kjaer state that a further improvement can be obtained by fitting a nose cone, although they produce no measurements to support this claim.

The superior frequency response and directivity of the 1/8" microphone might presuppose its adoption for use in the chamber calibration tests. However, its low sensitivity limited the maximum separation distance between source and receiver to 50 cm. In view of this, the ¼" microphone was adopted as standard, and the 1/8" used primarily to check the ¼" at short separation distances. The 1/8" was also used to measure the directivity of the sound sources.

7.4 Requirements of a Model Sound Source

Like a receiver, the source should be omni-directional, have a wideband frequency response, and perhaps most important should generate adequate signal power.

Model noise sources fall into two categories, continuous or impulsive. The impulsive source, such as an electrical spark, generates a short duration energy pulse of high intensity and large bandwidth which propagates along an infinite number of paths. Each path can be identified by the time delay between the energy discharge and the arrival of the pulse at the receiver. This feature is particularly useful for examining the influence of the model geometry.

The major drawback of impulsive sources is the possibility of non-linear wavefront propagation within the vicinity of the source. This imposes a minimum separation distance between source and receiver, and so limits the usefulness of such a device.

On the other hand, continuous sources emit their energy continuously and so it is not possible to distinguish between the effects of individual propagation paths. The main advantages of the use of such sources are the absence of non-linear propagation and the simplicity of the measurement instrumentation.

Two sources were selected for the model experiments. The first was the air jet described by Delany et al [7.2], and shown in Figure 7.5. Measurements of the directivity in both the vertical and horizontal planes indicate that this design is a good approximation to an omni-directional source even at 100 kHz.

One particularly important feature of this source is its excellent long term stability. For example over a period of 6 months the third octave spectrum varied by less than 0.5 dB.

The useful bandwidth of this air jet is 1-100 kHz, as dictated by the measurement system and the low frequency performance of the anechoic chamber. Figure 7.6 shows the free-field spectrum of the air jet measured at a distance of 100 cm.

The second model source was a spark discharge device designed by the author. A detailed description of this source is given in Appendix B.

The design operates at very low energy levels, and so non-linear effects are virtually eliminated, as is electro-magnetic radiation.

The useful bandwidth of the spark is also 1-100 kHz, although the actual spectrum extends beyond 150 kHz. Examples of the spark spectrum are given in Appendix B.

7.5 Modelling Environment

The major advantage of acoustic modelling of point to point propagation is that experiments can be conducted indoors within a controlled environment. However, this environment may influence the measurements, for example by introducing reflections from the walls and ceilings.

In the case of impulsive source measurements, these unwanted reflections may be removed by the means of time gating. That is the output of the receiver is switched on and off to control the measurement period. If the unwanted reflections occur when the receiver output is switched off, they will not contribute to the measurement. The technique does require that the enclosed space is sufficiently large to ensure that the travel time of the first

unwanted reflection is greater than that of the last wanted one.

Continuous sources are more demanding of the modelling environment; since it is not possible to use time gating, the surfaces of the enclosure must absorb the incident energy. The normal solution is to conduct the experiments within an anechoic chamber.

The design and calibration of a small anechoic chamber, suitable for the acoustic modelling associated with this study, is described in Appendix A, together with the results of calibration experiments.

This chamber has been used for both the impulsive and continuous source experiments.

7.6 Modelling Instrumentation

Acoustic modelling is demanding of instrumentation. The low sensitivity of small microphones requires that the pre-amplifiers and main amplifiers have low electrical noise floors over a very wide frequency range.

A typical microphone amplifier chain comprises of a pre-amplifier to convert the high output impedance of the microphone to a low impedance suitable for driving long cables, and a measuring amplifier to provide the polarization voltage for the microphone, power supplies for the pre-amplifier, and variable gain.

An estimate of the electrical noise can be obtained by summing the contribution from each stage in the receiver amplification chain. The following figures are taken from the relevant manufacturer's specifications.

(a) Pre-amplifier Noise. B & K 2619 and 2618

The inherent noise of the pre-amplifiers is primarily a function of microphone cartridge capacitance. For the 2618 ¼" pre-amp the noise floor is almost independent of frequency at 5 μV for a ¼" microphone. The 2619 noise level decreases with frequency, from 13 μV at 20 Hz to 4 μV at 5 kHz, and then remains independent of frequency. The total noise over the range 20 Hz to 200 kHz is <120 μV for both pre-amplifiers.

(b) Measuring Amplifier B & K 2607

The noise floor of the measuring amplifier is determined by the thermal noise of the electrical components. The input section noise floor is quoted as ≤5 μV, and the output section ≤50 μV. The signal to noise ratio for a 100 mV input is claimed to be better than 100 dB. This last figure implies a noise floor of 1 μV over the range 20 Hz to 200 kHz.

The equivalent sound pressure level (SPL) of the electrical noise can be calculated using the open circuit sensitivity of the microphone. The ¼" microphone has a nominal sensitivity of 4 mV/Pa and the 1/8" 1 mV/Pa.

Assuming that the measuring amplifier noise can be neglected compared to the pre-amplifier noise, the equivalent SPL is:

¼" microphone 63.5 dB

1/8" microphone 75.5 dB

If non-linear propagation effects from the source are to be avoided, the maximum sound pressure level of the source must be kept below 140 dB. Therefore, the maximum useful dynamic range of the amplifier chain is of the order of 75 dB and 65 dB for the ¼" and 1/8" microphones respectively.

In practise these figures may be reduced because the measuring amplifier gain will be greater than unity, hence the relative noise level contributed by the pre-amplifier will be increased.

7.7 Atmospheric Absorption

The overall signal to noise ratio is further degraded by atomospheric absorption. It is well known that high frequency sound is attenuated as it propagates through the air; due to a combination of thermal and viscous effects, and oxygen and nitrogen molecular relaxation. Delany [7.3] has made an extensive study of these effects, and has derived a set of equations for calculating the total attenuation as a function of distance, air temperature and pressure and relative humidity.

By means of these equations it has been possible to program a computer to correct the experimental measurements to take account of atmospheric absorption. Air temperature, pressure and relative humidity measurements were made prior to the commencement of each experimental run, and the results input to the computer. This technique is particularly simple and dispenses with the need for

complicated electronic compensation circuitry adopted by some experimenters.

A more detailed description of the absorption mechanisms is given in Appendix C, together with equations for calculating the absorption coefficients.

References Chapter 7

7.1 Bruel and Kjaer.: Microphones and Microphone Preamplifiers. 1975.

7.2 Delany, M.E., Rennie, A.J. and Collins, K.M.: A Scale Model Technique for Investigating Traffic Noise Propagation. J.S.V. (56) 325-340. 1978.

7.3 Delany, M.E. and Bazley, E.N.: Values of Air Attenuation for use in the Free-Field Calibration of Microphones. NPL Areo Report, Ac45. 1970.

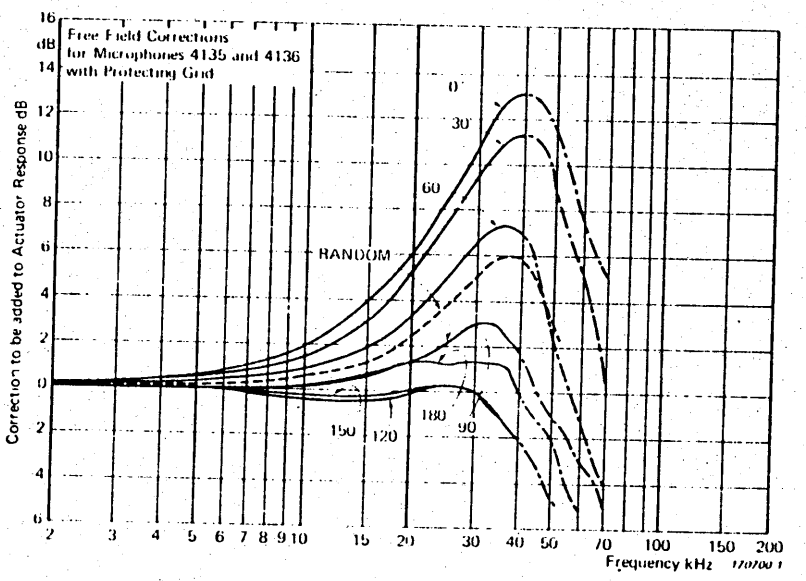

Figure 7.1
Free Field Corrections for Microphones 4135 and 4136 with Protecting Grid

Correction to be added to Actuator Response dB

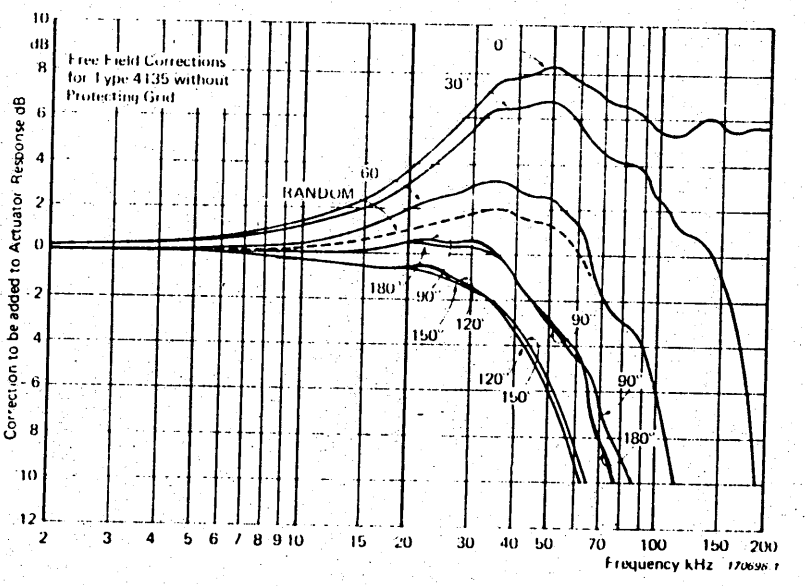

Figure 7.2
Fee Field Corrections for Type 4135 without Protecting Grid

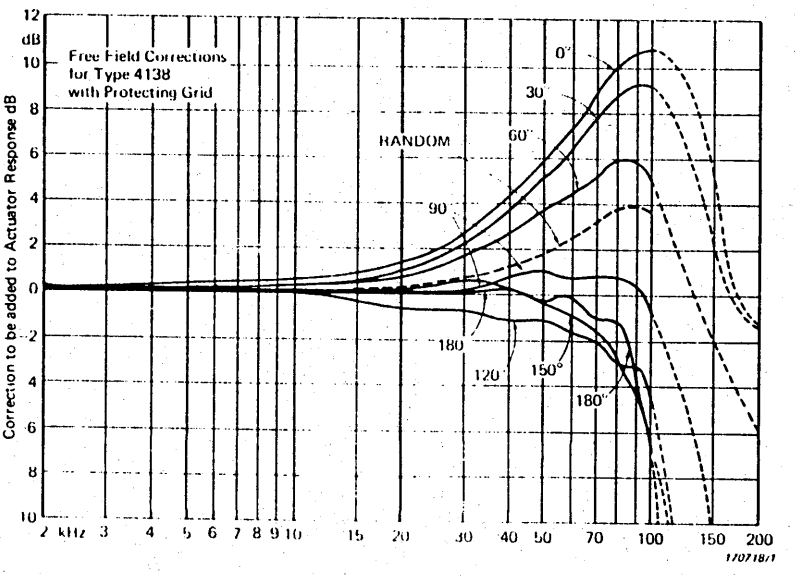

Figure 7.3
Free Field Corrections for Type 4138 with Protecting Grid

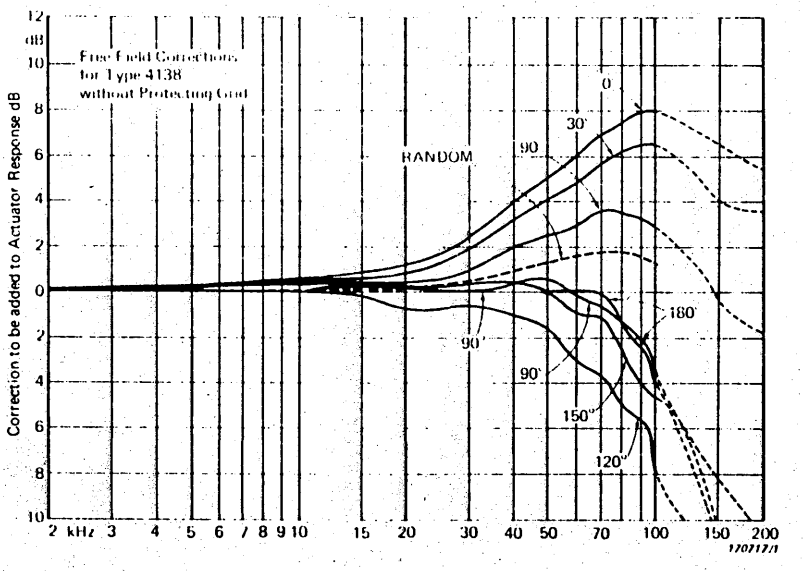

Figure 7.4
Free Field Corrections for Type 4138 without Protecting Grid

Correction to be added to Actuator Response dB

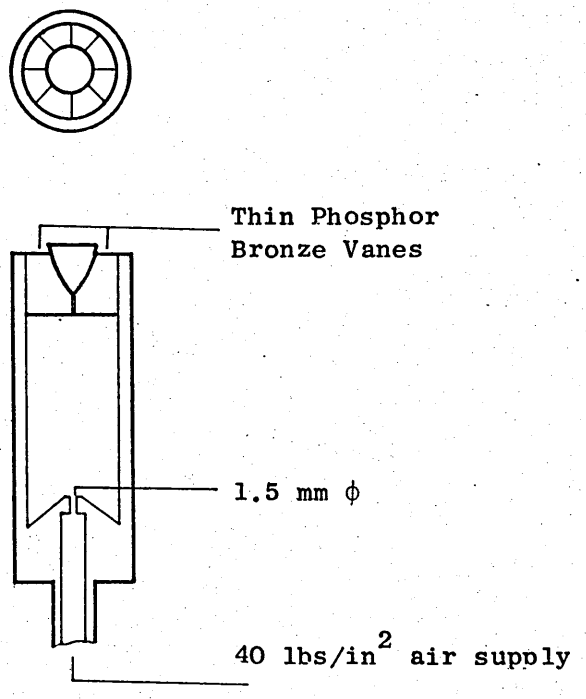

Figure 7.5
Air Jet Model Noise Source

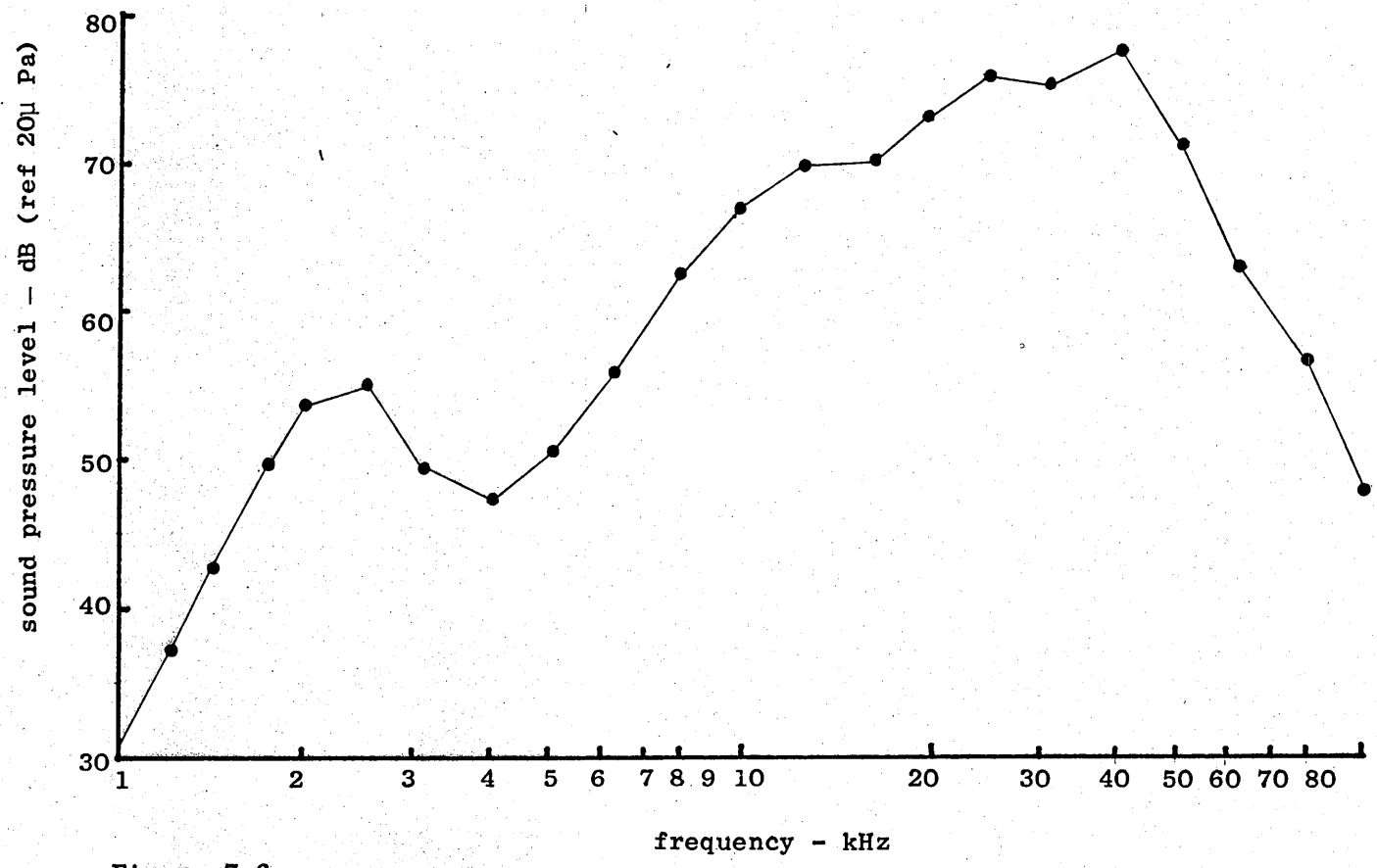

Figure 7.6
1/3rd Octave Free Field Spectrum of Air Jet Noise Source

Chapter 8

Acoustic Impedance Measurements

Previous chapters have shown that for the purpose of predicting propagation near to the ground, many surfaces can be characterised by their normal (or oblique) incidence acoustic impedance. Such surfaces are locally reacting. Other surfaces show marked differences between the normal and oblique incidence impedance and exhibit external reaction. To characterise such surfaces, one must also know the propagation constant of the lower medium.

Various methods for measuring these impedances have been reviewed in Chapter 5, together with details of the particular methods adopted for this study. Of particular interest has been the development and evaluation of those techniques suitable for use at the ultra-sonic frequencies associated with modelling at a notional scale of 100:1 propagation distances of 10 λ < 2 m.

Three materials were selected for investigation,

(a) varnished blockboard - assumed rigid over the frequency range of interest,
(b) artificial grass,
(c) fibreboard.

The last two were selected on the basis that they are relatively hard (acoustically) but have finite impedance, as do ground surfaces in the audio frequency range.

The remainder of this chapter describes the experimental procedures and numerical techniques used to obtain estimates of the two finite impedances and to test that the varnished blockboard was rigid to an adequate approximation over the frequency range of interest.

The impedance tube and free-field measurements for the artificial grass material were conducted by the author whilst on study leave at the Noise Control Laboratory, Pennsylvania State University. The experiments formed part of a study on noise reduction by barriers and the artificial grass material was used to model real grassland ground cover at $\frac{1}{5}$ th scale. Although this scale factor is much smaller than the notional 1/100th used in this study, the experience with the measurement techniques and the impedance information over the range 1-31.5 kHz are of use here also.

8.1 Impedance Tube Measurements

8.1.1 Description of the Tube Apparatus

The impedance tube chosen for these experiments was the Bruel and Kjaer type 4002 Standing Wave Apparatus. This comprises two measuring tubes, the larger has an internal diameter of 10 cm for use over the frequency range 90 - 1800 Hz, and the smaller an internal diameter of 3 cm for the frequency range 800 - 6500 Hz. A set of sample holders is provided for each tube. Two holders have fixed depths of 1" and 2" respectively, the third allows for a variable depth. All these holders have a thick base to ensure a rigid backing for the sample. Figure 8.1 shows the main

components of the assembled apparatus.

The measuring tube and track scale are both fixed onto the loudspeaker box. The microphone probe tube passes through the centre of the loudspeaker and one end screws into the microphone trolley. The free end of the probe tube is supported centrally in the measuring tube by a small trolley.

8.1.2 Instrumentation

A block diagram of the instrumentation used for the tube measurements is shown in Figure 8.2. The loudspeaker was driven by a Bruel and Kjaer 1024 Sine-Random Generator, which in the sine mode is continuously tunable over the range 20 Hz - 20 kHz. The output of the probe microphone was fed to a Bruel and Kjaer 2606 amplifier. A Bruel and Kjaer 1612 filter bank was used to minimise the effects of extraneous noise. The frequency of the pressure signal within the tube was measured by the means of a Heath EU805 frequency meter.

8.1.3 Measurement Range

The object of the measurements was to obtain impedance data for the artificial grass material for use in scale model experiments of traffic noise propagation over the frequency range 100 - 6300 Hz. A scale factor of 1/5th was chosen for the model, hence impedance data was required over the range 500 - 31,500 Hz. For convenience of measurement the actual frequencies chosen correspond to the notional centre frequencies of the one third octave analysis bands.

The 10 cm diameter tube was used for the range 500 to 1600 Hz and the 3 cm tube for the range 800 - 6300 Hz. The upper limit on both tubes is determined by the onset of cross-modes within the tube. These result in a non-plane incident wavefront.

The impedance tube measurements were conducted on only one of the modelling materials, namely the artificial grass. This material consists of clumps of plastic tufts some 10 mm long, embedded in a fibrous rubber backing approximately 6 mm thick.

Four sets of measurements were made:

(i) single layer, tufts facing source
(ii) double layer, tufts facing source
(iii) single layer, backing facing source
(iv) double layer, backing facing source

The object of inverting the active surface of the sample material was to try to assess the relative importance of the tufts and the backing. If the impedance varied little between the two sets of measurements, this would imply that the tufts play an insignificant role in determing the properties of the surface.

8.1.4 Probe-End Corrections

Probe end corrections were estimated for each impedance tube and probe tube configuration, by measuring the distances to the first two minima, d_1 and d_2, in a rigidly terminated tube. The correction C_e is given by equation 5.9.

Locating a minimum in the tube with a rigid termination is difficult, because of the high degree of cancellation between the direct and reflected waves. In view of this, two independant measurements of d_1 and d_2 were made and the mean value used to calculate C_e. The results are given in Table 8.1.

Table 8.1

Probe End Corrections

10 cm standing wave tube

Frequency Hz	d_1 cm	d_2 cm	C_e cm
500	17.49	51.99	-0.24
630	13.99	41.39	-0.29
800	11.00	32.64	-0.29
1000	8.82	26.09	-0.19
1250	7.09	20.87	-0.19
1600	5.55	16.36	-0.15

3 cm standing wave tube

Frequency Hz	d_1 cm	d_2 cm	C_e cm
800	10.93	32.51	-0.14
1000	8.78	26.00	-0.17
1250	7.02	20.88	-0.09
1600	5.56	16.31	-0.19
2000	4.44	13.08	-0.12
2500	3.59	10.49	-0.14
3150	2.85	8.36	-0.10
4000	2.27	6.61	-0.10
8000	1.84	5.34	-0.09
6300	1.51	4.23	-0.15

In general the results show a decrease in the end correction with increasing frequency and compare quite well with the value calculated from an expression derived by Ando, [8.1] his estimate being:

$$\hat{C}_e = -a(0.11ka-0.64)$$

where a is the radius of the probe tube and k is the wave number. For the probe tubes in question, a = 0.3 cm and C_e = -0.19 cm. The result is effectively independent of frequency, because $0.11\ ka \simeq 3.10^{-6}$.

The end correction is added to the measured values of d_1 and d_2.

8.1.5 Measurement Procedure

Several samples of the artificial grass material for use in both the 10 cm and 3 cm tube were cut from a single sheet. For the case of tufts facing the sound source (tufts up) the samples's rubber backing was fixed to the rigid termination by a thin coating of adhesive.

The phase estimate of the impedance is sensitive to errors in the measurement of the distance from the sample surface to the first and second minima, and for artificial grass materials, the surface is (physically) poorly defined. For the purposes of these experiments it was assumed that the active acoustic surface would exhibit a pressure maximum, hence the reference point for all distance measurements was taken to be the location of the first maximum.

Six parameters were measured at each frequency:

(i) Min_1 and Min_2, the sound pressure level at the first and second minima,

(ii) Max_1, the sound pressure level at the first maximum,

(iii) d_1 and d_3 the distance from the sample surface to the first and second minima respectively,

(iv) d_2 the distance from the sample surface to the second maximum.

In view of the difficulty in locating the minima and the measuring the minimum sound pressure levels, four independant measurements of d_1, d_3, Min_1 and Min_2 were taken and the mean values used to calculate the normal impedance ratio. An example of the raw data recorded is given in Table 8.2.

Table 8.2

Recorded Data

zero point 0.25 cm

Frequency	Min_1 dB	d_1 cm	Max_1 dB	d_2 cm	Min_2 dB	d_3 cm
500	61.4	17.49	96.8	35.55	63.5	52.02
	61.4	17.50			63.4	52.02
	61.4	17.50			63.4	52.04
	61.4	17.50			63.3	52.03
1250	54.8	7.02	85.6	13.84	53.6	16.40
	55.0	7.04			53.7	16.40
	54.6	7.05			53.6	16.40
	54.5	7.05			53.6	16.41

It was observed that over the short time it took to determine the pressure values, the signal frequency could change by a few hertz, which resulted in a shift in the location of the minima. For this reason a frequency meter was used to monitor the probe tube output so as to detect such changes.

8.1.6 Data Reduction

Expressions for the real and imaginary parts of the surface impedance were given in Chapter 5. These may be written in terms of the measured parameters:

SPLMAX = sound pressure level of first maximum

SPLMIN = sound pressure level of first minimum

FSTMIN = distance from sample surface to first minimum

DEFMIN = distance between first and second minima

in the form:

$$\frac{R}{\rho c} = \frac{10^{(SPLMIN-SPLMAX)/20}\left\{1+\tan^2\left[\pi\left(0.5 - \frac{FSTMIN}{DIFMIN}\right)\right]\right\}}{10^{(SPLMIN-SPLMAX)/20} + \tan^2\left[\pi\left(0.5\ \frac{FSTMIN}{DIFMIN}\right)\right]}$$

$$\frac{X}{\rho c} = \frac{\tan\left[\pi\left(0.5 - \frac{FSTMIN}{DIFMIN}\right)\right] \cdot \left[1-10^{(SPLMIN-SPLMAX)/20}\right]}{10^{(SPLMIN-SPLMAX)/20} + \tan^2\left[\pi\left(0.5 - \frac{FSTMIN}{DIFMIN}\right)\right]}$$

The values of FSTMIN and DIFMIN must be adjusted to take account of the probe end correction and the sample thickness.

SPLMIN must be corrected for air and tube absorption. The method adopted for these experiments is that due to Joffe [8.2] who suggests that a better estimate of the sound pressure minimum at the sample surface can be obtained from the expression:

$$SPLMIN_S = 20 \log_{10} (10^{SPLMIN/20} - \alpha.x.\ 10^{SPLMAX/20})$$

where α is the attenuation constant

and x is the distance from the surface to the first minimum

Joffe gives some experimental values of α for the Bruel and Kjaer 4002 Standing Wave Tubes.

8.1.7 Results

The normal surface impedance calculated from the impedance measurements are given in Tables 8.3 to 8.6. For the four cases examined the values obtained from the large and small tubes are in reasonable agreement for the overlapping frequency range. However, results for individual frequencies can differ by a factor of 2, and in one instance by a factor of 16.

The results of the two single layer measurements are very similar over most of the frequency range but the general scatter of the values makes it difficult to draw any positive conclusions about the relative contributions of the tufts and the rubber backing.

In view of this a further set of measurements were made on the artificial grass materials after the tufts had been clipped-off at

the surface. The measurements were made, using the small diameter impedance tube, on both faces of the sample. The results are given in Table 8.7. Although the results show considerable scatter, the mean trend of the values obtained from the two faces of the sample are very similar.

Comparing these results with those of Table 8.3, it is clear that the impedance of the clipped sample is greater than that of the sample with tufts. The tufts would therefore appear to reduce the impedance of the material and hence increase the absorption.

One might expect the results of Table 8.5 to be similar to those of Table 8.7(a), because both give values for the bottom face of the artificial grass material. In fact the values of Table 8.5 are generally smaller than those of Table 8.7(a). The most probable cause of this difference is the 10 mm air gap produced by the tufts between the rubber backing of the sample and the rigid termination of the tube. Such air gaps are known to reduce low frequency impedance |A.4| and to cause a change in sign of the reactive part of the impedance at those frequencies for which the air-gap width equals a quarter wavelength.

Table 8.3

Single Layer Impedance

frequency	Large Tube		Small Tube	
kHz	R/ρc	X/ρc	R/ρc	X/ρc
0.275	25.17	32.56		
0.315	12.77	22.69		
0.4	35.99	48.08		
0.5	4.37	16.39		
0.63	1.79	12.69		
0.8	2.39	9.78	2.73	11.05
1.0	1.25	7.39	1.56	7.49
25	1.76	7.11	1.34	7.41
1.6	1.36	5.05	0.63	4.85
2.0			1.06	5.64
2.5			0.65	3.84
3.15			0.46	2.81
4.0			0.55	1.93
5.0			0.64	1.65
6.3			0.34	0.87

Table 8.4

Double Layer Impedance

Frequency	Large Tube		Small Tube	
kHz	R/ρc	X/ρc	R/ρc	X/ρc
0.275	5.92	14.69		
0.315	7.27	13.01		
0.4	2.96	9.87		
0.5	2.15	6.55		
0.63	2.10	5.36		
0.8	1.84	3.33	1.31	4.86
1.0	2.27	1.99	1.14	3.72
1.25	2.23	0.96	1.08	2.91
1.6	1.68	-0.50	1.07	1.77
2.0			1.17	1.40
2.5			1.19	0.80
3.15			1.65	0.89
4.0			2.82	0.66
5.0			2.69	1.52
6.3			2.13	0.57

Table 8.5

Single Inverted Layer Impedance

Frequency	Large Tube		Small Tube	
kHz	R/ρc	X/ρc	R/ρc	X/ρc
0.275	34.4	28.8		
0.315	14.9	17.1		
0.4	9.76	21.2		
0.5	6.22	13.4		
0.63	3.7	9.13		
0.8	3.15	5.9	3.48	11.74
1.0	2.72	3.25	1.56	7.49
1.25	3.73	0.54	1.57	8.02
1.6	2.84	-0.77	0.7	4.83
2.0			0.81	3.11
2.5			0.91	1.82
3.15			0.46	2.81
4.0			1.48	-0.06
5.0			0.79	-0.78
6.3			0.47	-0.67

Table 8.6

Double Inverted Layer Impedance

Frequency	Large Tube		Small Tube	
kHz	R/ρc	X/ρc	R/ρc	X/ρc
0.275	6.62	14.0		
0.315	2.96	8.1		
0.4	3.44	7.23		
0.5	3.63	7.87		
0.63	2.50	4.69		
0.8	1.66	1.95	1.77	4.28
1.0	1.53	0.36	1.56	3.02
1.25	1.14	-0.79	1.57	2.12
1.6	0.87	-1.27	1.59	0.96
2.0			1.59	0.47
2.5			1.96	-0.75
3.15			1.73	-1.41
4.0			1.17	-1.84
5.0			3.61	-1.4
6.3			0.68	-1.13

Table 8.7

Artificial Grass - tufts clipped off at surface

(a) Single layer stubble facing rigid backing

frequency kHz	R/pc	X/pc
0.8	20.32	33.53
1.0	22.23	28.62
1.25	65.88	-10.12
1.6	12.60	24.86
2.0	38.55	21.21
2.5	7.68	16.35
3.15	17.36	15.13
4.0	12.57	8.22
5.0	4.46	0.34
6.3	2.60	3.02

(b) Single layer stubble facing source

frequency kHz	R/pc	X/pc
0.8	57.71	31.37
1.0	13.88	24.81
1.25	12.84	25.01
1.6	13.39	23.69
2.0	34.65	15.93
2.5	9.06	14.17
3.15	22.39	0.0
4.0	8.84	3.2
5.0	3.67	1.67
6.3	1.62	0.41

8.2 Free Field Standing Wave Measurements

8.2.1 The useful upper frequency limit of the impedance tube is dictated by the onset of cross mode propagation, and is related to the tube diameter. In order to extend the range beyond 6300 Hz, the limit of the 3 cm tube, the free-field method of Sides and Mulholland [8.4] was adapted for normal incidence measurements.

The measurement system was mounted in the anechoic chamber of the Department of Mechanical Engineering, Noise Control Laboratory, of the Pennsylvania State University (P.S.U.).

The backing surface used to support the sample materials was 1.8 m long and 1.2 m wide and consisted of a 7 mm aluminium sheet fixed to a 21 mm thick stiffened plywood board. Once cut to size the sample was fixed to the backing with double sided adhesive tape to prevent it lifting during the course of the measurements. Considerable care was taken to ensure that the sample lay flat against the backing, to minimise errors due to a non-plane surface.

8.2.2 Source and Receiver Transducers

The source transducer was a Phillips T8 pressure dome loudspeaker unit. Previous experience at the P.S.U. Noise Control Laboratory had shown this unit to have adequate power output and bandwidth for these experiments.

The receiving transducer was a Bruel and Kjaer 4133 ½" condenser microphone and 2615 cathode follower, fitted with a 3 mm (outside

diameter) probe tube 24 cm long. No attempt was made to modify the frequency response of this combination. Normally damping material would be inserted within the probe to reduce resonance effects, but since the impedance test only requires measurement of the standing wave ratio, such damping was considered unnecessary.

The probe tube was used to explore the standing wave set up in front of the sample and determine the location of the maxima. In view of the large number of tests to be conducted a special motorised probe positioning mechanism was developed. A synchronous motor, appropriately geared down, was connected to a short length of tapped studding. The microphone and probe tube were fixed to this studding by a small carriage, so that as the motor turned the probe would traverse the length of the studding.

The positioning mechanism was screwed to the underside of the backing board, so that the probe could traverse along a vertical path above the sample. The maximum traverse length available was 7.75". Limit switches at the ends of the studding, activated by the microphone carriage, disconnected the power supply to the motor when an endstop was reached.

8.2.3 Instrumentation

A block diagram of the instrumentation used for these impedance measurements is shown in Figure 8.3. The source signal (pure tone) was derived from either the HP3310B or the SD104A-2 oscillators, depending upon the frequency, since neither unit covered the entire range of interest, the HP3310B was used for all measurements above 20 kHz and the SO104A-2 for those below.

The Mackintosh 3500 provided the power amplification necessary to drive the T8 loudspeaker to ensure an adequate signal to noise ratio.

The Heath EU805 frequency counter was used to monitor the oscillators, because the tuning dials were not sufficiently accurate to obtain repeatable settings.

The microphone output was connected to the Brüel and Kjaer 2606 amplifier. This provided the polarisation voltage for the microphone, and power for the 2615 cathode follower as well as amplication for the low level signal.

The HP 400FL voltmeter provided a high impedance input for the long connecting cable from the 2606. It also simplified gain changes because these could be made at a point outside the chamber.

After amplification the received signal was filtered, rectified and converted to a d.c. log voltage by the SD101B tracking filter. This device works on the hetrodyne principle and is capable of very narrow band filtering.

The output of the tracking filter formed the Y input to the HP 7045A X-Y plotter. The X input was obtained from a linear potentiometer attached to the microphone traverse mechanism.

8.2.4 Measurement Range

The free-field experiments were carried out in order to extend the frequency range of the impedance measurements. The lower limit of the range was determined by the need to locate two minima in a single

traverse above the sample. Experiments showed that the lowest frequency which satisfied this requirement was 1300 Hz. The upper limit of 32 kHz was set by the scale factor of the model experiments.

Measurements were conducted for the same four material configurations, as described in 8.1.3.

8.2.5 Probe End Corrections

Corrections for the probe-end effect were estimated using the rigid backing surface and measuring the location of the first two minima. The results are shown in Table 8.8.

Above 2 kHz the results are comparable with those obtained for the similar diameter impedance tube probe, and with the theoretical correction $\hat{C}_e = -0.19$ cm.

At low frequencies the sign of the corrections imply that the apparent location of the probe end is behind the physical end.

Table 8.8

Free Field Probe-End Corrections

Frequency Hz	d_1 cm	d_2 cm	C_e cm
1300	6.71	18.92	0.64
1310	6.71	18.80	0.71
1334	6.68	18.29	0.89
1600	5.38	15.34	0.41
2000	4.01	12.32	-0.15
2500	3.22	9.91	-0.13
3150	2.62	7.82	0.03
4000	1.91	6.17	-0.23
5000	1.55	4.85	-0.10
6300	1.12	3.84	-0.25
8000	0.89	3.00	-0.18
10000	0.74	2.41	-0.10
12500	0.48	1.83	-0.20
16000	0.33	1.45	-0.23
20000	0.28	1.12	-0.15
25000	0.18	0.81	-0.15
31500	0.15	0.71	-0.13

It was felt the most probable cause of this discrepancy was a lack of rigidity in the backing surface. Measurement of the impedance of the backing, given in Table 8.9, supports this conclusion.

8.2.6 Measurement Procedure

The sample material was laid flat on the rigid backing, and in the case of the single layer was attached with double sided adhesive tape.

The probe tube was set flush with the rigid backing, regardless of the material thickness. This provided a convenient reference point for setting the X scale of the plotter from the linear potentiometer displacement transducer. The Y scale of the plotter was set to 10 dB/in.

Table 8.9

Backing Surface Impedance

Frequency kHz	R/ρc	X/ρc
1.36	2.8	-9.6
1.66	3.34	-12.72
1.98	5.84	-30.79
2.48	8.65	-57.51
3.18	29.19	-354.1
3.88	0.84	-16.73
5.02	0.09	-43.61
7.86	0.55	8.22
9.88	1.33	-1.92
12.30	0.35	-1.94
14.82	0.18	1.37
19.76	0.46	-0.35
26.08	0.46	-0.61
29.64	0.51	0.39

Figure 8.4 shows a typical trace of the pressure variation with height above the rigid backing surface as recorded by the plotter. The left hand limit represents the rigid surface. Figure 8.5 shows a trace for a single layer of artificial grass.

It was observed that in many cases the recorded minima were very broad, possibly because the probe was moving too quickly. The traverse rate was therefore reduced by driving the synchronous motor from a variable frequency power supply rather than directly from the mains. Unfortunately the low frequency performance of this supply only permitted a 2:3 reduction of the motor speed.

The maximum and minimum pressures were read directly from the plotter traces, together with their locations. The location of the first maximum was taken as the reference location.

8.2.7 Data Reduction

The real and imaginary parts of the normal impedance can be obtained by substituting the measured values into equation 5.16, 5.17 and 5.18.

The source-receiver distance for all the normal incidence measurements was 70.5".

The standing wave ratio can be calculated from the measured variables using the expression:

$$r = \frac{10^{SPLMIN/20}}{10^{SPLMAX/20}} = 10^{(SPLMIN-SPLMAX)/20}$$

where SPLMIN and SPLMAX are the sound pressure levels of the first minimum and the maximum respectively.

8.2.8 Results

The normal surface impedance calculated from the free-field measurements are shown in Tables 8.10 through to 8.13.

Comparing the normal and inverted layer results, it can be seen that in general the inverted layers have a smaller impedance than the normal layers. This is probably due to the existence of the air gap created by the tufts as described in section 8.1.7.

The single layer 'tufts-up' results do not compare well with the impedance tube values at low frequencies. In part this may be due to the lack of rigidity of the backing surface, but the sample size and edge diffraction effects may also be important. The impedance tube uses a relatively small sample size that may not be representative of the whole sample. Furthermore, any clamping of the sample edges in the tube would tend to raise the calculated values of the resistance |8.13|.

8.2.9 Regression Analysis

The individual impedance measurements are not very convenient to use in the point to point propagation solutions of Chapter 3. A monotonic impedance versus frequency characteristic is more suitable for computation purposes than scattered data points.

Table 8.10

Free-Field Impedance - Single Layer

Frequency kHz	R/ρc	X/ρc
1.6	7.43	34.29
2.0	0.12	1.59
2.5	2.28	4.26
3.15	8.32	31.60
4.0	1.86	5.71
5.0	1.91	4.84
6.3	0.93	0.44
8.0	0.51	-2.35
10.0	0.79	0.09
12.5	0.41	1.04
16.0	0.41	-0.70
20.0	0.36	-0.17
25.0	0.45	-0.42
32.8	0.53	0.20

Table 8.11

Free-Field Impedance - Double Layer

Frequency kHz	R/ρc	X/ρc
1.6	2.88	8.25
2.0	6.72	11.89
2.5	5.46	13.50
3.15	2.41	8.48
4.0	2.27	7.22
5.0	2.39	6.21
6.3	1.00	-0.82
8.0	2.47	-6.48
10.0	0.71	0.64
12.5	2.42	3.01
16.0	0.60	-0.14
20.0	0.72	-0.51
25.0	0.99	-0.5
27.0	1.03	-0.99
32.0	0.67	0.19

Table 8.12

Free-Field Impedance Single Inverted Layer

Frequency kHz	R/ρc	X/ρc
1.6	3.28	5.48
2.0	4.73	5.02
2.5	3.56	3.99
3.15	1.33	3.16
4.0	0.60	2.30
5.0	0.51	1.26
6.3	0.50	-0.23
8.0	0.15	-0.45
10.0	0.24	0.41
12.5	0.21	-0.47
20.0	1.87	0.91
25.0	0.63	0.92

Table 8.13

Free Field Impedance Double Inverted Layer

Frequency	R/ρc	X/ρc
1.6	0.9	6.55
2.0	0.52	1.77
2.5	0.53	2.48
3.15	0.47	2.03
4.0	0.15	1.25
5.0	0.23	0.67
6.3	0.14	-0.16
8.0	0.16	-0.51
10.0	0.14	0.34
12.5	0.29	0.31
16.0	1.61	0.22
20.0	3.0	1.83
25.0	0.41	0.12
27.0	1.30	-0.12
32.0	0.49	0.14

In view of this and the considerable scatter in the data, it was decided to derive a power law relationship along the lines suggested by Delaney and Bazley |8.3|. Following this model a linear regression of the form:

$$\begin{matrix} \text{Ln } (R/\rho c) \\ \text{Ln } (X/\rho c) \end{matrix} = A + B.\ \text{Ln}(f)$$

was performed on the artificial grass impedance data from both the impedance tube and free field measurements.

The values of the intercept, slope and correlation coefficient are given in Table 8.14.

The correlation coefficients for the double layer resistance and both inverted layer's reactance terms are significantly lower than the other coefficients.

One possible cause is the increase in scatter of the data points associated with the uncertainty in the location of the sample surface |8.14|. The reference position for all distance measurements was established by pushing the probe tube into the sample until resistance was met. In the case of the single layer surface, the rubber backing of the sample was fixed to the rigid termination of the tube and it was possible to identify the point at which the probe tube had reached the rubber surface. For the other three samples, it would have been very easy to cause bowing of the sample surface, because of the small resistance offered by the tufts when establishing the reference position. Unfortunately it was not possible to investigate

these effects further during the author's short stay at the Pennsylvania State University.

Table 8.14

Log-Log

Layer Type	Impedance Variable	Intercept A	Slope B	Correlation Coefficient
Single	R/ρc	7.19	-0.89	-0.86
	X/ρc	9.88	-1.14	-0.94
Double	R/ρc	3.22	-0.34	-0.74
	X/ρc	7.66	-0.94	-0.92
Single Inverted	R/ρc	9.37	-1.18	-0.97
	X/ρc	10.0	-1.21	-0.73
Double Inverted	R/ρc	8.02	-1.08	-0.88
	X/ρc	8.87	-1.18	-0.79

8.2.9 Bulk Properties of the Artificial Grass Material

The linear regression equations for the single and double thickness surface impedance values can be used to calculate the bulk propagation constant k_2 and the characteristic impedance Z_c. According to Pyett |8.9|, k_2 can be obtained from the relationship

$$\cosh(-2ik_2 d) = \frac{|R^1(R-R^1)+X^1(X-X^1)|+i|R^1(X-X^1)+X^1(R-R^1)|}{(R-R^1)^2+(X-X^1)^2}$$

and Z_c from

$$Z_c = 2(d)\ \text{tank}\ (-ik_2 d)$$

where R, X and R^1, X^1 are the real and imaginary parts of the single (d) and double (Zd) thickness impedance values respectively.

Calculated values for the refractive index, bulk propagation constant and characteristic impedance (for both normal and inverted layers) are givne in Table 8.15.

The refractive index n, can be used to determine the range of frequencies for which a material may be considered to be locally reacting. Section 3.8 showed that a sufficient condition is $|n| >> |$ so that

$$R_p = \frac{Z\cos\theta_i - \sqrt{1-\sin^2\theta_i/n^2}}{Z\cos\theta_i + \sqrt{1-\sin^2\theta_i/n^2}} \simeq \frac{Z\cos\theta_i - 1}{Z\cos\theta_i + 1}$$

Table 8.15

Bulk Propagation for the Artificial Grass Material

Frequency kHz	Magnitude of Refractive Index n	Propagation Constant k_2	Characteristic Impedance (normal) Z_{cn}	Characteristic Impedance (inverted) Z_{ci}
1.0	2.1	29.7 +i 25.0	4.2 +i.2.0	3.8 +i 0.88
1.25	1.7	30.0 +i 27.8	3.3 +i 1.8	2.8 +i 0.71
1.6	1.5	31.4 +i 29.6	2.7 +i 1.4	2.2 +i 0.57
2.0	1.2	34.6 +i 24.5	2.3 +i 1.1	1.6 +i 0.45
2.5	1.0	41.0 +i 26.5	2.1 +i 0.67	1.2 +i 0.36
3.15	0.95	52.0 +i 21.4	2.2 +i 0.29	0.95 +i 0.29
4.0	0.93	67.2 +i 16.1	2.6 +i 0.036	0.72 +i 0.23
5.0	0.92	85.0 +i 12.5	3.8 +i 0.32	0.54 +i 0.18
6.3	0.88	103.0 +i 17.8	2.4 +i 3.2	0.41 +i 0.14
8.0	0.70	101.1 +i 24.3	1.5 +i 1.8	0.32 +i 0.11
10.0	0.54	99.0 +i 26.5	1.2 +i 1.2	0.24 +i 0.089
12.5	0.43	98.0 +i 26.7	0.95 +i 0.84	0.18 +i 0.070
16.0	0.34	97.4 +i 26.1	0.79 +i 0.63	0.14 +i 0.055
20.0	0.26	97.2 +i 25.1	0.67 +i 0.48	0.11 +i 0.043
25.0	0.21	97.1 +i 23.9	0.56 +i 0.37	0.080 +i 0.034

Table 8.15 (Cont'd)

Frequency kHz	Magnitude of Refractive Index n	Propagation Constant k_2	Characteristic Impedance (normal) Z_{cn}	Characteristic Impedance (inverted) Z_{ci}
31.5	0.17	97.1 +i 22.6	0.48 +i 0.28	0.060 +i 0.026
40.0	0.13	97.2 +i 21.2	0.41 +i 0.22	0.040 +i 0.020
50.0	0.10	97.4 +i 20.0	0.35 +i 0.17	0.035 +i 0.016
63.0	0.084	97.6 +i 18.8	0.29 +i 0.13	0.027 +i 0.012
80.0	0.067	97.9 +i 17.6	0.25 +i 0.097	0.020 +i 0.0096
100.0	0.054	98.1 +i 16.6	0.22 +i 0.095	0.016 +i 0.0075

If $n > 3.16$, the error in the square root is less than 10%, whilst if $n > 1.5$ the error is less than 25%. The calculated values indicate that the material is unlikely to be locally reacting above 1.6 kHz.

The problem lies in assuming that this material can be modelled as a homogeneous porous medium for the purposes of calculating the reflected and transmitted waves. Comparing the characteristic impedance values for the normal and inverted layers, the large differences indicate that the material is inhomogeneous above 2.5 kHz. In view of the construction of the artificial grass, this is not an unexpected result. Furthermore, it would explain why the magnitude of the refractive index tends to zero at high frequencies rather than unity. As the wavelength of the incident sound decreases, it becomes comparable with the physical dimensions of the tufts, hence a scattering theory would be more appropriate to describe the reflected field.

8.3 Indirect Impedance Measurements

8.3.1 A normal surface impedance estimate can be obtained using the theoretical prediction equations of Chapter 3 as part of an iterative search procedure.

An initial guess is made for the normal impedance of the surface and the excess attenuation calculated for the particular source receiver geometry. The difference between this and the measured excess attenuation is stored as an error. The impedance value is then incremented a fixed amount plus and minus creating a set of impedance values for which new errors are calculated. The value of impedance producing the smallest error is then used as the initial guess in a new cycle of the search procedure, with a smaller impedance increment. This process is repeated until the best impedance value is determined to within 0.1. ρc.

Chessell |8.11| has suggested that the impedance values required for the predicted algorithm can be obtained from the Delaney and Bazley |8.3| flow resistivity model for fibrous porous media outline in section 5.7.

The model provides estimates of the characteristic impedance and the propagation constant of the medium, whereas the theoretical predictions are based upon normal surface impedance.

The relationship between these two impedances is determined by the nature of the surface. Three surface models have been examined.

The first model assumes that the surface is a locally reacting thin layer. The normal surface impedance, Z_s, is therefore given by

$$Z_s = Z_c \coth(-ik_b d)$$

where Z_c is the characteristic impedance, k_b is the propagation constant of the layer and d the thickness of the layer. The predicted excess attenuation is based upon equation 3.64 for local reaction.

Although theoretical prediction equations have been given for the rigid backed layer surface model, they are not applicable at the short separation distances and grazing angles of incidence used in this study.

The second model assumes that the surface can be model as a semi-infinite medium with a normal surface impedance equal to the characteristic impedance, therefore

$$Z_s = Z_c$$

The predicted excess attenuation is based upon equation 3.53.

The third model assumes that the surface is locally reacting, in which case the Delany and Bazley model gives

$$Z_s = Z_c$$

due to the very high rate of attenuation obtained for k_b. The predicted excess attenuation is based upon equation 3.64.

A least squares criteria can be established to obtain the best agreement between the measured and predicted excess attenuation values and hence estimates for the normal surface impedance.

The method, as used here, limits the range of frequency values employed in the iteration procedure to the range 2-40 kHz, corresponding to the first dip in the excess attenuation curve; because the location of the second dip is less sensitive to the surface impedance than to the source receiver geometry.

Figure 8.6 illustrates the influence of the normal impedance upon the location of the interference dips. The curves of Figure 8.6(a) were calculated for an impedance value similar to that for the artificial grass surface and those of (b) for a value similar to the fibreboard surface. The dashed line curves, either side of the solid line, were calculated for impedance values of the nominal $\pm$25% and $\pm$50%. The smaller values of impedance show a larger dip at lower frequencies.

The location, with respect to frequency, of the interference dip at about 70 kHz shows much small variation with impedance than does the low frequency dip. The amplitude variations are comparable.

8.3.2 Instrumentation

A block diagram of the instrumentation used to obtain the epxerimental values of excess attenuation is shown in Figure 8.7.

The air jet was used as the signal source and a B & K 4135 ¼" microphone as the receiver. The useful measurement range of this combination is approximately 10 Hz-70 Hz.

The Nicolet spectrum analyser was used in the dual channel mode with summation averaging. A Hanning squared window was employed to smooth the spectral estimates, together with 50% overlap processing. The instrument was set to average 128 measurement samples.

The spectral estimates were stored on the Nova 4/C computer and then transferred to the VAX 11/780 computer for subsequent processing.

8.3.3 Measurement procedure

The backing surface used to support the sample materials was a 1.8 m long, 1.2 m wide, 25 mm thick sheet of varnished blockboard.

The two other model materials were cut to the same size and laid directly onto the blockboard. In the case of the artificial grass, great care was taken to ensure that the sample lay flat to minimize the possibility of errors due to surface roughness. The fibreboard sample was sufficiently rigid to prevent such errors.

A hole was cut through the blockboard and sample to allow the air jet source to move along a vertical axis above the surface. The microphone was suspended from the chamber ceiling and aligned so that the diaphragm was normal to the source.

For these experiments the source and receiver were located 5 cm above the surface 100 cm apart.

8.3.4 Data Reduction

An iterative procedure was developed to estimate the normal surface impedance for the model materials from experimental measurements of the excess attenuation, based upon the local and extended reaction theoretical predictions.

The experiments actually measured the total field at the receiver and were reduced to the form excess attenuation by dividing the measured spectrum by the free-field spectrum. The latter had been measured previously and stored on the computer.

8.3.5 Results

The iterative procedure was used to estimate the impedance of the three surfaces: blockboard, artificial grass and fibreboard, using the single parameter (flow resistivity) model. The minimum error between measured and predicted excess attenuation for the blockboard surface occured for a flow resistivity value greater than 1.10^{10} mks units. At such high values the iterative procedure is not very

sensitive to small changes in flow resistivity.

The impedance calculated from the flow resistivity is very large, but the real and imaginary parts are comparable, whereas one would expect zero reactance to ensure no phase change on reflection. Such anomolies are a consequence of extropolating the flow resistivity model to non-porous materials. It is therefore difficult to determine from these measurements whether the blockboard does indeed behave as a rigid surface over the frequency range of interest. However, experimental results described in sections 8.4.4 and 8.5.7 indicate that it is reasonable to assume the blockboard is rigid over the frequency range 1-15 kHz.

The flow resistivity estimates for the two model materials are shown in Table 8.16.

Table 8.16

Flow Resistivity Estimates for the Model Materials

Surface Model	Artificial Grass mks units	Fibreboard mks units
locally reacting thin layer	1.122 10^6	2.691 10^6
semi-infinite medium	1.162 10^6	2.765 10^6
local reaction	1.125 10^6	2.695 10^6

The poor agreement between 50 and 100 kHz can be attributed to two factors, first the effective height of the source above the acoustic (rather than physical) surface and the second the destruction of the interference pattern by near surface turbulence. Both these factors are considered in Chapter 9.

A further consideration at high frequencies is the receiver directivity. Although the direct wave arrives at normal incidence, the reflected wave does not. For the geometry in question the angle of incidence of the reflected wave is 6 deg. According to the Bruel and Kjaer data book [8.6], the difference in sensitivity of the 4135 microphone at these two angles at 80 kHz is of the order of 1 dB, and increases at higher frequencies.

Although the microphone manufacturers published directivity data, it is usually published in the form of correction curves, such as Figure 7.1, which are not convenient for use with the propagation prediction schemes. Unfortunately, there is no simple method for deriving a continuous directivity function at high frequencies, so it has not been possible to correct for this effect as part of the excess attenuation calculation.

The major criticism levelled against this indirect method of determining normal surface impedance, is that a single calculation procedure is used for both estimation and comparison. However, the degree of confidence in the technique can be improved by using two different source receiver geometries, one for estimation and another for comparison.

A reasonable test would be to compare the measured and predicted excess attenuation curves for a geometry with lower source and receiver heights where the theory is more sensitive to impedance values. However, the air movement created by the air jet sound source introduced considerable disturbance to the sound field around a low level microphone. It was therefore decided to measure the excess attenuation with the source and receiver heights increased.

Figure 8.10 compares the measured and predicted curves for a source height of 9 cm, receiver height of 10 cm and separation distance of 100 cm. The predicted curve is based upon the local reaction surface model and the flow resistivity estimate obtained for the artificial grass material. Below 60 kHz the agreement between the curves is comparable with that of Figure 8.8. Above 60 kHz the prediction is not good due to a combination of source height error, surface turbulence and transducer directivity. However, the results indicate the usefulness of the indirect method over a broad frequency range.

Section 8.2.9 showed that the artificial grass material is not locally reacting above 1.6 kHz. This might indicate that the extended reaction surface model impedance values should provide a better estimate of the surface impedance. However, it is clear from Tables 8.17 and 8.18 that the differences between the local and extended reaction impedance values are negligibly small. In view of this and the fact that the mixed impedance prediction equations assume the impedance surface to be locally racting, it was decided to use the local reaction impedance values as the indirect method impedance estimates.

The three surface models produce very similar flow resistivity estimates. This is not unexpected, since it has been shown [8.15] that the flow resistivity model tends to over predict the values of the propagation constant. For the extended reaction solution this produces a large refractive index, whilst for the thin layer model the coth term of the surface impedance is approximately unity. The effect is that these two surface models give results equal to the local reaction model.

The normal surface impedance values for the two materials, calculated from these estimates, are given in Tables 8.17 to 8.22. The main differences between the surface models occur at low frequencies, such that the higher the flow resistivity the greater the real and imaginary parts of the impedance. At high frequencies the results are comparable.

The differences between the three surface models can best be seen by comparing the measured and predicted excess attenuation curves. Figure 8.8 shows the results for the artificial grass material.

The results are virtually identical, over the whole frequency range. The agreement with the measured excess attenuation is seen to be good except between 5-7 kHz and 70-90 kHz.

The comparable results for the fibreboard material are shown in Figure 8.9. Again the three models produce identical results, but the agreement with the measured attenuation is poor between 2.5 and 5 kHz and also 50-100 kHz.

Table 8.17 Impedance of Artificial Grass

Local Reaction (flow resistance = 1125000)

Frequency kHz	R/ρc	X/ρc
1.0	10.9	13.0
1.25	9.3	11.0
1.6	8.0	9.2
2.0	6.9	7.8
2.5	5.9	6.6
3.15	5.1	5.6
4.0	4.5	4.7
5.0	3.9	3.9
6.3	3.5	3.3
8.0	3.1	2.8
10.0	2.7	2.4
12.5	2.5	2.0
16.0	2.2	1.7
20.0	2.0	1.4
25.0	1.9	1.2
31.5	1.7	1.0
40.0	1.6	0.87
50.0	1.5	0.73
63.0	1.4	0.62
80.0	1.4	0.52
100.0	1.3	0.44

Table 8.18 Impedance of Artificial Grass

Extended Reaction (flow resistance = 1162000)

Frequency kHz	R/ρc	X/ρc
1.0	11.1	13.3
1.25	9.5	11.2
1.6	8.1	9.5
2.0	7.0	8.0
2.5	6.0	6.7
3.15	5.2	5.7
4.0	4.6	4.8
5.0	4.0	4.1
6.3	3.5	3.4
8.0	3.1	2.9
10.0	2.8	2.4
12.5	2.5	2.1
16.0	2.3	1.7
20.0	2.1	1.5
25.0	1.9	1.2
31.5	1.7	1.0
40.0	1.6	0.89
50.0	1.5	0.75
63.0	1.4	0.63
80.0	1.4	0.53
100.0	1.3	0.45

Table 8.19 Surface impedance of artificial grass

Thin layer (flow resistance = 562400)

Frequency kHz	R/ρ	X/ρc
1	10.9	13.0
1.25	9.3	10.9
1.6	7.9	9.2
2.0	6.8	7.8
2.5	5.9	6.6
3.15	5.1	5.5
4.0	4.5	4.7
5.0	3.9	4.0
6.3	3.4	3.3
8.0	3.1	2.8
10.0	2.7	2.4
12.5	2.5	2.0
16.0	2.2	1.7
20.0	2.0	1.4
25.0	1.9	1.2
31.5	1.7	1.0
40.0	1.6	0.86
50.0	1.5	0.73
63.0	1.4	0.62
80.0	1.4	0.52
100.0	1.3	0.44

Table 8.20 Impedance of Fibreboard

Local Reaction (flow resistance = 2695000)

Frequency kHz	R/ρc	X/ρc
1.0	20.1	24.6
1.25	17.0	20.7
1.6	14.5	17.5
2.0	12.3	14.8
2.5	10.5	12.5
3.15	9.0	10.5
4.0	7.7	8.9
5.0	6.6	7.5
6.3	5.7	6.3
8.0	5.0	5.4
10.0	4.3	4.5
12.5	3.8	3.8
16.0	3.4	3.2
20.0	3.0	2.7
25.0	2.7	2.3
31.5	2.4	1.9
40.0	2.2	1.6
50.0	2.0	1.4
63.0	1.8	1.2
80.0	1.7	0.99
100.0	1.6	0.83

Table 8.21 Impedance of Fibreboard

Extended Reaction (flow resistance = 2765000)

Frequency kHz	R/ρc	X/ρc
1.0	20.5	25.0
1.25	17.4	21.0
1.6	14.7	17.8
2.0	12.5	15.0
2.5	10.7	12.7
3.15	9.1	10.7
4.0	7.8	9.1
5.0	6.7	7.7
6.3	5.8	6.5
8.0	5.1	5.5
10.0	4.4	4.6
12.5	3.9	3.9
16.0	3.4	3.3
20.0	3.0	2.8
25.0	2.7	2.3
31.5	2.4	2.0
40.0	2.2	1.7
50.0	2.0	1.4
63.0	1.8	1.2
80.0	1.7	1.0
100.0	1.6	0.85

Table 8.22 Impedance for fibreboard

Thin layer (flow resistance = 4365000)

Frequency kHz	R/ρc	X/ρc
1.0	20.1	24.5
1.25	17.0	20.7
2.0	12.3	14.8
2.5	10.5	12.5
3.15	9.0	10.5
4.0	7.7	8.9
5.0	6.6	7.5
6.3	5.7	6.3
8.0	4.9	5.4
10.0	4.3	4.5
12.5	3.8	3.8
16.0	3.4	3.2
20.0	3.0	2.7
25.0	2.7	2.3
31.5	2.4	1.9
40.0	2.2	1.6
50.0	2.0	1.4
63.0	1.8	1.2
80.0	1.7	0.99
100.0	1.6	0.83

8.4 Direct and reflected pulse measurements

8.4.1 The spherical wave reflection coefficient, and hence impedance, can be calculated from the ratio of reflected to incident energy. Using a transient signal source it is possible to separate the direct and reflected pulses by employing a large path length difference.

The spectrum of each pulse can be calculated using a Fourier Transform algorithm and the spherical reflection coefficient obtained by dividing the reflected pulse spectrum by the direct pulse spectrum.

Two source-receiver geometries were employed for these experiments. For the first the receiver was positioned high above the surface, giving a path length difference of the order to 30 cm. For the second source and receiver were both 15 cm above the surface giving a path length difference of 4 cm.

The most difficult problem with this type of experiment is to obtain a reliable estimate of the phase of the reflection coefficient. Two phase components can be identified, one due to the pure time delay between the arrival of the direct and reflected pulses at the receiver, the other due to the properties of the reflecting surface. It is impossible to attribute the measured phase to one component or the other, given the uncertainty in the location of the surface.

At the maximum sampling frequency of the Nicolet spectrum analyser, the sampling interval is 3.9 μs. Hence the smallest phase increment that can be measured for a 100 kHz sinewave is

$$\Delta\phi = \frac{100}{256} \times 2\pi = 140 \text{ deg}$$

Even at 32 kHz the increment is 45 deg. It is therefore unlikely that the phase estimate of the reflection coefficient coefficient will be very accurate.

Under these circumstances the rigid surface provides a useful guide to the accuracy of the data reduction process because the phase of the reflection coefficient is known.

8.4.2 Instrumentation and Measurement Procedure

A block diagram of the instrumentation used for the pulse separation experiments is shown in Figure 8.11.

The pulse source was the small spark unit described in Appendix B, the receiver a B & K 4135 ¼" microphone.

The Nicolet spectrum analyser was used in the dual channel signal enhancement mode, with summation averaging. No window function was applied to the sampled data; because the whole transient is captured in a single window period. The instrument was set to average 128 samples.

The enhanced signal was stored on the Nova 4/C computer and later transferred to the VAX 11/780 computer for subsequent processing.

The measurement procedure follows that outlined in section 8.3.2, except for the differences in the source receiver geometry.

8.4.3 Data Reduction

The data reduction process consists of separating the direct and reflected pulses, calculating their spectra and dividing the reflected spectrum by the direct spectrum.

Figure 8.12 shows an averaged measurement of the direct and reflected pulses for source and receiver heights of 15 cm and 60.3 cm respectively, and a separation distance of 52.7 cm.

The direct pulse is obtained by first removing the short delay between the start of the measurement period and the onset of the pulse. After this the reflected pulse is removed simply by setting to zero all the samples from the end of the direct pulse to the end of the measurement period.

The reflected pulse is obtained in a similar manner. The direct pulse automatically disappears when the time delay to the onset of the reflected pulse is removed.

It is good practice to zero the samples after the reflected pulse to minimise the effects of other reflections within the chamber.

The direct pulse and its spectrum and the reflected pulse and its spectrum are shown in Figures 8.13(a),(b),(c) and (d) respectively. The spectral magnitudes have been plotted with respect to a reference of 1 Volt for convenience.

8.4.4 Results

The reflection coefficient obtained for the rigid surface is shown in Figure 8.14. Up to 15 kHz the magnitude and phase agree quite well with the theoretical values of 0 dB and 0 deg. Above 15 kHz the measured values fluctuate quite rapidly, the magnitude dropping to a minimum of -6.5 dB and the phase rising to +130 deg.

The large phase deviation is most probably due to an error in the time delay estimate. This contributes a linear phase term $\exp(i\omega\tau)$, where τ is the time delay error. At 100 kHz τ is less than the sampling interval of the Nicolet spectrum analyser.

The magnitude fluctuations may be due to lack of rigidity of the blackboard. Vibrations could be induced by the airborn wave, but it is more likely to result from mechanical coupling between the air jet and the blackboard. The equipment necessary to test such a hypothesis was not available.

A second measurement for the rigid surface, but with the source and receiver 15 cm above the surface and 1 m apaprt, is shown in Figure 8.15. Although the phase measurement is good, the magnitude exhibits the same high frequency variability.

A further factor contributing to the errors at high frequency is the receiver directivity. For both geometries the error is approximately -3 dB at 80 kHz and -2 dB at 125 kHz. The error fluctuates between 0 dB and 3 dB as the ratio (incident wave length)/(microphone diaphragm diameter) changes. The range of the reflection coefficient

magnitude fluctuations are comparable with the directivity error between 70 and 100 kHz.

The calculated reflection coefficients for the artificial grass and fibreboard materials are shown in Figure 8.16 and 8.17.

The general shape of the magnitude estimates agree with values calculated from the impedance data of Section 8.3, but the phase estimate shows a large deviation due to an error in the time delay estimate.

The normal surface impedance values calculated from these reflection coefficients are given in Tables 8.23 and 8.25.

Table 8.23 Normal surface impedance of artificial grass calculated from pulse separation measurements

Frequency kHz	R/ρc	X/ρc
1.0	5.6	6.6
2.0	5.7	6.2
3.0	5.7	6.0
4.0	5.2	5.8
5.0	5.1	6.0
6.0	3.8	5.6
8.0	2.1	4.7
10.0	1.5	3.9
12.0	1.21	2.2
16.0	0.92	2.8
20.0	0.75	2.4

Table 8.24 Normal Surface Impedance of Fibreboard Calculated from Pulse Separation Measurements

Frequency kHz	R/ρc	X/ρc
1.0	15.2	0
2.0	9.1	7.9
3.0	5.1	7.7
4.0	2.7	6.8
5.0	1.5	5.7
6.0	0.75	4.8
8.0	0.15	3.8
10.0	0.16	3.2
12.0	0.14	2.6
16.0	0.12	2.1
20.0	0.10	1.6

In view of the large fluctuations in the reflection coefficients at high frequencies, the impedance values are given only for the range 1-20 kHz.

8.5 Cepstrum Processing

8.5.1 The pulse separation procedure for estimating surface normal impedance can only be used for source receiver geometries that result in a large path length difference. For the model geometries examined so far this restricts the source and receiver heights to those greater than 15 cm, or alternatively, angles of incidence less than 73^{o}.

In many cases of interest the angle of incidence may be greater than this; hence the need to explore alternative impulse methods of estimating the surface impedance.

Cepstrum processing is one such method. Two forms are in common use, one using the power cepstrum and the other using the complex cepstrum. This section describes a series of experiments and data processing techniques that utilise cepstrum processing to obtain the surface reflection coefficient.

8.5.2 Instrumentation and Measurement Procedure

The instrumentation and measurement procedure used for the cepstrum processing experiments was exactly the same as that described in Section 8.4.2 for the pulse separation experiments.

Five different geometries were examined as shown in Table 8.25. The last column of the table gives the calculated time delay between the direct and reflected pulses.

At the maximum sampling frequency of the Nicolet analyser the time delay of geometry 1 corresponds to only 3 sample intervals and that of geometry 3 to only 15 intervals.

Table 8.25 Cepstrum Measurement Source Receiver Geometry

Geometry	Source Height cm	Receiver Height cm	Direct Path Length cm	Reflected Path Length cm	Time Delay μs
1	5	5	100	100.5	14.7
2	10	5	100.125	101.0	29.4
3	10	10	100	102.0	58.8
4	15	10	100.125	103.0	88.2
5	15	15	100	104.0	117.6

Such short delays precluded extraction of the impulse response from the cepstrum. For this reason only the results of the last two geometries are reported here.

8.5.3 Data Reduction

Cepstrum processing is a recent development in the field of surface impedance estimation. In view of this the main stages of the data reduction process are described in some detail and illustrated by way of an example, the rigid surface.

Figure 8.18(a) shows the measured direct and reflected pulses for the case of an elevated receiver. This geometry was chosen for illustration only; because, as shown in Figure 8.18(b) the power cepstrum of the impulse response is well separated from that of the direct pulse. The structure of each component is clearly distinguishable.

The cepstrum values occuring near zero time are referred to as the low-time components, whilst the remainder are called the high time components. Hence the direct pulse component always occurs at low time, but the impulse response may not.

The impulse response can be extracted from Figure 8.18(b) by simply zeroing the direct pulse contribution and the higher order terms of the impulse response as shown in Figure 8.19. The result is multipled by the ratio of the path lengths for the two pulses, to correct for spherical divergence, and then inverse Fourier Transformed.

8.5.4 Cepstrum Enhancement

As the direct and reflected pulses merge it becomes difficult to determine the onset of the impulse response. Furthermore, the features characteristic of the direct pulse cepstrum spread into the impulse response. Figure 8.20(a) shows the power cepstrum for source and receiver 15 cm high. Although the impulse response is reasonably well defined, the tail of the direct pulse cepstrum exhibits a slowly decaying oscillation, which will degrade the extracted impulse response.

If a good estimate of the direct pulse cepstrum exists, it can be subtracted from the combined cepstrum. Such an estimate can be obtained with the aid of the complex cepstrum. The signal is transformed into the cepstral domain in the normal way, and all but the direct pulse component removed. Inverse transformation produces an estimate of the direct pulse. The power cepstrum of this pulse can be used for the subtraction process.

Figure 8.20(b) shows the improvement in the cepstrum of the impulse response train that can be achieved using this technique.

The final reflection coefficient is very sensitive to the shape of the impulse response. In particular care must be taken to truncate the tail of impulse response if the reflection coefficient is not to exhibit oscillations at high frequency. Figure 8.21(a) shows an impulse response with a long tail (arbitrary delay), and Figure 8.21(b) the corresponding reflection coefficient. Figure 8.22(a) shows a similar impulse response, but with a shortened tail. The corresponding reflection coefficient Figure 22(b) shows only a single dip at high frequency. Note that the effect of truncating the tail of the impulse response has a minor effect upon the phase of the reflection coefficient.

8.5.5 Phase Estimation Techniques

Bolton and Gold [8.7] suggest two ad-hoc methods for improving the phase estimate. The first relies upon cross-correlating the estimated surface impulse response with the impulse response of a digital filter used to smooth the power cepstrum. The two sequences are first padded with zeroes to increase their length from 256 samples to 4096 samples, corresponding to a 64 fold increase in the sampling rates.

The cross correlation function can be used to obtain the time delay of the impulse. The increase in sampling rate, ensures that any error in estimating the duration of the delay contributes a much smaller linear phase component to the phase of the reflection coefficient.

This method is no longer recommended in view of the problems associated with the use of acausal finite impulse response filters.

The second method for improving the time delay estimate is based upon a calculation of a minimum phase component of the extracted impulse response. The minimum phase component is assumed to have no delay and can be used to align the impulse response in the time domain. The approach is based upon the supposition that "for simple low pass systems the deviation of the extracted impulse response from minimum phase is due to the pure delay in the extracted response" [8.7]

The minimum phase component of the impulse response can be obtained from the procedure suggested by Oppenheim and Schafer [8.8]. It is based on the fact that for a minimum phase signal the acausal components of the power cepstrum are zero. The following procedure can be used to calculate the minimum phase component of the impulse response.

(a) compute power cepstrum

(b) multiply power cepstrum by window function U(n), such that:

$$U(n) \begin{cases} = 1 & n = 0, N/2 \\ = 2 & 1 < n < N/2 \\ = 0 & N/2 < n < N-1 \end{cases}$$

(c) compute inverse power cepstrum

The resulting minimum phase impulse response is cross-correlated with the full extracted impulse response to obtain a time delay estimate. Bolton and Gold have shown this technique to be useful for low pass and bandpass systems up to 10 kHz.

The zero padding technique should also be applied to increase the sampling rate of the impulse responses. The required increase is determined by the desired resolution of the phase estimate at high frequencies. Suppose 10 degrees resolution is required, then the sampling rate for a 100 kHz signal is given by:

$$\frac{360}{10} \times 100\ 000 \text{ Hz samples/second}$$

that is 3.6 million samples per second. This is 14 times faster than that available on the Nicolet spectrum analyser.

Given that the Fourier Transform algorithm used for these calculations is based upon powers of 2, the sampling rate would need to be increased by 16, corresponding to a transform length of 16384 sample points. Unfortunately sufficient arrays this size could not be accommodated within the existing computer facility. However, it was possible to employ an 8 fold increase in the sampling rate, which results in a phase resolution of 17.5 degrees.

8.5.6 Minimum Phase Impulse Response

A minimum phase impulse response was calculated, using the procedure outlined above, for the rigid surface measurements. Figure 8.23 shows the extracted impulse and the reconstructed minimum phase

impulse. The minimum phase version does not exhibit an initial negative spike, since this is attributable to the acausal component.

The reflection coefficients calculated from these impulses responses are shown in Figure 8.24.

The time delay of the extracted impulse was calculated using the cross-correlation procedure outlined above. It can be seen that most of the linear phase term present in Figure 8.22(b) has been removed. The small differences in the magnitudes of Figures 8.22(a) and 8.24(b) arise from minor variations in the window applied when extracting the impulse response from the power cepstrum.

Although the result is not exact, it is a reasonable experimental estimate given that the measurement accuracy of the pulse amplitudes is of the order of $\pm$1 dB.

The minimum phase reflection coefficient exhibits no linear phase term as expected. However, the magnitude shows a redistribution of energy into the high frequencies components due to the truncation of the acausal time samples.

8.5.7 Results

The theoretical reflection coefficient, or surface transfer function, of a rigid surface is well known, hence its inverse Fourier transform, the impulse function, can be calculated.

For a digital transform the impulse function would consist of a single non-zero sample point of unit amplitude located at the time origin. This fact has been used as a guide when estimating the duration of the time window to be applied to the cepstrum for the extraction of the impulse response for the blackboard measurements.

The reflection coefficients for the other two model surfaces (artificial grass and fibreboard) are not known, hence there is no general rule for determining the duration of the impulse response. Figure 8.25(a) shows the extracted impulse response (arbitrary delay) for the artificial grass sample. The tail has not been truncated, so the amplitude variations transform to high frequency oscillations in the reflection coefficient as shown in Figure 8.25(b). Shortening the impulse tail reduces these oscillations, but increases the mean value of the impulse and hence the low frequency magnitude, as shown in Figure 8.26.

In order to obtain some guidance as to the shape of the impulse response of the impedance materials, the impulse responses and reflection coefficients were caluclated using the flow resistance model for impedance.

The magnitude and phase of the spherical wave reflection coefficient (local reaction) for the artificial grass and fibreboard materials are shown in Figure 8.27. The values were calculated from the flow resistivity estimates given in Table 8.16.

At low frequencies (1 kHz) the phase is small and positive, increasing to +180 degrees at 100 kHz. This accords with the change in sign of the reflection coefficient of +1 at low frequencies to -1 at high frequencies. The magnitude of the reflection coefficient is plotted on a logarithmic scale, hence $R_p = |1|$ is shown as 0 dB.

Figure 8.28 and (b) show the impulse responses calculated from the plane wave and spherical wave reflection coefficients respectively. It is interesting to note that both results show non-zero negative time components, corresponding to acausal systems (i.e. non-minimum phase).

The shape and duration of these idealised impulse responses have been used as an aid in estimating the duration of the extracted impulse response from the power cepstrum measurements.

The extracted impulse, the minimum phase impulse and the corresponding reflection coefficients for the artificial grass and fibreboard materials are shown in Figures 8.29 to 8.32.

The normal impedance of the samples have been calculated using equation 5.1 over the frequency range 1-20 kHz. The results are shown in Tables 8.26 and 8.27.

Table 8.26 Artificial Grass Normal Impedance Estimated from the Extracted Impulse Response

Frequency kHz	R/ρc	X/ρc
1	11.5	4.3
2	10.1	4.9
3	8.9	5.5
4	7.5	6.0
5	5.8	6.0
6	4.8	5.8
8	3.4	5.0
10	2.3	4.0
12	1.9	3.5
16	1.6	3.1
20	1.4	2.7

Table 8.27 Fibreboard Normal Impedance Estimated from the Extracted Impulse Response

Frequency kHz	R/ρc	X/ρc
1	13.4	2.6
2	12.6	4.0
3	12.0	4.7
4	11.3	5.2
5	9.1	6.2
6	8.4	6.4
8	6.9	6.4
10	5.8	6.2
12	5.1	6.0
16	4.6	5.8
20	4.1	5.2

The values of the real part of the impedance of the artificial grass agree well with those obtained from the indirect method of Section 8.3 over whole of the frequency range for which results were calculated. The values for the imaginary part of the impedance however, only agree for frequencies between 2 and 5 kHz.

Apart from the 1 kHz value, the real part of impedance for the fibreboard surface also compare well with those obtained from the indirect method as given in Table 8.17. The 1 kHz value is approximately 50% too small.

The values of the imaginary part of the impedance only agree with the values in Table 8.17 for frequencies above 4 kHz.

Table 8.27

Frequency Range of Pole Contribution

Method	Artificial Grass	Fibreboard
Standing wave	0.2-5.0 kHz	-
Indirect	1-5.0 kHz	1-12.5 kHz
Pulse Separation	1-20 kHz	3-20 kHz
Cepstrum	5-20 kHz	10-20 kHz

The experimental measurement of excess attenuation would tend to support the range of frequencies indicated by the standing wave and indirect methods.

In view of this, and the fact that the standing wave impedance values do not give a good prediction of excess attenuation, it was decided to use the indirect method impedance values for evaluating the theoretical predictions in Chapter 9.

The main problem with the indirect method employed in this study is that it utilises a single parameter model to obtain impedance values. Such a single parameter model does not allow sufficient degrees of freedom in the impedance estimates and tends to produce a very smooth predicted excess attenuation. Furthermore, it constrains the real and imaginary parts of the impedance to be of comparable magnitude. A simple improvement would be that, having obtained an estimate of the impedance from the flow resistivity

model, to repeat the iterative search procedure about this estimate but allow the real and imaginary parts of the impedance to vary independantly.

Alternatively, it would be possible to alter the flow resistance model such that the frequency dependance can be modified within the iterative procedure.

Although this type of modification should improve the impedance estimate, it seems clear that the basic flow resistance model is inadequate for ground surfaces. Thomasson |8.5| has proposed a four parameter model that is capable of reproducing the fine detail of the excess attenuation curve as illustrated in Figure 8.37.

Attenborough |8.17| has also proposed a four parameter model, based upon porisity, flow resistivity, tortuosity and shape factor ratio, with the advantage that the parameters can either be measured directly, or their ranges estimated with confidence.

Chessell |8.11| has argued against the need for better impedance estimation models, on the basis that they are not required to obtain reasonable accuracy for community noise problems. The A weighted frequency response characteristic tends to obscure the fined detail of the excess attenuation curve. This point is examined further in Chapter 9, however, the findings indicate that whilst it may be time for elevated noise sources, such as lorries or aeroplanes, it is not tru for cars and trains. For such low sources the impedance estimate needs to be obtained with an error bound of about $\pm$10%.

Unfortunately this may be difficult to achieve in practice, especially for the transient source methods. The sampling rate and conversion resolution of the commercially available signal processing systems need to be significantly improved to obtain this degree of accuracy. The limitations are particularly significant for the phase estimates, which require a sampling rate in excess of 36 times the signal bandwidth to obtain 10% resolution. Many current systems employ sampling rates only 2.56 times the bandwidth.

For both the artificial grass and fibreboard surfaces, the low frequency values of the imaginary part of the impedance are lower than the real parts. According to the theoretical solutions of Chapter 3, this implies that there would be no surface wave contribution to the field at the receiver.

8.6 Transfer Function Method

Chapter 5, section 5.9 described a method of estimating the normal surface impedance using the transfer function measured between two microphones positioned above the surface.

A series of experiments was conducted with two $\frac{1}{4}$" microphones and the air jet noise source. One microphone was mounted with its diaphragm normal to the incident wavefront. The other microphone was mounted with its diaphragm parallel to the incident wavefront and flush with the surface. This was necessary to minimise the distance between the two microphones and thus increase the high frequency limitation imposed by the requirement that:

$$S \leqslant \frac{c}{f_u}$$

where S is the distance between the two microphones, c the velocity of sound and f_u the upper frequency limit of the measurement.

For f_u = 100 kHz, $S \leqslant 3.4$ mm, but the minimum spacing between two normal incidence microphones is equal to the sum of their radii, in this case 6 mm. By positioning one microphone parallel to the incident wavefront it is possible to reduce the spacing to 3 mm.

This arrangement of the microphones introduces several unknown factors into the experiment. For example to what extent the upper microphone masks the lower one. Unfortunately, these factors could not be investigated due to the poor quality of the transfer function measurements.

The statistical properties of the transfer function can be determined from the coherence function [8.9]. The normalised random error ε of the transfer function is given by:

$$\varepsilon[H_1(\omega)] = \frac{(1-\gamma^2(\omega))^{\frac{1}{2}}}{\gamma(\omega)\sqrt{2N}}$$

where $H(\omega)$ is the transfer function,

$\gamma^2(\omega)$ is coherence function,

and N is the number of samples

The values of $\gamma^2(\omega)$ calculated for these experiments were in the range $0 \leqslant \gamma(\omega) \leqslant 0.25$, which gives a lower limit on $\varepsilon[H(\omega)]$ of 0.1. However, for most of the frequency range of interest $\gamma^2(\omega) \leqslant 0.01$ and hence $\varepsilon[H(\omega)] \geqslant 0.6$.

Such a large normalised random error made it impossible to obtain consistent estimates of the transfer function and so the experiments were abandoned.

The most probable cause of these large errors was near-surface turbulence created by the air jet noise source. The effect is described more fully in Chapter 9, Sections 9.2.2 and 9.2.3.

8.7 Impedance Measurements - Comparison of Results

8.7.1 This chapter has described five methods of estimating the normal surface impedance and reported experimental results for two model materials. The object of these experiments was to obtain normal surface impedance data that could be used to evaluate the theoretical predictions of point to point propagation reviewed in Chapter 3.

8.7.2 Impedance Estimates of Artificial Grass

The experimental estimates of the real and imaginary parts of the normal surface impedance of artificial grass material are compared in two groups: (i) those obtained from the high frequency methods, (ii) all methods.

The high frequency estimates are compared with Figures 8.33 and 8.34.

The results show considerable scatter and in particular, the free-field resistance values are generally much smaller than the values obtained from the other three methods. The reactance values obtained from the free-field method are also much smaller and become negative at some frequencies. As already stated, it is felt these values may be erroneous due to the lack of rigidity of the backing surface.

The two transient source measurements, pulse separation and cepstrum, show good agreement above 5 kHz. Below 5 kHz the results diverge, possibly because of the effects of the finite size of the sample. Jones |8.10| has shown that if the smallest dimension of the sample

is less than 10 wavelengths, diffraction effects start to be important. For the samples in question this implies a lower frequency limit of about 3 kHz.

The indirect method results are comparable with the transient source results over the range 2-20 kHz. However, the actual differences correspond to a factor of 2 for the resistance and 0.5 for the reactance, relative to the mean of the transient source results.

The resistance and reactance estimates obtained from the impedance tube are compared with the other results in Figures 8.35 and 8.36.

The resistance values obtained with the two tubes are much smaller over the whole of the overlapping frequency range.

Furthermore, the data points lie on a flatter curve, indicating a reduced dependance upon frequency. Resistance values independant of frequency have been reported in the literature for grass covered ground surfaces |8.12|.

The reactance values obtained from the tube measurements exhibit the same general trend with frequency as do the other results, but the values are some 1.5-2 times smaller than the mean of the values obtained from the high frequency methods.

Assuming experimental errors associated with each method to be of a similar order of magnitude, there is no obvious reason for the difference in the impedance estimates except that of sample size and edge diffraction effects. Clamping of the sample within the impedance

tube would, according to Donato [8.13], only increase the resistance estimates.

The effect of impedance variations of the order exhibited by the experimental results can be seen by reference to Figure 8.37. Increasing both the resistance and reactance by 10% causes the first interference dip to shift from 7.8 kHz up to 8.2 kHz and reduces the excess attenuation by about 1 dB. The differences are negligible for practical purposes.

Increasing the impedance by 50% does produce significant differences as shown in Figure 8.37(b). The frequency location of the first minimum increases by some 2 kHz and the excess attenuation is reduced by about 4 dB.

The significance of a factor of 2 variation in the impedance, typical of the measured data, can be seen by comparing the +50% and -50% attenuation curves. The location of the dip shifts downward by about 7 kHz and the excess attenuation increases from 6 dB to 12 dB.

The impedance tube measurements suggest that the real and imaginary parts of impedance may vary in range independantly. The effect of such variation upon the predicted excess attenuation can be seen in Figures 8.37 (c) and (d).

The solid line shows the excess attenuation predicted for a nominal impedance of $Z = R+iX$. The dashed line corresponds to a doubling of the variable (R or X) and the dash-dot line a halving of the variable (R or X).

Increasing the resistance extends the frequency range over which the excess attenuation is positive and moves the interference dip to a high frequency. The maximum attenuation is increased relative to the nominal impedance value. Reducing the resistance produces the converse effects.

Varying the reactance has little effect at the lower frequencies. Increasing the reactance causes an upward shift in frequency of the dip location, as per the resistance increase, but reduces the value of the minimum, opposite to the resistance increase. Reducing the reactance produces the converse effects.

8.7.3 Impedance Estimates of Fibreboard

The measurements of the resistance and reactance of the fibreboard surface are compared in Figures 8.38 and 8.39 respectively. There are no standing wave measurements for this model material.

The indirect and cepstrum resistance values agree well over the frequency range 2-20 kHz, but the pulse separation values are much smaller, although they show the same underlying trend with increasing frequency.

The reactance values also show reasonable agreement over the range 4-20 kHz. Below 4 kHz the pulse separation and cepstrum values are much smaller than the indirect method results and the cepstrum values show a distinct decrease with decreasing frequency.

Much of this low frequency behaviour of the cepstrum data can be traced back to the phase estimate of the reflection coefficient. At low frequencies the phase is approximately zero, hence the reactance of the surface will be very small corresponding to a rigid surface zero phase is a direct result of failing to distinguish between the acousal terms of the extracted impulse response and phase change due to the acoustical characteristics of the surface. The effect is exaggerated by cross-correlating the extracted impulse response with the minimum phase version of the impulse response to determine the travel time difference between the direct and reflected pulses; because this technique cannot distinguish between travel time delay and phase shift.

If the low frequency phase estimate of the reflection coefficient were increased, the calculated reactance would increase and the resistance decrease. The indirect and cepstrum results would then be in very good agreement over the whole of the overlapping frequency range.

8.7.4 Selection of Impedance Estimates for the Model Materials

Specific reasons for the differences between the standing wave impedance values and the indirect, pulse and cepstrum values are difficult to defend; because of the many measurement uncertainties. Problems associated with sample fixing, tuve attenuation, probe end correction and atmospheric absorption may introduce significant errors into the impedance tube measurements, whereas sampling rate, time delay estimation, impulse response duration and edge diffraction contribute to the errors in the transient source methods. An

additional factor to consider for the transient source methods is the significance of any surface wave contribution. Donato |8.13| has shown that the surface wave travels at a lower velocity than the air borne waves and therefore has a different travel time. The energy contributed by the surface wave may be lost due to windowing of the reflected pulse in which case the absorption coefficient of the surface would increase. This could in part explain the so-called sphericty errors observed by some experimenters |8.16|.

The indirect method has gained wide acceptance in recent years |8.5, 4.7, 7.2, 8.11| and does lead to a predicted excess attenuation curve that agrees reasonably well with measured results for soft surfaces.

A useful guide when selecting impedance estimates is to examine the relative magnitude of the resistive (R) and reactive (X) terms. The local reaction theoretical prediction for grazing incidence (equation 364) showed that when X > R the total pressure field at the receiver includes a contribution from a pole which gives rise to a term with surface wave like behaviour. The existence of this pole reduces the excess attenuation at low frequencies.

The range of frequencies for which this pole is part of the total solution, as indicated by the different measurement methods, for each material is shown in Talbe 8.24.

References Chapter 8

8.1 Ando, Y.: The Directivity and Acoustic Centre of a Probe Microphone.
J. Acoustic Soc. Japan (24) 335-342. 1968.

8.2 Joffe, L.: A criterion for the use of Linear Regression Analysis in the Determination of Low Values of Absorption Coefficient using the Impedance Tube.
Applied Acoustics (7) 139-147. 1974.

8.3 Delany, M.E. and Bazley, E.N.: Acoustical Properties of Fibrous Absorbents.
NPL Aero Report Ac 37 March 1969.

8.4 Sides, D.J. and Mulholland, K.A.: The Variation of Normal Layer Impedance with Angle of Incidence.
J.S.V. (14) 139-142. 1971.

8.5 Thomasson, S.I.: Theory and Experiments on Sound Propagation Above an Impedance Boundary.
Report 75 Lund Institute of Technology. 1977.

8.6 Bruel and Kjaer: Microphones and Microphone Preamplifiers.
January 1975.

8.7 Bolton, J.S. and Gold, E.: The Application of Cepstral Techniques to the Measurement of Reflection Coefficients.
In situ. Part 1 Simulations.
Royal Melbourne Institute of Technology Report 121007.

8.8 Oppenheim, A.V. and Schafer, R.W.: Digital Signal Processing. Prentice-Hall. 1975.

8.9 Bendat, J.S.: Statistical Errors in Measurement of Coherence Functions and Input/Output Quantities. J.S.V. (59) 405-442. 1978.

8.10 Jones, M.H.: The Measurement of Absorption Coefficient Using a Correlation Technique. British Acoustical Soceity: Absorption of Sound. University of Salford. 1971.

8.11 Chessell, C.I.: Propagation of Noise Along a Finite Impedance Boundary. J.A.S.A. (62) 825-834 1977.

8.12 Dickinson, P.J. and Doak, P.E.: Measurements of the Normal Acoustic Impedance of Ground Surfaces. J.S.V. (13) 309-322 1970.

8.13 Donato, R.J.: Model Experiments on Surface Waves. J.A.S.A. (63) 700-703 1978.

8.14 Talaske, R.H.: The Acoustic Impedance of a Layered Forest Floor. M.Sc Thesis Pennsylvania State University 1979.

8.15 Attenborough, K.A.: private communication.

8.16 Davies, J.C. and Mulholland, K.A.: An Impulse Method of Measuring Normal Impedance at Olbique Incidence.
J.S.V. (67) 135-149 1979

8.17 Attenborough, K.A.: Acoustical Characteristics of Porous Materials.
Physics Reports (82) 179-227 1982

8.18 Pyett, J.S.: The Acoustic Impedance of a Porous Layer at Oblique Incidence.
Acustica (3) 375 1953

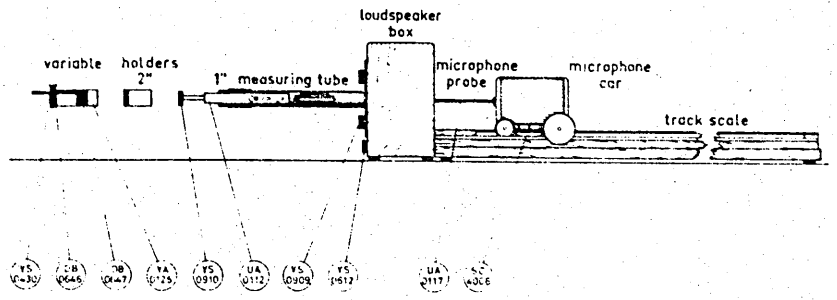

(a) 3 cm tube

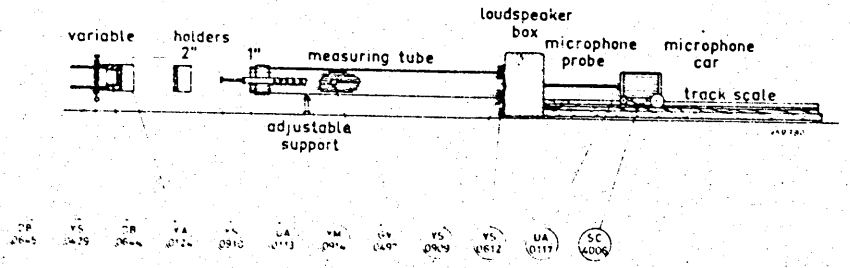

(b) 10 cm tube

Figure 8.1
Bruel and Kjaer Standing Wave Apparatus Type 4002

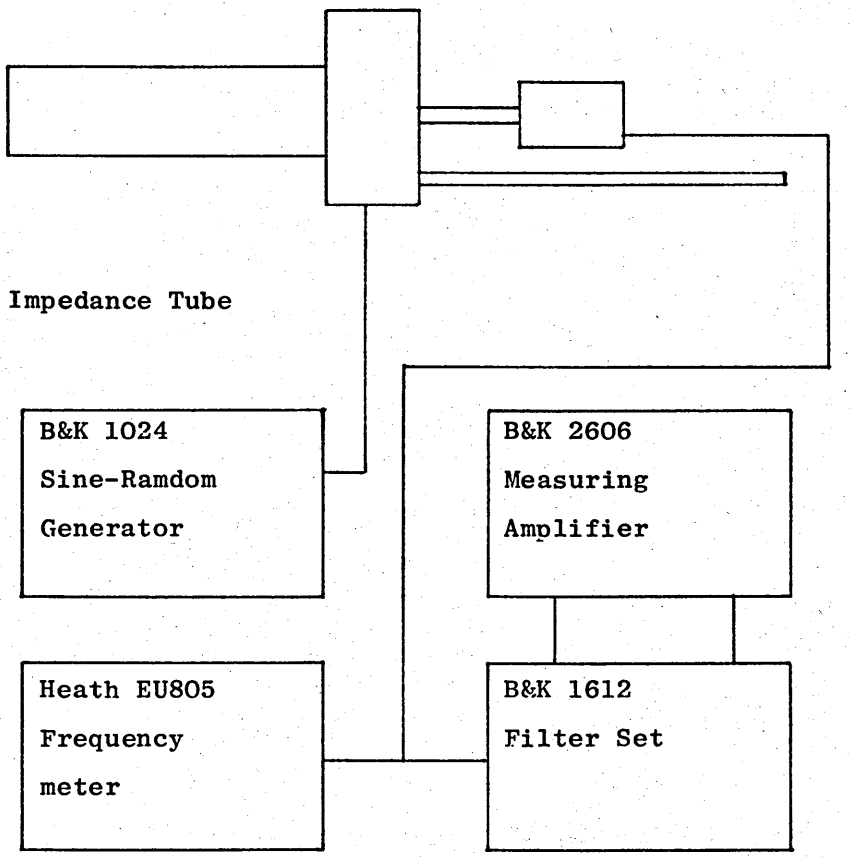

Figure 8.2
Block diagram of the instrumentation used for the Impedance Tube measurements

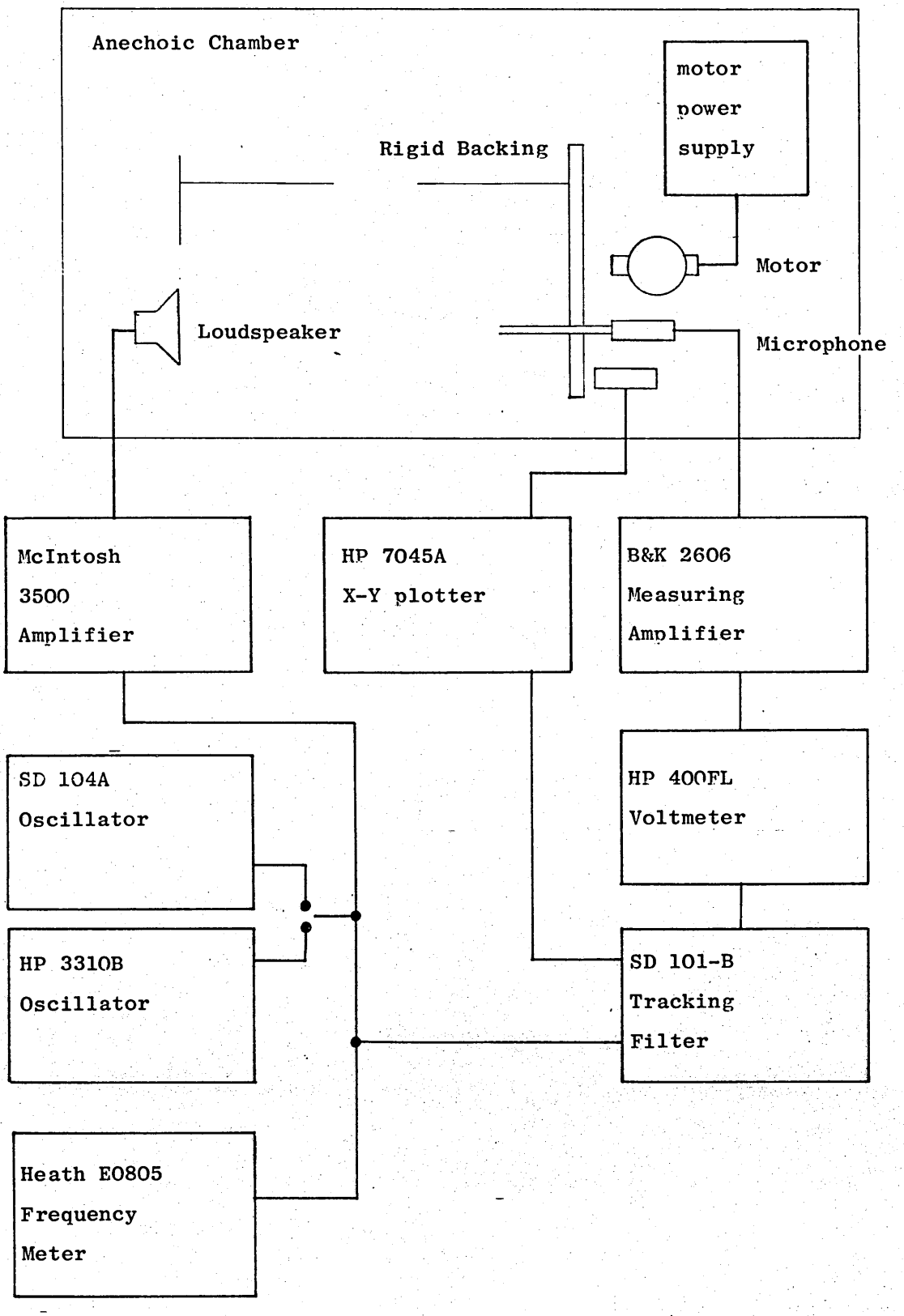

Figure 8.3

Block diagram of the instrumentation used for the Free-Field impedance measurements

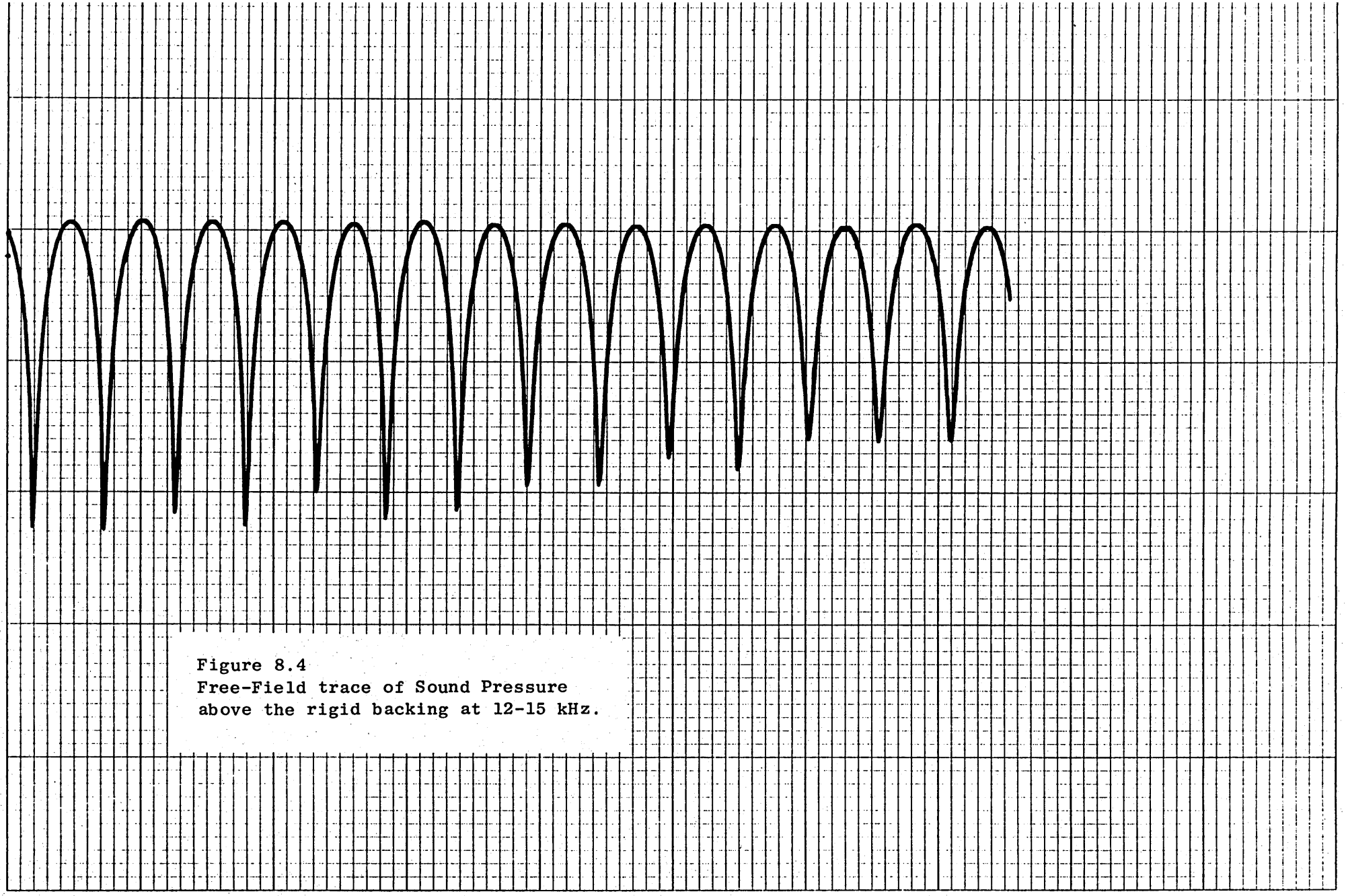

Figure 8.4
Free-Field trace of Sound Pressure
above the rigid backing at 12-15 kHz.

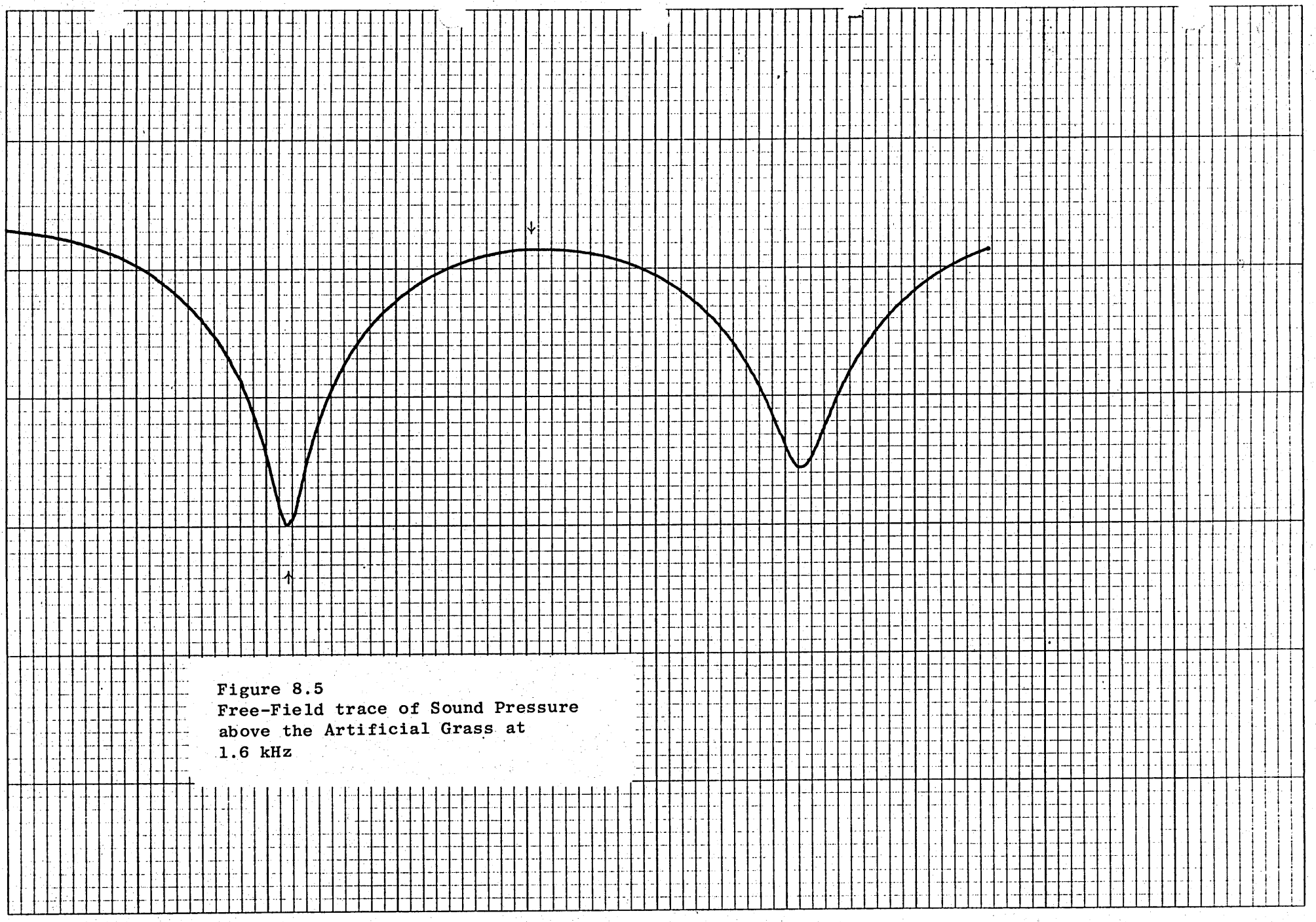

Figure 8.5
Free-Field trace of Sound Pressure above the Artificial Grass at 1.6 kHz

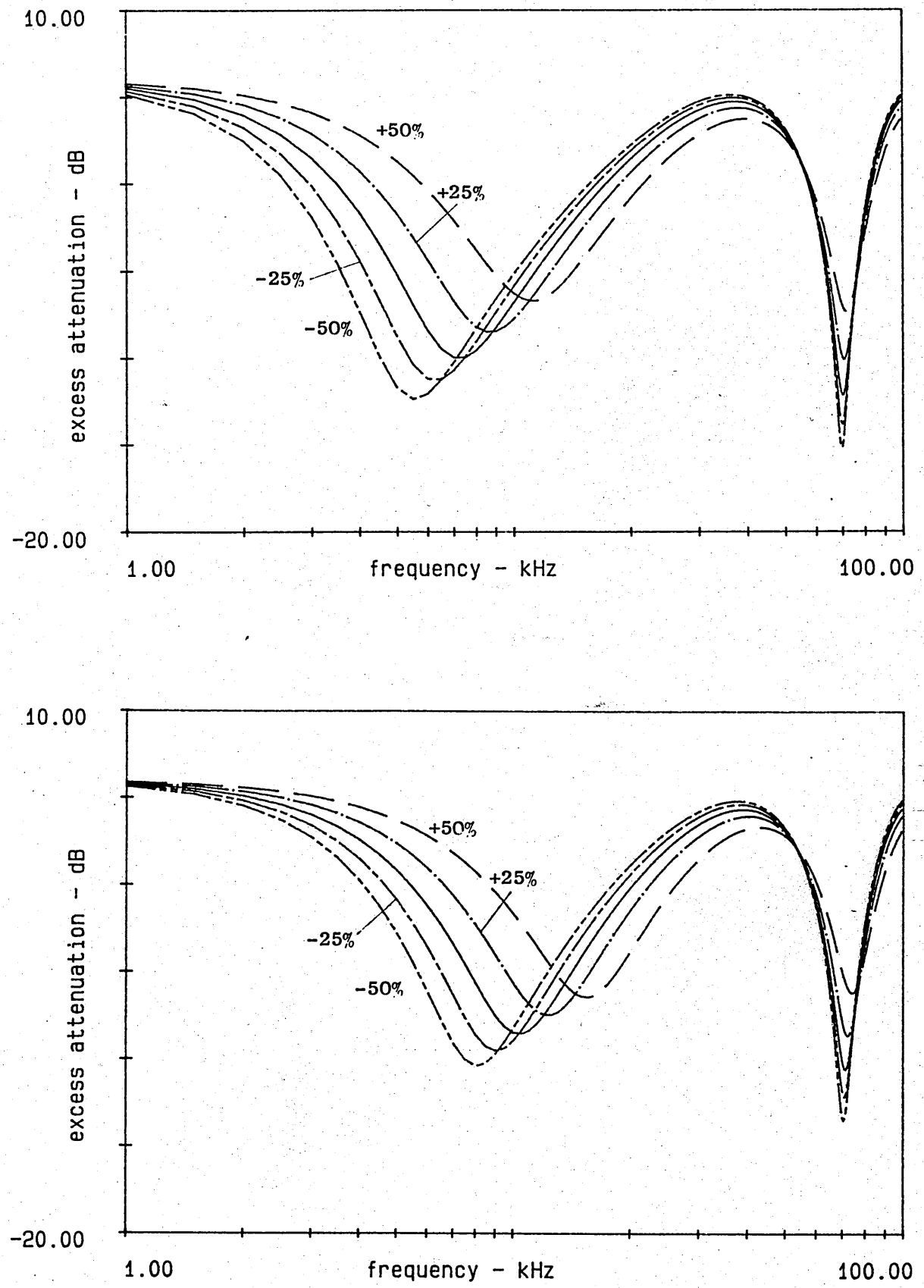

Figure 8.6
Effect of normal surface impedance value upon the location of the interference minima

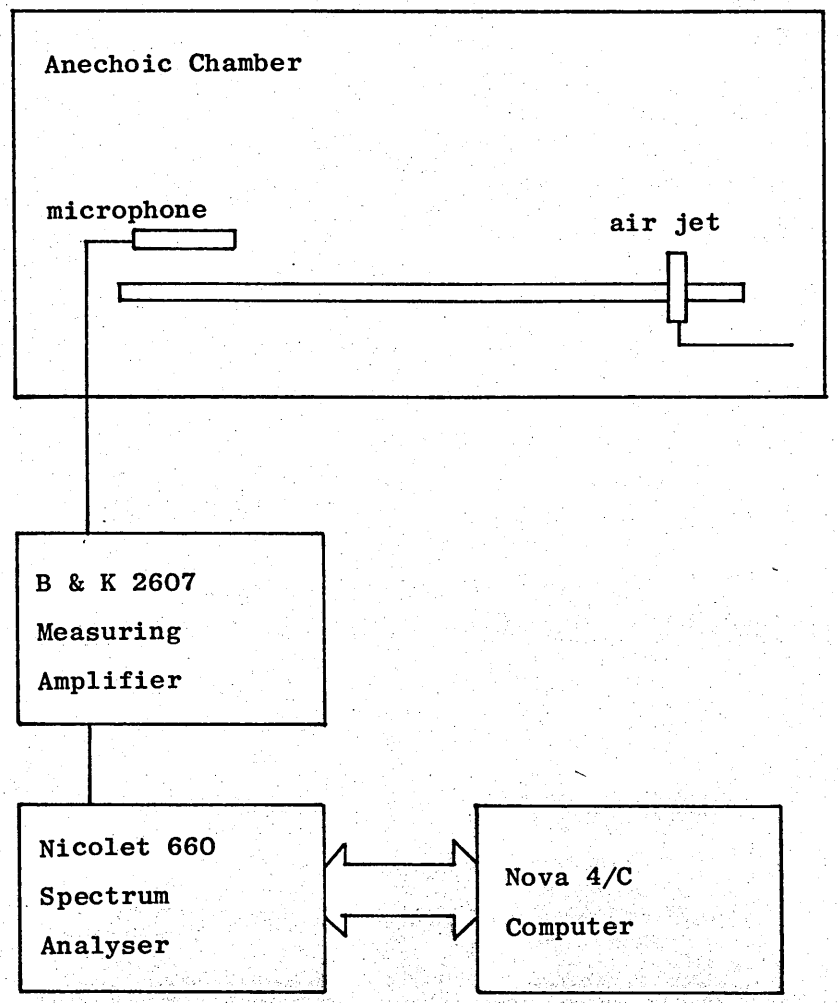

Figure 8.7
Block Diagram of Instrumentation used for the Experimental Determination of Excess Attenuation

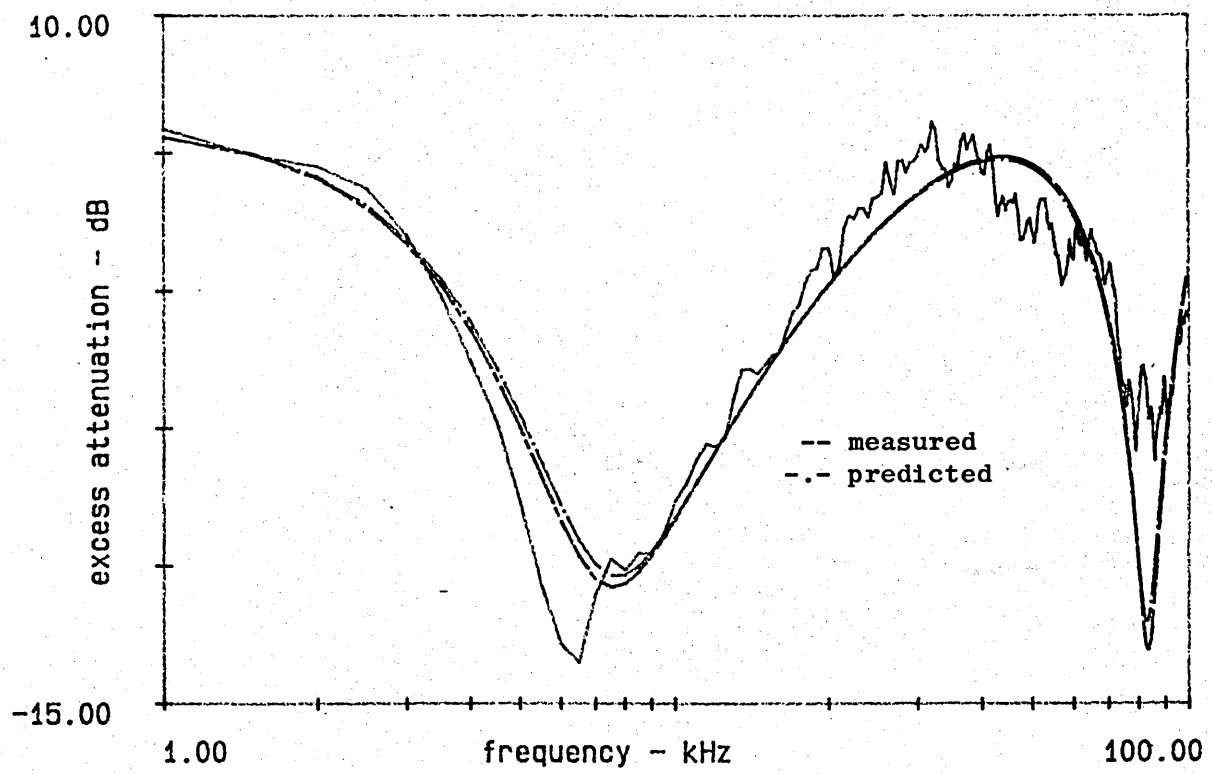

Figure 8.8
Comparison of predicted and measured excess attenuation for propagation over the artificial grass surface. Source height 5 cm, receiver height 5 cm, separation distance 100 cm.

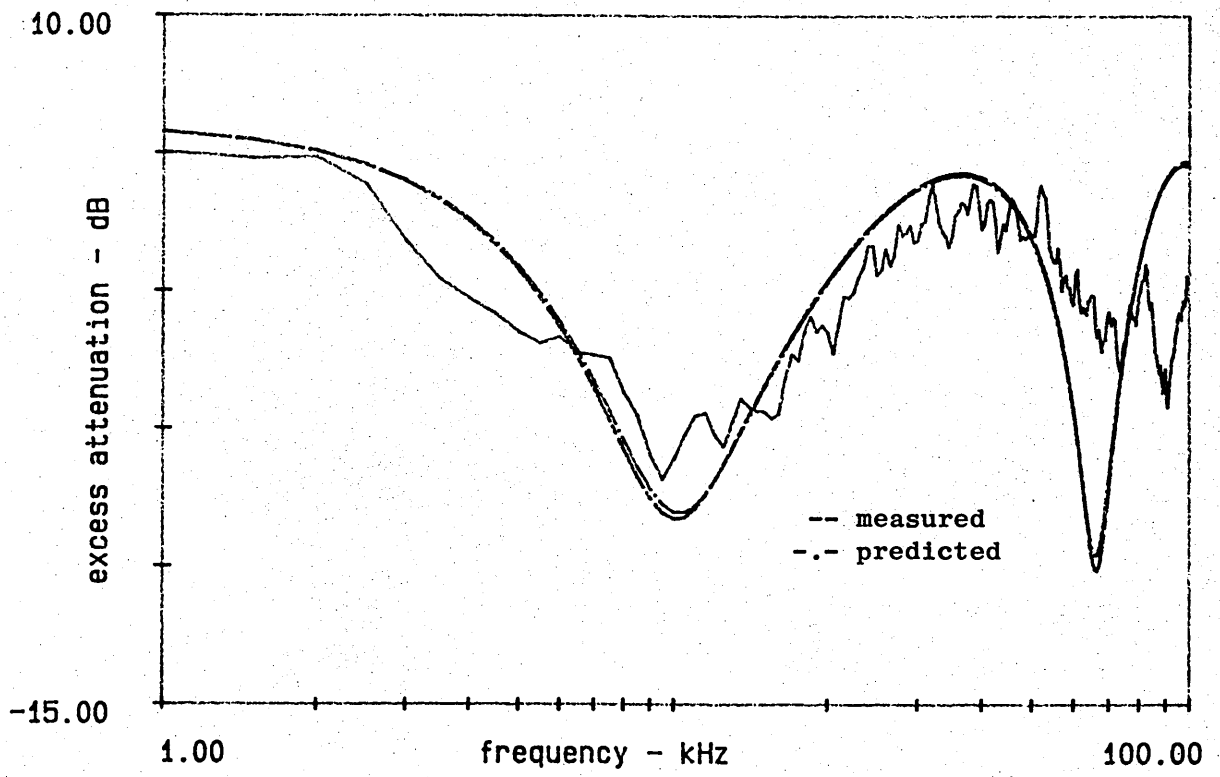

Figure 8.9
Comparison of predicted and measured excess attenuation for propagation over the fibreboard surface. Source height 5 cm, receiver height 5 cm, separation distance 100 cm.

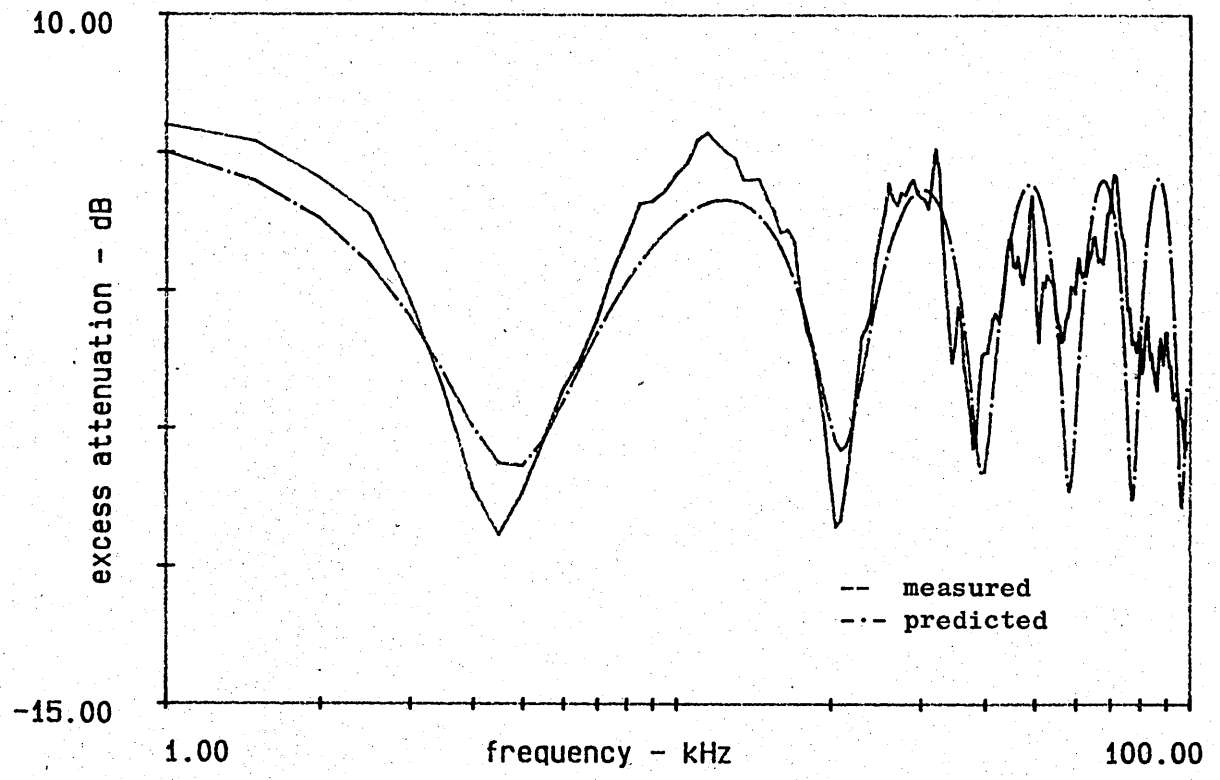

Figure 8.10
Comparison of predicted and measured excess attenuation for propagation over the fibreboard surface. Source height 9 cm, receiver height 10 cm, separation distance 100 cm

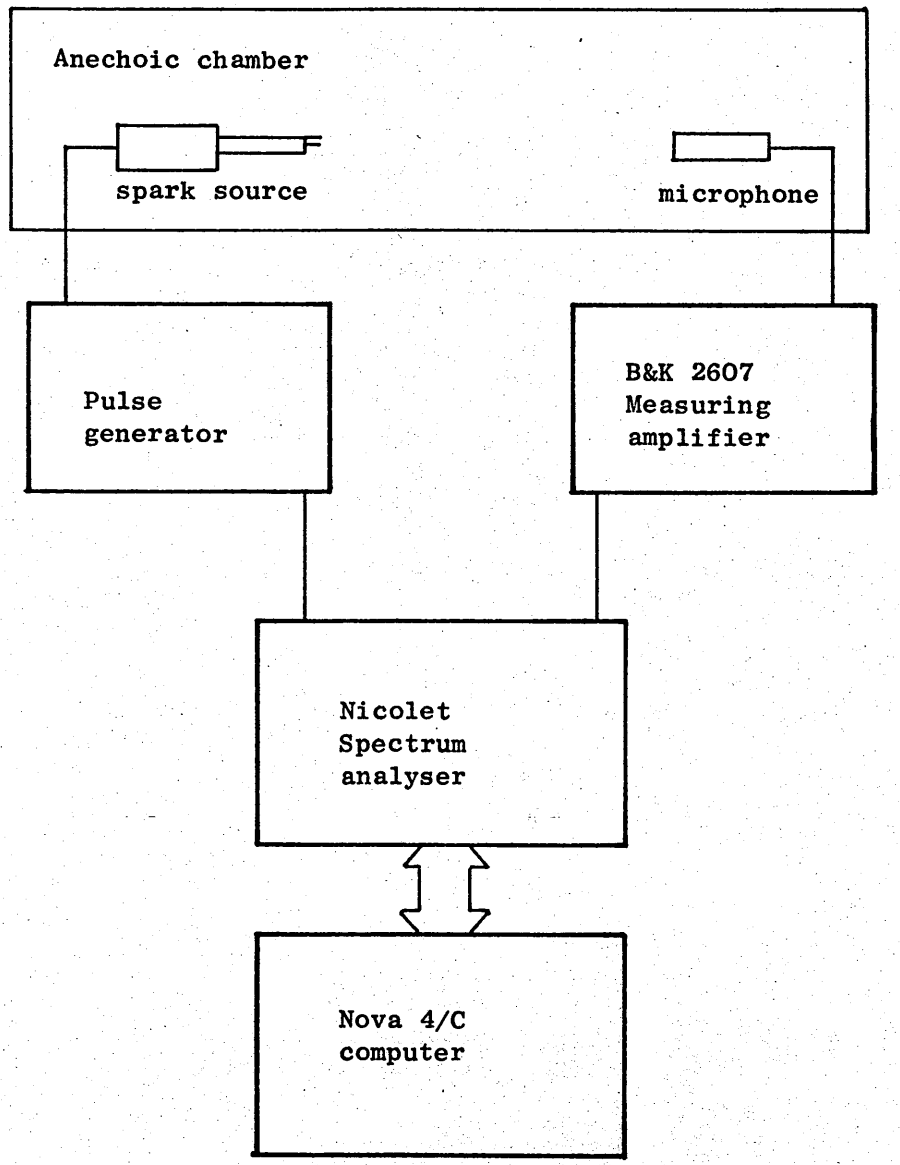

Figure 8.11
Block diagram of the instrumentation used for the direct and reflected pulse measurements

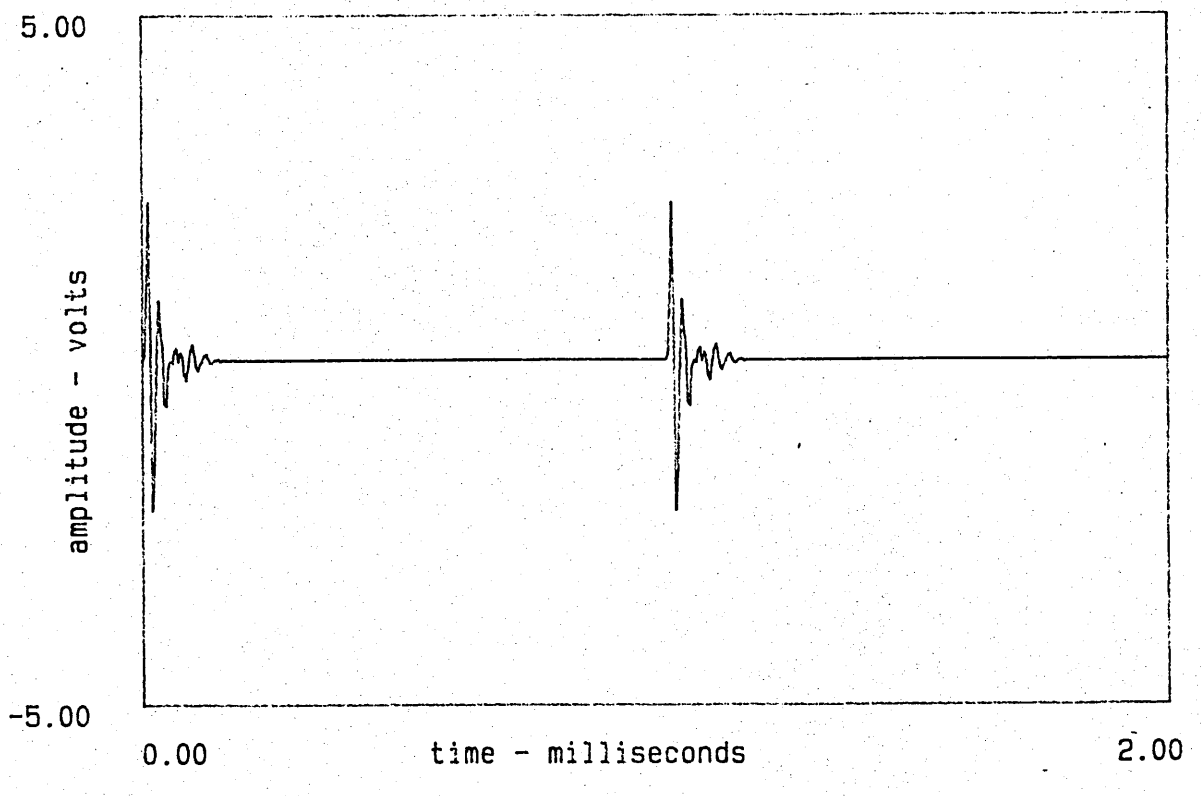

Figure 8.12
Measured direct and reflected pulses. Source height 15 cm, receiver height 60.3 cm, separation distance 52.7 cm.

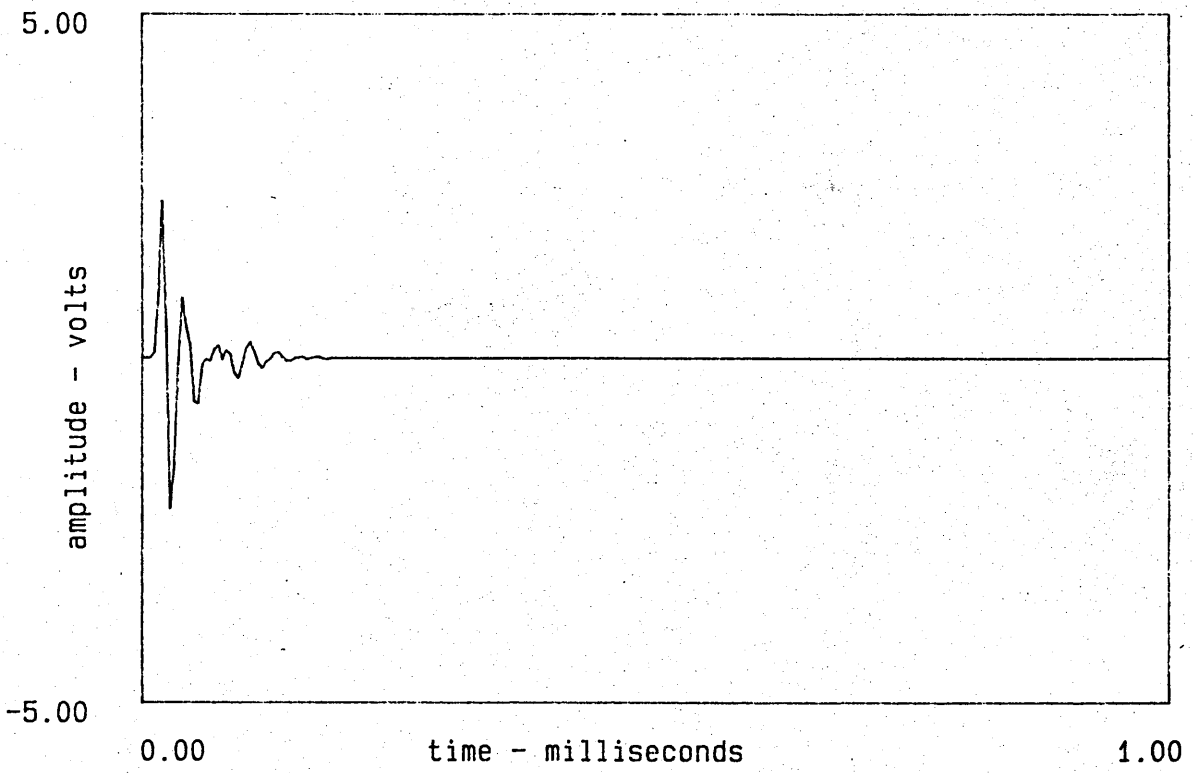

direct pulse - rigid surface (15,60.3,52.7)

Figure 8.13(a)

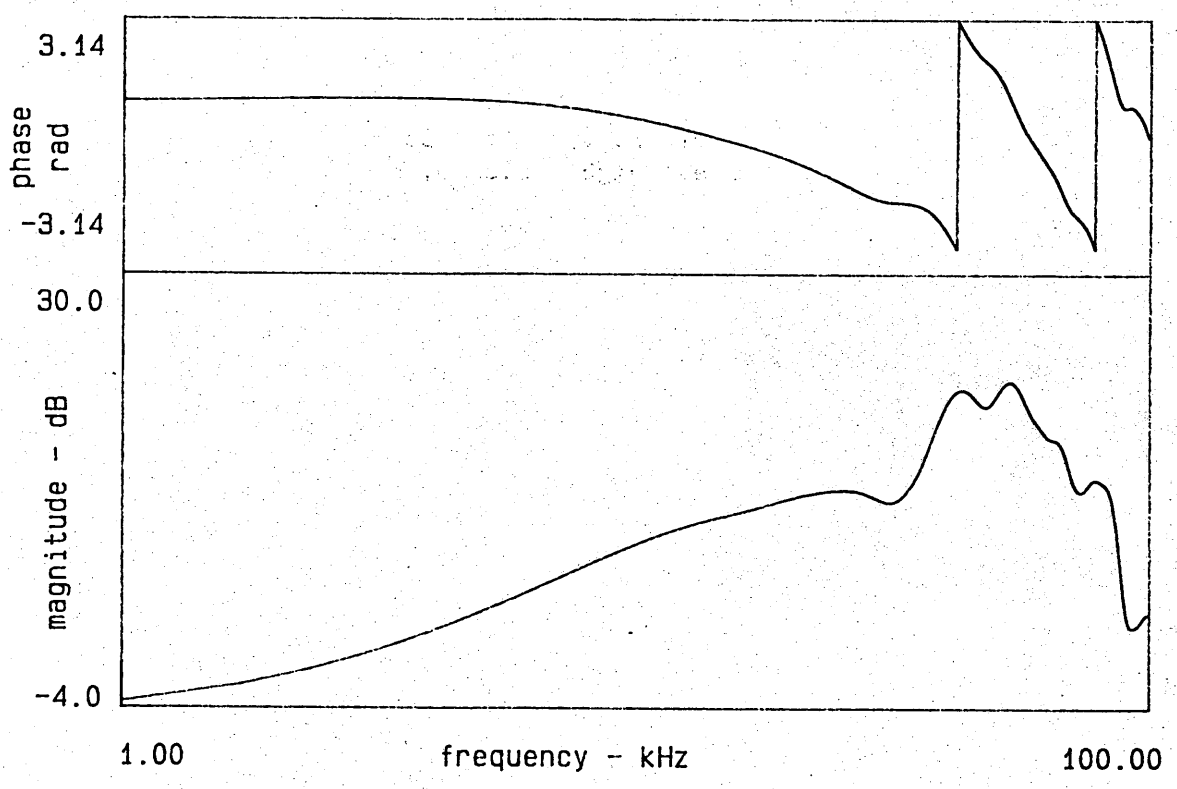

direct pulse spectrum - rigid surface (15,60.3,52.7)

Figure 8.13(b)

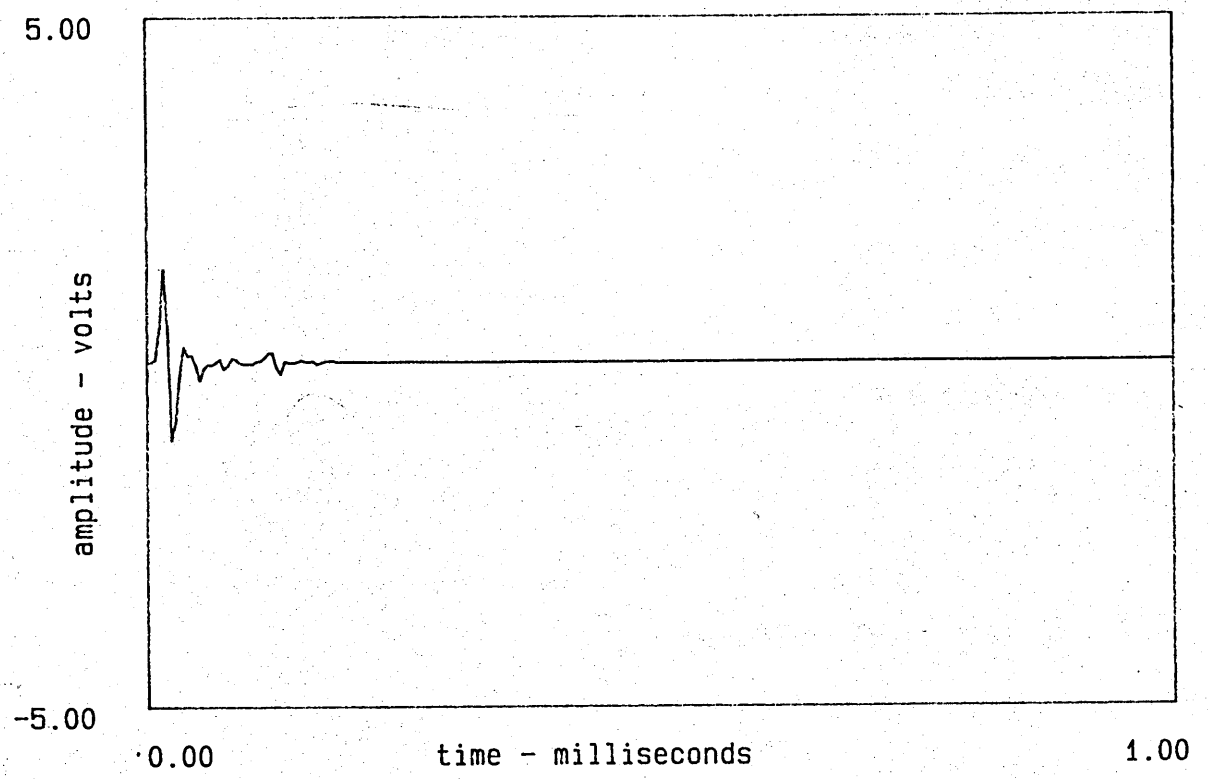

reflected pulse - rigid surface (15, 60.3, 52.7)

Figure 8.13(c)

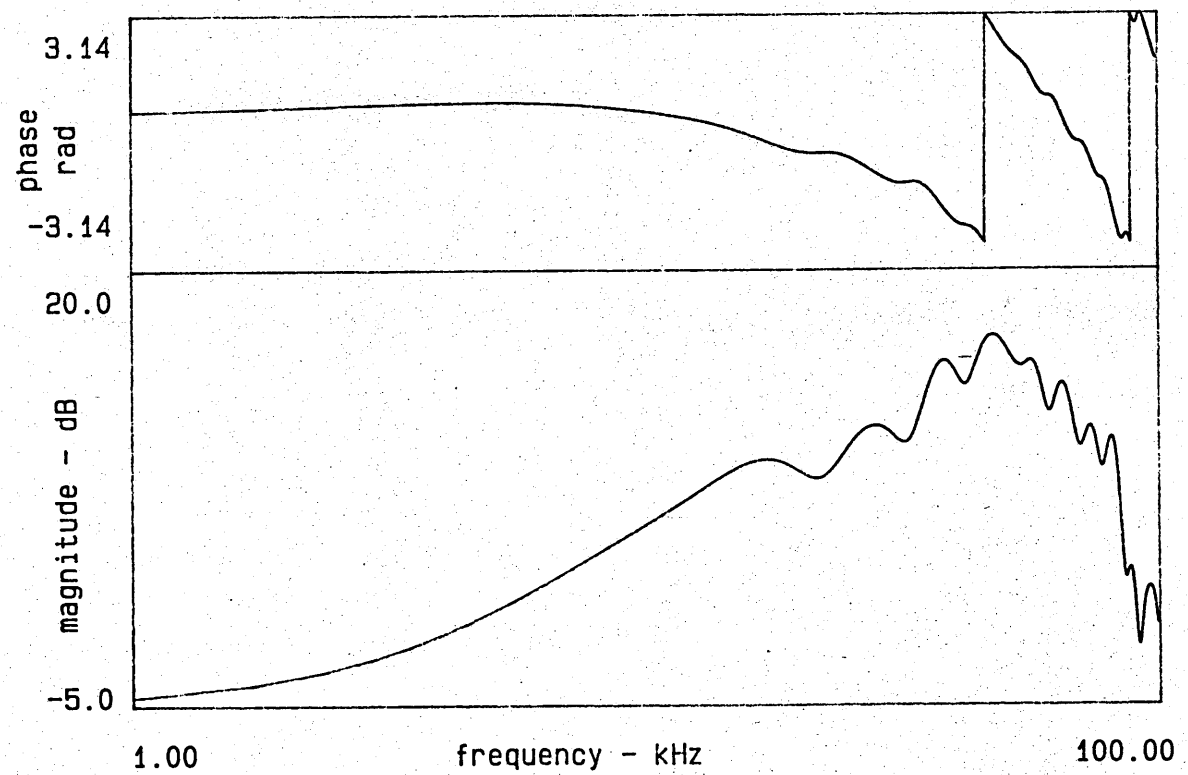

reflected pulse spectrum - rigid surface (15, 60.3, 52.7)

Figure 8.13(d)
Direct and reflected pulses and their corresponding spectra

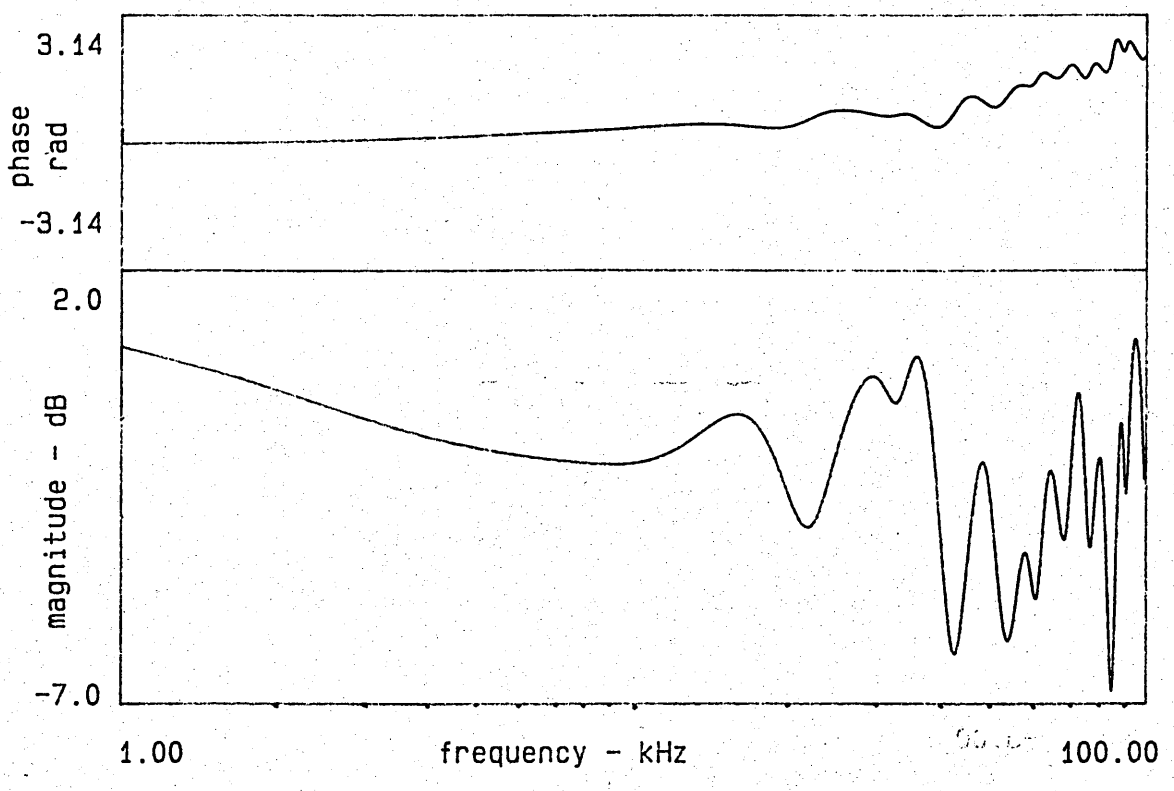

Figure 8.14
Calculated reflection coefficient for the rigid surface. Source height 15 cm, receiver height 60.3 cm, separation distance 52.7 cm.

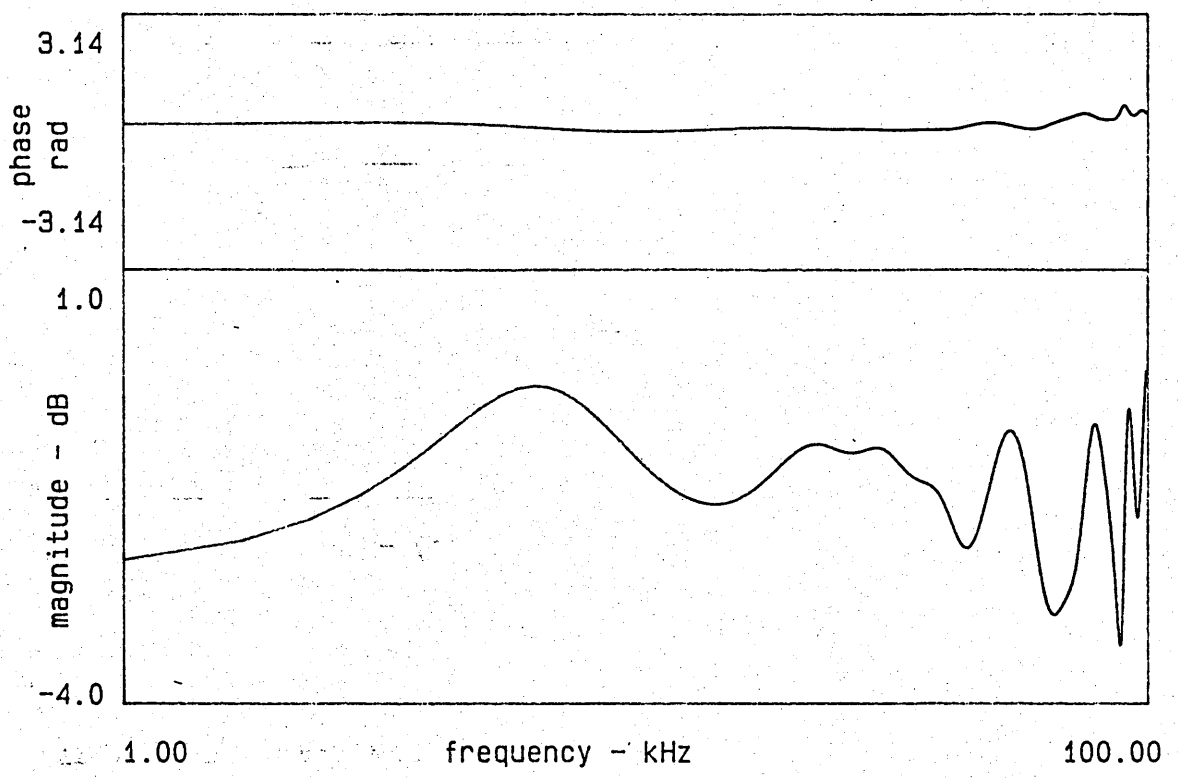

Figure 8.15
Calculated reflection coefficient for the rigid surface. Source height 15 cm, receiver height 15 cm, separation distance 100 cm.

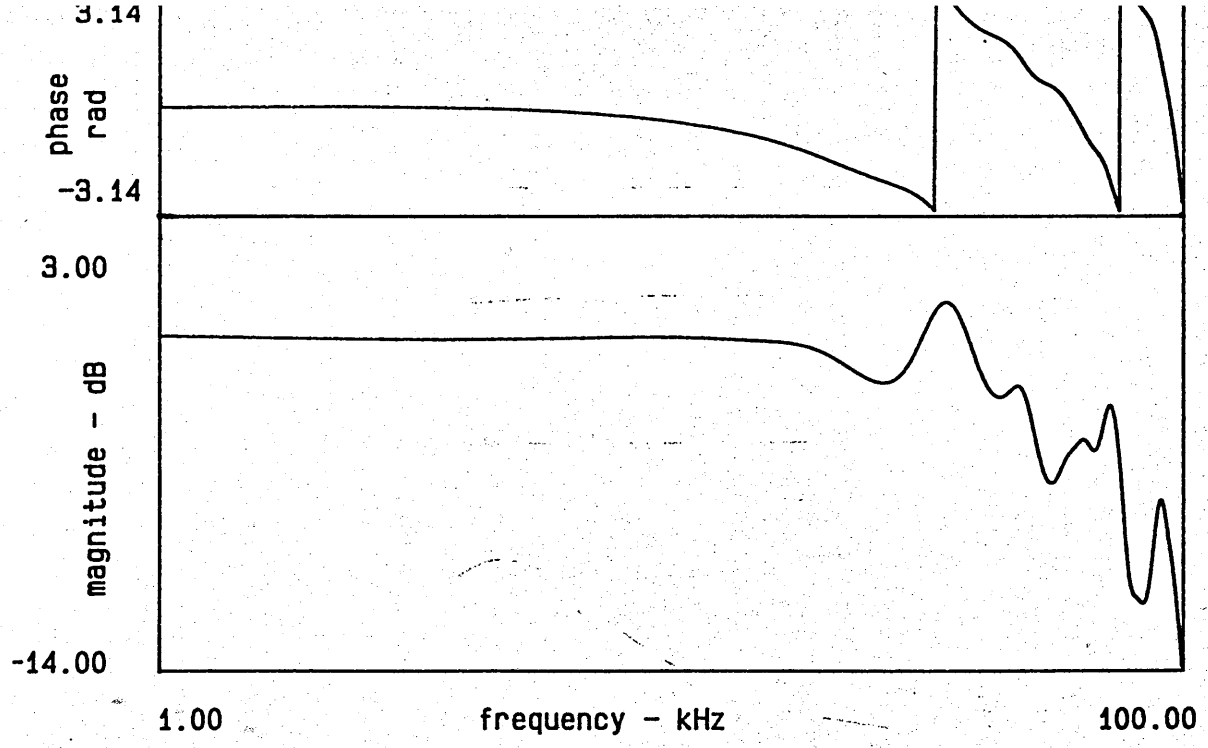

Figure 8.16
Calculated reflection coefficient for the artificial grass surface. Source height 15 cm, receiver height 62 cm, separation distance 49.5 cm.

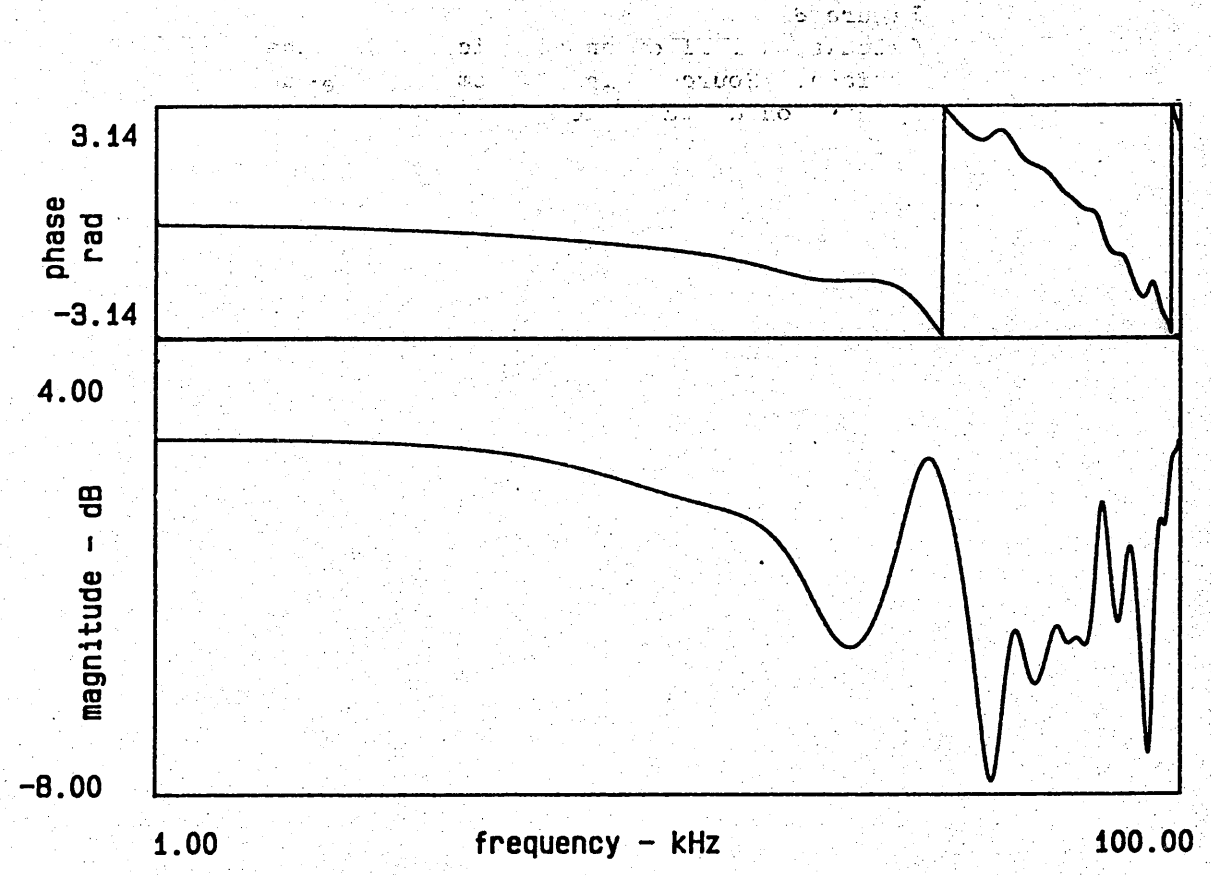

Figure 8.17
Calculated reflection coefficient for the fibreboard surface. Source height 15 cm, receiver height 70.3 cm, separation distance 49.2 cm.

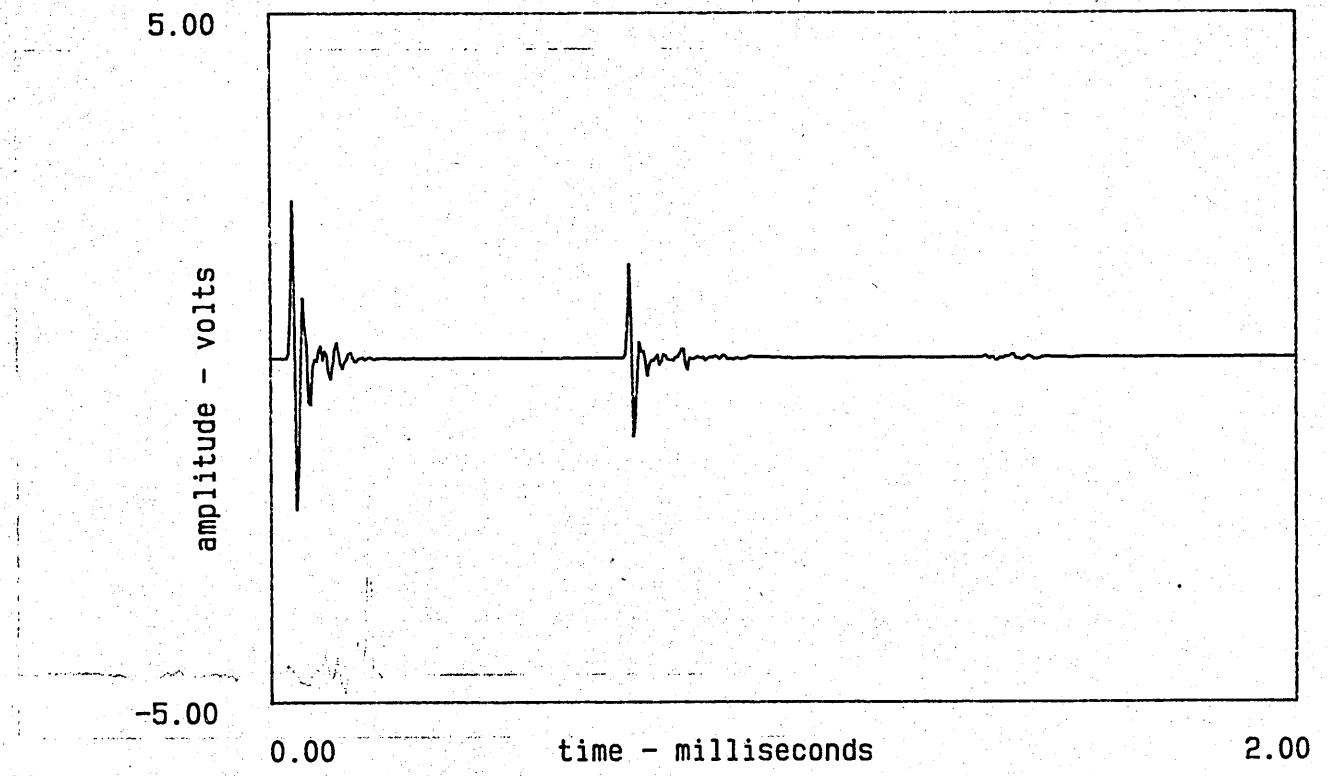

Figure 8.18(a)

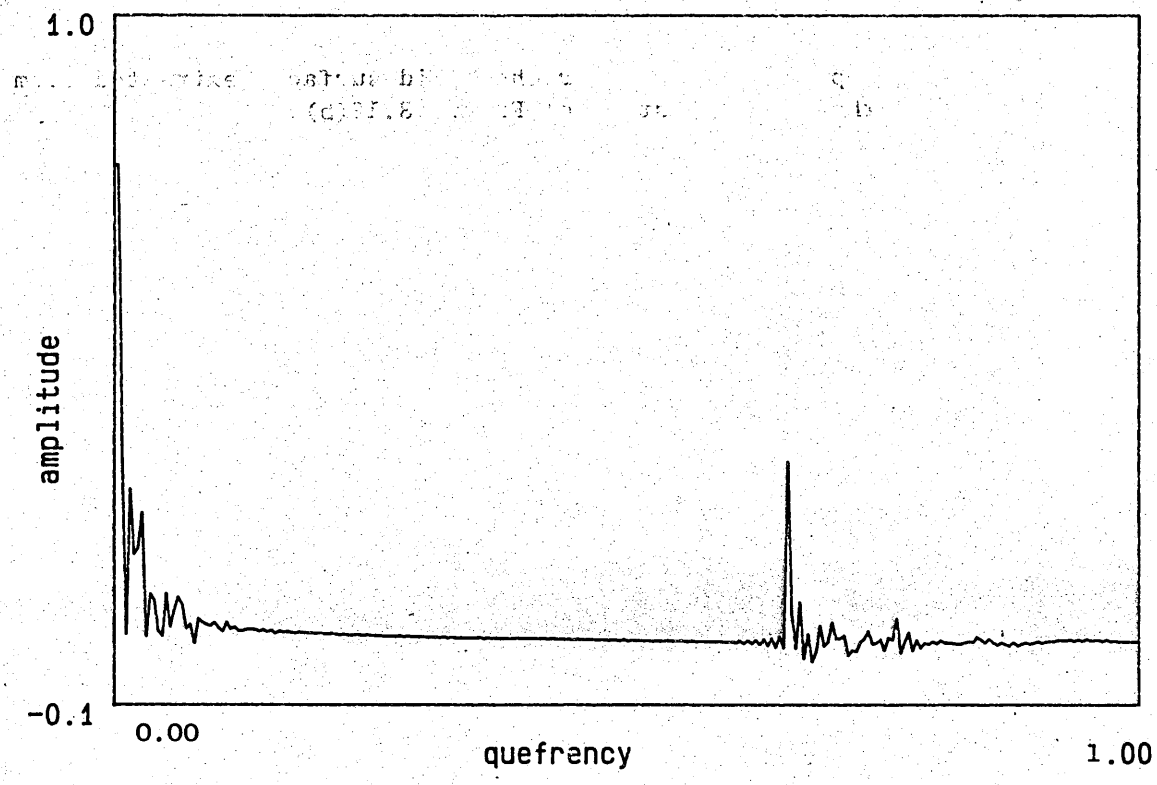

Figure 18.18(b)
Measured direct and reflected pulses and corresponding power cepstrum for the rigid surface. Source height 15 cm, receiver height 60.3 cm, separation distance 52.7 cm

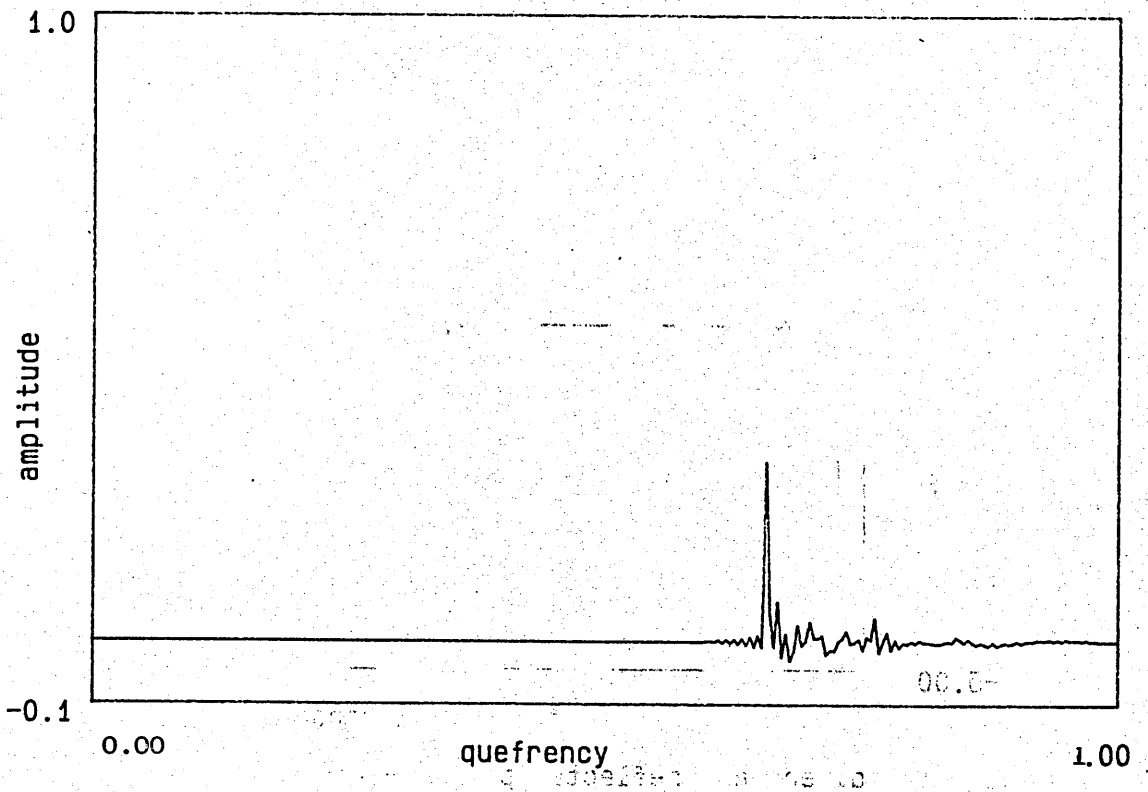

Figure 8.19
Impulse response for the rigid surface, extracted from the Power Cepstrum of Figure 8.18(b).

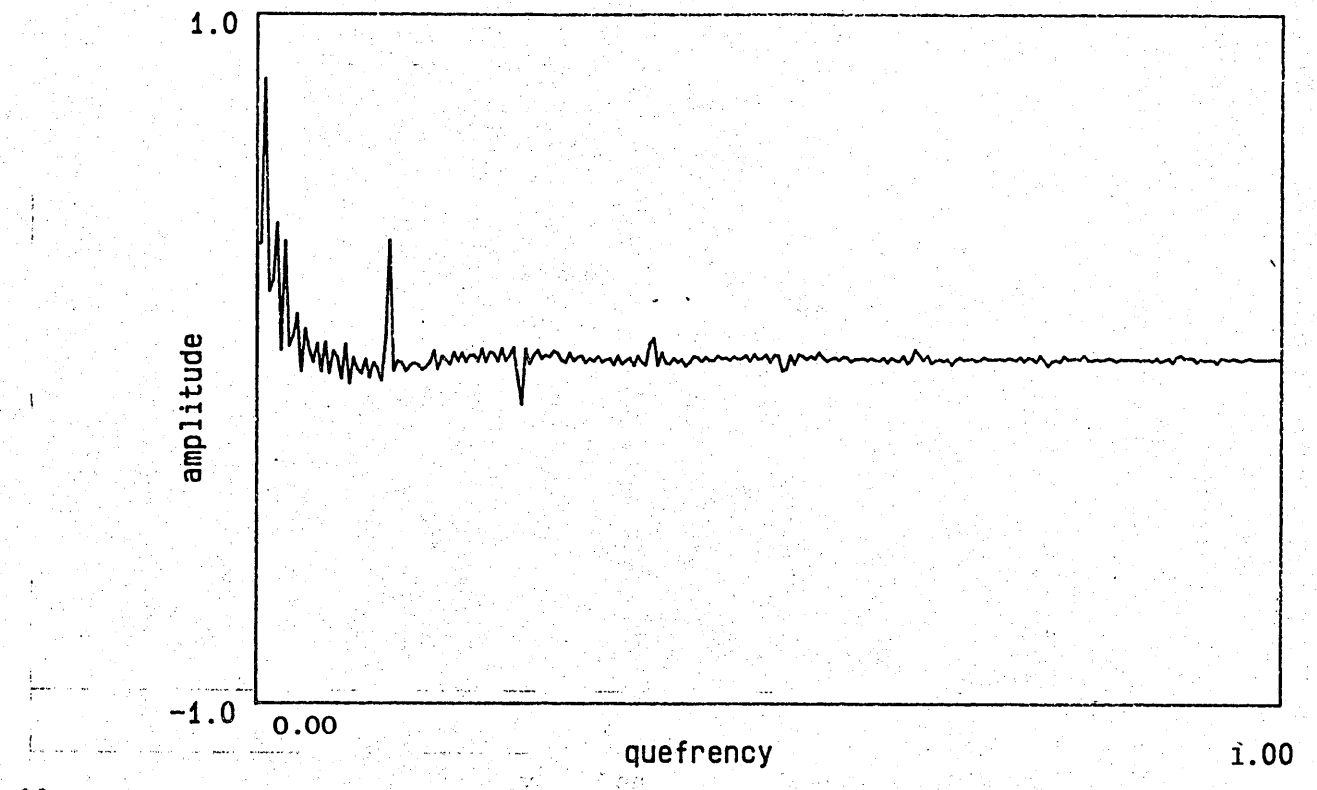

Figure 8.20(a)

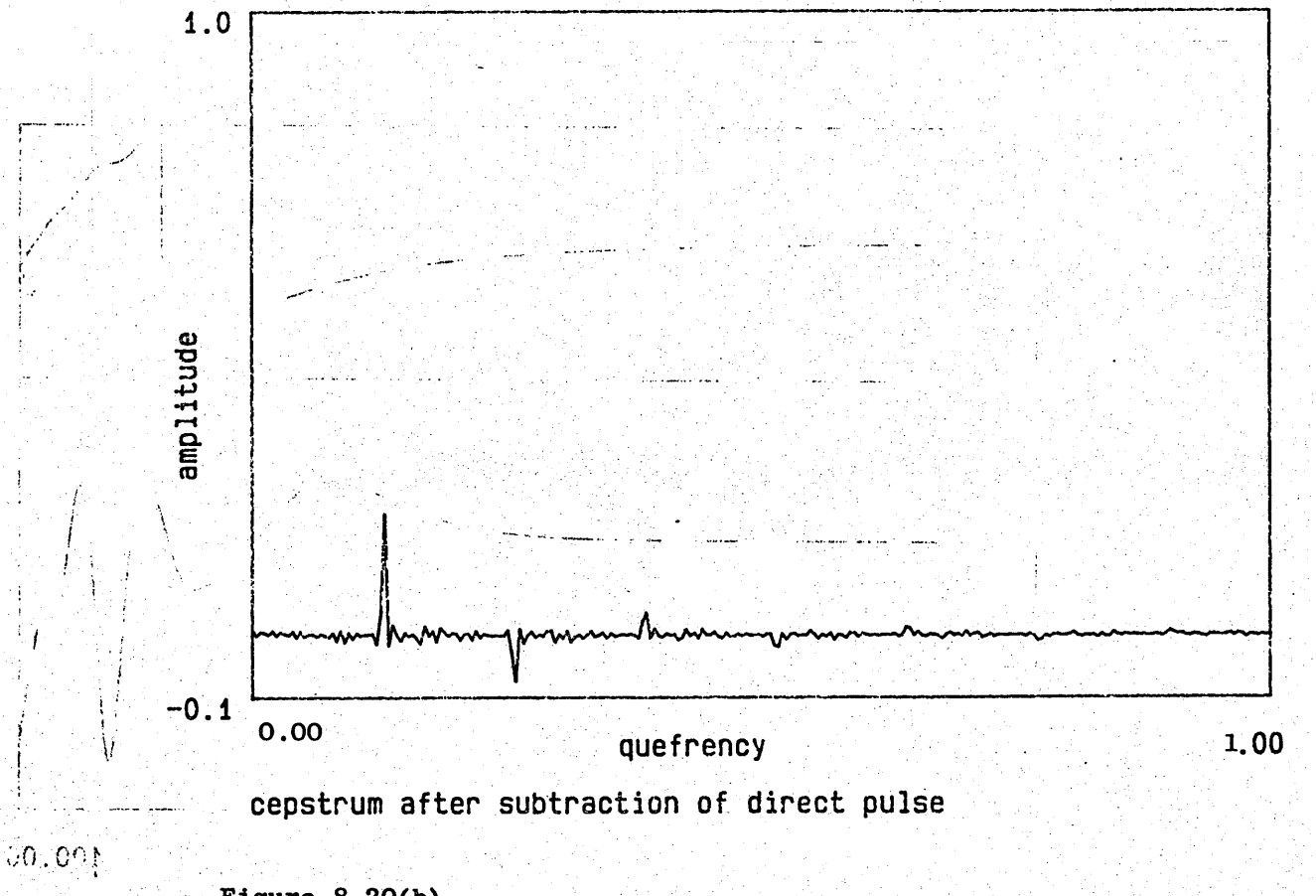

Figure 8.20(b)
Power Cepstrum before and after subtraction of the direct pulse contribution

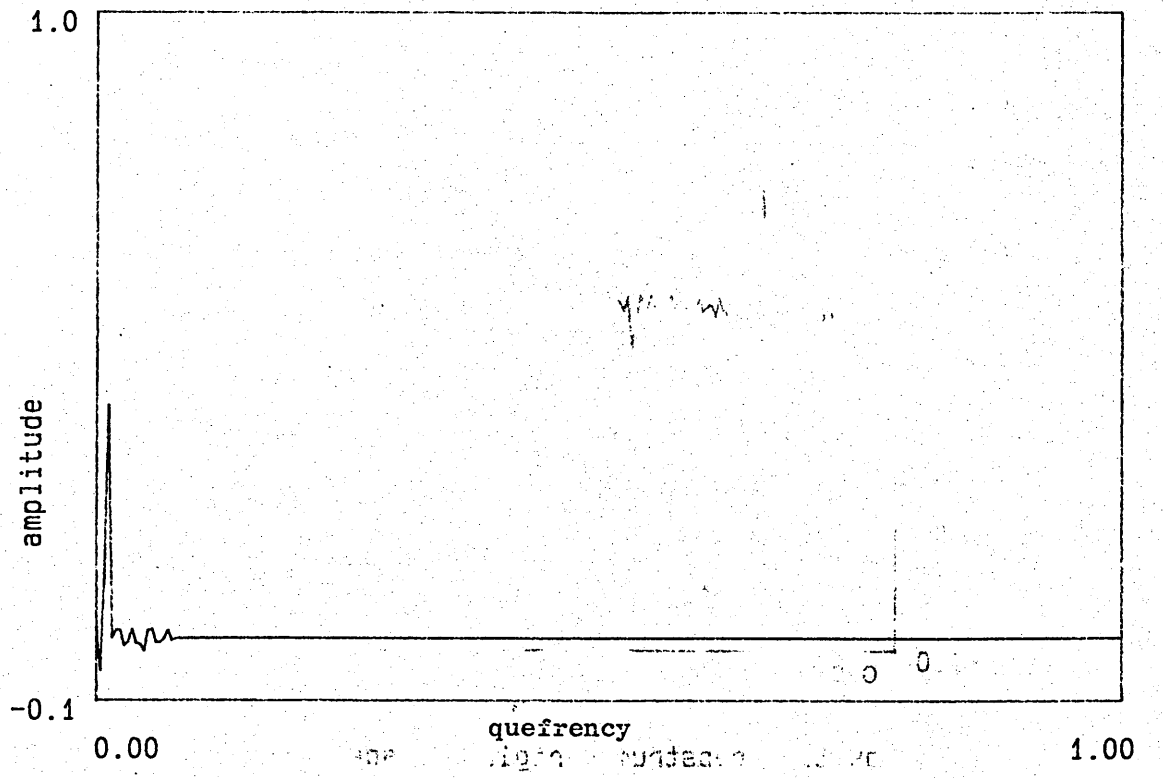

impulse response - rigid surface

Figure 8.21(a)

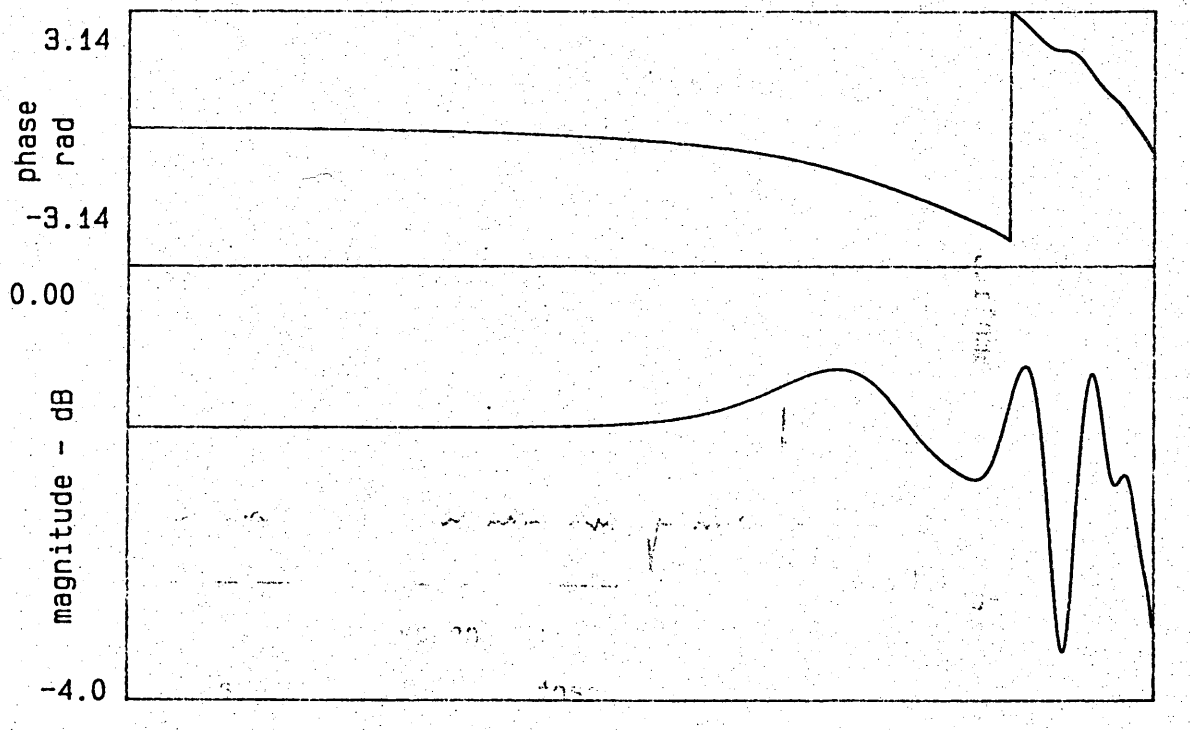

reflection coefficient - rigid surface

Figure 8.21(b)
Long duration impulse response and corresponding reflection coefficient for a rigid surface

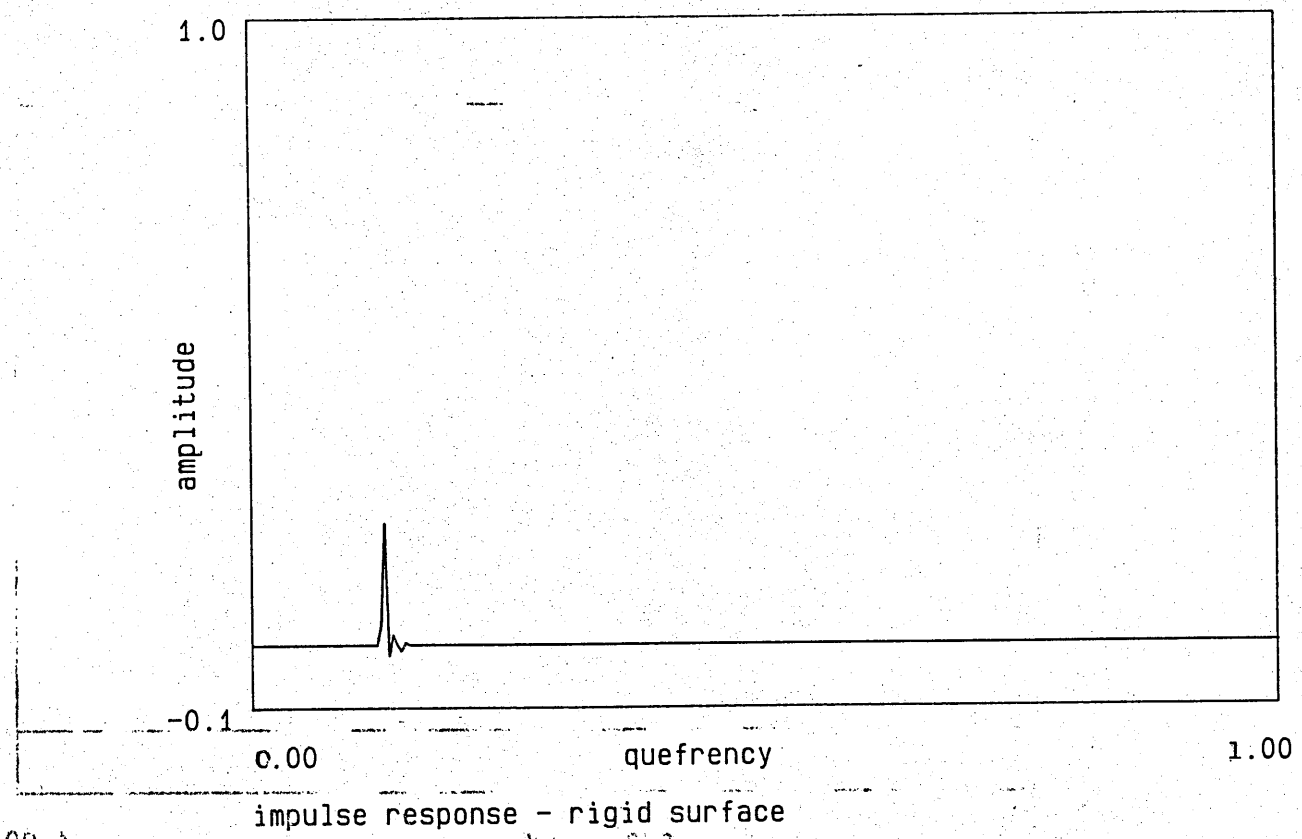

Figure 8.22(a)

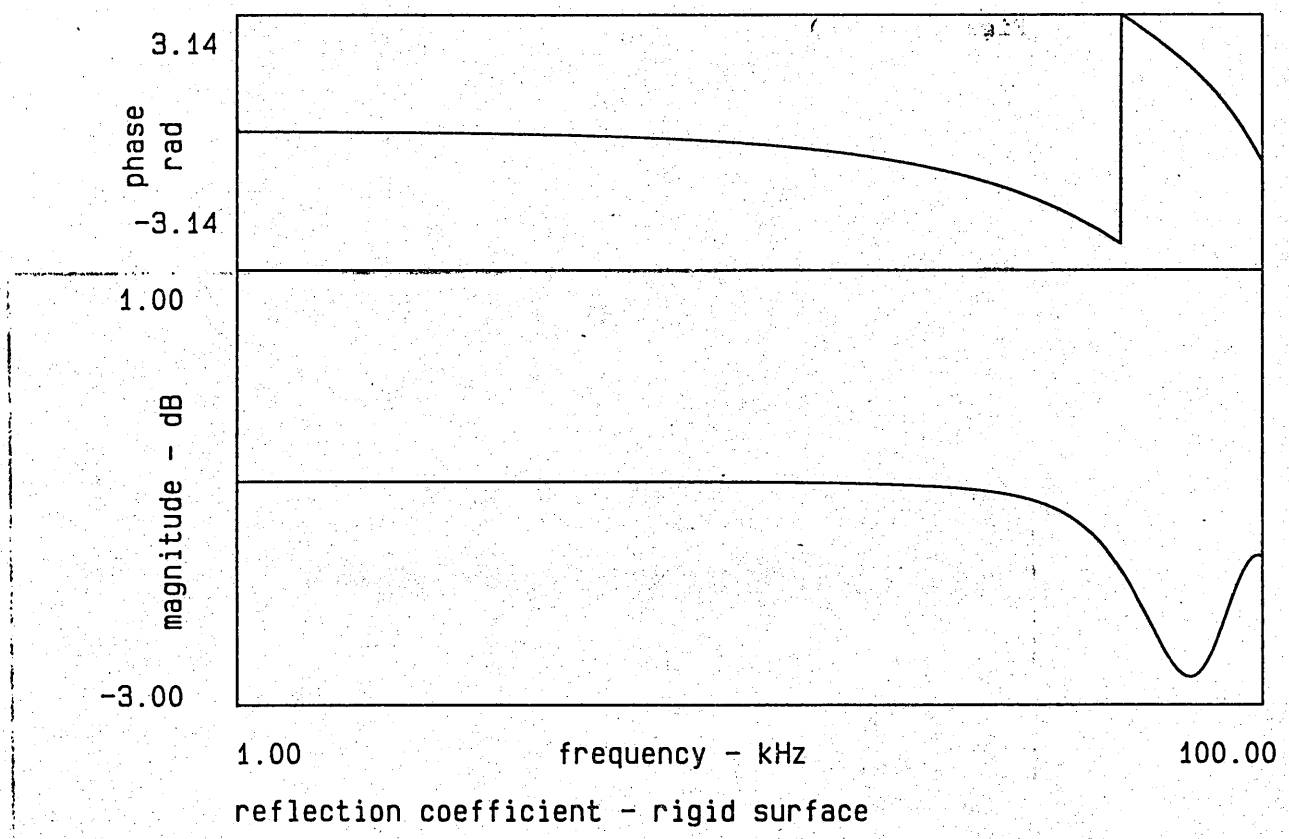

Figure 8.22(b)

Short duration impulse response and corresponding reflection coefficient for a rigid surface

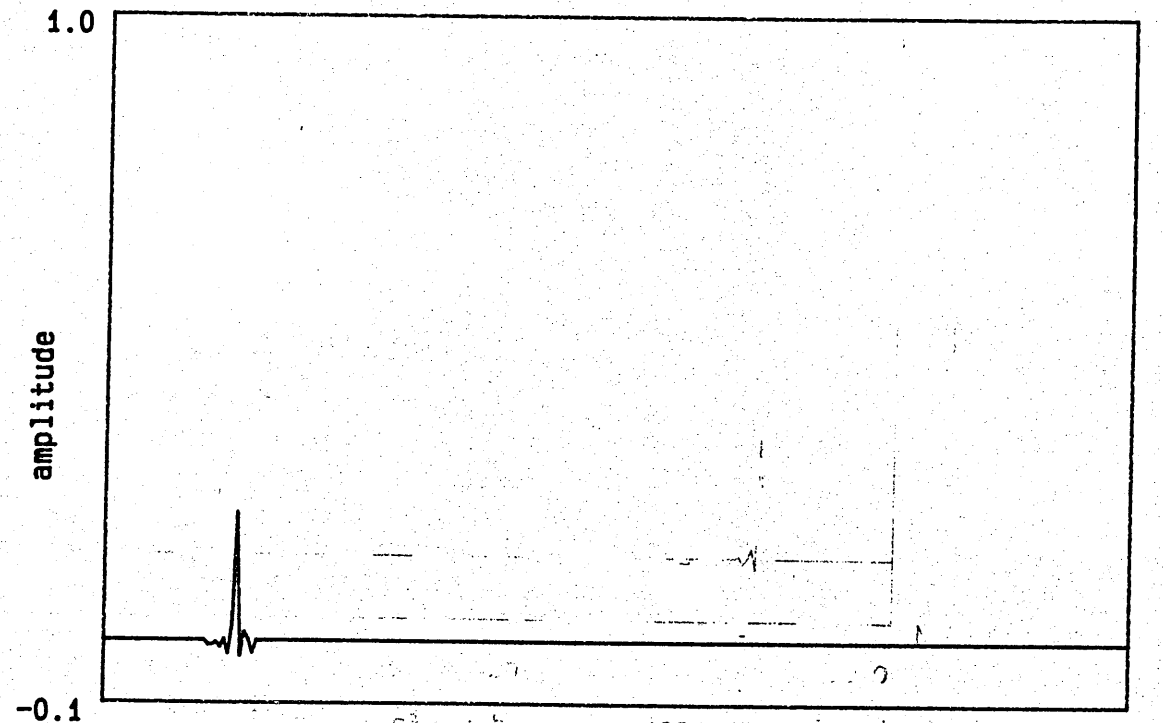

extracted impulse response (arbitrary delay)

Figure 8.23(a)

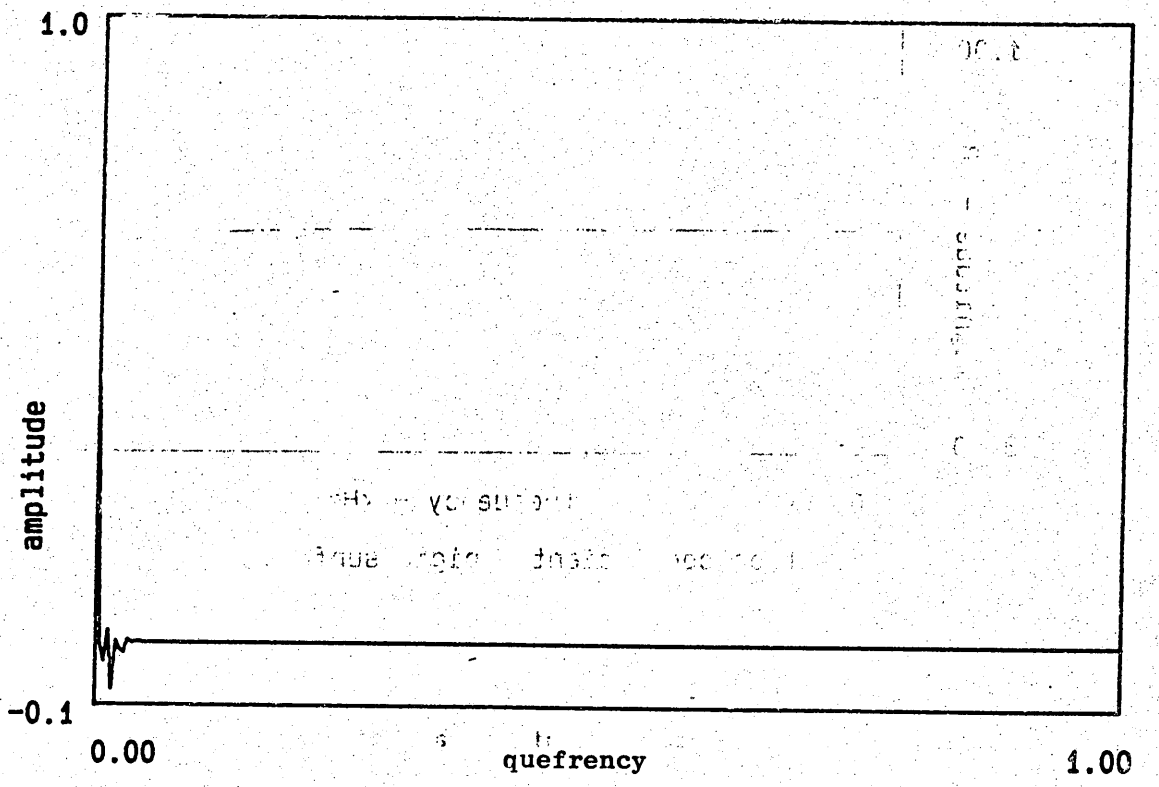

minimum phase reconstruction of impulse response

Figure 8.23(b)

Extracted impulse response and corresponding minimum phase impulse response for a rigid surface

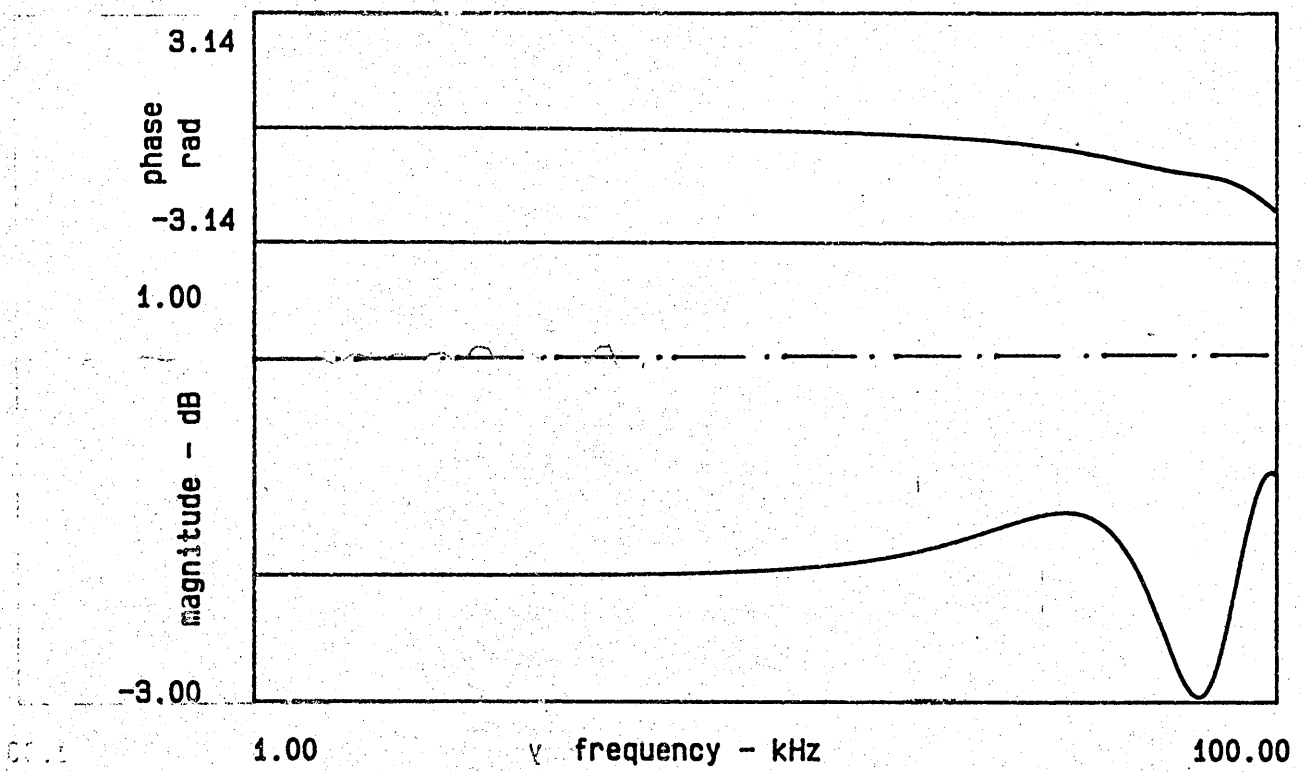

reflection coefficient from extracted impulse response

Figure 8.24(a)

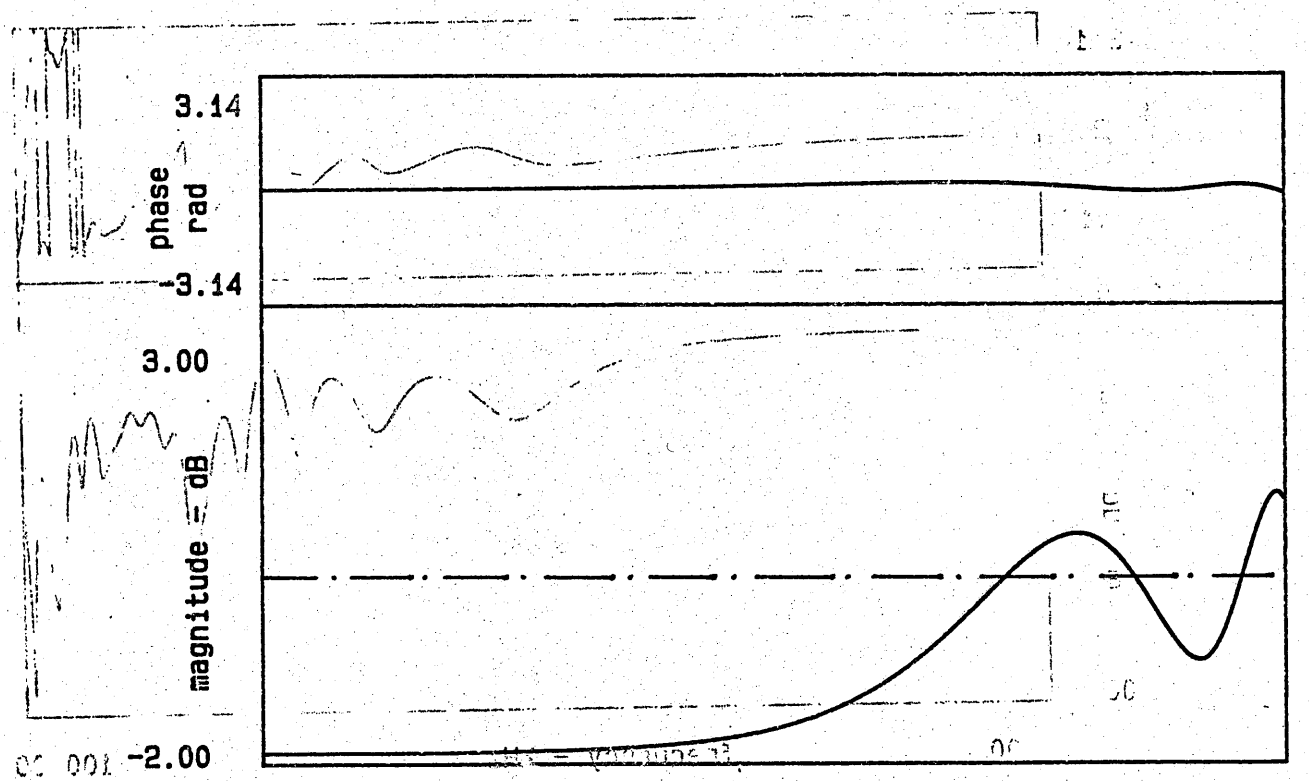

reflection coefficient from minimum phase impulse response

Figure 8.24(b)
Reflection coefficients calculated from the extracted impulse response and the minimum phase impulse response for a rigid surface

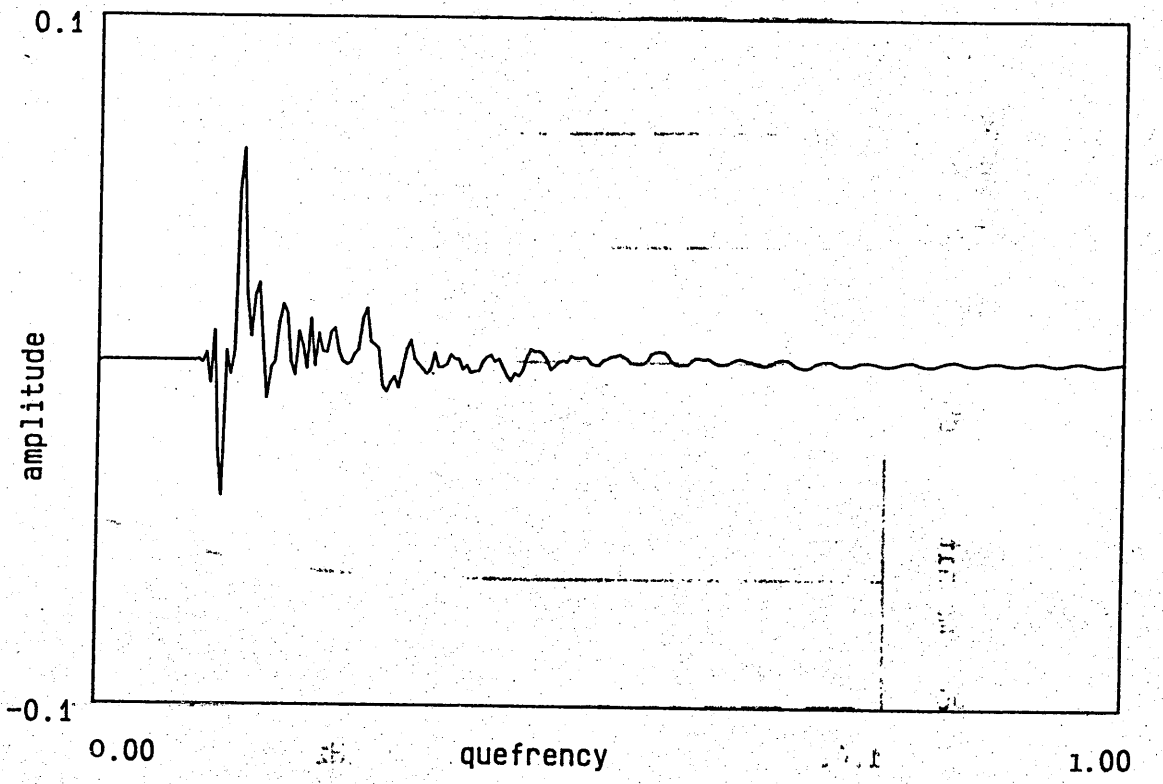

Figure 8.25(a)

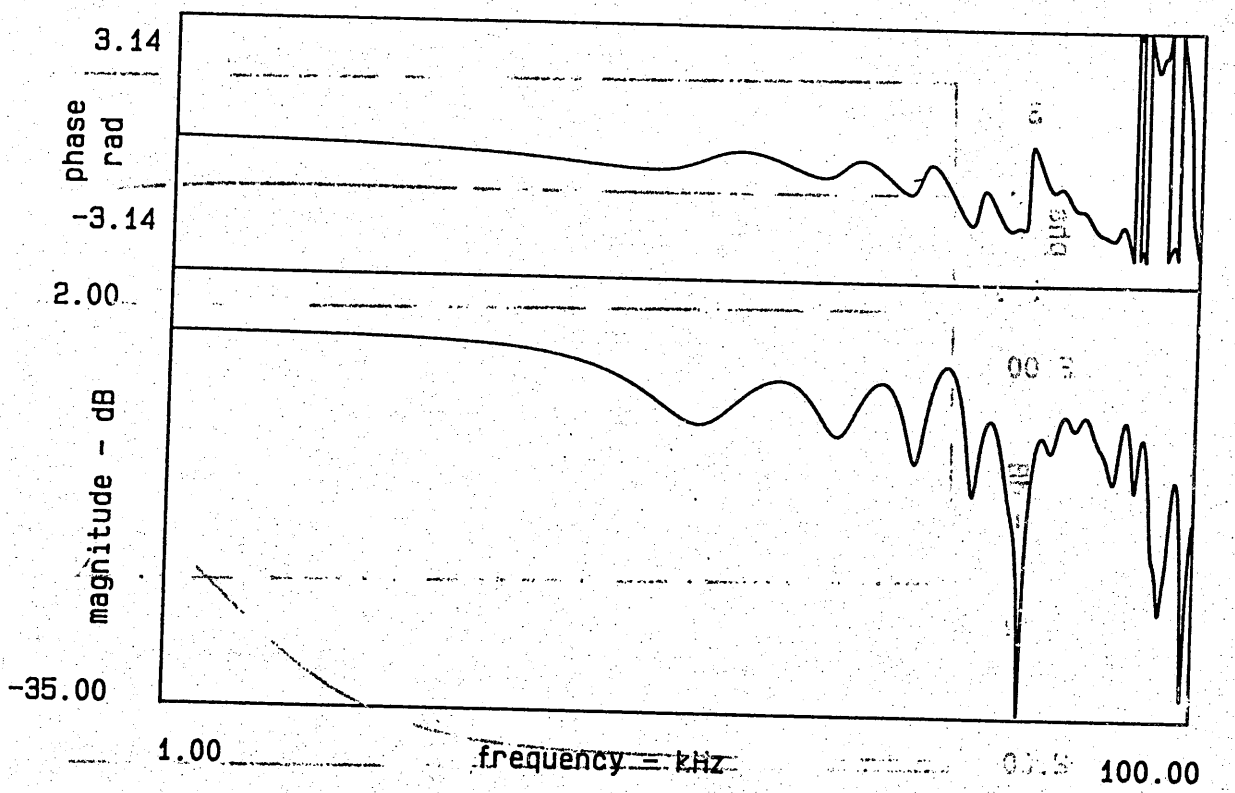

Figure 8.25(b)
Extracted impulse response and calculated reflection coefficient for the artificial grass surface.
Source height 15 cm, receiver height 15 cm, separation distance 100 cm.

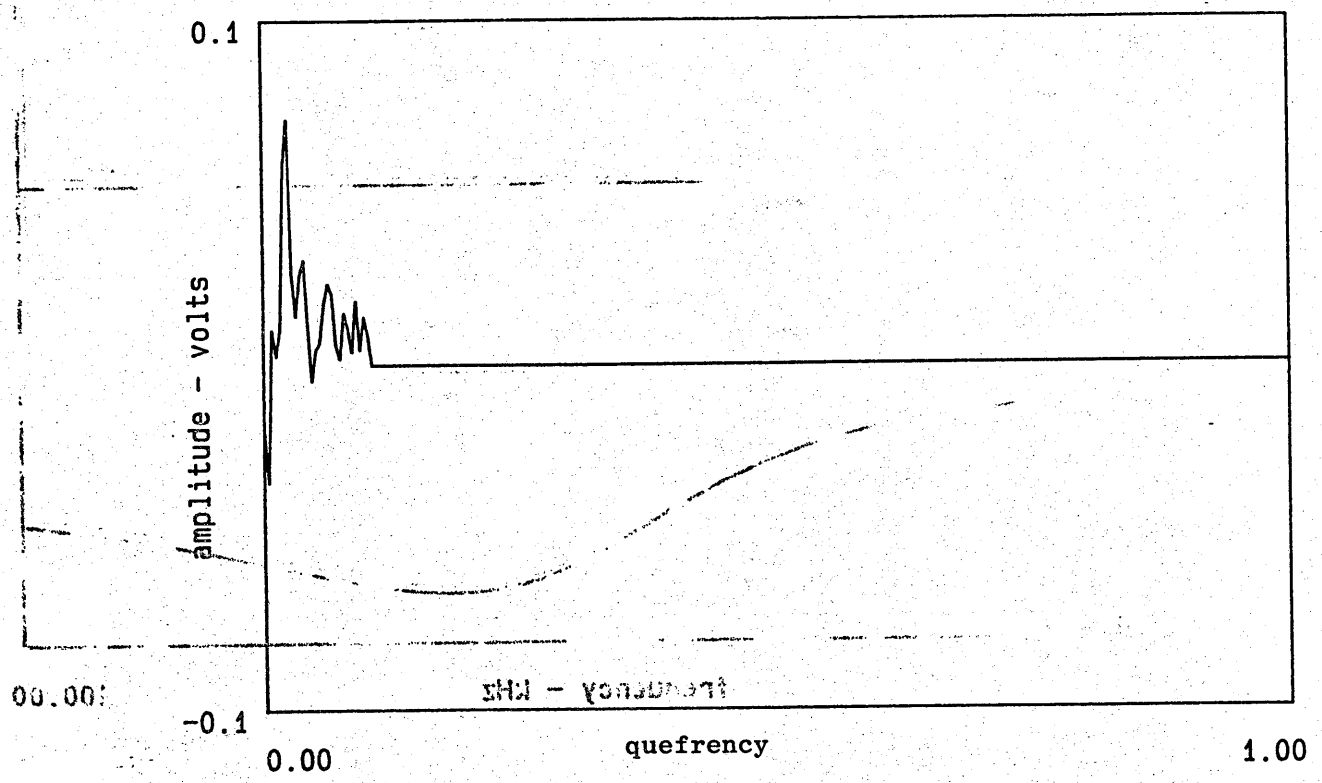

Figure 8.26(a)

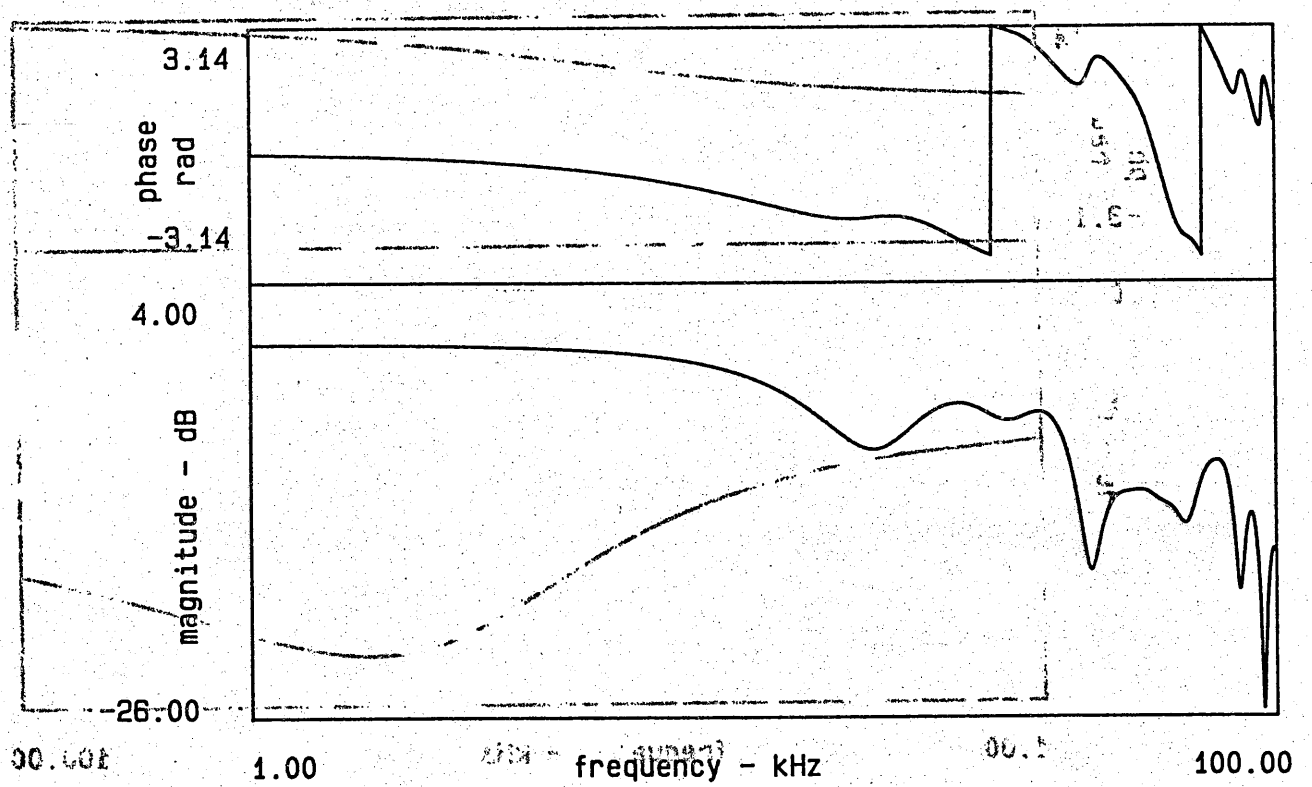

reflection coefficient - artificial grass

Figure 8.26(b)
Short duration impulse response and corresponding reflection coefficient for artificial grass. Surface height 15 cm, receiver height 15 cm, separation distance 100 cm.

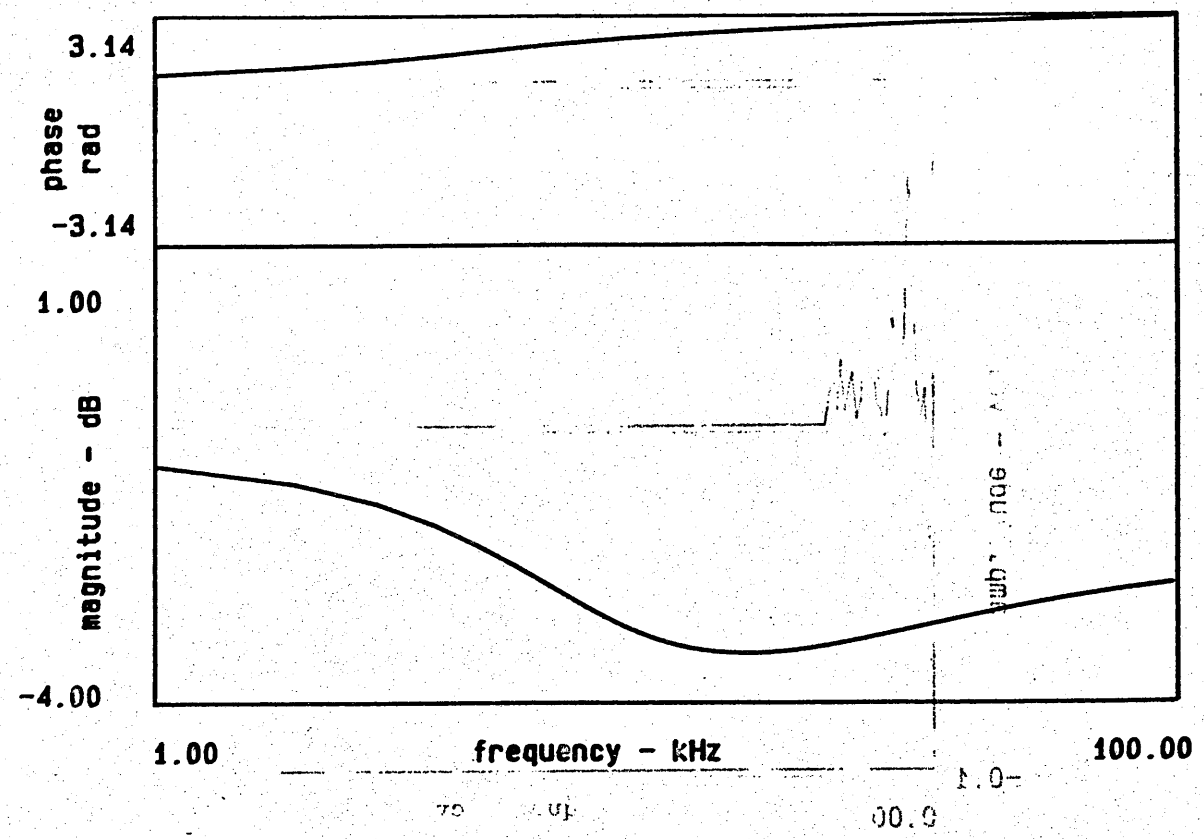

Figure 8.27(a)

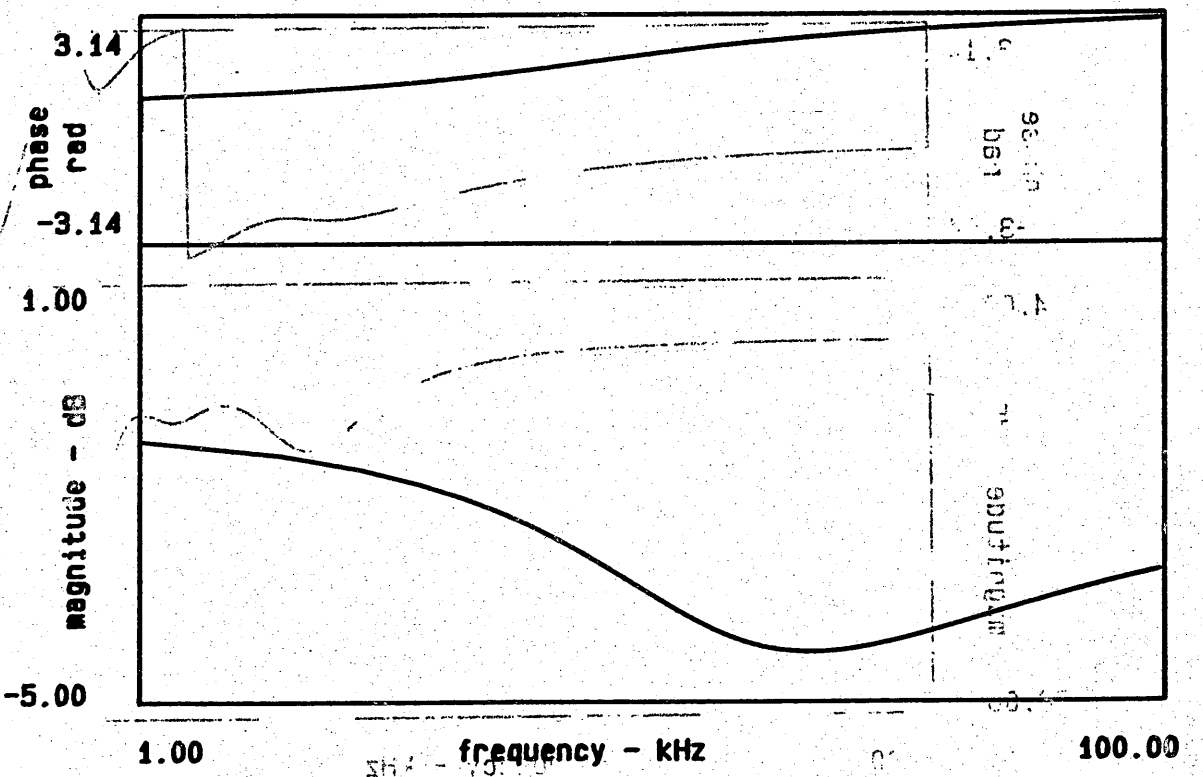

Figure 8.27(b)
Reflection coefficient calculated from flow-resistance impedance model for artificial grass and fibreboard.

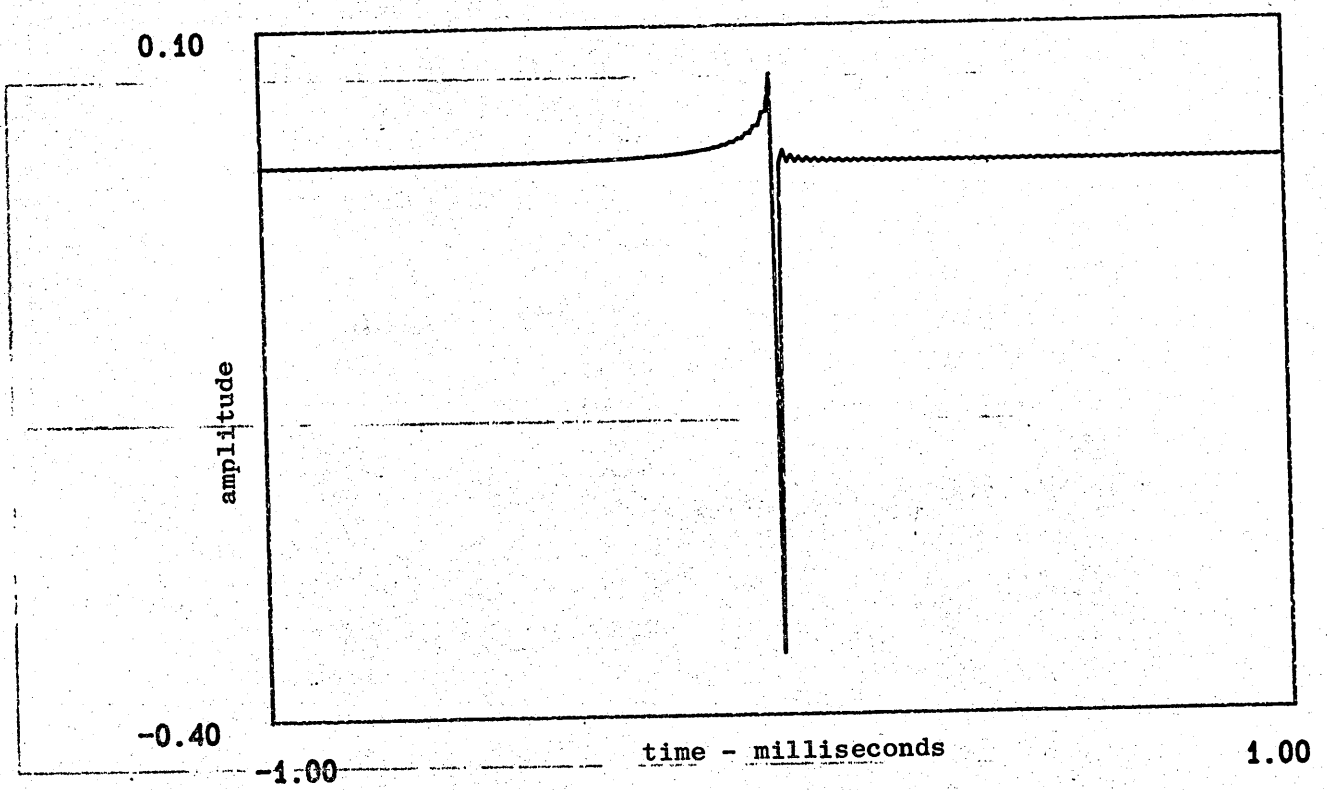

Figure 8.28(a)

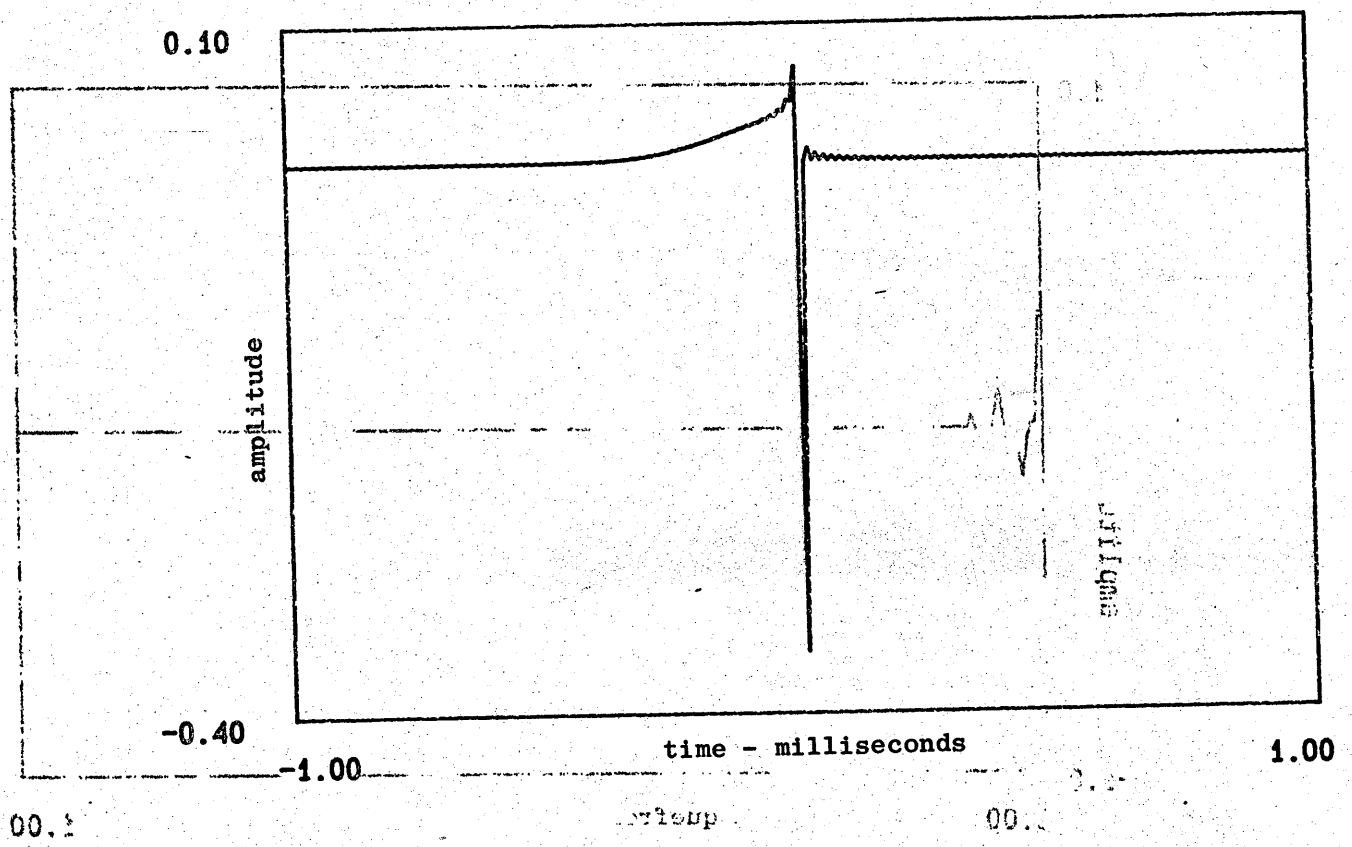

Figure 8.28(b)
Impulse response for artificial grass surface calculated from plane wave and spherical wave reflection coefficients.

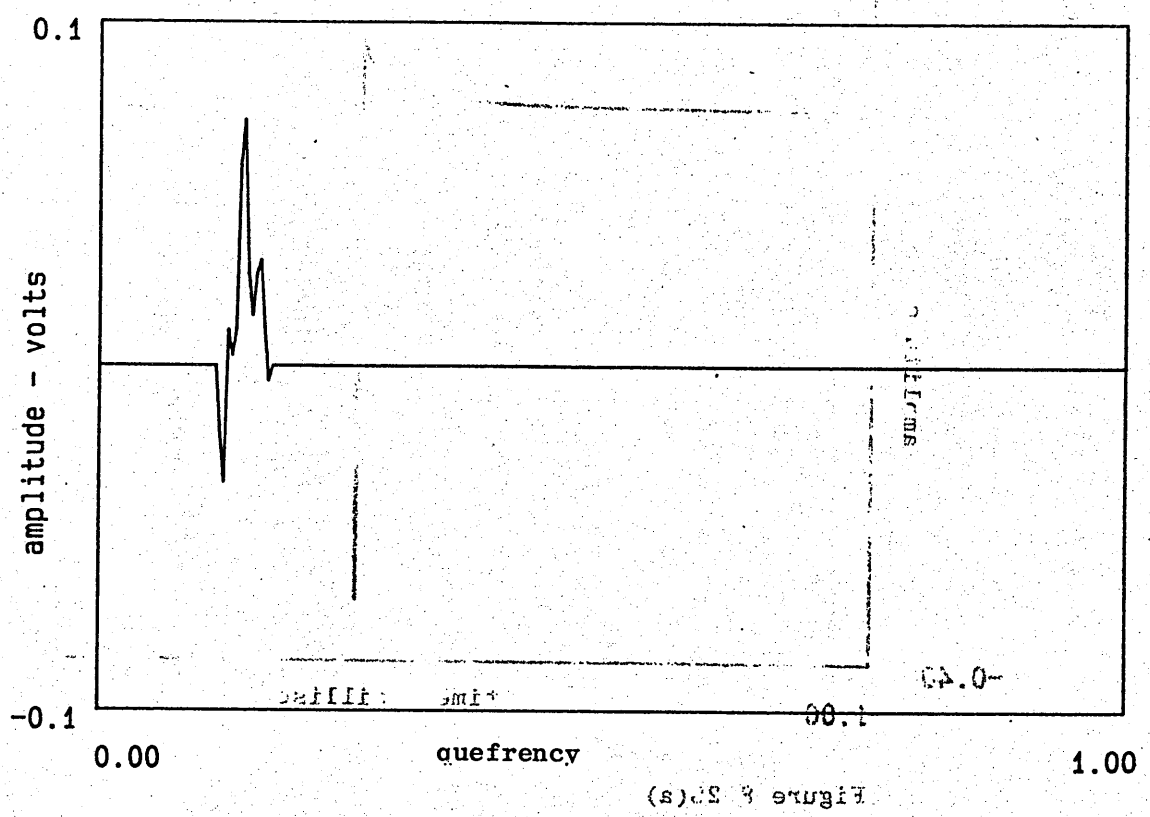

Figure 8.29(a)

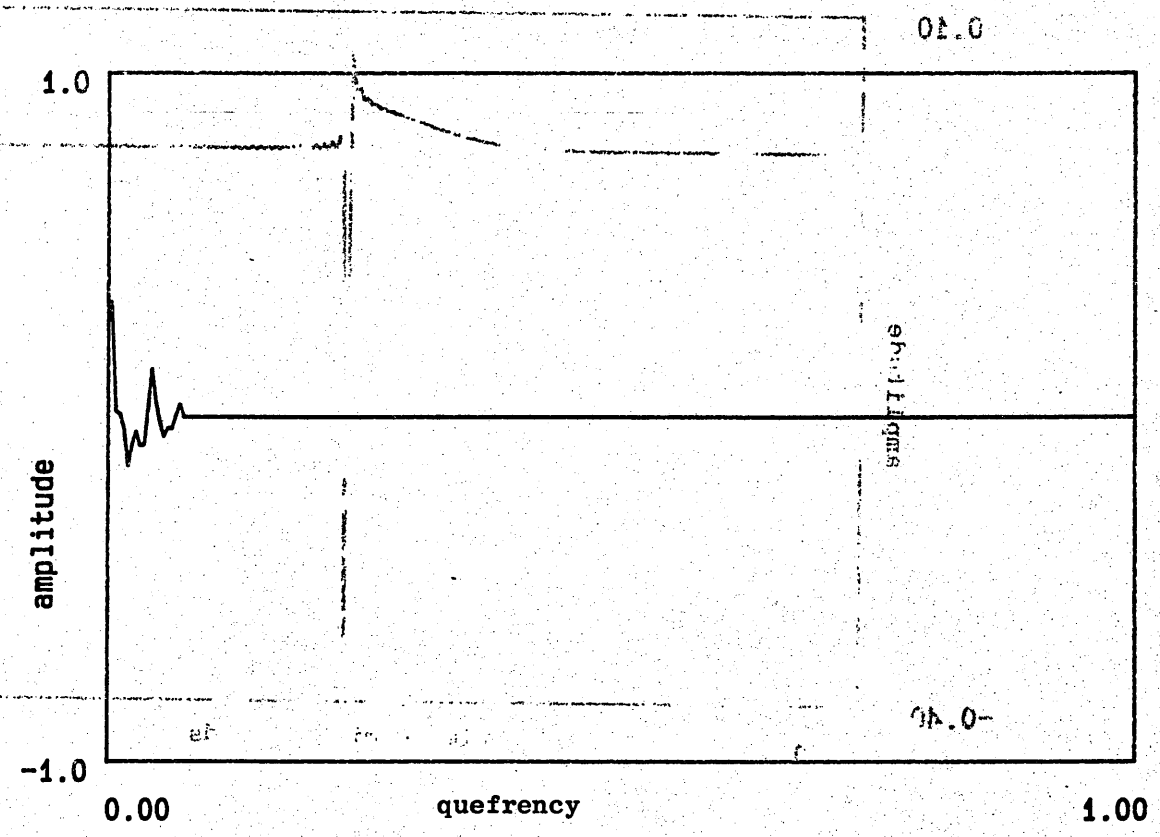

Figure 8.29(b)
Extracted and minimum-phase impulse responses for the artificial grass surface. Source height 15 cm, receiver height 15 cm, separation distance 100 cm.

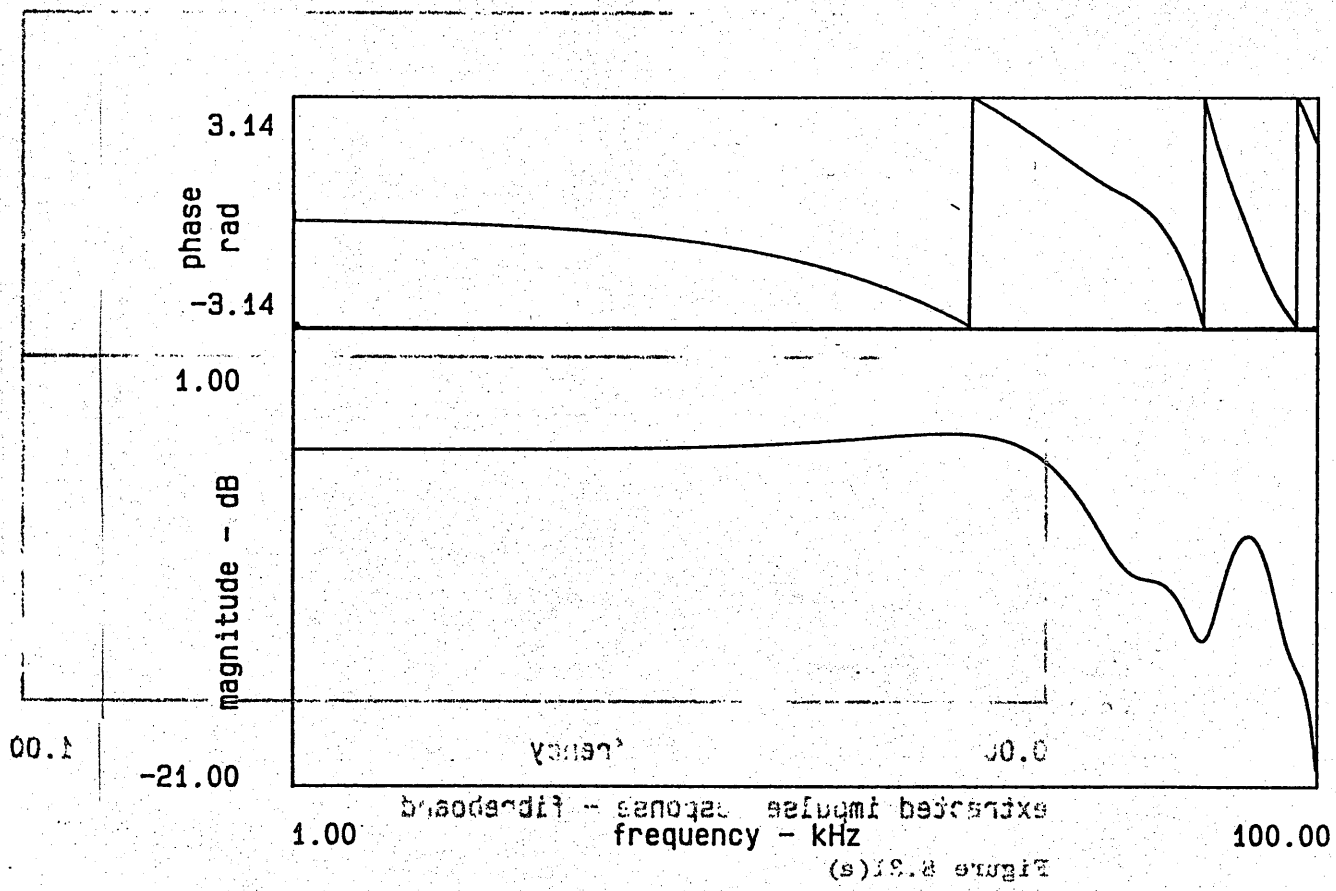

Figure 8.30(a)

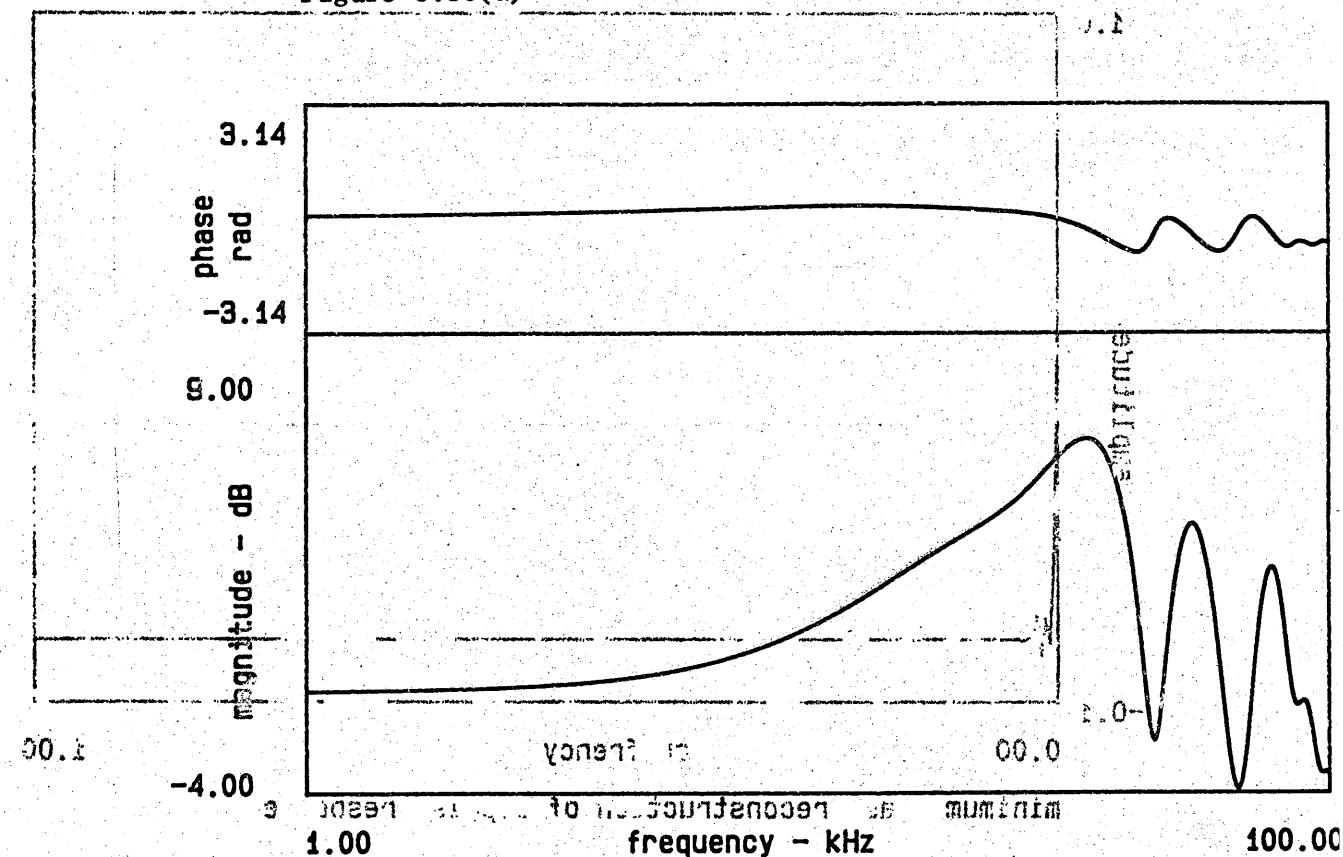

Figure 8.30(b) Reflection coefficient for the artificial grass surface calculated from Figure 8.29.

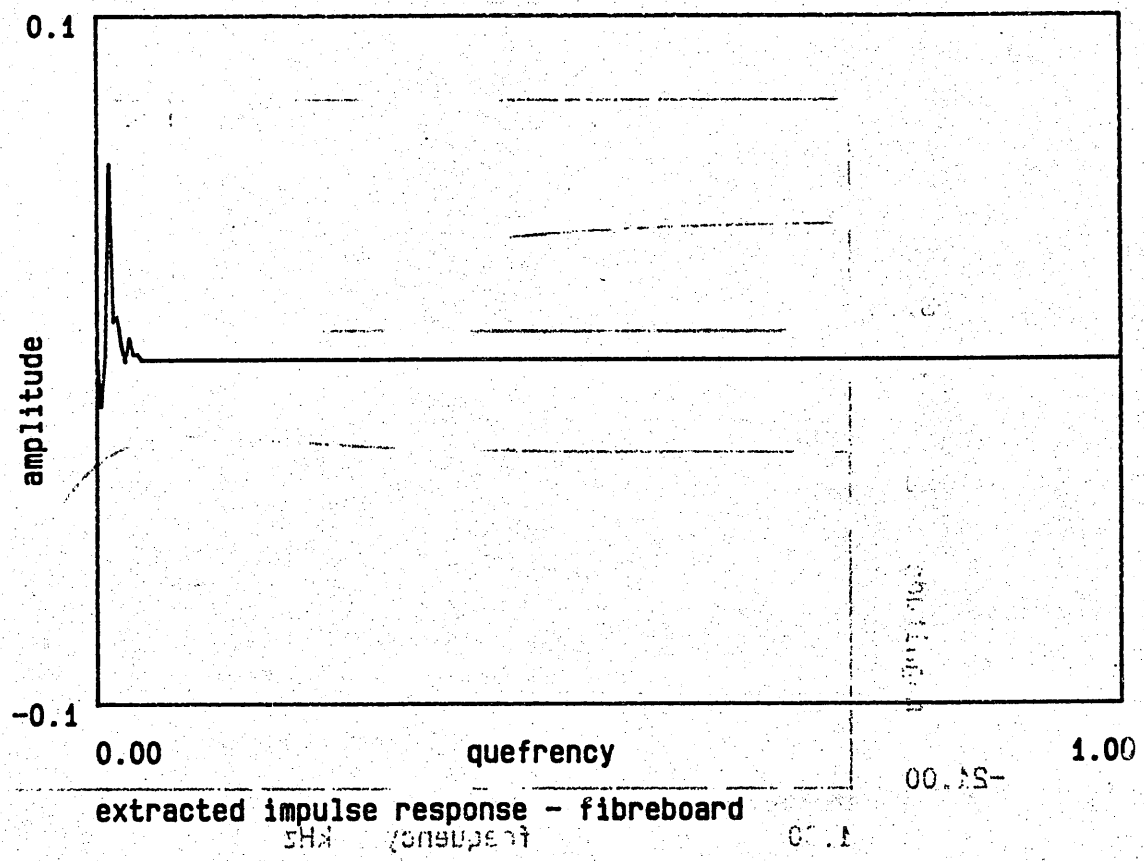

Figure 8.31(a)

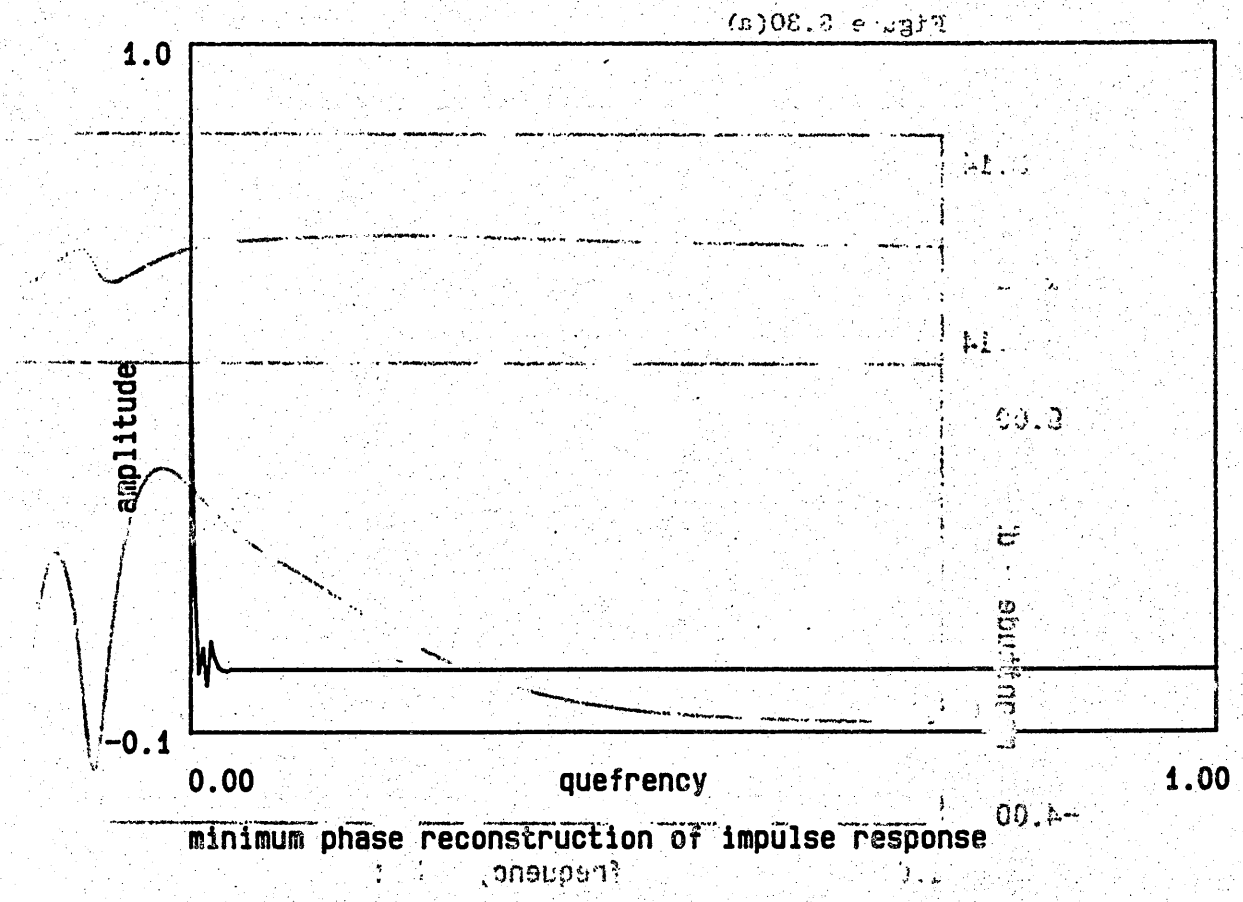

Figure 8.31(b)
Extracted and minimum phase impulse responses for the fibreboard surface. Source height 15 cm, receiver height 15 cm, separation distance 100 cm.

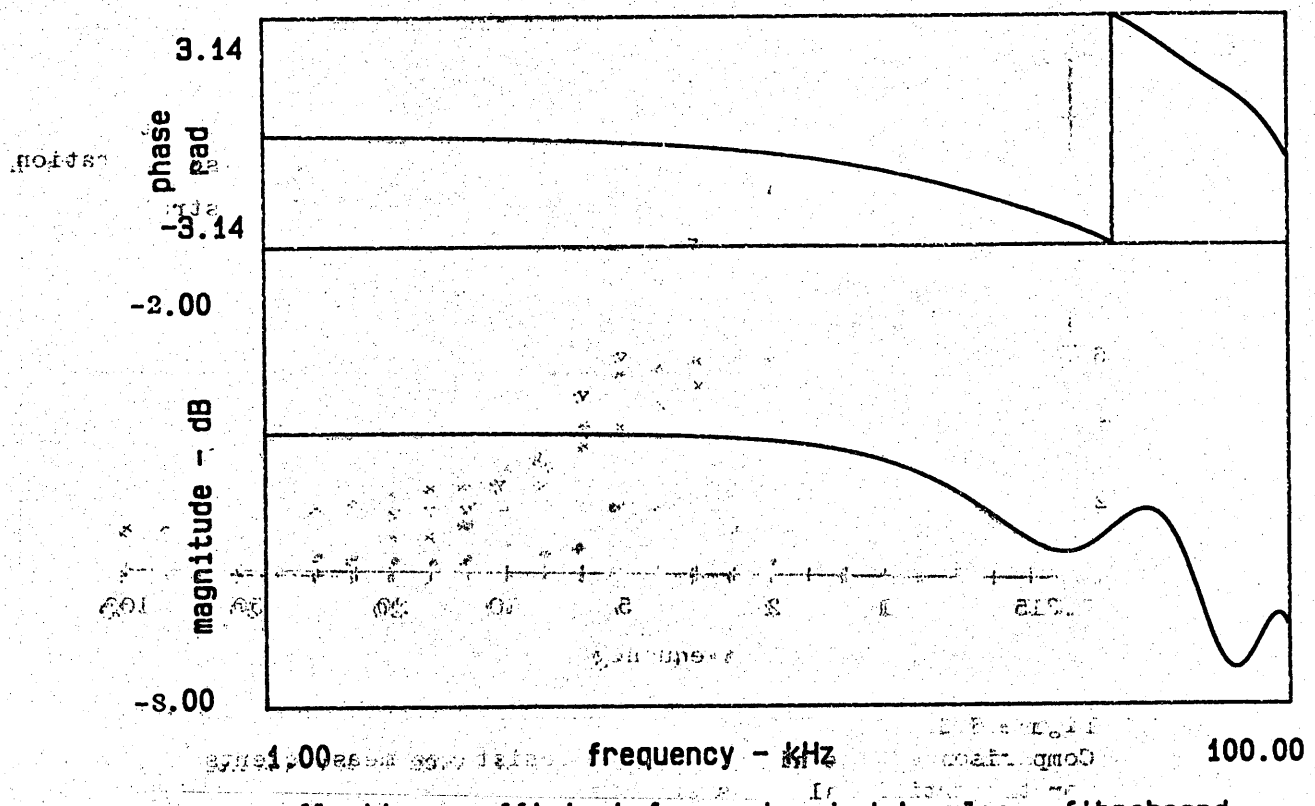

reflection coefficient from extracted impulse - fibreboard

Figure 8.32(a)

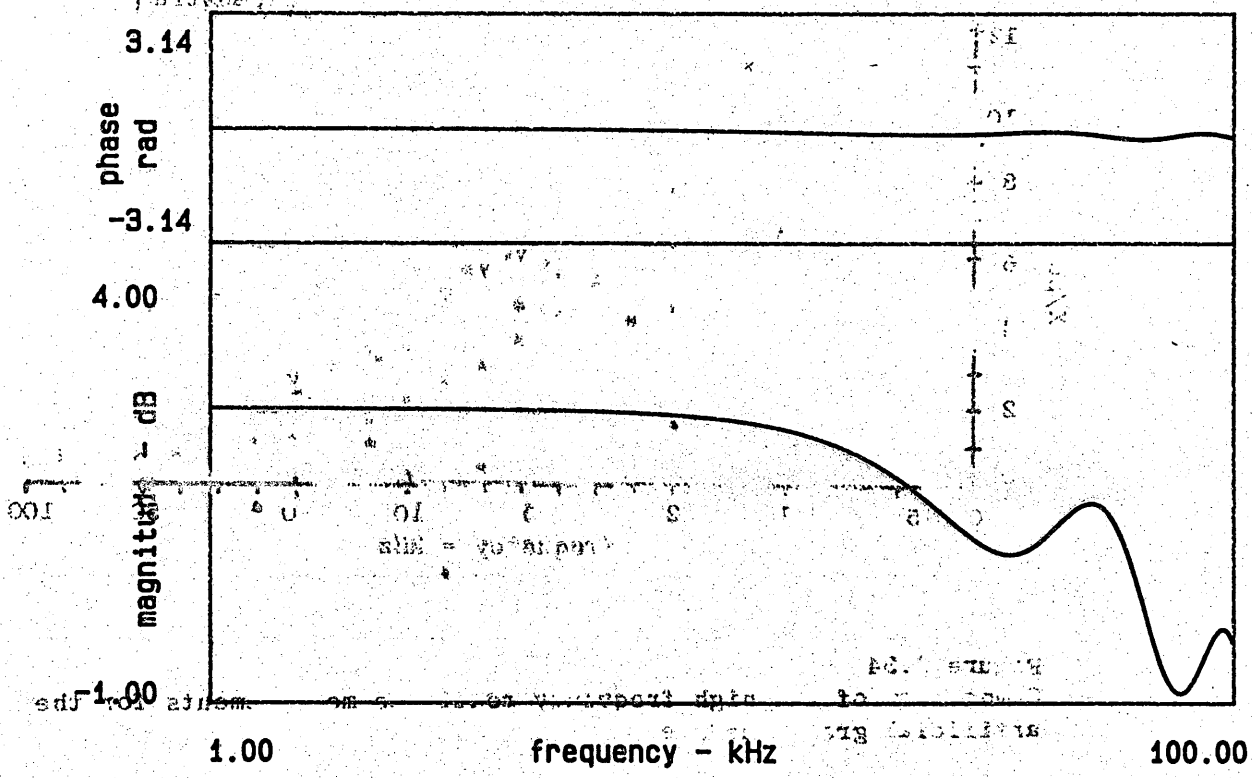

reflection coefficient from minimum phase impulse response

Figure 8.32(b)
Reflection coefficients for the fibreboard surface calculated from Figure 8.31.

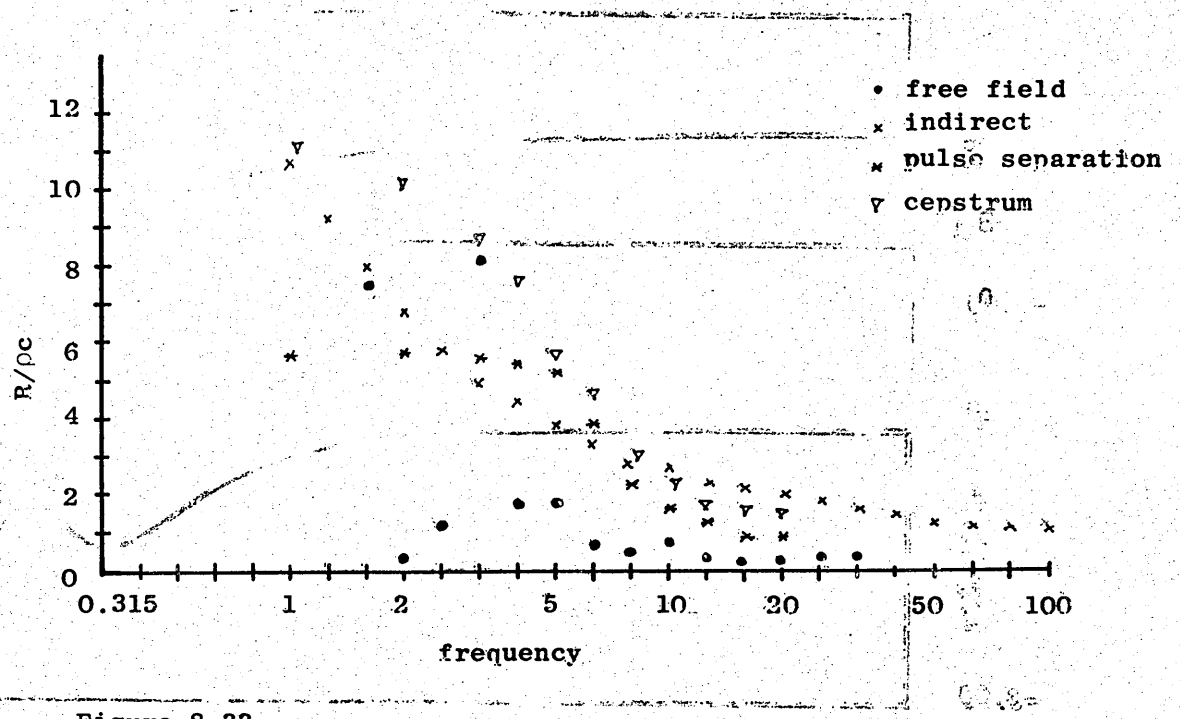

Figure 8.33
Comparison of the high frequency resistance measurements for the artificial grass surface

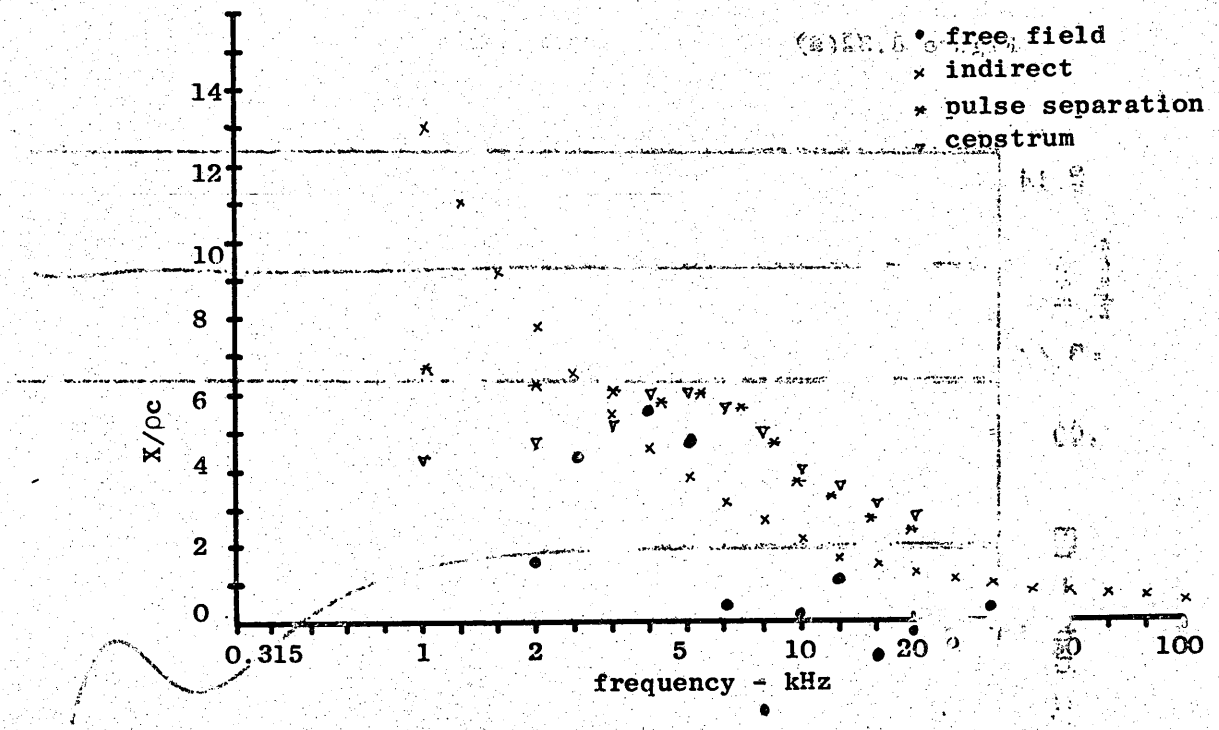

Figure 8.34
Comparison of the high frequency reactance measurements for the artificial grass surface

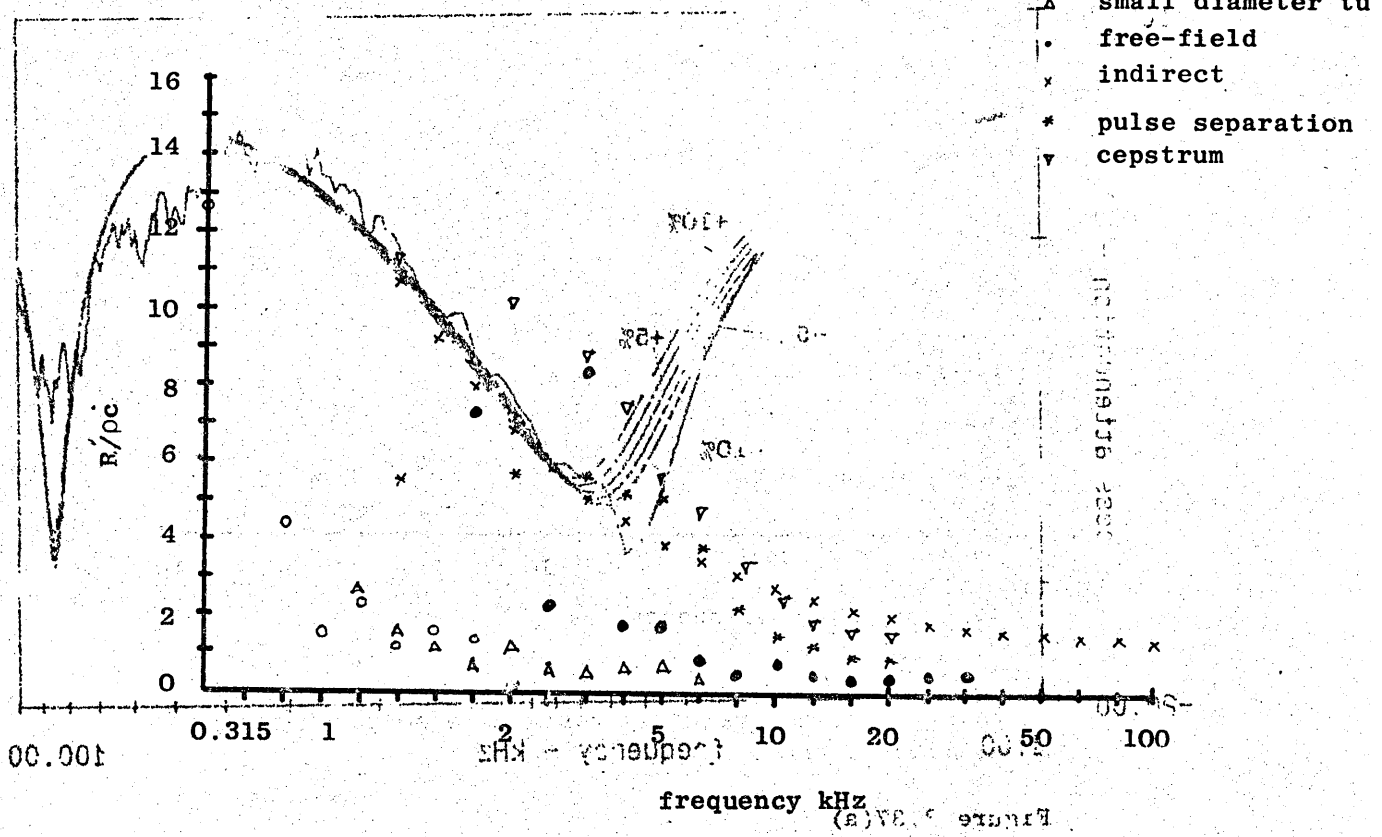

Figure 8.35
Comparison of all resistance measurements for artificial grass surface

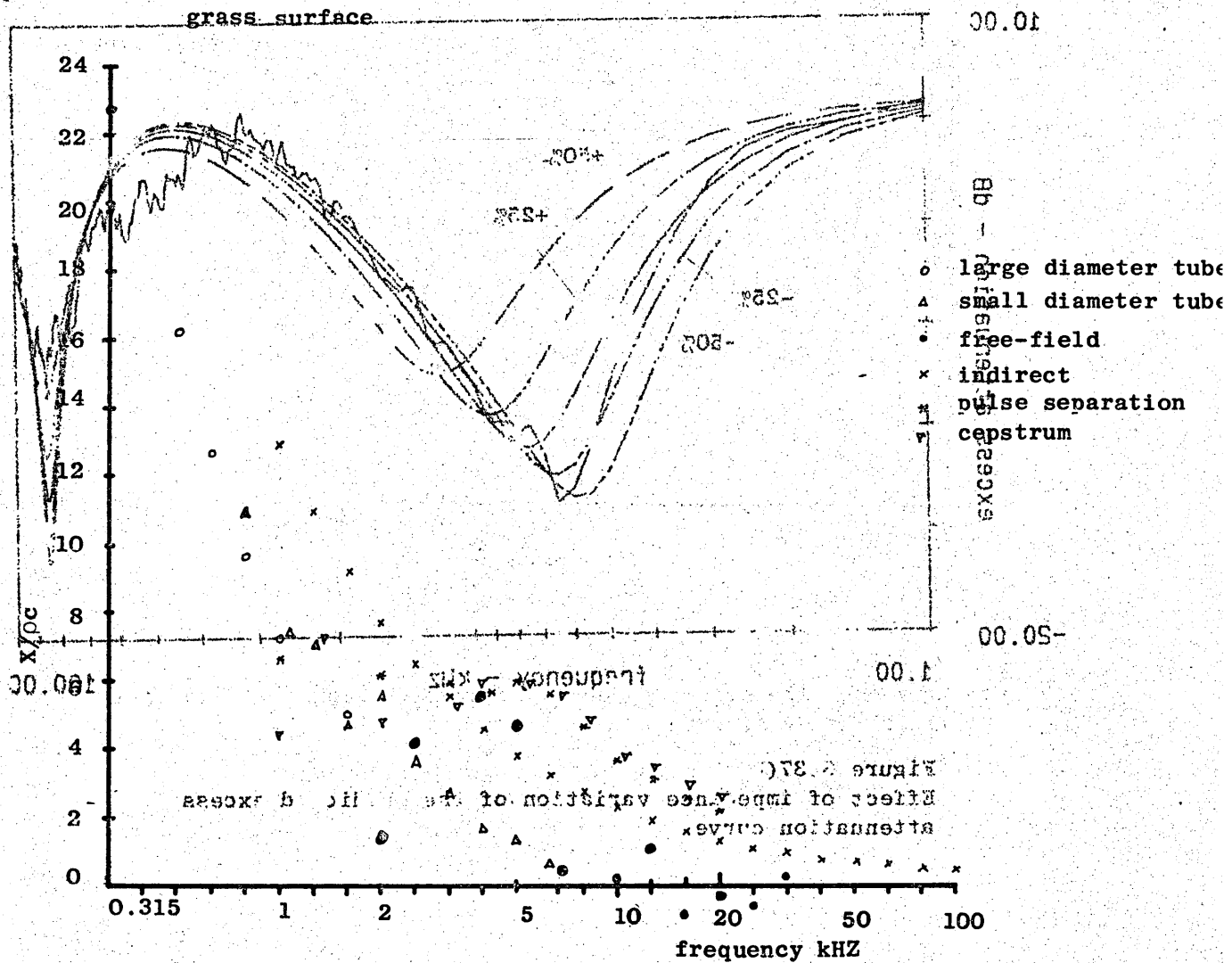

Figure 8.36
Comparison of all the reactance measurements for the artificial grass surface

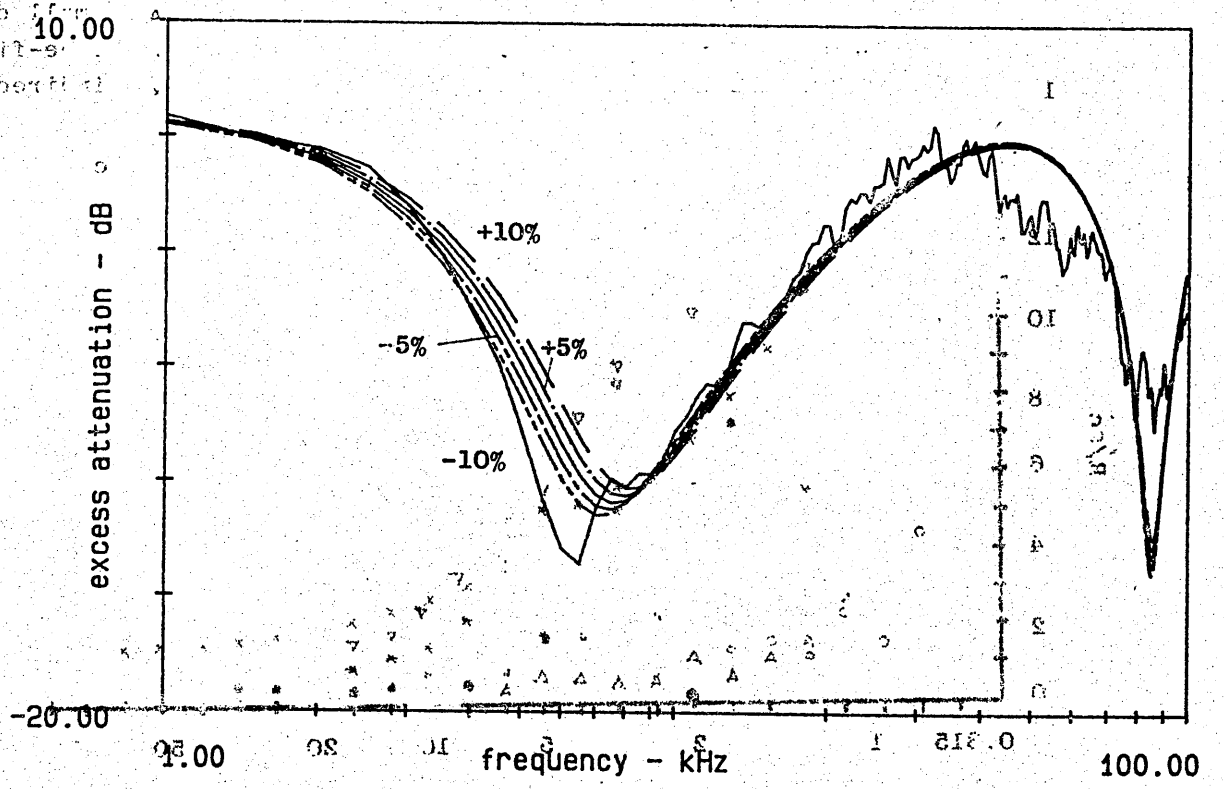

Figure 8.37(a)

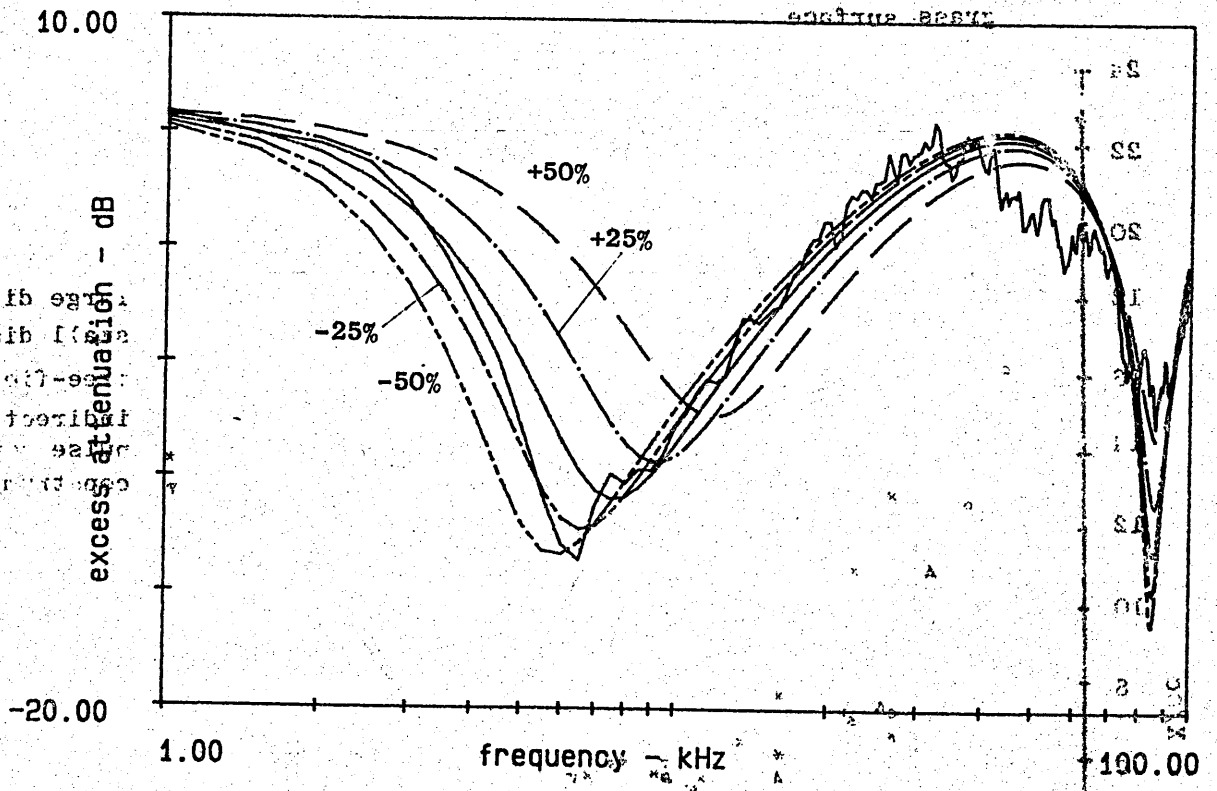

Figure 8.37(b)
Effect of impedance variation of the predicted excess attenuation curve

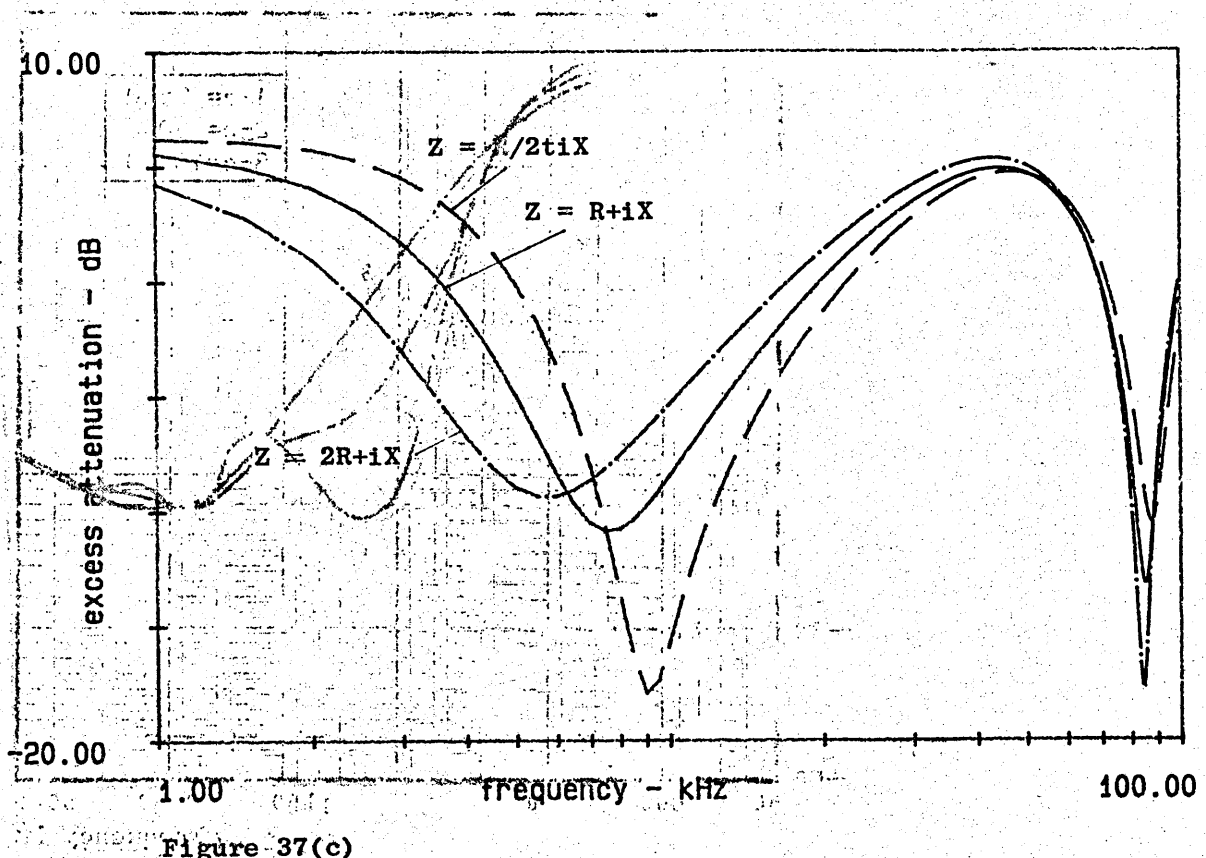

Figure 37(c)

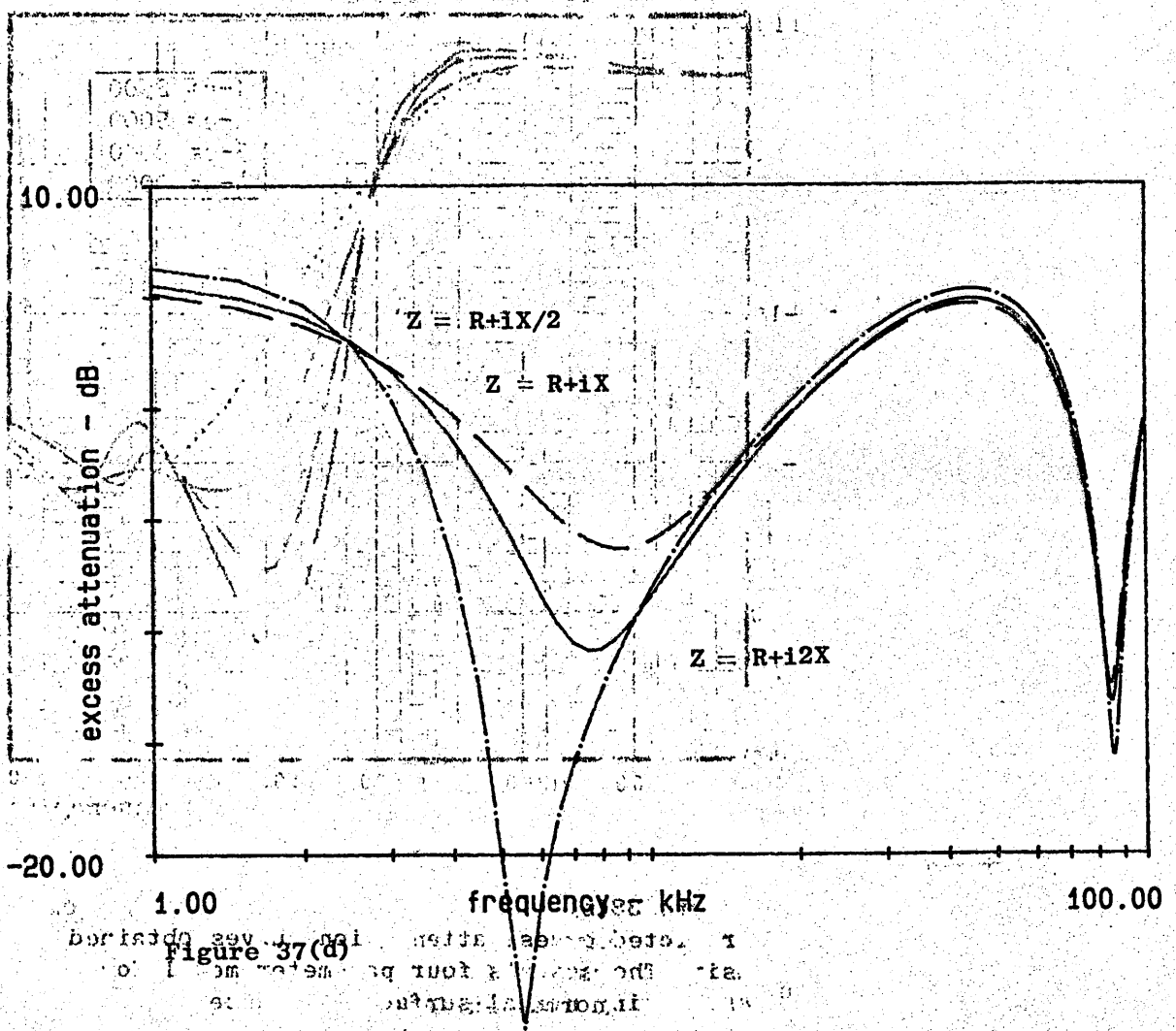

Figure 37(d)

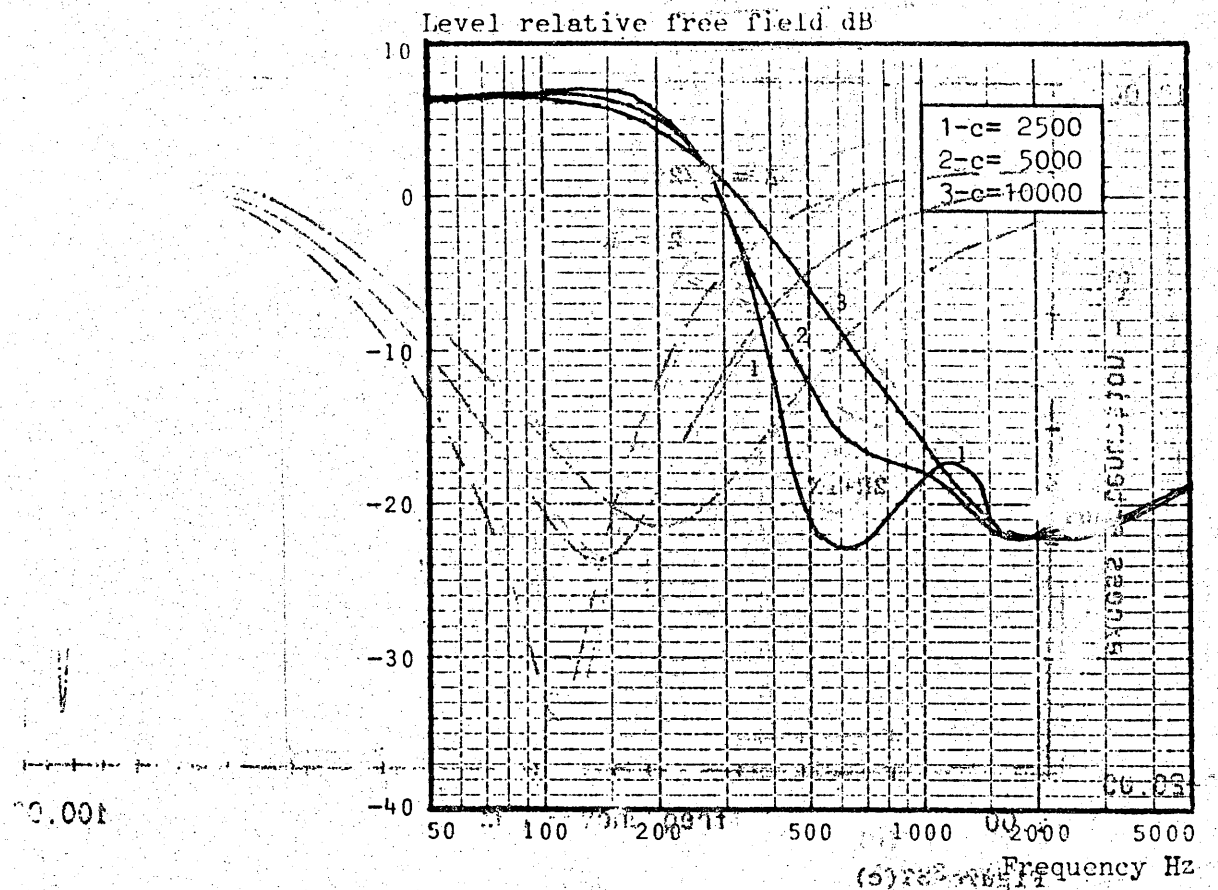

Figure 8.38(a)

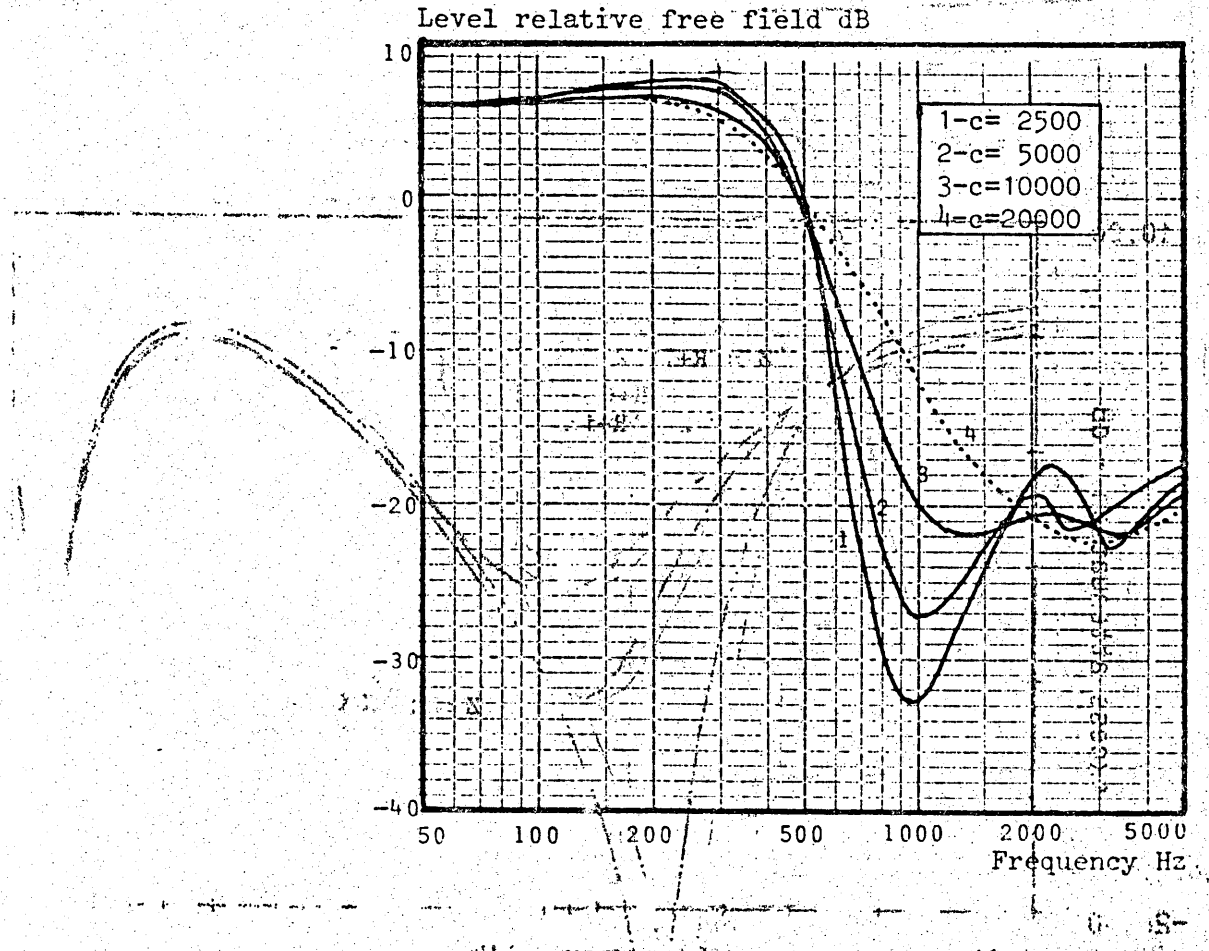

Figure 38(b)
Predicted excess attenuation curves obtained using Thomasson's four parameter model for estimating normal surface impedance

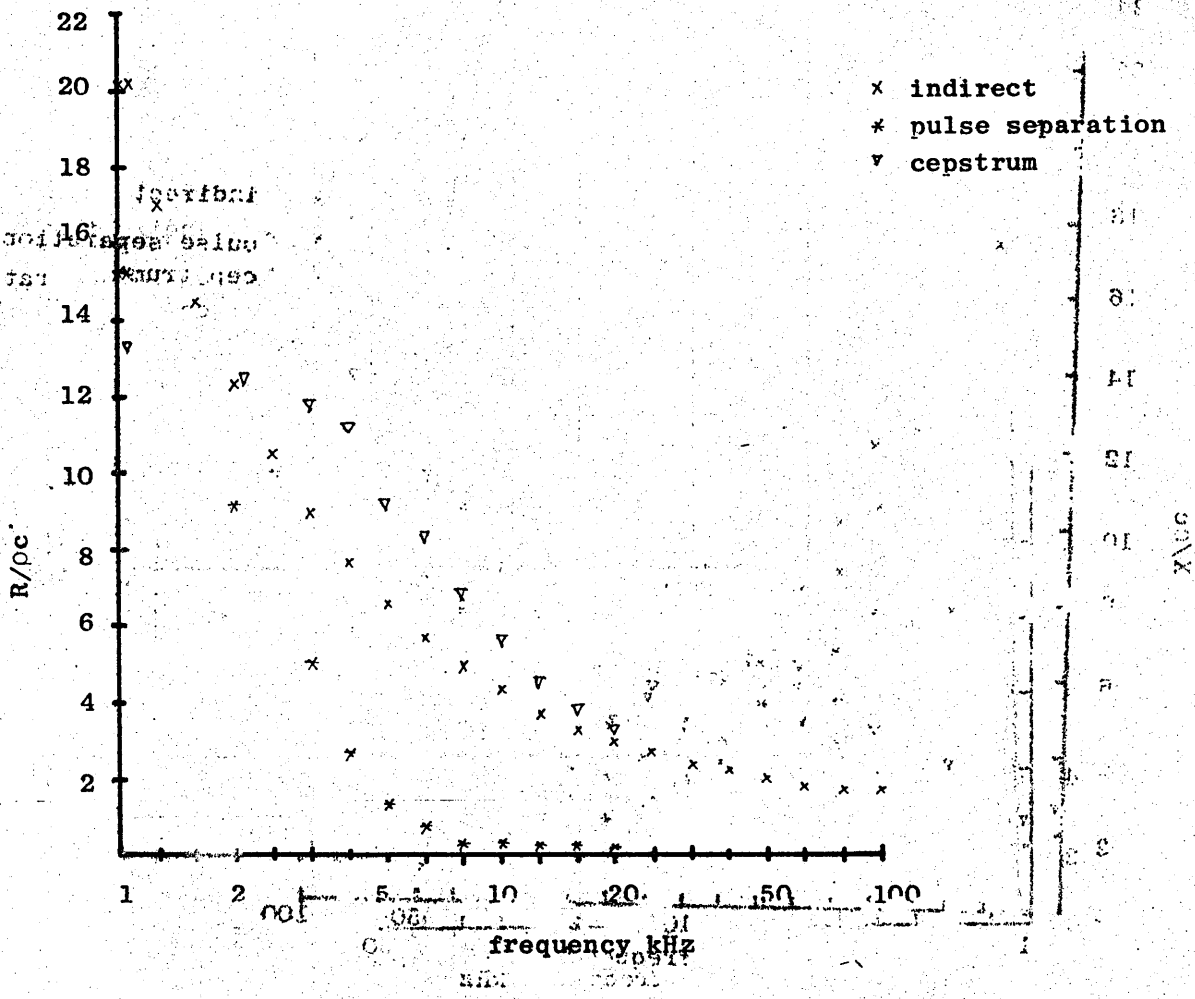

Figure 8.39
Comparison of the resistance measurements for the fibreboard surface

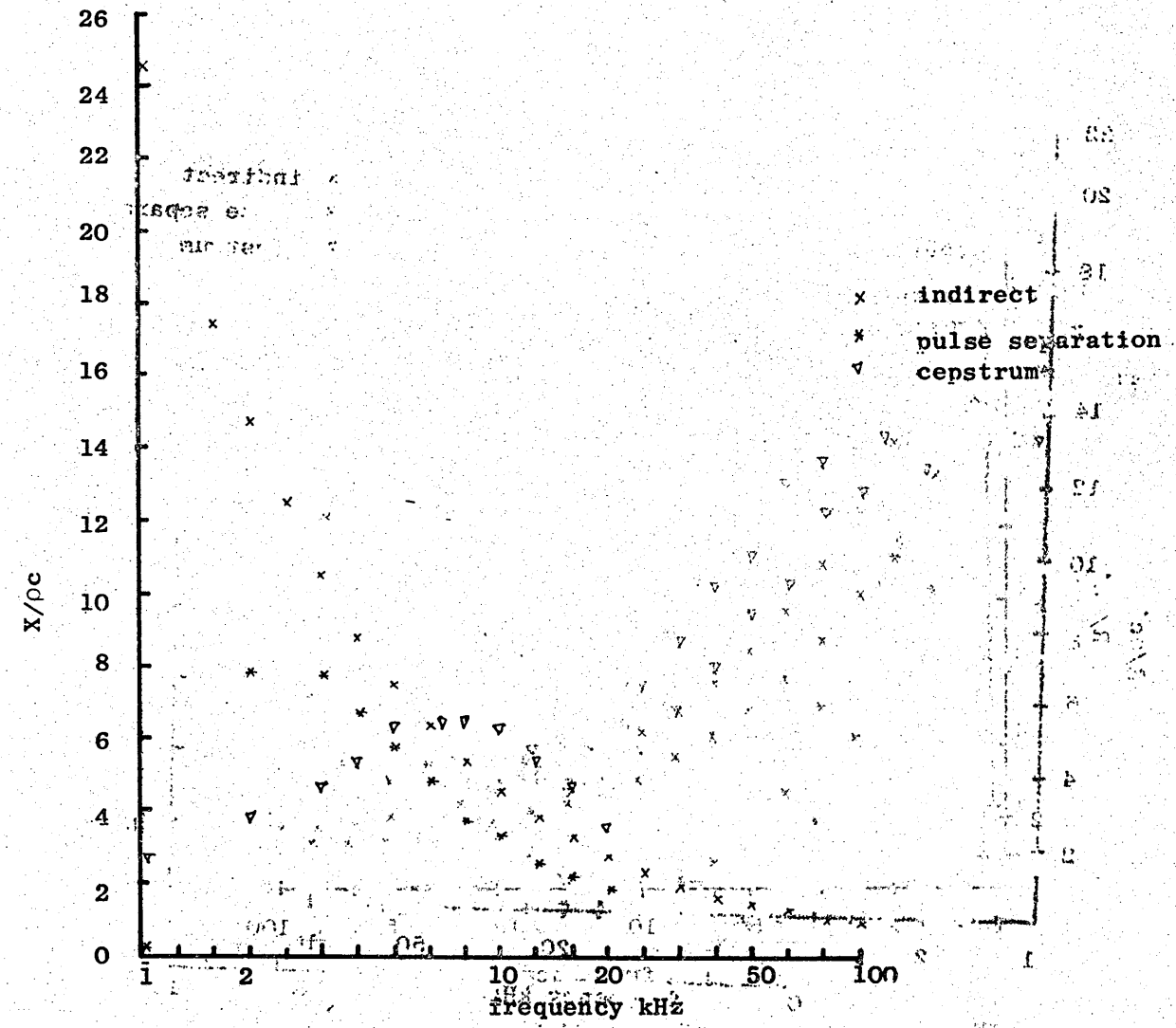

Figure 8.40
Comparison of the reactance measurements for the fibreboard surface

Chapter 9

Point to point propagation: a comparison of measurement and prediction

9.1 Introduction

Several reports describing the experimental evaluation of point to point propagation theoretical predictions have been published in recent years [9.1-9.4]. Some of the experiments were conducted outdoors, and therefore subject to the influence of wind and temperature gradients [9.4], others used prediction schemes based upon erroneous [9.2] or incomplete [9.1] solutions to the wave equation.

The prime objective of this study was to evaluate the more recent developments in the theoretical predictions for local and extended reaction and the rigid backed layer boundaries, with the aid of laboratory models.

The specific normal impedance values used for this evaluation are those based upon the flow resistivity values derived from the indirect method as described in Section 8.4. The high values of flow resistivity obtained for the two model materials preclude distinguishing between the different boundary types; due to the very high rate of attenuation of the transmitted wave over the range of frequencies employed. All boundaries therefore appear to behave as locally reacting. In view of this the predictions are based upon equation 3.64, the solution for a local reaction boundary.

Measurements of point to point propagation over plane absorbing and mixed impedance boundaries have been made in the small anechoic chamber. Three cases have been examined in detail:

(i) homogeneous finite impedance,

(ii) half rigid half finite impedance,

(iii) rigid strip and finite impedance.

The two materials selected to model finite impedance surfaces have been described elsewhere. For the mixed impedance boundaries, the rigid surface has been modelled by 1/16th inch thick aluminium sheet.

9.2 Rigid Surface Measurements

Prior to conducting experiments with the finite impedance materials, a limited set of measurements was made using the varnished blockboard backing to represent a rigid surface. The object of these measurements was to investigate the effects of:

(i) source height uncertainty,

(ii) broad band noise source,

(iii) near surface turbulence,

(iv) extended source and receiver size.

A block diagram of the experimental instrumentation is shown in Figure 9.1. The air jet was used as the sound source and B & K 4135 ¼" microphone as the receiver. The Nicolet spectrum analyser was set to the dual channel mode and summation averaging of 128 samples.

The results are presented in the form of excess attenuation relative to free field. Figure 9.2 shows the measured and predicted excess attenuation for source and receiver heights of 5 cm and a separation distance of 100 cm. Comparing the results, several observations can be made.

(i) The measured minima do not occur at the same frequency.

(ii) The predicted minima are much lower than the measured minima.

(iii) The measured high frequency minimum is much broader than the predicted minimum.

Possible causes for the differences between the two results are discussed below.

9.2.1 Source height error

For a rigid boundary the excess attenuation minima result from destructive interference as a consequence of the path length difference between the direct and reflected fields. The frequencies at which the minima occur are therefore very sensitive to the source-receiver geometry.

The predicted excess attenuation shown in Figure 9.2 was calculated for a source height of 5 cm, the distance from the rigid surface to the top of the air jet nozzle. The acoustic source location is unlikely to be at the top of the jet because of the large mass of air flowing through the nozzle.

An estimate of the acoustic source height can be obtained by varying the height used in the predictive algorithm until the locations of the measured and predicted minima coincide. The variation in minima location with source height can be seen in Figure 9.3. Increasing the source height increases the path length difference and so moves the minima to lower frequencies.

An attempt to establish a least squares criterion for determining the source height proved unsuccessful. The large differences between the measured and predicted attenuation at the minima dominated the summation of the error terms and so the small errors introduced by source height variations had neligible influence. In view of this a visual estimate of best fit was made by comparing the measured attenuation curve with the curves predicted for a range of source heights. Figure 9.4(a) compares the measured attenuation curve with the predicted for source heights of 5.2, 5.3, 5.4 and 5.5 cm. The best agreement appears to be obtained for a source height of 5.3 cm, as shown in Figure 9.4(b), but the 5.4 and 5.2 cm curves could also be considered as reasonable predictions. Obviously such a subjective estimation procedure is questionable and further work needs to be carried out in order to obtain some objective source height determination procedure.

Assuming a source height of 5.3 cm $\pm$ 1 mm, the acoustic source is located between 2 and 4 mm above the top of the air jet nozzle. The actual height appears to have negligible influence upon the value of the predicted attenuation at the minima. The differences exhibited in Figures 9.3 and 9.4(a) are due to arithmetic rounding errors in the computation process.

9.2.2 Finite analysis bandwidth

Part of the discrepancy between the depth of the measured and predicted minima arises from the finite analysis bandwidth.

Each of the spectral estimates calculated by the Nicolet corresponds to the average energy in a 250 Hz wide filter, whereas the predicted value is for pure tone interference. Correction procedures for the pure tone calculations are described in Appendix D. However, these cannot account for all the difference in the results, unless a very wide analysis bandwidth is assumed.

9.2.3 Near Surface Turbulence

Another factor to consider is the effect of near surface turbulence. A smoke source held near the receiver showed that there was considerable turbulent air motion in front of the microphone diaphragm. Such turbulence could only be caused by the air flowing through the air jet noise source. Other possible causes were elliminated by careful sealing of the chamber door and construction joints.

Daigle [9.5] has proposed modelling turbulent air movement as an additional propagation path length, with random direction and attenuation. The extra path length disturbs the strong interference pattern due to the boundary. A correction procedure, based upon the measurement of four meteorological parameters, shows good agreement with experimental measurements. The parameters are:

σ_V - variance of sound velocity deviations

σ_T - variance of air temperature deviations

L_V - sound velocity correlation length

L_T - temperature correlation length

L_V and L_T are measures of the autocorrelation function of the wind and temperature variations. The time delay corresponding to maximum correlation is converted to an equivalent path length difference by multiplying the velocity of sound by the time delay.

Unfortunately the experimental apparatus required to measure these parameters was not available, so no attempt was made to apply any corrections for turbulence. However, Daigle's results support the main observations of this study.

Figure 9.5 compares experimental sound level measurements with two theories. The dashed curve is the spectrum predicted by pure-tone coherent source theory and exhibits strong interference dips. The solid curve is the spectrum predicted for the long-term average pressure as given by Daigle's correction procedure. The interference dips are considerably reduced in amplitude and agree well with the experimental meausrements.

9.2.4 Finite size source and receiver

The measured excess attenuation curve of Figure 9.2 exhibits a much broader high frequency minimum than the low frequency minimum, whilst the predicted attenuation curve shows the two minima to have comparable width.

One possible cause is the directivity of the source and receiver, but for the geometry in question the effects are minimal. Another possible cause is that at high frequencies the transducers no longer behave as point sources, but take on the characteristics of extended or finite size sources.

The receiver could be modelled as a series of coherent point sources, but this cannot account for the difference in the width of the minima. Any symmetry in the location of the point sources cancels the finite size behaviour of the receiver. Although an incoherent point receiver model could account for the discrepancies, such a model would appear unreasonable in view of the mechanical construction of the microphone.

The air jet on the other could reasonably be modelled as an array of points sources, because of the turbulent air movement immediately above the top of the nozzle. Figure 9.6 shows the predicted attenuation assuming that the source can be modelled by a vertical array of incoherent elemental point sources spaced 1 mm apart.

A 7 point model is sufficient to correct for the observed differences between measured and predicted width of the high frequency minimum.

The width differences, however, could also be explained by turbulence effects. Given that turbulence can be modelled as a random length path difference, then the effect on the attenuation function would be to broaden the second minimum relative to the first. At low frequencies a small path length difference error will have only a minor effect on the interference pattern because the wave number is small. At high frequencies, large wave number, the effect will be greater, hence a much broader minimum.

Figure 9.7 shows the predicted vs measured excess attenuation after correcting the former for source height, broadband source and finite source size effects. The results are in good agreement over the whole frequency range. In this case the depth of the minima have been reduced by averaging power over adjacent filters. As already mentioned, the degree of averaging required to obtain reasonable agreement with the measured attenuation is considered to be excessive. Fortunately, this is not the case for finite impedance surfaces.

9.3 Finite impedance boundary meausrements

9.3.1 Measurements of point to point propagation over finite impedance surfaces were taken in the anechoic chamber using the instrumentation shown in the block diagram of Figure 9.1.

The sample materials were laid directly onto the rigid backing and a hole cut to allow the air jet sound source to traverse along a vertical path above the sample. The flexible artificial grass material was lightly stretched to remove small wrinkles and held in position with adhesive tape.

A limited range of source receiver geometries have been examined, covering source and receiver heights from 1 to 10 cm for a separation distance of 1 m. Shorter separation distances would have resulted in non-grazing angles of incidence, whilst longer distances might have introduced edge diffraction effects from the finite sample size or the chamber wedges.

For notional scale factors of 1/50th and 1/100th, the model heights used correspond to the source and receiver heights commonly encountered in road traffic and railway noise propagation problems.

9.3.2 Source height determination

As observed in Sections 8.3.5 and 9.2.1, the measured source height is not a good estimator of the effective source height. This is especially true for porous media where the moving air mass interacts with a rigid or flexible frame. Figure 9.8 compares the measured and predicted excess attenuation for the two impedance materials. The prediction is based upon a source height of 5 cm. For the artificial grass material this distance was measured from the top of the rubber backing, not the top of the tufts.

Although the location of the first minimum is predicted quite well for both materials, the second minimum is not. The effect of varying the source height for a finite impedance material can be seen in Figure 9.9. The amplitude and location of the first minimum are unaffected by small height variations, but the location of the second minimum is. This suggests that the curve fitting procedure outlined in Section 9.2.1 can be used to estimate the effective source height.

The results obtained for this proceudre are:

artificial grass	4.2 cm $\pm$ 1 mm
fibreboard	5.4 cm $\pm$ 1 mm

Assuming the output of the air jet is independent of the reflecting surface, it is possible to estimate the height of the acoustic surface for the two modelling materials. Allowing for source height estimation errors, the acoustic surface of the artificial grass is between 2 mm below and 2 mm above the top of the tufts, whilst for the fibreboard it is between 1 mm above and 3 mm below the physical surface. For a porous material one would expect the acoustic surface to lie just below the physical surface; because of the interaction of the pore frame and the air. The results obtained for the two materials indicate the magnitude of the errors that can be expected from the experimental procedures.

9.3.3 Comparison of Measurement and Predicted Attenuation

The predicted excess attenuation curves for the new source heights are shown in Figure 9.10. The results for the artificial grass show good agreement over most of the frequency range. The differences around 6 kHz are due in part to the logarithmic scaling used for plotting. The Nicolet spectrum analyser calculates spectra for linearly spaced frequency points. When the spectrum is plotted on a logarithmic scale there are fewer points to display at low frequencies than at high frequencies, that is the density of sample points increases with frequency.

The result is that the left hand side of the measured low frequency minimum is defined by 10 sample points, of which only 5 are significantly different from the predicted attenuation curve.

Significant differences between the two curves can also be seen in the range 35 - 60 kHz. Similar results are exhibited by all the surfaces examined in this study, independant of the source receiver geometry. The only common factor between the measured excess attenuation curves, is the free-field source spectrum used to normalise the measured data. This spectrum was measured several days before the point to point propagation experiments were completed, and it is possible that the measurement conditions, such as the air supply pressure, were not exactly the same for the two sets of measurements.

Experiments have shown that a 2 - 3lb/sq in change in the pressure supply to the air jet noise source does alter the high frequency spectrum by 1 or 2 dB.

Possible causes for the differences in the amplitudes of the second interference dip have been considered in Section 9.2.

Comparing the measured and predicted attenuation curves for fibreboard, it is clear that the prediction for this surface is not as good, especially at high frequencies. Between 1 and 50 kHz the agreement is reasonable, even though the maximum difference is about 4 dB. Above 50 kHz the two curves diverge; the measured curve appearing to exhibit two minima and the predicted curve just one. The double minima caused difficulty when trying to determine an appropriate source height. The predicted curve was eventually fitted to the minimum at 68 kHz; because the source height required to fit the minimum at 90 kHz resulted in an apparent acoustic surface 0.6 cm above the physical surface. This was considered to be unrealistic for the fibreboard. The most probably cause for the divergence of the two attenuation curves above 50 kHz is turbulence.

9.4 Half Rigid - Half Finite Impedance Boundary Measurements

9.4.1 Introduction

Excess attenuation measurements for the case of a half rigid/half soft boundary were made in the anechoic chamber using the instrumentation shown in the block diagram of Figure 9.1.

The air jet noise source was located above the rigid half of the surface and the $\frac{1}{4}$" microphone above the impedance half. The rigid surface was modelled by 1/16" thick polished aluminum. The dividing line between the two surfaces was set at the mid-point between the source and receiver.

For all the measurements the receiver height and separation distance were fixed at 5 cm and 100 cm respectively. Three source heights were examined; 1, 2.5 and 5 cm. The source and receiver heights were kept low so as to ensure the validity of the approximate solution.

The effect of the mixed boundary can be seen in Figure 9.12 which compares the measured attenuation for the single impedance and mixed impedance boundaries. For frequencies below 12 kHz, the mixed boundary exhibits much less attenuation than does the single impedance boundary, and the first minimum occurs at a higher frequency. In fact the measured attenuation is comparable to that of a single impedance surface having a flow resistance 2 or 3 times that of the experimental impedance half-surface.

Between 12 and 5o kHz the mixed boundary exhibits greater excess attenuation, with a second dip occuring in the region of 45 kHz. The attenuation then falls below that of the single impedance surface.

9.4.2 Theoretical Predictions

The theoretical predictions reported here are based upon Rasmussen's [9.3] approximate solution as given by equation 4.4. The impedance values for the soft half surface were calculated from the flow resistance model using the results obtained in section 8.3.

The predicted excess attenuation for two source heights is shown in Figure 9.13. The impedance half surface corresponds to artificial grass.

At low frequencies the boundary behaves as if there were no discontinuity in the impedance, whilst at high frequencies the excess attenuation curve exhibits an oscillatory behaviour.

Such behaviour has not been reported in the literature. However, it can be explained by a geometric ray propagation model. Assuming that the reflected energy is concentrated along the specularly reflected ray path, then the discontinuity will determine the total received pressure field. At low frequencies the discontinuity is transparent, hence the surface behaves as if it were a single impedance boundary with the impedance of the soft half surface. At middle frequencies the impedance of the surface increases corresponding to an average value of the soft and rigid half surfaces.

The oscillatory response at high frequencies suggests that the discontinuity behaves as a diffracting knife edge with the corresponding light and dark fringes.

For the case of the low source, the high frequency attenuation is positive and exceeds that for a rigid boundary, implying that the direct reflected and diffracted fields are all in phase. Increasing the source height increases the excess attenuation, the opposite effect to that for a homogeneous boundary.

9.4.3 Comparison of Measured and Predicted Attenuation

The mixed boundary surfaces do not exhibit a strong high frequency interference dip, so it was not possible to determine an effective source height by the curve fitting. However, the results of the rigid surface experiment showed that the effective source height was 3 mm above the top of the air jet.

The excess attenuation curves for the artificial grass half surface are shown in Figures 9.14 to 9.16.

The high frequency oscillatory behaviour of the predicted curves was found to be very sensitive to source height. In view of this two predicted curves are shown for each source height. The first was calculated for an effective source height of measured source height minus 0.5 cm, the second for an effective source height of measured height plus 0.5 cm.

For all the cases examined the measured and predicted attenuation curves show good agreement at low frequencies. In the case of the 1 cm high source the predictions do not reproduce the attenuation dip at 10 kHz. For the other two source heights the dip is predicted quite well, with maximum differences of about 3 dB. At high frequencies the two predicted curves give upper and lower bounds to the measured attenuation curves, but the differences above 70 kHz are significant and sometimes exceed 8 dB.

Comparisons for the fibreboard surface are given in Figures 9.17 to 19.19. Note that only one predicted curve is shown, corresponding to the measured source height plus 0.5 cm. In general the predicted attenuation curves show very good agreement with the measured curves for frequencies below 50 kHz. Between 50 and 80 kHz the maximum difference is about 3 dB, but above 80 kHz the two curves diverge regardless of the source height.

9.5 Rigid strip in a soft boundary measurement

9.5.1 Introduction

Measurements of the excess attenuation for the case of a rigid strip set in a finite impedance boundary were made in the anechoic chamber using the instrumentation shown in the block diagram of Figure 9.1

Modelling a rigid strip in an impedance boundary presents several problems. In the first case modelling just a rigid surface. Earlier experiments on 25 mm thick blackboard panels, varnished or covered with thin aluminium sheet, have shown how difficult it is to reproduce the acoustical properties of rigid surfaces. A second question that arises is where should the rigid surface be located relative to the acoustic surface of the soft boundary?

In view of these difficulties it was decided, in the first instance, to model the rigid strip with a 1.5 mm thick aluminium laid directly onto the finite impedance material. It was considered that such a thin sheet would not give rise to significant diffraction effects even at 100 kHz.

The strip was positioned midway between the air jet source and the $\frac{1}{4}$" microphone.

Four different strip widths were employed: 5,10,15 and 20 cm. The source height, receiver height and separation distance were fixed at 5 cm, 5 cm and 100 cm respectively.

The effect of a strip on the excess attenuation can be seen in Figures 9.20 and 9.21, which compare the measured attenuation of the single and mixed impedance boundaries.

Figure 9.20 (a) shows that the effect of a strip whose width corresponds to 5% of the separation distance is negligible. Apart from the first two frequency samples, the attenuation curves are almost identical. Increasing the strip width

to 20% of the separation distance is significant,however,as can be seen by reference to Figure 9.20(b). The excess attenuation at the first minimum is reduced by some 3-5 dB, and the second attenuation dip occurs between 40 and 70 kHz instead of 70 to 100 kHz.

Similar observations can be made for the fibreboard surface measurements shown in Figure 9.21, but in addition, the 20 cm rigid strip attenuation curve shows a distinct third dip between 80 and 100 kHz.

9.5.2 Theoretical predictions

The theoretical predictions reported here are based upon the asymptotic solution given by equation 4.23. The normal surface impedance values for the soft boundary were calculated from the flow resistance model using the results obtained in Section 8.3.

The predicted excess attenuation for two strip widths is shown in Figure 9.22. The impedance value used corresponds to that of the artificial grass. The solid line corresponds to a strip width of 5 cm and the dashed line to a strip 20 cm wide.

Increasing the strip width has two distinct effects. The first is to decrease the frequencies at which the two interference minima occur and the second is the decrease the maximum excess attenuation at these minima.

The oscillatory behaviour exhibited in the two curves at high frequencies is due to edge diffraction effects at the two impedance discontinuities.

9.5.3 Comparison of measured and predicted attenuation

For the purposes of predicting the excess attenuation, it has been assumed that the source heights obtained from the single surface measurements are applicable. This corresponds to postulating a high source impedance so that the source output is independent of the boundary impedance.

The measured and predicted excess attenuation curves for the artificial grass material are compared in Figures 9.23 to 9.26. The solid line represents the measured attenuation and the dashed line the predicted attenuation.

As already shown the attenuation for a 5 cm wide strip is the same as the case of no strip. The contribution from the rigid surface integral of equaiton 4.23 is negligible, hence the agreement between the two curves is comparable to that of Figure 9.10(a).

As the strip width increases, the attenuation minima shift in frequency and decrease in amplitude. This trend is duplicated by the predicted attenuation curves. It can be seen that the agreement between the two curves improves with strip width up to about 75 kHz. Above this frequency the measured curve appears to exhibit a third minimum at the point of a predicted maximum.

The main region of disagreement is seen to be that around the second minimum where the predicted excess attenuation is much greater than the measured. As with all the other measurements this is most probably due to surface turbulence effects.

The measured and predicted excess attenuation curves for the fibreboard material are compared in Figures 9.27 to 9.30. For this surface the best agreement is obtained for the 5 cm wide strip and is comparable to that of Figure 9.10(b).

As the strip width increases, the measured attenuation at the first dip decreases and the location of the second dip shifts to downward in frequency more rapidly than is predicted.

One possible explanation for this is the change in the relative magnitude of the real and imaginary parts of the surface impedance. The rigid strip should present a purely resistive impedance and so would increase the resistance of the average surface impedance around the point of specular reflection.

The effect can be seen in Figure 9.31 which shows the predicted excess attenuation for a source height receiver height and separation distance of 5.4, 5.0 and 100 cm respectively. The solid curve is the attenuation for a nominal surface impedance of $Z = R + iX$ corresponding to fibreboard. The dashed line is

the attenuation for a surface of $Z = 2R + iX$. Increasing just the resistance moves both minima to lower frequencies and reduces the attenuation at the first minimum. The increase in attenuation at the second minimum would not be observed experimentally due to the effects of surface turbulence.

Shifting the minima to lower frequencies would also allow for the prediction of the third minima measured between 80-100 kHz. These observations would suggest that it may be possible to obtain a practical prediction procedure by modifying the impedance estimate, rather than by introducing correction terms into the wave equation solution.

9.6 Road Traffic Noise Prediction

9.6.1 Evaluation of the theoretical predictions of excess attenuation for point to point propagation over homogeneous and hard/soft surfaces has shown that they are sensitive to impedance estimates. Current prediction schemes for estimating noise levels from road traffic however, only distinguish between two types of surface, hard and soft [9.6]. A surface is considered soft if it is covered with vegetation of any sort.

This limited classification would appear to be at conflict with the theoretical predictions because of the large range of impedance values possible within the classification of soft. The simple flow resistance model can be used to illustrate the effect upon the predicted attenuation as a function of distance.

9.6.2 Predicted Values of A-weighted Excess Attenuation

Typical values of flow resistivity have been used to predict the excess attenuation for point to point propagation over the frequency range 0.1-10 kHz for separation distances from 10 to 300 m. The predictions are based upon a car source height of 0.5 m and a lorry height of 2.4 m, with the spectra shown in Figure 9.32. The results have been A-weighted in common with the approved prediction scheme. Figure 9.33 shows the excess attenuation versus distance curve for four values of flow resistivity.

The graph shows that up to 50 m the attenuation is independant of flow resistivity and that even at 100 m the maximum range of the

values is about 1 dB(A). At 300 m the difference is about a 1 dB(A) increase in attenuation per halving of flow resistivity. The maximum attenuation of 300 m is -14dB(A) for a surface with a flow resistivity of 50 000 MKS units, typical of a forest floor.

The main influence of increasing flow resistivity would appear to be to decrease the attenuation rate at large separation distances.

The effect of increasing the source height to 2.4 m is to reduce the excess attenuation to less than approximately ±1 dB(A) even at 300 m, as can be seen in Figure 9.34.

These findings would suggest that the A-weighted prediction is insensitive to impedance, and that the prediction accuracy of ±2 dB can be achieved for distances up to 300 m. However, the flow resistivity model has been shown to constain the impedance estimates.

Attenborough [9.7] has recently published the results of similar calculations based upon measured impedance values of grassland, sand, stubble, forest floor and snow. Figure 9.35 shows the predicted A-weighted excess attenuation for distances up to 70 m for a car source over three types of grassland. At 70 m the difference between the curves is more than 1 dB. For the other ground surfaces the range of values at 70 m is greater than 6 dB(A), well outside the acceptable error margins. The calculations for a lorry source height are comparable with Figure 9.34.

9.6.3 A-weighted Attenuation for Source over a Rigid Surface

Clearly there is a need to re-examine the current classification of ground surface types for the purpose of predicting the excess attenuation for road traffic noise. However, the calculations just described assume that the noise source is travelling over the soft ground surface. Rasmussen's theoretical prediction for a mixed impedance boundary has been used to examine the effect of a source over a rigid surface. The source is located 3.5 m from the near kerbside of a single lane road and the receiver is located over a surface with a flow resistivity of 250,000 MKS units.

The predicted A-weighted excess attenuation for the soft and mixed surfaces are compared in Figure 9.36, for a source 0.5 m high and a receiver 1.2 m high. For distances of up to 50 m, the mixed surface shows a smaller excess attenuation than the soft surface and at 20 m the value is positive.

Between 50 and 100 m the results for the two surfaces are virtually identical. Beyond 100 m the two curves gradually diverge such that at 300 m the difference in the excess attenuation is approximately 1 dB(A).

Such a result is not unexpected. At short distances the source will see a hard surface (average of rigid plus soft) with an excess attenuation dip outside the frequency band of interest. As the separation distance increases the path length difference decreases keeping the interference minima at high frequencies. However, the increase in separation distance will also reduce the average surface impedance and so produce a low frequency minimum that will increase

the excess attenuation. The calculation suggest this change in surface impedance occurs over the range 20-30 m from the kerbside.

Beyond 30 m the average surface impedance approximates that of the soft surface.

The 1 dB(A) difference at 300 m is most probably due to an accumulation of calculation errors in the two prediction procedures, bearing in mind the surface integral approximation in Rasmussen's Model. This excess attenuation value, over the range 100-300 m as predicted by the single and mixed impedance surface models agrees well with the official prediction method [9.8], which is based upon outdoor measurements of road traffic noise propagation.

The effect of the rigid surface for a 2.4 m high source can be seen by reference to Figure 9.37, which compares soft and mixed impedance excess attenuation curves. Up to 100 m the soft surface model predicts a positive excess attenuation with a maximum value of 1.4 dB(A) at 60 m. The mixed surface model, however, predicts a zero or negative excess attenuation with a maximum value of -1 dB(A) at 40 m. Beyond 100 m both models predict an increase in excess attenuation with distance, but the rate of attenuation is markedly different, such that the mixed impedance model shows some 6 dB(A) more attenuation at 300 m.

The reasons for this difference are not clear, although as the experimental measurements have shown, increasing the source height does reduce the excess attenuation for a single impedance surface. It is interesting to observe that the mixed impedance model gives an excess attenuation value at 300 m approximately equal to that predicted by the official prediction method [9.8].

This official method gives a correction for the change in L_{10} for a source positioned over a road, but propagating over a vegetation covered ground surface. According to Scholes et al [9.9], the difference between L_{10} and the peak level is only 0.1 dB(A) at large separation distances, so it is not unreasonable to expect the calculations used here to give results comparable to the value of the L_{10} excess attenuation.

9.6.4 The calculations reported here have highlighted two basic requirements when developing models for predicting the A-weighted excess attenuation for road traffic noise. The first is the need to extend the range of classification used for ground surfaces. The simple hard or soft used in the current prediction scheme can introduce much greater errors than the ±2 dB(A) allowed.

The other requirement is to ensure that the physical description of the surface, upon which the theoretical prediction is based, in an adequate representation of the actual surface. The effect of locating the source over a hard rather than soft portion of the surface is just one example.

References Chapter 9

9.1 Johansson, H. G.: Sound Reduction by Barriers on the Ground. JSV (22) 113-126 1972.

9.2 Chessel, C. I.: Propagation of Noise Along a Finite Impedance Boundary. JASA (62) 825-834 1977.

9.3 Rasmussen, K. B.: Sound Propagation over Grass Covered Ground. JSV (78) 247-255 1981.

9.4 Sewell, E. J.: Calculations of the Sound Field Near the Ground Produced by a Point Source in a Calm Isothermal Atmosphere. DSJR Building Research Station Note No B262 1962.

9.5 Daigle, G. A.: Effects of Atmospheric Turbulence on the Interference of Sound Waves Near a Hard Boundary.

9.6 Delany, M. E., Harland, D. G., Hood, R. A. and Scholes, W.E.: The Prediction of Noise Levels L_{10} due to Road Traffic. JSV (48) 305-325 1976.

9.7 Attenborough, K.A.: Predicted Ground Effect for Highway Noise. JSV (81) 413-424 1982.

9.8 Calculation of Road Traffic Noise. Department of the Environment and Welsh Office Joint Publication. HMSO 1975

9.9 Scholes, W. E., Salvidge, A. C. and Sargent, J. W.: Barriers and Traffic Noise Peaks. Applied Acoustics (5) 205-222 1972.

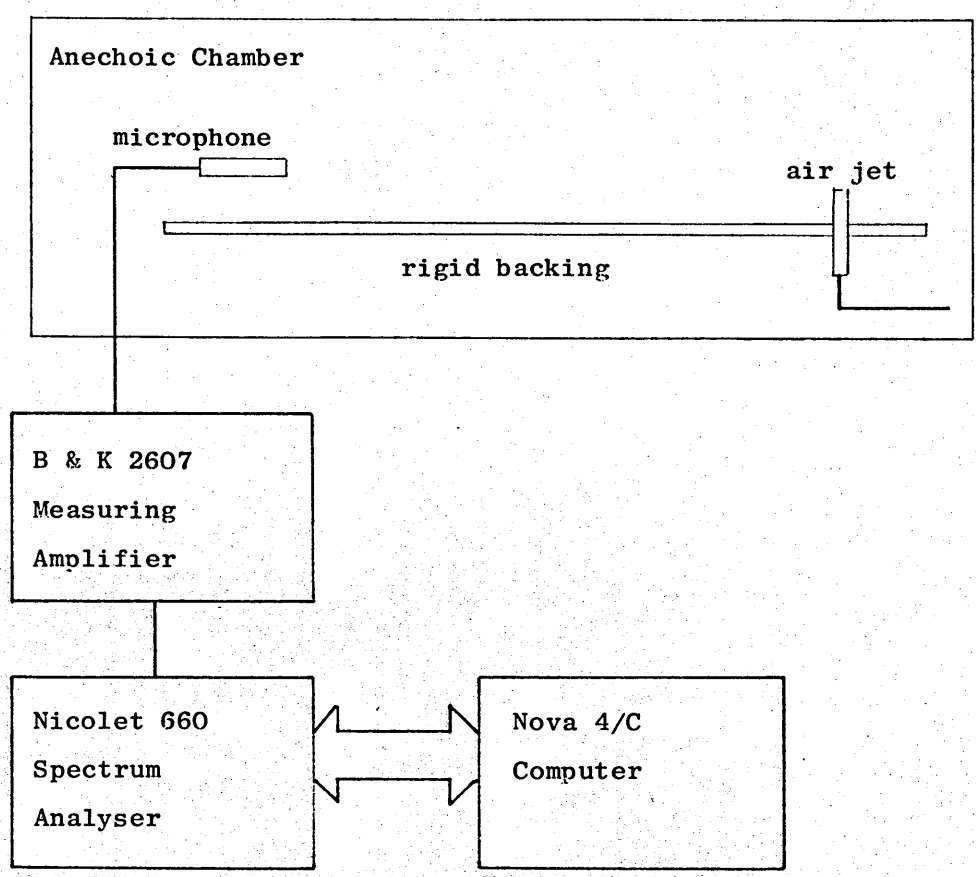

Figure 9.1
Block diagram of the instrumentation used for the point to point propagation measurements

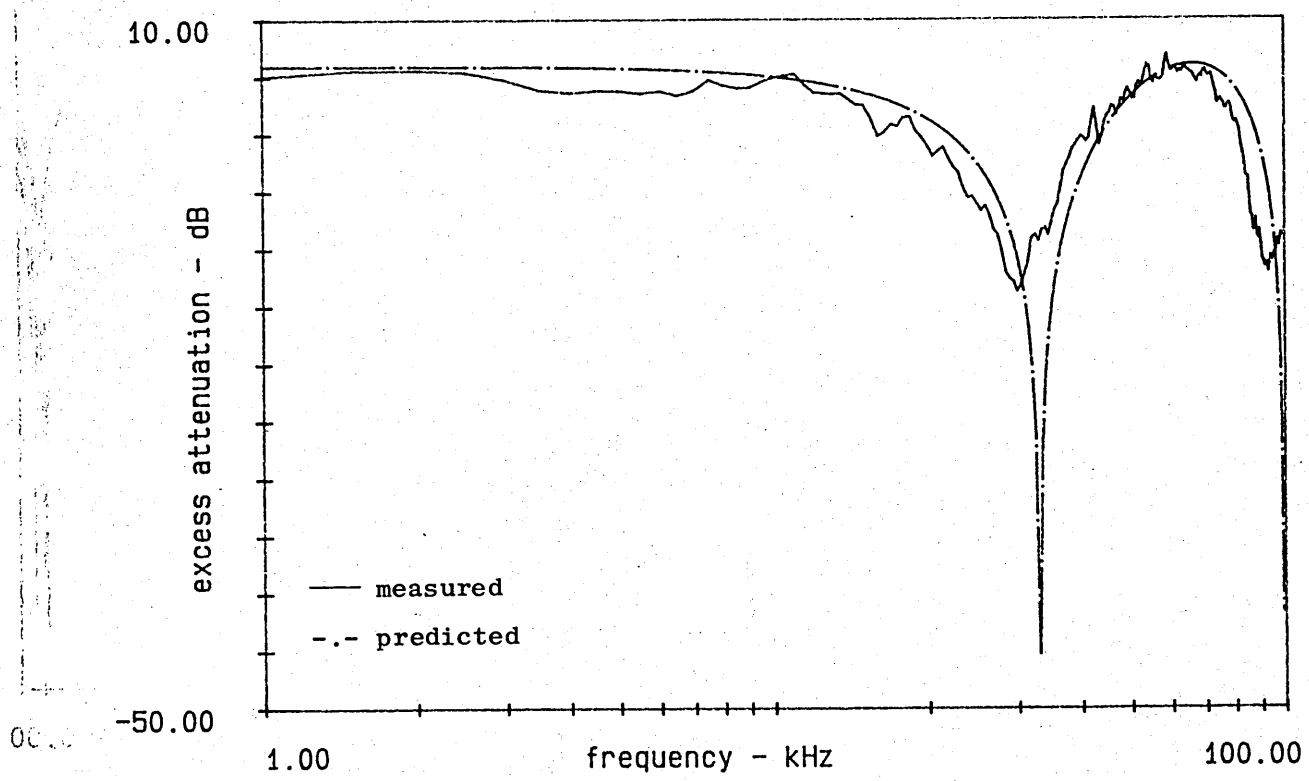

Figure 9.2
Comparison of measured and predicted excess attenuation for propagation over a rigid surface. Source height 5 cm, receiver height 5 cm, separation distance 100 cm.

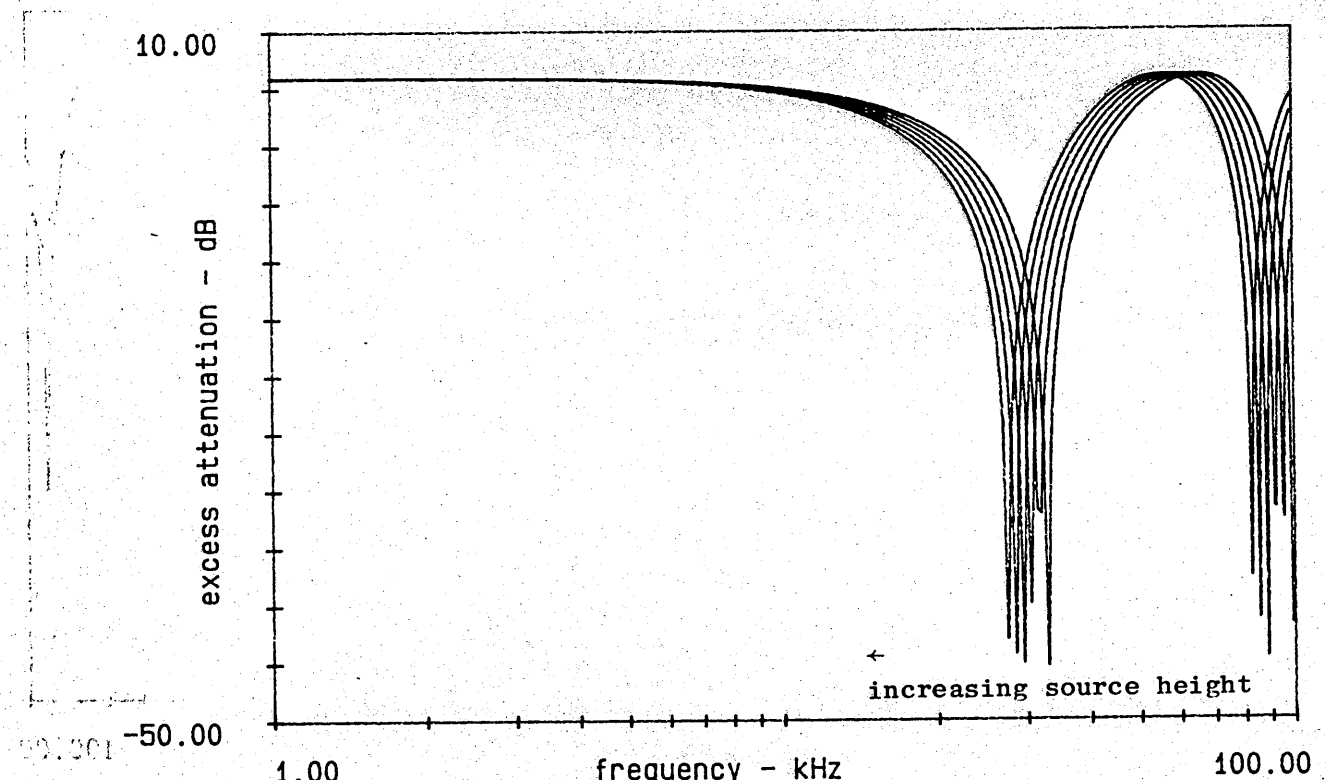

Figure 9.3
Effect of source height upon the location of the interference minima

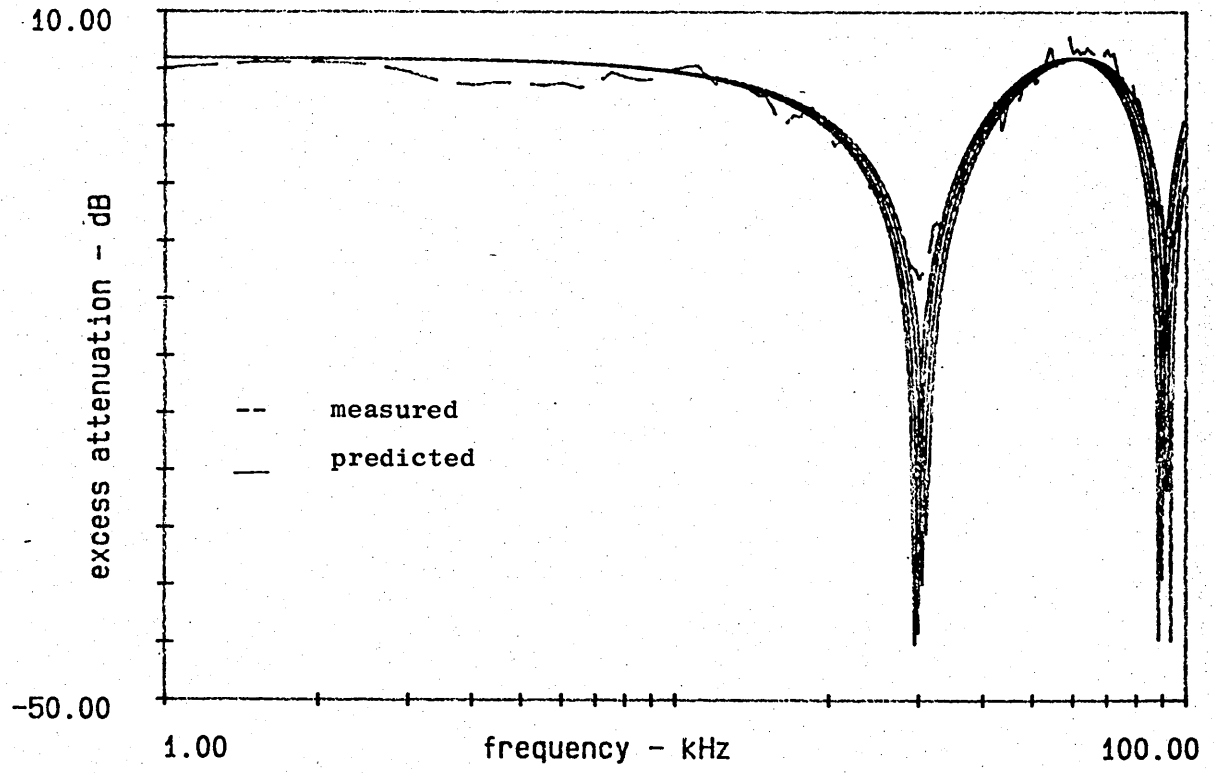

Figure 9.4(a)

Comparison of measured and predicted excess attenuation for a rigid surface versus source height

Figure 9.4(b)

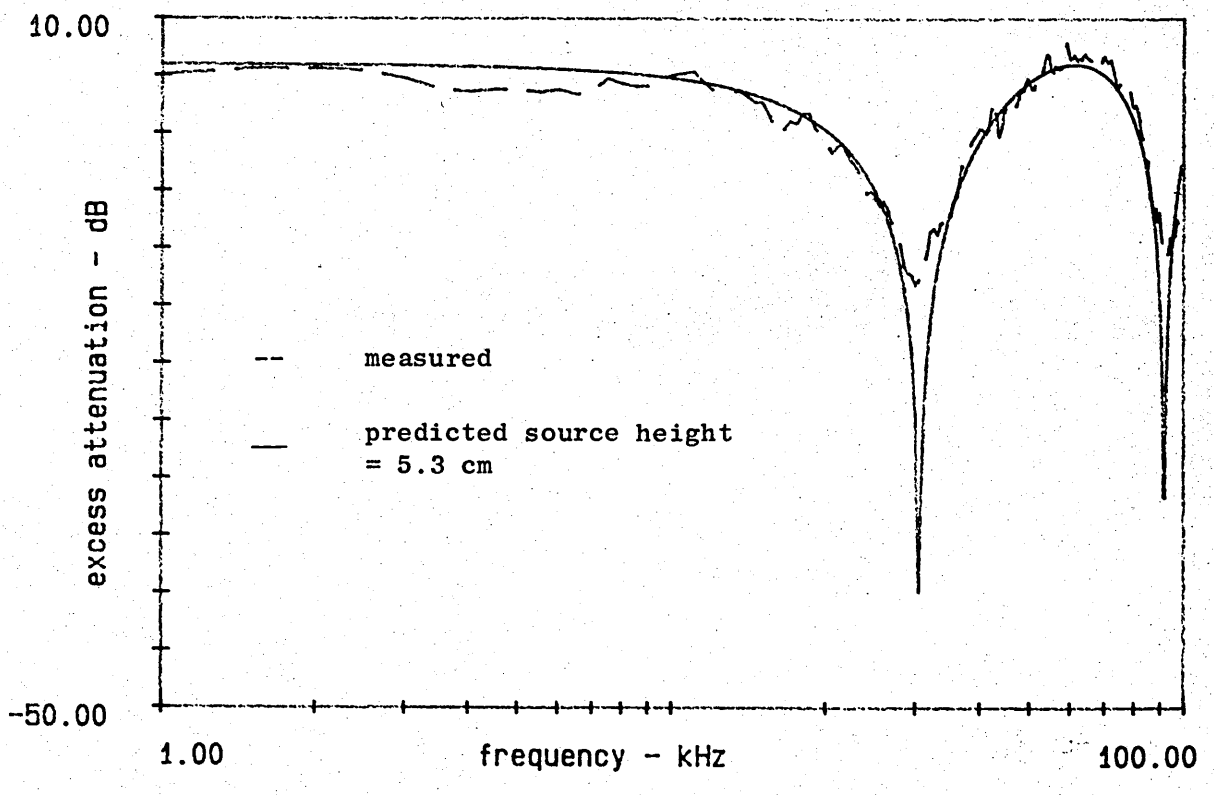

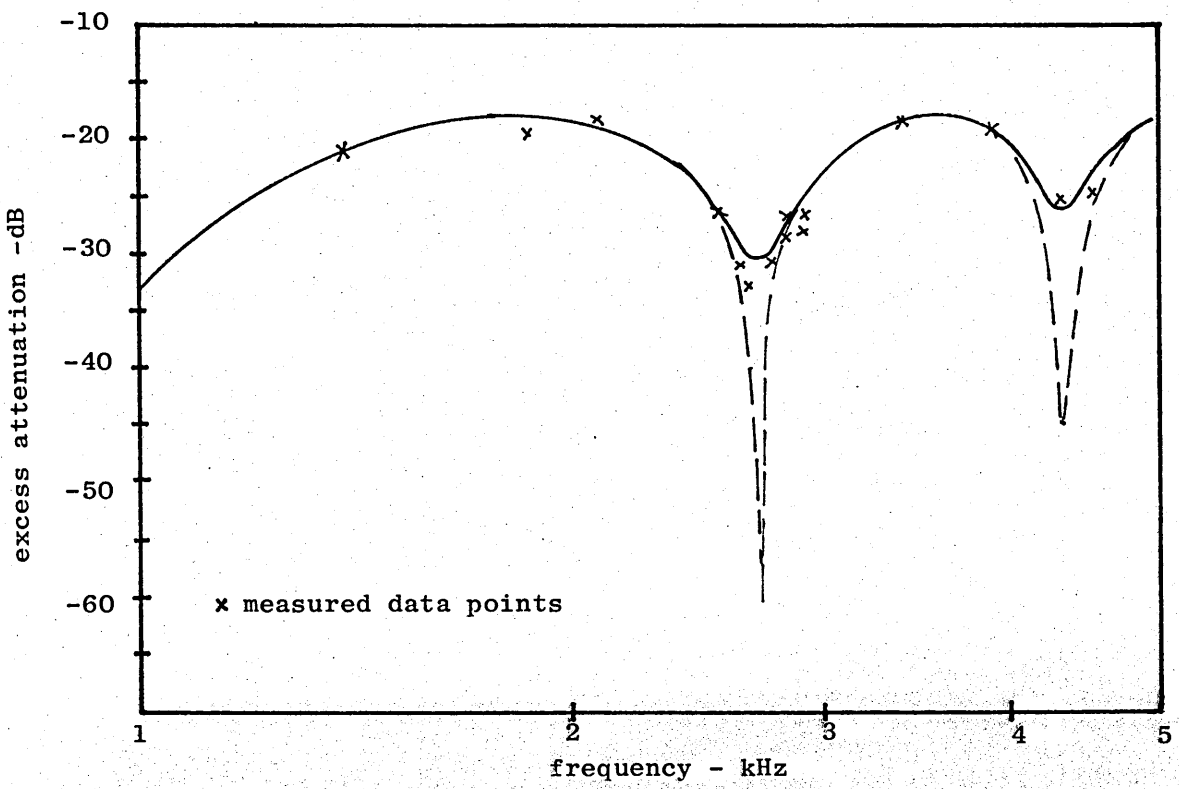

Figure 9.5
Comparison of excess attenuation over a rigid surface predicted by (a) coherent source theory (b) fluctuating spherical wave theory. Solid circles are measured values. Source and receiver heights 1.2 m, separation distance 15 m (after Daigle)

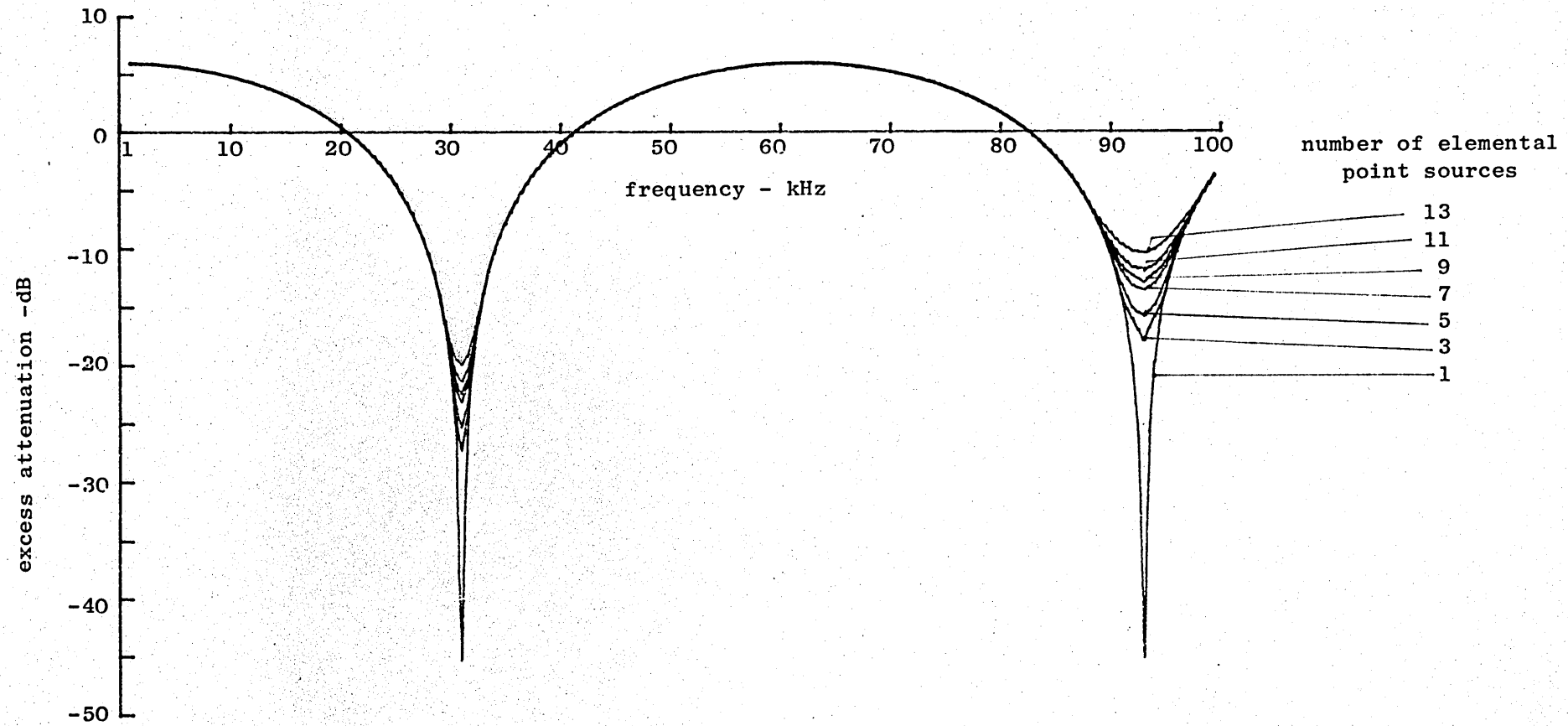

Figure 9.6
Predicted excess attenuation for propagation over a rigid surface
when the source is modelled as a linear array of point sources

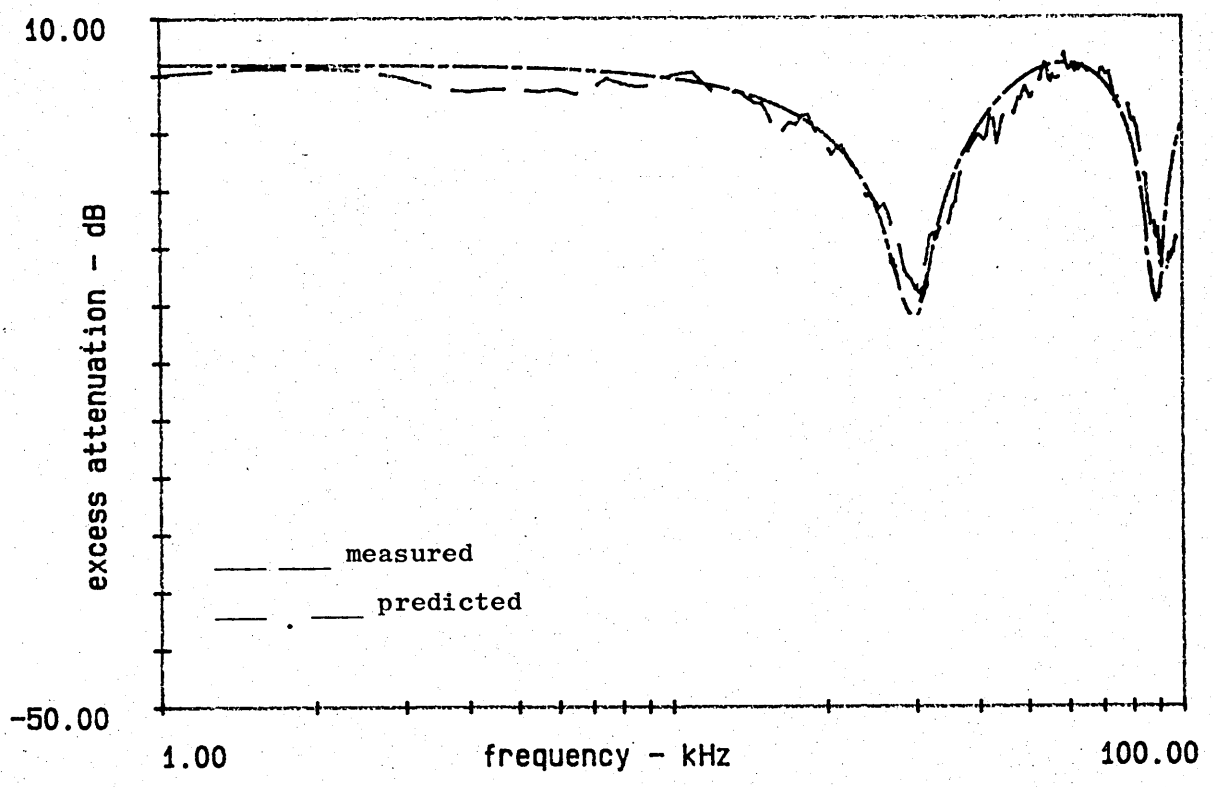

Figure 9.7
Comparison of measured and Predicted excess attenuation after correcting the predicted values for source height, broadband source and finite source size

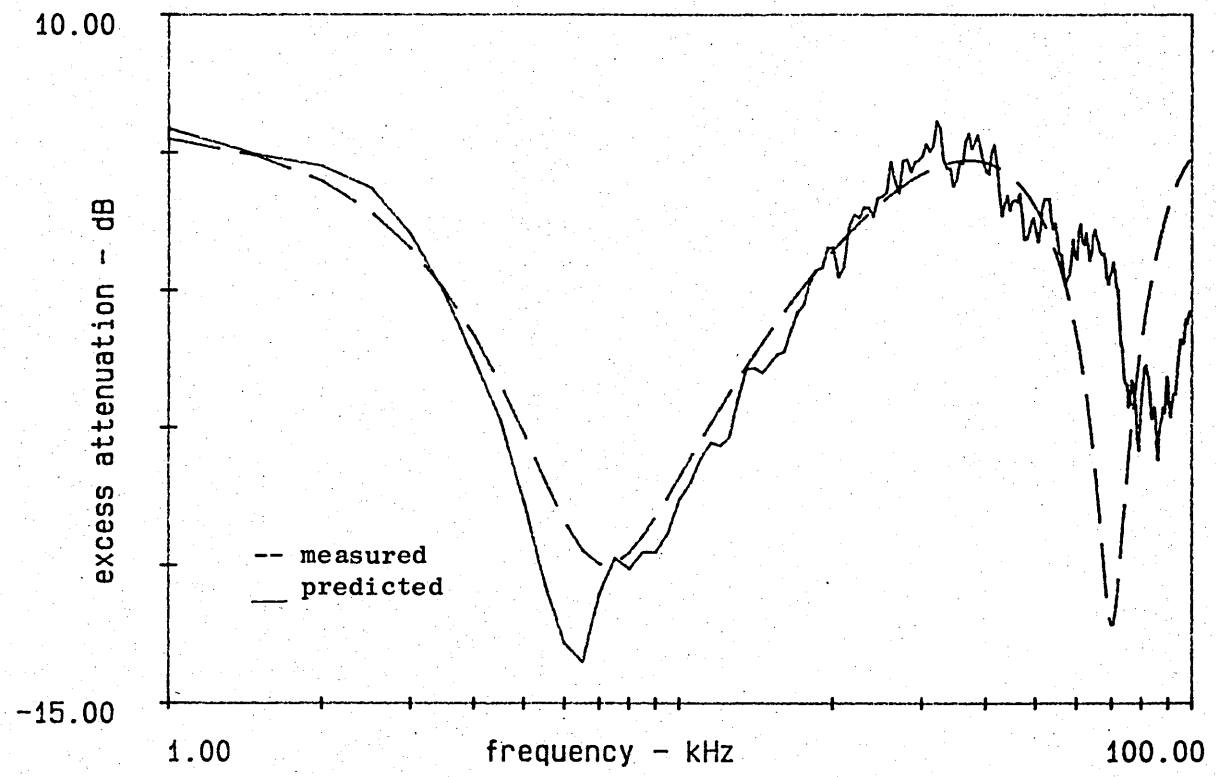

Figure 9.8(a) artificial grass

Comparison of measured and predicted excess attenuation for propagation over the two modelling materials. Receiver height 5 cm, separation distance 100 cm.

Figure 9.8(b) fibreboard

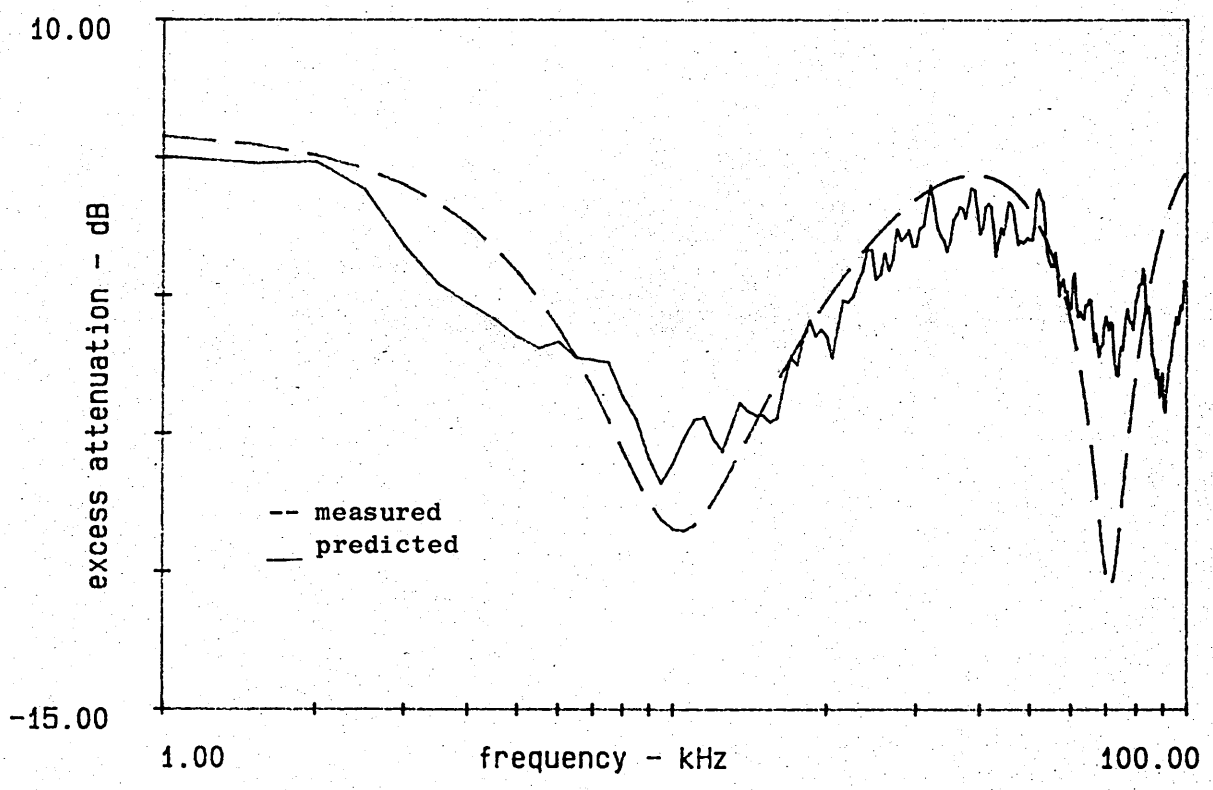

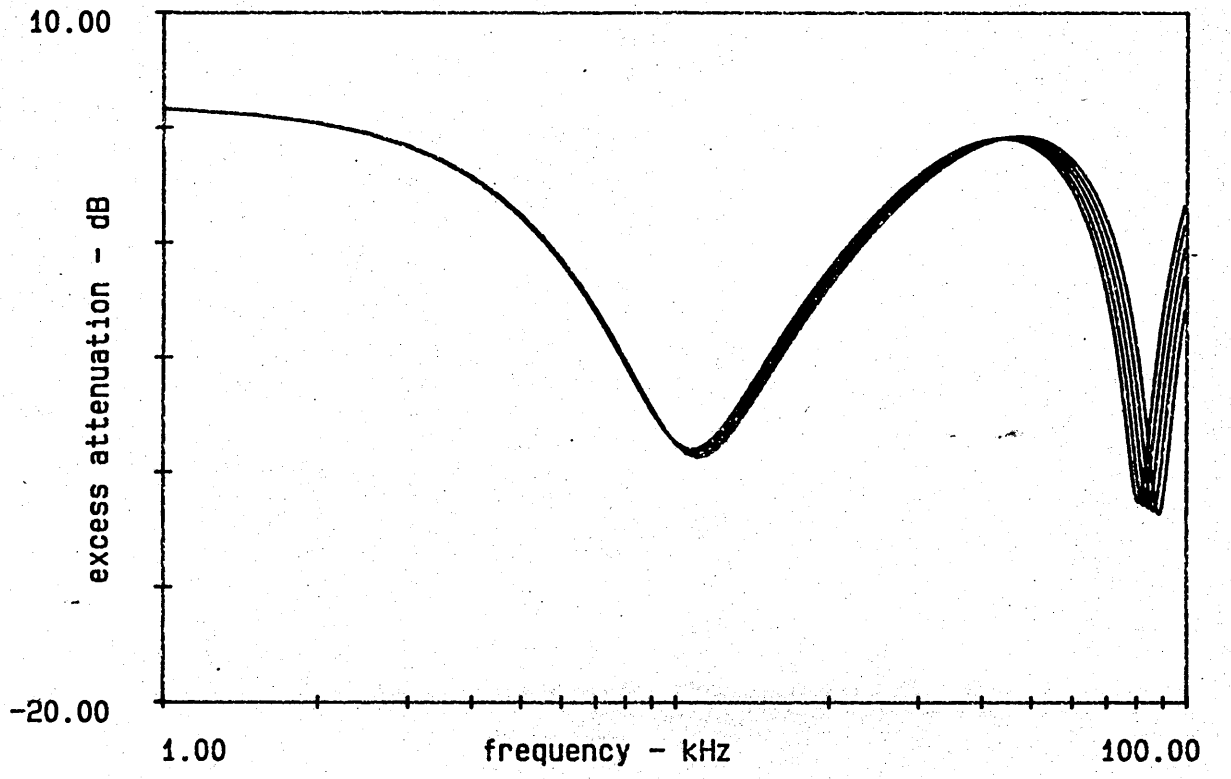

Figure 9.9
Effect of source height upon the location of the interference minima for propagation over an impedance surface

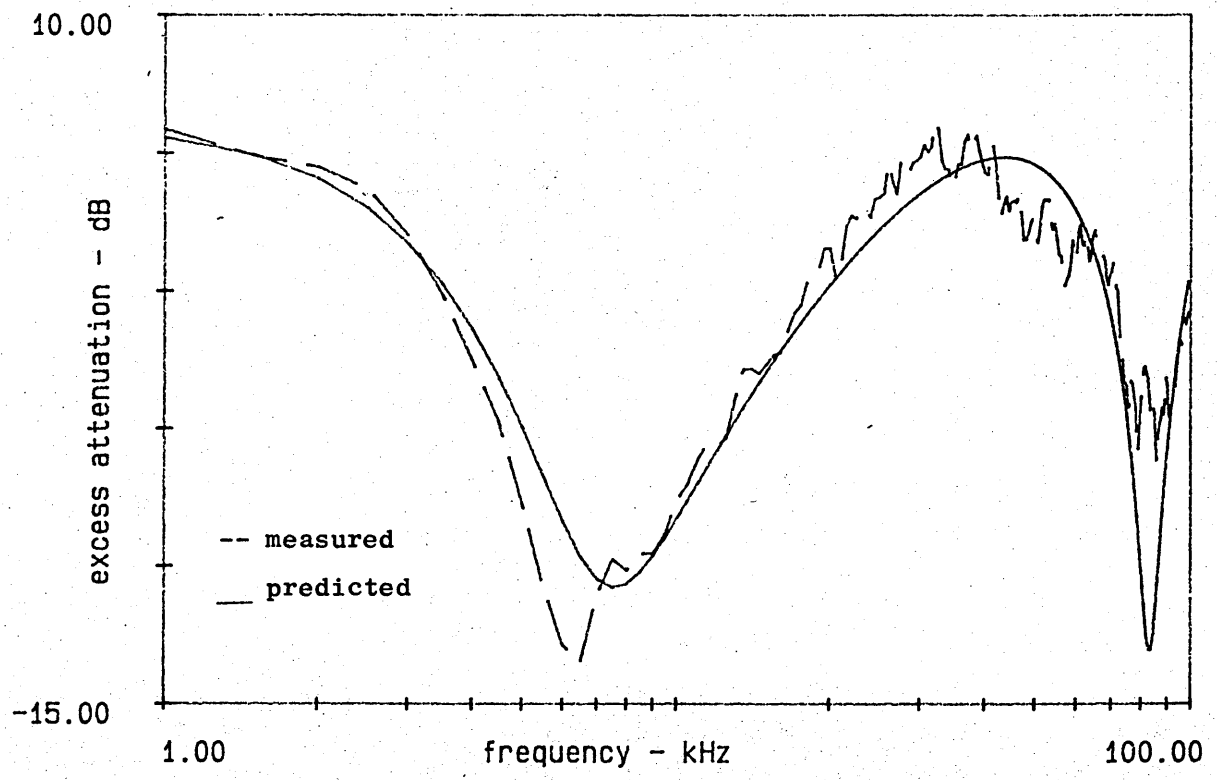

Figure 9.10(a) artificial grass

Comparison of measured and predicted excess attenuation for two modelling materials. Receiver height 5 cm, separation distance 100 cm.

Figure 9.10(b) fibreboard

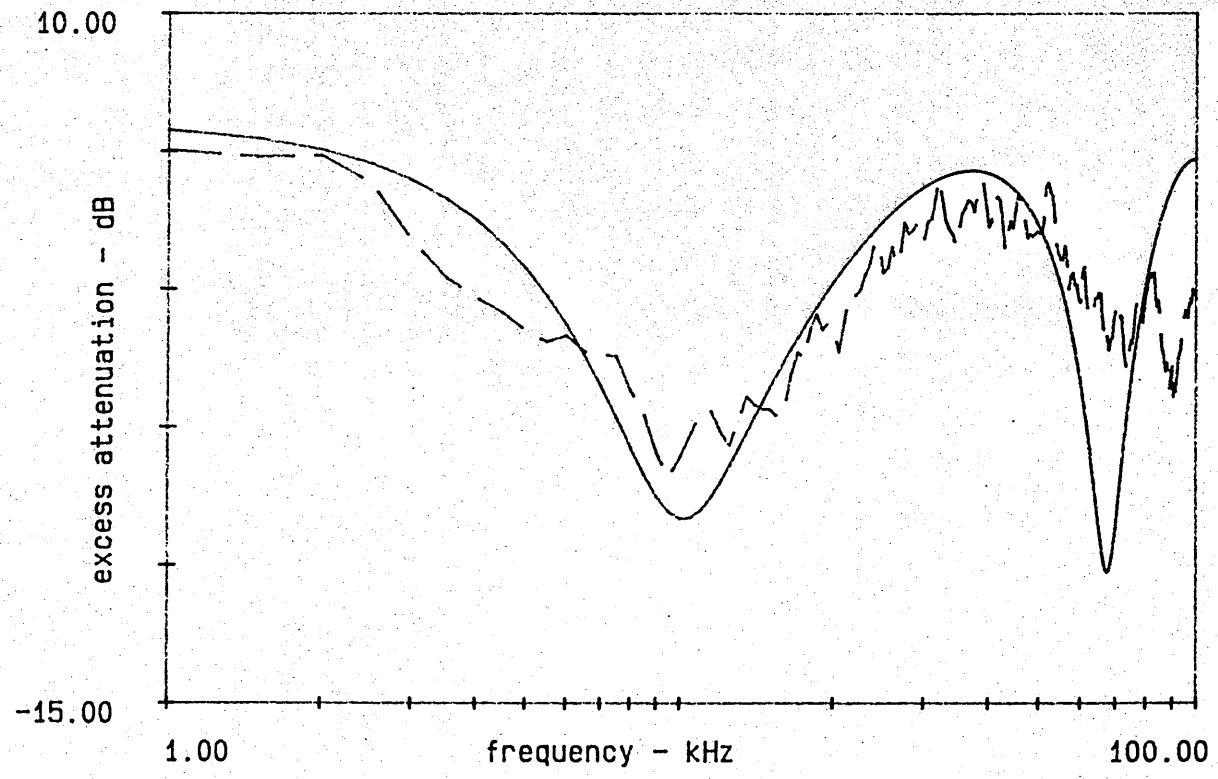

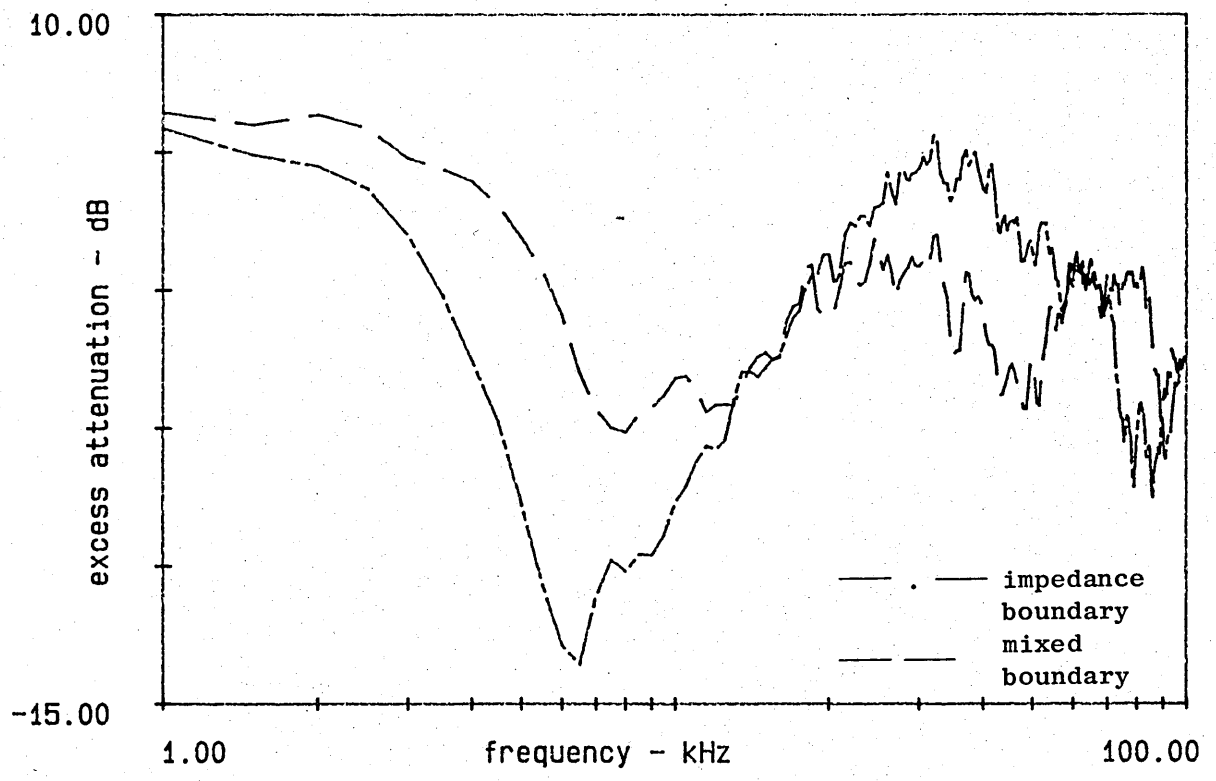

Figure 9.12
Comparison of the measured excess attenuation for propagation over a mixed impedance and single impedance boundaries. Source height 5 cm, receiver height 5 cm, separation distance 100 cm

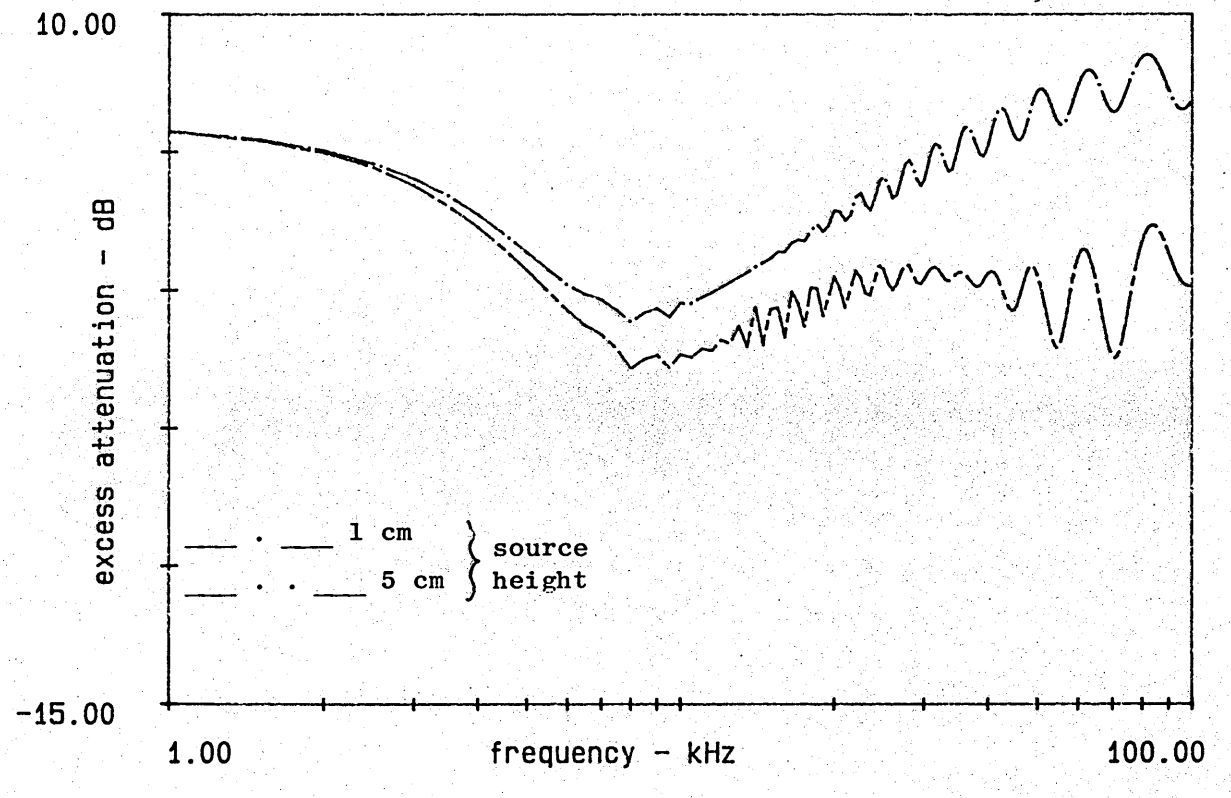

Figure 9.13
Comparison of the predicted excess attenuation for propagation over a mixed impedance boundary

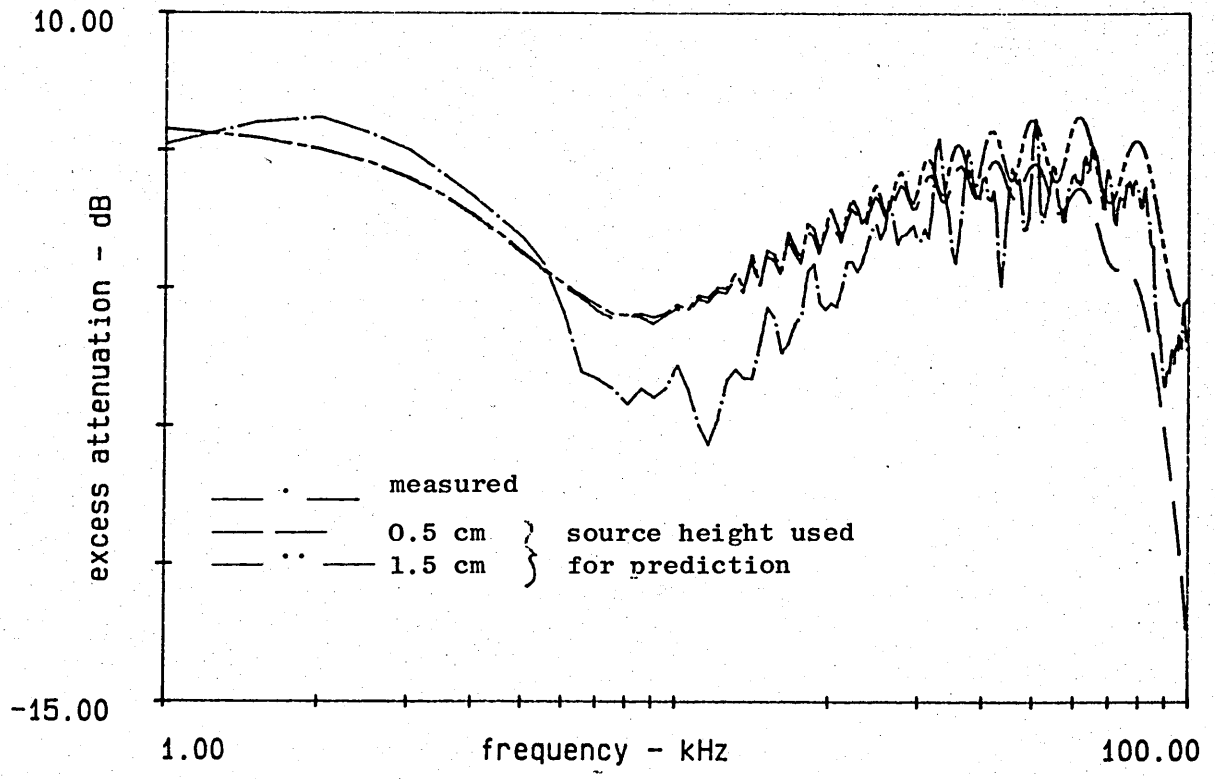

Figure 9.14
Comparison of measured and predicted excess attenuation for propagation over a half rigid artificial grass surface. Receiver height 5 cm, separation distance 100 cm, measured source height 1 cm

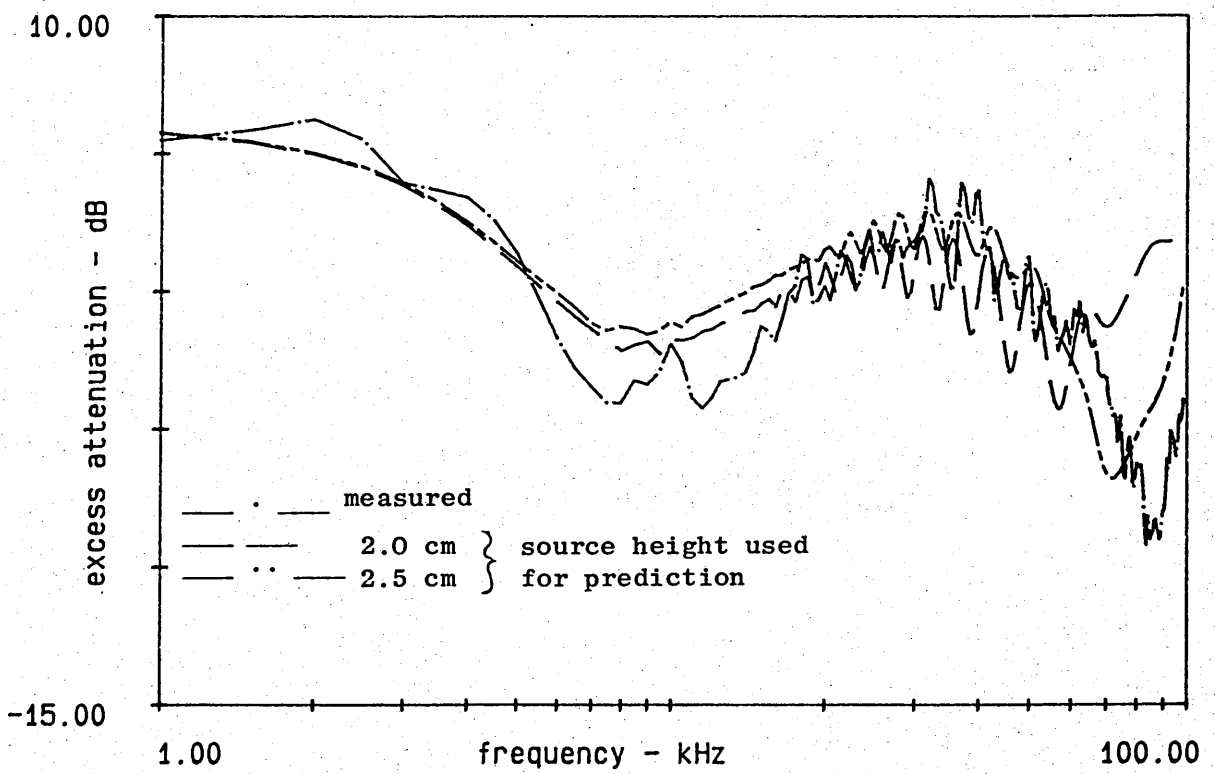

Figure 9.15
Comparison of measured and predicted excess attenuation for propagation over a half rigid half artificial grass surface. Receiver height 5 cm, separation distance 100 cm, measured source height 2.5 cm

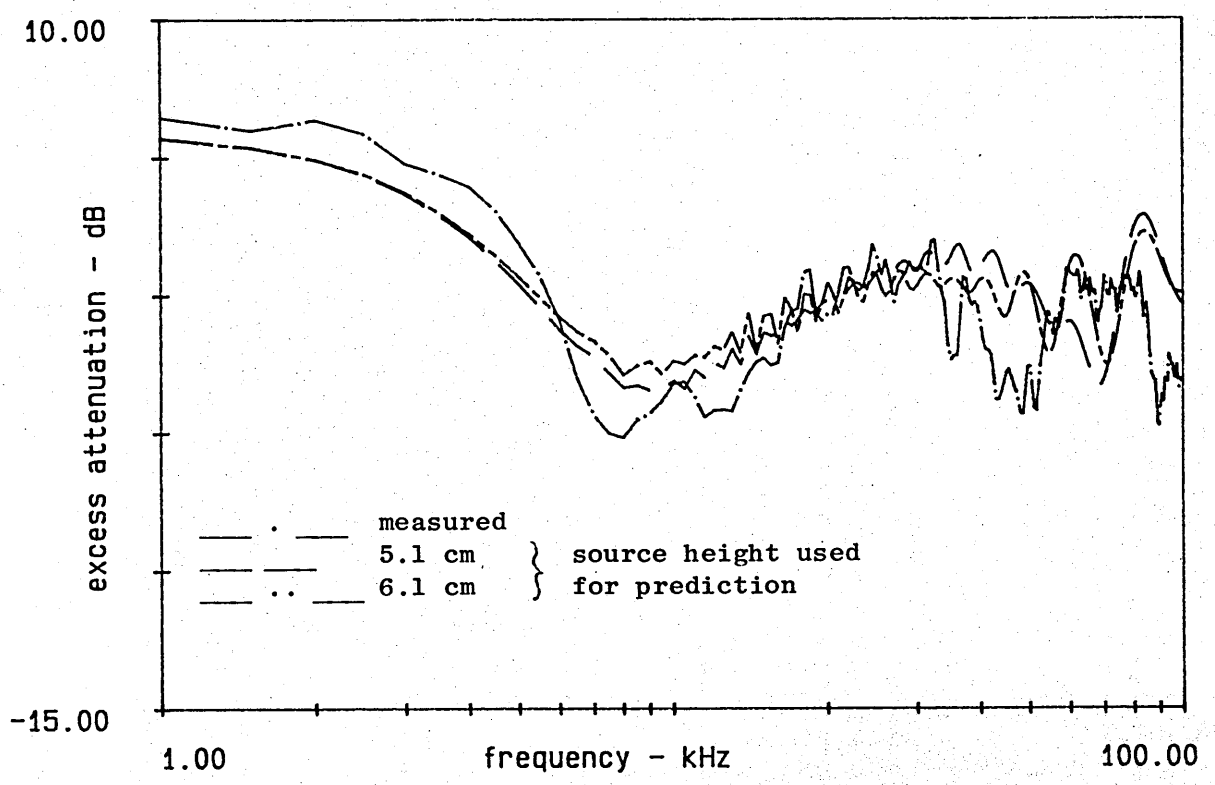

Figure 9.16
Comparison of measured and predicted excess attenuation for propagation over a half rigid half artificial grass surface. Receiver height 5 cm, separation distance 100 cm, measured source height 5 cm

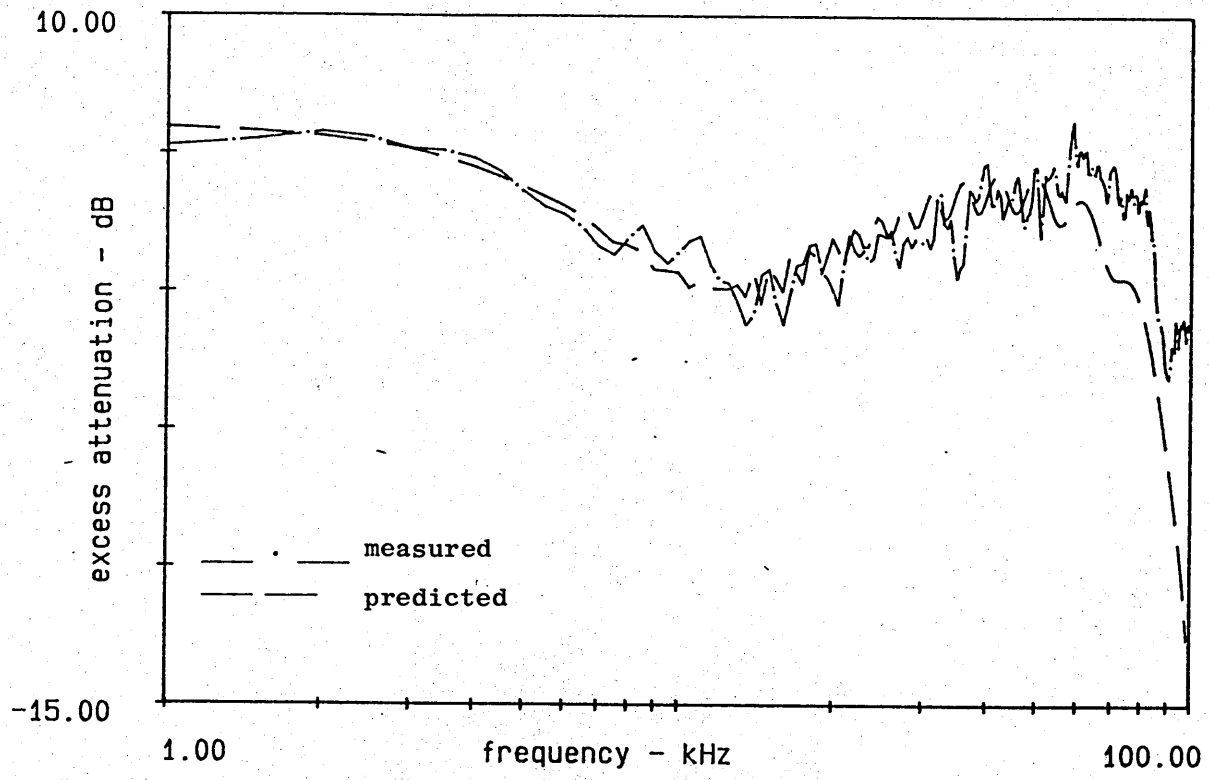

Figure 9.17
Comparison of measured and predicted excess attenuation for propagation over a half rigid half fibreboard surface. Receiver height 5 cm, separation distance 100 cm, measured source height 1 cm

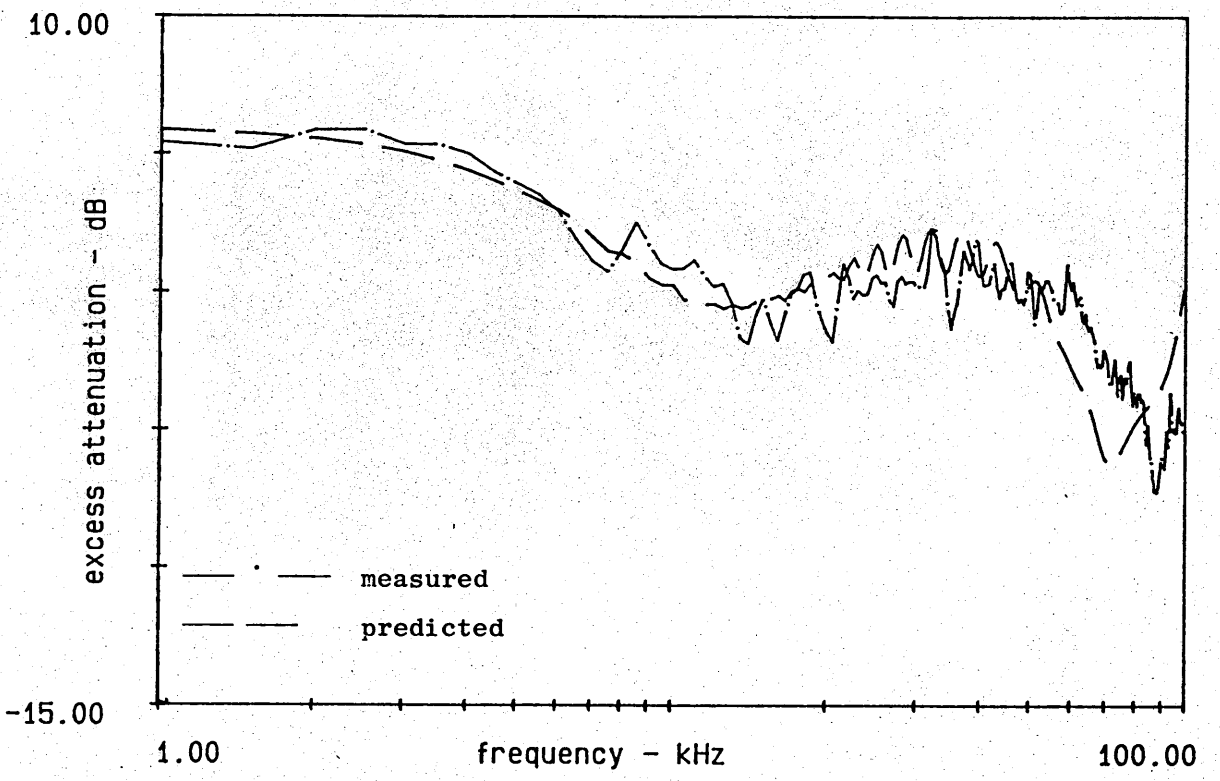

Figure 9.18
Comparison of measured and predicted excess attenuation for propagation over a half rigid half fibreboard surface. Receiver height 5 cm, separation distance 100 cm, measured source height 2.5 cm

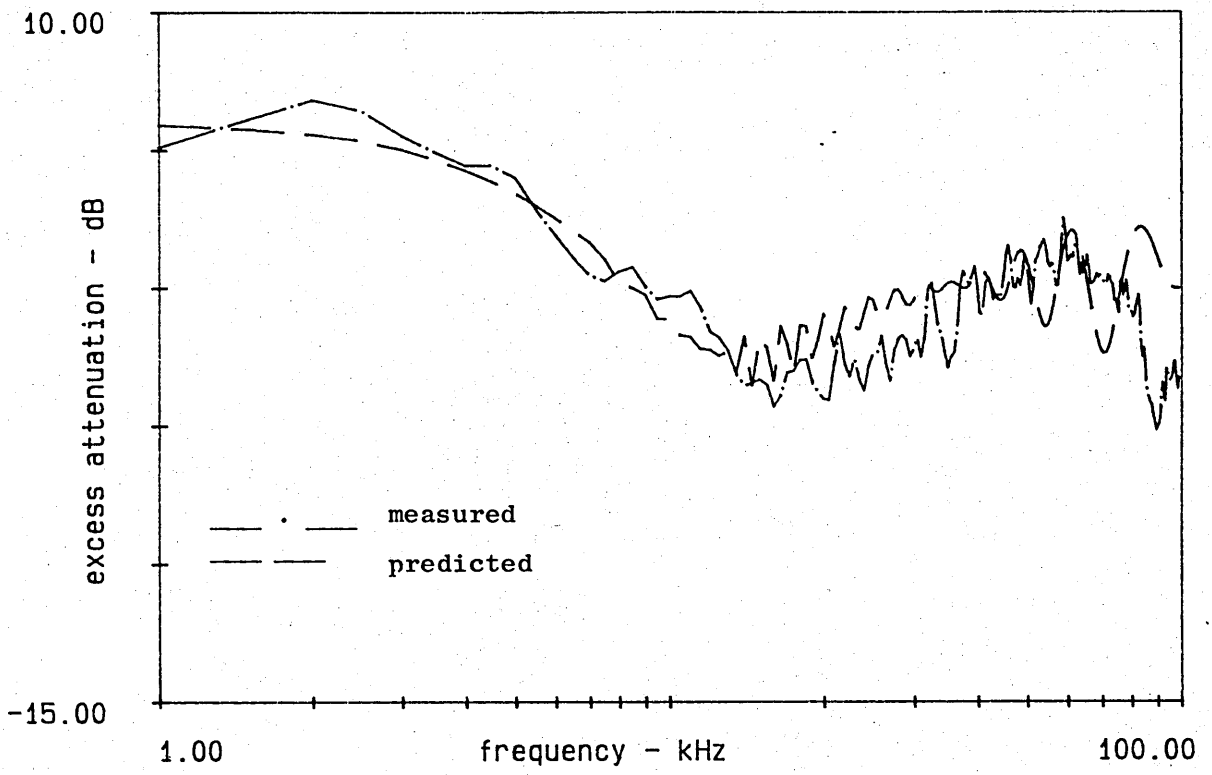

Figure 9.19
Comparison of measured and predicted excess attenuation for propagation over a half rigid half fibreboard surface. Receiver height 5 cm, separation distance 100 cm, measured source height 5 cm

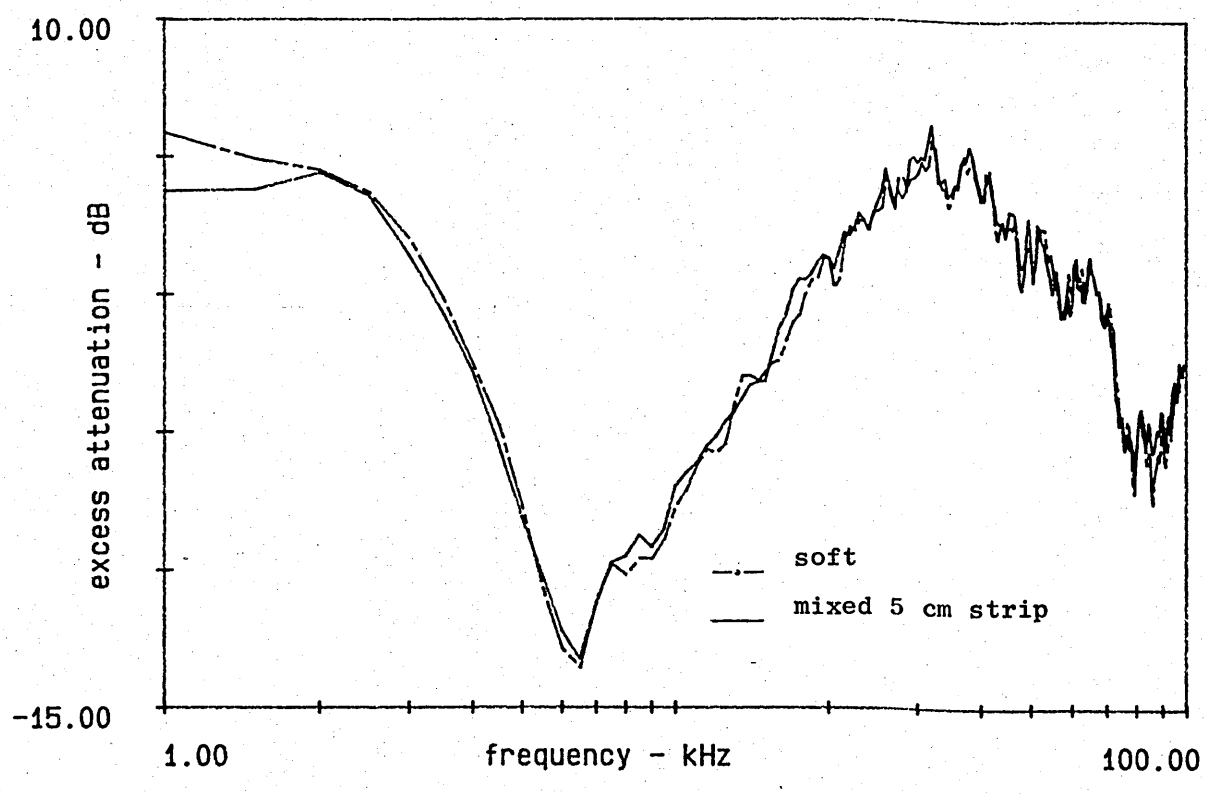

Figure 9.20(a) 5 cm rigid strip

Comparison of measured excess attenuation for soft and mixed impedance boundaries. Impedance surface is artificial grass

Figure 9.20(b) 20 cm rigid strip

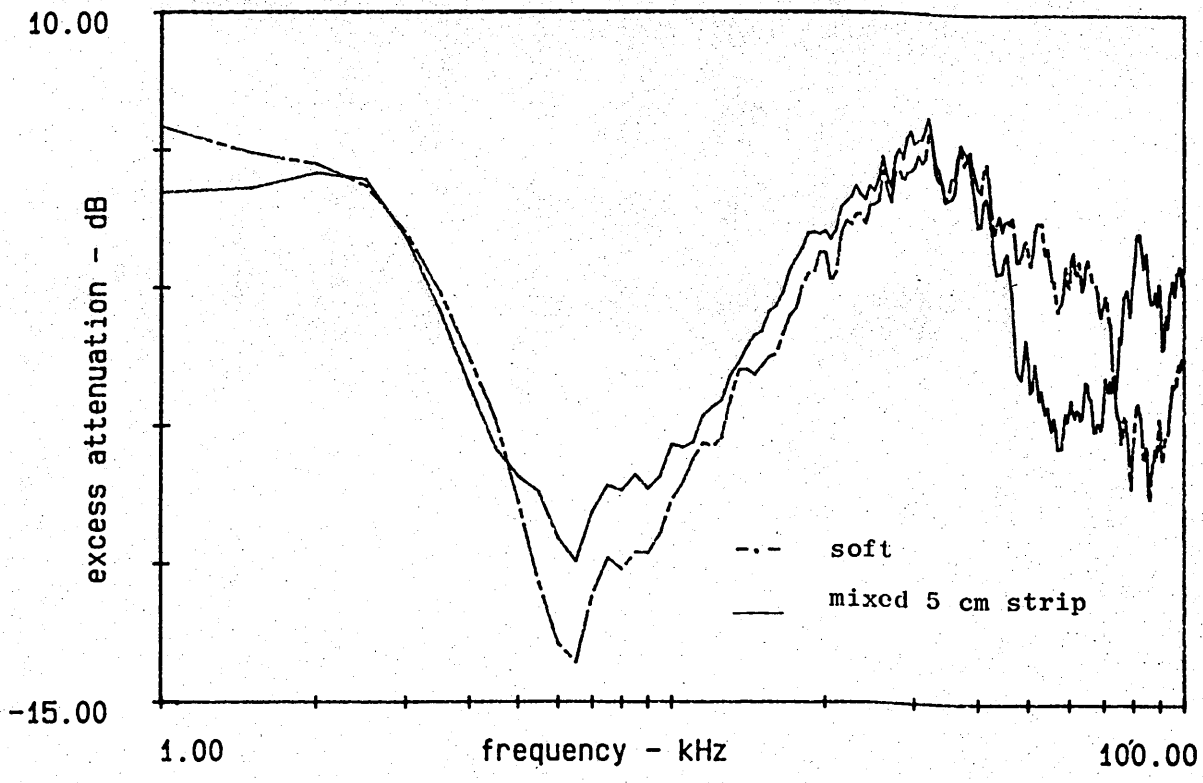

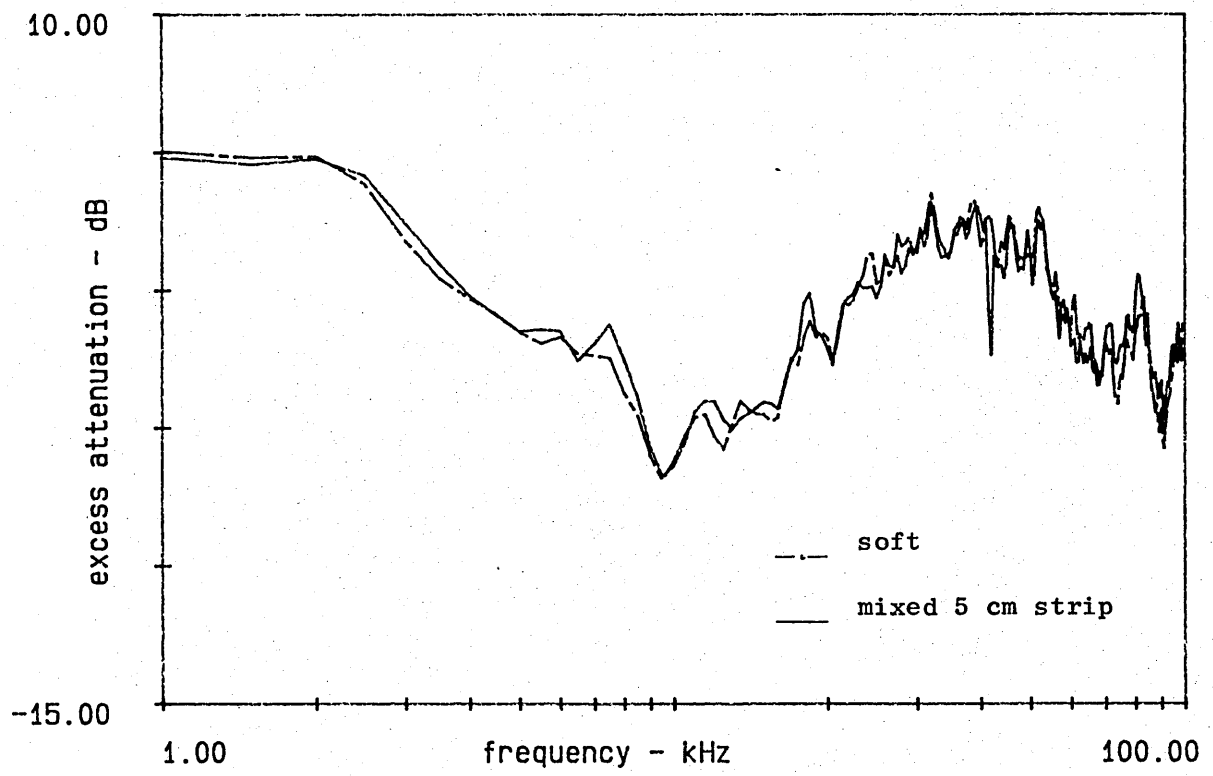

Figure 9.21(a) 5 cm rigid strip

Comparison of measured excess attenuation for soft and mixed impedance boundaries. Impedance surface is fibreboard.

Figure 9.21(b) 20 cm rigid strip

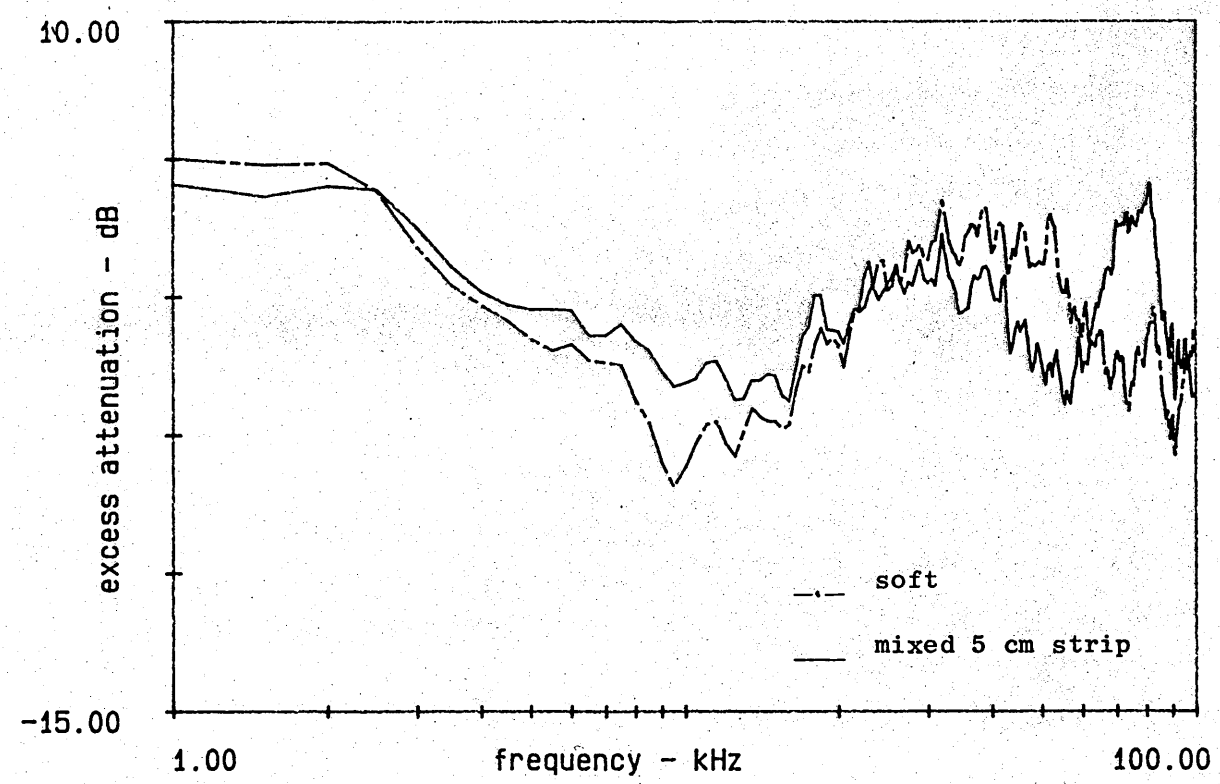

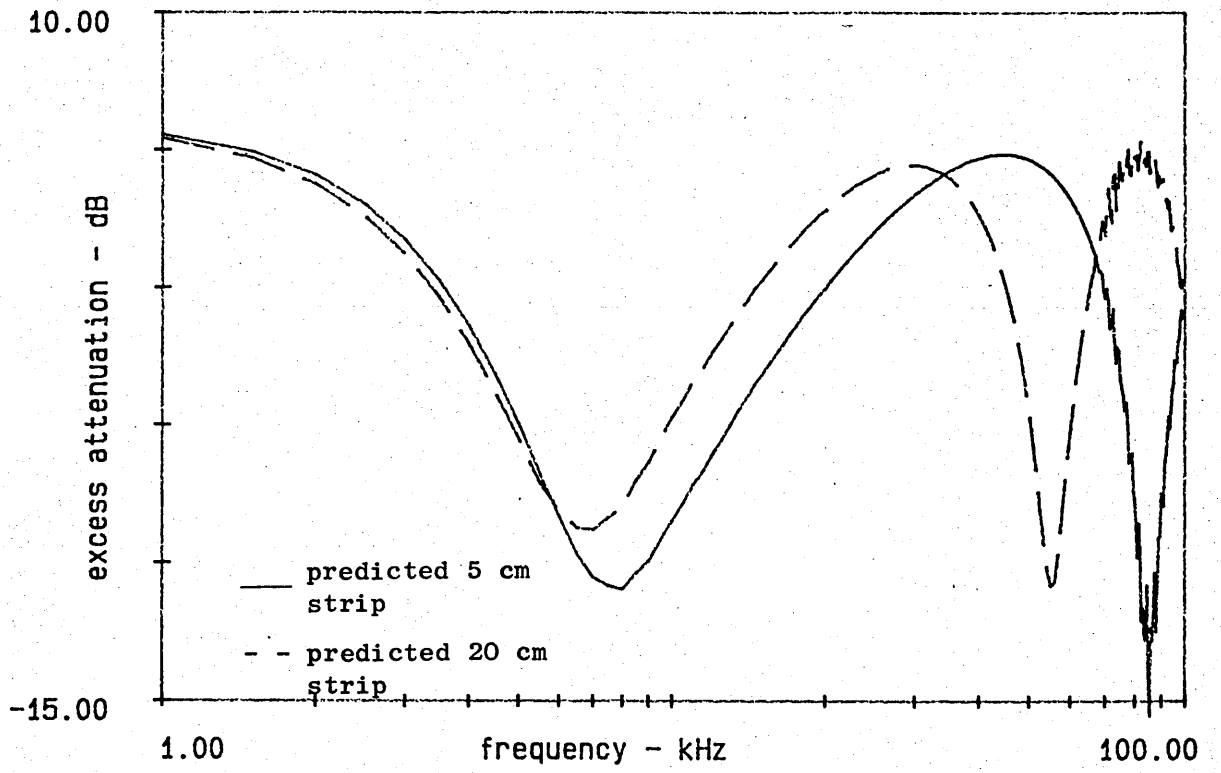

Figure 9.22 Comparison of predicted excess attenuation for a 5 cm and 20 cm rigid strip in an impedance boundary

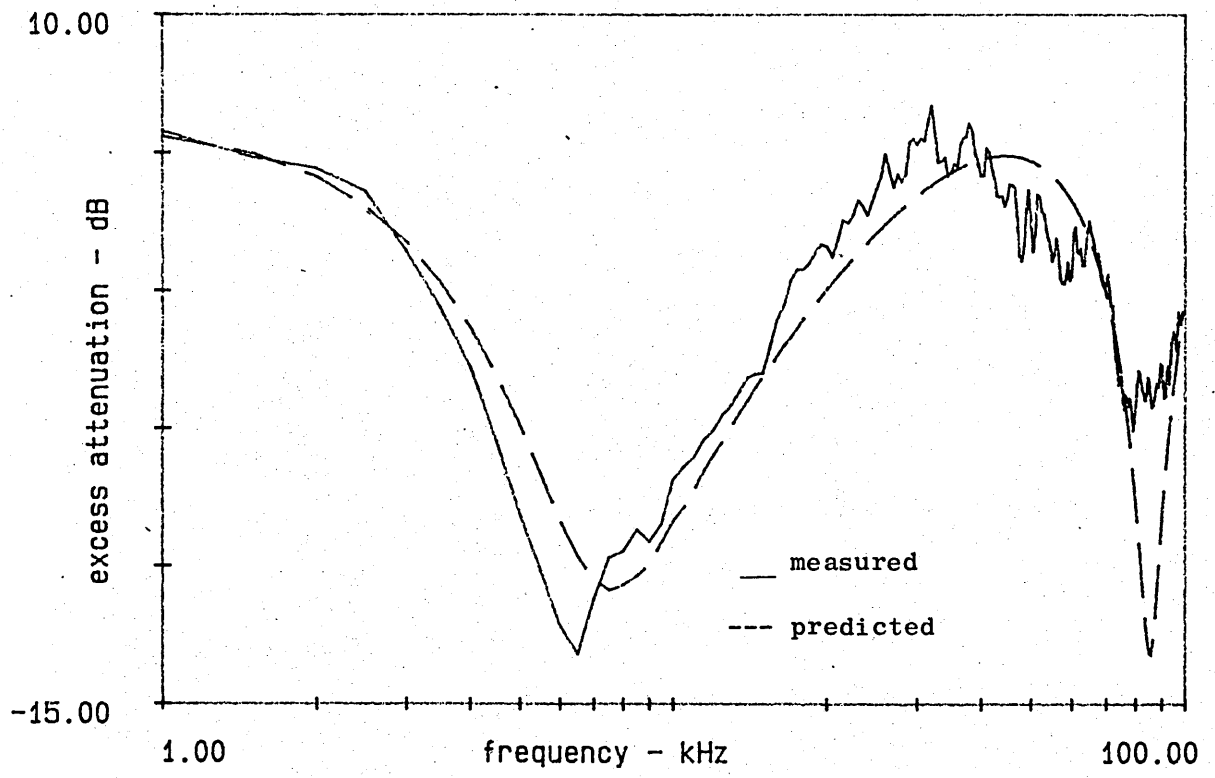

Figure 9.23 Comparison of measured and predicted excess attenuation for a mixed boundary of a 5 cm rigid strip in artificial grass

Figure 9.24 Comparison of measured and predicted excess attenuation for a mixed boundary of a 10 cm rigid strip in artificial grass

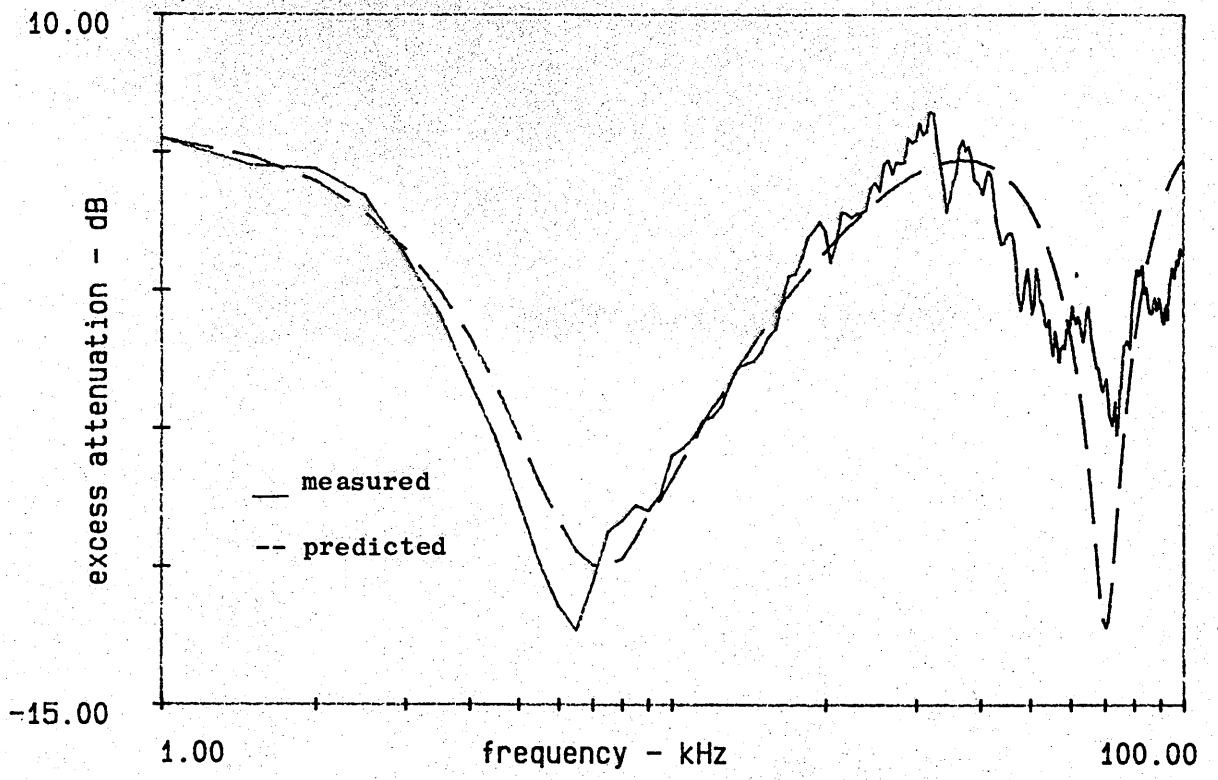

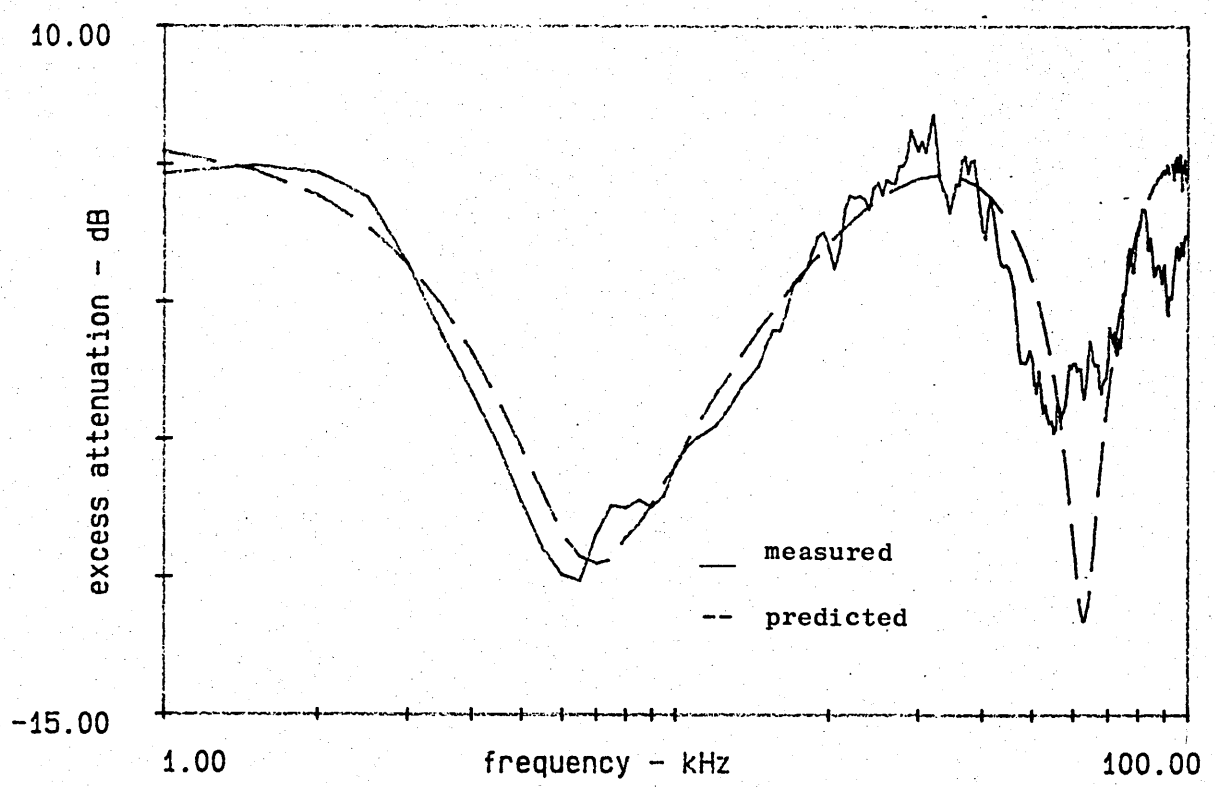

Figure 9.25 Comparison of measured and predicted excess attenuation for a mixed boundary of a 15 cm rigid strip in artificial grass

Figure 9.26 Comparison of measured and predicted attenuation for a mixed boundary of a 20 cm rigid strip in artificial grass

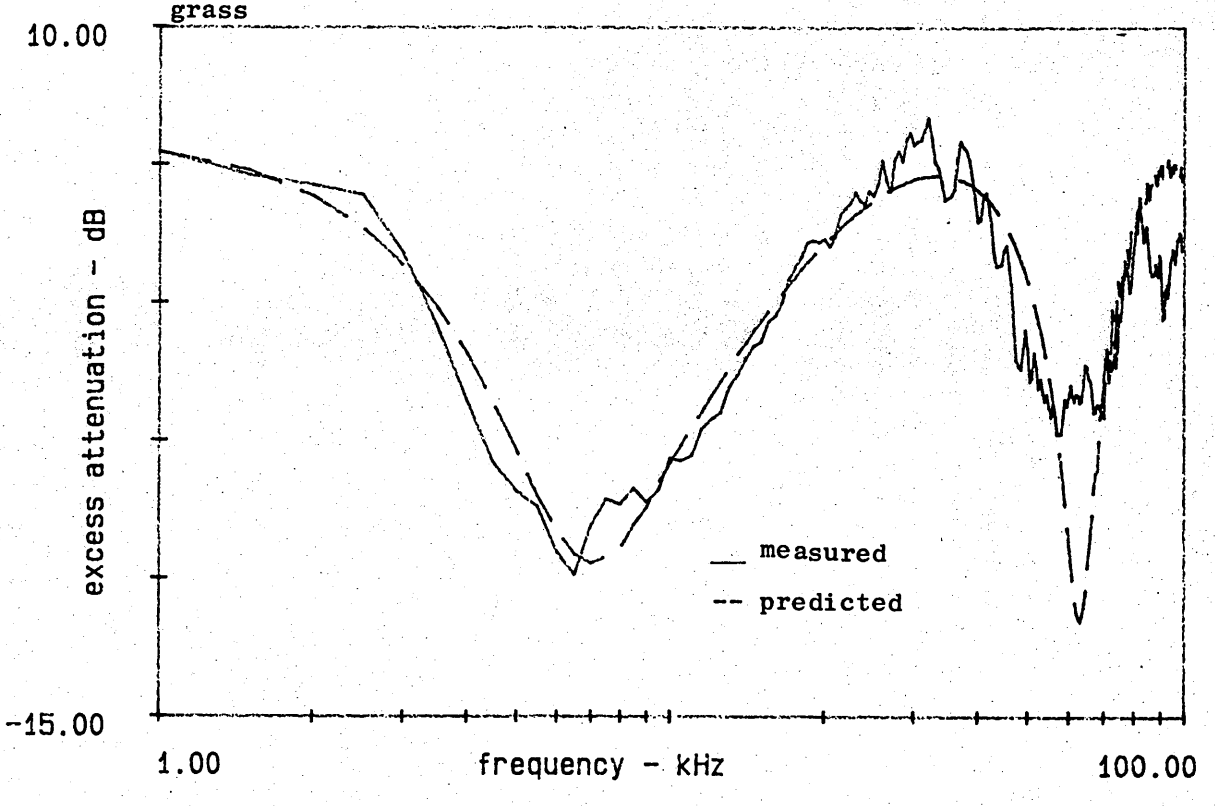

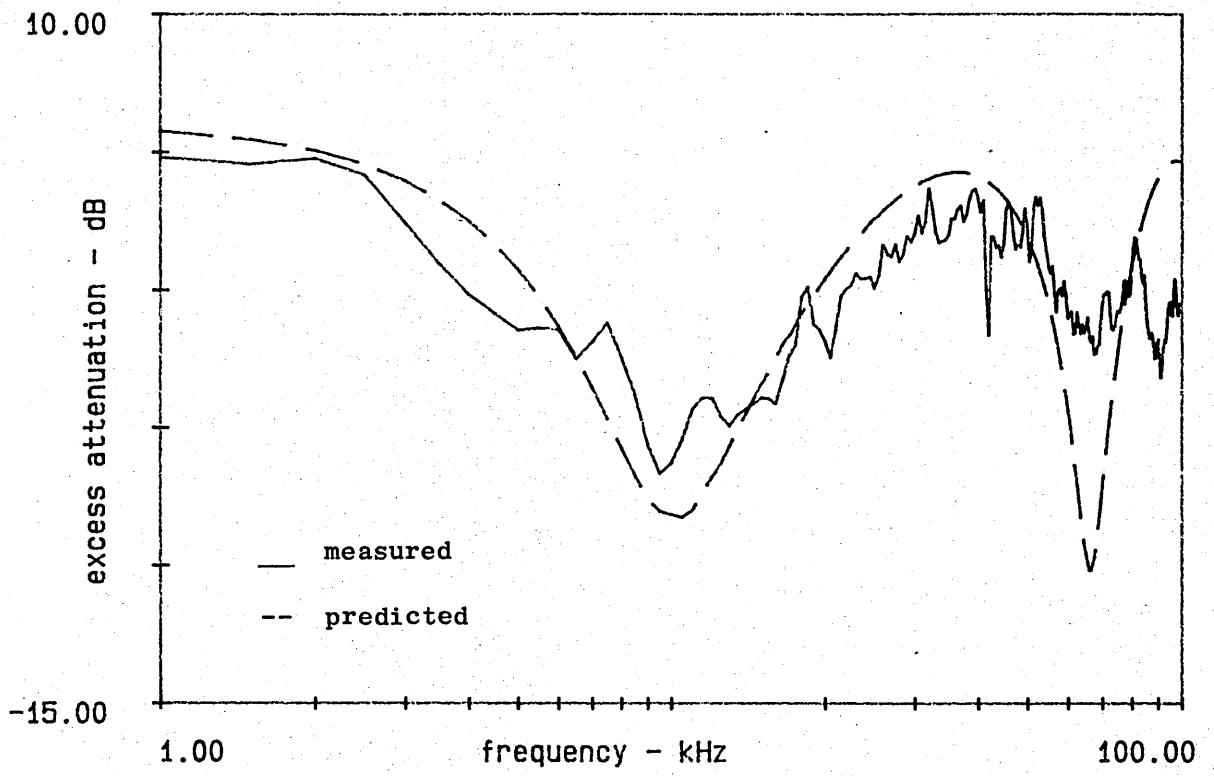

Figure 9.27 Comparison of measured and predicted excess attenuation for a mixed boundary of a 5 cm rigid strip in fibreboard

Figure 9.28 Comparison of measured and predicted excess attenuation for a mixed boundary of a 10 cm rigid strip in fibreboard

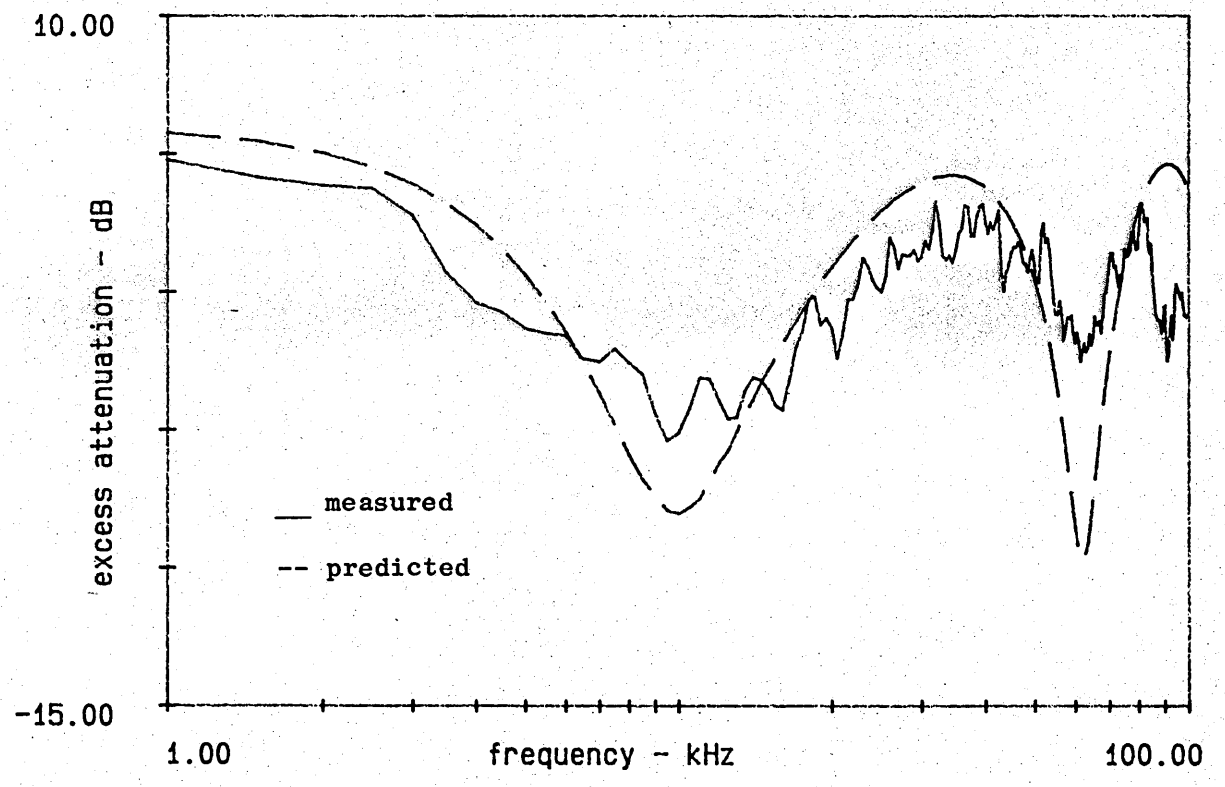

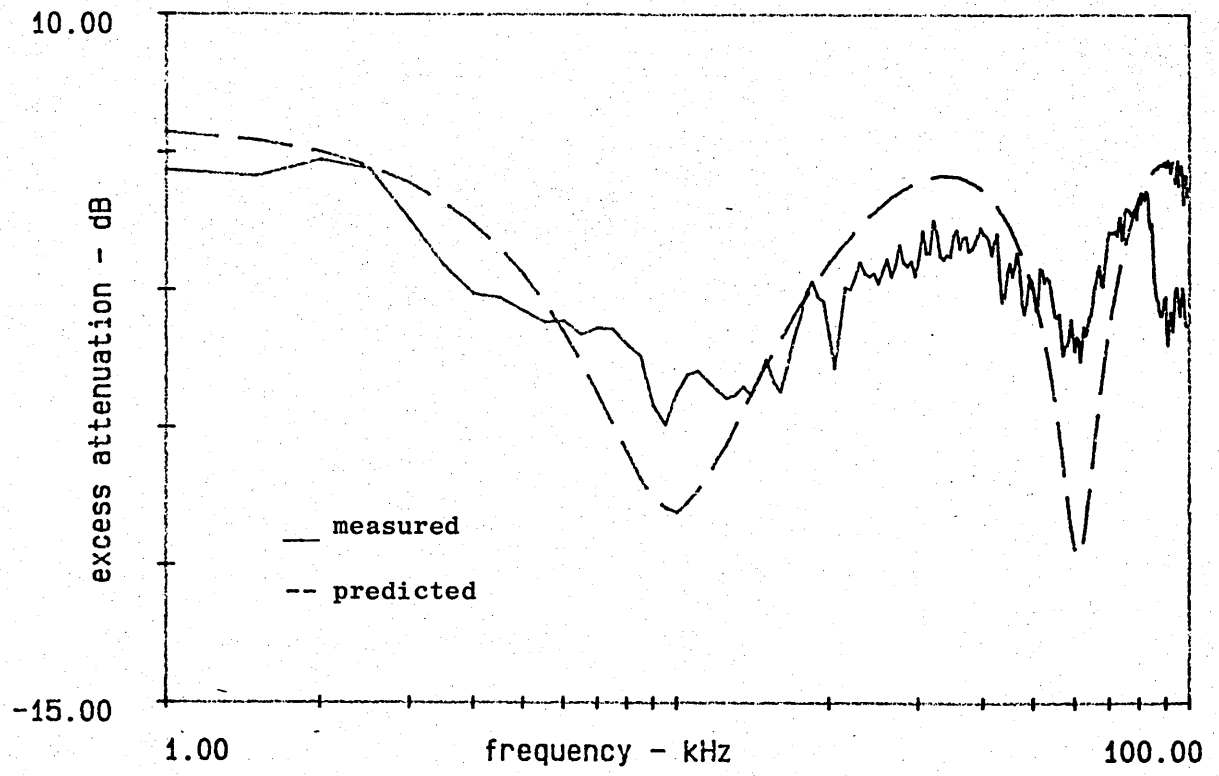

Figure 9.29 Comparison of measured and predicted excess attenuation for a mixed boundary of a 15 cm rigid strip in fibreboard

Figure 9.30 Comparison of measured and predicted excess attenuation for a mixed boundary of a 20 cm rigid strip in fibreboard

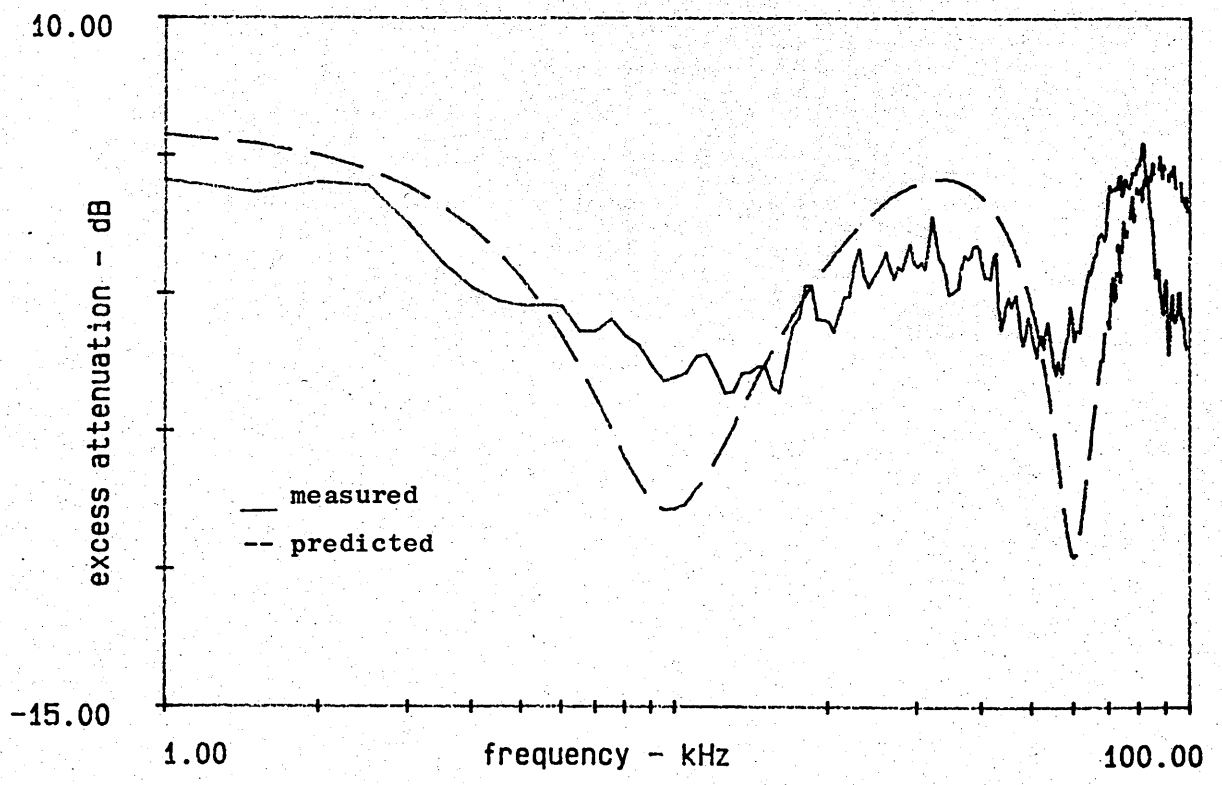

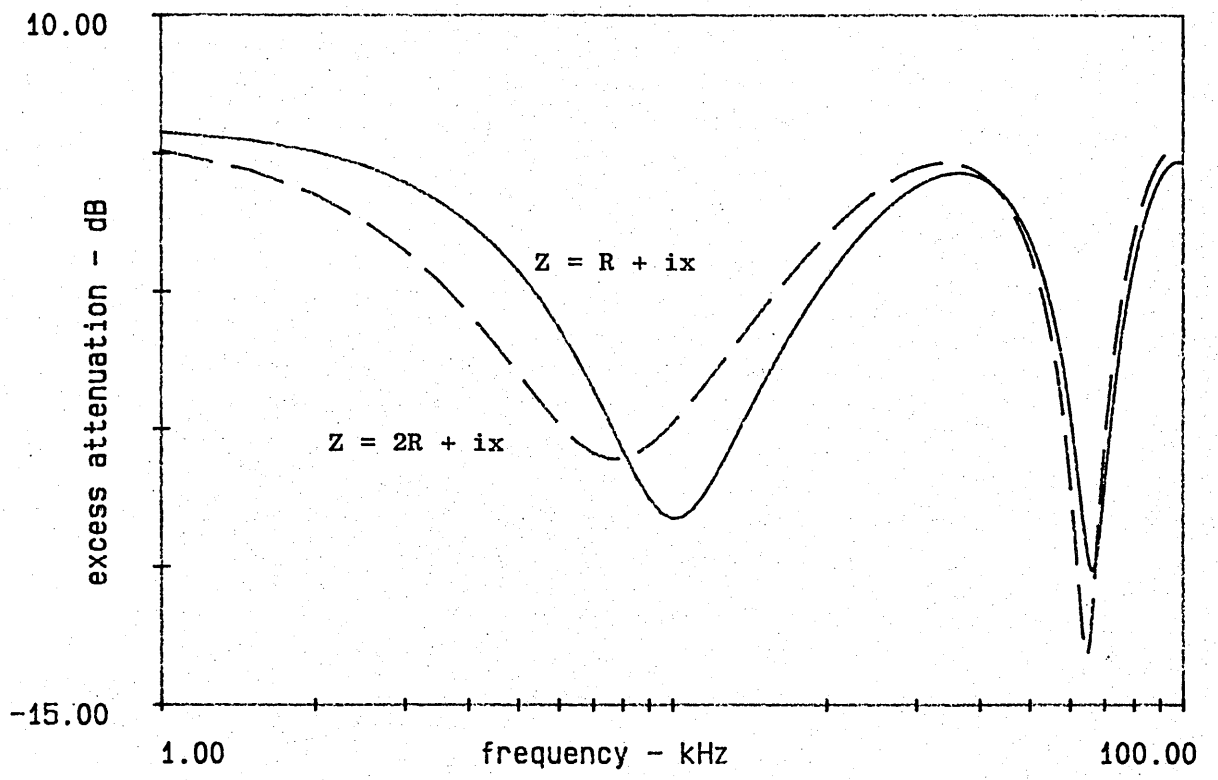

Figure 9.31 Effect of doubling the real part of the normal surface impedance on the predicted excess attenuation

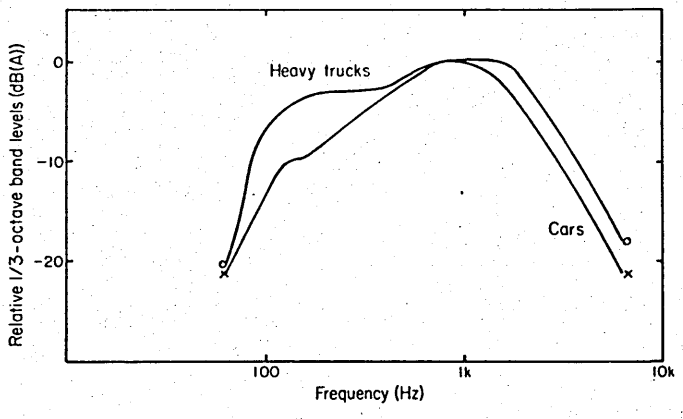

Figure 9.32 Car and lorry spectra used for the prediction of A-weighted excess attenuation

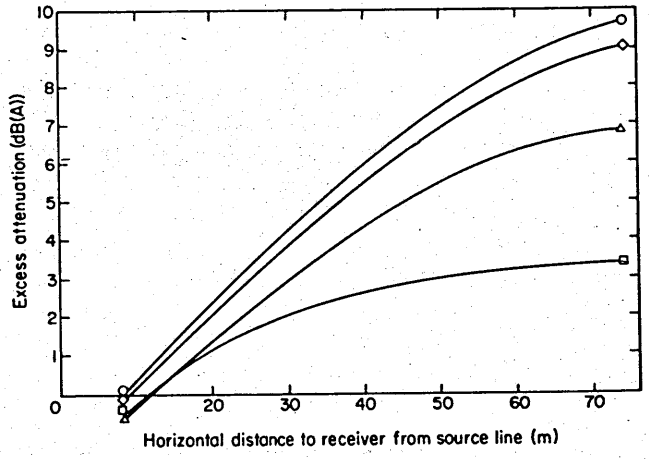

Figure 9.36

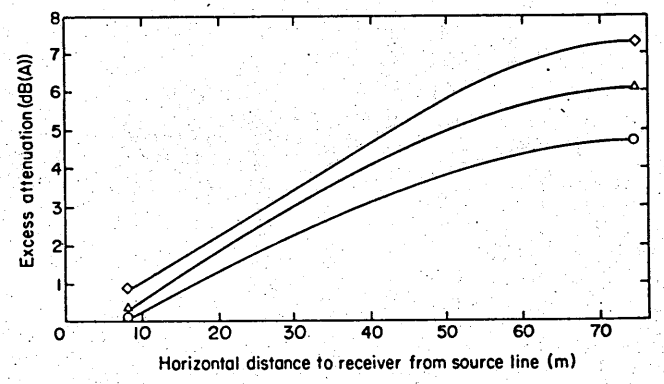

Figure 9.35
Predicted attenuation at 1.5 m above ground vs horizontal separation from a line of cars (source height 0.44 m) over three grass impedances (after Attenborough)

Figure 9.33 Predicted excess attenuation vs horizontal separation for four values of flow resistivity. Source height 0.5 m, receiver height 1.2 m

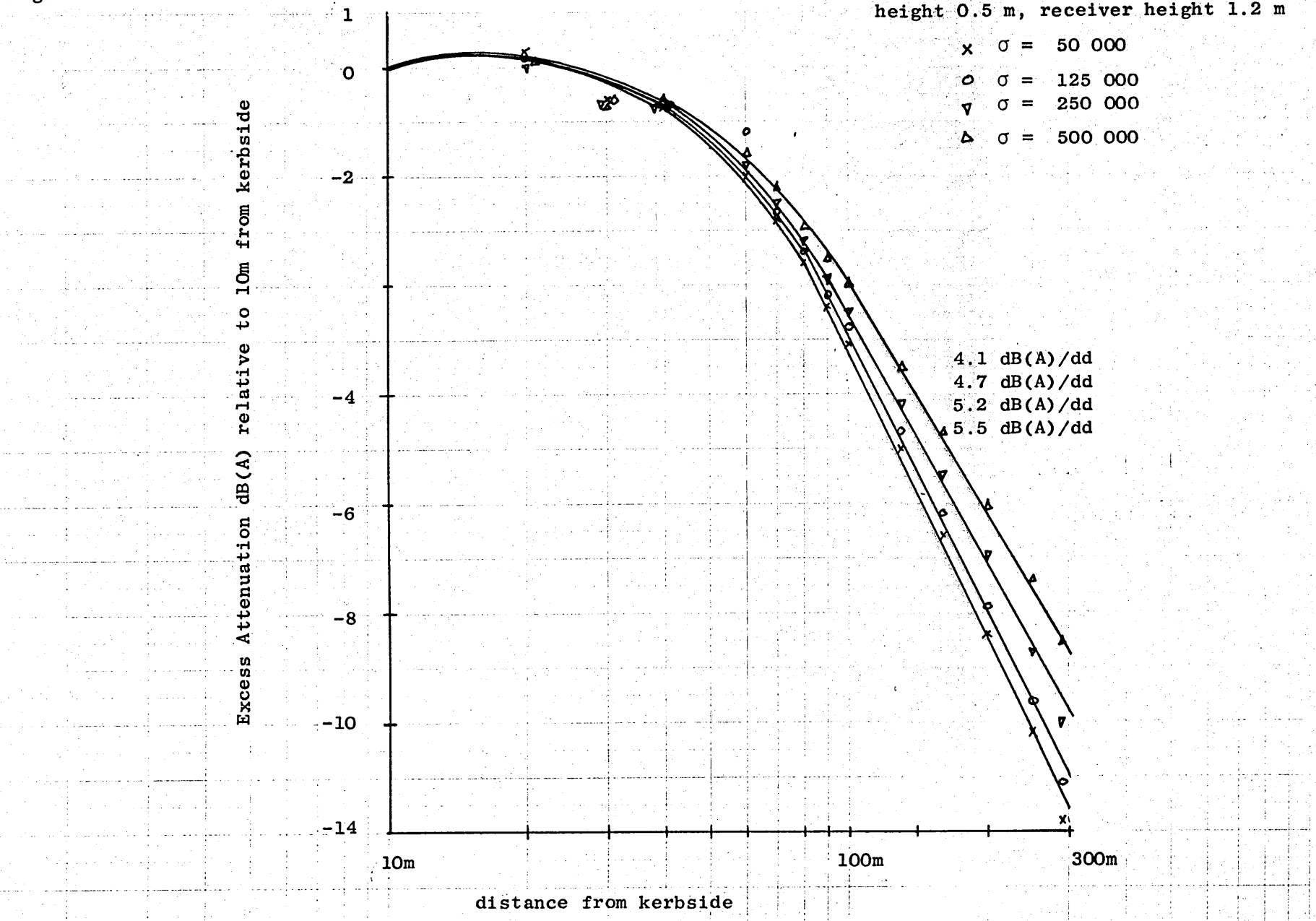

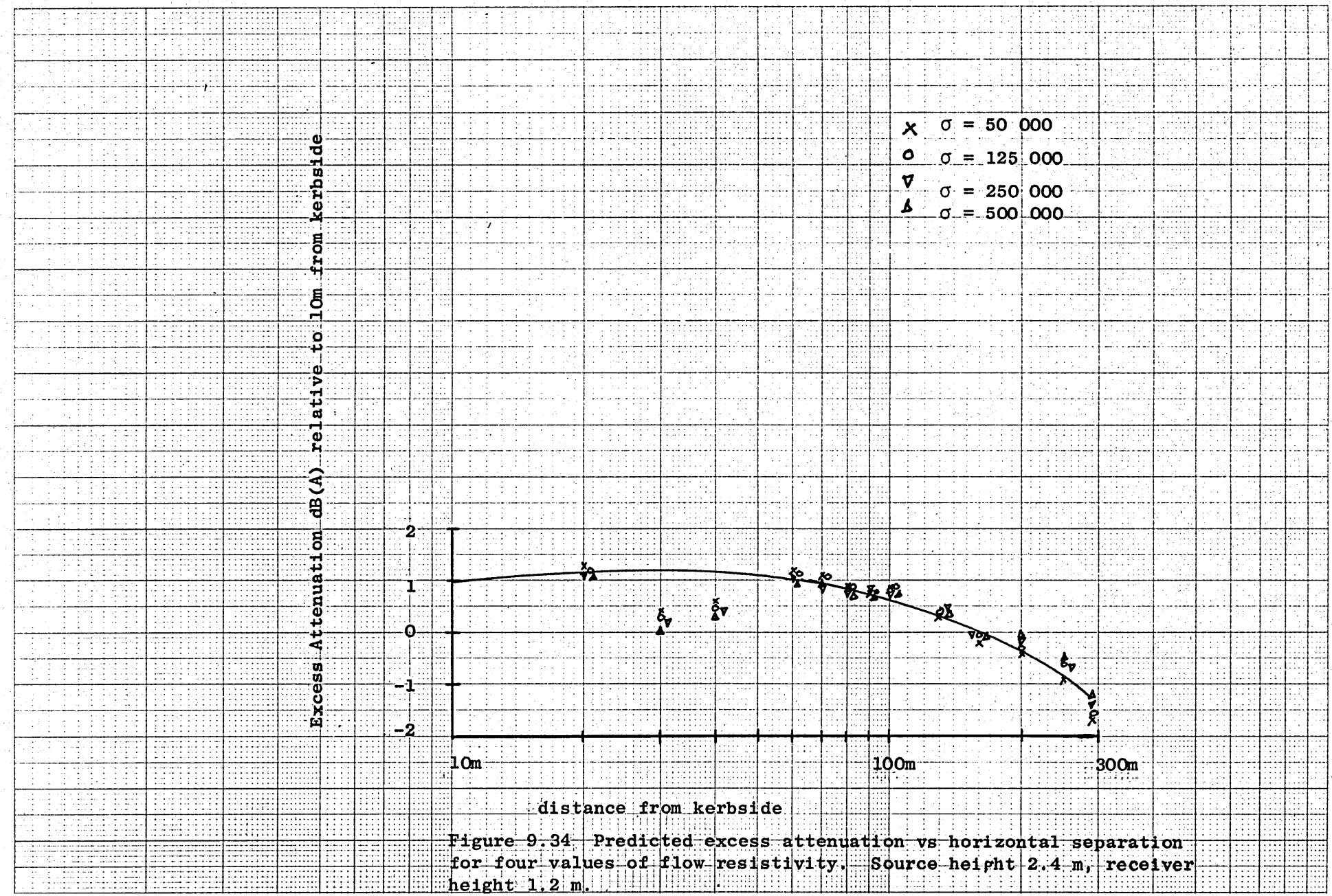

Figure 9.34 Predicted excess attenuation vs horizontal separation for four values of flow resistivity. Source height 2.4 m, receiver height 1.2 m.

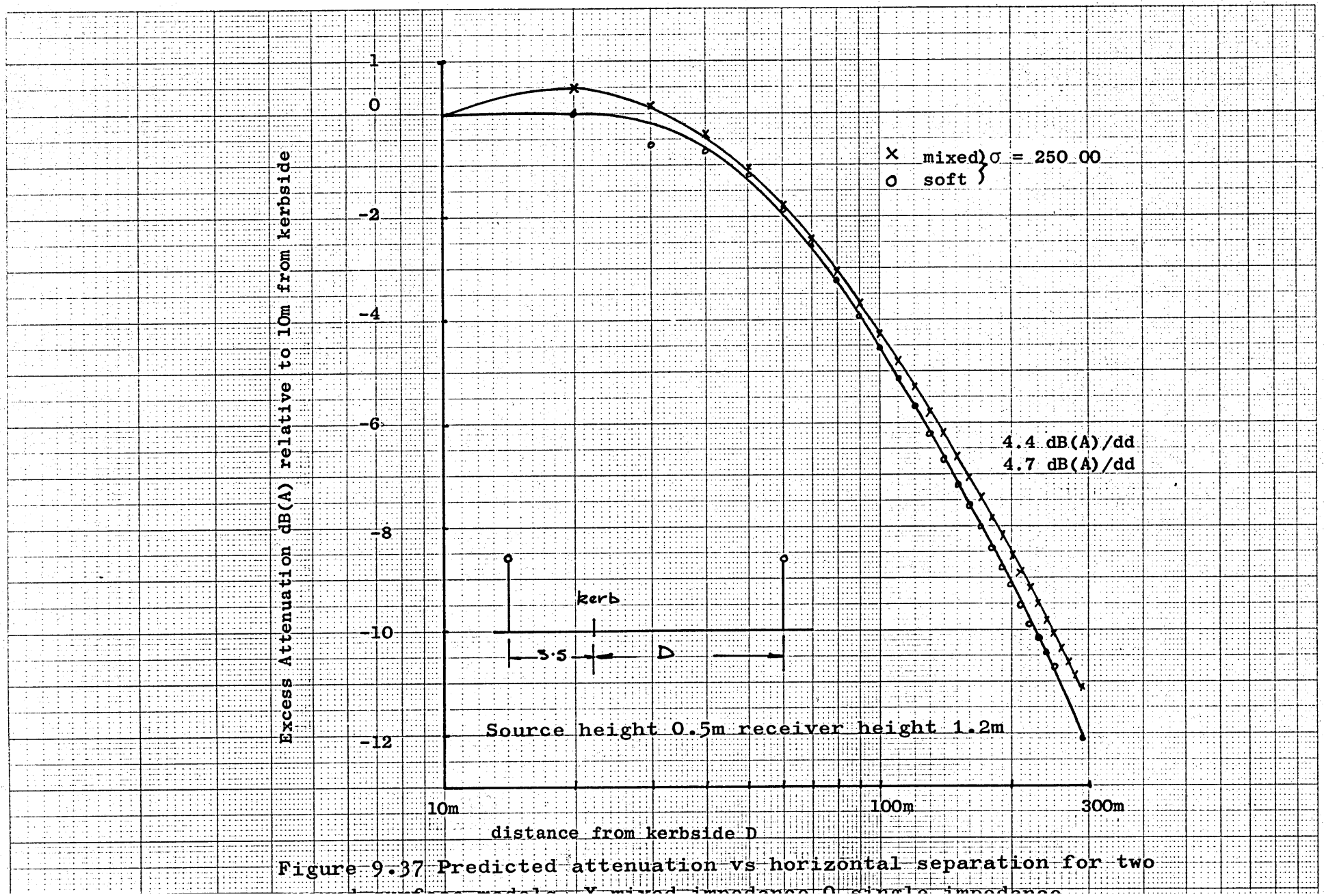

Figure 9.37 Predicted attenuation vs horizontal separation for two

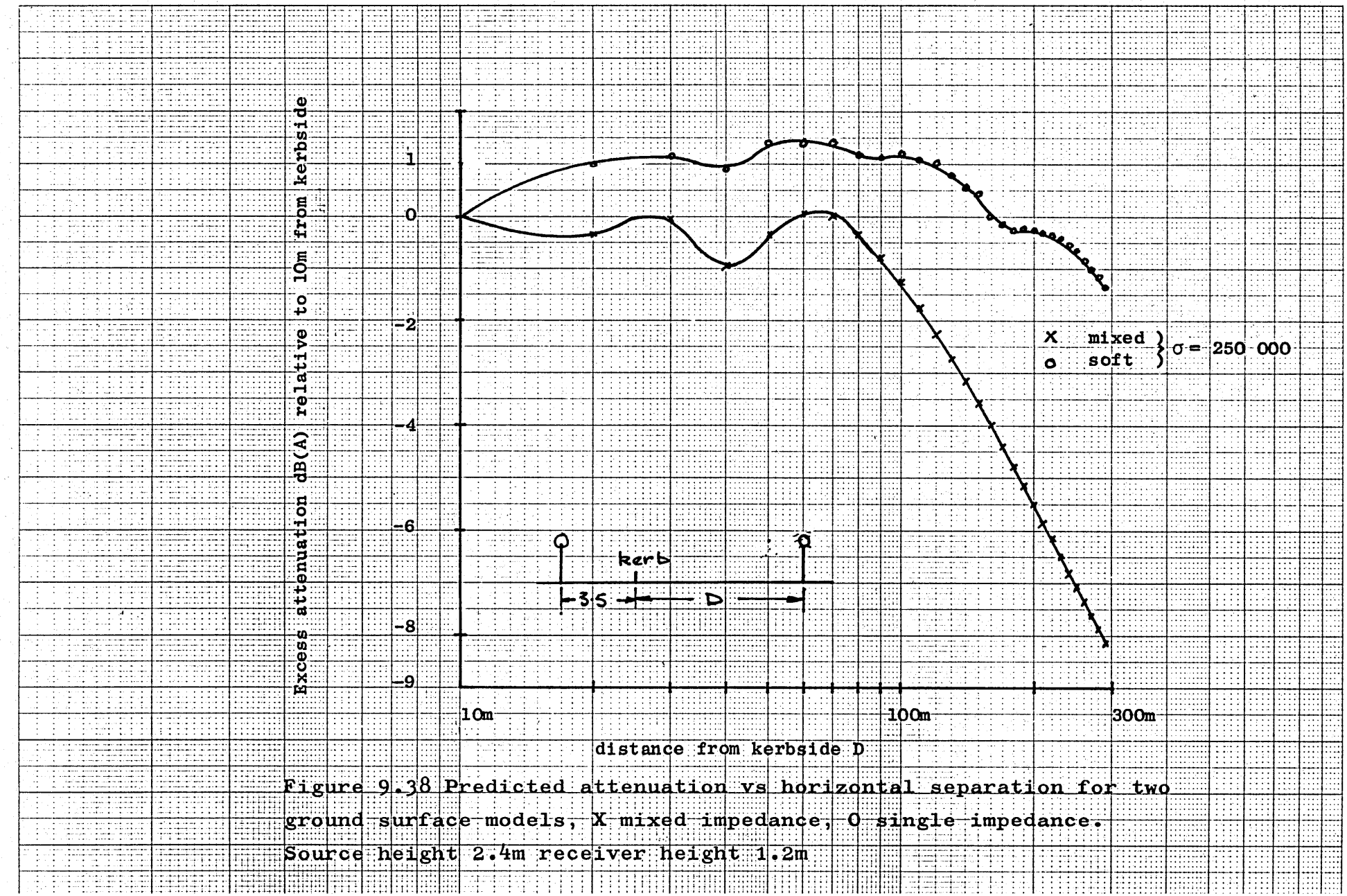

Figure 9.38 Predicted attenuation vs horizontal separation for two ground surface models, X mixed impedance, O single impedance. Source height 2.4m receiver height 1.2m

Chapter 10

Review and Conclusions

In the first chapter of this thesis the aims were given. These aims were to investigate methods of measuring the normal surface impedance at those frequencies normally associated with acoustic scale modelling and to evaluate the currently available theoretical predictions of point to point propagation over finite and mixed impedance boundaries. The results were to be applicable to the problems of road traffic and railway noise propagation.

To accomplish the first parts of the investigation a review of currently available theoretical predictions for single and mixed impedance boundaries was given in Chapters 3 and 4. Development of a new asymptotic solution for a rigid strip in a finite impedance boundary was also described in Chapter 4.

A review of impedance measurement methods was given in Chapter 5 together with a detailed discussion of the limitations and corrective procedures required to enable use of these methods for frequencies up to 100 kHz.

A brief description of the signal processing techniques and the scaling requirements for the laboratory models was given in Chapters 6 and 7.

A detailed account of the experimental measurement and signal processing techniques for estimating the normal surface impedance was given in Chapter 8. Pyett's method for estimating the bulk properties of a material were used to obtain values for the refractive index and

characteristic impedance of one of the model materials. The results suggest that a homogeneous porous medium model is inappropiated for the tufted artificial grass material, especially at high frequencies.

The considerable scatter in the impedance estimates obtained from the various models increased the problem of selecting values for use in the theoretical prediction evaluation stage of the study. The effect of a non-rigid backing introduced significant errors into the free-field estimates and precluded measurement of a frequency dependant probe end correction.

The sampling rate limitations of the available signal processing equipment introduced errors into the reflection coefficient phase estimation of both the pulse separation and cepstrum methods and for the latter led to results at variance with the measured excess attenuation data.

The indirect method proved simple to use, but the impedance estimates provided by the empirical single parameter flow resistivity model only gave quantitative agreement with the measured data.

The transfer function method proved to be unuseable due to the effects of near surface turbulence created by the air jet sound source.

Chapter 9 compared experimental and predicted excess attenuation values for locally reacting and mixed impedance boundaries. It was shown that source height, analysis bandwidth, source size and turbulence have a significant impact upon the measured excess attenuation. Where possible corrective procedures were applied and the improvement in the predicted attenuation discussed.

The major limitations to predicting attenuation for these boundaries were shown to be the values of normal surface impedance and near surface turbulence. However, the theoretical predictions did give good estimates of the excess attenuation for a single impedance and half soft-half rigid semi-infinite surface models.

The theoretical prediction for a rigid strip in a soft surface gave good agreement with the measured results for the artificial grass material, but not for the fibreboard material. This may in part have been due to the inadequacy of the impedance estimates used, since even the local reaction prediction for the fibreboard was not as good as that for the artificial grass.

The experimental measurements and theoretical predictions showed that for stripwidths less than 10% of the total propagation path, the pressure field at the receiver is approximately equal to that of a single impedance surface withthe same value of normal surface impedance. The effect of a wider strip is to reduce the level of the low frequency excess attenuation and shift the location of the high frequency minima to a lower frequency. This corresponds to an increase in the average surface impedance.

In terms of practical prediction procedures for use in road traffic and railway noise propagation problems, it was shown that current suggestions for schemes based upon the single parameter flow resistance model can lead to results with errors significantly larger than those allowed for by legislation. Furthermore, the simple hard/soft classification system used for ground surfaces was shown to be inadequate for most noise propagation problems.

The theoretical prediction for a mixed impedance surface was discussed. It was shown that for elevated sources (e.g. lorries) the difference between the excess attenuation predicted for distances greater than 100 m was significant and that the mixed boundary gives higher values of attenuation than the single boundary. However, the former shows much better agreement with measured values of attenuation for distances between 100 and 300 m.

For low source heights (e.g. cars) the difference between the excess attenuation predictions for the two types of boundary was very small and most probably due to computational rounding errors. Both theoretical predictions give very good agreement with measured values of attenuation.

The experienced gained using the five methods to measure the normal surface impedance of the modelling materials has shown the need for additional research to be conducted into the measurement of high impedance, particularly at grazing incidence.

For the impedance tube method, the major uncertainties are the effects of sample clamping and air gaps behind the sample. It is clear that tube absorption and probe-end corrections must be included in the calculation procedure, but the methods for estimating appropriate values appear reliable.

The free-field methods, interference pattern, pulse separation and cepstrum, all suffer as a consequence of assuming plane wave reflection when defining the relationship between the surface impedance and the reflection coefficient. This work has shown that the current theoretical predictions do provide an accurate description of point

to point propagation over a finite impedance surface. It should therefore, be possible to use equation 3.53 to define the relationship between the surface impedance and a spherical wave reflection coefficient.

The indirect method proved simple to use, but the empirical single parameter flow resistivity model used to predict the normal surface impedance was inadequate. Multiple parameter models should be capable of improving the usefulness of this technique, provided the parameters can be related to physically measureable properties of the surface.

The theoretical predictions for mixed impedance boundaries were shown to produce reliable estimates of excess attenuation. However, for the case of an elevated source the attenuation for the mixed boundary is significantly greater than that for a single boundary. No physical explanation for this behaviour was observed, but it may be due either to diffraction from the impedance discontinuity or from some form of descructive interference of the ground or surface waves. Such an anomoly between the two types of boundary is of sufficient practical importance to warrant further investigation.

The theoretical predictions examined in this study are based upon plane surfaces, but such surfaces are rarely encountered in outdoor noise propagation problems. Real surfaces show both impedance and height variations. The approximate techniques described in Chapter 4 are equally applicable to such surfaces and should enhance the prediction. At large separation distances, such refinement are unlikely to prove worthwhile due to the uncertainties of meterological factors. However, with the introduction of Noise Registers for

industrial premises the improvement for short propagation distance should prove beneficial.

APPENDIX A

This appendix describes the design and calibration of the small anechoic chamber used for the scale model experiments conducted during this study.

A.1 Description of the Anechoic Chamber

The Anechoic Chamber is situated on the ground floor of the B wing in the Venables Building at the Open University. Figure A.1 shows a floor plan of the chamber.

Although no special vibration isolation measures could be incorporated into the building, provision was made to isolate the floor of the chamber from the general concrete floor slab of the main building by means of an expansion joint. The limited headroom within the laboratory area prohibited the use of a suspended ceiling design, hence the underside of the 1st floor concrete slab forms the chamber ceiling.

In view of the limited vibration isolation, it was felt that the cost of double skin walls could not be justified since airborne sound transmission was unlikely to prove the major cause of noise leakage into the chamber, hence a single skin of 150 mm lightweight concrete building blocks, laid directly onto the isolated concrete floor, was specified.

It was anticipated that this would provide a minimum Sound Reduction Index of 40 dB.

The joints between the walls and ceiling were filled with expanded polystyrene foam, and an elastic sealant was applied to the joint to minimise air leakage.

A proprietary steel door, with double rubber seals, together with extract fans and ducting, were purchased from TMAT Engineering Limited. The Sound Reduction Index of these items was specified as 40 dB to match that of the chamber walls.

Tungsten filament lights were specified for the interior of the chamber; due to the high frequency noise output associated with florescent tube fittings. Electric power is available from four 13 amp sockets, and a telephone provides an emergency link to the outside.

Transducer interconnection cables run through the chamber wall via a separate metal conduit. This has been specially screened and positioned well away from any mains supplies, to mimimise induced noise problems.

A.2 Design of the Chamber Lining

The function of an anechoic chamber is to reproduce a free-field environment within a enclosure under controlled conditions. The primary requirements are:

(i) the total energy at any point contributed by reflection and scattering is small compared to the direct energy,

(ii) the total energy transmitted into the chamber from outside is small compared to that generated internally.

The second requirement has particular significance for scale model measurements, as will be shown in Section A.4.

Olson [A.1] gives an expression for the ratio of generally reflected to direct sound under steady state conditions as:

$$\frac{E_R}{E_D} = \frac{16 \pi D^2 (1-\alpha)}{\alpha S} \qquad \text{A.1}$$

where: E_R = energy density of generally reflected sound

E_D = energy density of direct sound

D = distance from source to receiver

S = surface area of absorbing material

α = absorption coefficient

Examination of this expression shows that the ratio of reflected to direct sound may be reduced by decreasing the source-receiver separation, increasing the absorption coefficient, or by increasing the surface area of the walls.

For the chamber in question limited space precluded increasing the wall surface area, hence the only parameter to be maximised was the absorption coefficient of the lining material.

In general the absorption of high frequency sound presents no problem, although the extent of reflection by the cell walls of plastic foams is not known. Low frequencies however are particularly difficult to absorb, so it is useful to introduce a notional low-frequency cut-off point of the chamber. This point is defined as the frequency at which the reflection coefficient exceeds 0.1. For an enclosure, the cut-off point is determined by three factors:

(i) the largest undisturbed dimension

(ii) the material used for, and the geometry of the absorbing surface

(iii) the construction of the enclosing walls.

Obviously the first two of these factors are inter-related, and determined by the chamber lining, whilst the third points to the need to minimise low frequency transmission through the chamber walls. Two types of lining were investigated, namely plane foam blocks and foam wedges.

A.3 Plane Foam Lining

The condition for undisturbed sound propagation parallel to a highly damped surface is given by Ingerslev [A.2] as:

$$h/\lambda > |Z|/1.2\ \rho c \qquad \text{A.2}$$

where:

h = the largest undisturbed dimension normal to the direction of propagation

λ = the wavelength

Z = the characteristic impedance of the surface

ρc = the characteristic impedance of air.

For plane waves at normal incidence, the ratio $|Z|/\rho c$ can be obtained from the equation for the plane wave reflection coefficient R_p given below:

$$R_p = \frac{Z - \rho c}{Z + \rho c} \qquad \text{A.3}$$

Substituting $R_p = 0$ into this expression gives the condition that $Z = \rho c$ for total absorption. Hence $Z/\rho c = 1.0$ and from equation A.2

$$\lambda < 0.83h$$

The low frequency cut-off can be found from equation A.3 by substituting $|R_p| = 0.1$, since R_p is in general complex, therefore:

$$\left|\frac{Z - \rho c}{Z + \rho c}\right| = 0.1 \qquad \text{A.4}$$

By means of the two inequalities:

$$|Z + \rho c| < |Z| + |\rho c| \qquad \text{A.5(a)}$$

and

$$|Z - \rho c| > |Z| - |\rho c| \qquad \text{A.5(b)}$$

it can be shown that a lower bound on the cut-off frequency is given by:

$$|Z|/\rho c \quad 1.22$$

and thus from equation A.2:

$$\lambda < \frac{1.2h}{1.22} = 0.9h \qquad \text{A.6}$$

The maximum undisturbed dimension, h, is found by subtracting twice the absorbent thickness from the chamber width.

The absorbent thickness can be estimated by assuming that absorption occurs due to the transformation of kinetic energy to heat energy at the point of maximum particle displacement. This implies a basic requirement for the material thickness to exceed $\lambda/4$ if the chamber walls are rigid. h can now be expressed in terms of the chamber width w and the wavelength λ as:

$$h = w - 2\,(\lambda/4) \qquad \text{A.7(a)}$$

$$h = w - \lambda/2 \qquad \text{A.7(b)}$$

The low-frequency cut-off can now be estimated from the expression:

$$\lambda < 0.98\,(w - \lambda/2)$$

$$\lambda \simeq 0.66w \qquad \text{A.8}$$

The smallest dimension of the chamber is the floor to ceiling height of 2.7 m. Substituting this value for w in equation A.8 gives an approximate wavelength of 1.78 m corresponding to a frequency of 191 Hz at 20°C.

In practice the actual cut-off frequency will be somewhat higher because the source or receiver cannot be placed at the lining surface. Allowing an additional $\lambda/4$ m between the source and lining and the receiver and lining would raise the cut-off frequency to 290 Hz at 20°C.

In view of the limited headroom within the chamber, a plane lining of 200 mm thick polyurethane foam was used for the floor and ceiling surfaces. A 100 cm air gap was introduced behind the foam to improve the low frequency absorption.

However, there are two distinct disadvantages to the use of a plane absorbent. Firstly the low impedance requirement can only be met by employing low flow-resistance materials, but these cease to be self-supporting for thick samples. Secondly the absorption coefficient decreases for increasing angles of incidence. These two problems can be overcome by employing wedge shaped absorbers.

A.4 Wedge Lining

Beranek and Sleeper [A.3] were amongst the first investigators to demonstrate both the utility and cost effectiveness of wedge shaped absorbers. They showed that the wedge shape precludes an abrupt

impedance mismatch at the lining surface. Instead it provides for a gradual transition region between the two media. Moreover, a random orientation of the wedge faces improves absorption by reducing the occurence of grazing incidence.

The most important parameters for a wedge shaped lining have been determined from the literature, they are:

wedge angle - according to Ingerslev [A.2] this should lie in the range $\tan^{-1}$ (0.1-0.5).

wedge length - increases low frequency absorption minimum value is $< = 0.2\lambda$.

wedge base length - increases low frequency absorption, but if too long produces fluctuations in absorption curve.

air gap between base and wall - increases low frequency absorption and sharpens the transition region of the low frequency roll-off.

Yegnanarayana [A.4] suggests an optimum ratio of air gap: base length: taper length as 1:4:18 for polyurethane foam materials.

After extensive examination of the literature, a final wedge shape of 15 cm square base and 45 cm taper was chosen. These wedges are held in position by a light steel lattice framework suspended 2.5 cm away from the wall surface.

A.5 Lining material

Various lining materials, such as fibreglass and polyurethane foams, were examined, and after much deliberation Prytex NG22 polyurethane foam was chosen. This material is easy to handle, as opposed to mineral fibres, and is classified as flame retardant. The specific flow resistance is:

$$15.10^3 \text{ kg/Sm}^2$$

A.6 Chamber calibration instrumentation

Several test methods have been suggested for evaluating the performance of an anechoic room, of which the most basic is to measure the deviation from true inverse pressure/distance law, for sound radiated from a nominal point source.

In practice the performance of an anechoic chamber depends not only upon the geometry of the room, the lining, and the source/receiver separation distance, but also on such factors as source and receiver size, their directivity, the test spectrum, and the bandwidth used in the analysis. For example, the measured room performance can be enhanced by the use of a receiver that is large compared to the pressure field fluctuations (say $\lambda/2$), due to spatial averaging effects. Similarly, frequency averaging will result from the introduction of broadband filters or noise sources.

Hence the deviation from true inverse pressure/distance law measured using a small nominally omni-directional source and receiver does not necessarily constitute a direct test of a chamber's performance, since the performance will vary with the test conditions.

In view of this, it was decided to determine the deviation under conditions similar to those to be used for the scale model experiments.

A block diagram of the instrumentation system is shown in Figure A.2. The system comprises a Nova computer, an Analogic analogue to digital converter, a Hewlett Packard 7203A digital plotter, and a 2619 pre-amp, 2607 Measuring Amplifier and 1614 Third Octave Filter Set Manufactured by Bruel and Kjaer (B & K).

The experimental procedure adopted was as follows:

(1) The microphone was positioned 10 cm from the source, and the filters set to 1 kHz. These formed the initial conditions for the commencement of an experimental run.

(2) The microphone was traversed across the chamber in 10 cm steps, out to a maximum source/receiver separation of 190 cm.

(3) At the end of a traverse the filter set was advanced to the next highest third octave band, and the microphone then returned to its initial position 10 cm from the source. Advancing the filter before the return traverse ensured that the new filter output would settle before sampling recommenced.

This cycle was repeated for each of 21 filters covering the frequency range 1-100 kHz, and required approximately 20 minutes for completion. At each of the 19 measurement positions the computer calculated the mean and standard deviation of 256 samples of the sound pressure level. Advantage was taken of the fact that the 2607 provides a d.c. output voltage between 0 and -4.5 volts, which is directly related to the sound pressure level in dB.

Use of this d.c. output ensured aliasing errors could not arise in the sampling process, and also avoided the need to calculate a root mean square pressure level from an a.c. signal.

A.7 Calibration Sound Sources

The main sound source used for the calibration experiments was the air jet described in Chapter 7, which has a useful bandwidth of 1-100 kHz.

A few experimental measurements were made to investigate the averaging effects of wide bandnoise. A pure tone omni-directional source was made by adding a 48 cm long probe tube to a small high frequency loudspeaker. The useful bandwidth of this source was 200 Hz-20 kHz.

A.8 Calibration Receivers

Bandwidth requirements limit the choice of microphone for use in the calibration experiments to either the B&K 4135 ¼" or the B&K 4138 1/8".

The superior bandwidth and directivity of the 1/8" microphone might presuppose its adoption, but its low sensitivity limited the maximum separation to 150 cm. In view of this, the ¼" microphone was adopted as the standard. The 1/8" was used primarily to check the ¼" at short separation distances and to measure the directivity of the sound source.

A.9 Experimental Measurements

The prime object of the experimental measurements was to determine the performance of the anechoic chamber. However, additional measurements were made in order to examine the spatial and frequency averaging effects of a broadband noise source, and the influence of a diffuser over the microphone diaphragm.

The measurements fall into three categories, namely, pure tone, narrowband noise and broadband noise.

A.9.1 Pure tone measurements

The pure tone measurements cover the frequency range 100 Hz to 10 kHz in 21 third octave bands. The receiver was a B and K 4135 ¼" free-field response microphone and the source a pressure-dome drive unit fitted with a probe tube.

The measured values were corrected for atmospheric absorption and the final results plotted as attenuation versus log distance. This choice of ordinates is convenient, since under ideal conditions the curve should be a straight line with a slope of 6 dB per doubling of distance. The results are shown in Figures A.3 (a) to (g).

In general the plotted curves show considerable deviation from true inverse pressure/distance law, but it is significantly worse for frequencies below 1.25 kHz. Above 1.25 kHz the curves appear to have approximately the right slope, but exhibit minor oscillations to either side.

The low frequency deviations are to be expected in view of the fact that the wavelength of the sound is comparable with the maximum free path length between the wedge tips, and that the distance between source and wedge tips was approximately 10 cm.

At low frequencies a greater proportion of the incident sound energy will be reflected by the chamber lining. The interference pattern created by these reflections will be most pronounced near the surface where the path length difference between direct and reflected waves is smallest. If the source is also close to the surface, then one could not expect the true inverse pressure/distance law to be obeyed within the vicinity of the source. Furthermore, the wedge tips could be sources of the secondary wavefronts associated with diffraction. These reflection and diffraction effects could well explain the poor performance of the chamber at low frequencies.

The high frequency oscillations could possibly be due to reflections from the traverse support framework, but are more probably the result of instability in the signal source. During a single traverse it was noticed that the oscillator frequency drifted from the initial setting by as much as 20 Hz. Upon further investigation, with the aid of a frequency counter and manual tuning, it was found that even a few hertz error in

oscillator setting could produce a 3 or 4 dB variation in the sound pressure level.

A.9.2 Narrow band random noise

As a further test of the low frequency performance of the chamber a series of measurements was made using narrow bands of random noise. The source and receiver transducers were the same as those used for the pure tone tests, but the frequency range covered was 200 Hz to 20 kHz in 21 third octave bands.

The results, after correction for atmospheric absorption, were plotted as before and are shown in Figures A.4(a) to (f). In general they confirm the poor performance of the chamber at frequencies below 1 kHz. The improved performance above 1 kHz is probably due in part to better control of the signal source, but frequency averaging effects cannot be discounted. Above 5 kHz the results show virtually no deviation from the true inverse pressure/distance law, and even allowing for all averaging effects, indicate that the chamber performs satisfactorily.

A.9.3 Broadband random noise

The final set of measurements to be discussed utilize the air jet sound source. In addition to investigating

the inverse square law characteristic of the chamber, an attempt was made to determine the effect of a microphone diaphragm diffuser. The combinations of microphone and diffuser used were:

(i) ¼" microphone with normal protection diffuser
(ii) ¼" microphone without diffuser
(iii) ¼" microphone with nosecone diffuser
(iv) 1/8" microphone with nosecone diffuser

Measurements were made over the frequency range 50 kHz in 21 third octave bands. The results, as shown in Figures A.5 to A.8 would suggest an almost perfect free field, but since it is virtually impossible to quantify the averaging effects,one must maintain a certain degree of scepticism. One observation of interest is that whilst it is very difficult to distinguish between the results of 1/8" microphone with nosecone and those of the ¼" microphone with nosecone or without a grid, the results of the ¼" microphone with grid show a distinct deviation at high frequencies. This would appear to confirm the manufacturers claim of an improved high frequency directional response for a microphone and nosecone combination.

A.10 Conclusion

The extensive measurements made in the anechoic chamber indicate that it produces a free-field environment adequate for scale modelling studies over the frequency range 1-100 kHz. Below 1 kHz the chamber is too small to enable one to model propagation paths of 200 m, at a minimum scale of 1:100, and yet maintain a minimum distance of $\lambda/4$ between the wedge tips and the source.

The measurements have also confirmed the improvement in the directional response of a microphone when a nosecone is employed.

Furthermore, the air jet noise source has been shown to behave as a nominally omni-directional source, with adequate power output to overcome the problems of microphone sensitivity and air absorption.

References Appendix A

A.1 Olson, H.F.: Elements of Acoustical Engineering.
D. Von Nostrand. 1947.

A.2 Ingersler, F., Pedersen, O.J., Moller, P.K. and Kristensen, J.:
The Anechoic Chambers at the Technical University of Denmark.
Bruel & Kjaer Technical Review (2) 1968.

A.3 Beranek, L.L. and Sleeper, H.P.: The Design and Construction of
Anechoic Sound Chambers.
J.A.S.A. (18) 140-150. 1946.

A.4 Yegnanarayana, B.: Anechoic Chambers at I.I.Sc.
Indian Institute of Science, Bangalore. 1971.

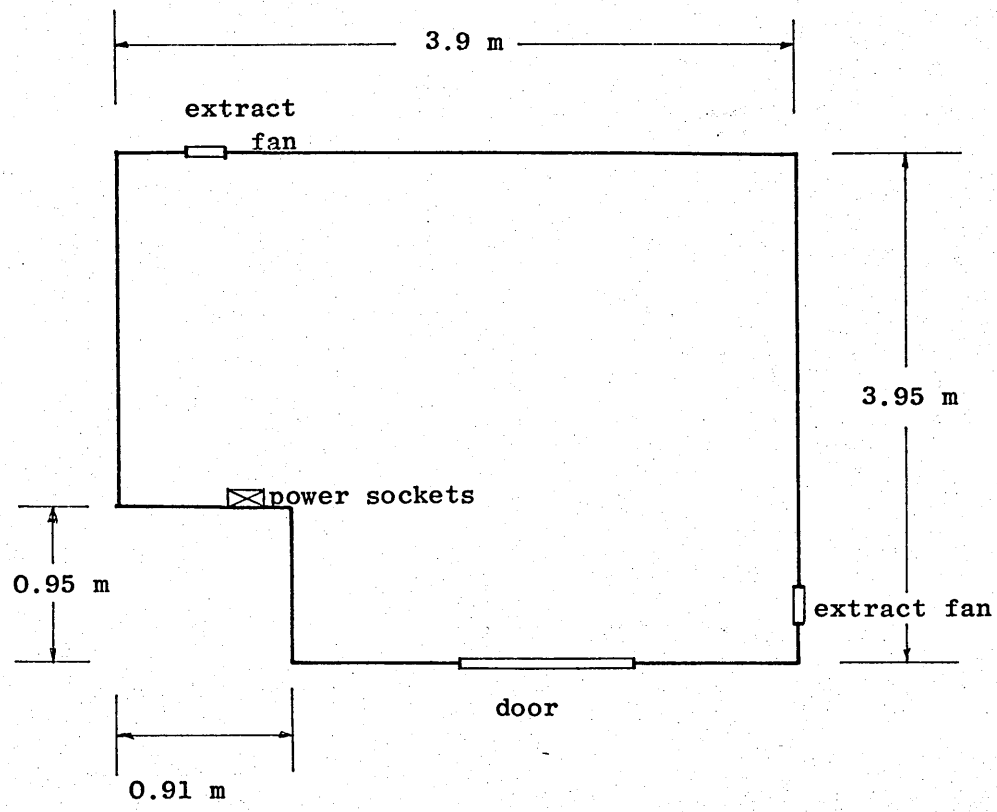

Figure A.1
Floor Plan of Anechoic Chamber

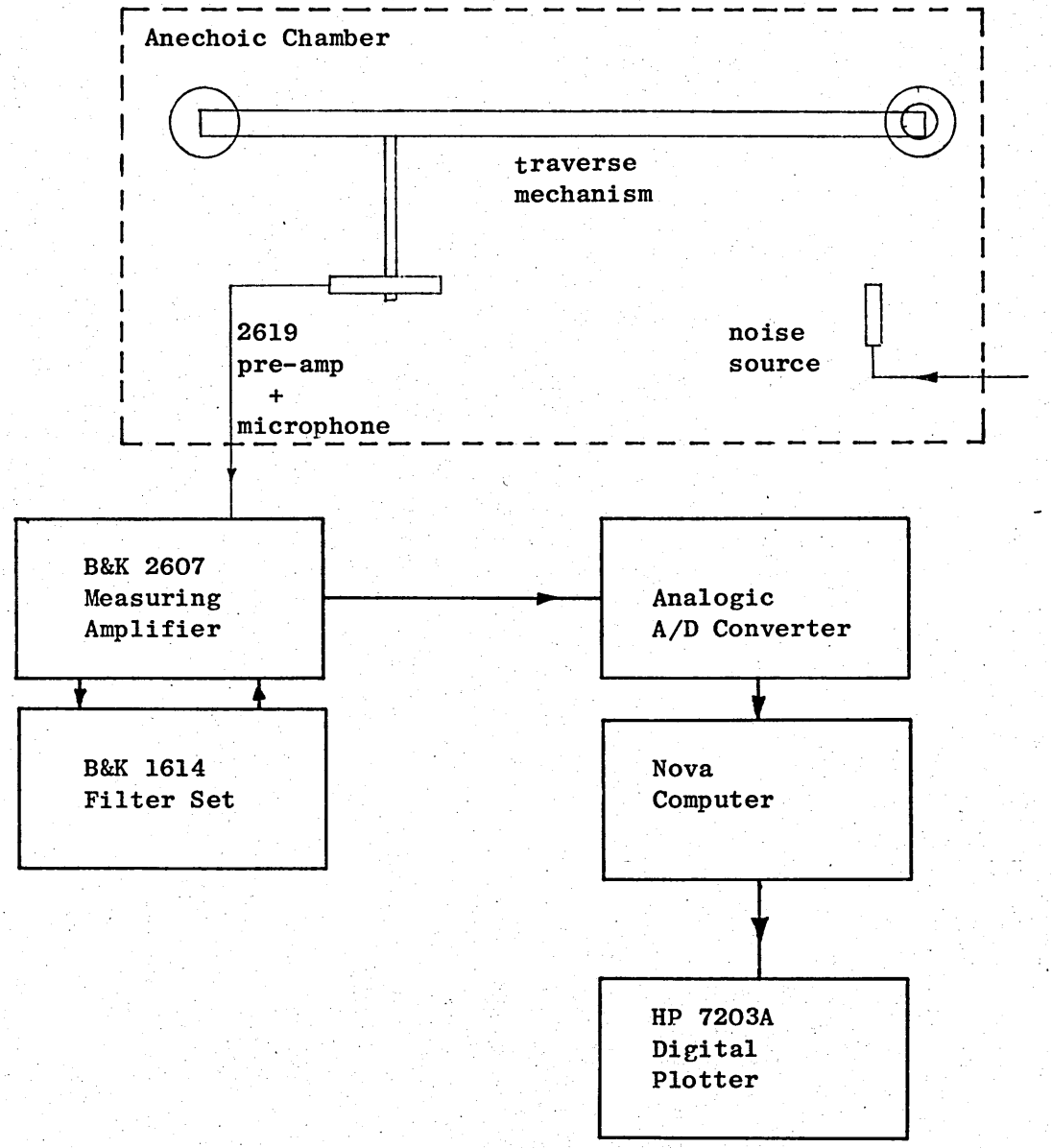

Figure A.2
Block Diagram of the Anechoic Calibration
Experiments Instrumentation

Figure A.3(a)
Spherical Divergence Measurements - Pure Tones ½" Microphone + Protection Grid

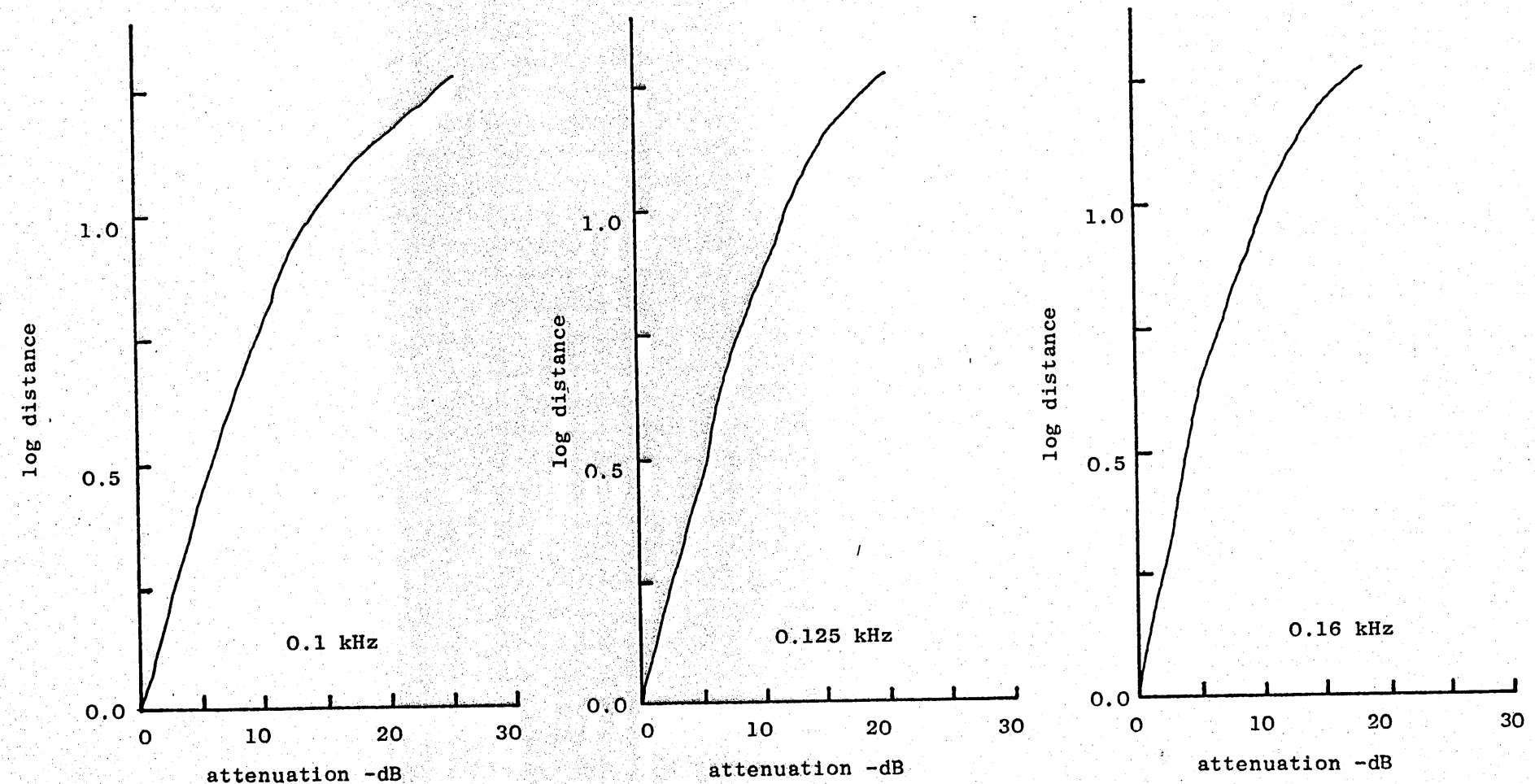

Figure A.3(b)

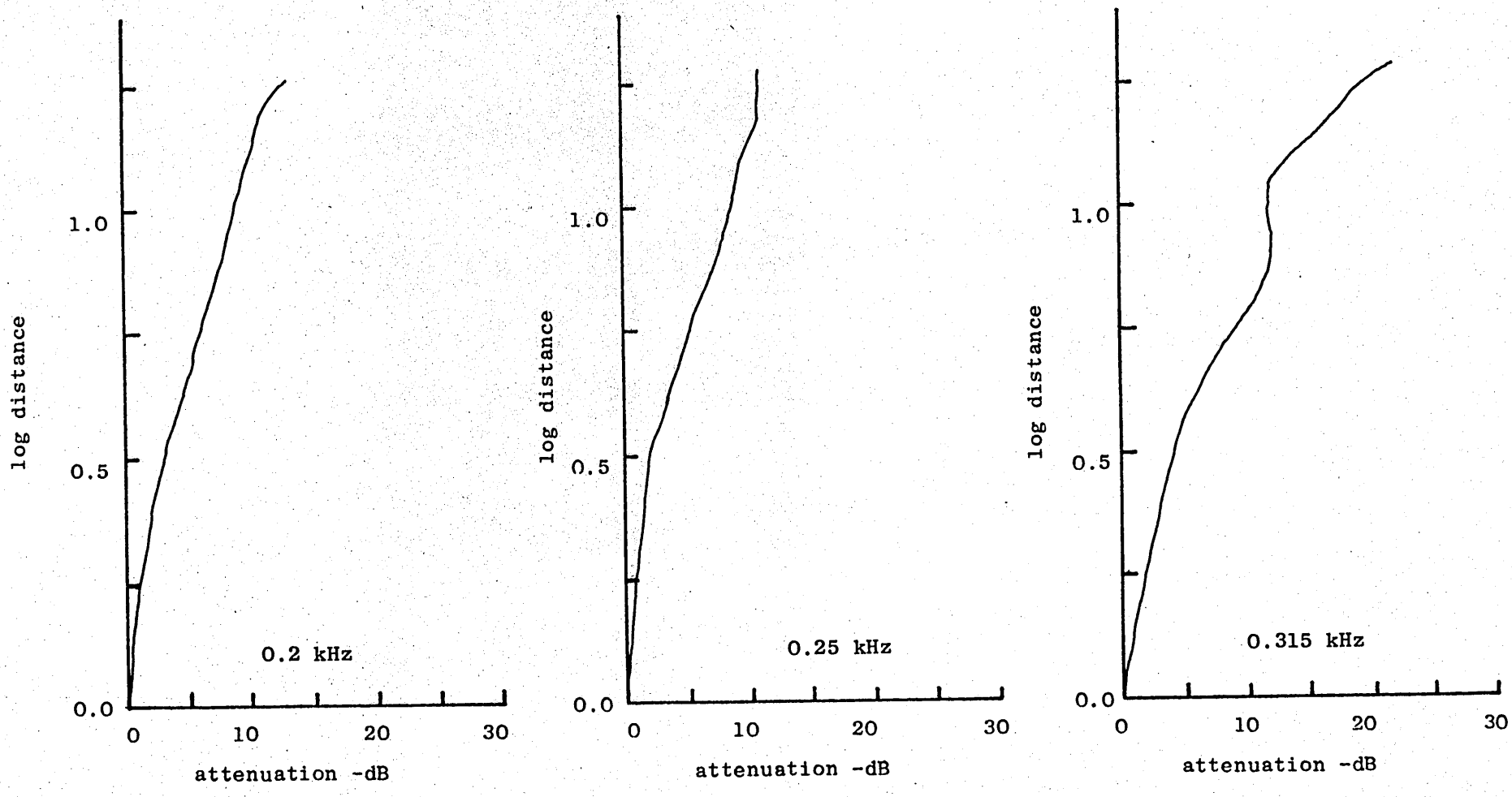
log distance
1.0
0.5
0.0
0.2 kHz
0
10
20
30
attenuation -dB
log distance
1.0
0.5
0.0
0.25 kHz
0
10
20
30
attenuation -dB
log distance
1.0
0.5
0.0
0.315 kHz
0
10
20
30
attenuation -dB

Figure A.3(c)

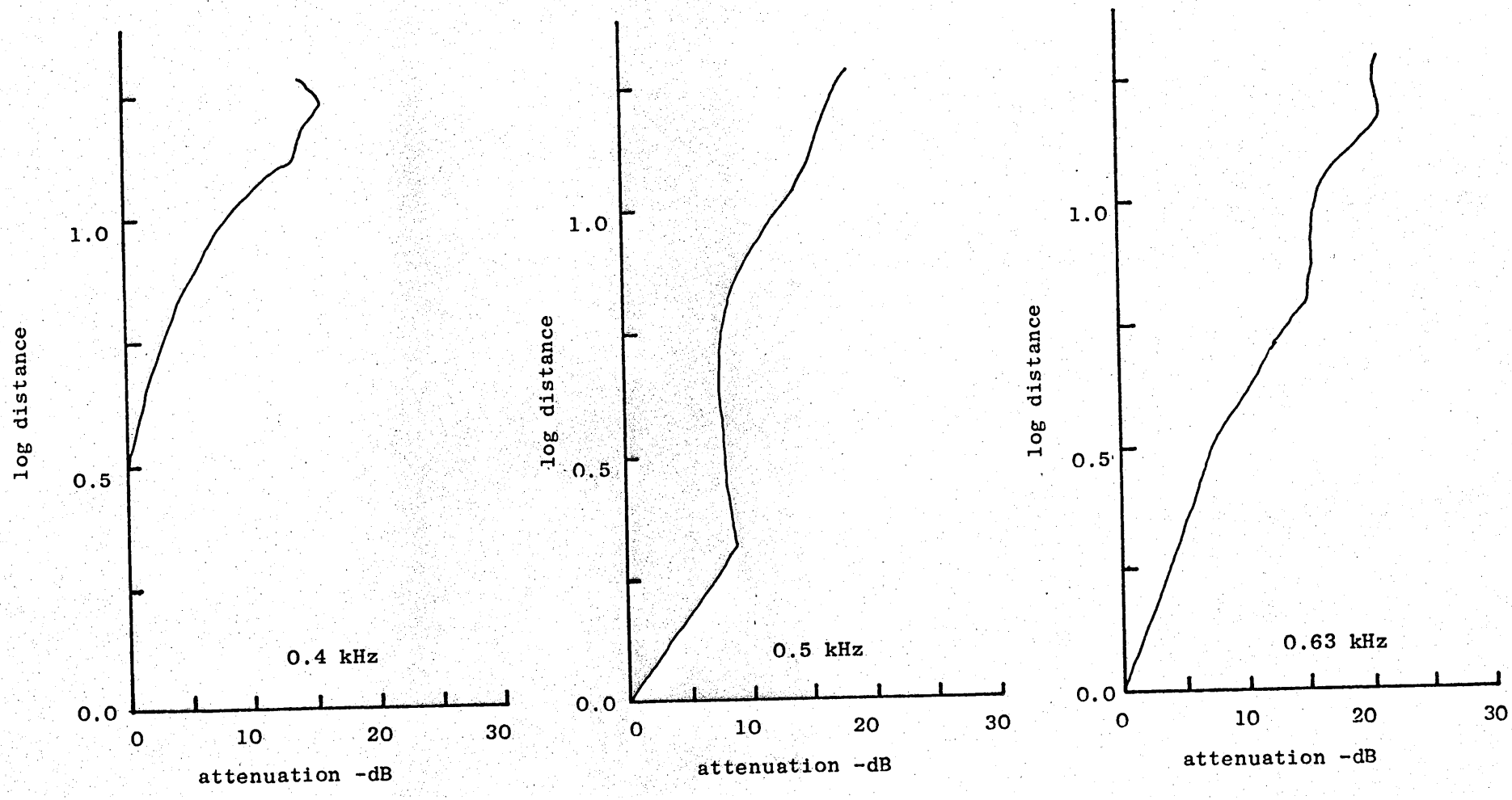
log distance
1.0
0.5
0.0
0.4 kHz
0
10
20
30
attenuation -dB
log distance
1.0
0.5
0.0
0.5 kHz
0
10
20
30
attenuation -dB
log distance
1.0
0.5
0.0
0.63 kHz
0
10
20
30
attenuation -dB

Figure A.3(d)

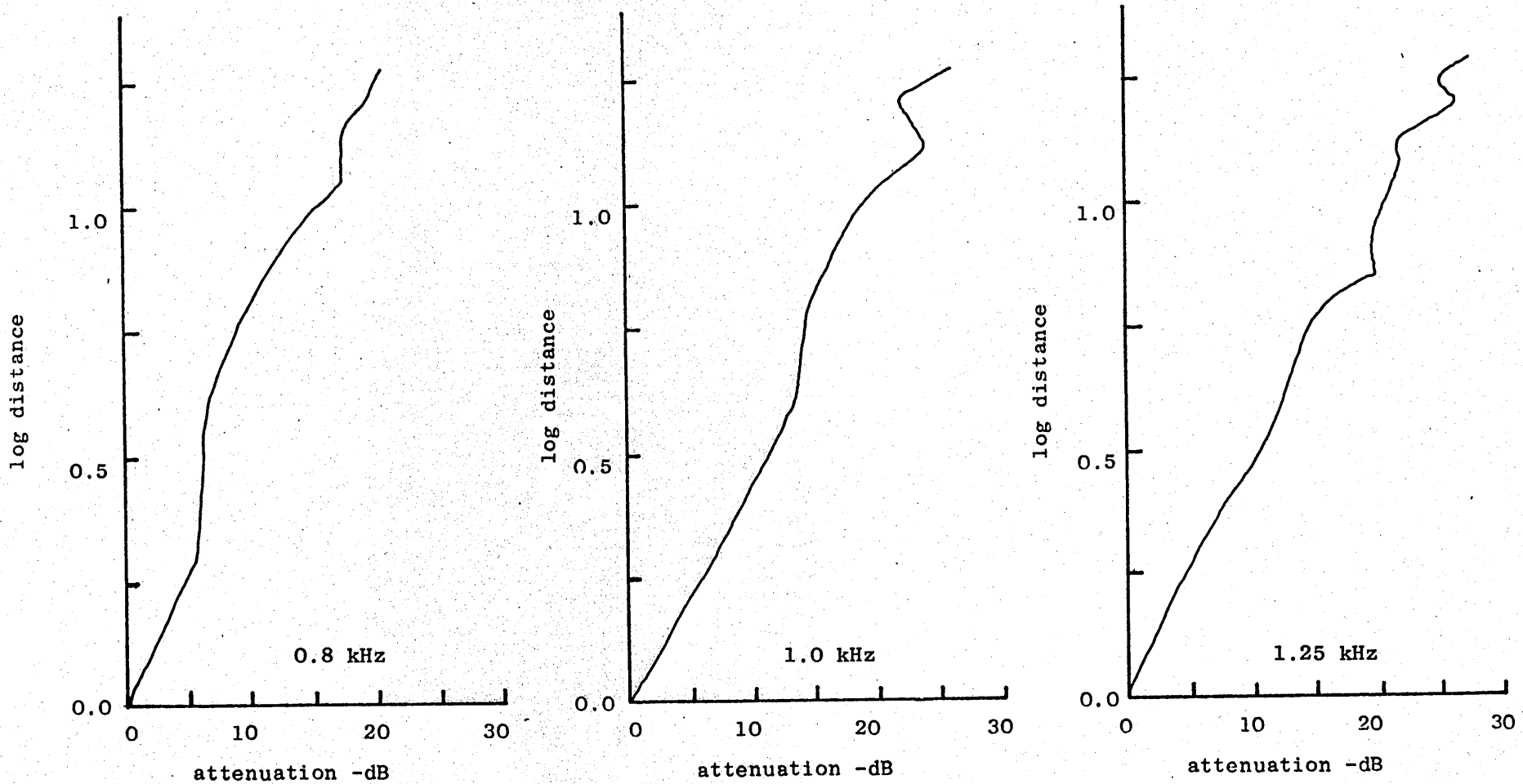
log distance
1.0
0.5
0.0
0.8 kHz
0
10
20
30
attenuation -dB
log distance
1.0
0.5
0.0
1.0 kHz
0
10
20
30
attenuation -dB
log distance
1.0
0.5
0.0
1.25 kHz
0
10
20
30
attenuation -dB

Figure A.3(e)

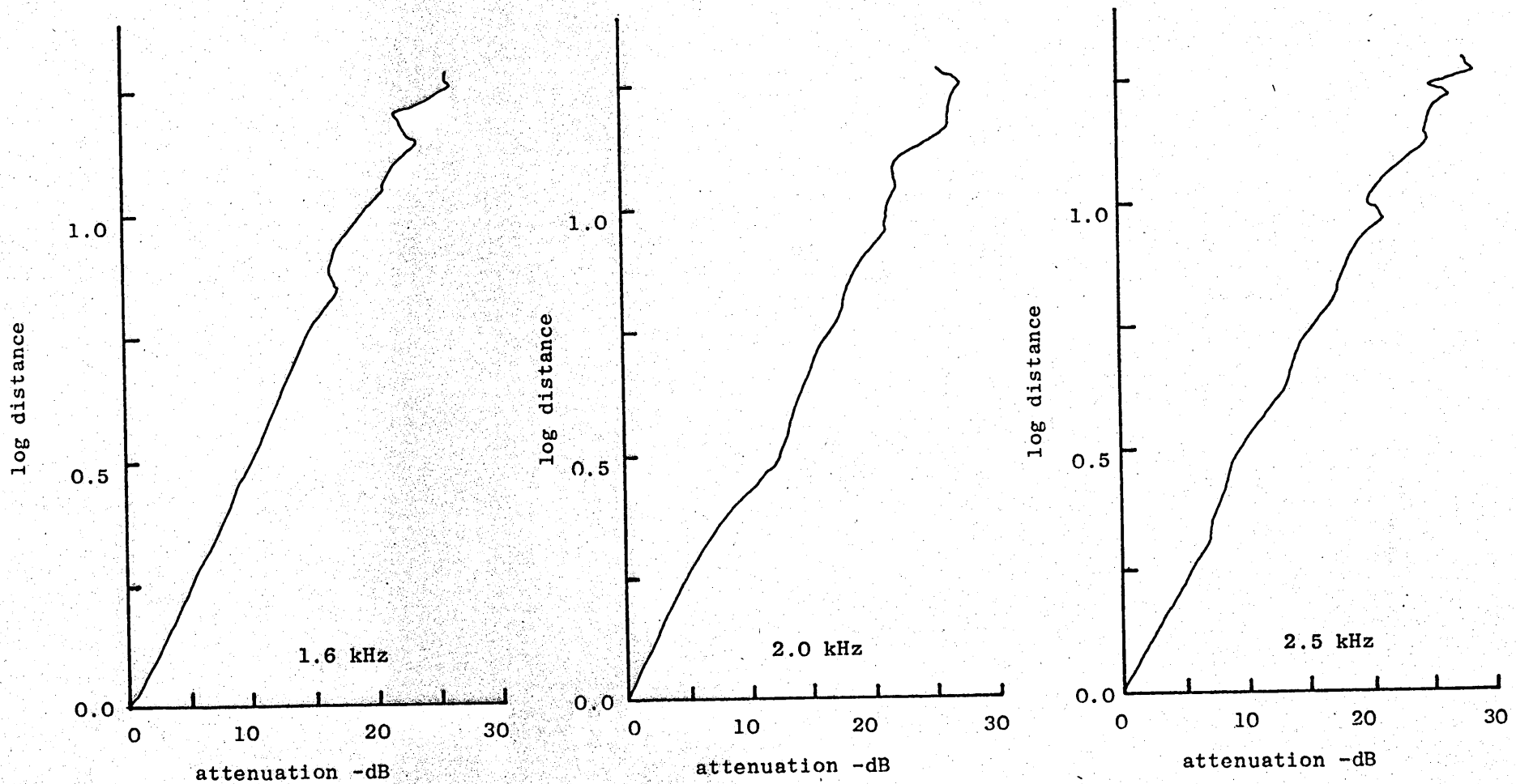
log distance
1.0
0.5
0.0
1.6 kHz
0
10
20
30
attenuation -dB
log distance
1.0
0.5
0.0
2.0 kHz
0
10
20
30
attenuation -dB
log distance
1.0
0.5
0.0
2.5 kHz
0
10
20
30
attenuation -dB

Figure A.3(f)

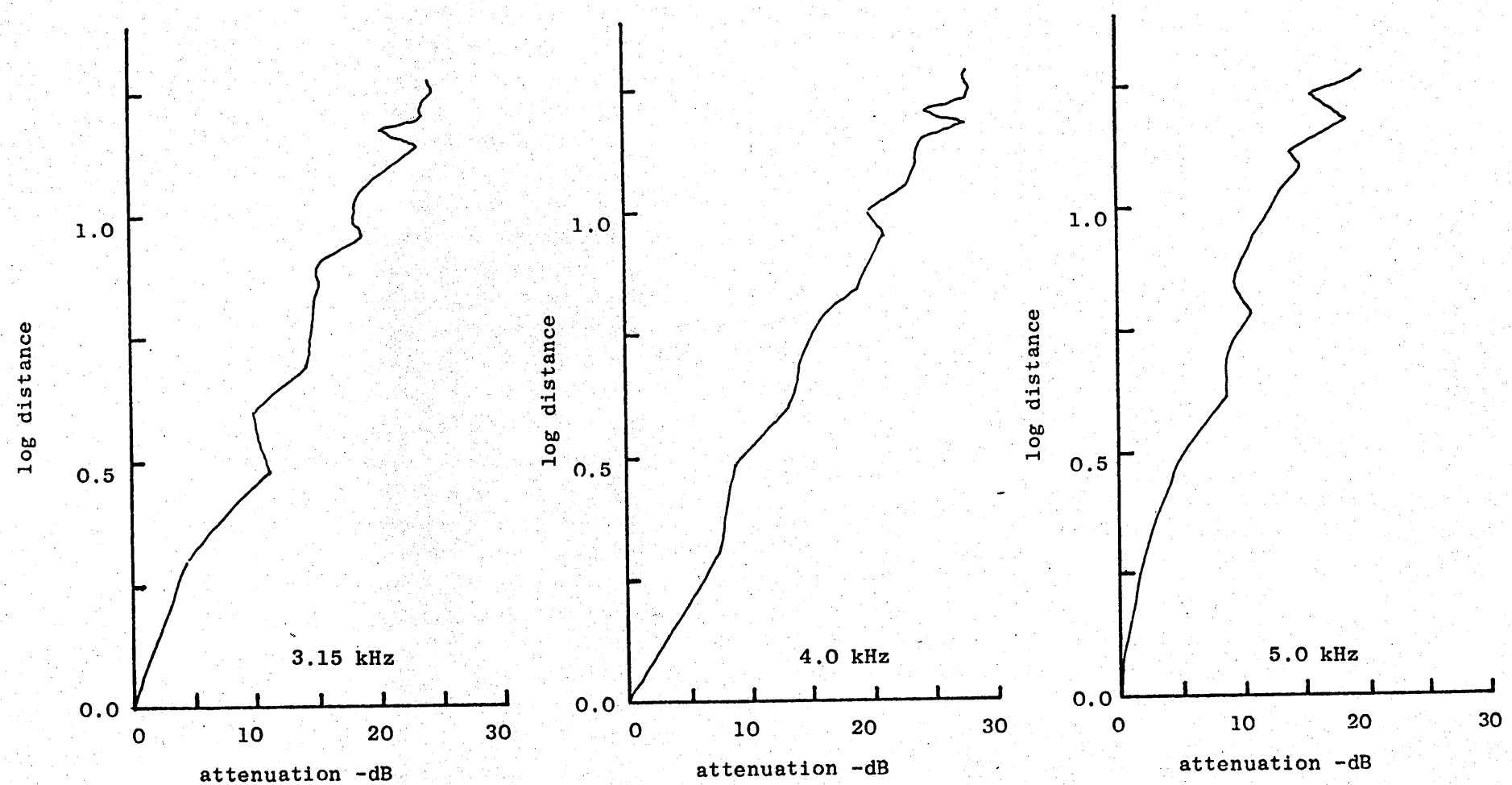
log distance
1.0
0.5
0.0
3.15 kHz
0
10
20
30
attenuation -dB
log distance
1.0
0.5
0.0
4.0 kHz
0
10
20
30
attenuation -dB
log distance
1.0
0.5
0.0
5.0 kHz
0
10
20
30
attenuation -dB

Figure A.3(g)

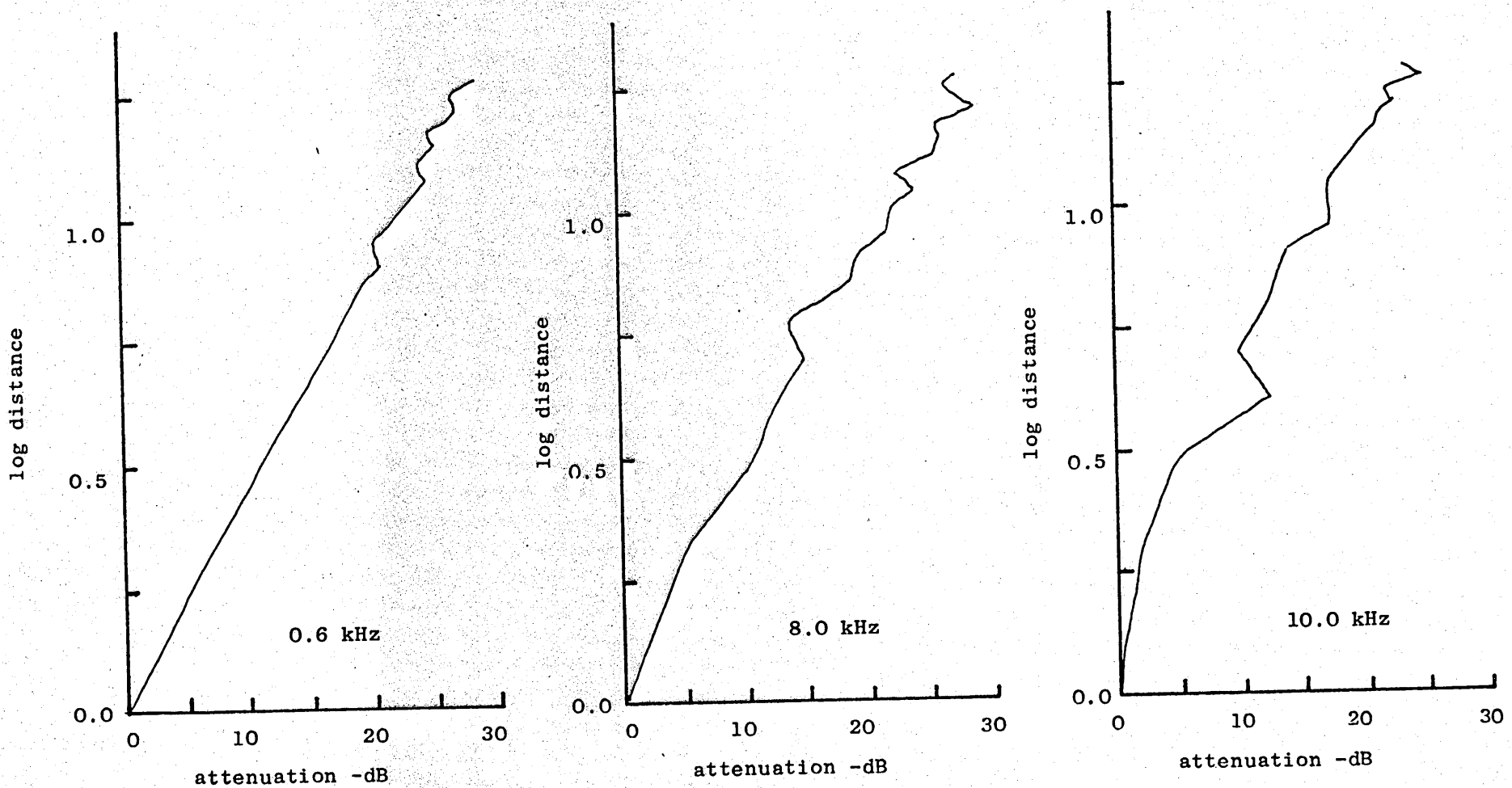
log distance
1.0
0.5
0.0
0.6 kHz
0
10
20
30
attenuation -dB
log distance
1.0
0.5
0.0
8.0 kHz
0
10
20
30
attenuation -dB
log distance
1.0
0.5
0.0
10.0 kHz
0
10
20
30
attenuation -dB

Figure A.4(a)
Spherical Divergence Measurements - Random Noise, ½" Microphone + Protection Grid

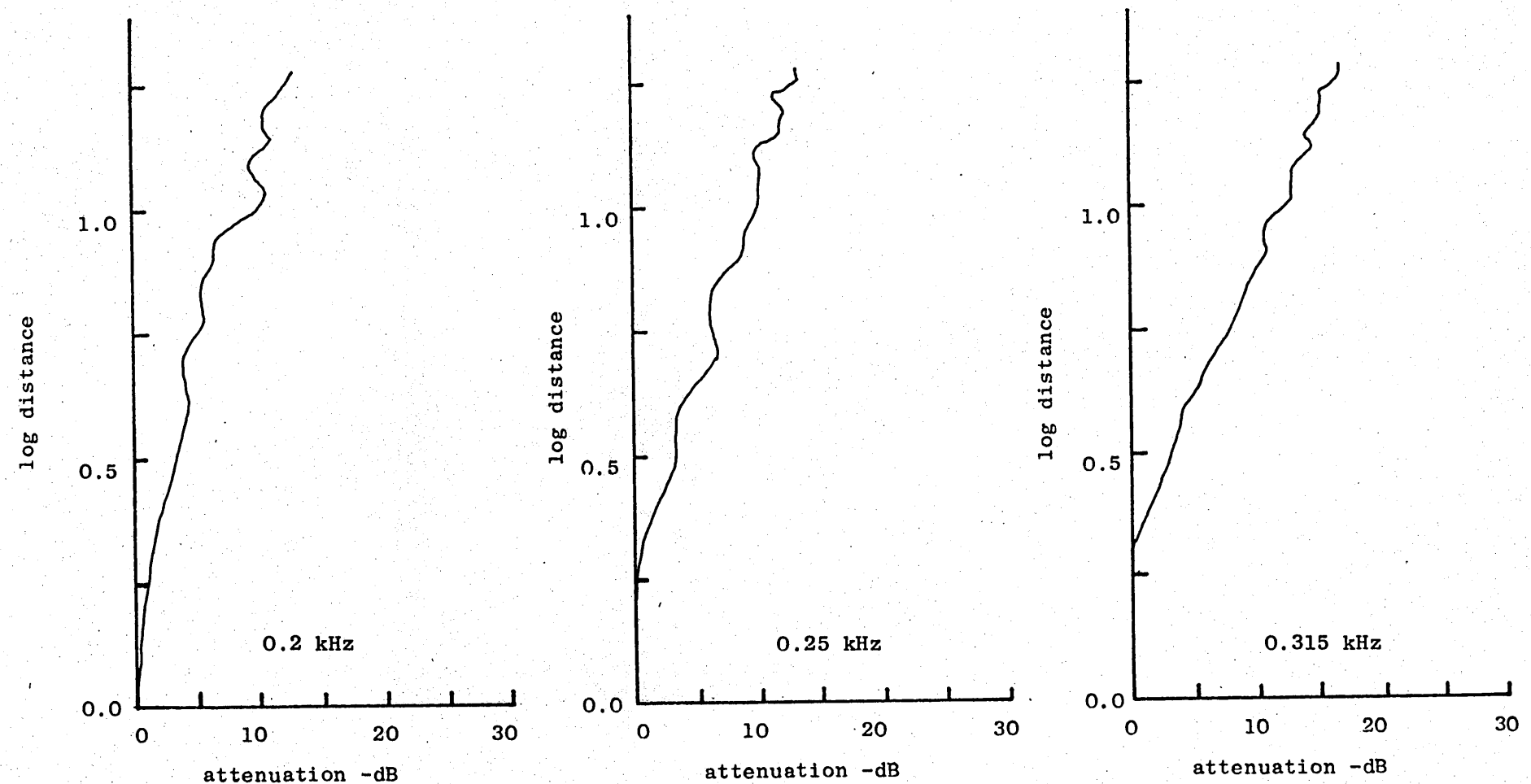

Figure A.4(b)

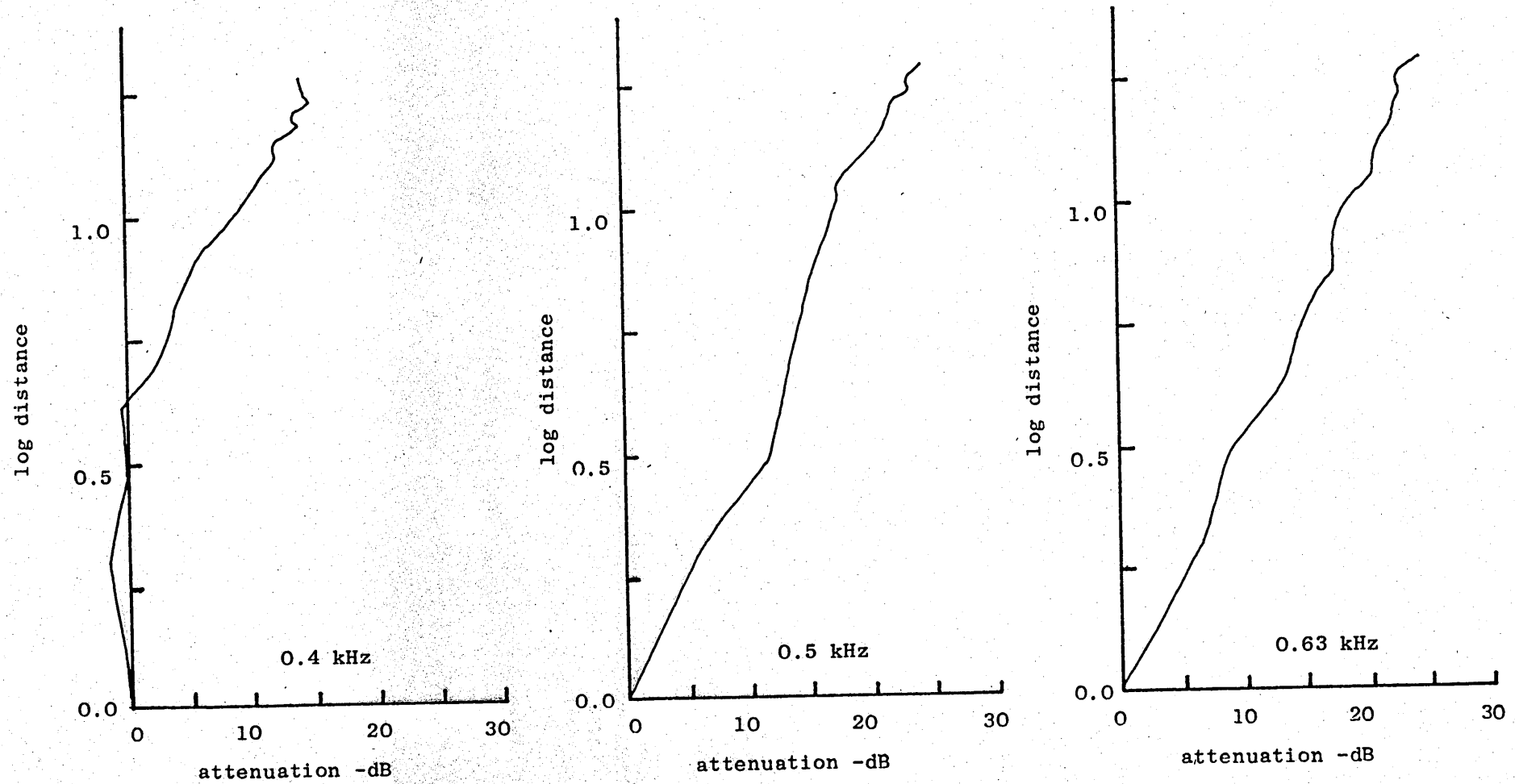
log distance
1.0
0.5
0.0
0.4 kHz
0
10
20
30
attenuation -dB
log distance
1.0
0.5
0.0
0.5 kHz
0
10
20
30
attenuation -dB
log distance
1.0
0.5
0.0
0.63 kHz
0
10
20
30
attenuation -dB

Figure A.4(c)

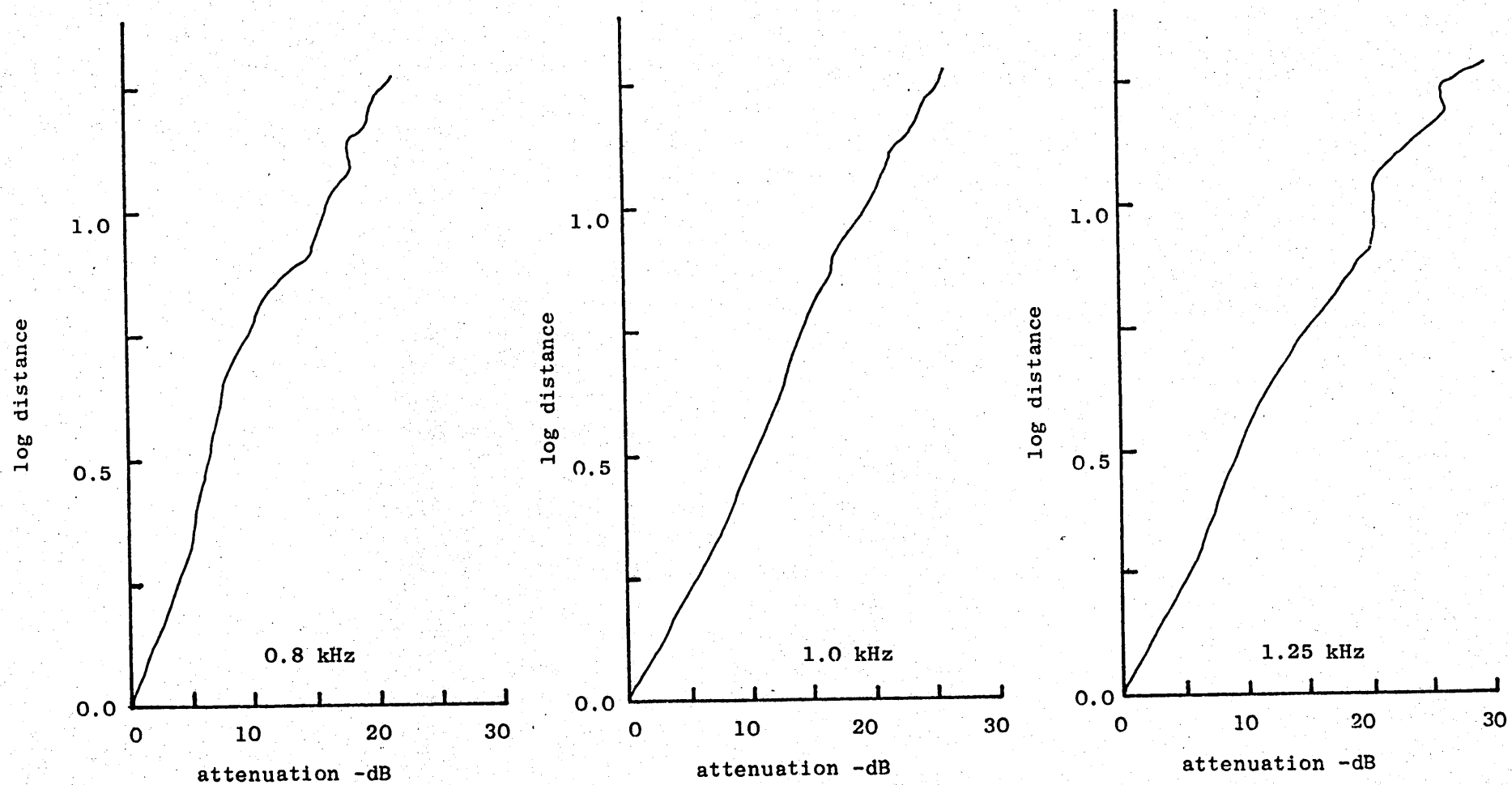
log distance
1.0
0.5
0.0
0.8 kHz
0
10
20
30
attenuation -dB
log distance
1.0
0.5
0.0
1.0 kHz
0
10
20
30
attenuation -dB
log distance
1.0
0.5
0.0
1.25 kHz
0
10
20
30
attenuation -dB

Figure A.4(d)

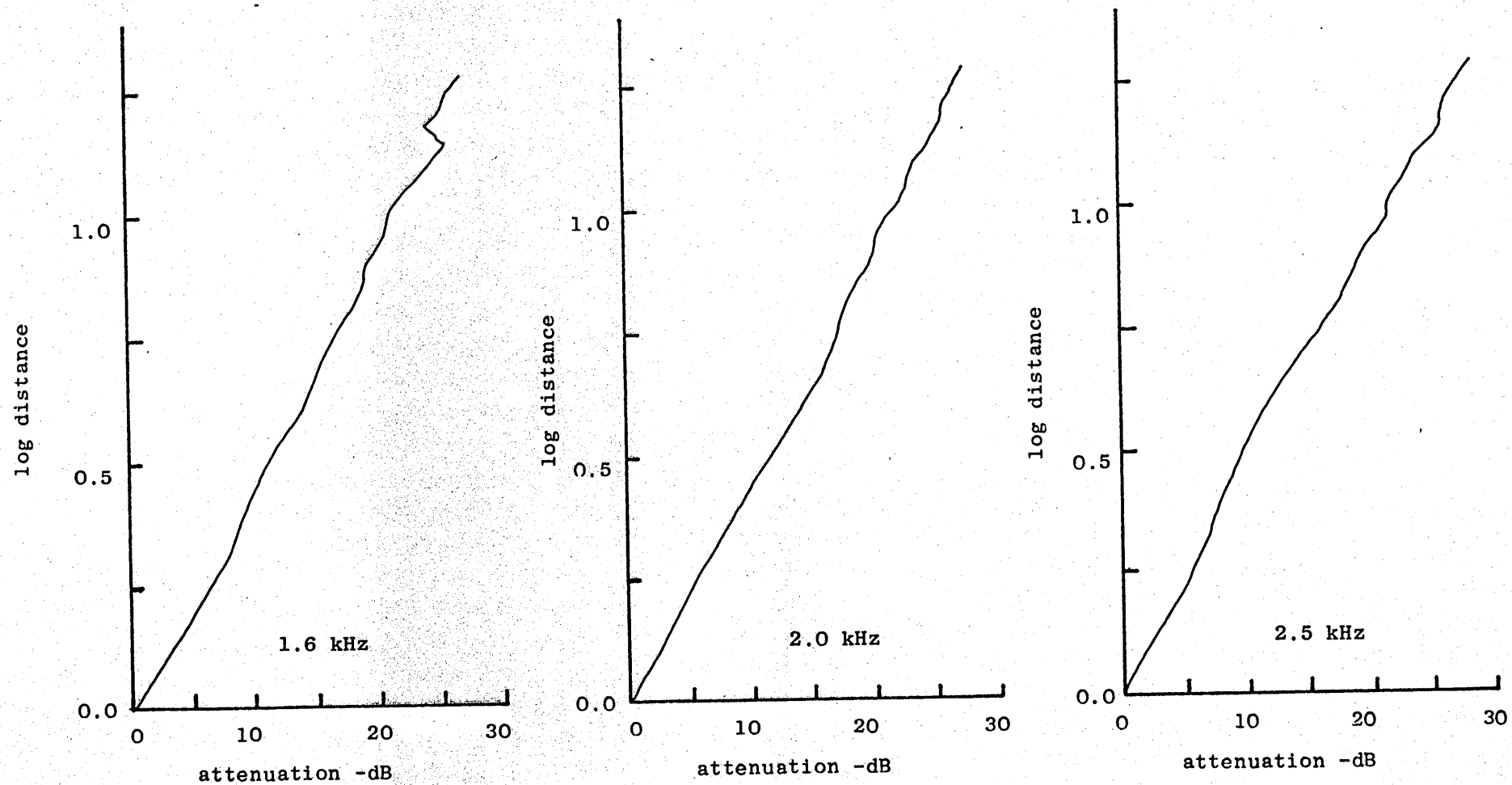
log distance
1.0
0.5
0.0
1.6 kHz
0
10
20
30
attenuation -dB
log distance
1.0
0.5
0.0
2.0 kHz
0
10
20
30
attenuation -dB
log distance
1.0
0.5
0.0
2.5 kHz
0
10
20
30
attenuation -dB

Figure A.4(e)

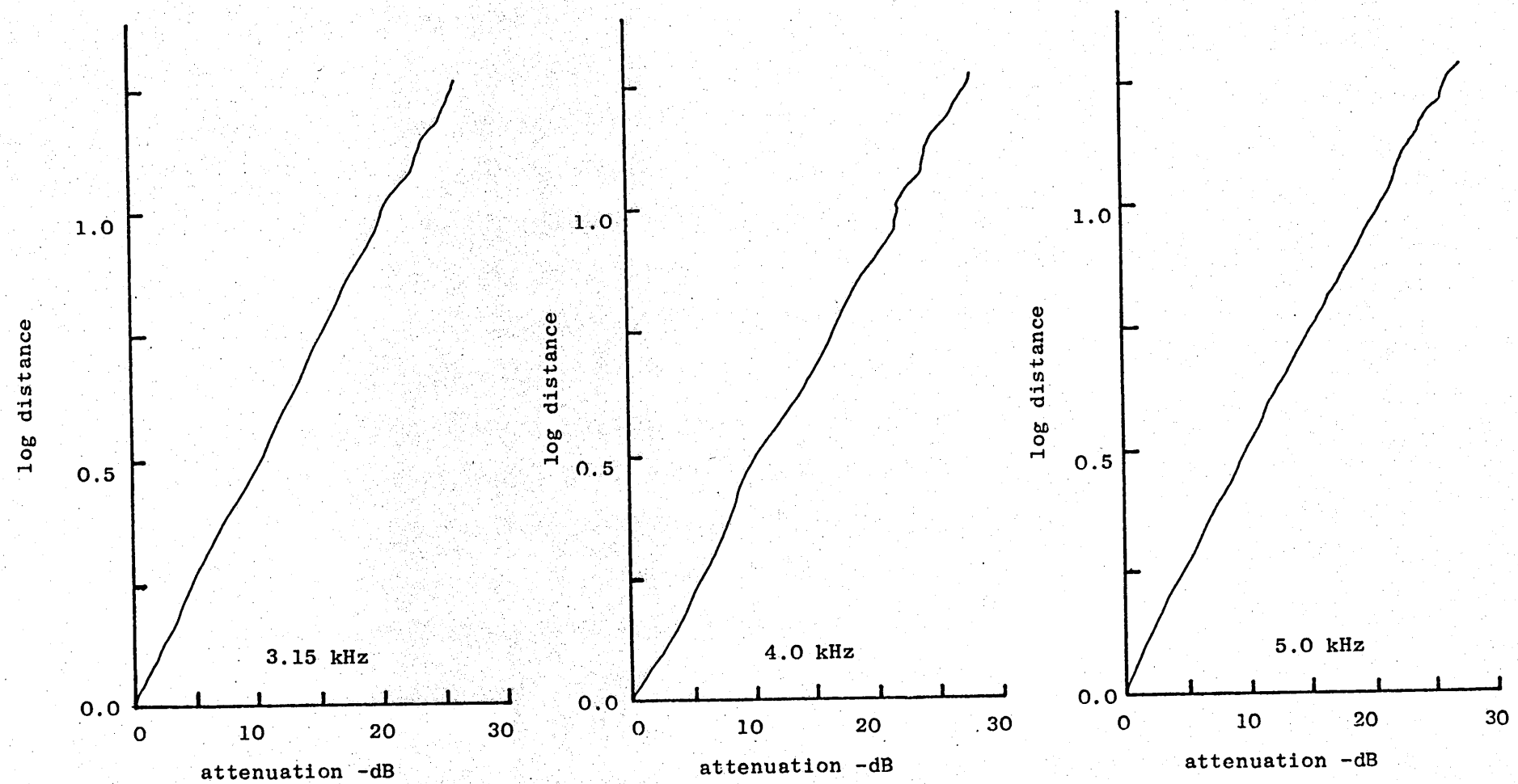
log distance
1.0
0.5
0.0
3.15 kHz
0
10
20
30
attenuation -dB
log distance
1.0
0.5
0.0
4.0 kHz
0
10
20
30
attenuation -dB
log distance
1.0
0.5
0.0
5.0 kHz
0
10
20
30
attenuation -dB

Figure A.4(f)

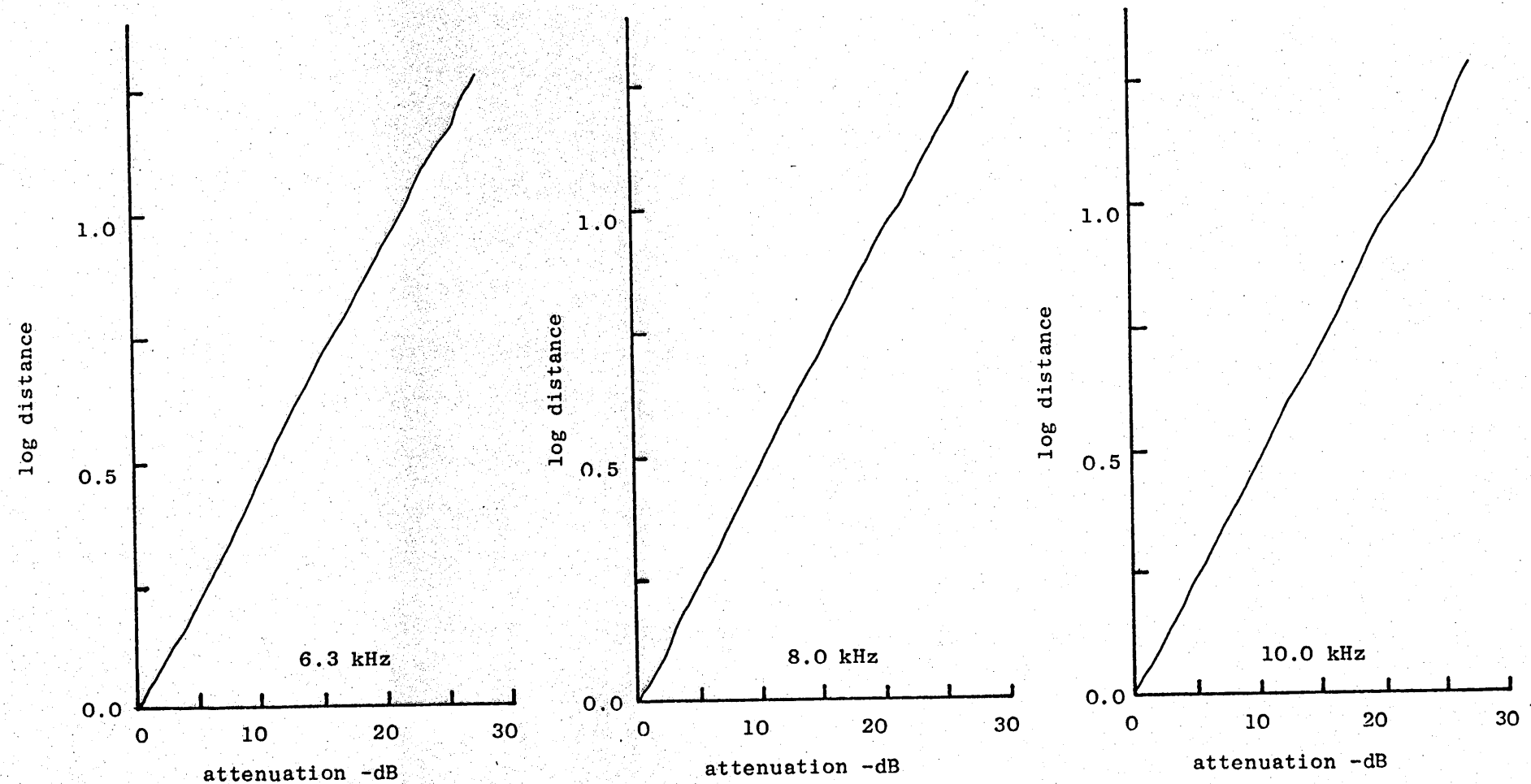
log distance
1.0
0.5
0.0
6.3 kHz
0
10
20
30
attenuation -dB
log distance
1.0
0.5
0.0
8.0 kHz
0
10
20
30
attenuation -dB
log distance
1.0
0.5
0.0
10.0 kHz
0
10
20
30
attenuation -dB

Figure A.4(g)

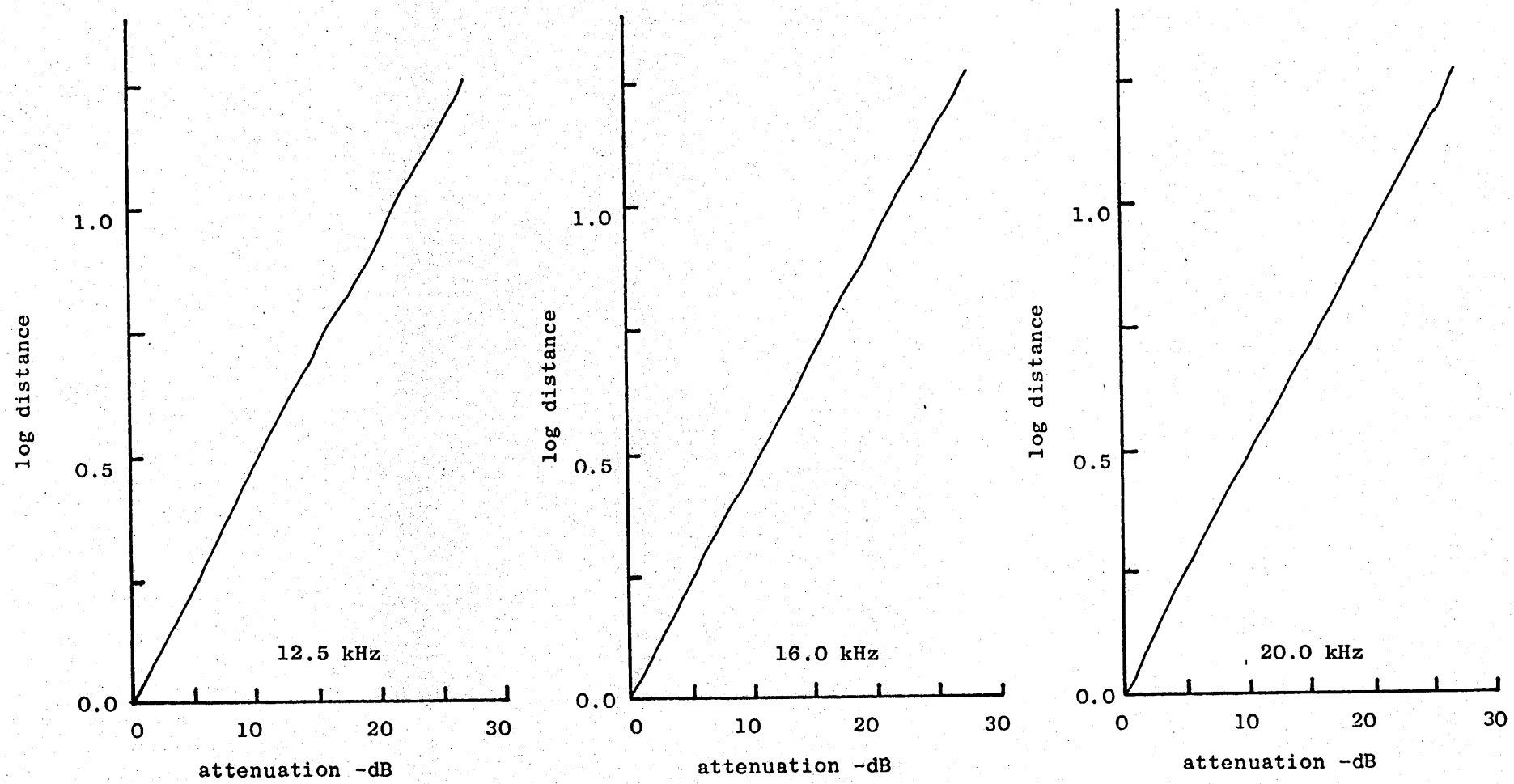
log distance
1.0
0.5
0.0
12.5 kHz
0
10
20
30
attenuation -dB
log distance
1.0
0.5
0.0
16.0 kHz
0
10
20
30
attenuation -dB
log distance
1.0
0.5
0.0
20.0 kHz
0
10
20
30
attenuation -dB

Figure A.5(a)
Spherical Divergence Measurements - Air Jet Source $\frac{1}{4}$" Microphone + Protection Grid

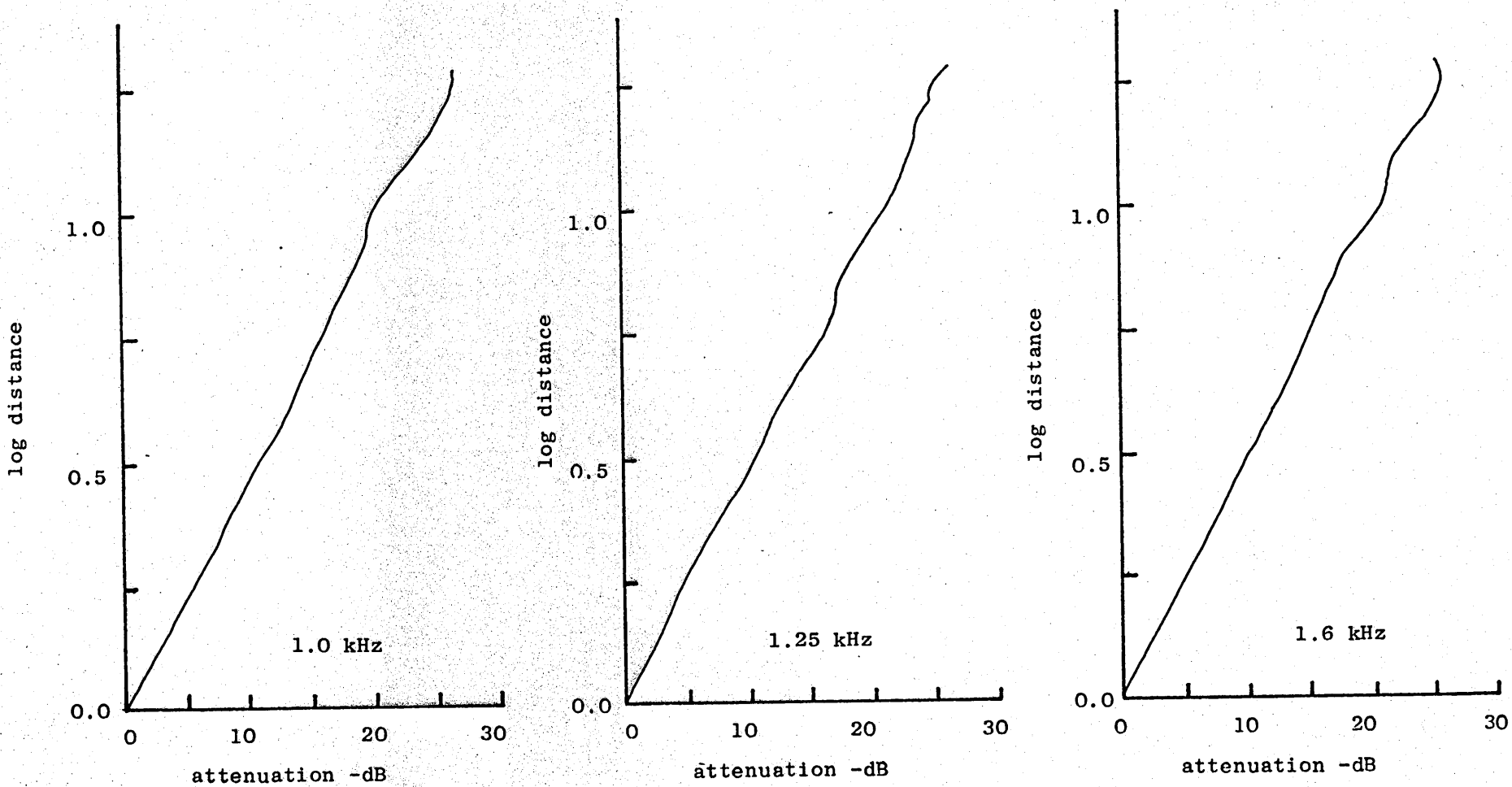

Figure A.5(b)

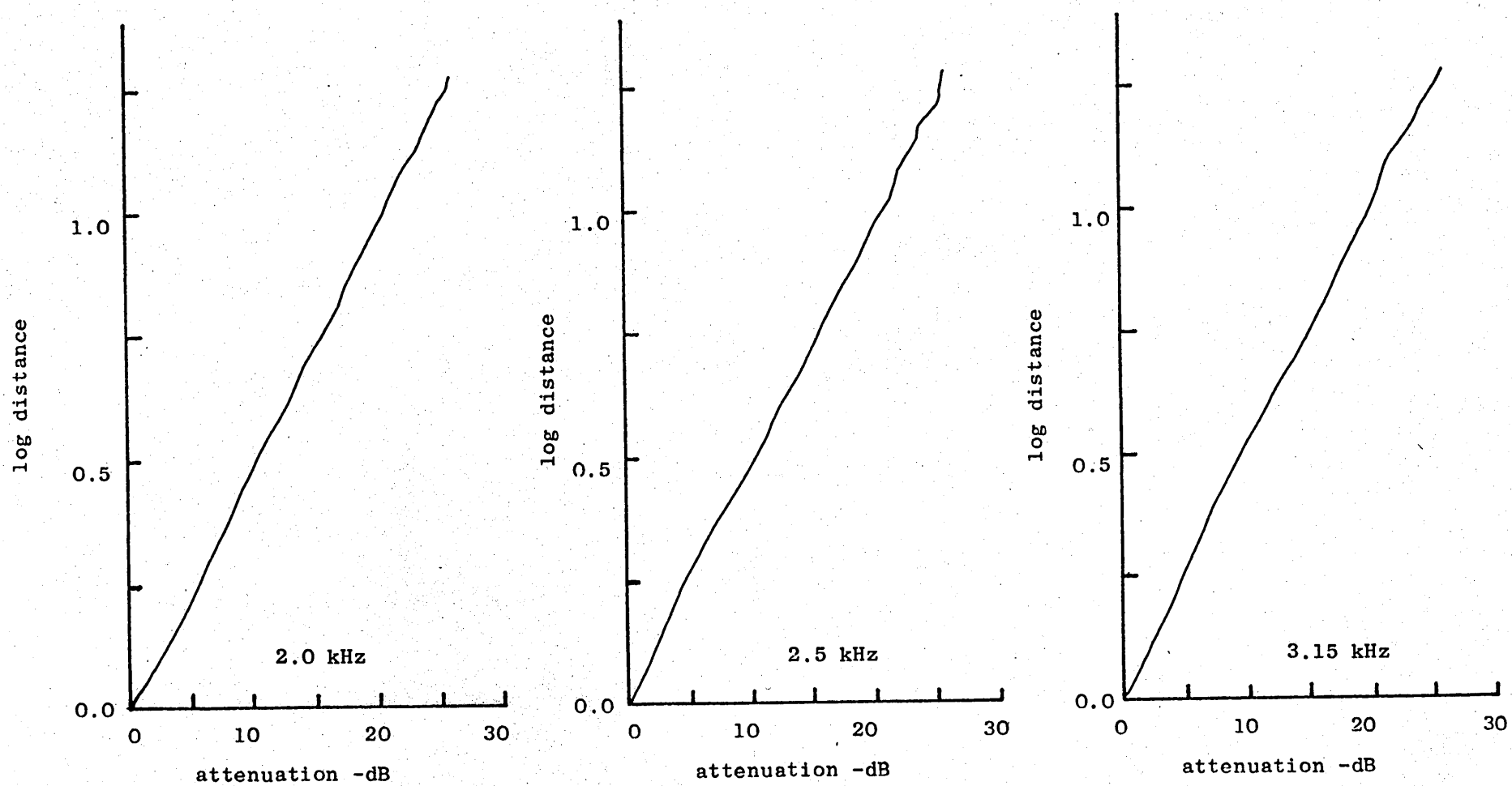
log distance
1.0
0.5
0.0
2.0 kHz
0
10
20
30
attenuation -dB
log distance
1.0
0.5
0.0
2.5 kHz
0
10
20
30
attenuation -dB
log distance
1.0
0.5
0.0
3.15 kHz
0
10
20
30
attenuation -dB

Figure A.5(c)

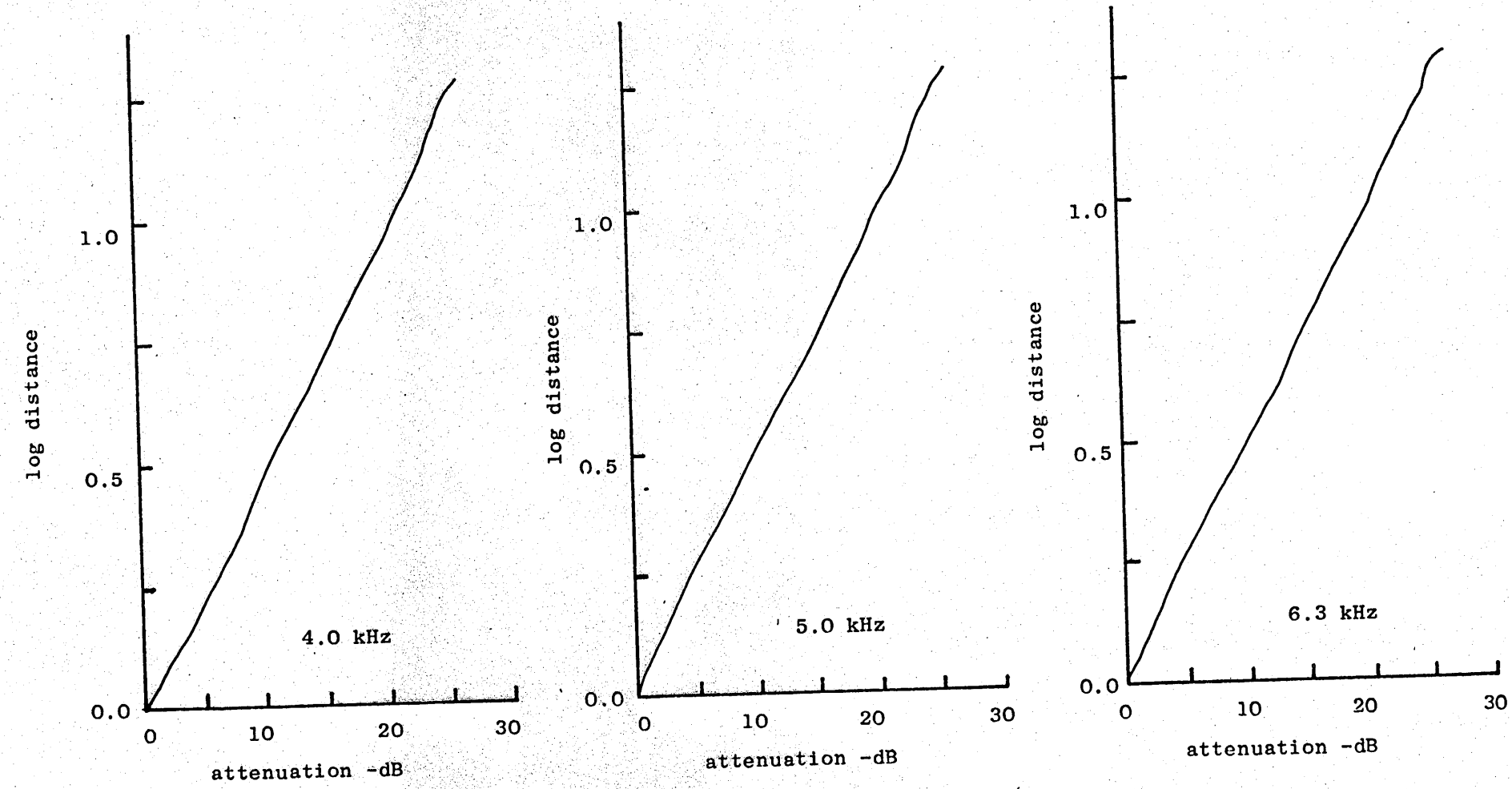
log distance
1.0
0.5
0.0
0
10
20
30
attenuation -dB
4.0 kHz
log distance
1.0
0.5
0.0
0
10
20
30
attenuation -dB
5.0 kHz
log distance
1.0
0.5
0.0
0
10
20
30
attenuation -dB
6.3 kHz

Figure A.5 (d)

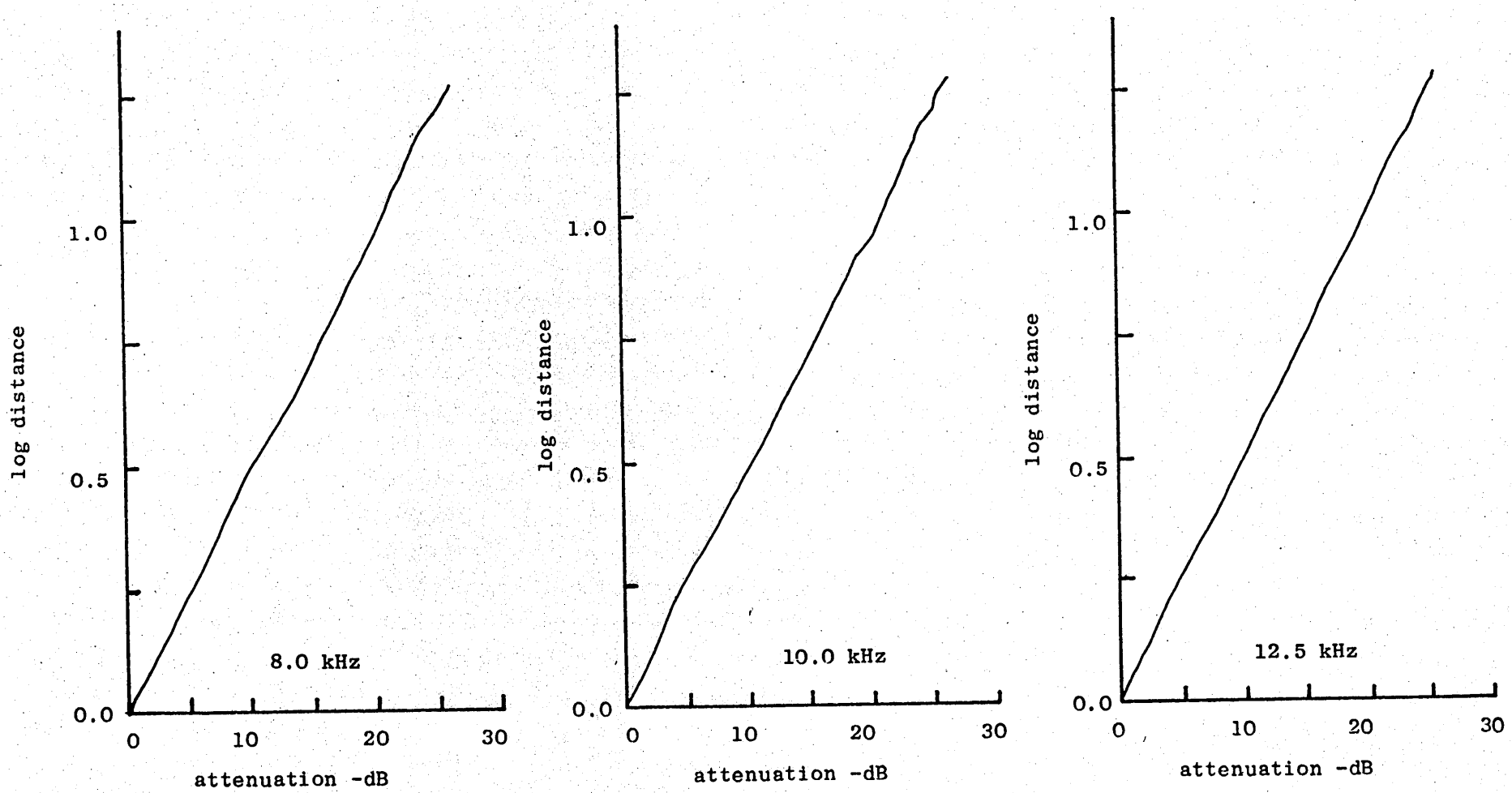
log distance
1.0
0.5
0.0
8.0 kHz
0
10
20
30
attenuation -dB
log distance
1.0
0.5
0.0
10.0 kHz
0
10
20
30
attenuation -dB
log distance
1.0
0.5
0.0
12.5 kHz
0
10
20
30
attenuation -dB

Figure A.5(e)

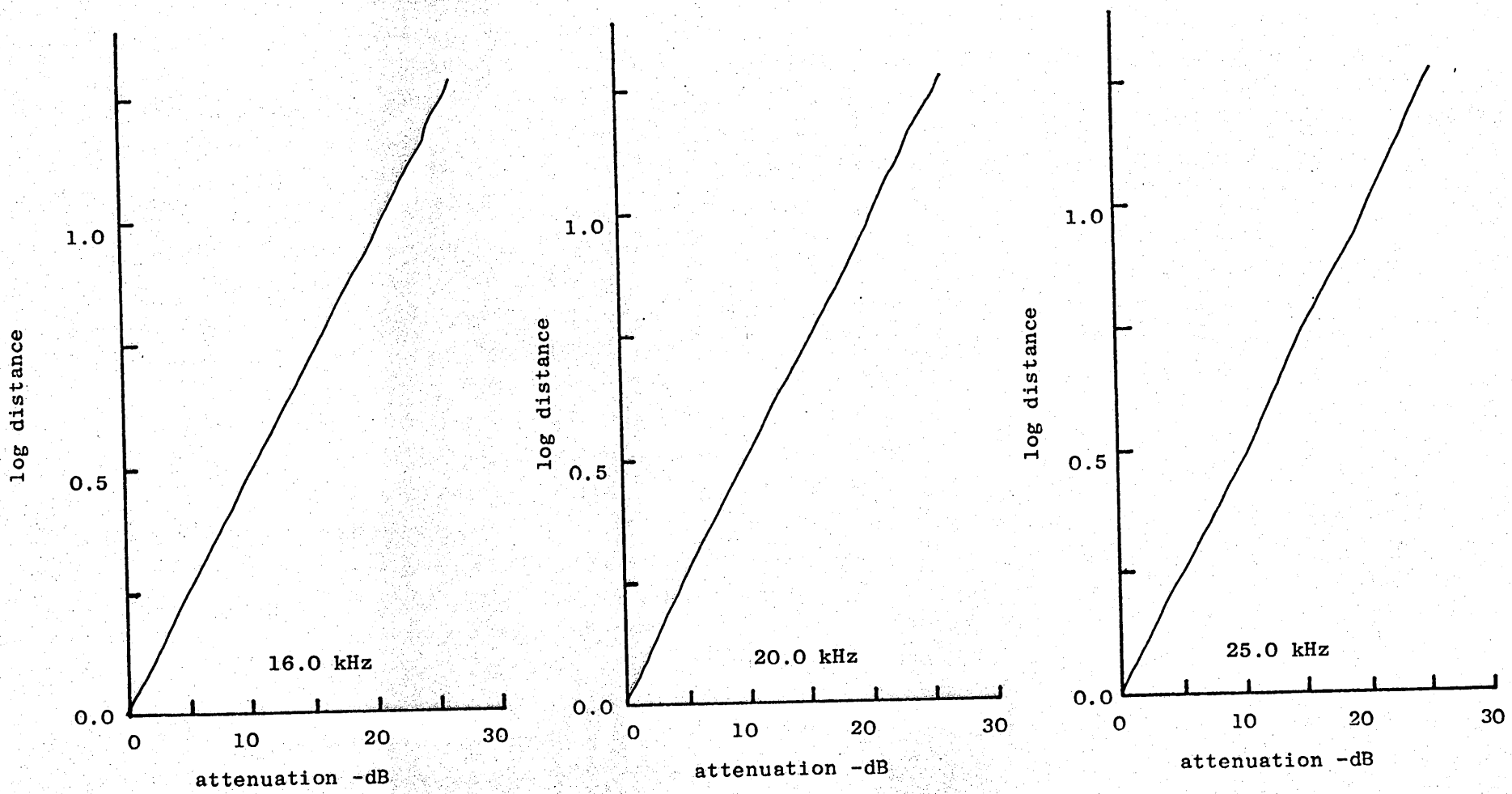
log distance
1.0
0.5
0.0
16.0 kHz
0
10
20
30
attenuation -dB
log distance
1.0
0.5
0.0
20.0 kHz
0
10
20
30
attenuation -dB
log distance
1.0
0.5
0.0
25.0 kHz
0
10
20
30
attenuation -dB

Figure A.5(f)

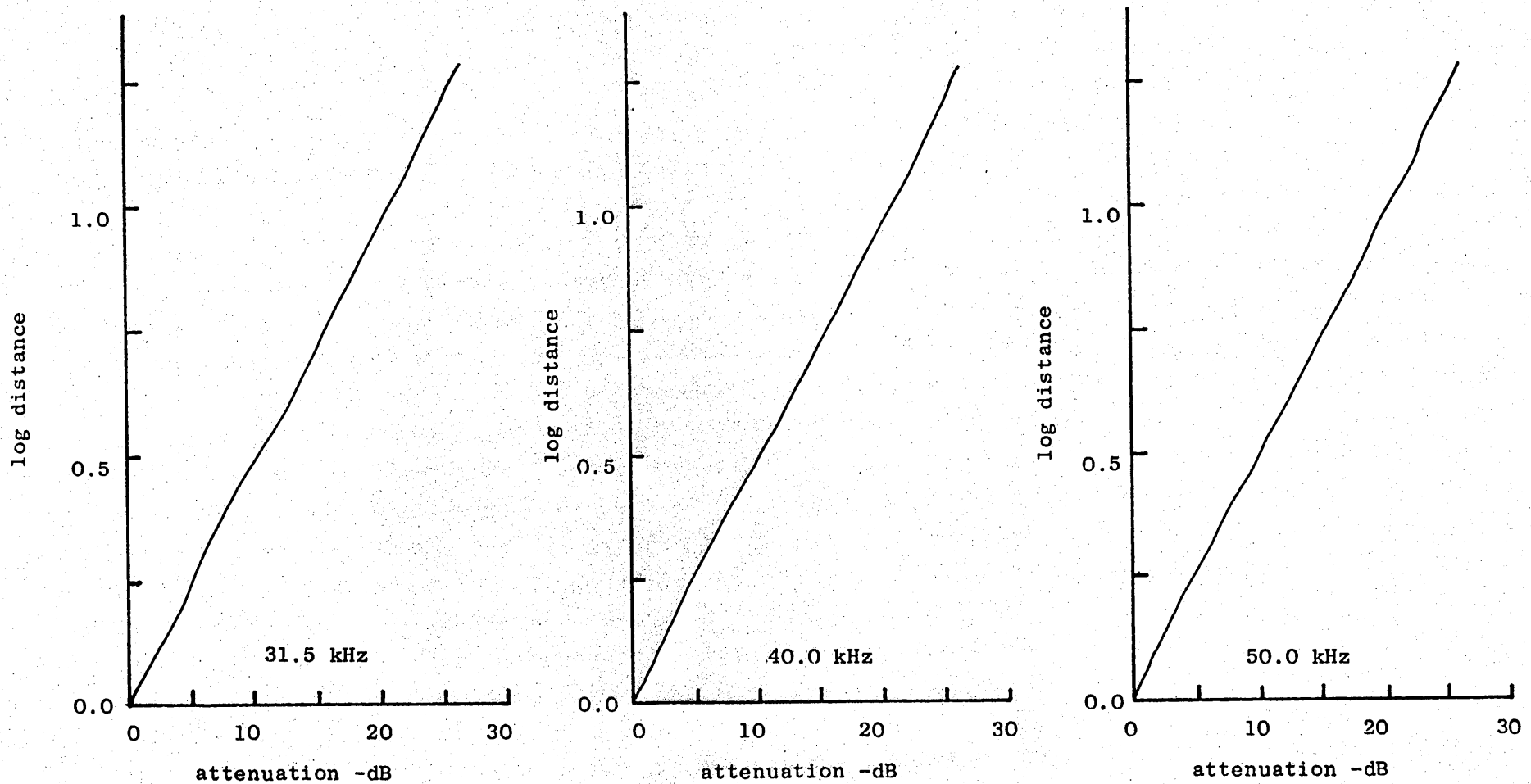
log distance
1.0
0.5
0.0
31.5 kHz
0
10
20
30
attenuation -dB
log distance
1.0
0.5
0.0
40.0 kHz
0
10
20
30
attenuation -dB
log distance
1.0
0.5
0.0
50.0 kHz
0
10
20
30
attenuation -dB

Figure A.5(g)

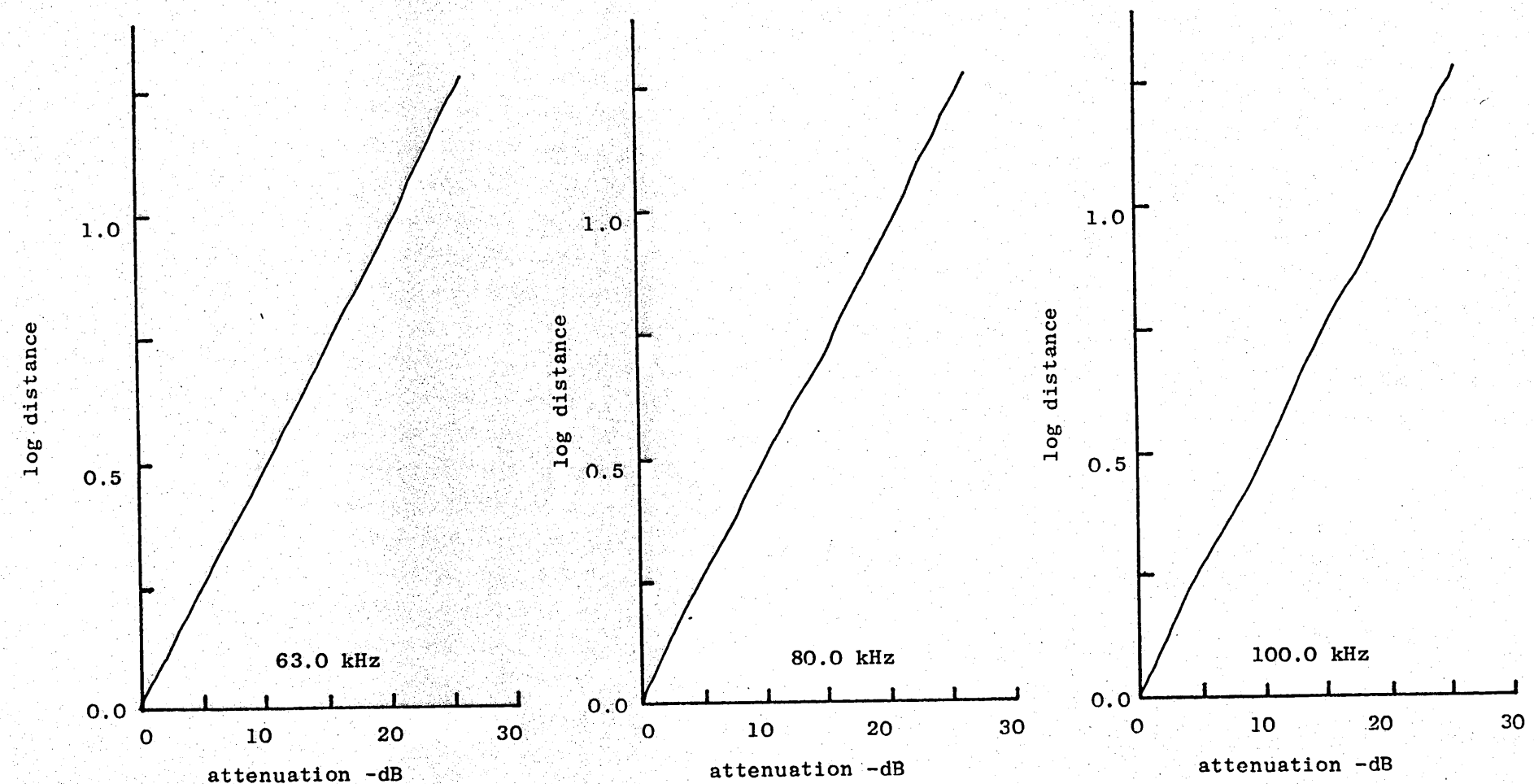
log distance
1.0
0.5
0.0
63.0 kHz
0
10
20
30
attenuation -dB
log distance
1.0
0.5
0.0
80.0 kHz
0
10
20
30
attenuation -dB
log distance
1.0
0.5
0.0
100.0 kHz
0
10
20
30
attenuation -dB

Figure A.6(a)
Spherical Divergence Measurements - Air Jet Source ¼" Microphone without Protection Grid

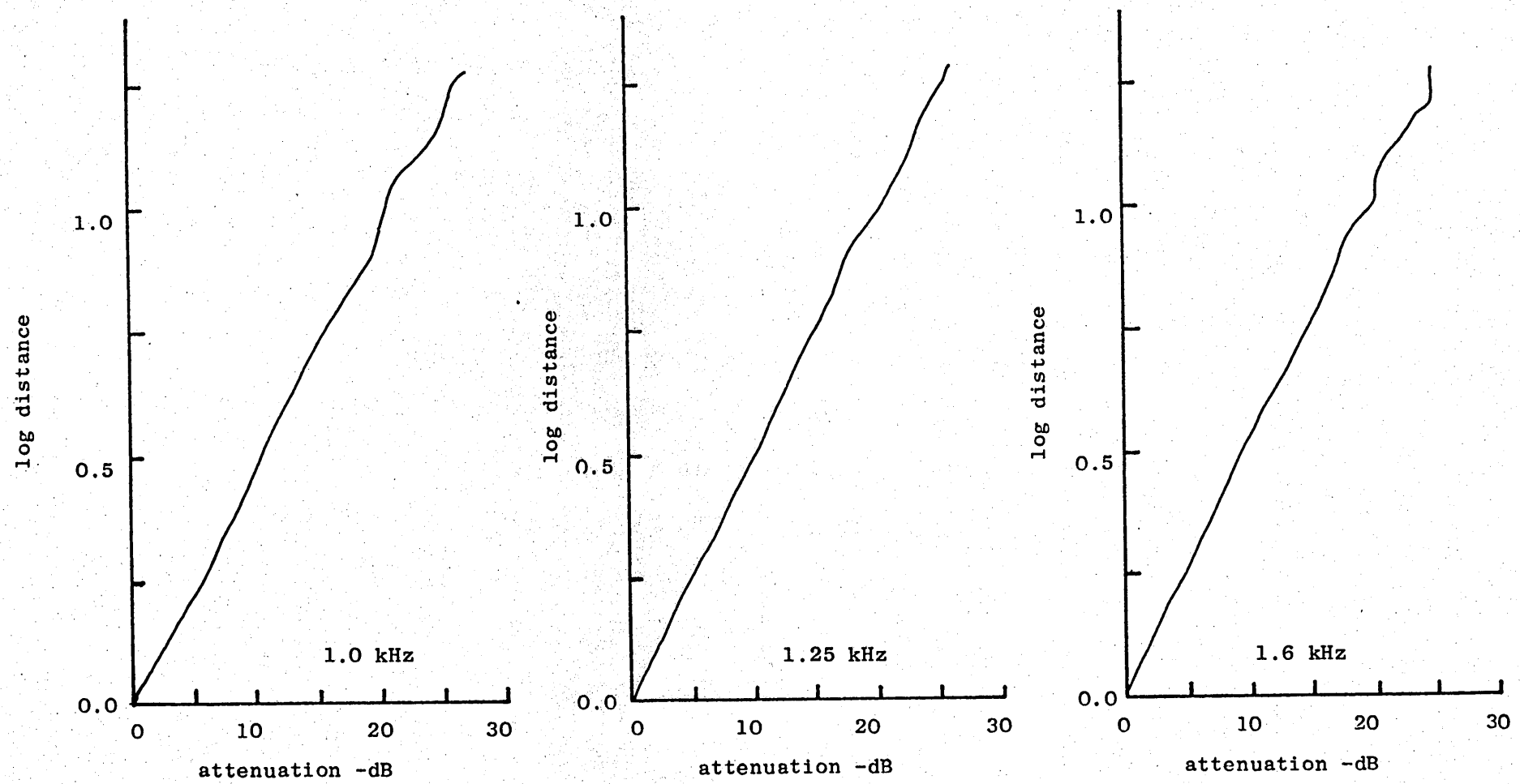

Figure A.6(b)

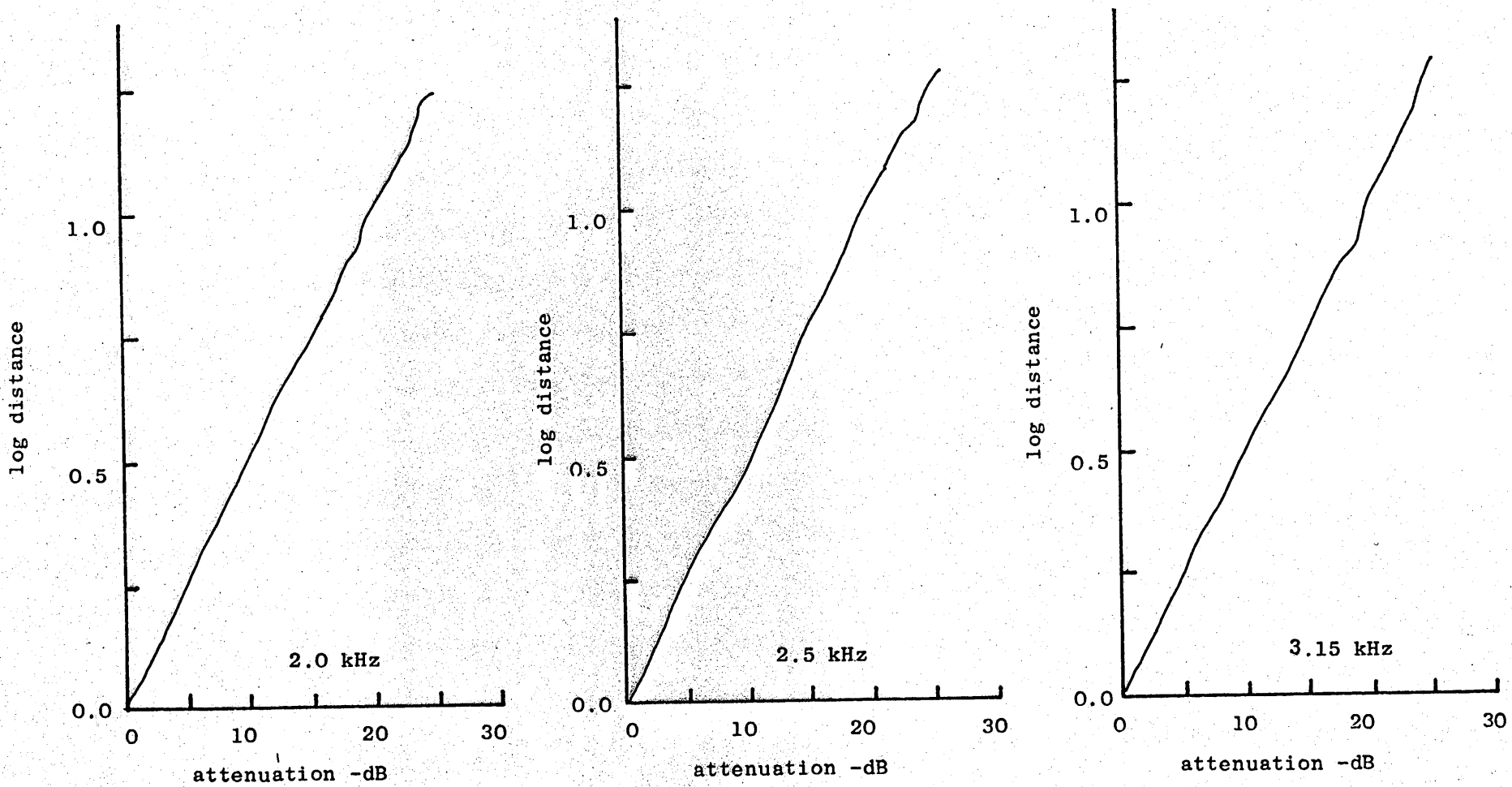
log distance
1.0
0.5
0.0
2.0 kHz
0
10
20
30
attenuation -dB
log distance
1.0
0.5
0.0
2.5 kHz
0
10
20
30
attenuation -dB
log distance
1.0
0.5
0.0
3.15 kHz
0
10
20
30
attenuation -dB

Figure A.6(c)

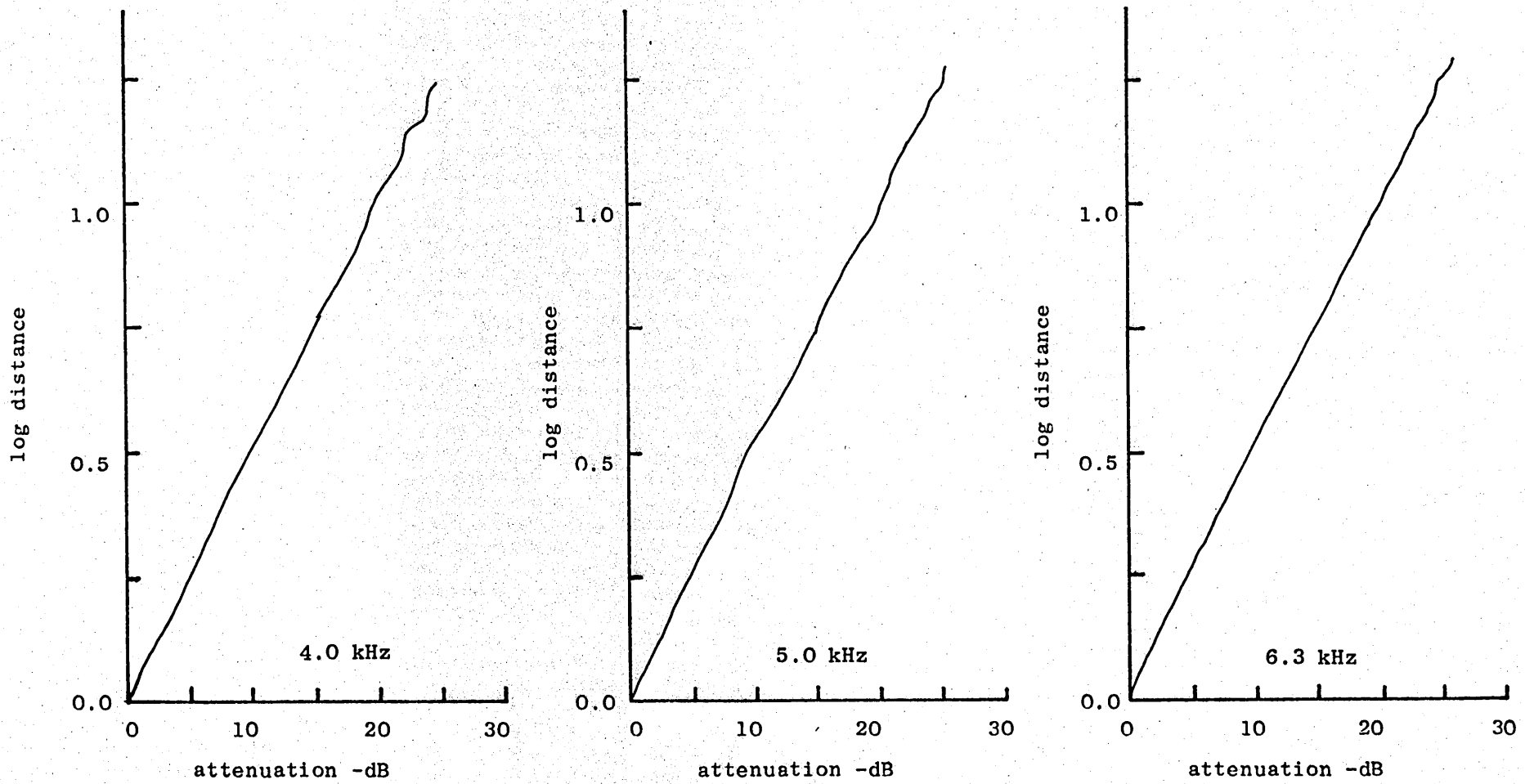
log distance
1.0
0.5
0.0
4.0 kHz
0
10
20
30
attenuation -dB
log distance
1.0
0.5
0.0
5.0 kHz
0
10
20
30
attenuation -dB
log distance
1.0
0.5
0.0
6.3 kHz
0
10
20
30
attenuation -dB

Figure A.6(d)

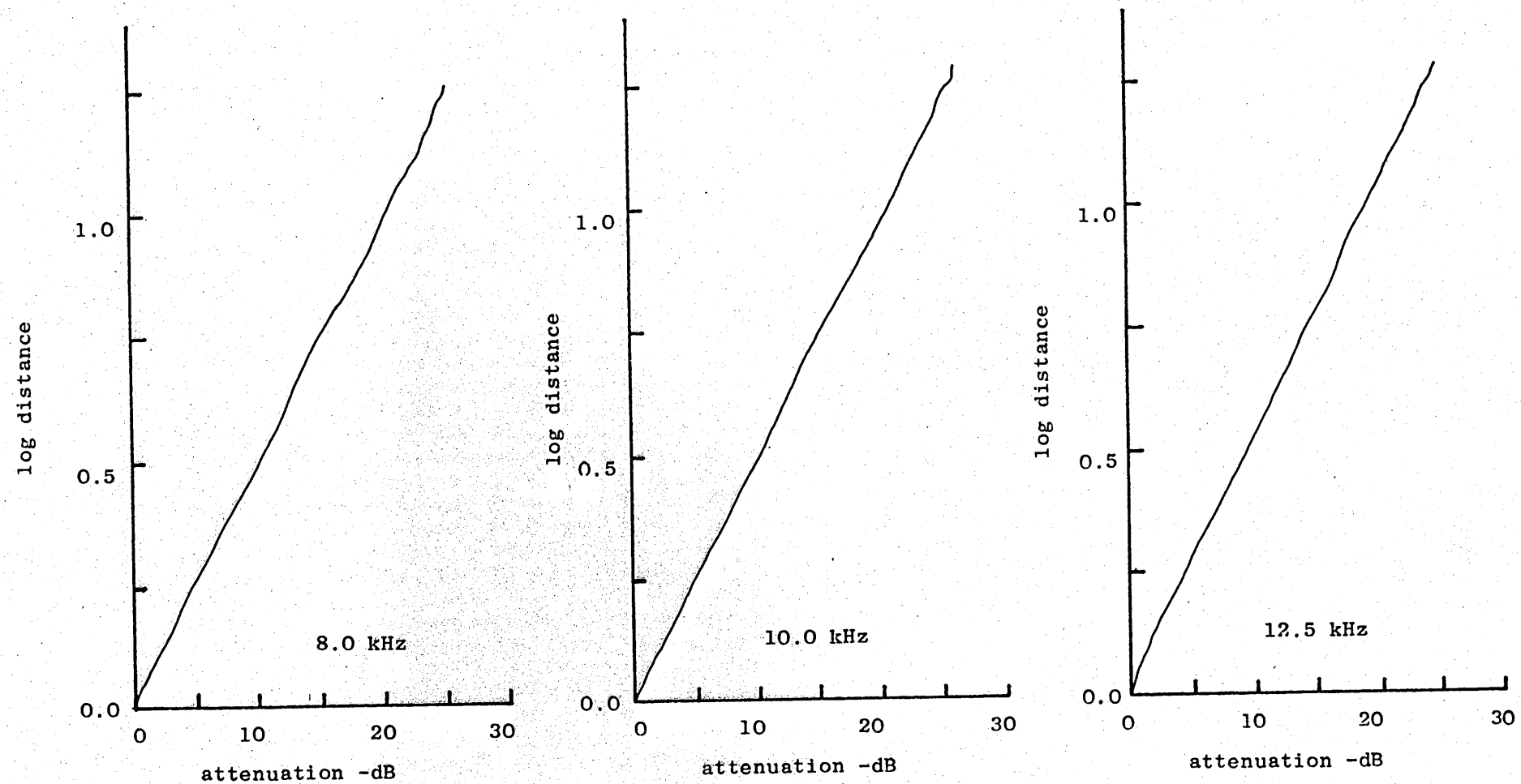
log distance
1.0
0.5
0.0
8.0 kHz
0
10
20
30
attenuation -dB
log distance
1.0
0.5
0.0
10.0 kHz
0
10
20
30
attenuation -dB
log distance
1.0
0.5
0.0
12.5 kHz
0
10
20
30
attenuation -dB

Figure A.6(e)

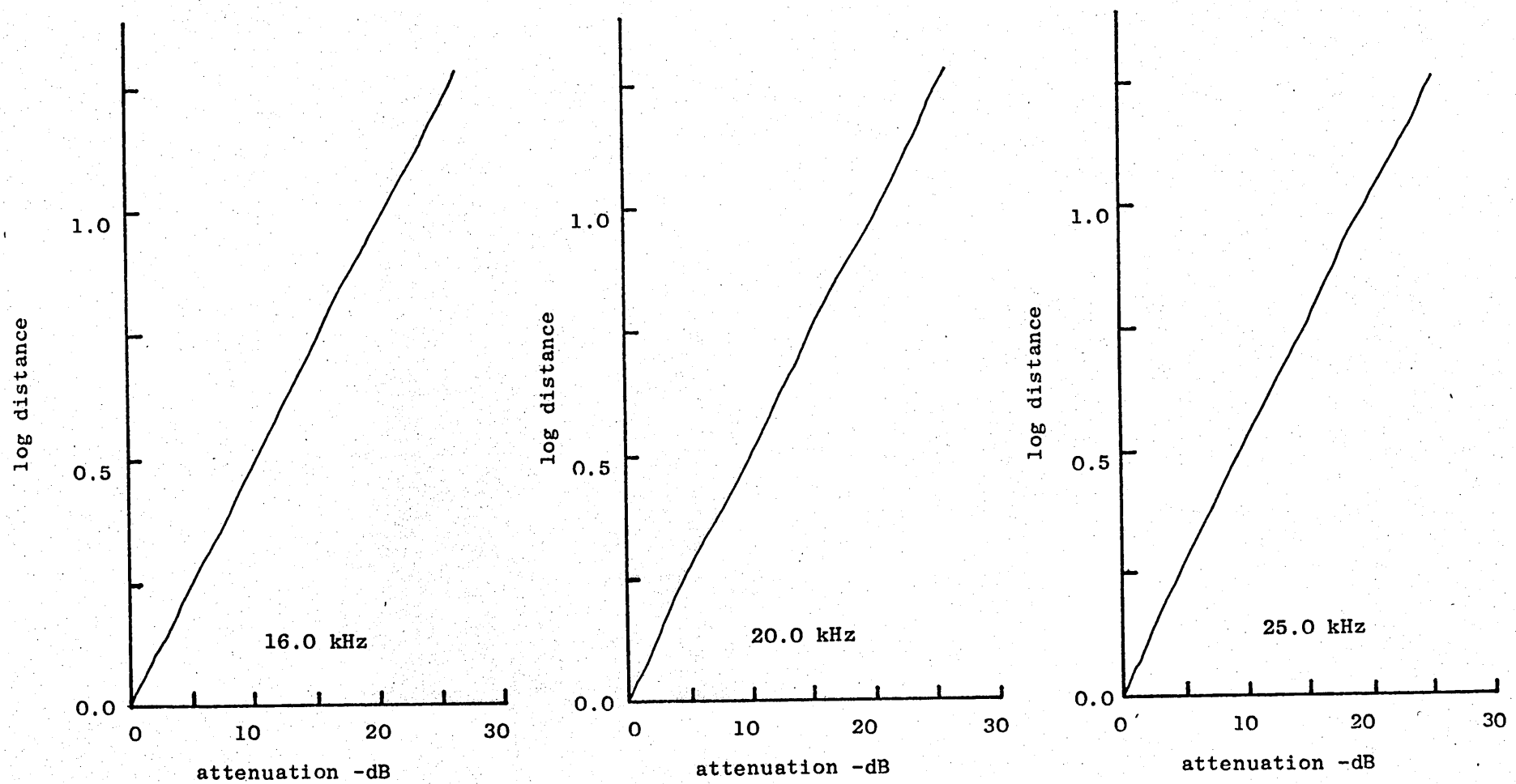
log distance
1.0
0.5
0.0
16.0 kHz
0
10
20
30
attenuation -dB
log distance
1.0
0.5
0.0
20.0 kHz
0
10
20
30
attenuation -dB
log distance
1.0
0.5
0.0
25.0 kHz
0
10
20
30
attenuation -dB

Figure A.6(f)

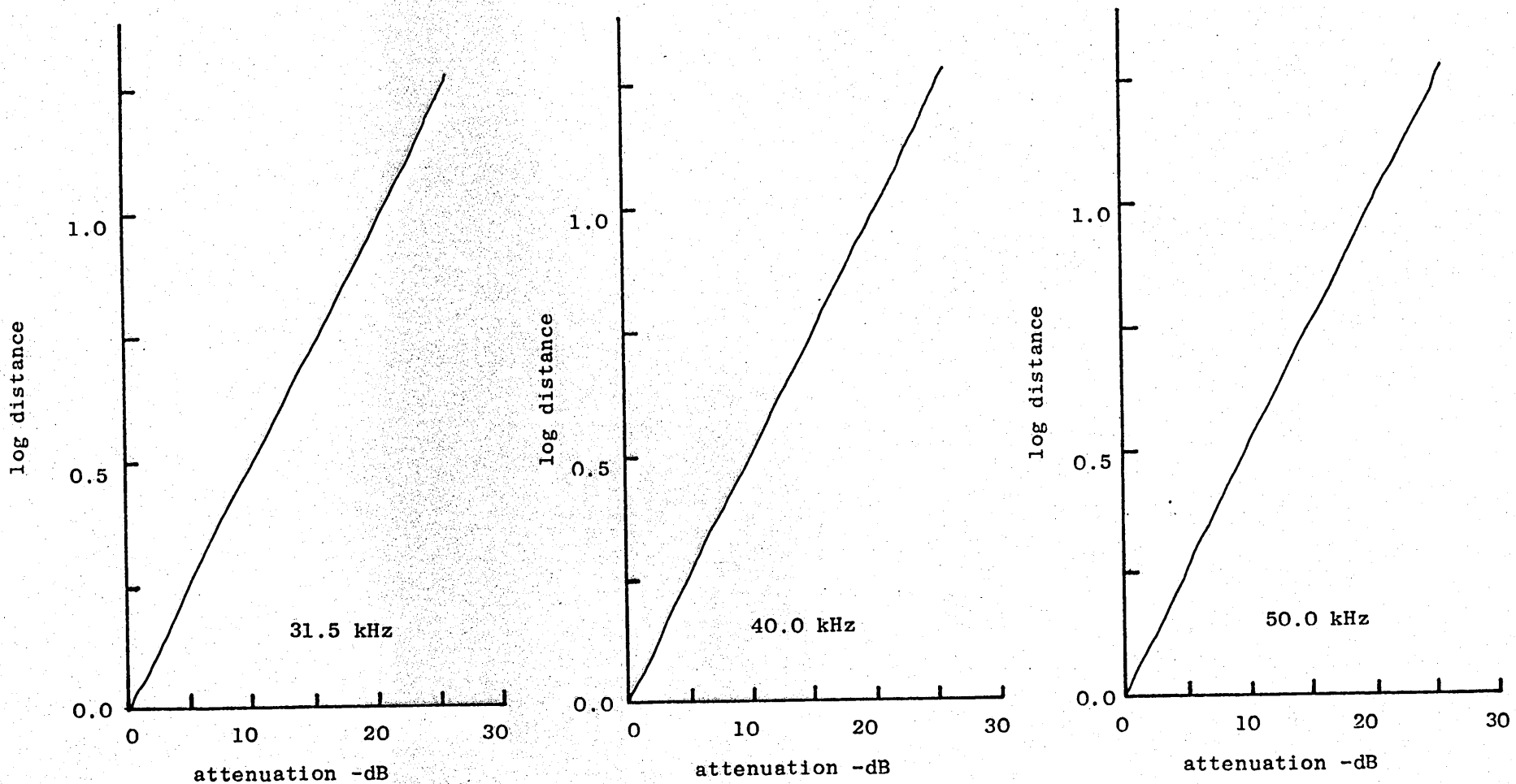
log distance
1.0
0.5
0.0
0
10
20
30
attenuation -dB
31.5 kHz
40.0 kHz
50.0 kHz

Figure A.6(g)

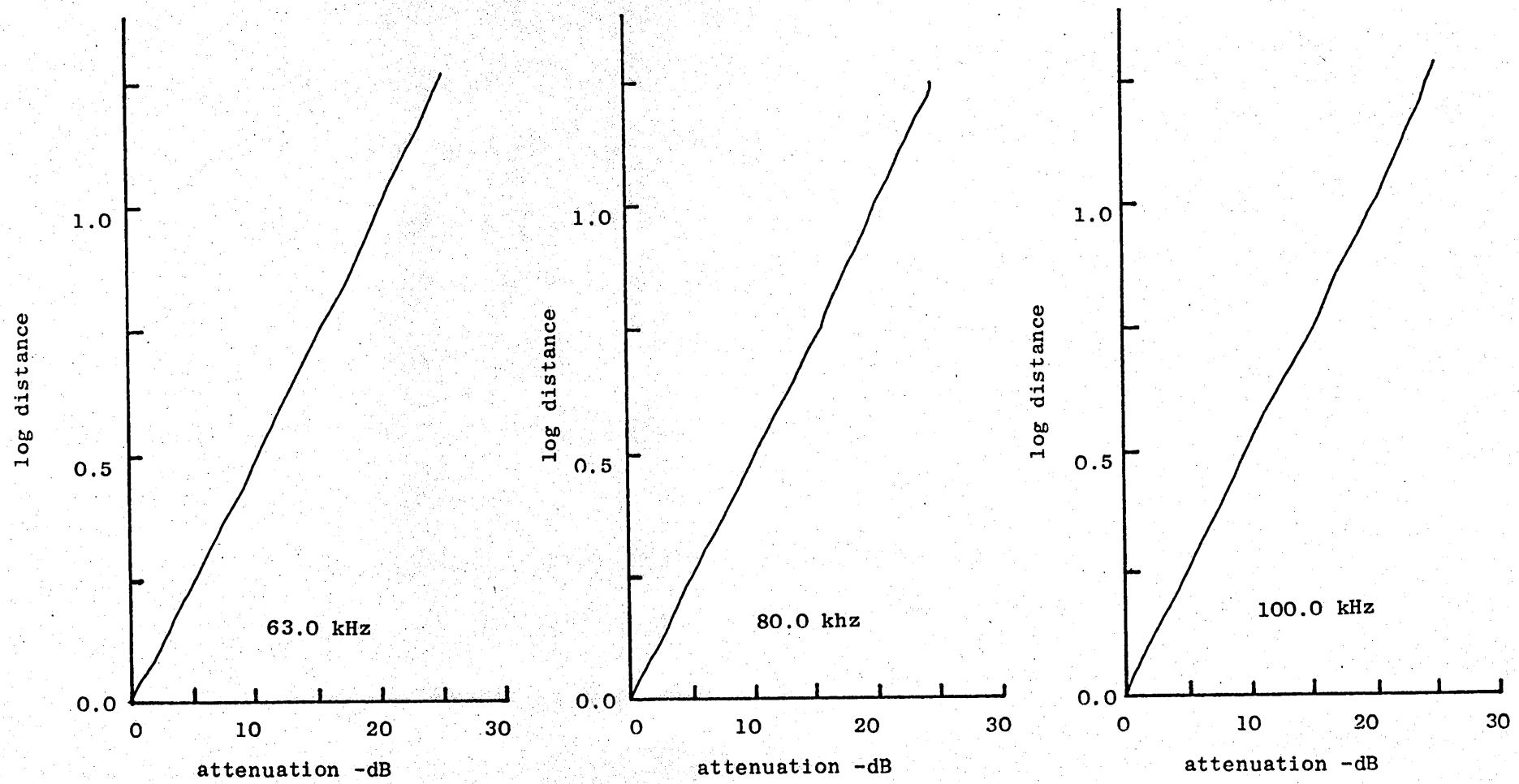
log distance
1.0
0.5
0.0
63.0 kHz
0
10
20
30
attenuation -dB
log distance
1.0
0.5
0.0
80.0 khz
0
10
20
30
attenuation -dB
log distance
1.0
0.5
0.0
100.0 kHz
0
10
20
30
attenuation -dB

Figure A.7(a)
Spherical Divergence Measurements - Air Jet Source $\frac{1}{4}$" Microphone + Nosecone

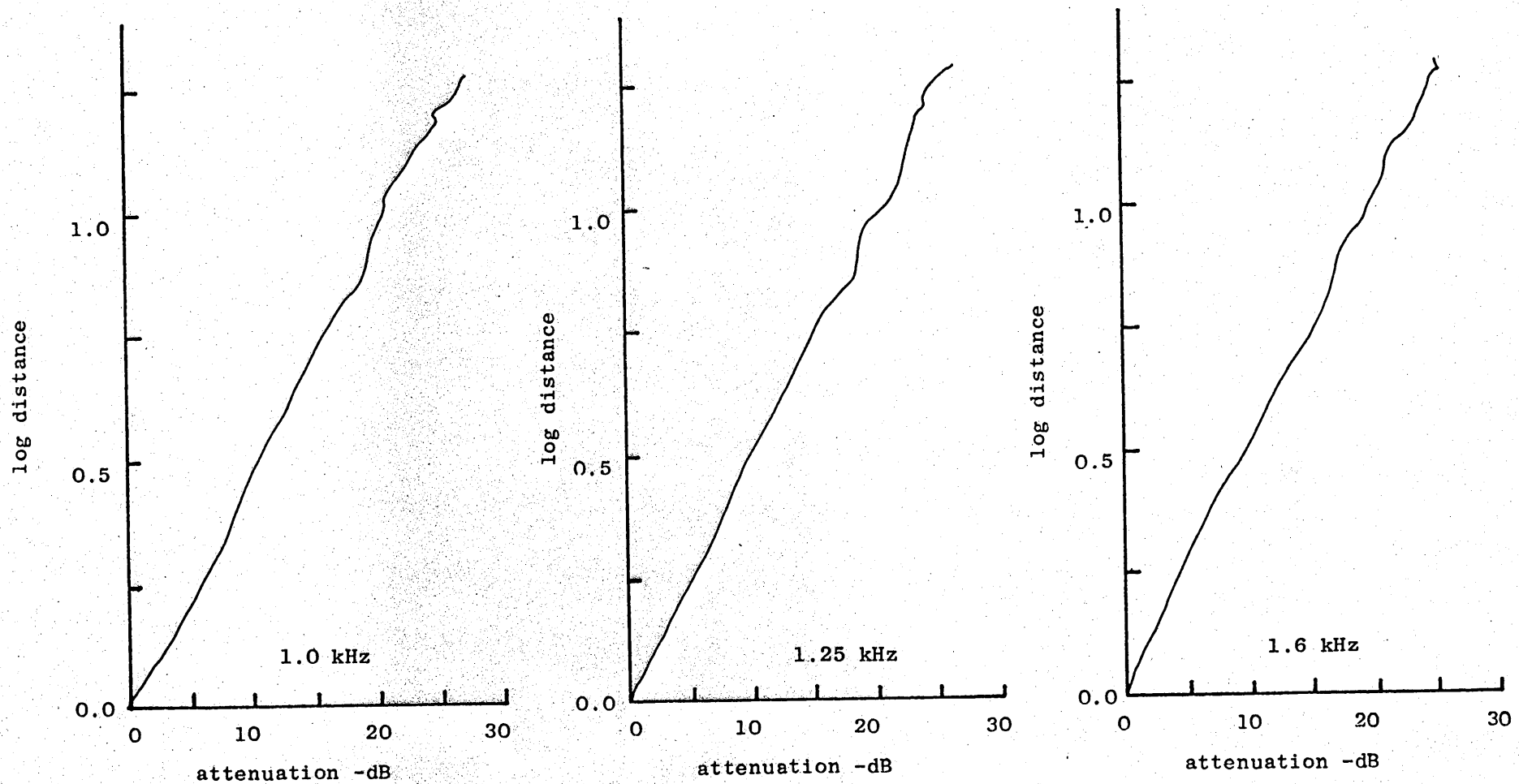

Figure A.7(b)

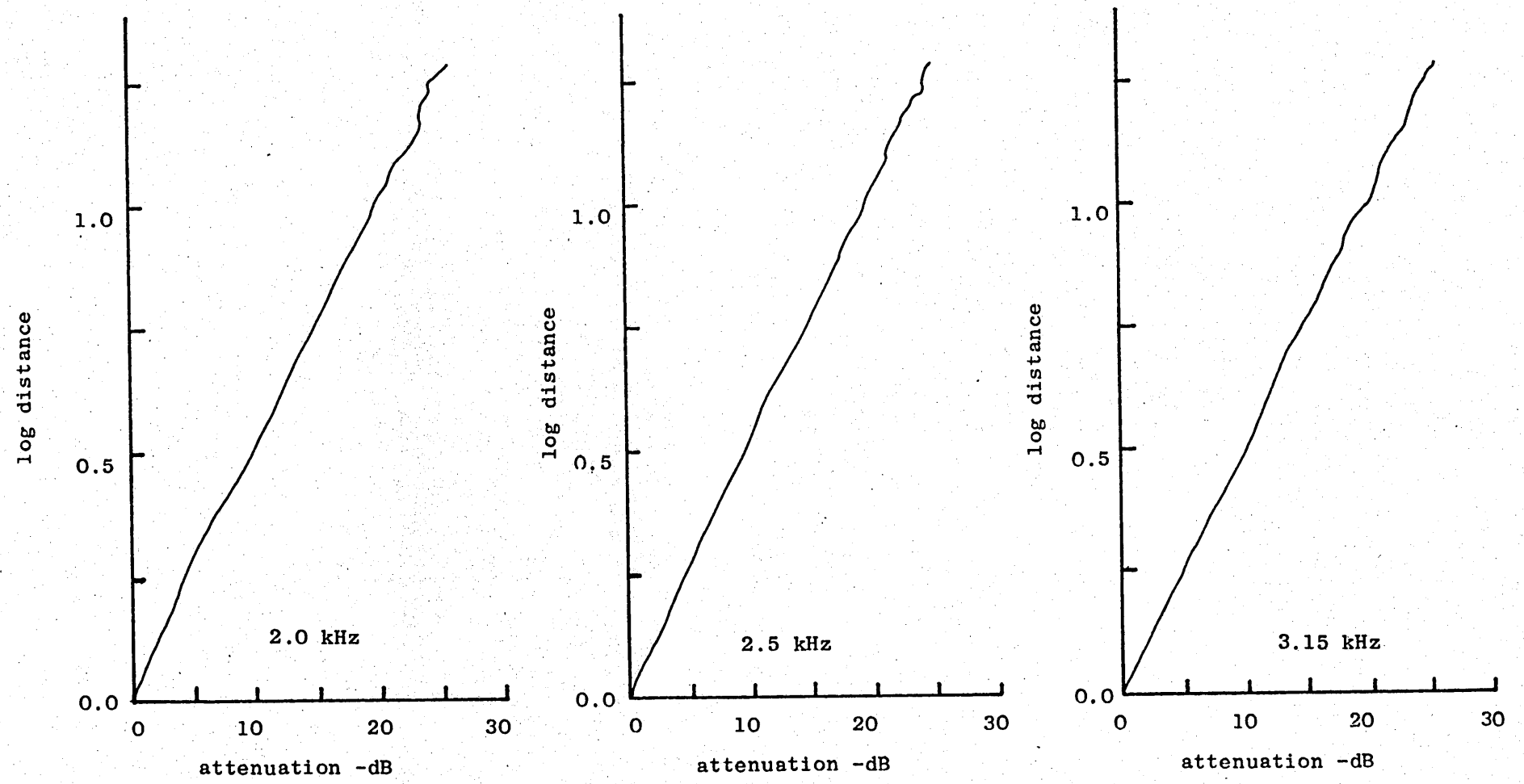
log distance
1.0
0.5
0.0
2.0 kHz
0
10
20
30
attenuation -dB
log distance
1.0
0.5
0.0
2.5 kHz
0
10
20
30
attenuation -dB
log distance
1.0
0.5
0.0
3.15 kHz
0
10
20
30
attenuation -dB

Figure A.7(c)

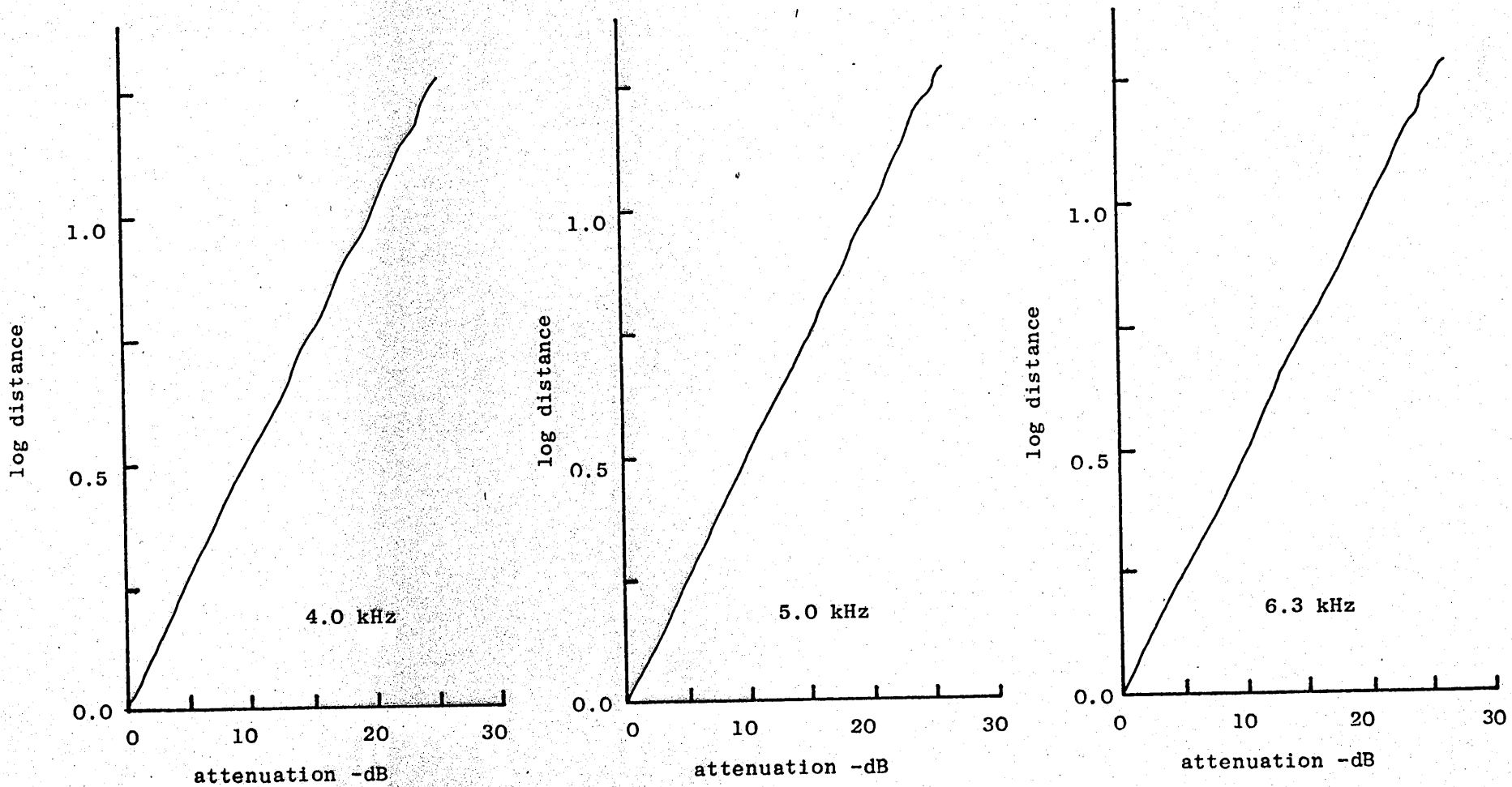
log distance
1.0
0.5
0.0
4.0 kHz
0
10
20
30
attenuation -dB
log distance
1.0
0.5
0.0
5.0 kHz
0
10
20
30
attenuation -dB
log distance
1.0
0.5
0.0
6.3 kHz
0
10
20
30
attenuation -dB

Figure A.7(d)

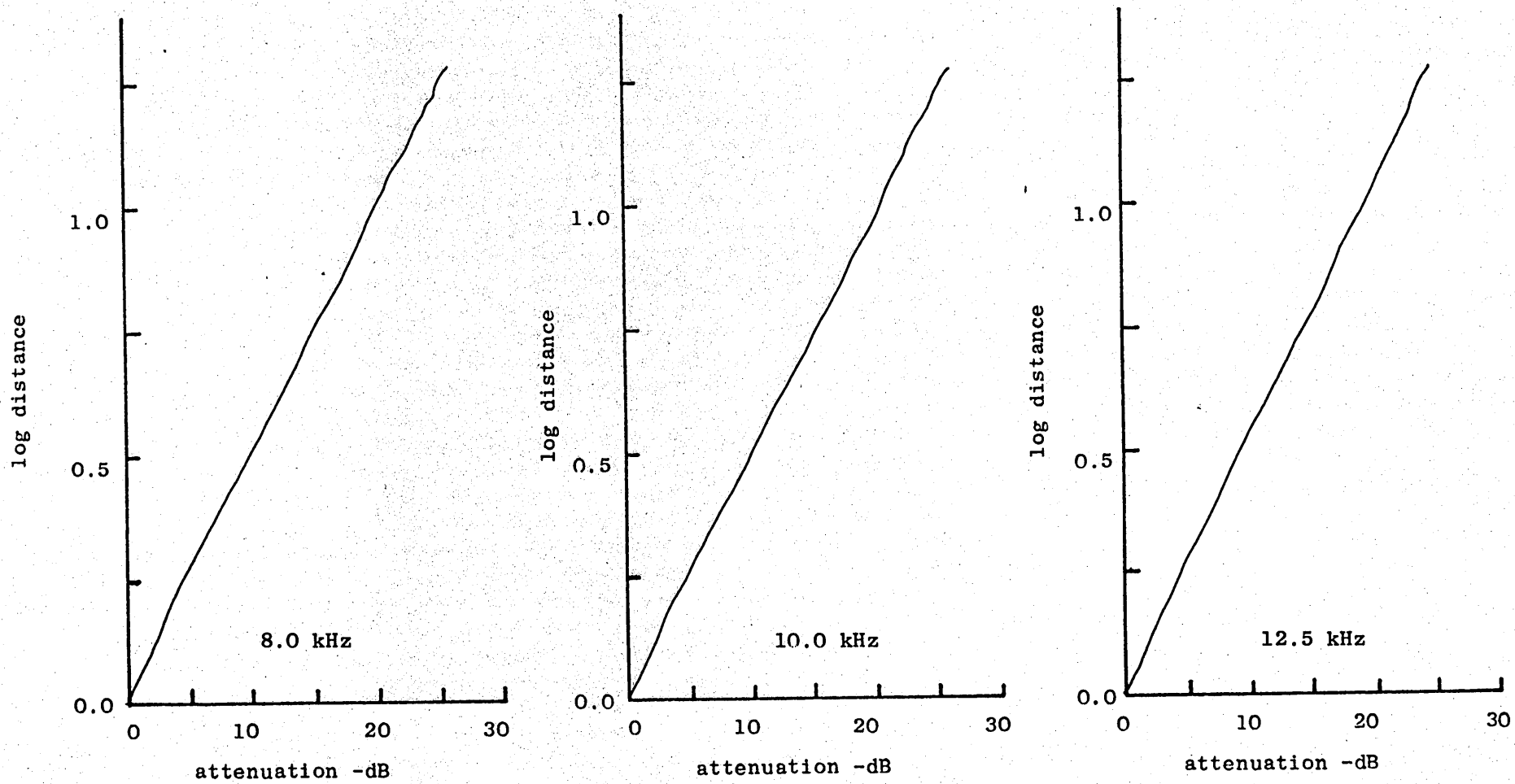
log distance
1.0
0.5
0.0
8.0 kHz
0
10
20
30
attenuation -dB
log distance
1.0
0.5
0.0
10.0 kHz
0
10
20
30
attenuation -dB
log distance
1.0
0.5
0.0
12.5 kHz
0
10
20
30
attenuation -dB

Figure A.7(e)

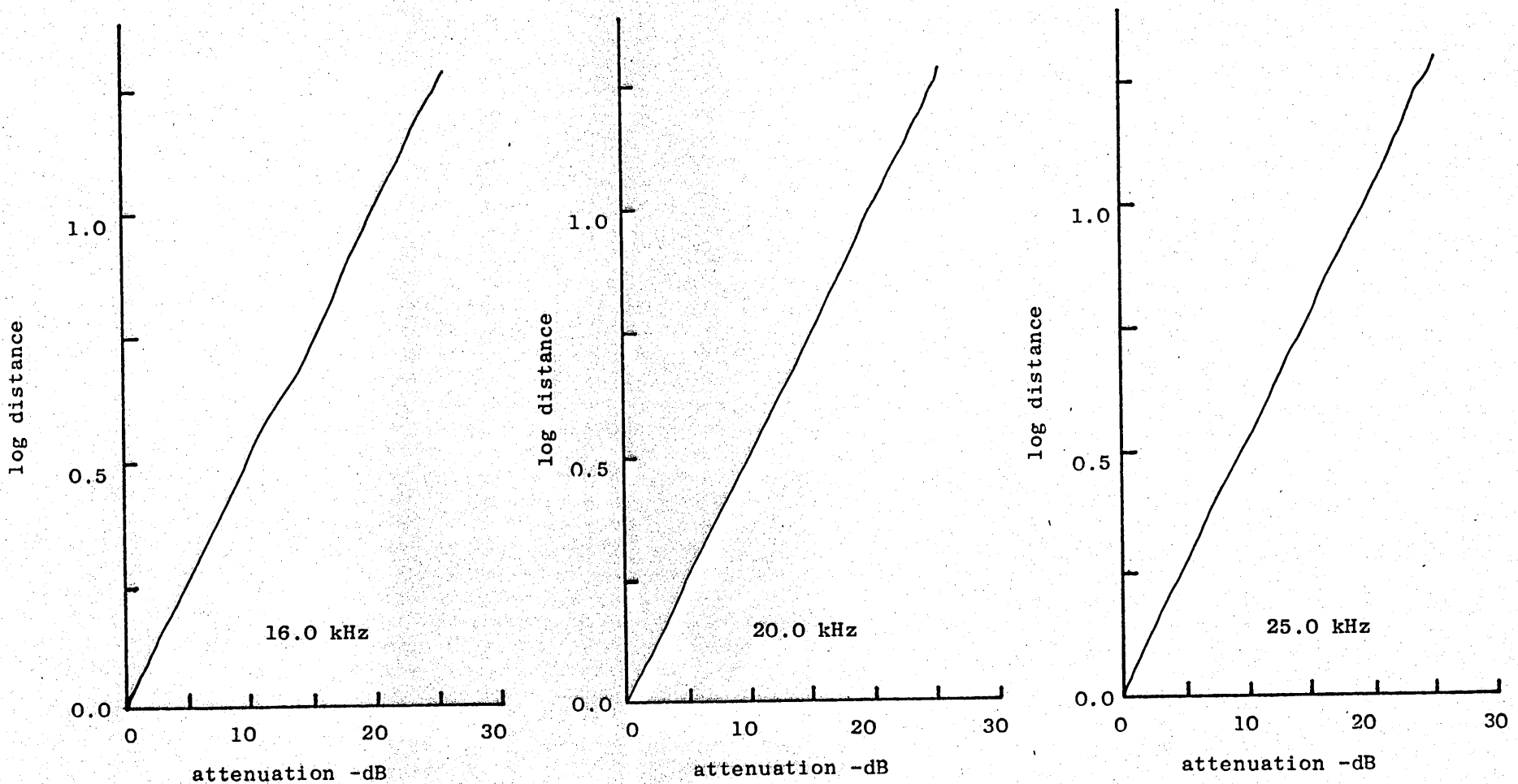
log distance
1.0
0.5
0.0
16.0 kHz
0
10
20
30
attenuation -dB
log distance
1.0
0.5
0.0
20.0 kHz
0
10
20
30
attenuation -dB
log distance
1.0
0.5
0.0
25.0 kHz
0
10
20
30
attenuation -dB

Figure A.7(f)

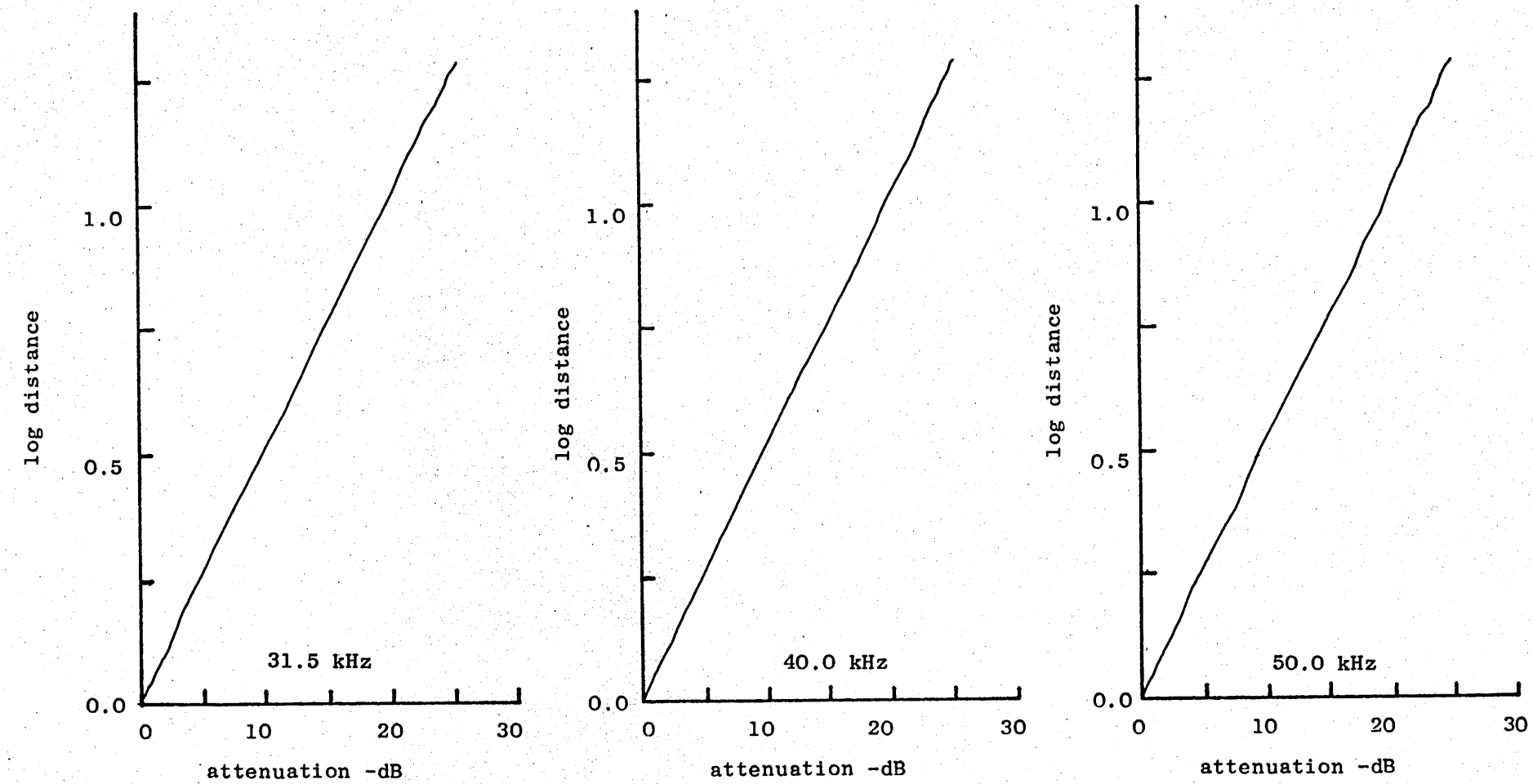
log distance
1.0
0.5
0.0
31.5 kHz
0
10
20
30
attenuation -dB
log distance
1.0
0.5
0.0
40.0 kHz
0
10
20
30
attenuation -dB
log distance
1.0
0.5
0.0
50.0 kHz
0
10
20
30
attenuation -dB

Figure A.7(g)

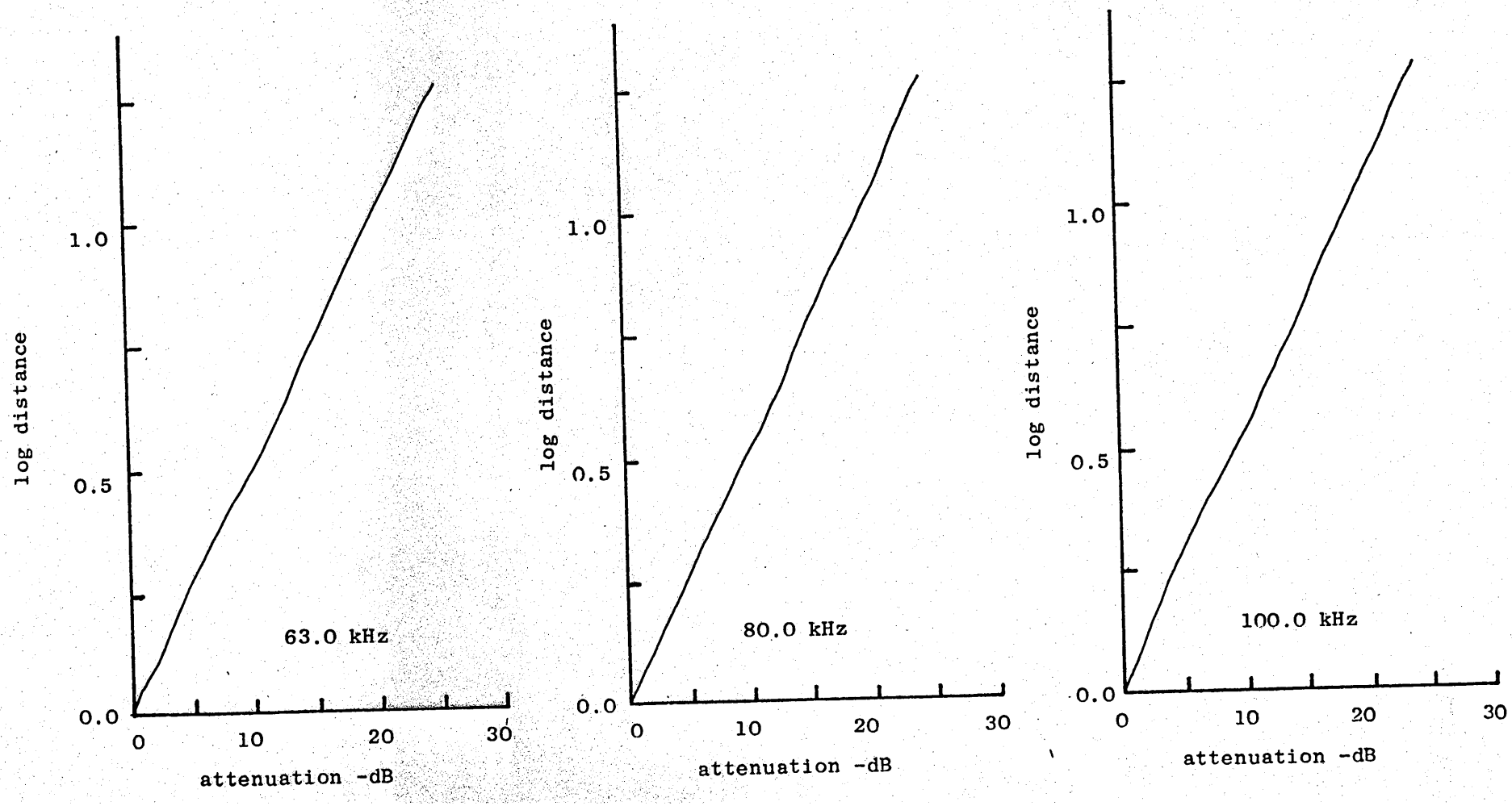
log distance
1.0
0.5
0.0
63.0 kHz
0
10
20
30
attenuation -dB
log distance
1.0
0.5
0.0
80.0 kHz
0
10
20
30
attenuation -dB
log distance
1.0
0.5
0.0
100.0 kHz
0
10
20
30
attenuation -dB

Figure A.8(a)
Spherical Divergence Measurement - Air Jet Source 1/8" Microphone + Nose cone

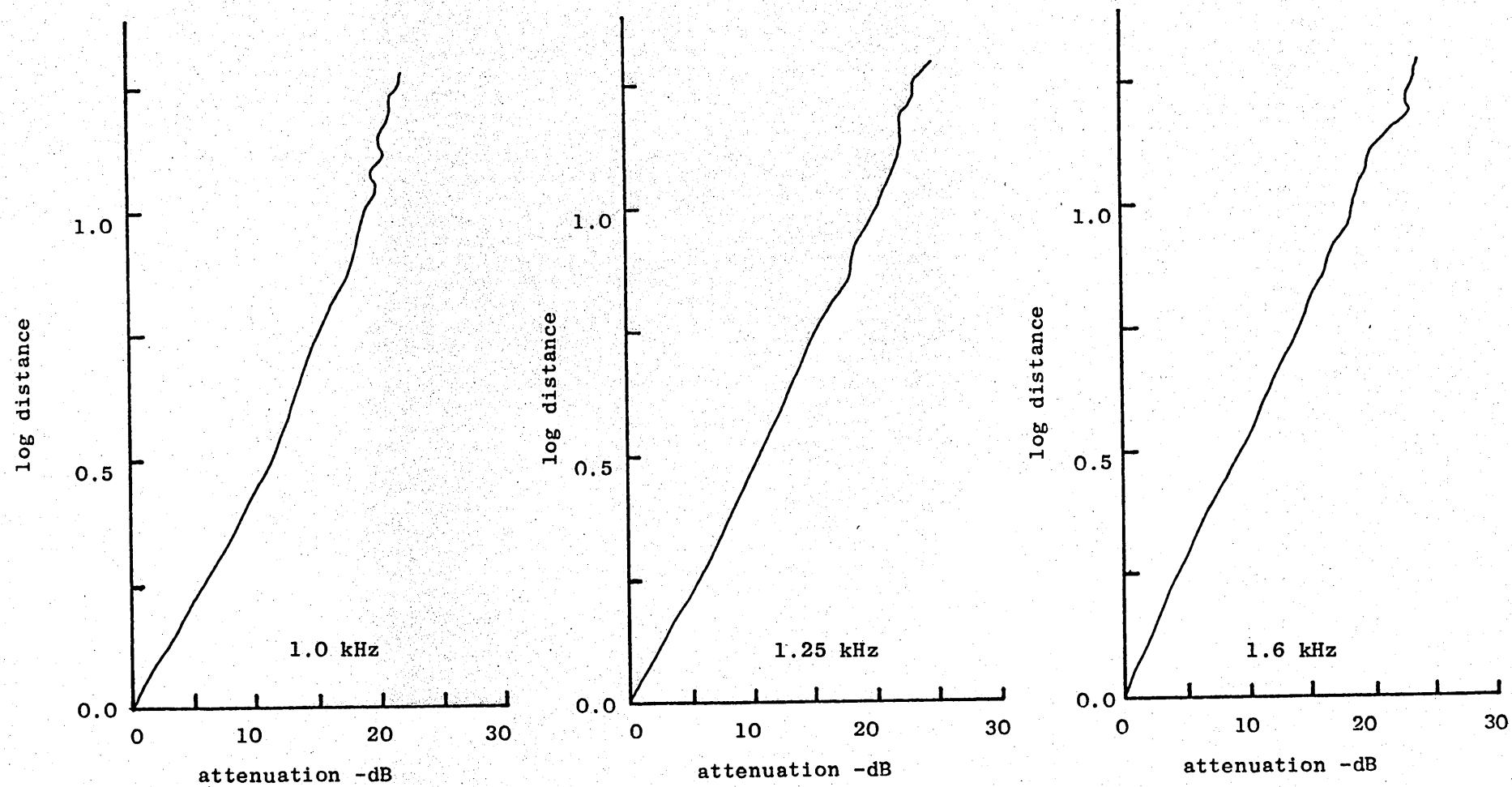

Figure A.8(b)

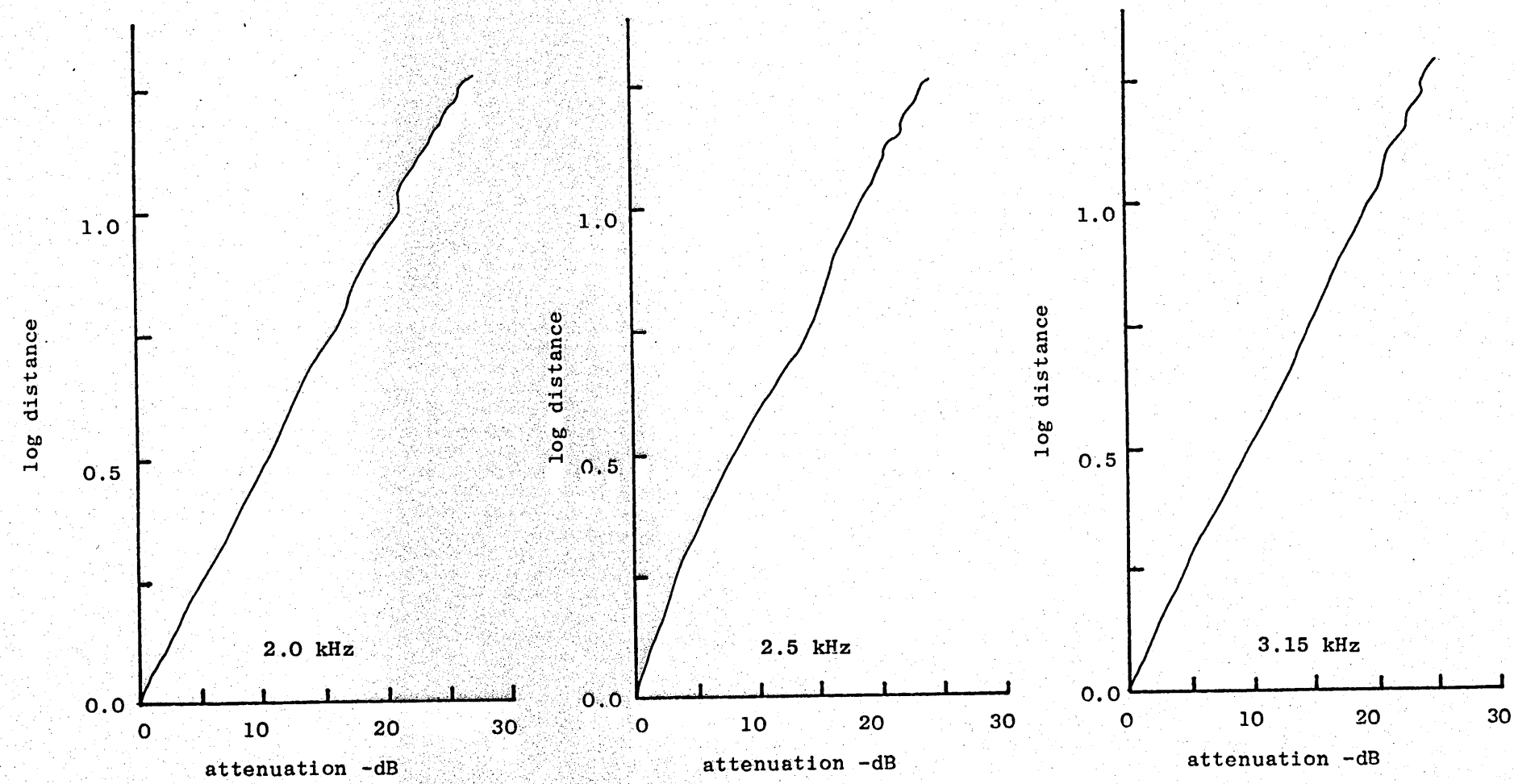
log distance
1.0
0.5
0.0
2.0 kHz
0
10
20
30
attenuation -dB
log distance
1.0
0.5
0.0
2.5 kHz
0
10
20
30
attenuation -dB
log distance
1.0
0.5
0.0
3.15 kHz
0
10
20
30
attenuation -dB

Figure A.8(c)

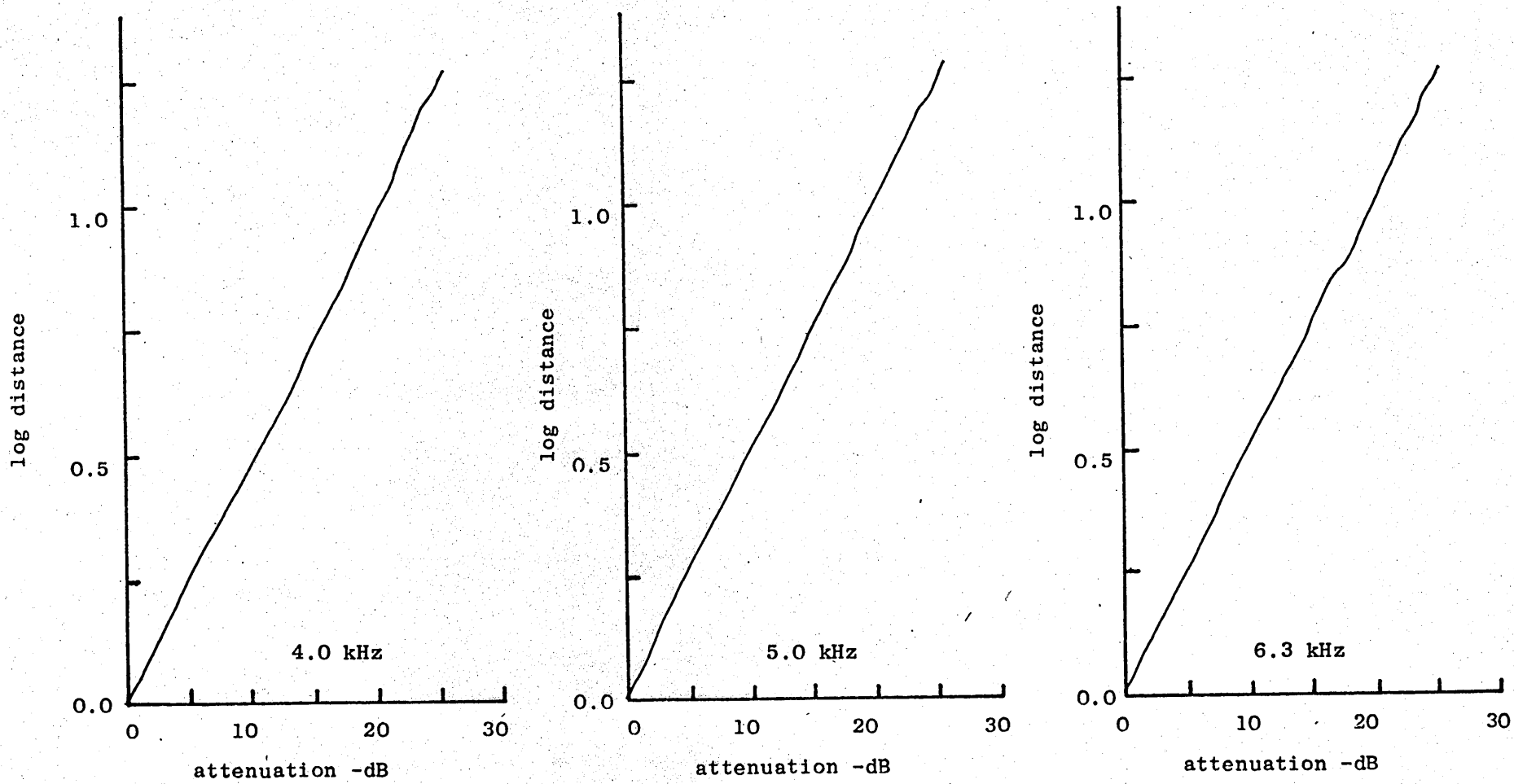
log distance
1.0
0.5
0.0
0
10
20
30
attenuation -dB
4.0 kHz
5.0 kHz
6.3 kHz

Figure A.8(d)

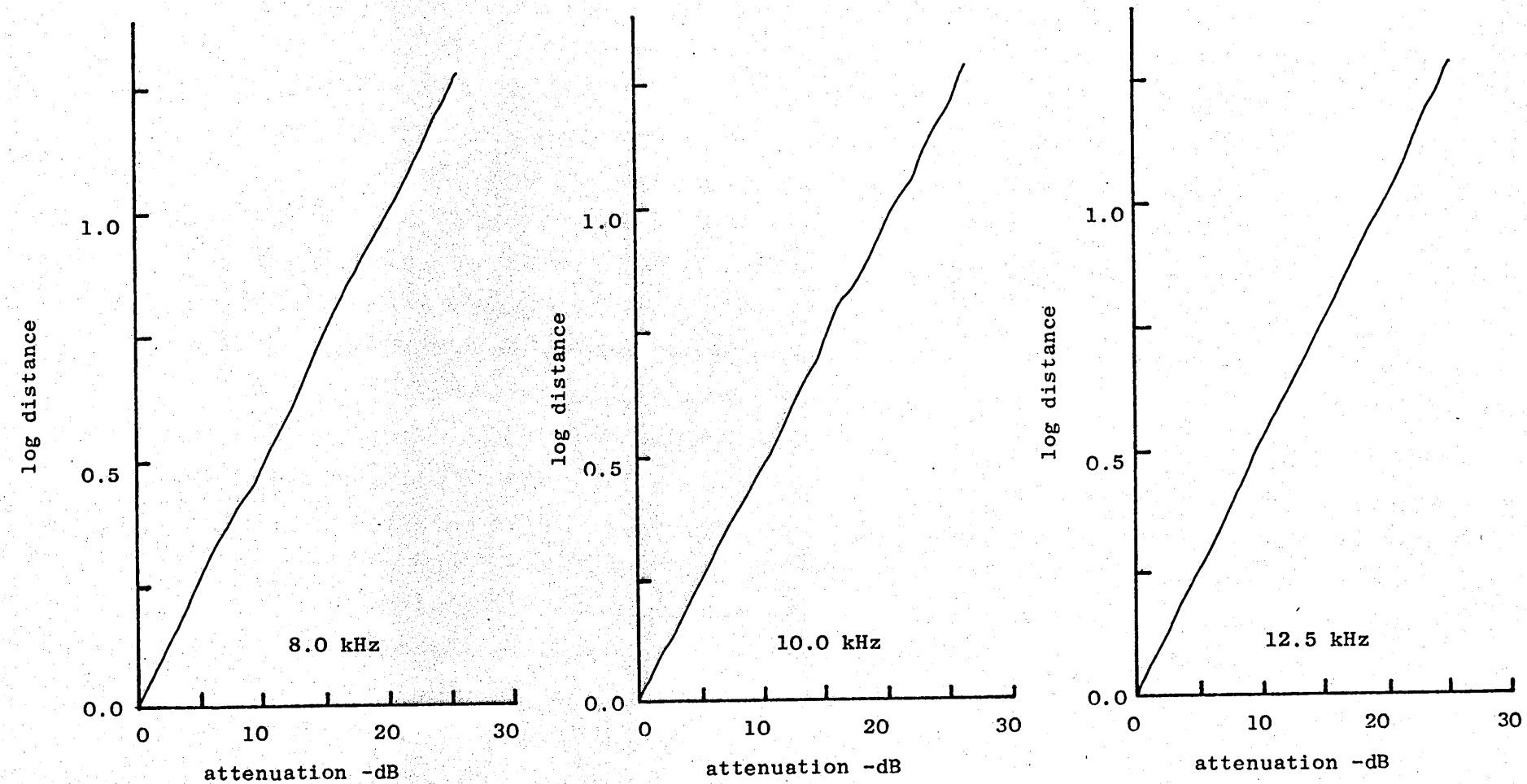
log distance
1.0
0.5
0.0
0
10
20
30
attenuation -dB
8.0 kHz
10.0 kHz
12.5 kHz

Figure A.8(e)

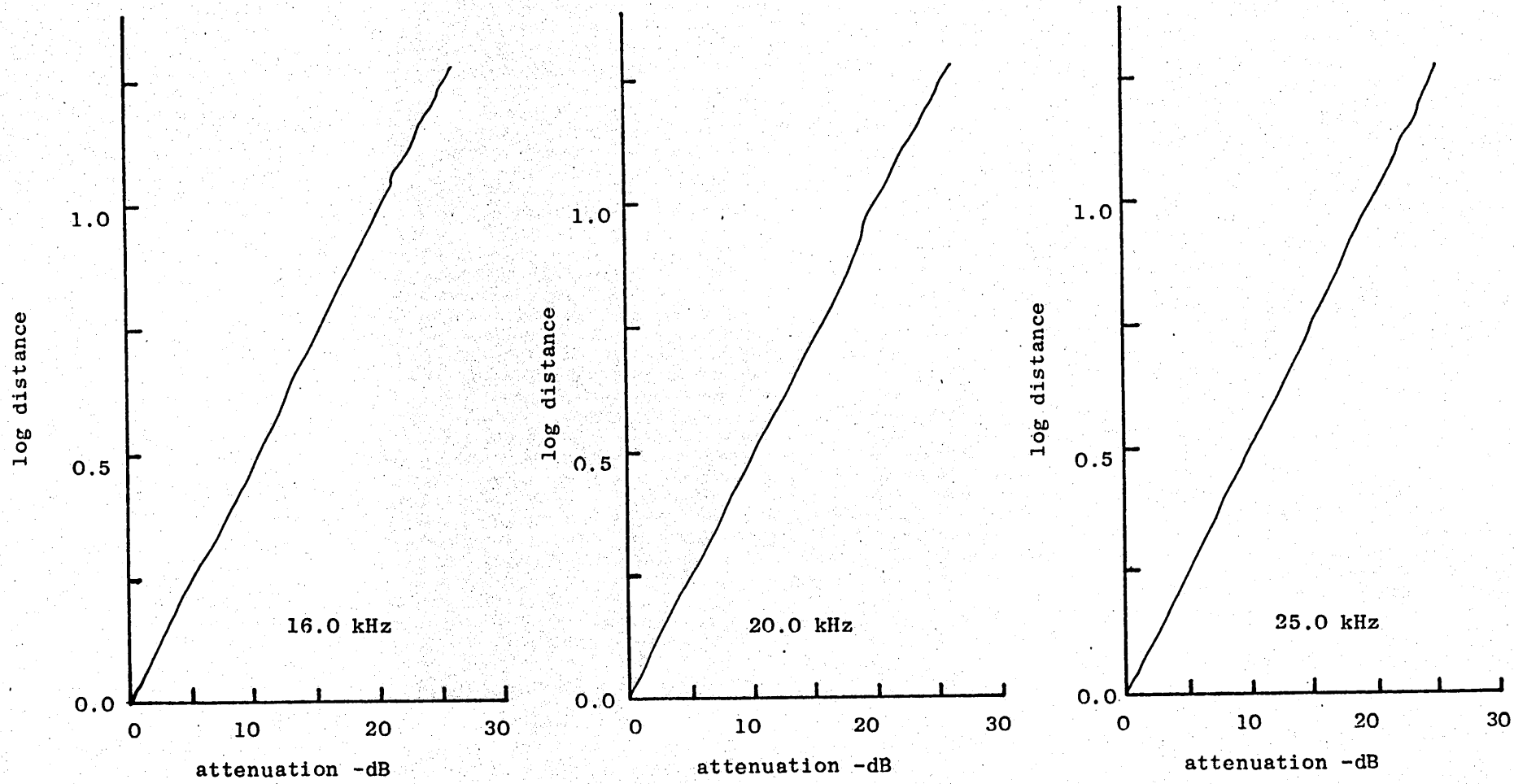
log distance
1.0
0.5
0.0
16.0 kHz
0
10
20
30
attenuation -dB
log distance
1.0
0.5
0.0
20.0 kHz
0
10
20
30
attenuation -dB
log distance
1.0
0.5
0.0
25.0 kHz
0
10
20
30
attenuation -dB

Figure A.8(f)

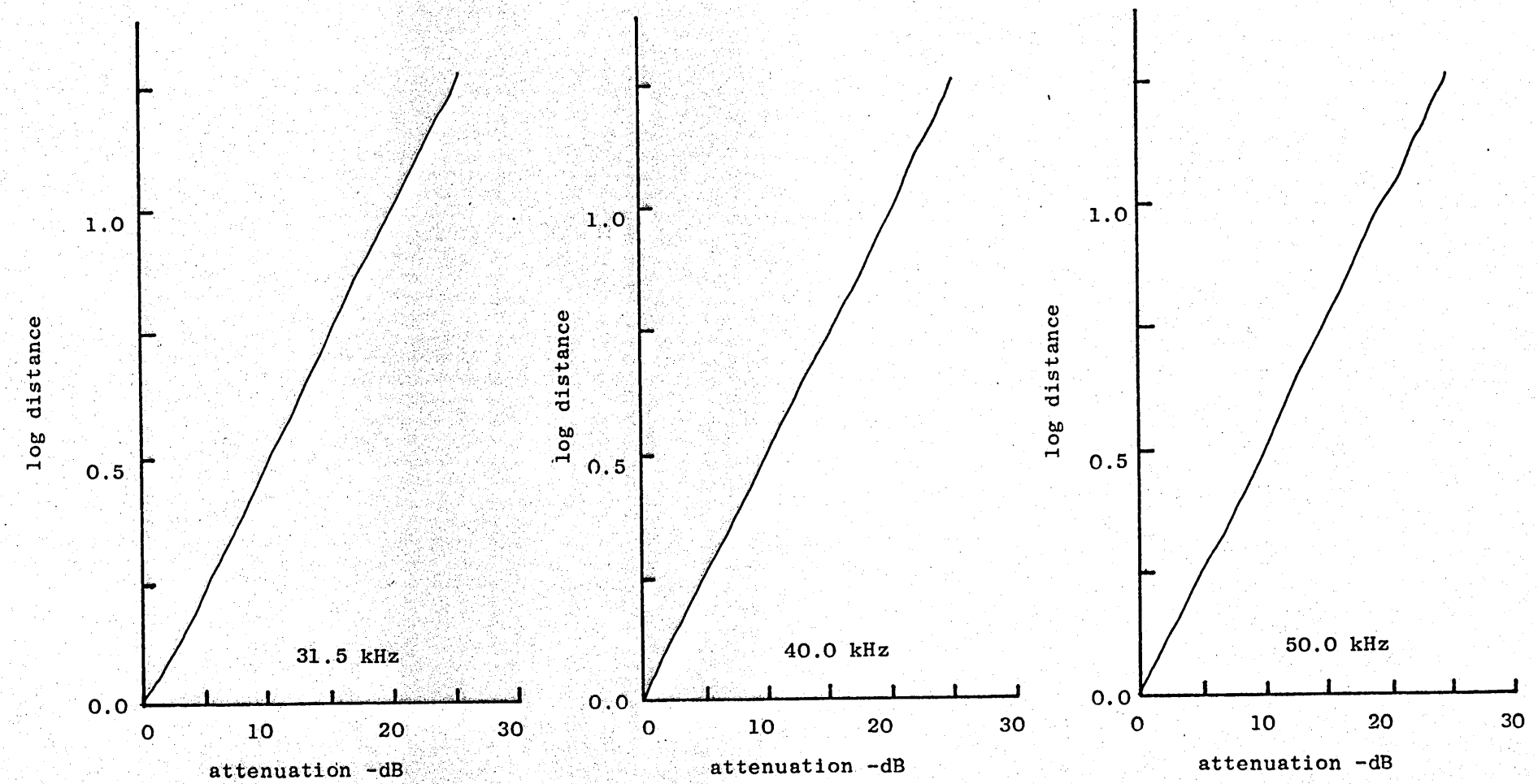
log distance
1.0
0.5
0.0
31.5 kHz
0
10
20
30
attenuation -dB
log distance
1.0
0.5
0.0
40.0 kHz
0
10
20
30
attenuation -dB
log distance
1.0
0.5
0.0
50.0 kHz
0
10
20
30
attenuation -dB

Figure A.8(g)

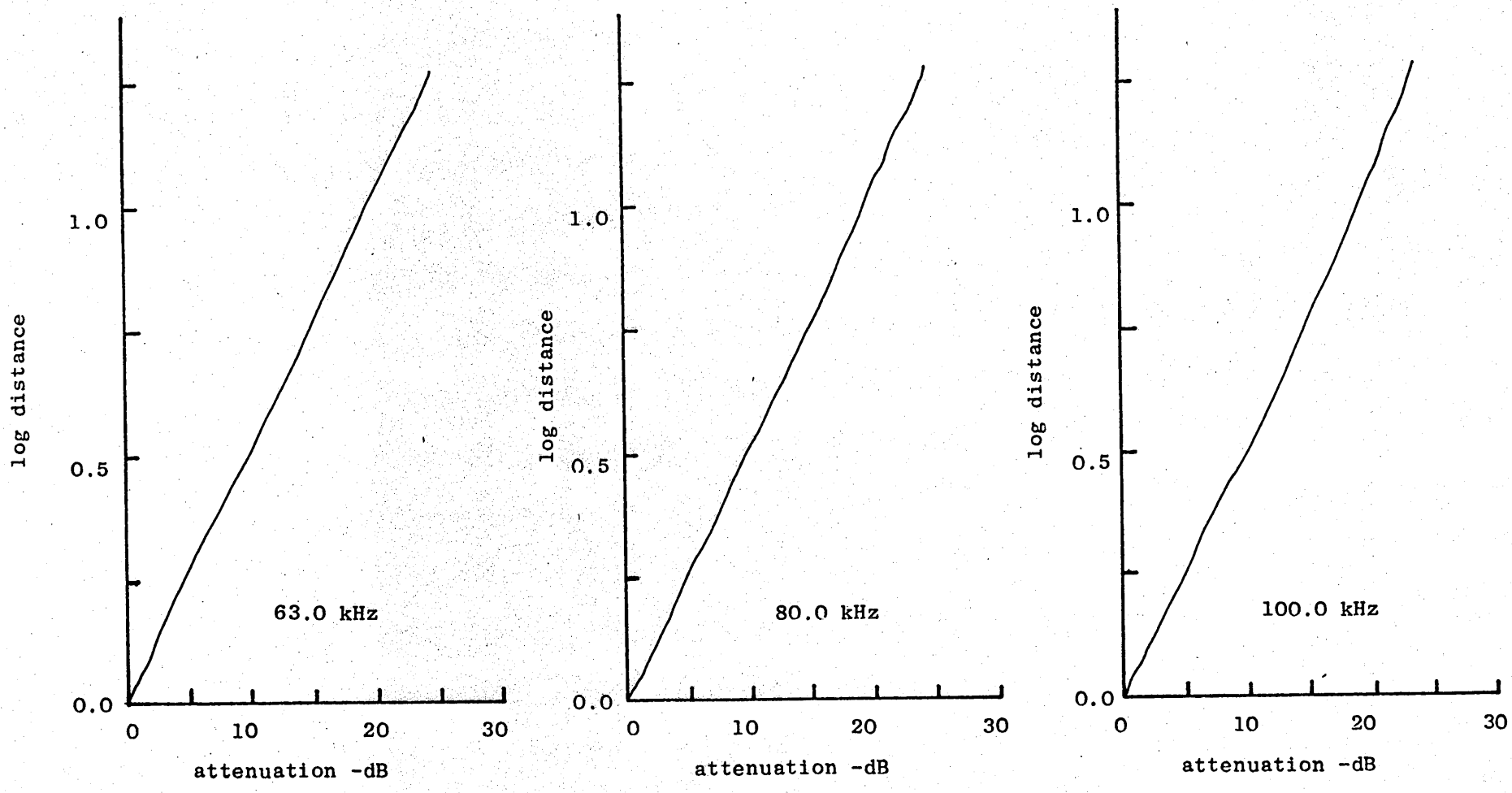
log distance
1.0
0.5
0.0
63.0 kHz
0
10
20
30
attenuation -dB
log distance
1.0
0.5
0.0
80.0 kHz
0
10
20
30
attenuation -dB
log distance
1.0
0.5
0.0
100.0 kHz
0
10
20
30
attenuation -dB

APPENDIX B

A Spark Discharge Noise Source for Use with Acoustic Scale Models

B.1 The Spark Discharge has proved to be one of the most successful impulsive noise sources for acoustic modelling. This is due primarily to the high sound power level it produces, typically in excess of 120dB, but also because of its small size and repeatable output spectrum.

The basic spark discharge circuit is shown in Figure B.1. It is comprised of a capacitor for storage of electric charge, a resistor, switch and a pair of electrodes. A high voltage power supply charges the capacitor through the resistor which limits the rate of flow of current. The change in voltage measured across the capacitor, as a function of time is shown in Figure B.2. At time t, the switch is closed and the voltage increases exponentially. Eventually the voltage across the capacitor, and hence the electrodes, is sufficient to cause ionization of the air between the electrodes. This is shown as time t_2.

Ionization of the air gap causes a narrow cylindrical region of air between the electrodes to fall in resistance and thus conduct the electric charge stored on the capacitor. The charge surges through this region raising the temperature to several thousand degrees Kelvin (B.1), thus causing a rapid expansion of the air leading to the generation of a shock wavefront.

The initial shock leaves the gap region within 1μs and the shock wavefront is ellipsoidal with its major axis along the axis of the gap. Within 10μs, however, it assumes a nearly perfect spherical shape (B.2).

It has been found experimentally that the acoustic energy radiated by a spark source is dependant upon the initial air gap as well as the electrical energy. Wyber (B.3) for example suggests that up to 7% of the input energy may be converted to useful acoustic energy. Klinkowstein (B.1) on the otherhand quotes efficiencies of the order 0.85-2.85%, depending upon the gap width. Wright (B.4) indicates values around 1% when the gap resistance drops to below 1Ω.

The electrical input energy can be calculated from the expression $VC^2/2$, where V is the voltage across the gap and C is the capacitance of the circuit.

B.2 Triggering the Spark Discharge

Although simple to construct, the basic circuit of Figure B.1 is of little practical use for two reasons. Firstly, the spark is not very repeatable because small variations in the environment of the air gap causes ionization at different voltages. This results in fluctuations of the energy released and hence the acoustic output of the source.

Secondly, there is no mechanism to enable synchronisation between the source and the measurement system. In the case of the basic

circuit the current flowing to the electrodes changes from zero to maximum when the breakdown voltage is reached. This rapid change can be used to provide a trigger signal for the measurement system [B.5] [B.6] [B.7].

Both these problems can be overcome by introducing a separate trigger circuit to control the actual spark discharge [B.1] [B.5] [B.8]. The trigger circuit provides a low energy high voltage pulse which is guarenteed to cause ionization of the gap and hence release the energy stored on the capacitor in a controlled manner. Furthermore, the trigger pulse can be used to synchronise the discharge and measurement instrumentation.

A further advantage of the trigger circuit is that the stored energy on the capacitor can be varied to suit the experiment because ionization is now independant of the stored charge level.

There are two types of triggering circuit in common use, the series and the parallel.

2.1 Series Triggering

A typical series triggering circuit is shown in Figure B.3. The capacitor is charged to a voltage below that required for breakdown. To activate the spark a high voltage pulse is superimposed upon the d.c. voltage of the capacitor by means of the transformer. This high voltage pulse, which is much greater than the breakdown voltage, causes ionization allowing the charge stored on the capacitor to flow.

An alternative series technique employs a high voltage switch such as a thyratron. In this case the capacitor is charged to a voltage well above breakdown, and the spark is activated by closing the switch.

B.2.2 Parallel Triggering

Parallel triggering circuits use three electrodes as shown in Figure B.4 . The capacitor is charged to a voltage below breakdown. To activate the spark a voltage pulse is input to the primary of the transformer. This generates a high voltage pulse on the secondary, which is sufficient to ionise the gap between the trigger electrode and the common electrode. Once ionised the resistance of this small gap drops sufficiently to allow the main gap to ionise.

B.3 The Design of the Spark Source

The initial design for a spark followed closely the parallel triggered circuit of Figure B.4, and used an automobile ignition coil for the pulse transformer. Although this design generated a good spark, it was found to be un-useable, because the intensity of the pulse induced in the microphone by the electromagnetic radiation from the coil was sufficient to swamp the actual sound pressure pulse.

Various methods were used to try and improve the e.m. shielding of the coil, but none proved very successful.

A second spark discharge source, based on components from a domestic gas lighter, did prove successful. The circuit is shown in Figure B.5. The capacitor is charged to 130V or 240d.c. through a current limiting resistor R4. Under normal conditions no current flows through the transformer primary winding; because the Thyristor is held in the 'off' state by the photo transistor. To activate the spark the light emitting diode is forward biassed by means of a TTL level signal. This causes the photo-transistor to 'source' current to the gate terminal of the Thyristor, thus turning it on. The current stored in the capacitor then flows through the high turns ratio transformer, generating a high voltage pulse sufficient to ionise the air gap between the electrodes.

The light emitting diode and photo-transistor provide an isolation barrier capable of withstanding a 1-5kV d.c. voltage. This barrier ensures protection from the high voltage circuit for the measurement system that generates the trigger signal.

B.4 Measurement of the acoustic output of the spark source

A series of measurements were undertaken to determine acoustic characteristics of the spark source. In particular it was decided to determine:-

(i) the repeatability of the source
(ii) the effect of pulse gate width on the source spectrum
(iii) the degree of non-linearity
(iv) the amount of e.m. interference

A block diagram of the instrumentation used for these measurements is shown in Figure B.6. Two microphones were used for all tests, a B&K 4138 1/8" inch and a B&K 4135 1/4" inch. The smaller of these was used as a reference microphone; because although superior in terms of bandwidth and directionality it is less sensitive than the 4135 so cannot be used for large separation distances.

The Nicolet 660 was set up in the Signal Enhancement mode to maximise the signal to noise ratio of the measurements. Test measurements indicated no significant improvement in the signal to noise ratio above 32 samples.

The instrument was set to trigger on the rising edge of signal channel A, with various amounts of pre-trigger. Pre-trigger is a term used to define the fact that a digital recording device can store the signal that

occurred prior to the trigger point. This feature is particularly useful for analysing transient events, otherwise the early part of the signal may not be available for analysis.

Figure B.7 shows the acoustic pulse received by the two microphones after averaging 32 samples. The upper trace is that of the 4138 and the lower that of the 4135. The total duration of the sample is 0.004 secs (4 ms), and each horizontal division corresponds to 500 μs. The vertical divisions are 0.5 V, and the input amplifiers were set for 5 V full scale.

The small negative spike on the top trace at 300 μs and a similar one on the bottom trace at 1600 μs is the result of the e.m. radiation caused by the spark. Although very small, its presence cannot be neglected as will be shown later.

The spectra calculated from these two pulses are shown in Figure B.8. The horizontal divisions of this figure equal 10 kHz and the vertical divisions 10 dB. The top trace shows that the magnitude of the low frequency response increases at a rate of 6 dB per octave, typical of N-wave excitation, and eventually flatterns off at a maximum up to 100 kHz.

The bottom trace shows a similar envelope up to 50 kHz, but then exhibits a strong dip at about 68 kHz and eventually rolls off at 6 dB per octave. The dip results from the response of the microphone, and coincides with the point when the diaphragm motion changes from stiffeness controlled to mass controlled (B.9). All the measurements made have produced similar spectra.

B.4.2 Repeatability of the source

The repeatability of the source was tested by calculating the total energy received from each pulse and calculating the standard deviation of the measurements. Over a series of 100 measurements the standard deviation was less than 0.5 dB.

B.4.3 Effect of gate pulse width

The second question to be answered was whether the source spectrum could be controlled by varying the length of the pulse applied to the thyristor gate. Figures B.9 a,b,c,d,e show the measured pulses for gate pulse widths of 12,100, 200, 400, 1000 μs respectively, and Figures B.10 a,b,c,d,e, show the calculated spectra.

Comparing these results shows that the spectrum of the spark is independant of the applied gate pulse width.

The exact reason for this is not yet clear, since the longer the gate pulse the longer the thyristor conducts and hence the longer the duration of the spark. One possible explanation is that all the stored energy is completely dissipated within the first few micro seconds, thus extending the conduction period of the thyristor has no effect.

4.4 Non-linear effects

Several authors [B.9] have pointed out that spark discharge sources may exhibit some non-linear behaviour in terms of the spherical divergence law for a point source. The over pressure produced by the shock wavefront may approach or even exceed the ambient pressure, and so nullify the assumptions implicit in the derivation of the wave equation.

The most direct and simplest test for non-linearity is that of spherical divergence, that is, does the sound pressure at any frequency decrease at a rate of 6 dB per doubling of distance.

A series of measurements were conducted in the anechoic chamber to test the pressure variation with distance. The reference distance was taken as 10 cm, and spectra measured at 20, 40, 80 and 160 cm.

The results are shown in Figure B.11 for the frequencies 5, 10, 20, 50 and 100 kHz. All these results include corrections for atmospheric absorption.

It can be seen that the spark source does obey the spherical divergence law over this range of distances.

B.4.5 Electro-magnetic Interferences

The basic design of a spark discharge noise source can lead to considerable electromagnetic radiation. The major source is the secondary winding of the transformer, but electrical cables will act as an aerial and radiate into free space.

The early designs of the spark source using the automobile ignition coil exhibited considerable e.m. radiation. At first it was thought that the diaphragm of the microphone was acting as a receiving aerial, but even with the cartridge removed, peak levels in excess of 140 dB could be measured. Electromagnetic shield techniques proved inadequate to reduce the effect to an acceptable level.

The new design of source uses a very small pulse transformer and very low energy, hence the initial radiation levels are considerably reduced relative to that of early designs. Enclosing the transformer in a grounded metal box, together with the use of a ground-plane printed circuit board was sufficient to reduce e.m. effects to an acceptable level.

Figure B.7 shows the relative size of the e.m. pulse compared to the acoustic one. However, even at this samll level, the pulse can cause

the Nicolet Spectrum Analyser to mis-trigger in the time averaging mode.

The problem can be overcome by using an external trigger pulse, the one used to fire the spark source.

References Appendix B

B.1 Klinkowstein, R.E.: "A study of Acoustic Radiation from an Electrical Spark Discharge in Air".
M.Sc Thesis MIT Acoustics and Vibration Laboratory. 1974.

B.2 Lyman, O.: "A study of the Shock Wave Growth from a weak Electrical Discharge".
Ballistics Research Laboratory Report 1300. 1960.

B.3 Wyber, R.J.: "The Design of a Spark Discharge Acoustic Impulse Generator".
IEEE Trans. A.S.S.P. 1975 (23) 157-162.

B.4 Wright, W.M. and Mendendorp, N.W. "Acoustic Radiation from a Finite Line Source with N-Wave Excitation".
J.A.S.A. (43) 966-971.

B.5 Dejong, R.: "A Model Study of the Effects of Wind On The Sound Attenuation of Barriers".
MIT Acoustics and Vibration Laboratory. 1974.

B.6 Cann, R.G. and Lyon, R.H.: "New Acoustical Modelling Instrumentation".
J.A.S.A. (61) 1094-1097. 1977.

B.7 Wyber, R.J.: "The Application of Digital Processing to Acoustic Testing".
IEEE Trans. A.S.S.P. (22) 66-72. 1974.

B.8 Walters, B.G.: "Instrumentation for Acoustic Modelling". J.A.S.A. (47) 413-418. 1979.

B.9 Barron, M.: "Analogue Scale Modelling of Auditoria." IOA Meeting Edinburgh, September 1980.

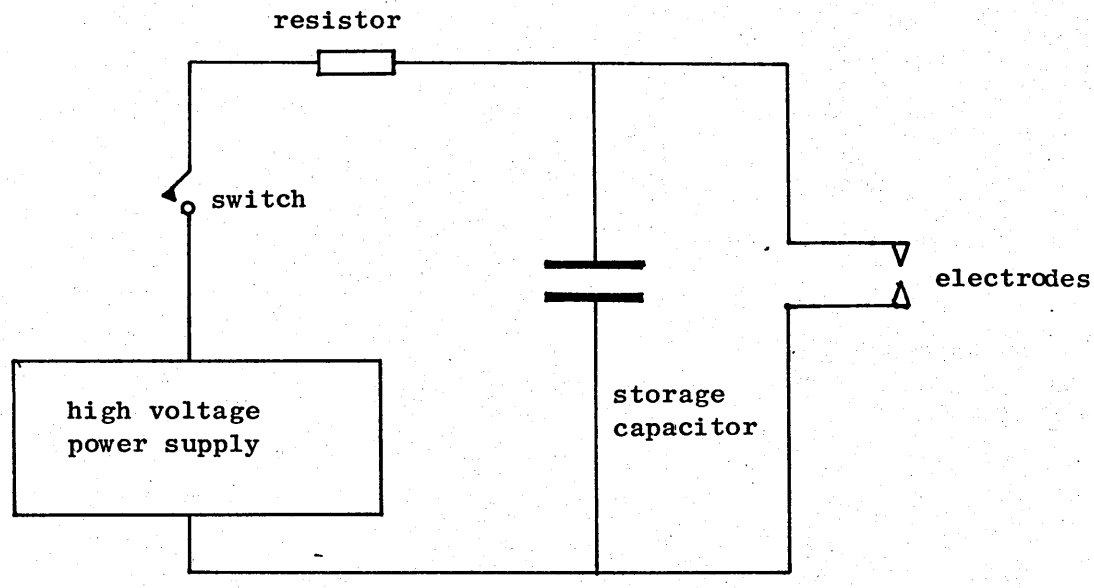

Figure B.1
Block diagram of basic spark discharge circuit

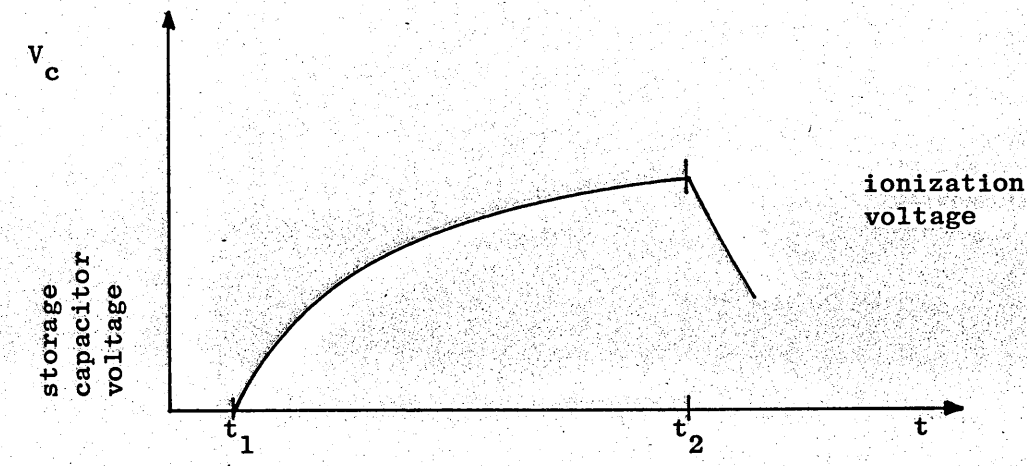

Figure B.2
Storage capacitor voltage versus time

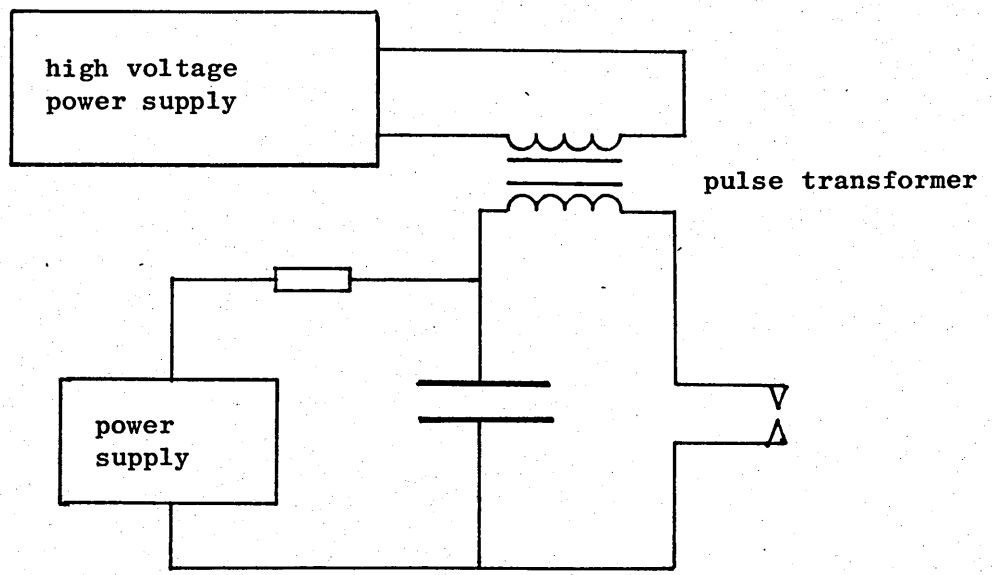

Figure B.3
Series triggered spark discharge circuit

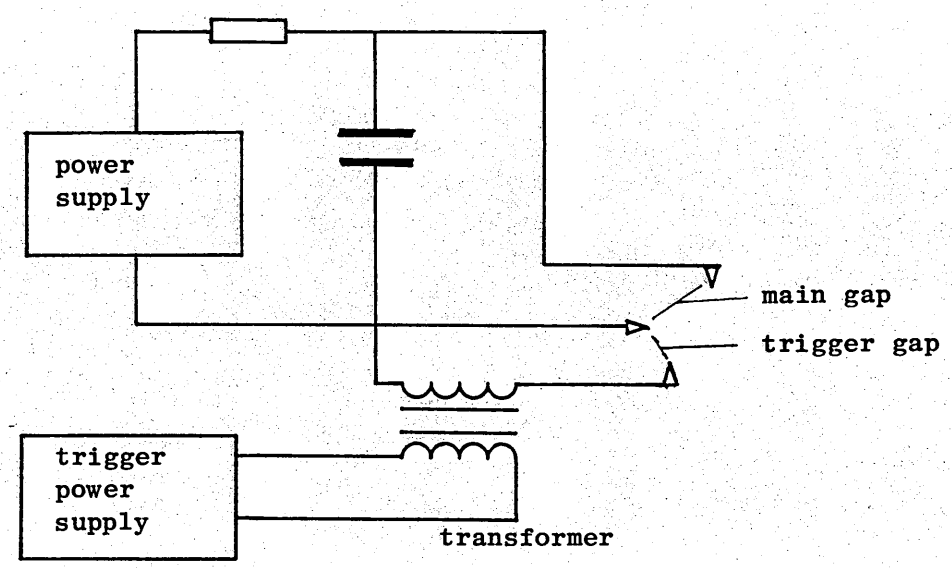

Figure B.4
Parallel triggered spark discharge circuit

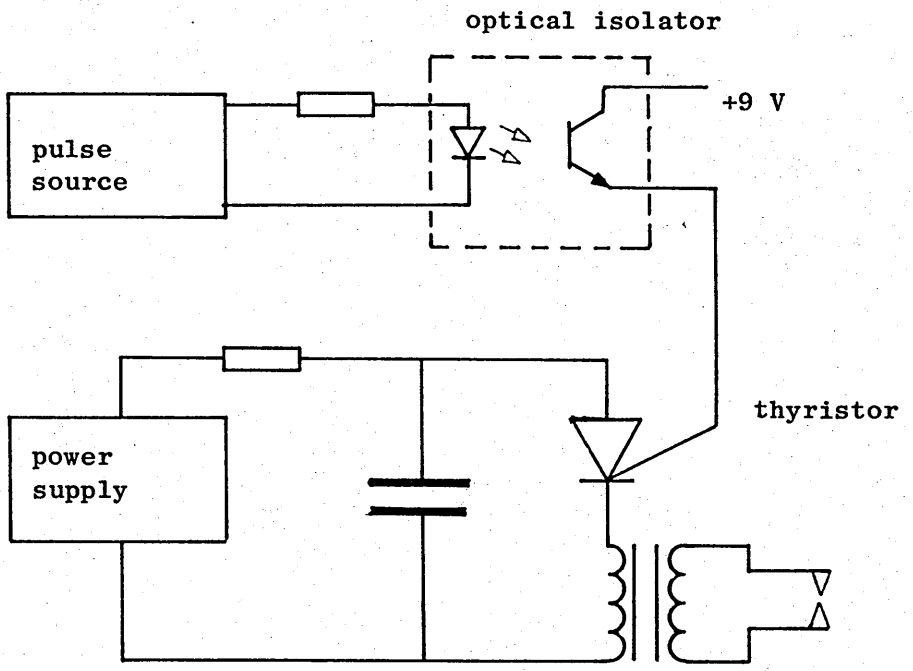

Figure B.5
Spark discharge circuit with thyristor switch

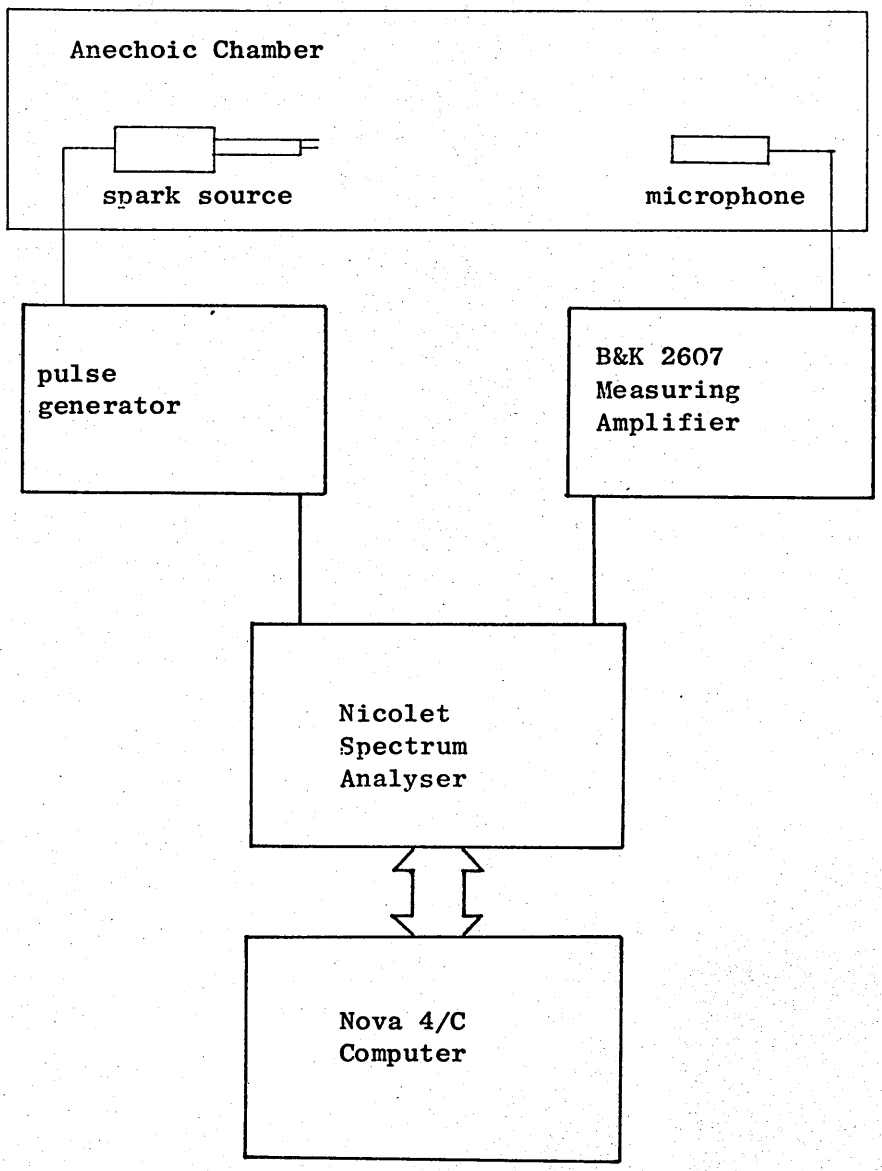

Figure B.6
Block diagram of spark source
calibration instrumentation

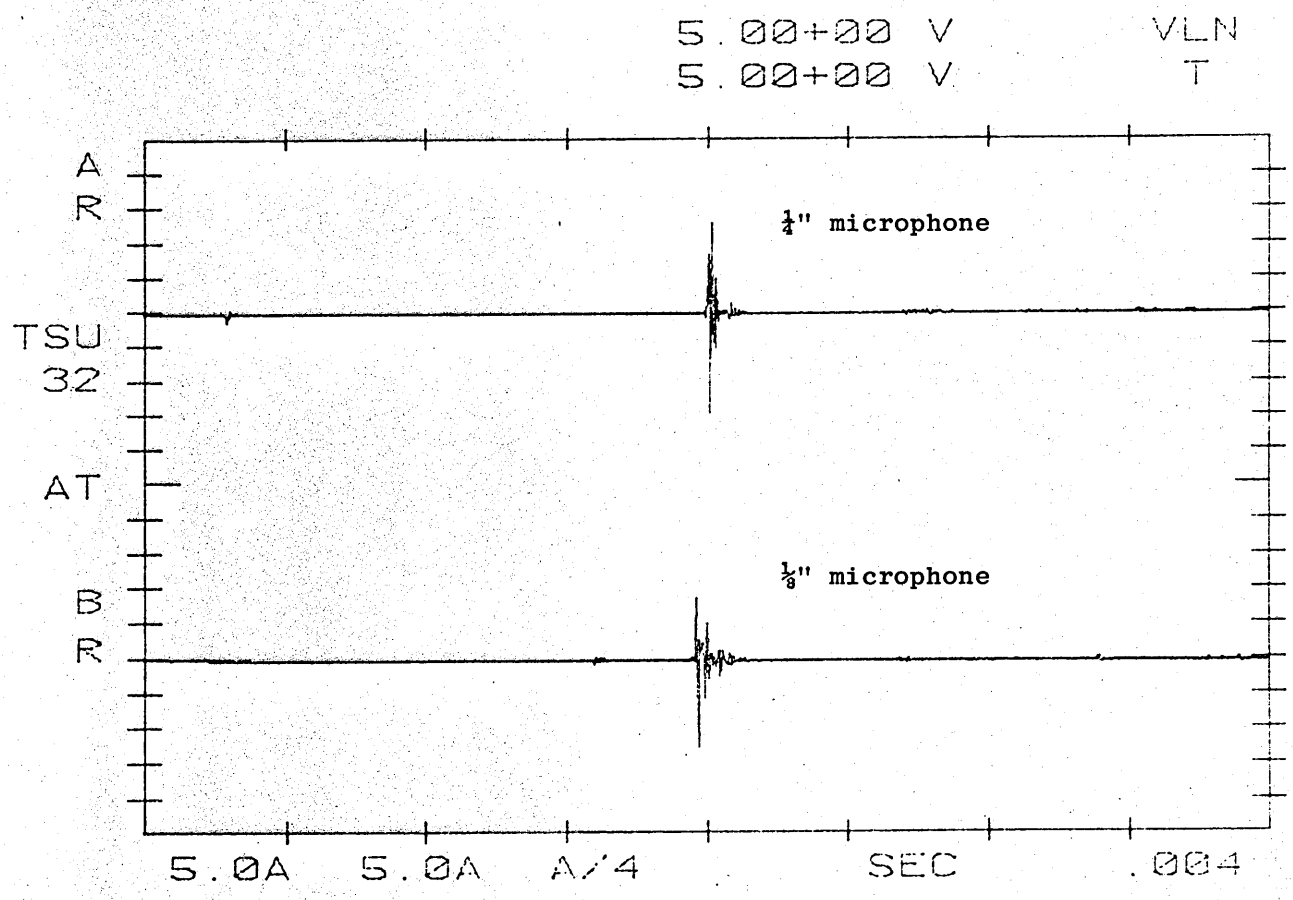

Figure B.7
Measured spark discharge

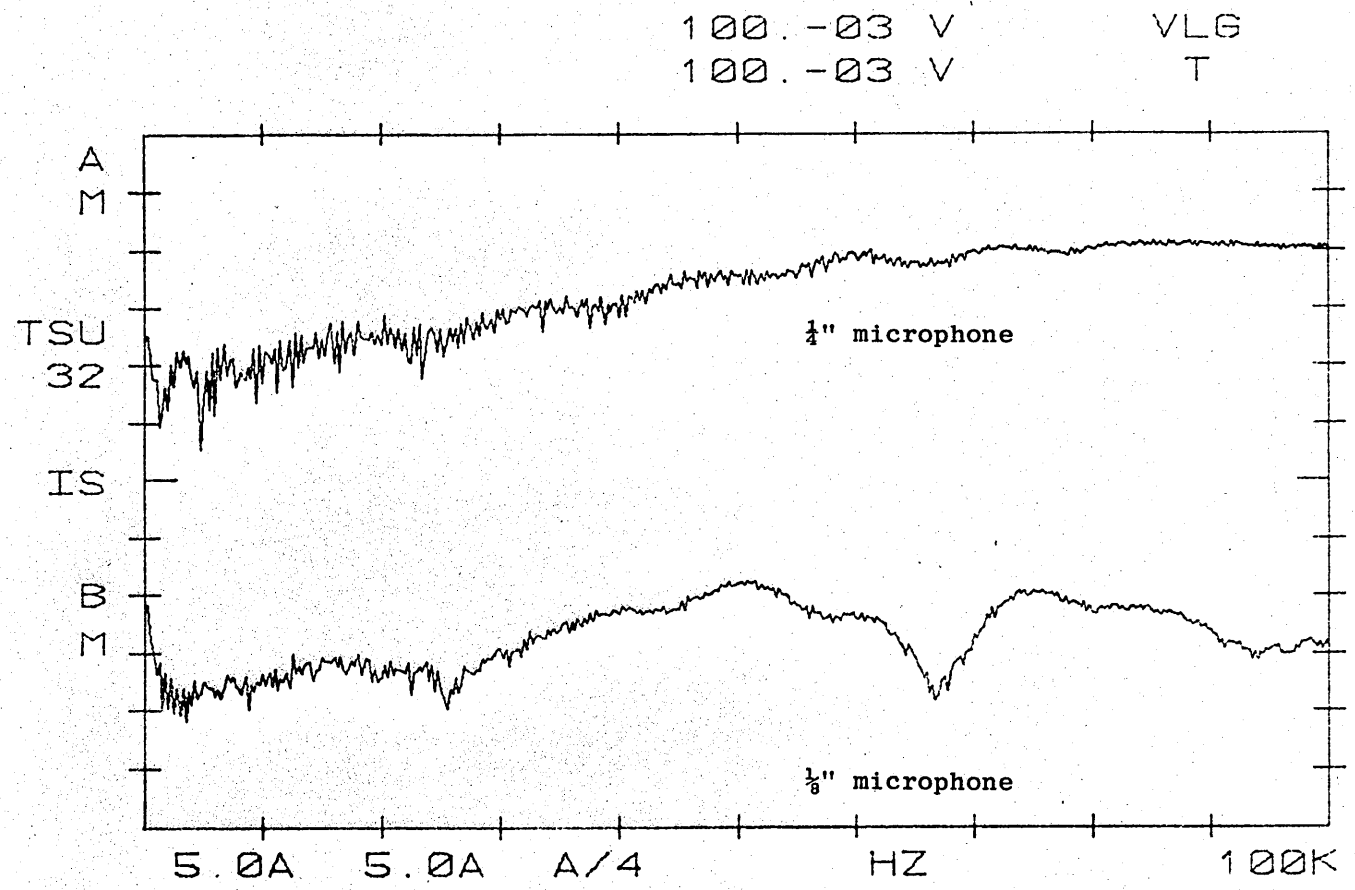

Figure B.8
Measured Spectra of spark discharge

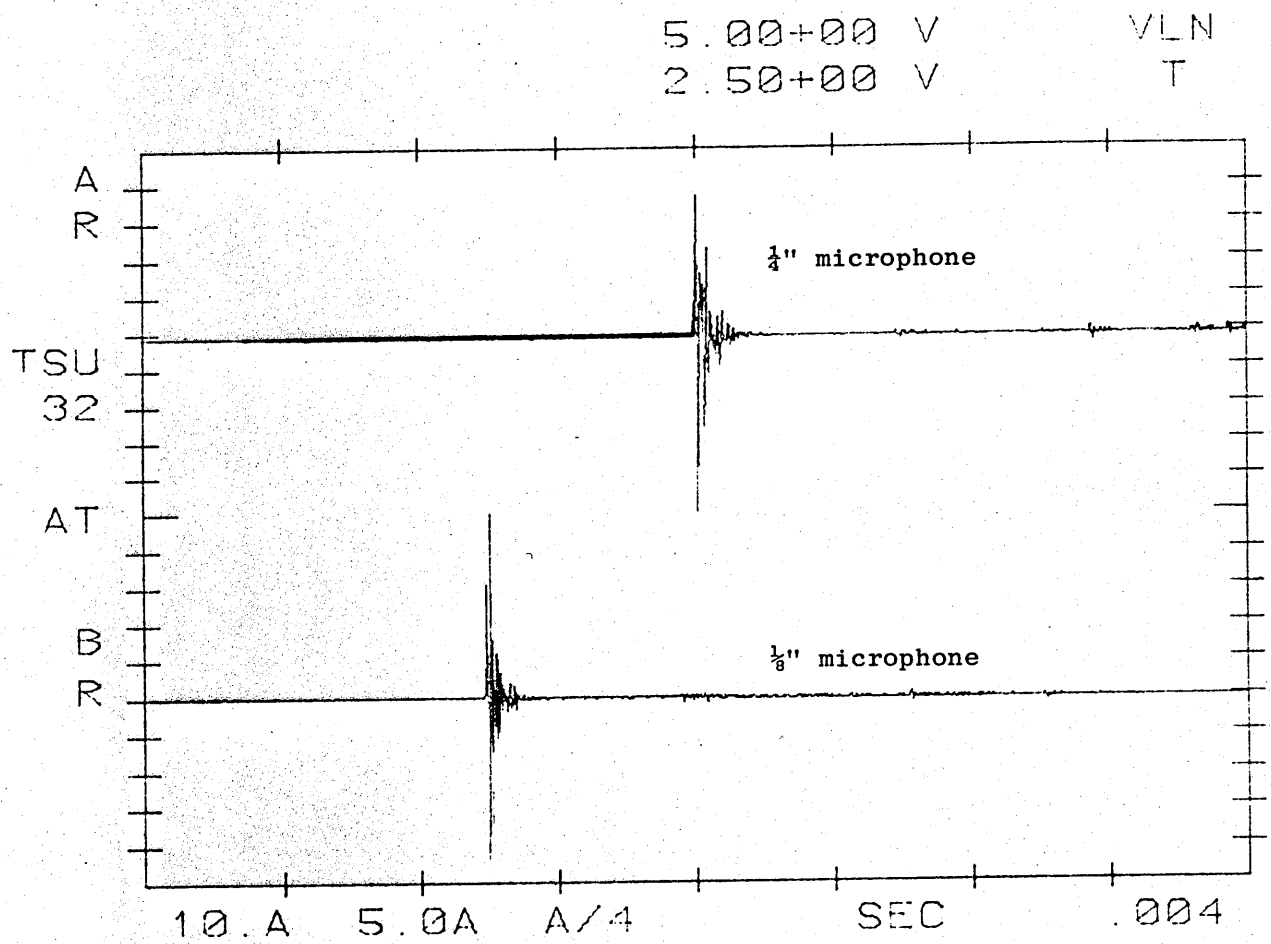

Figure B.9
Spark discharge pulse duration versus trigger pulse duration
(a) trigger pulse duration 12 μs

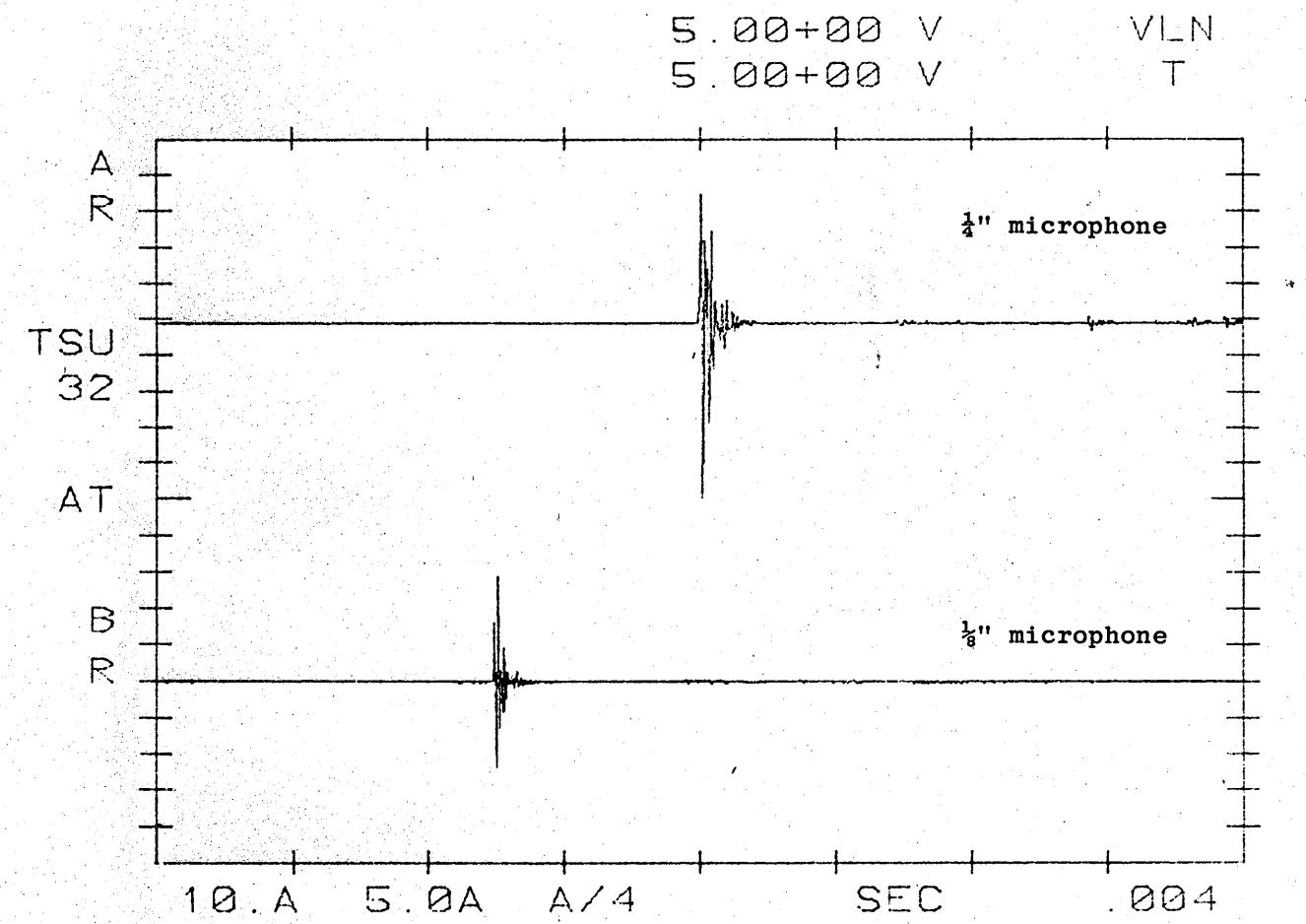

Figure B.9(b)
Trigger pulse duration 100 µs

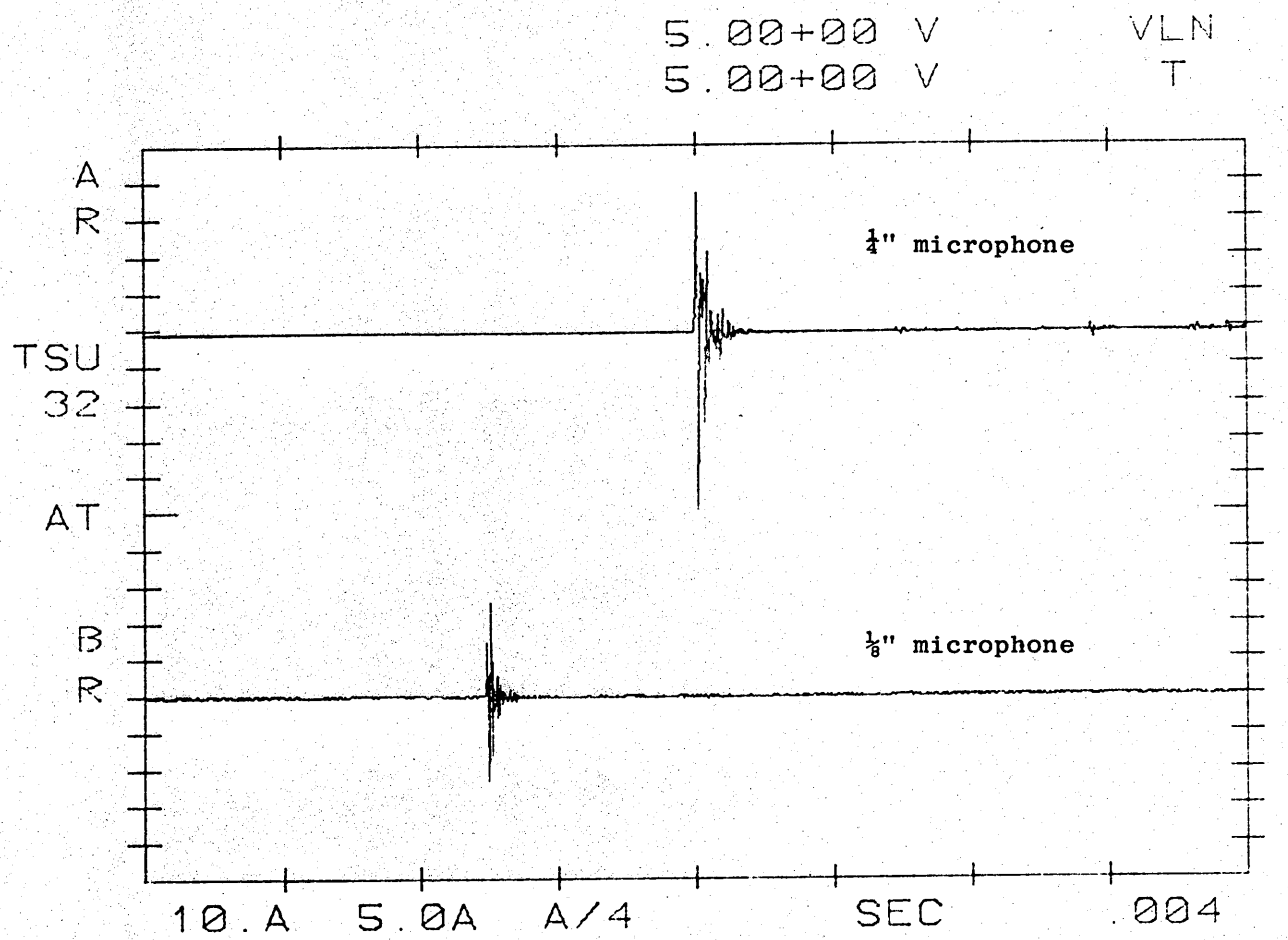

Figure B.9(c)
Trigger pulse duration 200 µs

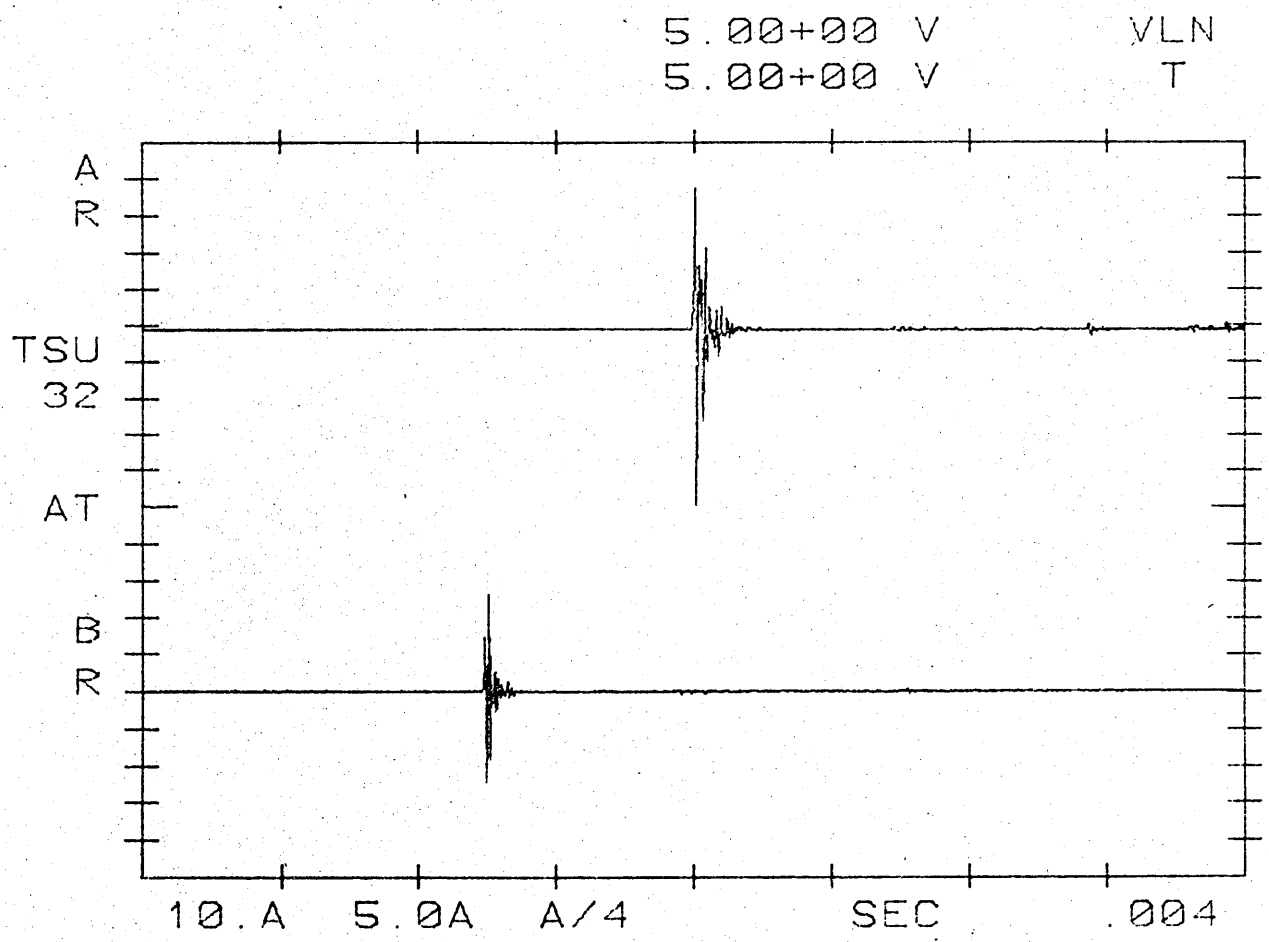

Figure B.9(d)
Trigger pulse duration 400 µs

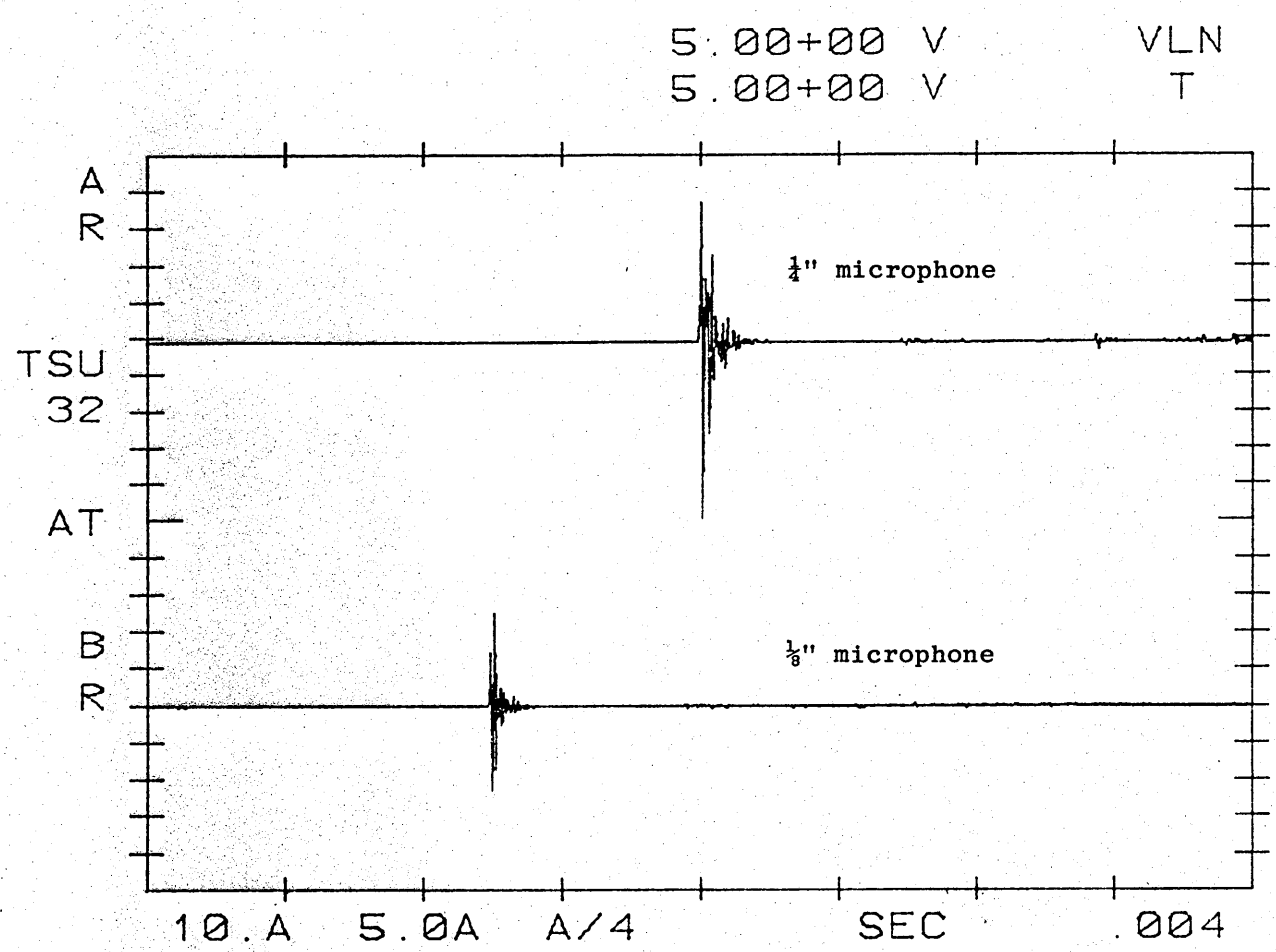

Figure B.9(e)
Trigger pulse duration 1000 µs

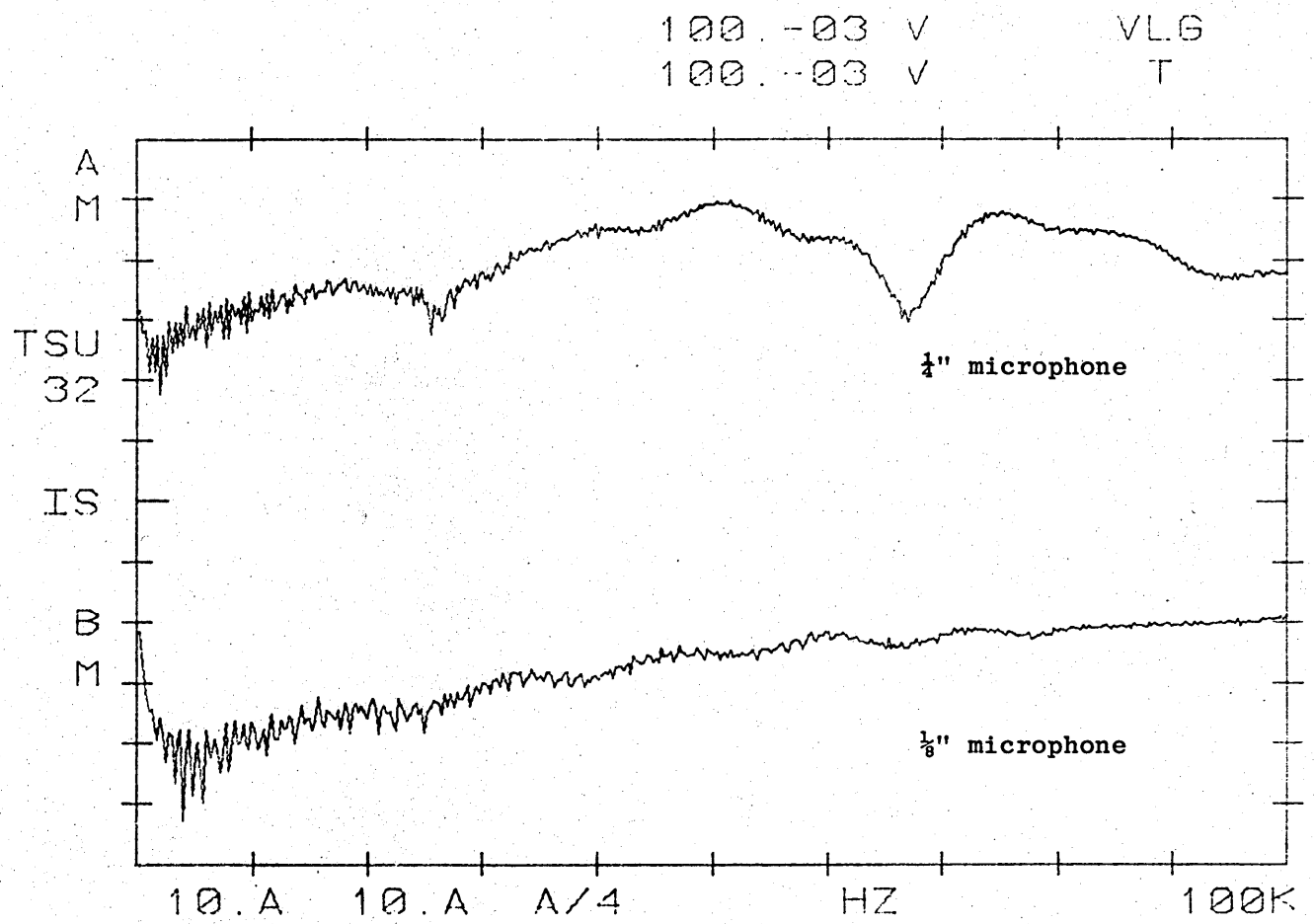

Figure B.10 Spark source spectrum versus trigger pulse duration
(a) trigger pulse duration 12 μs

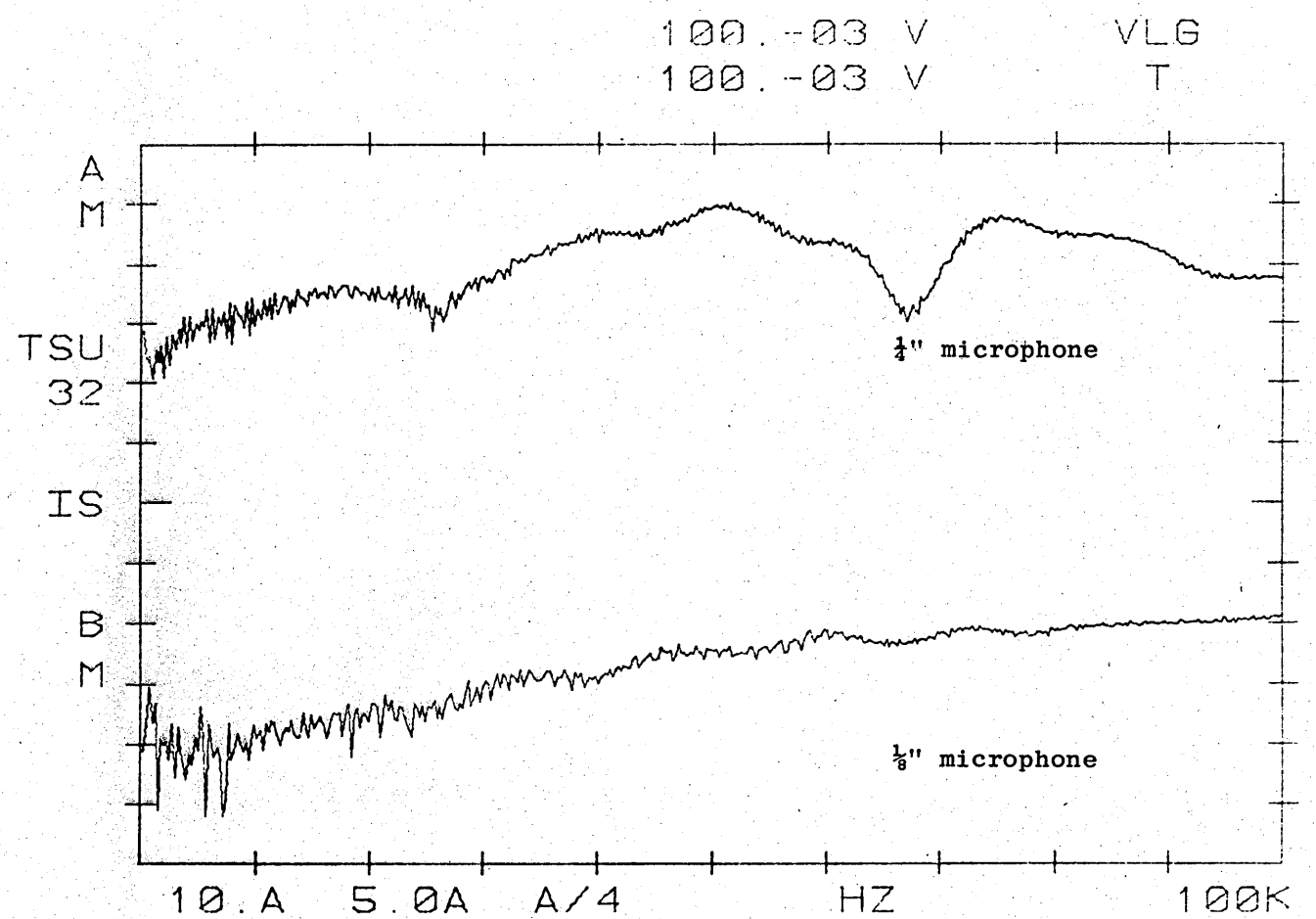

Figure B.10(b)
Trigger pulse duration 100 µs

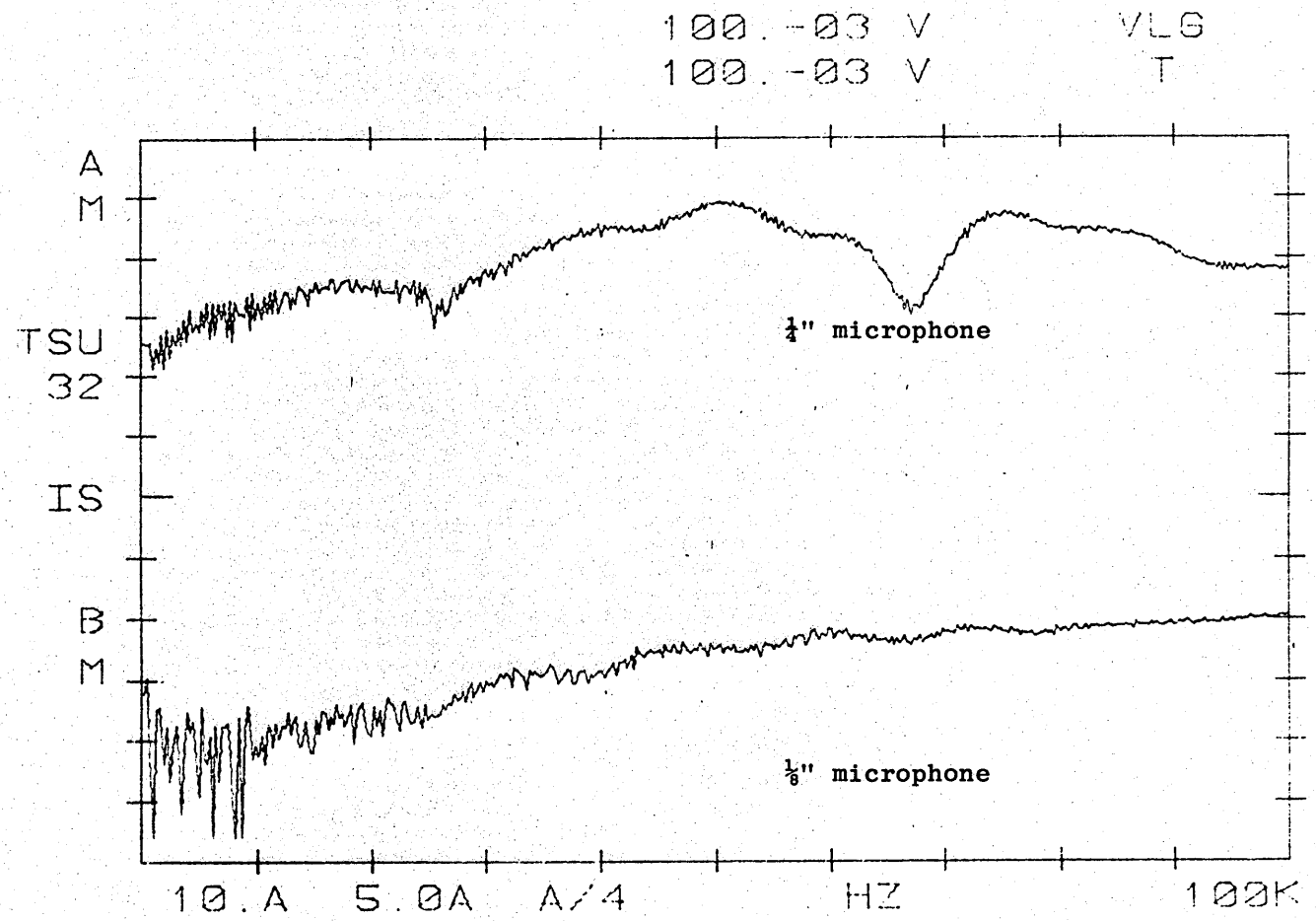

Figure B.10(c)
Trigger pulse duration 200 µs

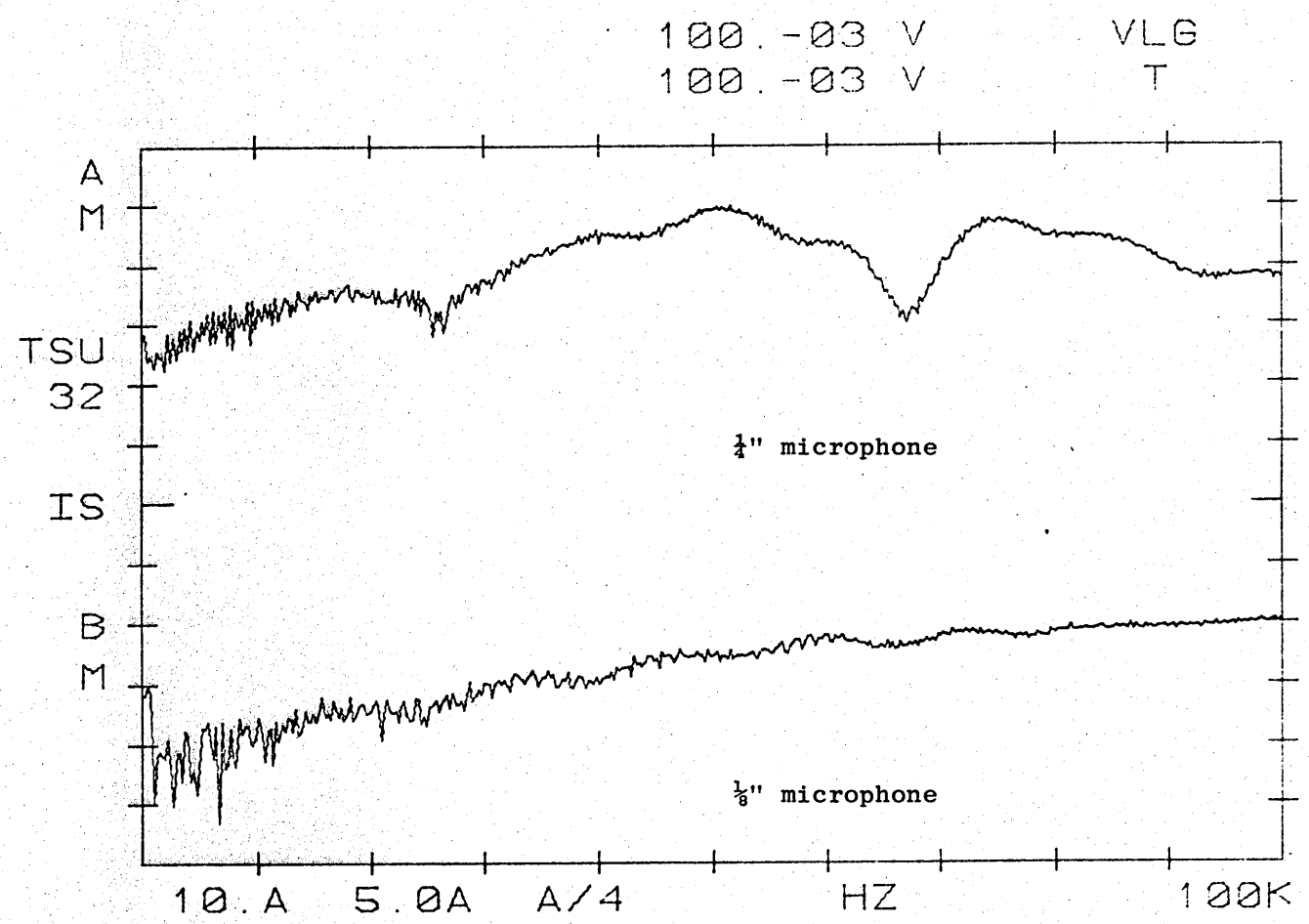

Figure B.10(d)
Trigger pulse duration 400 µs

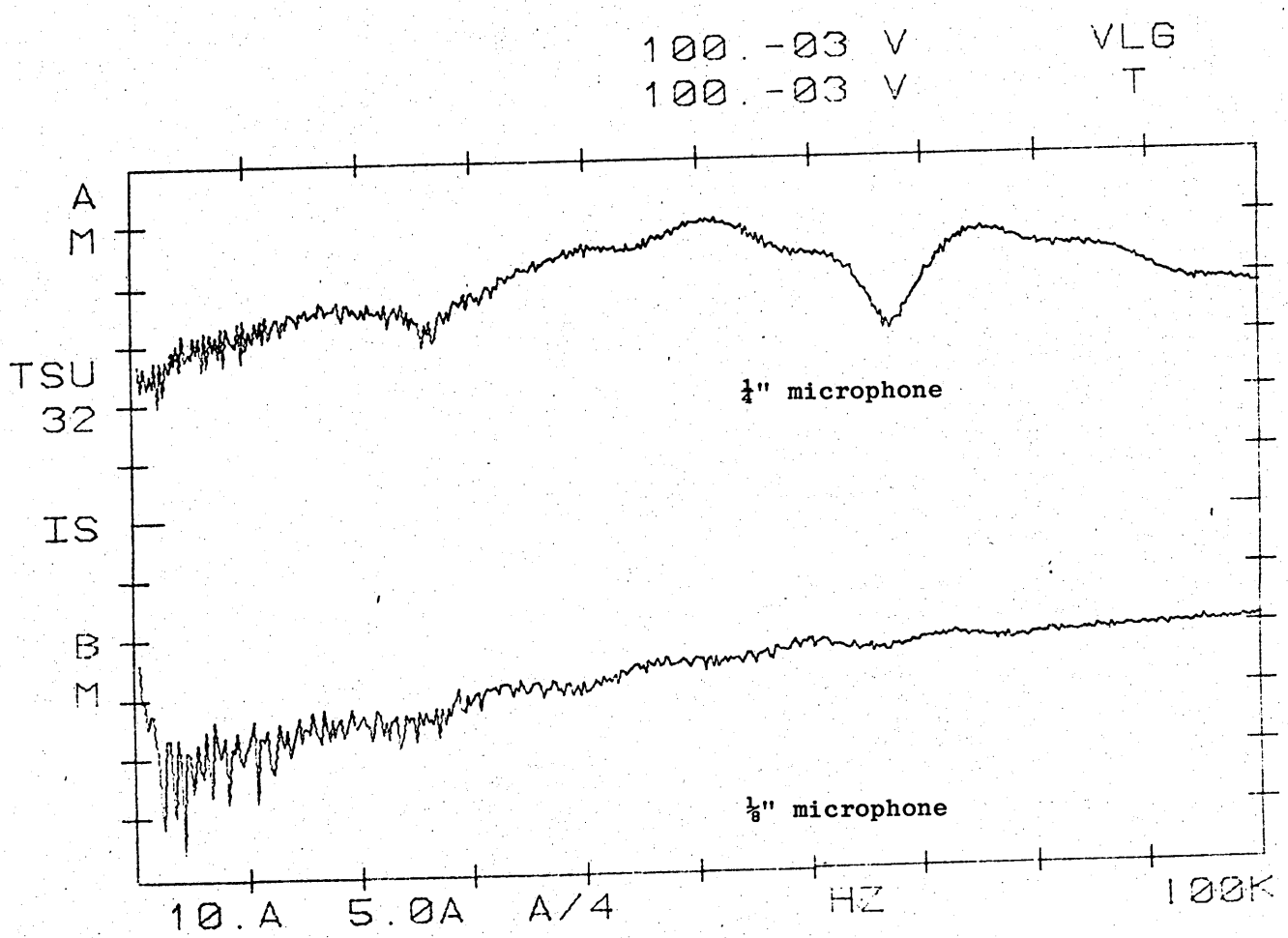

Figure B.10(e)
Trigger pulse duration 1000 µs

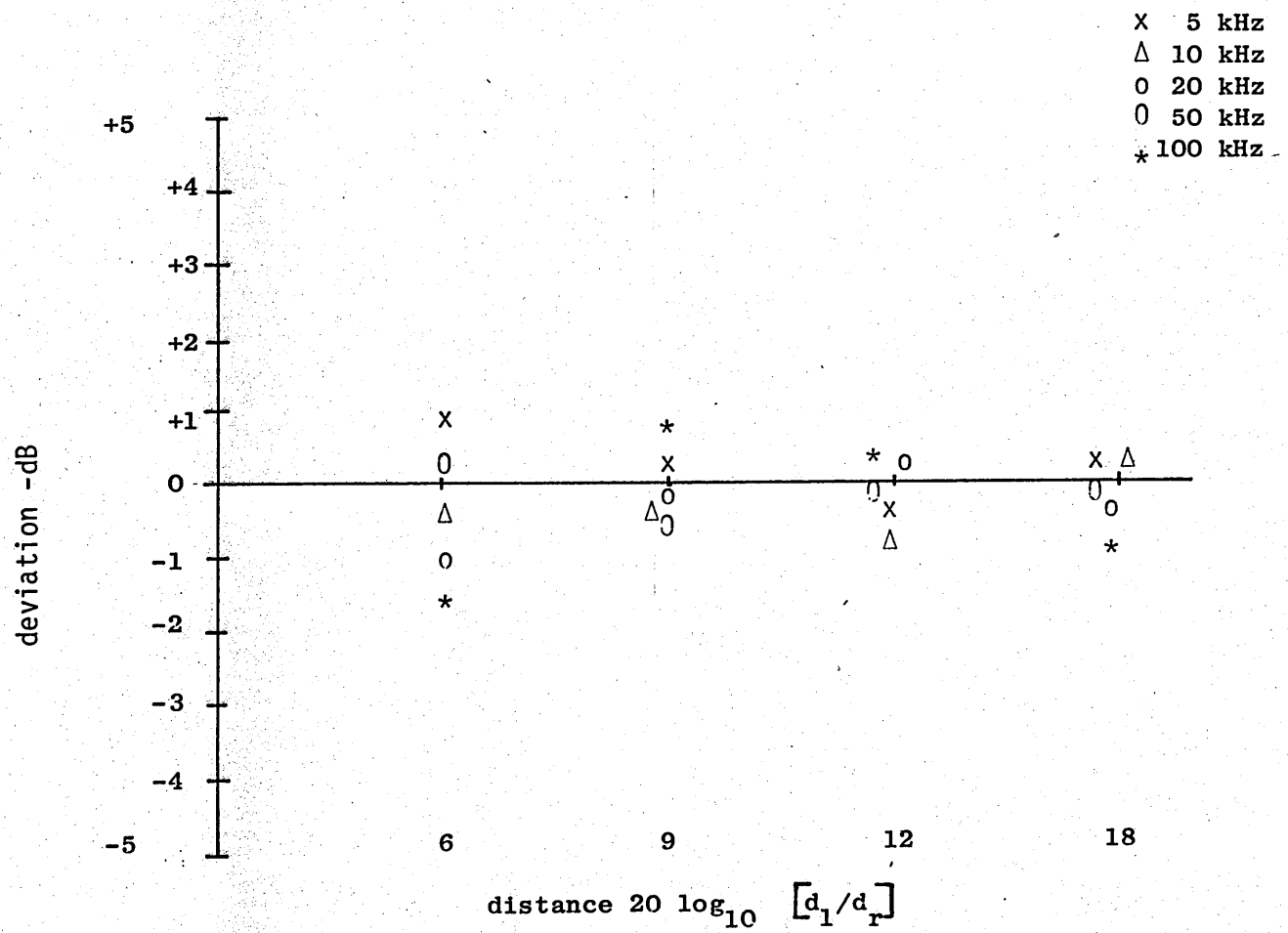

Figure B.11
Deviation from Inverse Square Law for Spark Source

APPENDIX C

Atmospheric Absorption

Sound propagating through an unbounded medium is subject to attenuation due to viscous and thermal losses associated with transport phenomena in the medium and that due to molecular relaxation effects of losses in the transfer of energy between the excited and ground states of the molecules during the passage of the sound waves.

For the range of frequencies associated with this study, the different sources of attenuation may be considered to be simply additive due to the wide separation of the frequencies of maximum effect and the magnitufe of attenuation from each source: Two types of sound source must be considered, pure tone and broadband.

C.1 Pure Tone Absorption Coefficients

Formulae for predicting the magnitude of such absorption for pure tones have been taken from the work of Evans and Bazley [C.1] and Bazley [C.2]. These formulae are based on the assumption that the attenuation can be expressed in the form

$$\text{attenuation} \sim \exp(mx) \qquad \text{C.1}$$

where x is the distance and m the absorption coefficient.

C.1.1 Classical Absorption

Classical absorption is the term given to the losses due to viscous and thermal effects when sound travels through a gaseous medium. The attenuation is dependant upon the temperature, frequency and ambient pressure.

According to Bazley [C.2] the energy attenuation coefficient M_{cr} can be calculated from the expression

$$M_{cr} = 3.62.10^{-11}(1+0.001t)f^2/P \qquad C.2$$

where t is the temperature in ^{o}C

f is the frequency in Hz

and P is the ambient pressure in atmospheres.

C.1.2 Molecular Absorption

Molecular absorption arises from relaxation losses associated with the exchange of energy between the translational and vibrational modes of the molecules of oxygen and nitrogen.

The energy attenuation coefficient for the nitrogen molecules M_N is given by

$$M_N = \frac{1.71.10^{-8}}{(1+0.00366t)^{\frac{1}{2}}} \left\{ \frac{hpf^2}{2.77.10^{-5}f^2+h^2p^2} \right\} \qquad C.3$$

h is the percentage of water molecules in the air, and can be calculated if the relative humidity, RH, is known from the expression

$$h = \frac{RH}{P} \quad T^{-4.922} \quad \text{antilog}_{10}(20.5318-2939/T) \qquad C.4$$

where T is the ambient temperature in ^{o}K.

The attenuation for the oxygen molecules is given by

$$M_o = 2 \frac{\mu max}{C_o} \qquad \frac{f}{f/F_o+F_o/f} \qquad C.5$$

where $F_o = 30560.P.h^{1.3}$ C.6

and $\frac{\mu max}{C_o} = 4,2425.10^{-6}+8,8168.10^{-8}t+5.4834.10^{-10}t^2$ C.7

1.3 Total Absorption Coefficient

The total absorption coefficient is the sum of the three components, namely

$$M = M_{cr}+M_N+M_O \quad \text{nepers/m.} \qquad C.8$$

A more useful expression in terms of dB/m can be obtained by multiplying equation C.8 by 4.343 so that:

$$M = 4.343\left[M_{cr}+M_N+M_O\right] \text{dB/m} \qquad C.9$$

C-2 Broadband Noise Absorption Coefficients

Pure tone sources rarely exist in practice. Instead one is normally faced with a source whose energy is spread continuously over a band of frequencies.

The previous subsection showed that absorption increases with frequency. As a result, when a band of noise propagates through the air the higher frequencies are attenuated more than the lower ones of the band. The atmosphere behaves as a spectrum shaping mechanism which can introduce significant errors in the measurement of the source spectrum.

Several techniques for correcting for this effect have been proposed. If the source spectrum is flat within the band, then an underestimate of the attenuation will be obtained if the pure tone absorption coefficient for the frequency at the lower limit of the band is used for the whole band. This is the procedure recommended by the S.A.E. [C.3].

Sutherland and Bass [C.4] have proposed a more rigorous correction based upon integration of the absorption loss across the whole band. Furthermore, they also address the problem of the receiver frequency response characteristic, but this topic is left to Appendix D.

2.1 Absorption Loss for a Band of Noise

The difference Δ_I, in decibels, between the absorption loss, for a fixed path length ℓ, of pure tone at the centre of the band and the loss for the total power in the band is given by

$$\Delta_I = 4.343m(f).\ell.10 \log_{10}\left\{ \int_{f_1}^{f_2} P^2(f).10^{\frac{-4.343m(f).\ell}{10}} df \right\} = 1$$

$$-10 \log_{10}\left\{ \int_{F_1}^{f_2} P^2(f)df \right\} \qquad \text{C.9}$$

where m(f) is the pure tone absorption coefficient at frequency f calculated from equation C.8.

ℓ is the path length

P(f) is the pressure spectral density of the source

and f_1, f_2 are the nominal lower and upper cut off frequencies of the noise band.

Equation C.9 cannot normally be expressed in a closed form, hence Sutherland and Bass propose a numerical integration scheme based upon subdivision of the band f_1 to f_2. Assuming a constant slope to the pressure spectral density of the source, Δ_I can be written as

$$\Delta_I = 10 \log_{10} \left\{ S\beta \sinh\left[\beta(S_A+S_B)\right]/(S_A+S_B)\sinh(\beta S_B) \right\} \qquad \text{C.10}$$

where $\beta = 1/20 \log_{10}(e) = 0.11513$

The terms S_A and S_B correspond to the slope of the absorption loss and the slope of the source spectrum over the band f_1 to f_2.

An approximate value for S_A can be obtained from the expression

$$S_A \simeq 4.343\left|m(f_{c-1})-m(f_{c+1})\right|. \; 1/2$$

$m(f_{c-1})$ is the attenuation coefficient at the centre frequency of the filter one bandwidth below f_c, and $m(f_{c+1})$ that at the centre frequency one bandwidth above f_c.

S_B can be calculated using a similar procedure for the source spectrum.

References Appendix C

C.1 Evans, E.J. and Bazley, E.N.: The Absorption of Sound in Air at Audio Frequencies.
Acustica (6) 238-243. 1956.

C.2 Bazley, E.N.: Sound Absorption in Air at Frequencies up to 100 kHz.
NPL Acoustics Report, Ac 74. 1976.

C.3 Society of Automotive Engineers.: Standard Values of Atmospheric Absorption as a Function of Temperature and Humidity for use in Evaluating Aircraft Flyover Noise.
Areospace Recommended Practice, ARP 866. 1964.

C.4 Sutherland, L.C. and Bass, H.E.: Influence of Atmospheric Absorption on the Propagation of Bands of Noise.
J.A.S.A. (66) 885-894. 1979.

APPENDIX D

Finite Analysis Bandwidth Effects

The theoretical models for point to point propagation described in Chapters 3 and 4 are essentially puretone ones, that is they assume an infinitely narrow analysis bandwidth for the source and receiver. However, typical source and receivers used for modelling or community noise measurements have a finite bandwidth, and this difference has certain implications when comparing prediction with measurement, especially at model frequencies.

The energy of a broadband source can be thought of as being produced by an infinite number of puretone sources (Fourier Integral). Each such puretone source will behave as predicted by the theoretical model with interference dips related to the frequency, source receiver geometry and ground surface. However, because of the receiver bandwidth, the occurrence of strong interference dips at some frequencies will be masked by the high pressure levels at other frequencies.

Figure D.1 compares the received pressure measured over a rigid surface for a puretone, 1/3 octave and octave band sources.

The pure tone shows pronounced interference dips, whilst the broadband sources do not. The masking of the dips is greatest at high frequencies.

This problem was recognised by Franken [D.1] as early as 1955, but seems to have been ignored by many others since then.

Consider first the problem of reflection from a rigid boundary. The mean square pressure at a receiver is given by the expression:

$$\overline{P_t^2} = \overline{P_i^2} + \overline{P_r^2} + 2\overline{P_i P_r} \qquad \text{D.1}$$

where $\overline{P_i^2}$ is the mean square pressure contributed by the direct path, $\overline{P_r^2}$ that from the reflected, and $\overline{P_i P_r}$ the mean pressure of the cross product.

For a rigid surface P_r is just a delayed version of P_i, therefore the mean value of the cross product may be written in the form:

$$\overline{P_i P_r} = \frac{1}{T} \int_o^T P_i(t)\, P_i(t-\tau)\, d\tau \qquad \text{D.2}$$

But this integral defines the auto-correlation function $R(\tau)$. Equation D.1 may therefore be written as:

$$\overline{p_t^2} = \overline{p_i^2} + \overline{p_r^2} + 2R(\tau) \qquad \text{D.3}$$

since the mean square pressure of the reflected wave is independant of τ.

For a band limited receiver, with limits f_1 and f_2, it can be shown [D.2] that for $P_i = A\cos(\omega t)$, then:

$$R(\tau) = \frac{1}{\pi\tau(f_2-f_1)} \cos[\pi\tau(f_2+f_1)] \sin[\pi\tau(f_2-f_1)] \qquad \text{D.4}$$

The total pressure at the receiver, relative to free field can be obtained by dividing equation D.3 by $\overline{p_i^2}$.

Expressing this in decibels gives:

$$p_t^2 = 20 \log_{10} [2 + 2R(\tau)] \qquad \text{D.5}$$

If $f_2 = f_1$, then:

$R(\tau) = \cos 2\pi f\tau$ and $\overline{p_t^2}$ becomes

$$\overline{p_t^2} = 20 \log_{10} [2 + \cos 2\pi f\tau] \qquad \text{D.6}$$

which is the result for pure tone propagation over a rigid boundary.

Franken extends this solution to include reflection from a finite impedance surface, using Ingard's solution for a local reaction boundary. Unfortunately the errors in Ingard's solution reduces the value of Frankens results.

An alternative technique suggested by Sutherland and Bass [D.3] enables one to correct for the bandwidth effects regardless of the propagation path. The method uses a numerical integration process similar to that outlined in Appendix C, but includes the effect of real filter attenuation skirts.

The filter correction factor, in dBs, is given by:

$$\Delta_F = 10 \log_{10}\left[\int_{f_L}^{f_u} P^2(f)\ 10^{-TL(f)/10} df \Big/ \int_{f_1}^{f_2} P^2(f) df\right] \qquad D.7$$

TL(f) is the transmission loss of the filter, f_L and f_u are the lower and upper frequency limits of the filter, and $P^2(f)$ is the pressure spectral density at the input, whilst f_2 and f_1 are the limits of the input signal. For practical purposes $f_U = 8f_2$ and $f_L = f_1/8$.

Equation D.7 is solved numerically by dividing the bands f_U-f_L and f_2-f_1 into smaller constant percentage bandwidth filters. The range f_2-f_1 becomes 'b' bands and f_U-f_L 'n.b' bands.

The pressure spectral density in each of these small bands is assumed to have constant slope, therefore, if strong interference bands are known to exist these bands must be made very narrow.

The numerical solution for Δ_F can be written as:

$$\Delta_F = 10 \log_{10} \left[\sum_j^{nb} B_j'\right] - 10 \log \left[\sum_j^{b} B_j\right] \qquad D.8$$

where:

$$B_j = P^2(f)\ f_j\ (r^{(m_j+1)/b}-1)/(m_j+1)$$

$$B_j' = P^2(f)\ 10^{-TL(f)/10}\ fj(r^{(m_j+1)/b}-1)/(m_j+1)$$

f_j is the centre frequency of the jth band.
r is the ratio of the nominal band edges of the filter f_2/f_1.
m_j is the slope of the pressure spectal density given by:

$$m_j = \left[L_s(f_{j+1}) - L_s(f_j)\right]/\left[10/b \log_{10} r\right]$$

$L_s(f_j)$ is the sound pressure level at frequency f_j and
TL(f) is the transmission loss of the real filter at frequency f.

A approximate solution for TL(f) is:

$$TL(f) = 10 \log_{10} \{A+B \left[(C(f/f_c)-(f_c/c_f)\right]^6\}$$

For 1/3 octave filters the constants are:

$A = 8/13,\ B = 2547,\ C = 10^{-1/60} \quad f \leqslant f_1'$

$A = 1,\ B = C = 0,\ f_1' < f < f_2'$

$A = 8/13,\ B = 2547,\ C = 10\ 1/60 \quad f \geqslant f_2'$

$f_2' = 10^{1/30} f_c \quad f_1' = 10^{-1/30} f_c$

f_c is the centre frequency of the filter.

References Appendix D

D.1 Franken, P.A.: A Theoretical Analysis of the Field of a Random Noise Source Above an Infinite Plane.
National Advisory Committee for Aeronautics, Technical Note 3557. 1955.

D.2 Pernet, D.F.: Interference and Correlation.
Paper K66 ICA Liege. 1965.

D.3 Sutherland, L.C. and Bass, H.E.: Influence of Atmospheric Absorption on the Propagation of Bands of Noise.
J.A.S.A. (66) 885-894. 1979.

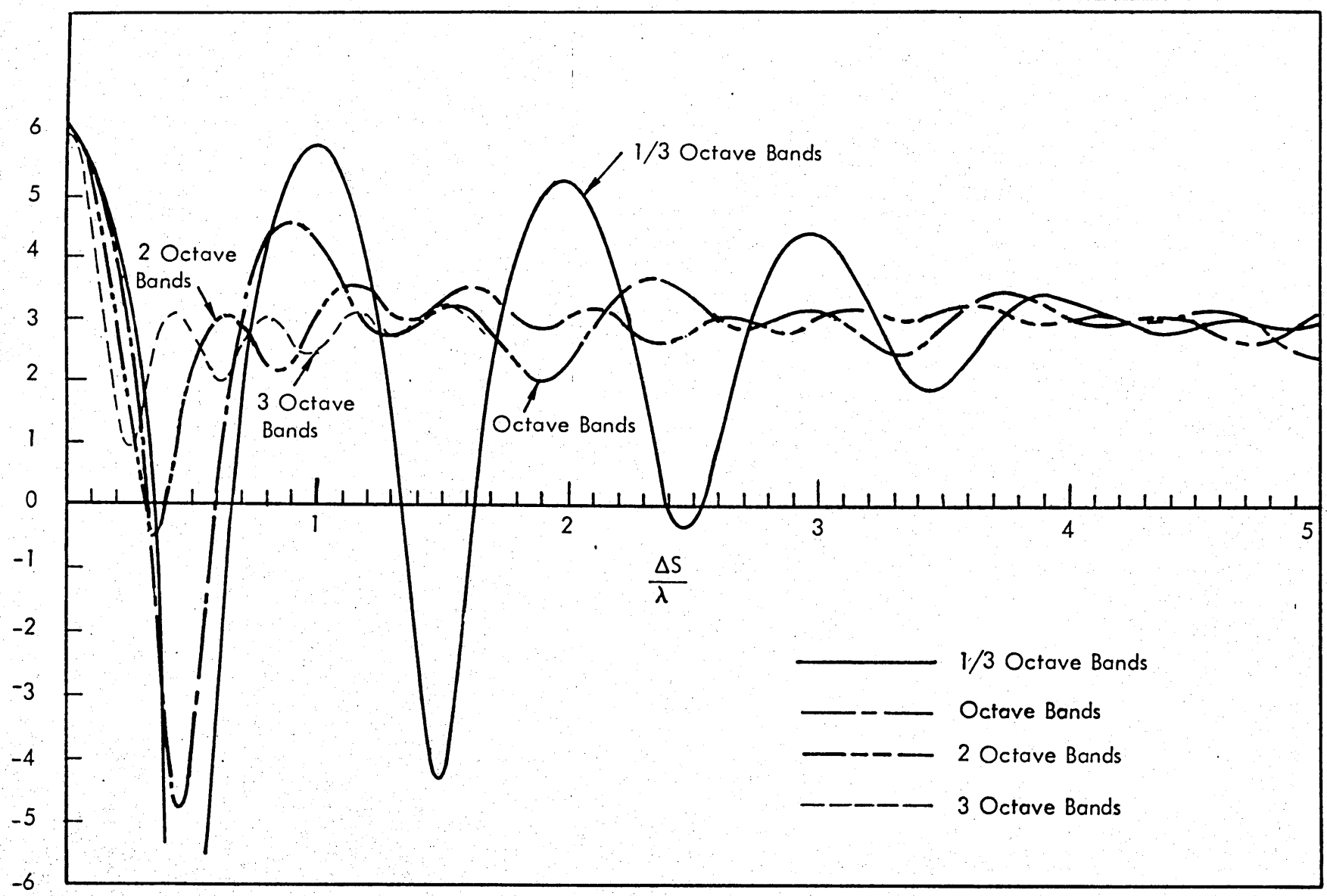

Figure D.1 Predicted excess attenuation above a rigid surface for octave bands of noise (after Sutherland)

APPENDIX E

Computer program listings

This appendix describes the more important computer programs developed during this study. The programs have been divided into two groups, those derived from the theoretical predictions of Chapter 3, and those developed for the impedance measurement methods. The programs consist of a main program for initializing variables and files and sub-programs (subroutines or functions) for computing the numerical results.

In view of the many differences between computer software and hardware systems, the main program listings are not described here. However, the parameters required by each sub-program are fully described so that a reader may develop suitable main programs for any computer installation.

The programs have been written in Fortran/77 for use on a Digital Equipment VAX/780 computer operating under VMS/3.0. The parameters for each module are described under the headings: name, equivalent parameter and data type. The equivalent parameter descriptor provides a cross reference to the defining equation in the main text.

A listing for each module is given at the end of this appendix.

E.1 Theoretical prediction sub-programs

Five sub-program modules have been developed for predicting the total pressure at a receiver. Modules CHEN and EXTEND provide numerical values for the local and extended reaction boundaries respectively. Module RASMUSSEN computes the solution for the half soft,half rigid boundary and modules STRIP1 and STRIP2 compute solutions for the rigid strip in an impedance boundary.

E.1.1 Module CHEN

CHEN computes the total pressure at a receiver according to equation 3.64. Three input variables are passed to the subroutine in the parameter list, the other variables are passed in the common block ALL.

Parameter list

Name	Equivalent parameter	Data type	Comment
H	h	real	sum of ns + nr
HS	z_s	real	source height
HR	z_r	real	receiver height
R	r	real	horizontal separation distance
R1	r_1	real	direct path length
R2	r_2	real	reflected path length
BETA	β	complex	admittance ratio
J	i	complex	$\sqrt{-1}$
K1	k_1	real	wave number in air
STH	$\sin \theta_i$	real	sine of angle of incidence

Name	Equivalent parameter	Data type	Comment
CTH	$\cos \theta_i$	real	cosine of angle of incidence
RP	R_p	complex	plane wave reflection coefficient
PI	π	real	constant 3.1415927
ZR	Z	complex	surface impedance
P1	$\frac{e^{ikr_1}}{4\pi r_1}$	complex	direct field
PTOT	Φ_{LR}	complex	total pressure field

Subroutines called

W(PE2,W1Z) computes erfc $(+ix_o/\sqrt{2})$

E.1.2 Module EXTEND

EXTEND computes the total pressure for a receiver above an extended reaction boundary according to equation 3.53.

Parameter list

Name	Equivalent parameter	Data -type	Comment
AKOR1	$k_1 r_1$	real	product of wave number in air and direct path length
AKOR2	$k_1 r_2$	real	product of wave number in air and reflected path length
M	M	complex	ratio of the densities of the two media
N	n	complex	refraction index
PHIT	Φ_t	complex	total pressure

Subroutines called

W(WO,WIZ) computes erfc $(+ix_o/\sqrt{2})$

E.1.3 Module RASMUSSEN

RASMUSSEN computes the total pressure above a half soft,half rigid surface according to equation 4.2. The summation is carried out over a vertical surface 20 wavelengths square and the result doubled to take account of the horizontal symmetry.

Parameter list

Name	Equivalent parameter	Data type	Comment
LAMDA	λ	real	wavelength
PHI		complex	intermediate summation variable
RD	D	real	distance of source from surface discontinuity
PHID	$\frac{e^{ikr_1}}{4\pi r_1}$	complex	direct field
HORIZ		real	horizontal increment across vertical plane
SD		real	horizontal distance from source to point on plane
R1	r_1/r_3	real	direct path length
R2	r_2/r_4	real	reflected path length
AMN	$A_{m,n}$	complex	elemental source strength
PHI	$\emptyset_t$	complex	total pressure field

Subroutines called

CHEN (BETA2,P21,P2TOT) computes total field from elemental source to receiver over an impedance boundary.

E.1.4 Module STRIP1

STRIP1 calculates the surface integral over a rigid strip according to equation 4.23.

Parameter list

Name	Equivalent parameter	Data type	Comment
LAMDA	λ	real	wavelength
K	k_1	real	wavelength
XMAX	a	real	half strip width
YMAX		real	maximum Y value for integration
XS	d	real	horizontal distance of source from origin
TP	r_2	real	distance from source to origin
SUMB		complex	intermediate
SUMC		complex	summation variables
VALUE		complex	value of surface integral

E.1.5 Module STRIP2

STRIP2 computes the surface integral of equation 4.23 using a Gaussian numerical integration procedure employing 16,32 or 64 weighting term [E.1]. The integration over Y can be expressed in terms of a Hankel function, leaving just the integration over X which is computed from the numerical procedure. The Hankel function is calculated from the relationship

$$H_o'[Z] = J_o(Z) + iY_o(Z)$$

Parameter list

Name	Equivalent parameter	Data type	Comment
SUM		complex	intermediate summation variable
Y		complex	numerical integration variable
VAL		complex	value of integrand
K	k_1	real	wave number
J	i	complex	$\sqrt{-1}$
NOP		integer	number of points in Gaussion integration
X(I)		real	abscissas
W(I)		real	weight
ARG1		real	Hankel function argument for positive x half of strip
ARG2		real	Hankel function argument for negative x half of strip

Functions called

HO1(ARG1/ARG2) computes the Hankel function of first kind and zeroth order.

E.1.6 Utility subroutines

The following set of subroutines have been used to calculate specific variables required for the theoretical solutions.

(i) Subroutine PWRC (BETA,CTH,RP)

Computes plane wave local reaction reflection coefficient (RP) from equation 3.62, assuming $|n| >> 1$, given the admittance (BETA) and the cosine of the angle of incidence (CTH).

(ii) Subroutine CMRC(CTH,STH,M,N,RC)

Computes the plane wave extended reaction reflection coefficient (RC) from equation 3.62, given the sine and cosine of the angle of incidence (STH,CTH), the complex ratio of the densities of the two media (M) and the refractive index (N).

(iii) Subroutine CWVN(F1,K1,OM,CV,K2,N)

Computes the propagation constant (K2) and the refractive index (N) of the fibrous porous material from the flow resistivity model of Delaney and Bazley. The input parameters are:

F1 flow resistivity divided by frequency;

K1 wave number in air;

OM frequency in radians;

CV velocity of sound in air.

(iv) Subroutine CIMP(F1,ZR)

Computes the characteristic impedance (ZR) of a fibrous porous material from the flow resistivity model of Delany and Bazley. The single input parameter is F1 the flow resistivity divided by frequency.

(v) Subroutine CADM(FR,B)

Computes the admittance of a fibrous porous material from the reciprocal of the characteristic impedance. The input parameter F1 is flow resistivity divided by frequency.

(vi) Subroutines PREAT and ATMOS

Compute the value of atmospheric absorption per metre given the frequency and the atmospheric temperature, pressure and relative humidity.

E.2 Impedance mesurement sub-programs

Three modules are described in this section. Module FFIMP calculates the real and imaginary parts of the surface impedance from free-field measurements of the standing wave ratio and distance to the first and second minima. Module PYETKB calculates the propagation constant and characteristic impedance of a material from impedance measurements on samples of single and double thickness. Module CCEPs calculates the complex cepstrum and its inverse as well as the power cepstrum and its inverse.

E.2.1 Module FFIMP

FFIMP calculates the normal surface impedance of a material from equations 5.17 and 5.18.

Parameter list

Name	Equivalent variable	Data type	Comment
THETA	θ	real	angle of incidence
SPLMIN		real	sound pressure level at first minimum
DIS1	d_1	real	distance from surface to first minimum
SPLMAX		real	sound pressure level at first maximum

Name	Equivalent variable	Data type	Comment
DIS3		real	distance from surface to second minimum
FREQ		real	frequency

E.2.2 Module PYETKB

PYETKB calculates propagation constant and characteristic impedance according to Pyett's method outlined in Section 8.2.9.

Parameter list

Name	Equivalent parameter	Data type	Comment
A,B,C,D		real	regression coefficients of the power law for the resistance and reactance of a single thickness sample
E,F,G,H		real	regression coefficients of the power law for the resistance and reactance of a double thickness sample
FREQ	f	real	frequency

E.2.3 Module CCEPS

Although very long this module has been included here for those readers not familiar with cepstral analysis. The main feature of the sub-program is the so called 'phase unwrapping' technique based upon an algorithm due to Tribolet [E.2].

```
C
CPROPAGATION MODEL DUE TO CHIEN AND SOROKA
C
      SUBROUTINE CHEN(ZR,P1,PTOT)
      COMMON/ALL/H,HS,HR,R,R1,R2,BETA,J,K1,STH,CTH,RP,PI
      COMPLEX P1,P2,P3,J,PTOT,BETA,ZR,RP
      COMPLEX PE,PE2,WIZ,F
      COMPLEX C1,C2,C4,CG,CK1,CR1,CR2,CPI
      REAL K1

      C1=(1.,0.)
      C2=(2.,0.)
      C4=(4.,0.)
      CK1=CMPLX(K1,0.)
      CG=CMPLX(CTH,0.)
      CR1=CMPLX(R1,0.)
      CR2=CMPLX(R2,0.)
      CPI=CMPLX(PI,0.)
      RP=(CG-BETA)/(CG+BETA)
      P1=CEXP(J*CK1*CR1)/(C4*CPI*CK1*CR1)
      P2=RP*CEXP(J*CK1*CR2)/(C4*CPI*CK1*CR2)
      PE=CSQRT(J*CK1*CR2/C2)*(CG+BETA)
      PE2=-C1*J*PE

      CALL W(PE2,WIZ)
      F=C1+J*CSQRT(CPI)*PE*WIZ
      P3=(C1-RP)*F*CEXP(J*CK1*CR2)/(C4*CPI*CK1*CR2)
      PTOT=P1+P2+P3
      RETURN
      END
```

```
C
C  CALCULATES VELOCITY POTENTIAL ABOVE SURFACE WITH
C  EXTENDED REACTION
C
      SUBROUTINE EXTEND(M,N,PHIT)
      REAL K1
      COMPLEX J,K2,BETA,M,N,RP
      COMMON/ALL/H,HS,HR,R,R1,R2,BETA,J,K1,K2,STH,CTH,RP,PI,AKOR1,AKOR2
      COMPLEX WO,WIZ
      COMPLEX REF,ROOT1,ROOT2,ROOT3,ROOT4,ROOT5,ROOT6,ROOT7
      COMPLEX BT1,BT2,BB1,BB2,B,W1,W2,F
      COMPLEX U,PH1,PH2,PHIT
      U=M*N
      ROOT1=CSQRT(N*N-STH*STH)
      REF=(CTH-M*ROOT1)/(CTH+M*ROOT1)
      ROOT2=CSQRT((1.0,0.0)-STH*STH/(N*N))
      ROOT3=CSQRT((1.0,0.0)-(1.0,0.0)/(N*N))
      ROOT4=CSQRT((1.0,0.0)-M*M)
      ROOT5=CSQRT((1.0,0.0)-U*U)
      ROOT6=ROOT2
      ROOT7=ROOT5
      BT1=(CTH+U*ROOT6)*ROOT3
      BB1=(CTH+U*ROOT3/ROOT4)*ROOT2
      BT2=CSQRT(ROOT4+U*ROOT3*CTH+STH*ROOT5)
      BB2=ROOT4**3*SQRT(2.0*STH)*CSQRT(ROOT7)
      B=BT1*BT2/(BB1*BB2)
      W2=J*K1*R2*(CTH+U*ROOT3/ROOT4)**2
     &    /(1.0+(U*CTH*ROOT3+STH*ROOT5)/ROOT4)
      W1=CSQRT(W2)
      WO=-J*W1
      CALL W(WO,WIZ)
      F=(1.0,0.0)+J*SQRT(PI)*W1*WIZ
      PH1=(1.0,0.0)
      PH2=(R1/R2)*CEXP(J*K1*(4.0,0.0)*HS*HR/(R1+R2))
      PHIT=PH1+PH2*(REF+B*((1.0,0.0)-REF)*F)
      RETURN
      END
```

```
C       TO CALCULATE THE FIELD AT THE GRID POINT M,N.

        LAMDA = 0.2*LAMDA
        PHI = (0.0,0.0)
C       CALCULATE THE FREE FIELD
        RD = SQRT((HS-HR)**2 + R*R)
        PHID = CEXP(J*K1*RD)/RD
        APHID = CABS(PHID)
        DO 2 IHOR = 1,IHORF
        HORIZ = (IHOR-1)*LAMDA + LAMDA*0.5
        SD = SQRT( 0.25*R*R + HORIZ*HORIZ )
                DO 3 IVER = 1,IVERF
                HRM = (IVER-1)*LAMDA
                R1 = SQRT ( (HS-HRM)*(HS-HRM) + SD*SD )
                R2 = SQRT( (HS+HRM)*(HS+HRM) + SD*SD )
                CTH = (HS+HRM)/R2
                STH = SD/R2


                CALL CHEN(BETA,P1,P2)
                CALL SOSTH(AMN)
        IF(IVER.EQ.1) AMN = 0.5*AMN
                HS2 = HRM
                R1 = SQRT( (HR-HS2)*(HR-HS2) + SD*SD )
                R2 = SQRT( (HR+HS2)*(HR+HS2) + SD*SD )
                CTH = (HS2+HR)/R2
                STH = (SD)/R2
                CALL CHEN(BETA2,P21,P2TOT)
                PHIMN = AMN*(P21+P2TOT)
                PHI = PHI+PHIMN
3       CONTINUE
2       CONTINUE
        PHI = PHI*LAMDA*LAMDA
        APHI = CABS(PHI/(2.0*PI*PHID))
50      CONTINUE
        END
C       TO CALCULATE SOURCE STRENGTH AMN.
        SUBROUTINE SOSTH(AMN)
        COMMON/ALL/H,HS,HR,R,R1,R2,J,K1,STH,CTH,RP,PI
        COMMON /BLK1/ P1,P2,LAMDA
        COMPLEX AMN,P1,P2,J
        REAL K1,LAMDA
        DZ = 0.5*R

        AMN = 2.0*(-J*K1 + 1.0/R1)*P1*DZ/R1
     1      + 2.0*(-J*K1 + 1.0/R2)*P2*DZ/R2
        RETURN
        END
```

```
      SUBROUTINE FUN(A,R,YUP,HS,VALUE)
      COMMON /C/ LAMDA,K,VAL1
      COMMON /LIMS/ XMAX,YMAX,XSTEP,YSTEP
      COMPLEX J
      REAL LAMDA,K
      INTEGER XMAX,YMAX
      XS=R/2.
      J=(0.,1.)
      DY = YSTEP*LAMDA
      XMAX=200
      DX=A/400.
      YMAX = AINT( (YUP/DY) + 0.5 )
      SUMB=0.
      SUMC=0.
      DO 1 IX = 1,XMAX
      DO 1 IY = 1,YMAX
         X = (IX-1)*DX
         Y = (IY-1)*DY
         TP=Y*Y+HS*HS
         RB=SQRT((XS-X)*(XS-X)+TP)
         RC=SQRT((XS+X)*(XS+X)+TP)
      ARB=K*RB
      ARC=K*RC
          SUMB = SUMB + CEXP(J*ARB)/RB
          SUMC=SUMC+CEXP(J*ARC)/RC
1     CONTINUE
      VALUE=2.*DX*DY*(SUMB+SUMC)
      RETURN
      END
```

```
      SUBROUTINE INTL(K,NOP,A,R,HS,VAL)
C     COMPUTES THE VALUE OF THE INTEGRAL USING QUADRATURES.

      DOUBLEPRECISION X(32),W(32),AB,WT
      COMPLEX SUM,Y,VAL,J
      REAL K
      COMMON /FLAGS/ IFJIN,IFYIN,IFJOUT,IFYOUT


      J = (0.0,1.0)
      N = NOP
      IF(N.EQ.64) THEN
              OPEN(UNIT=16,NAME='ABWT64.DAT',TYPE='OLD')
              DO 502 I = 1,32
              READ(16,200) AB,WT
              X(I) = AB
              W(I) = WT
502           CONTINUE
      CLOSE(UNIT=16)
      ELSEIF(N.EQ.32) THEN
              OPEN(UNIT=16,NAME='ABWT32.DAT',TYPE='OLD')
              DO 501 I=1,16
              READ(16,200) AB,WT
              X(I) = AB
              W(I) = WT
501           CONTINUE
      CLOSE(UNIT=16)
      ELSEIF(N.EQ.16) THEN
              OPEN(UNIT=16,NAME='ABWT16.DAT',TYPE='OLD')
              DO 500 I=1,8
              READ(16,200) AB,WT


200           FORMAT(1X,F23.21,2X,F23.21)
              X(I) = AB
              W(I) = WT
500           CONTINUE
      CLOSE(UNIT=16)
      ENDIF

      SUM = (0.0,0.0)
      N = N/2
      DO 1 I = 1,N
      XX = X(I)
      ARG1 = SQRT( (1.0+(A/R)*XX)**2.0 + (HS/R)**2.0 )
      ARG1 = ARG1*K*R*0.5
      ARG2 = SQRT( (1.0-(A/R)*XX)**2.0 + (HS/R)**2.0 )
      ARG2 = ARG2*K*R*0.5
      Y = W(I)*( HO1(ARG1) + HO1(ARG2) )
      SUM = SUM + Y
1     CONTINUE

      IF(IFJOUT.EQ.1) TYPE*,'ARGUMENT TOO LARGE FOR JO'
      IF(IFYOUT.EQ.1) TYPE*,'ARGUMENT TOO LARGE FOR YO'
      VAL = A*J*SUM*0.25
      RETURN

      END
```

```
C
C ROUTINE TO CALCULATE THE PLANE WAVE REFLECTION COEFFICIENT
C FOR A NORMAL IMPEDANCE BOUNDARY
C
      SUBROUTINE PWRC(BETA,CTH,RP)
      COMPLEX BETA,RP
      RP=(CTH-BETA)/(CTH+BETA)
      RETURN
      END
C
C ROUTINE TO CALCULATE COMPLEX REFLECTION COEFFICIENT
C FOR AN EXTENDED REACTION BOUNDARY
C
      SUBROUTINE CMRC(CTH,STH,M,N,RC)
      COMPLEX M,N,RC
      RC=CTH-M*CSQRT(N*N-STH*STH)
      RC=RC/(CTH+M*CSQRT(N*N-STH*STH))
      RETURN
      END

C
C ROUTINE TO CALCULATE COMPLEX WAVE-NUMBER AND REFRACTIVE
C INDEX FROM FLOW RESISTANCE
C
      SUBROUTINE CWVN(F1,K1,OM,CV,K2,N)
      COMPLEX K2,N
      REAL K1
      FR=F1*1000.
      RHO=1.21
      A=1.+0.0978*(FR/RHO)**0.7
      B=0.189*(FR/RHO)**0.595
      N=CMPLX(A,B)
      A=A*OM/CV
      B=B*OM/CV
      K2=CMPLX(A,B)
      RETURN
      END


C
C ROUTINE TO CALCULATE COMPLEX IMPEDANCE FROM FLOW RESISTANCE
C
      SUBROUTINE CIMP(F1,ZR)
      COMPLEX ZR
      FR=F1*1000.
      RHO=1.21
      R=1.+0.0571*(FR/RHO)**0.754
      X=0.087*(FR/RHO)**0.732
      ZR=CMPLX(R,X)
      RETURN
      END


C
C ROUTINE TO CALCULATE COMPLEX ADMITTANCE FROM FLOW RESISTANCE
C
      SUBROUTINE CADM(FR,B)
      COMPLEX B,Z
      CALL CIMP(FR,Z)
      B=1.0/Z
      RETURN
      END
```

```
C
C ROUTINE TO CALCULATE CONSTANTS FOR AIR ABSORPTION
C
      SUBROUTINE PREAT(AT,AP,ARH,FO,CO,HO,CV)
      TK=273.15+AT
      A=20.5318-2939./TK
      B=1./(TK**4.922)
      HO=(ARH/AP)*B*(10.**A)
      FO=30560.*AP*(HO**1.3)
      CO=4.2425E-6+8.8168E-8*AT+5.4834E-10*AT*AT
      CV=331.55*SQRT(1.+AT/273.15)
      RETURN
      END

C
C ROUTINE TO CALCULATE AIR ABSORPTION
C
      SUBROUTINE ATMOS(F,AP,AT,HO,CO,FO,AA)
      AMO=2.*CO*(F/(F/FO+FO/F))
      B1=1.7E-8/SQRT(1.+3.66E-3*AT)
      B2=HO*AP*F*F/(2.77E-5*F*F+HO*HO*AP*AP)
      AMN=B1*B2
      AMC=3.6E-11*(1.+1.E-3*AT)*F*F/AP
      AA=(AMO+AMN+AMC)*4.343
      RETURN
      END
C
C FUNCTION TO CALCULATE TANGENT OF COMPLEX ARGUMENT
C
      COMPLEX FUNCTION CTAN(Z)
      COMPLEX Z,J
      REAL X,Y
      J=(0.0,1.0)
      X=2.*REAL(Z)
      Y=2.*AIMAG(Z)
      CTAN=(SIN(X)+J*SINH(Y))/(COS(X)+COSH(Y))
      RETURN
      END
C
C FUNCTION TO CALCULATE HYPERBOLIC TANGENT OF COMPLEX ARGUMENT
C
      COMPLEX FUNCTION CTAH(Z)
      COMPLEX Z,J
      REAL X,Y
      J=(0.0,1.0)
      X=2.*REAL(Z)
      Y=2.*AIMAG(Z)
      CTAH=(SINH(X)+J*SIN(Y))/(COSH(X)+COS(Y))
      RETURN
      END
$
```

```
      C=13385.8
      PI=3.1415927
      CORF=7.75/7.5
      TYPE*,'INPUT H,SMPSIZ '
      ACCEPT*,H,SMPSIZ
100   TYPE*,'INPUT THETA,SPLMIN,DIS1,SPLMAX,DIS3,FREQ ? '
      ACCEPT*,DTHETA,SPLMIN,DIS1,SPLMAX,DIS3,F
      PEC=0.
      GOTO 50
      IF(F.EQ.5.)PEC=0.55
      IF(F.EQ.6.3)PEC=0.39
      IF(F.EQ.8.)PEC=0.31
      IF(F.EQ.10.)PEC=0.26
      IF(F.EQ.12.5)PEC=0.16
      IF(F.EQ.16.)PEC=0.11
      IF(F.EQ.20.)PEC=0.09
      IF(F.EQ.25.)PEC=0.06
      IF(F.EQ.27.)PEC=0.06
      IF(F.EQ.31.5)PEC=0.05
50    CONTINUE
      PEC=PEC*CORF
      DIS1=DIS1*CORF
      DIS3=DIS3*CORF
      SMPSIZ=SMPSIZ+PEC
      DIS1=DIS1-SMPSIZ
      DIS3=DIS3-SMPSIZ
      THETA=DTHETA*PI/180.
      WAVEL=2.*(DIS3-DIS1)
      FREQ=C/WAVEL
      DIS2=DIS1+WAVEL/(4.*COS(THETA))
      DL=SPLMIN-SPLMAX
      R=10.**(DL/20.)
      SWR=20.*ALOG10(1./R)
      Z1=-DIS1*COS(THETA)/H
      Z2=-DIS2*COS(THETA)/H
      Z3=-Z1
      Z4=-Z2
      ALPHA=(ALOG((EXP(Z1)+R*EXP(Z2))/(EXP(Z3)-R*EXP(Z4))))/2.
      PRC=2.*PI/WAVEL
      RP=PRC*H*(PRC*H*SINH(2.*ALPHA)+SIN(2.*PRC*DIS1*COS(THETA)))
     1/(2.*COS(THETA)*(1.+PRC*PRC*H*H))/((COSH(ALPHA)*COSH(ALPHA))
     2-(SIN(PRC*DIS1*COS(THETA)))**2)
      XIP=PRC*H*(SINH(ALPHA)-PRC*H*SIN(2.*PRC+DIS1*COS(THETA)))
     1/(2.*COS(THETA))/(1.+PRC*PRC*H*H)/((COSH(ALPHA))**2
     2-(SIN(PRC*DIS1*COS(THETA)))**2)
      FREQ=FREQ/1000.
      TYPE*,FREQ,THETA,SWR,RP,XIP
      GOTO 100
      END
```

```
C       PROGRAM TO CALCULATE BULK PROPAGATION CONSTANT KB FROM
C       SMOOTHED IMPEDANCE DATA FOR TWO LAYERS.

        COMPLEX CARCSH,CTAH
        COMPLEX Z,KB,V
        COMPLEX ZC,N

        OPEN (UNIT=1, NAME='PYETKB.DAT', TYPE='NEW')
        OPEN (UNIT=2, NAME='TOCTF.DAT ', TYPE='OLD')
        OPEN(UNIT=3,NAME='PYNZ.DAT',TYPE='NEW')

        TYPE*,'R=A+B*ALOG(FREQ), X=C+D*ALOG(FREQ)'
        TYPE*,' ENTER A,B,C,D FOR SINGLE LAYER'
        ACCEPT*,A,B,C,D
        TYPE*,' ENTER A,B,C,D FOR DOUBLE LAYER'
        ACCEPT*,E,F,G,H

        DO 50 I=1,21

        READ (2,*) FREQ
        FR=ALOG10(FREQ)-3.

        R1=A+B*ALOG(FREQ)
        X1=C+D*ALOG(FREQ)
        R2=E+F*ALOG(FREQ)
        X2=G+H*ALOG(FREQ)
        R1=EXP(R1)
        R2=EXP(R2)
        X1=EXP(X1)
        X2=EXP(X2)

        W=(R2*(R1-R2)+X2*(X1-X2))/((R1-R2)*(R1-R2)+(X1-X2)*(X1-X2))
        Y=(R2*(X1-X2)+X2*(R1-R2))/((R1-R2)*(R1-R2)+(X1-X2)*(X1-X2))
        Z=CMPLX(W,Y)


        V=CARCSH(Z)
        V=(0.0,1.0)*V
        KB=V/0.03
        KB=CMPLX(ABS(REAL(KB)),ABS(AIMAG(KB)))


        AKO=2.*3.1415927*FREQ/340.
        N=KB/AKO
        AN=CABS(N)
        ZC=CMPLX(R1,X1)
        N=(0.0,1.0)*KB*0.015
        N=-N
        ZC=ZC*CTAH(N)
 60     WRITE(1,100) FR,R1,X1,R2,X2,KB
100     FORMAT(1X,7F11.6)
        WRITE(3,*) FR,AN,ZC

 50     CONTINUE

        END
```

```
C
C SUBROUTINE TO COMPUTE THE COMPLEX CEPSTRUM
C OF A REAL DATA SEQUENCE X(N)
C
      SUBROUTINE CCEPS(NX,X,ISNX,ISFX,ISSUC,CX,AUX)
C
C DESCRIPTION OF ARGUMENTS
C
C       NX      = LENGTH OF SEQUENCE X(N)
C        X      = ARRAY CONTAINING SEQUENCE X(N)
C     ISNX      = SIGN OF REVERSAL OF X(N)
C     ISFX      = SHIFT OF X(N) FOR LIN PHASE COMPONENT
C    ISSUC      = LOGICAL INDICATOR OF PHASE UNWRAPPING
C       CX      = ARRAY CONTAINING COMPLEX CEPSTRUM
C      AUX      = AUXILIARY ARRAY FOR INTERNAL CALCS
C
      DIMENSION X(1),CX(1),AUX(1)
C
C DIMENSION REQUIREMENTS
C
C NX    .LE. NFFT
C DIM(X).LE. NFFT
C DIM(CX).GE.NFFT+2
C DIM(AUX).GE.NFFT+2
C
      COMMON/CEPS/PI,TWOPI,THLINC,THLCON,NFFT,NPTS,N,L,H,H1,DVTMN2
      COMMON/TMPS/TMP1,TMP2
      LOGICAL ISSUC
C
C DESCRIPTION OF VARIABLES
C
C THLINC = PHASE INCREMENT THRESHOLD
C THLCON = PHASE CONSISTENCY THRESHOLD
C NFFT   = LENGTH OF FFT (REAL DATA)
C NPTS   = HALF LENGTH OF FFT (COMPLEX PAIRS)
C DVTMN2 = TWICE THE MEAN OF THE PHASE DERIVATIVE
C
C SUBROUTINES CALLED
C
C FFT TO COMPUTE FOURIER TRANSFORMS
C
C FUNCTIONS CALLED
C
C AMODSQ = TO COMPUTE MOD SQUARED OF COMPLEX NUMBER
C PHADVT = TO COMPUTE PHASE DERIVATIVE OF SEPCTRAL VALUE
C PRVPHA = TO COMPUTE PRINCIPLE VALUE OF PHASE
C PHAUNW = TO COMPUTE UNWRAPPED PHASE OF SPECTRAL VALUE
C
C INITIALISATION
C
      NPTS=NFFT/2
      N=12
      L=2**N
      H=FLOAT(L)*FLOAT(NFFT)
      H1=PI/H
      ISSUC=.TRUE.
      ISNX=1
C
C TRANSFORM X(N) AND NX(N)
C
      DO 10 I=1,NX
      CX(I)=X(I)
      AUX(I)=FLOAT(I-1)*X(I)
```

```
10      CONTINUE
        INITL=NX+1
        IEND=NFFT+2
        DO 20 I=INITL,IEND
        CX(I)=0.
        AUX(I)=0.
20      CONTINUE

        AM=ALOG(FLOAT(NPTS))/ALOG(2.)
        M=INT(AM)
        CALL FFT(CX,NPTS+1,M,1)
        CALL FFT(AUX,NPTS+1,M,1)
C
C CHECK IF SIGN REVERSAL REQUIRED
C
        IF(CX(1).LT.0.0) ISNX=-1
C
C COMPUTE MAGNITUDE OF SPECTRUM STORE IN ODD AUX(I)
C COMPUTE PHASE DERIVATIVE STORE IN EVEN AUX(I)
C COMPUTE LINEAR PHASE ESTIMATE AND STORE DOUBLED IN DVTMN2
C
        I0=-1
        DVTMN2=0.
        IEND=NPTS+1
        DO 30 I=1,IEND
        I0=I0+2
        IE=I0+1
        AMAGSQ=AMODSQ(CX(I0),CX(IE))
        PDVT=PHADVT(CX(I0),CX(IE),AUX(I0),AUX(IE),AMAGSQ)
        AUX(I0)=AMAGSQ
        AUX(IE)=PDVT
        DVTMN2=DVTMN2+PDVT
30      CONTINUE
        DVTMN2=(2.*DVTMN2-AUX(2)-PDVT)/FLOAT(NPTS)
C
C COMPUT LOG E MAGNITUDE STORE IN ODD CX(I)
C COMPUTE UNWRAPPED PHASE STORE IN EVEN CX(I)
C
        PPDVT=AUX(2)
        PPHASE=0.
        PPV=PPVPHA(CX(1),CX(2),ISNX)
        CX(1)=0.5*ALOG(AUX(1))
        CX(2)=0.
        TMP1=CX(1)
        TMP2=CX(2)
        I0=1

        DO 50 I=2,IEND
        I0=I0+2
        IE=I0+1
        PDVT=AUX(IE)
        PPV=PPVPHA(CX(I0),CX(IE),ISNX)
        PHASE=PHAUNW(X,NX,ISNX,I,PPHASE,PPDVT,PPV,PDVT,ISSUC)
C
C IF PHASE ESTIMATION SUCCESSFUL CONTINUE, ELSE RETURN
C
        IF(ISSUC)GOTO 40
        ISSUC=.FALSE.
        RETURN
40      PPDVT=PDVT
        PPHASE=PHASE
        CX(I0)=0.5*ALOG(AUX(I0))
        CX(IE)=PHASE
50      CONTINUE
```

```
C
C REMOVE LINEAR PHASE COMPONENT
C
        ISFX=(ABS(PHASE/PI)+0.1)
        IF(PHASE.LT.0.0)ISFX=-ISFX
        H=PHASE/FLOAT(NPTS)
        IE=0
        DO 60 I=1,IEND
        IE=IE+2
        CX(IE)=CX(IE)-H*FLOAT(I-1)
60      CONTINUE
C SAVE POWER SPECTRUM IN AUX
C
        DO 70 I=1,NFFT+2
        AUX(I)=CX(I)
70      CONTINUE
C
C REMOVE MEAN VALUE OF LOG SPECTRUM FROM REAL VALUES
C
        IO=-1
        IEND=NPTS+1
        AM=0.
        DO 80 I=1,IEND
        IO=IO+2
        AM=AM+CX(IO)
80      CONTINUE
        AM=AM/FLOAT(IEND)
        IO=-1
        DO 90 I=1,IEND
        IO=IO+2
        CX(IO)=CX(IO)-AM
90      CONTINUE
C
C COMPUTE COMPLEX CEPSTRUM
C
        CALL FFT(CX,NPTS+1,M,-1)
        RETURN
        END
C
C SUBROUTINE TO COMPUTE SPECTRAL VALUE AT FREQUENCY
C FREQ FOR SEQUENCES X(N) AND N*X(N)
C
        SUBROUTINE SPCVAL(NX,X,FREQ,XR,XI,YR,YI)
        DIMENSION X(1)
        DOUBLE PRECISION U0,U1,U2,W0,W1,W2,A,B,C,D,A1,A2,SA0,CA0
C
C DESCRIPTION OF ARGUMENTS
C
C NX    = LENGTH OF SEQUENCE X(N)
C X(N)  = ARRAY CONTAINING X(N)
C FREQ  = FREQUENCY
C XR    = REAL PART OF SPECTRAL VALUE OF X(N)
C XI    = IMAGINARY PART OF SPECTRAL VALUE OF X(N)
C YR    = REAL PART OF SPEC VAL OF N*X(N)
C YI    = IMAGINARY PART OF SPEC VAL OF N*X(N)
C
C METHOD:- MODIFIED GOERTZEL BY BONZANIGO
C          ( IEEE TRANS ASSP VOL 26 NO 1 FEB 1978)
C
C INITIALISATION
C
        CA0=DBLE(COS(FREQ))
        SA0=DBLE(SIN(FREQ))
        A1=2.D+0*CA0
```

```
      U1=0.0+0
      U2=U1
      W1=U1
      W2=U1
C
C MAIN LOOP (GOERTZEL ALOGORITHM)
C
      DO 10 J=1,NX
      XJ=DBLE(X(J))
      U0=XJ+A1*U1-U2
      W0=DBLE(FLOAT(J-1))*XJ+A1*W1-W2
      U2=U1
      U1=U0
      W2=W1
      W1=W0
10    CONTINUE
C
C BONZANIGO'S PHASE CORRECTION
C
      A=U1-U2*CA0
      B=U2*SA0
      C=W1-W2*CA0
      D=W2*SA0
      A2=DBLE(FREQ*FLOAT(NX-1))
      U1=DCOS(A2)
      U2=-DSIN(A2)
      XR=SNGL(U1*A-U2*B)
      XI=SNGL(U2*A+U1*B)
      YR=SNGL(U1*C-U2*D)
      YI=SNGL(U2*C+U1*D)
      RETURN
      END
C
C FUNCTION PHAUNW
C PHASE UNWRAPPING BASED ON TRIBOLET'S ADAPTIVE INTEGRATION SCHEME
C THE UNWRAPPED PHASE ESTIMATE IS RETURNED IN PHAUNW
C
      FUNCTION PHAUNW(X,NX,ISNX,I,PPHASE,PPDVT,PPV,PDVT,ISCONS)
C
C DESCRIPTION OF THE ARGUMENTS
C
C NX    = NUMBER OF POINTS IN SEQUENCE X(N)
C X     = ARRAY CONTAINING X(N)
C ISNX  = SIGN OF REVERSAL OF X(N)
C I     =INDEX OF PHASE ESTIMATE ON FFT GRID
C PPHASE= PHASE ESTIMATE AT INDEX I-1
C PPDVT = PHASE DERIVATIVE AT INDEX I-1
C PPV   = PHASE PRINCIPLE VALUE AT INDEX I
C PDVT  = PHASE DERIVATIVE AT INDEX I
C ISCONS= SET FALSE IF PHASE ESTIMATION UNSUCCESSFUL
C
C SUBROUTINES CALLED
C
C SPCVAL= TO COMPUTE SPECTRAL VALUE
C PHCHCK= TO CHECK PHASE CONSISTENCY
C
C FUNCTIONS CALLED
C
C PPVPHA= TO COMPUTE PRINCIPLE VALUE OF PHASE
C PHADVT= TO COMPUTE PHASE DERIVATIVE
C AMODSQ= TO COMPUTE MOD SQUARED OF COMPLEX NUMBER
C
      DIMENSION SDVT(17),SPPV(17),X(1)
      INTEGER SINDEX(17),PINDEX,SP
```

```
      LOGICAL ISCONS,FIRST
      COMMON/CEPS/PI,TWOPI,THRINC,THRCON,NFFT,NPTS,N,L,H,H1,DVTMN2
C
C DESCRIPTION OF ARRAYS AND VARIABLES
C
C SINDEX= INDEX STACK
C SDVT  = PHASE DERIVATIVE STACK
C SPPV  = PHASE PRINCIPLE VALUE STACK
C SP    = STACK POINTER
C
C INTIALISATION
C
      FIRST=.TRUE.
      PINDEX=1
      SP=1
      SPPV(SP)=PPV
      SDVT(SP)=PDVT
      SINDEX(SP)=L+1
C
C ENTER MAJOR LOOP
C
      GOTO 40
C
C UPDATE PREVIOUS ESTIMATE
C
10    PINDEX=SINDEX(SP)
      PPHASE=PHASE
      PPDVT=SDVT(SP)
      SP=SP-1
      GOTO 40
C
C IF SOFTWARE STACK DOES NOT ALLOW FURTHER STEP REDUCTION, RETURN
C
20    IF(SINDEX(SP)-PINDEX.GT.1)GOTO 30
      ISCONS=.FALSE.
      PHAUNW=0.
      RETURN
C
C DEFINE INTERMEDIATE FREQUENCY
C W=(TWOPI/NFFT)*(I-2+(K-1)/L)
C
30    K=(SINDEX(SP)+PINDEX)/2
C
C CALC INTERMEDIATE FREQUENCY
C
      FREQ=TWOPI*(FLOAT(I-2)*FLOAT(L)+FLOAT(K-1))/H
      CALL SPCVAL(NX,X,FREQ,XR,XI,YR,YI)
C
C COMPUTE PHASE DERIVATIVE AND PRINCIPLE VALUE
C
      SP=SP+1
      SINDEX(SP)=K
      SPPV(SP)=PPVPHA(XR,XI,ISNX)
      XMAG=AMODSQ(XR,XI)
      SDVT(SP)=PHADVT(XR,XI,YR,YI,XMAG)
C
C EVALUATE THE PHASE INCREMENT ACROSS SPECTRAL INTERVAL
C
40    DELTA=H1*FLOAT(SINDEX(SP)-PINDEX)
      PHAINC=DELTA*(PPDVT+SDVT(SP))
C
C IF PHASE INCREMENT, REDUCED BY EXPECTED LIEAR PHASE INCREMENT
C IS GREATER THAN SPECIFIED THRESHOLD, ADAPT STEP SIZE
C
```

```
      IF(ABS(PHAINC-DELTA*DVTMN2).GT.THLINC)GOTO 20
C
C FORM PHASE ESTIMATE, CHECK CONSISTENCY
C
      PHASE=PPHASE+PHAINC
      CALL PHCHCK(PHASE,SPPV(SP),ISCONS)
      IF(.NOT.ISCONS)GOTO 20
C
C IF RESULTING PHASE INCREMENT IS GREATER THAN PI, ADAPT STEP SIZE
C FOR MORE CONFIDENT ESTIMATE, OTHERWISE UPDATE PREVIOUS ESTIMATE
C IF STACK IS NOT EMPTY
C
      IF(ABS(PHASE-PPHASE).GT.PI)GOTO 20
C
C WHEN STACK IS EMPTY, THE UNWRAPPED PHASE AT
C W= TWOPI*(I-1)/NFFT IS HELD IN PHASE
C
      IF(SP.NE.1)GOTO 10
      PHAUNW=PHASE
      RETURN
      END
C
C
C FUNCTION PPVPHA COMPUTE PRINCIPLE VALUE OF PHASE
C
      FUNCTION PPVPHA(XR,XI,ISNX)
C
C DESCRIPTION OF ARGUMENTS
C
C XR    = REAL PART OF SPECTRAL VALUE
C XI    = IMAGINARY PART OF SPECTRAL VALUE
C ISNX  = SIGN OF SPECTRAL VALUE AT ZERO FREQUENCY
C
      IF(ISNX.EQ.1) PPVPHA=ATAN2(XI,XR)
      IF(ISNX.EQ.-1) PPVPHA=ATAN2(-XI,-XR)
      RETURN
      END
C
C
C FUNCTION PHADVT COMPUTE PHASE DERIVATIVE OF X(N)
C
      FUNCTION PHADVT(XR,XI,YR,YI,XMAG)
C
C DESCRIPTION OF ARGUMENTS
C
C XR    = REAL PART OF SPECTRAL VALUE X(N)
C XI    = IMAGINARY PART OF SPECTRAL VALUE X(N)
C YR    = REAL PART OF SPECTRAL VALUE N*X(N)
C YI    = IMAGINARY PART OF SPECTRAL VALUE N*X(N)
C XMAG  = MAGNITUDE SQUARED OF SPECTRAL VALUE X(N)
C
      PHADVT=-SNGL((DBLE(XR)*DBLE(YR)+DBLE(XI)*DBLE(YI))/DBLE(XMAG))
      RETURN
      END
C
C
C FUNCTION AMODSQ COMPUTE MODULOUS SQUARED OF COMPLEX NUMBER
C
      FUNCTION AMODSQ(ZR,ZI)
C
C DESCRIPTION OF ARGUMENTS
C
C ZR    = REAL PART OF COMPLEX NUMBER
C ZI    = IMAGINARY PART OF COMPLEX NUMBER
```

```
C
      AMODSQ=SNGL(DBLE(ZR)*DBLE(ZR)+DBLE(ZI)*DBLE(ZI))
      RETURN
      END
C
C
C SUBROUTINE PHCHCK CHECK CONSISTENCY OF PHASE ESTIMATE
C
      SUBROUTINE PHCHCK(PH,PV,ISCONS)
C
C DESCRIPTION OF ARGUMENTS
C
C PH     = PHASE ESTIMATE
C PV     = PRINCIPLE VALUE OF PHASE AT FREQUENCY OF ESTIMATE
C ISCONS= FALSE IF ESTIMATE INCONSISTENT
C
      COMMON/CEPS/PI,TWOPI,THLINC,THLCON,NFFT,NPTS,N,L,H,H1,DVTMN2
      LOGICAL ISCONS
C
C FIND THE TWO ADMISSABLE PHASE VALUES CLOSEST TO PH
C
      A0=(PH-PV)/TWOPI
      A1=FLOAT(IFIX(A0))*TWOPI+PV
      A2=A1+SIGN(TWOPI,A0)
      A3=ABS(A1-PH)
      A4=ABS(A2-PH)
C
C CHECK CONSISTENCY
C
      ISCONS=.FALSE.
      IF(A3.GT.THLCON.AND.A4.GT.THLCON)RETURN
      ISCONS=.TRUE.
C
C FIND CLOSEST UNWRAPPED PHASE ESTIMATE
C
      PH=A1
      IF(A3.GT.A4)PH=A2
      RETURN
      END
C
C*********************************************************************
C
C
C SUBROUTINE TO COMPUTE INVERSE CEPSTRUM
C OF THE SEQUENCE CX
      SUBROUTINE ICEPS(NX,X,ISNX,ISFX,ISSUC,CX,AUX)
C
C DESCRIPTION OF ARGUMENTS
C
C NX     = LENGTH OF ORIGINAL TIME SEQUENCE X(N)
C X      = ARRAY CONTAINING TIME SEQUENCE
C ISNX   = SIGN OF INITIAL PHASE OF X
C ISFX   = SHIFT OF X(N) FOR LINEAR PHASE COMPONENT
C ISSUC  = LOGICAL INDICATOR OF PHASE UNWRAPPING
C CX     = ARRAY CONTAINING COMPLEX CEPSTRUM
C AUX    = AUXCILLARY ARRAY FOR CALCULATIONS
C
      DIMENSION X(1),CX(1),AUX(1)
C
C DIMENSION REQUIREMENTS
C
C NX .LE. NFFT
C DIM(X) .LE. NFFT
C DIM(CX) .LE. NFFT+2
```

```
      DIMENSION X(1),CX(1),AUX(1)
C
C INITIALISE VARIABLES
C
      NPTS=NFFT/2
      AM=ALOG(FLOAT(NPTS))/ALOG(2.)
      M=INT(AM)
C
C COPY REAL SEQUENCE INTO CX
C
      DO 10 I=1,NX
      CX(I)=X(I)
10    CONTINUE
      IEND=NX+1
      DO 20 I=IEND,NFFT+2
      CX(I)=0.
20    CONTINUE
C
C PERFORM FIRST TRANSFORM
C
      CALL FFT(CX,NPTS+1,M,1)
C
C CONVERT TO POWER SPECTRUM AND SET PHASE TO 0.0
C
      AN=0.
      IO=-1
      DO 30 I=1,NPTS+1
      IO=IO+2
      IE=IO+1
      RMAG=CX(IO)**2+CX(IE)**2
      CX(IO)=0.5*ALOG(RMAG)
      CX(IE)=0.
      AN=AN+CX(IO)
30    CONTINUE
C
C REMOVE MEAN OF LOG SPECTRUM FROM CX
C
      AN=AN/FLOAT(NPTS+1)
      IO=-1
      DO 31 I=1,NPTS+1
      IO=IO+2
      CX(IO)=CX(IO)-AN
31    CONTINUE
C
C PERFORM INVERSE TRANSFORM
C
      CALL FFT(CX,NPTS+1,M,-1)

      RETURN
      END
C
C*************************************************************
C
C SUBROUTINE IRCPS
C COMPUTES THE INVERSE POWER CEPSTRUM OF A REAL DATA SEQUENCE
C
      SUBROUTINE IRCPS(NX,X,CX,AUX)
C
C NX    = NUMBER OF DATA POINTS IN REAL SEQUENCE
C X     = ARRAY THAT WILL RETURN THE REAL SEQUENCE
C CX    = ARRAY CONTAINING COMPLEX CEPSTRUM
C AUX   = AUXILARY ARRAY
C
      COMMON/CEPS/PI,TWOPI,THLINC,THLCON,NFFT,NPTS,N,L,R,RI,DVTHR2
```

```
C DIM(AUX) .LE.NFFT+2
C
      COMMON/CEPS/PI,TWOPI,THLINC,THLCON,NFFT,NPTS,N,L,H,H1,DVTMN2
      COMMON/TMPS/TMP1,TMP2
      LOGICAL ISSUC
C
C TRANSFER CX INTO AUX ARRAY
C
      IEND=NFFT+2
      DO 10 I=1,IEND
      AUX(I)=CX(I)
10    CONTINUE
C
C INITIALISATION
C
      NPTS=NFFT/2
      AM=ALOG(FLOAT(NPTS))/ALOG(2.)
      M=INT(AM)
C
C COMPUTE FORWARD TRANSFORM
C
      CALL FFT(AUX,NPTS+1,M,1)
C
C ADD BACK LINEAR PHASE COMPONENT
C
      IE=0
      DO 15 I=1,NPTS+1
      IE=IE+2
      AUX(IE)=AUX(IE)+H*FLOAT(I-1)
15    CONTINUE
C
C EXPONENTIATE RESULT
C
      IO=-1
      DO 20 I=1,NPTS+1
      IO=IO+2
      IE=IO+1
      RMAG=EXP(AUX(IO))
      AUX(IO)=RMAG*COS(AUX(IE))
      AUX(IE)=RMAG*SIN(AUX(IE))
20    CONTINUE
      AUX(1)=EXP(TMP1)
      AUX(2)=TMP2
C
C INVERSE TRANSFORM
C
      CALL FFT(AUX,NPTS+1,M,-1)
      RETURN
      END
C
C**********************************************************************
C
C
C SUBROUTINE RCEPS
C ROUTINE TO CALCULATE THE POWER CEPSTRUM OF A REAL SEQUENCE X(N)
C
      SUBROUTINE RCEPS(NX,X,CX,AUX)
C
C NX    = LENGTH OF REAL SEQUENCE
C X     = REAL DATA SEQUENCE
C CX    = ARRAY CONTAINING CEPSTRUM
C AUX   = AUXILARY ARRAY
C
      COMMON/CEPS/PI,TWOPI,THLINC,THLCON,NFFT,NPTS,N,L,H,H1,DVTMN2
```

References Appendix E

E.1 Abramowitz, E and Stegun, I. A.: Handbook of Mathematical Functions

Dover 1965

E.2 Tribolet, J.M.: Seismic Applications of Homomorphic Signal Processing

Prentice-Hall 1978

```
      IP=I+LE1
      A=X(IP)*U
      X(IP)=X(I)-A
10    X(I)=X(I)+A
20    U=U*W
C
C CHECK IF FORWARD OR INVERSE TRANSFORM
C IF INVERSE SCALE DATA
C
      IF(ILN.EQ.-1)GOTO 40

      X(N+1)=X(1)
25    PIBN=PI/N
      U=CMPLX(0.0,-FLOAT(ILN))
      A1=COS(PIBN)
      B1=-SIN(PIBN)*ILN
      W=CMPLX(A1,B1)
      K=N2+1
      DO 30 I=1,K
      A=X(I)+CONJG(X(N-I+2))
      B=(X(I)-CONJG(X(N-I+2)))*U
      U=U*W
      X(I)=A+B
30    X(N-I+2)=CONJG(A-B)
      IF(ILN.EQ.-1)GOTO 4
      GOTO 50
C
C SCALE DATA
C
40    DO 45 I=1,NMX
      X(I)=X(I)/FLOAT(N*4)
45    CONTINUE
C
C EXIT IF FORWARD TRANSFORM
C
50    RETURN
      END
$
```

```
      COMMON/TMPS/TMP1,TMP2
      DIMENSION X(1),CX(1),AUX(1)
C
C INITIALISE VARIABLES
C
      NPTS=NFFT/2
      AM=ALOG(FLOAT(NPTS))/ALOG(2.)
      M=INT(AM)
C
C PERFORM FORWARD TRANSFORM
C
      CALL FFT(CX,NPTS+1,M,1)
C
C EXPONENTIATE
C
      I0=-1
      DO 10 I=1,NPTS+1
      I0=I0+2
      IF=I0+1
      RMAG=EXP(CX(I0))
      CX(I0)=RMAG*COS(CX(IE))
      CX(IE)=RMAG*SIN(CX(IE))
10    CONTINUE
C
C INVERSE TRANSFORM
C
      CALL FFT(CX,NPTS+1,M,-1)
      RETURN
      END
      SUBROUTINE FFT(X,NMX,M,ILN)
      COMPLEX X(NMX),U,W,A,B
      N=NMX
      N=N-1
      N2=N/2
      PI=3.1415926
      IF(ILN.EQ.-1)GOTO 25

C FORWARD TRANSFORM SO BIT REVERSE DATA

4     NM1=N-1
      J=1
      DO 7 I=1,NM1
      IF(I.GE.J)GOTO 5
      A=X(I)
      X(I)=X(J)
      X(J)=A
5     K=N2
6     IF(K.GE.J)GOTO 7
      J=J-K
      K=K/2
      GOTO 6
7     J=J+K

C BIT REVERSAL FINISHED

      DO 20 K=1,M
      LE=2**K
      LE1=LE/2
      U=(1.0,0.0)
      A1=COS(PI/LE1)
      B1=-SIN(PI/LE1)*ILN
      W=CMPLX(A1,B1)
      DO 20 J=1,LE1
      DO 10 I=J,N,LE
```